Secondary Organic Aerosol Formation from Volatile Chemical Products: Understanding Aerosol Yields and Dynamics

Thesis by
Sophia Mohini Charan

In Partial Fulfillment of the Requirements for the
Degree of
Doctor of Philosophy

Caltech

CALIFORNIA INSTITUTE OF TECHNOLOGY
Pasadena, California

2021
Defended May 21, 2021

ACKNOWLEDGMENTS

There are innumerable people to thank for making this thesis possible, and merely writing an acknowledgement section cannot do justice to all the gratitude that these people deserve.

First of all, I want to thank my advisor John Seinfeld and the other members of my thesis committee for their support throughout my tenure as a graduate student. John, thank you for always making the time to meet, for the freedom you gave me, and for patiently going over manuscripts again and again. It was an honor to work with you. Rick Flagan, it is impossible to leave a conversation with you without learning some interesting tidbit and appreciating an instrument a little more; you have been an immense help to my research and understanding. To Paul Wennberg, thank you for welcoming me into your group meetings and for the numerous insights into chemical systems delivered while walking to lunch. John Brady, in your classes, you always illuminated interesting phenomena in a way that made it thoroughly enjoyable to spend hours and hours on problem sets.

Thank you to Nathan Dalleska, who patiently answered all my chromatography questions; to John Crounse, whose insight into the chemistry and physics of the instruments in lab is unparalleled; to Lu Xu, who really understands aerosol formation; and to Josh Laughner, who taught me how to responsibly organize my code.

The former members of the Seinfeld Lab all helped, in some way or the other, to orient me to the lab. Becky Schwantes, thank you for teaching me about the chamber and for answering numerous emails when I was starting out. Your attention to detail is something to which I have always aspired. Kelvin Bates, I always enjoyed seeing you at conferences and in Monterey. To Ran Zhao, thank you for long and wide-ranging conversations about science and your career. To Stephanie Kong, thank you for teaching me about the SMPS and, really, about chemical engineering at Caltech. Brigitte Rooney, I appreciated your insights and loved chatting with you.

To my current colleagues in the Seinfeld Lab, who should better be called friends, you have all helped me immeasurably and made graduate school quite a bit of fun. Thank you for the feedback on ideas, presentations, and everything else. Yuanlong Huang, I have loved every minute spent sitting in the office or standing next to a broken instrument brainstorming with and learning from you. Chris Kenseth, thank you for answering phone calls about the AMS in the middle of the night.

Elyse Pennington, thank you for always being willing to breeze into the office and gossip with me. Reina Buenconsejo, thank you for incalculable help and support on the VCP project and for conversations about the morning's radio programs. Ben Schulze, I always enjoyed chatting over coffee and am only sad not to have seen your puppy more. Ryan Ward, thank you for unabashedly displaying a Zoom background that captured the feeling that, indeed, the world was on fire.

To Paul's lab—or, more accurately, the members and honorary members of Paul's lab that I have not already thanked—it was great fun to bounce ideas off of you and to drink coffee in the upstairs office. Harrison Parker, thanks for untangling the intricacies of Caltech with me in our first few years and for always being down for a board game. Hannah Allen, thank you for leading SEPAC and eating dumplings and driving to see the eclipse with me. Sara Murphy, thanks for always being willing to talk about linguistics or do a crossword. Lily Dove, thanks for getting us all to stick hand turkeys on the door. Ariana Tribby, I loved running into you walking Benji on campus. Krystal Vasquez, thank you for advocating for all of us.

Without Heidi Klumpe, I would not appreciate many corners of campus. I loved our meetings to talk about the podcast or really anything else, and I am so honored to have worked on *Not My Thesis* (when not working on this thesis) with you. I also want to thank everyone at *Caltech Letters* who edited or assisted in the podcast's production.

To Sophie Miller and Alex Welch, thank you for making my first year at Caltech a great one and for many adventures since. Food is also chemistry, and I want to thank Dan Jacobson and Camilla Kjeldbjerg, for sharing many delicious meals. Thank you, as well, to Anna Ho for long conversations: characteristic, perhaps, of the ones found in Proust. And to Lee Rosenthal, for many great dinners and for making graduate school a *Good Place*.

Throughout my Ph.D., I have had the great pleasure of collaborating with and learning from many people. While I was in Monterey, Armin Sorooshian, Andrew Metcalf, and Haf Jonsson taught me about the intricacies of field campaigns. At the RAND Corporation, I had the pleasure of working with Rob Lempert, Ben Preston, Liisa Ecola, and Laura Fraade-Blanar: I am immensely grateful to all of them for teaching me about the policy implications of my (and my field's) research. Through the VCP project, I worked with David Cocker, Qi Li, Weihan Peng, and Chen Le: thank you for the opportunity to investigate the dynamics in other environmental chambers.

ABSTRACT

Particulate matter impacts public health and climate. A major component of small particulate matter, called secondary organic aerosol (SOA), is formed from the condensation of the oxidation products of organic compounds emitted into the atmosphere in the gas phase. Recent analysis suggests that volatile chemical products are responsible for a large fraction of the particulate matter formed from petroleum sources: perhaps more than motor vehicles. This is especially the case in urban areas, which have significant air pollution burdens.

Understanding exactly which precursors are responsible for this large SOA formation and under which conditions is difficult: for each compound, different chemical pathways dominate and even similar molecules can form vastly varied amounts of aerosol. Even if one could study every compound, extrapolating data to the atmosphere is non-trivial. SOA formation is principally understood through laboratory chamber studies, but these studies require a rigorous, quantitative grasp of chamber phenomena to meaningfully interpret the results.

In this dissertation, computational simulations of environmental chambers illuminate the physico-chemical processes that occur within a chamber and the manner in which these processes interact, in order to help extrapolate data to real-world conditions. In particular, the contribution of particle charge to the rate of particle-wall deposition within environmental chambers is investigated.

With this understanding, the amount of aerosol formed per precursor emitted, called the secondary organic aerosol yield, is investigated for benzyl alcohol and decamethylcylopentasiloxane (D5). At atmospherically relevant concentrations, benzyl alcohol and D5 have disparate SOA mass yields: as much as 100% for benzyl alcohol and ~1% for D5. Both of these findings differ from what was previously modeled and measured, indicating the importance of performing experiments on the compounds of interest and evaluating the oxidation products under atmospherically relevant conditions.

PUBLISHED CONTENT AND CONTRIBUTIONS

Charan, Sophia M., Yuanlong Huang, Reina S. Buenconsejo, Qi Li, David R. Cocker III, and John H. Seinfeld (2021). "Secondary organic aerosol formation from the oxidation of decamethylcyclopentasiloxane at atmospherically relevant OH concentrations". [Submitted]. DOI: 10.5194/acp-2021-353.
SMC designed and conducted the experiments, performed the data analysis, and wrote the manuscript.

Charan, Sophia M., Reina S. Buenconsejo, and John H. Seinfeld (2020). "Secondary organic aerosol yields from the oxidation of benzyl alcohol." In: *Atmospheric Chemistry and Physics* 20.21, pp. 13167–13190. DOI: 10.5194/acp-20-13167-2020.
SMC designed the experiments, conducted all experiments except for U1 and U3–5, performed the modeling, did the data analysis (except of the filters with UPLC-MS), and wrote the manuscript.

Charan, Sophia M., Yuanlong Huang, and John H. Seinfeld (2019). "Computational simulation of secondary organic aerosol formation in laboratory chambers." In: *Chemical Reviews*. DOI: 10.1021/acs.chemrev.9b00358.
SMC wrote the model used for this project, performed all the modeling and calculations, and led the writing of the manuscript.

Charan, Sophia M., Weimeng Kong, Richard C. Flagan, and John H. Seinfeld (2018). "Effect of particle charge on aerosol dynamics in Teflon environmental chambers." In: *Aerosol Science and Technology* 52.8, pp. 854–871. DOI: 10.1080/02786826.2018.1474167.
SMC designed and performed the experiments, did the data analysis, and wrote the manuscript.

Schulze, Benjamin C., Sophia M. Charan, Christopher M. Kenseth, Weimeng Kong, Kelvin H. Bates, Walt Williams, Andrew R. Metcalf, Haflidi H. Jonsson, Roy K. Woods, Armin Sorooshian, Richard C. Flagan, and John H. Seinfeld (2020). "Characterization of aerosol hygroscopicity over the northeast Pacific Ocean: impacts on prediction of CCN and stratocumulus cloud droplet number concentrations." In: *Earth and Space Science* 7.7, pp. 1–26. DOI: 10.1029/2020EA001098.
SMC assisted with data calibrations and collection, participated in discussions about the data analysis, and edited the manuscript.

Schwantes, Rebecca H., Sophia M. Charan, Kelvin H. Bates, Yuanlong Huang, Tran B. Nguyen, Huajun Mai, Weimeng Kong, Richard C. Flagan, and John H. Seinfeld (2019). "Low-volatility compounds contribute significantly to isoprene secondary organic aerosol (SOA) under high-NO$_x$ conditions." In: *Atmospheric Chemistry and Physics* 19.11, pp. 7255–7278. DOI: 10.5194/acp-19-7255-2019.
SMC performed four of the chamber experiments, did the wall-loss analysis, and participated in the writing of the manuscript.

Sunol, Alp M., Sophia M. Charan, and John H. Seinfeld (2018). "Computational simulation of the dynamics of secondary organic aerosol formation in an environmental chamber." In: *Aerosol Science and Technology* 52.4, pp. 470–482. DOI: 10.1080/02786826.2018.1427209.

SMC adapted AMS's model so that it was fixed bin and included coagulation-corrected particle-wall deposition, prepared all figures, performed all simulations, wrote the section on particle-wall deposition, and extensively edited and added to the rest of the manuscript.

Huang, Yuanlong, Ran Zhao, Sophia M. Charan, Christopher M Kenseth, Xuan Zhang, and John H. Seinfeld (2018). "Unified theory of vapor–wall mass transport in Teflon-Walled environmental chambers." In: *Environmental Science & Technology* 52.4, pp. 2134–2142. DOI: 10.1021/acs.est.7b05575.

SMC participated in discussions about the data analysis and edited the manuscript.

TABLE OF CONTENTS

LIST OF ILLUSTRATIONS

LIST OF TABLES

NOMENCLATURE

Aerosol. Small liquid or solid particles suspended in air.

AMS. Aerosol mass spectrometer; used to measure the chemical composition of the particle phase.

CCN. Cloud condensation nuclei; particles onto which water condenses to form cloud droplets.

CIMS. Chemical ionization mass spectrometer; an instrument that measures compounds in the gas phase (the one used here has a CF_3O^- reagent ion).

CPC. Condensation particle counter; the component of an SMPS that counts the particles that emerge from the DMA.

DMA. Differential mobility analyzer; the component of an SMPS that separates the charged particles in the electric field.

GC-FID. Gas chromatograph with a flame ionization detector; measures the gas-phase concentration of different compounds.

NO_x. The nitrogen oxide chemical family, including both nitric oxide (NO) and nitrogen dioxide (NO_2).

OH. The hydroxyl radical; the major daytime oxidant in the troposphere.

$PM_{2.5}$. The mass concentration (often in $\mu g \ m^{-3}$) of particulate matter with an aerodynamic diameter less than 2.5 μm.

RH. Relative humidity; the concentration of water vapor in air at a given temperature compared to the maximum possible concentration of water vapor at that temperature, expressed in a percentage.

SMPS. Scanning mobility particle sizer; an instrument that measures the aerodynamic diameter of particles by applying a known charge distribution to aerosol, passing that aerosol through a varying electric field, and measuring the number of particles that emerge at each electric field strength.

SOA. Secondary organic aerosol; particulate matter formed when organic compounds emitted in the gas-phase react and condense into the particle phase.

VCPs. Volatile chemical products; compounds often used as organic solvents that originate from petrochemical sources and are used in consumer products such as paints and coatings, personal care products, cleaning products, pesticides, printing, and asphalt.

VOCs. Volatile organic compounds; highly evaporative molecules with carbon atoms in them.

Y. Secondary organic aerosol yield; the ratio of the mass of aerosol formed to the mass of reacted precursor.

Chapter 1

INTRODUCTION

1.1 Background and Motivation

Particulate matter is a local and a global problem. Particulate matter smaller than 2.5 μm ($PM_{2.5}$) caused ~4.2 million deaths, globally, in 2015 (Cohen et al., 2017). In 2016, $PM_{2.5}$ pollution was ranked sixth in global risk factors for mortality, and 95% of the world's population lived in areas where $PM_{2.5}$ concentrations exceeded the guidelines from the World Health Organization (Shaddick et al., 2018; EPA, 2021c). In the U.S. alone, more than 20 million people live in areas classified as non-compliant with the 2012 $PM_{2.5}$ standards from the Environmental Protection Agency (EPA, 2021a), and $PM_{2.5}$ pollution disproportionately affects people from marginalized communities (Bell and Ebisu, 2012).

Reducing particulate matter pollution is important for public health, but understanding its formation, composition, and global distribution is also critical for understanding climate: particulate matter can absorb or reflect radiation and act as cloud condensation nuclei. The interaction between particulate matter and clouds is one of the most uncertain components in the Earth's radiation budget and, therefore, in climate predictions (IPCC, 2014). Knowing the effect of particulate matter on climate is critically important as global carbon dioxide concentrations continue to rise (see Fig. 1.1) and global climate continues to change.
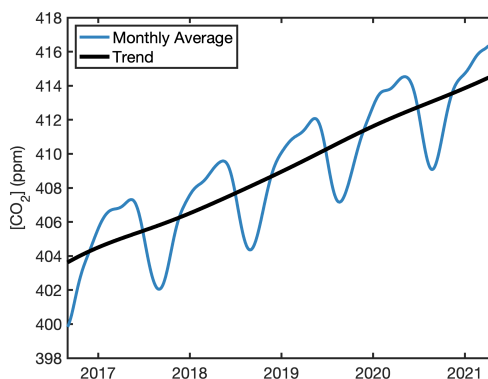
Figure 1.1: The estimated global monthly average and trend in the CO_2 concentration since I began the research in this dissertation (as reported by Dlugokencky and Tans, 2021).

A major component of small particulate matter is secondary organic aerosol (SOA), which is emitted into the atmosphere in the gas phase and later reacts to form particulate matter (Shrivastava et al., 2017; Goldstein and Galbally, 2007). Because it is not directly emitted and its formation is highly condition-dependent, SOA is difficult to regulate and predict.
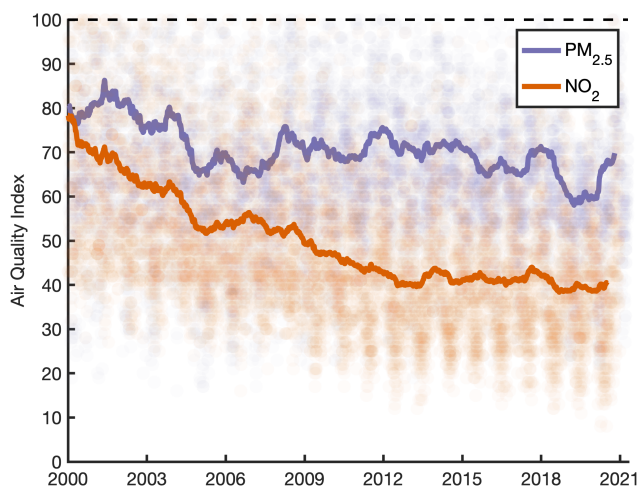
Figure 1.2: Air Quality Index of $PM_{2.5}$ and NO_2 in the Los Angeles Basin since 2000 as reported by EPA (2021b). Each point represents data from one day, and the curves are a 365-day moving average. Since 2000, NO_2 concentrations have decreased much faster than $PM_{2.5}$ concentrations have.

Traditionally, anthropogenic particulate matter from the transportation sector was understood to be the main cause of $PM_{2.5}$ non-compliance in urban areas (McDonald et al., 2018). However, even as concentrations of other pollutants, such as NO_2, have decreased due to successful regulations of motor vehicles, $PM_{2.5}$ concentrations have not fallen as fast. This indicates that there is a significant non-transportation source of $PM_{2.5}$. Figure 1.2 shows the change in NO_2 and $PM_{2.5}$ concentrations in the Los Angeles Basin since 2000. NO_2 concentrations are correlated with motor vehicle use much more significantly than $PM_{2.5}$ (see Fig. 1.3).

In recent years, it has become clear that volatile chemical products (VCPs) are responsible for a large fraction of anthropogenic particulate matter, especially in urban areas (Gkatzelis et al., 2021; McDonald et al., 2018). Understanding exactly which precursors are responsible for this large SOA formation and under which conditions is difficult, though; for each compound, different chemical pathways dominate and even similar molecules can form vastly varied amounts of aerosol. For example, toluene has a SOA yield that is 70% higher at low NO_x concentrations than at high concentrations (Zhang, Cappa, et al., 2014). In order to formulate policy to reduce urban particulate matter pollution, understanding which precursors form the most aerosol under which conditions is critically important.

Both the detailed mechanisms of SOA formation and the understanding of SOA yield (Y), which is the ratio of the aerosol mass formed to the mass of the precursor reacted
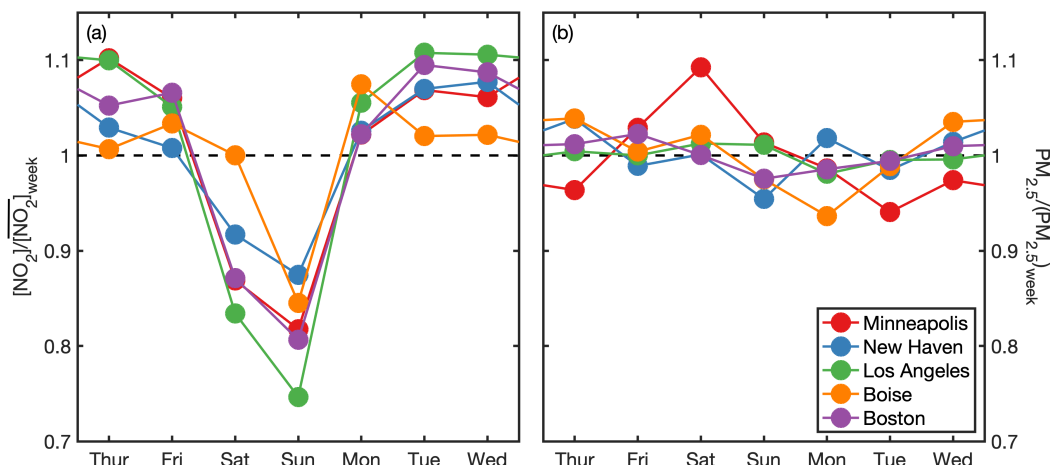
Figure 1.3: The (a) NO_2 concentrations and (b) $PM_{2.5}$ concentrations by day of the week, normalized to the weekly average, for some U.S. metro areas between 2016 and 2019 (data from EPA, 2021b, analysis inspired by Beirle et al., 2003). The decrease in NO_2 concentrations on weekends and, especially, on Sundays, indicates that NO_2 concentrations correlate with driving more so than $PM_{2.5}$ concentrations do.

(Odum et al., 1996), are predominantly understood through data obtained from laboratory chamber studies (Burkholder et al., 2017; Abbatt et al., 2014; Schwantes et al., 2017). The Caltech Environmental Chamber (shown in Fig. 1.4) and many other laboratory chambers are run in batch mode: typically the precursor compound undergoes oxidation within the chamber, and time-resolved data are collected. Other reactors, like the Caltech Photooxidation Flow Tube (CPOT), are run under steady-state conditions (Huang et al., 2017).

Extrapolating data from laboratory reactors to the outdoor environment is non-trivial: for example, chambers are necessarily smaller than the atmosphere, so wall effects will have a disproportionate influence on the data. Since, generally, only the bulk, suspended phase of the

Figure 1.4: The 19 m^3 Caltech Environmental Chamber.

reactor is measured, any particles or low-volatility compounds that are lost to the walls will not be considered, and the SOA yield will be underestimated without careful accounting (Zhang, Schwantes, et al., 2015; Trump et al., 2016).

This thesis describes the physico-chemical processes that occur within a chamber, how the various processes interact, how to account for these processes when extrapolating data from environmental chambers to the atmosphere, and, perhaps most importantly, how to design experiments to avoid needing to perform large corrections.

Equipped with this understanding of the environmental chamber, this thesis then investigates two compounds found in volatile chemical products: one has a larger-than-expected SOA yield and the other has a smaller-than-expected one. The former varies based on the temperature and NO_x concentration; the latter depends on the experimental conditions, requiring comparisons between reactors run at steady-state and in batch mode to discern this dependence. This demonstrates the importance of ascertaining the aerosol formation potential under the conditions and for the compounds that are important for the atmosphere.

1.2 Organization of Thesis

Chapter 2 is an overview of all the chemical and physical processes that occur in an environmental chamber. Using a computational model of the environmental chamber (which I first developed and further discuss in Appendix A), this chapter describes the parameters for each of these processes and then discusses the manner in which these processes interact. By modeling secondary organic aerosol formation in the environmental chamber, different phenomena (like the seed-surface-area effect) and different regimes important for aerosol growth are identified and explained in terms of the underlying chemistry and physics. While these parameters and regimes may not be known ab initio, this chapter also describes how to extract parameter information from experimental data and how to extrapolate the information to the atmosphere.

Because of the effects of vapor-wall deposition, a chamber process which is discussed in Appendix B as it applies to Teflon-walled chambers, for some experiments it is necessary to use large amounts of seed aerosol. This, in turn, increases the effect and complexity of another chamber process, particle-wall deposition; if there is more aerosol present initially, then more mass is lost to the chamber wall, and accounts of particle-wall deposition must also include particle-particle coagulation.

Chapter 3 discusses this important chamber process, particle-wall deposition. In particular, this chapter focuses on the effect of particle charge on the loss of aerosol to the walls of Teflon environmental chambers. Using the chamber model described in

Chapter 2 and Appendix A, I evaluate the size- and charge-dependent particle-wall deposition in the Caltech Environmental Chamber, ascertain the effect of charge on particle-particle coagulation, and demonstrate the large increase in particle-wall deposition that occurs when Teflon environmental chambers are heavily charged.

A charge- and size-dependent particle-wall-deposition correction is needed in Appendix C to understand the SOA formation potential of isoprene, necessitating the use of these methods developed in this chapter.

Chapter 3 also elucidates how, with the appropriate preparation, experiments in environmental chambers can be performed so that particle-wall deposition is only size-dependent (and not charge-dependent) and data extrapolation to the atmosphere has minimal uncertainty.

In Chapter 4, the particle-wall deposition of aerosol formed from the oxidation of benzyl alcohol, a volatile chemical product species, is merely size-dependent. I calculate SOA yields for benzyl alcohol that account for both particle- and vapor-wall deposition and use the results to extract parameters related to aerosol growth for the chamber and for benzyl alcohol. Because it is important to understand aerosol formation under different conditions, I investigate the temperature- and NO_x-dependence of the aerosol formation of benzyl alcohol. Under atmospherically relevant urban conditions ([NO]≈80 ppb and 291 K), SOA yields from benzyl alcohol can reach 100%, which is larger than was previously used in emission and particulate matter inventories.

Chapter 5 investigates the SOA yield from another volatile chemical product species, decamethylcyclopentasiloxane (D5), and comes to the opposite conclusion: aerosol yields from D5 used in inventories are too high and, under atmospherically relevant conditions ([OH] $\lesssim 10^{7.5}$ molec cm^{-3}), SOA yields are likely ∼1%. In the case of D5, it is the OH concentration that matters the most for predicting the SOA yield. To reconcile reports of higher yields in the literature, I performed and compared experiments from different reactors to determine that, at OH mixing ratios much higher than achieved in the atmosphere (∼5×10^9 molec cm^{-3}), SOA yields can exceed 100%.

Once in the atmosphere, secondary organic aerosol is important not only for its impact on human health, but also for the way that it interacts with clouds and therefore climate. Appendix D investigates the link between aerosol hygroscopicity and cloud condensation nuclei.

References

Abbatt, Jon, Christian George, Megan Melamed, Paul Monks, Spyros Pandis, and Yinon Rudich (Feb. 2014). "New directions: fundamentals of atmospheric chemistry: keeping a three-legged stool balanced." In: *Atmos. Environ.* 84, pp. 390–391. ISSN: 13522310. DOI: `10.1016/j.atmosenv.2013.10.025`.

Beirle, S., U. Platt, M. Wenig, and T. Wagner (2003). "Weekly cycle of NO_2 by GOME measurements: a signature of anthropogenic sources." In: *Atmos. Chem. Phys.* 3.6, pp. 2225–2232. DOI: `10.5194/acp-3-2225-2003`.

Bell, Michelle L. and Keita Ebisu (2012). "Environmental Inequality in Exposures to Airborne Particulate Matter Components in the United States." In: *Environmental Health Perspectives* 120.12, pp. 1699–1704. DOI: `10.1289/ehp.1205201`.

Burkholder, James B. et al. (2017). "The essential role for laboratory studies in atmospheric chemistry." In: *Environ. Sci. Technol.* 51.5, pp. 2519–2528. ISSN: 0013-936X. DOI: `10.1021/acs.est.6b04947`.

Cohen, Aaron J. et al. (2017). "Estimates and 25-year trends of the global burden of disease attributable to ambient air pollution: an analysis of data from the Global Burden of Diseases Study 2015." In: *The Lancet* 389.10082, pp. 1907–1918. DOI: `10.1016/S0140-6736(17)30505-6`.

Dlugokencky, Ed and Pieter Tans (2021). *Trends in Atmospheric Carbon Dioxide (NOAA/GML)*. URL: `www.esrl.noaa.gov/gmd/ccgg/trends/` (visited on 04/21/2021).

EPA, United States Environmental Protection Agency (2021a). *Green Book: PM-2.5 (2012) Designated Area/State Information with Design Values*. URL: `https://www3.epa.gov/airquality/greenbook/kbtcw.html` (visited on 04/26/2021).

– (2021b). *Outdoor Air Quality Data*. URL: `https://www.epa.gov/outdoor-air-quality-data/air-data-multiyear-tile-plot` (visited on 04/21/2021).

– (2021c). *Particulate Matter (PM) Pollution: Timeline of Particulate Matter (PM) National Ambient Air Quality Standards (NAAQS)*. URL: `https://www.epa.gov/pm-pollution/timeline-particulate-matter-pm-national-ambient-air-quality-standards-naaqs` (visited on 04/26/2021).

Gkatzelis, Georgios I., Matthew M. Coggon, Brian C. McDonald, Jeff Peischl, Jessica B. Gilman, Kenneth C. Aikin, Michael A. Robinson, Francesco Canonaco, Andre S. H. Prevot, Michael Trainer, and Carsten Warneke (2021). "Observations Confirm that Volatile Chemical Products Are a Major Source of Petrochemical Emissions in U.S. Cities." In: *Environ. Sci. Technol.* DOI: `10.1021/acs.est.0c05471`.

Goldstein, Allen H. and Ian E. Galbally (Mar. 2007). "Known and Unexplored Organic Constituents in the Earth's Atmosphere." In: *Environ. Sci. Technol.* 41.5, pp. 1514–1521. ISSN: 0013-936X. DOI: `10.1021/es072476p`.

Huang, Yuanlong, Matthew M. Coggon, Ran Zhao, Hanna Lignell, Michael U. Bauer, Richard C. Flagan, and John H. Seinfeld (2017). "The Caltech Photooxidation Flow Tube reactor: Design, Fluid Dynamics and Characterization." In: *Atmos. Meas. Tech.* 10.10, pp. 839–867. DOI: `10.5194/amt-10-839-2017`.

IPCC (2014). *Climate Change 2014: Synthesis report.* Tech. rep. Geneva, Switzerland: Intergovernmental Panel on Climate Change, p. 151. DOI: `10.1017/CB09781107415324`.

McDonald, Brian C. et al. (Feb. 2018). "Volatile chemical products emerging as largest petrochemical source of urban organic emissions." In: *Science* 359.6377, pp. 760–764. ISSN: 0036-8075. DOI: `10.1126/science.aaq0524`.

Odum, Jay R., Thorsten Hoffmann, Frank Bowman, Don Collins, Richard C. Flagan, and John H. Seinfeld (1996). "Gas–particle partitioning and secondary organic aerosol yields." In: *Environ. Sci. Technol.* 30.8, pp. 2580–2585. ISSN: 0013-936X. DOI: `10.1021/es950943+`.

Schwantes, Rebecca H., Renee C. McVay, Xuan Zhang, Matthew M. Coggon, Hanna Lignell, Richard C. Flagan, Paul O. Wennberg, and John H. Seinfeld (2017). In: *Advances in Atmospheric Chemistry Volume I.* Ed. by J.R. Barker, A.L. Steiner, and T.J. Wallington. Singapore: World Scientific. Chap. Science of the environmental chamber, pp. 1–93. ISBN: 978-981-3147-34-8.

Shaddick, Gavin et al. (2018). "Data Integration for the Assessment of Population Exposure to Ambient Air Pollution for Global Burden of Disease Assessment." In: *Environmental Science and Technology* 52.16, pp. 9069–9078. DOI: `10.1021/acs.est.8b02864`.

Shrivastava, Manish et al. (2017). "Recent advances in understanding secondary organic aerosol: implications for global climate forcing." In: *Rev. Geophys.* 55.2, pp. 509–559. DOI: `10.1002/2016RG000540`.

Trump, Erica R., Scott A. Epstein, Ilona Riipinen, and Neil M. Donahue (Nov. 2016). "Wall effects in smog chamber experiments: a model study." In: *Aerosol Sci. Technol.* 50.11, pp. 1180–1200. ISSN: 0278-6826. DOI: `10.1080/02786826.2016.1232858`.

Zhang, Xuan, Christopher D. Cappa, Shantanu H. Jathar, Renee C. McVay, Joseph J. Ensberg, Michael J. Kleeman, and John H. Seinfeld (2014). "Influence of vapor wall loss in laboratory chambers on yields of secondary organic aerosol." In: *Proc. Natl. Acad. Sci. U.S.A.* 111.16, pp. 5802–5807. DOI: `10.1073/pnas.1404727111`.

Zhang, Xuan, R. H. Schwantes, R. C. McVay, H. Lignell, M. M. Coggon, R. C. Flagan, and J. H. Seinfeld (Apr. 2015). "Vapor wall deposition in Teflon chambers." In: *Atmos. Chem. Phys.* 15.8, pp. 4197–4214. ISSN: 1680-7324. DOI: `10.5194/acp-15-4197-2015`.

Chapter 2

THE VERY MODEL OF MODERN MAJOR CHAMBERS: COMPUTATIONAL SIMULATION OF SECONDARY ORGANIC AEROSOL FORMATION IN LABORATORY CHAMBERS

Abstract

In the atmosphere, certain volatile organic compounds (VOCs) undergo oxidation. Some of these oxidation products then condense into the particle phase. Oxidation products that transform into the particle phase by this route are termed secondary organic aerosol (SOA). Understanding the route by which particulate matter is formed from these reactions is a key challenge in atmospheric chemistry. The principal understanding of SOA formation is derived from studies in laboratory chambers, for which determination of the amount of SOA formed requires a rigorous, quantitative understanding of chamber phenomena. With computational simulation of the processes occurring within an environmental chamber, the extrapolation to atmospheric conditions can be assessed. Moreover, computational chamber modeling of secondary organic aerosol formation will become an integral part of experimental design and data analysis. Here, we present a comprehensive review of processes involved in laboratory chamber SOA formation with a focus on the coupling between different physico-chemical processes and understanding that has recently emerged.
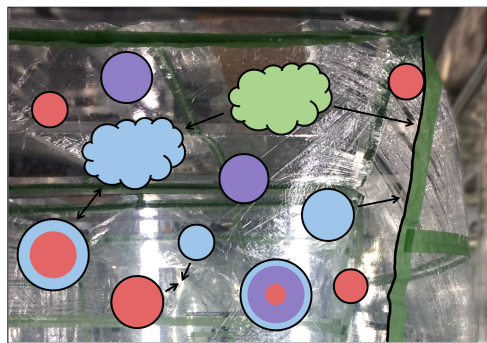
2.1 Introduction

Organic aerosol is a considerable fraction of global atmospheric particulate matter (Shrivastava et al., 2017; Goldstein and Galbally, 2007). A particle emitted into the atmosphere directly from its sources is called primary organic aerosol (POA), while

a particle formed when organic gas-phase compounds oxidize and condense into the particle phase is called secondary organic aerosol (SOA). The predominant source of fundamental data on the detailed mechanisms of SOA formation is laboratory chamber studies (Burkholder et al., 2017; Abbatt et al., 2014; Schwantes, McVay, et al., 2017). In a typical laboratory chamber experiment, a precursor volatile organic compound undergoes oxidation in a chamber filled with purified air and a source of oxidant (typically the OH radical). The goal of such chamber studies is to gain a quantitative, detailed description of the amount, chemical composition, and properties of the organic aerosol generated, via understanding of the atmospheric chemistry that underlies its formation (Kanakidou et al., 2005). The propensity of a given volatile organic compound (VOC) to form secondary organic aerosol is measured quantitatively by the *secondary organic aerosol yield*, the ratio of the mass of organic aerosol formed to the mass of the reacted parent compound (Odum et al., 1996; Kroll and Seinfeld, 2008). Results of laboratory chamber experiments show that SOA yield depends on a number of factors, including: (1) the concentration of oxides of nitrogen (NO_x), which, among other factors, governs the competitive chemistry of peroxy radicals (RO_2) formed in VOC oxidation; (2) relative humidity; and (3) temperature. The grand challenge is to design and interpret secondary organic aerosol laboratory chamber experiments so as to infer the underlying oxidation mechanism and determine the fundamental yield of SOA.

When oxidation products of sufficiently low volatility are generated, secondary organic aerosol forms. The conversion generally occurs as VOC oxidation products undergo progressive oxidation. In the absence of intentionally introduced seed particles, with a sufficiently high VOC concentration, oxidation products must accumulate in the chamber without going to the chamber wall until homogeneous nucleation of these products occurs. When nucleation does occur, the formed particles are often relatively small (below ~100 nm diameter).

The use of a seed aerosol stimulates the oxidation products to condense onto the seed aerosol, as opposed to onto the chamber walls. To determine the aerosol formed, the amount of particle mass that is lost to the chamber walls is quantified through an understanding of chamber dynamics. SOA formation experiments are generally carried out for some hours after consumption of the parent compound, since intermediate products may continuously condense and react. As noted above, the SOA yield of a precursor includes the condensed mass from many generations of oxidation reactions.

With the widespread use of laboratory chambers for investigating atmospheric chemistry and SOA formation, understanding the chamber-related physics and chemistry is paramount (Bzdek and Reid, 2017). Even for the largest chambers, one must carefully account for the interactions between the chamber walls and the gas- and particle-phase components housed within the chamber. If, for example, an appreciable fraction of low-volatility oxidation product vapors, as well as the particles on which such vapors have condensed, deposits on the wall of the chamber throughout an experiment, the measured SOA yield relative to that in the "wall-less" atmosphere, will be underestimated (Zhang, Schwantes, et al., 2015; Trump et al., 2016).

Typically, environmental reaction chambers are made from Teflon film (fluorinated ethylene propylene, FEP). Such film is essentially transparent to radiation in the spectral range of photooxidation, which facilitates placement of the radiation source outside of the chamber itself. Low-volatility vapor molecules characteristic of SOA are not inert with respect to Teflon and may partition into Teflon chamber walls (Huang et al., 2018; Matsunaga and Ziemann, 2010). Ample evidence also exists that particles deposit onto Teflon walls.

Here, we comprehensively present the processes involved in SOA formation in atmospheric chambers. The traditional chamber is operated as a batch reactor, into which all reactants are injected at the outset. An atmospheric chamber can also be run in steady-state as a continuously mixed flow reactor (CMFR) (Zhang, Ortega, et al., 2018; Han et al., 2019). In this setup, reactants are continuously introduced and the well-mixed reactor contents are continuously withdrawn. Most of our discussion focuses on the batch reactor, but we address the CMFR in Section 2.2.10.

Computational modeling affords quantification of the effect of reaction conditions, vapor-wall interactions, particle-wall interactions, particle-particle interactions, particle charging effects, aerosol levels, temperature, and humidity (Figure 2.1). With computational simulation of the processes occurring within an environmental chamber, the effect of parameters necessary for extrapolating to atmospheric conditions can be assessed. Moreover, computational modeling of secondary organic aerosol formation has become an integral part of experimental design and data analysis. We begin by discussing physico-chemical chamber processes individually: including fundamental theory, identification of key parameters, and coupling between different processes. Through chamber simulations, we will examine the effects that emerge when parameters and processes interact in specific ways and discuss how this ought to be addressed in experimental design.
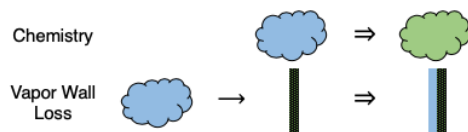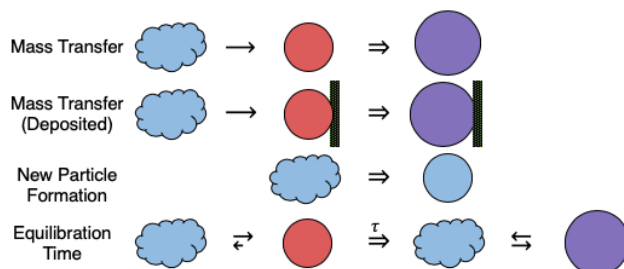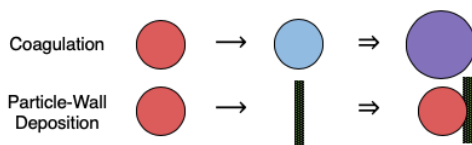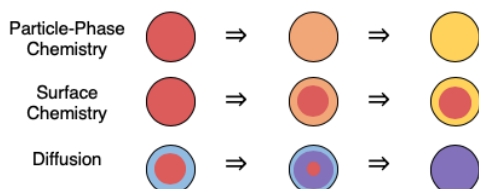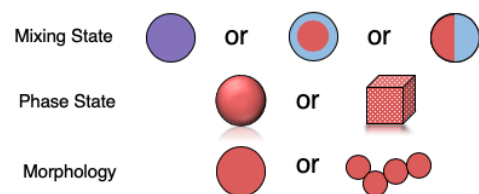
Figure 2.1: Atmospheric chamber phenomena. "→" indicates "goes to" and "⇒" indicates "becomes." The spheres represent particles, the clouds represent gas-phase species, and the rectangle represents the wall.

2.2 Physico-Chemical Processes Occurring in an Environmental Chamber

Atmospheric oxidation of a volatile organic compound is generally initiated by reaction with the hydroxyl radical (OH), the nitrate radical (NO_3), or ozone (O_3) (Seinfeld and Pandis, 2016). As an intact parent VOC molecule becomes progressively oxidized, its volatility decreases, and oxidized product molecules begin to nucleate into particles or to condense onto pre-existing aerosol. The mass of aerosol formed is governed by the degree of gas-particle partitioning of each generation of oxidation products. Oxidation products might be of higher- or lower-volatility than their precursors, since oxidation occurs both through addition of functional groups to form products of lower volatility and by molecular fragmentation to form higher volatility compounds (Isaacman-VanWertz et al., 2018; Hallquist et al., 2009; Saleh, Donahue, and Robinson, 2013; Ziemann and Atkinson, 2012). The extent of compound partitioning between the gas and particle phases hinges on the pure component volatilities (vapor pressures), the particle phase state, and the ambient temperature and relative humidity. Once condensed, particle-phase chemistry can also take place that further affects the volatility and, correspondingly, the vapor-aerosol partitioning of the oxidation products. Continued oxidation of the particle-phase species by impact with gas-phase OH or O_3 can also occur (Donahue, Henry, et al., 2012).

The propensity of an organic compound to form secondary organic aerosol is quantified by the SOA yield (Y), which is given by the ratio of the change in the mass of SOA (ΔSOA) to the mass of the reacted precursor (ΔVOC),

$$Y = \frac{\Delta\text{SOA}}{\Delta\text{VOC}} \tag{2.1}$$

where the magnitude of Y can depend on experimental conditions such as relative humidity, temperature, and NO_x concentration (Odum et al., 1996). The value of Y may exceed 1 since, during the process of oxidation, a compound may gain oxygen and therefore increase in molecular mass. Since oxidation of a VOC generally proceeds through several generations of reaction in the atmosphere before its oxidation products are of sufficiently low volatility to condense into SOA, chamber experiments are usually carried out until Y reaches essentially an ultimate value for the particular experimental conditions.

2.2.1 Qualitative Comparison of Chamber Processes

In the environmental chamber, the inherent gas-phase VOC oxidation chemistry is accompanied by four major processes: condensation of vapor molecules onto particles, particle-particle coagulation, particle deposition onto the chamber wall,

and deposition of vapors onto the chamber wall. A fifth process that may take place is nucleation of oxidation products to form fresh particles. In the absence of intentionally introduced seed particles, oxidation products, upon reaching a sufficient level of supersaturation, may nucleate to form nanometer-scale particles that grow upon subsequent condensation of VOC oxidation products. By and large, in the present review we confine our attention to the situation in which inert particles are introduced into the chamber as seeds to facilitate condensation of VOC oxidation products. In that case, homogeneous nucleation of VOC oxidation products is suppressed due to the presence of abundant aerosol surface area accessible for condensation of oxidation products. We also limit our discussion of chemical reactions primarily to those in the gas-phase. Note that multiphase aerosol processes can also be important, especially under high relative humidity conditions, in which case the aerosol may consist of a mixture of organic and aqueous phases (Pöschl and Shiraiwa, 2015).

Before we address each of these processes in detail, it is informative to illustrate their effects on condensing vapor concentration and particle size distribution as a function of particle diameter, D_p, over the course of VOC oxidation. The particle size distribution is expressed by $dN/d\log_{10}D_p$, where dN = an increment in total particle number concentration and $d\log_{10}D_p$ = an increment of the logarithm of particle diameter (see Box 2.2.1). Figure 2.2 shows the effect, individually, of the four key chamber processes on particle number and mass concentration, the concentration of oxidized vapor, and the overall particle size distribution.

Vapor condensation on particles leads to particle growth. For pure vapor condensation on particles, particle number concentration does not change, particle mass increases, and the condensing vapor concentration decreases (Figure 2.2: panels A, E, I, and M). With a continuous source of vapor, the rate of change of diameter due to vapor condensation on a particle is inversely proportional to the diameter of that particle (Seinfeld and Pandis, 2016). The consequence of this dependence is that smaller particles grow more rapidly than larger particles, so that the particle size distribution tends to compress (Figure 2.2M).

Particle-particle coagulation (Figure 2.2: panels B, F, L, and N) reduces the particle number concentration (panel B), but not the particle mass concentration (panel F). As the overall suspended particle number concentration decreases owing to coagulation, the particle size distribution shifts progressively towards larger sizes. The presence of coagulation indirectly affects both the amount of SOA formed, owing to the
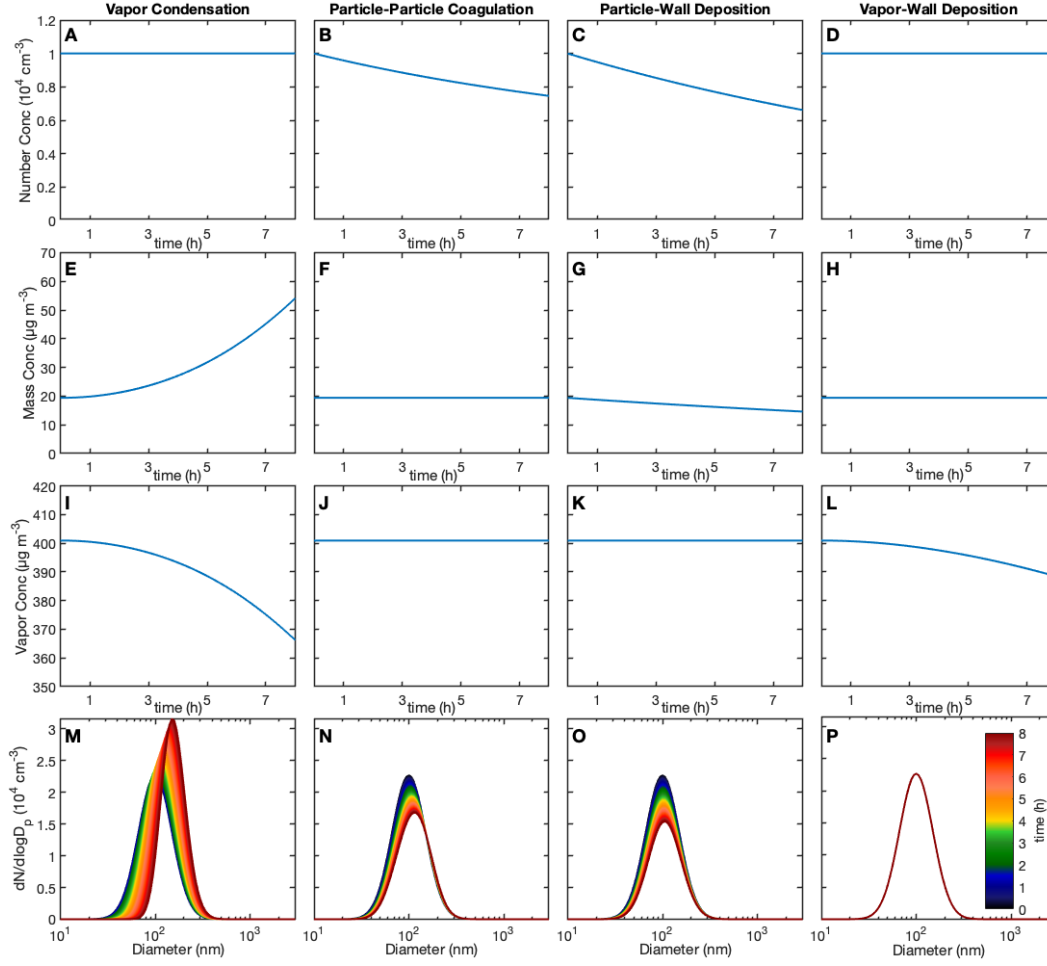
Figure 2.2: Effect of processes occurring in an environmental chamber on (A-D) particle number concentration, (E-H) particle mass concentration, (I-L) vapor mass concentration, and (M-P) particle size distribution over an 8-h simulation. In each panel, the initial particle number concentration is 10^4 cm^{-3} with a lognormal size distribution (D_{pg} = 100 nm and σ_g = 1.5). Chamber temperature is taken as 300 K with particles of density 1770 kg m^{-3}. The precursor VOC has mixing ratio of 100 ppb, molecular weight of 100 g mol^{-1}, and saturation mass concentration $C^* = 1 \times 10^2$ µg m^{-3} reacting to form a product with molecular weight of 100 g mol^{-1} and $C^* = 1$ µg m^{-3}. Panels A, E, I, and M assume a first-order VOC oxidation rate constant of $k_{OH} = 1 \times 10^{-5}$ s^{-1}, and a mass accommodation coefficient between the vapor and suspended particle phase $\alpha_p = 10^{-3}$. For coagulation (panels B, F, J, and N), a unity particle-particle sticking efficiency (α = 1) and no oxidation ($k_{OH} = 0$) is assumed. For panels C, G, K, and O, wall-deposition parameters for a 19.0 m^3 spherical chamber with an eddy-diffusion coefficient of mixing in the chamber of 0.2 s^{-1} are used (see Section 2.2.6). Panels D, H, L, and P assume the equivalent saturation mass concentration of the wall, C_w (to be addressed in Section 2.2.8), is 10^4 µg m^{-3} and the wall accommodation coefficients using the relation in Huang et al. (2018), also described in Section 2.2.8. Each process is shown individually in the absence of any of the other processes occurring.

Box 2.2.1: Aerosol Size Distribution Function

The aerosol size distribution function $n(D_p)$ is defined as: $n(D_p)dD_p$ = the number of particles per cm^3 of air with diameters in the range D_p to $D_p + dD_p$ (Seinfeld and Pandis, 2016). The units of $n(D_p)$, then, are usually μm^{-1} cm^{-3}. N, the total number of particles per cm^3, is

$$N = \int_0^\infty n(D_p)dD_p \tag{2.2}$$

If $dN = n(D_p)dD_p$ denotes the number concentration of particles in the size range D_p to $D_p + dD_p$, then $n(D_p)$ can also be expressed as dN/dD_p. The aerosol size distribution can be expressed as functions of $\ln D_p$ or $\log_{10} D_p$ instead of D_p. Note that $\ln D_p$ and $\log_{10} D_p$ implicitly assume that the "reference" particle diameter is 1 nm or μm (depending on the unit of D_p). The number distribution function $n^e(\ln D_p)$ is defined as $n^e(\ln D_p)d\ln D_p$ = particle number concentration in the size range $\ln D_p$ to $\ln D_p + d\ln D_p$. Likewise, $dN/d\log_{10} D_p$ expresses an increment dN in total aerosol number concentration and $d\log_{10} D_p$ = an increment of the logarithm of particle diameter D_p. Distributions are often initialized or fit to a lognormal distribution, defined by (Seinfeld and Pandis, 2016):

$$n(\log_{10} D_p) = \frac{N}{(2\pi)^{1/2} \log_{10} \sigma_g} \exp\left(-\frac{\left(\log_{10} D_p - \log_{10} D_{pg}\right)^2}{2 \log_{10}^2 \sigma_g}\right) \tag{2.3}$$

where D_{pg} is the median diameter and σ_g is the geometric standard deviation of the aerosol size distribution.

---

changing surface area of aerosol present, and the rate of vapor condensation over the size distribution.

Particle-wall deposition (Figure 2.2: panels C, G, K, and O) decreases both the number (panel C) and mass concentration of suspended particles (panel G). In the absence of other processes, larger particles settle faster due to gravity and smaller particles diffuse to the wall more rapidly, so intermediate-size particles tend to remain preferentially suspended as particles deposit on the wall (panel O, see Section 2.2.6). While particle-wall deposition itself does not directly affect the amount of condensable SOA formed, the process reduces the mass of SOA-laden suspended particles that can actually be measured.

Vapor-wall deposition (Figure 2.2: panels D, H, L, and P) decreases the mass concentration of suspended vapor, without affecting the suspended particle mass (panel L). In the ideal case, in which suspended vapor does not deposit on chamber walls, the decrease in VOC concentration results entirely from oxidation of the

parent VOC. If loss of vapor by wall deposition is occurring but not taken into account, then the SOA yield Y will be underestimated.

The evolution of chamber aerosol size distribution is affected by four processes quantified in Figure 2.2 as shown in panels M, N, O, and P. Panel M gives the aerosol size distribution evolution due purely to vapor oxidation product condensation. Characteristically, the aerosol size distribution shifts toward larger sizes. In the case of pure coagulation, the aerosol size distribution shifts in the direction of larger particle sizes and smaller number concentration (panel N). In the case solely of deposition of suspended particles on the chamber walls, particle number concentration decreases (panel C) and the particle size distribution shifts in a manner that reflects the complex particle-size-dependence of wall deposition (panel O). When considering vapor-wall deposition only, the vapor concentration decreases (panel L) without any growth of the suspended particles (panel P), since all the mass goes to the chamber walls instead of condensing onto suspended particles.

2.2.2 Dynamics of the Particle Size-Distribution Function: the Aerosol General Dynamic Equation

In theory, particles can be considered to be comprised of individual, molecular units. Because the molecules that constitute atmospheric organic aerosol are on the Angstrom scale, whereas the particles themselves are on the order of tens to hundreds of nanometers in diameter, resolving particles computationally according to the number of constituent molecules is not feasible. From a computational viewpoint, particles are characterized by their diameter and are apportioned into particle diameter size bins. Generally, though not always, particles are assumed to be spherical (Tian et al., 2017).

A mass balance on the suspended particle-phase includes the source from nucleation (if nucleation is occurring) and from vapor condensation. It also includes the loss by evaporation from particles and by deposition to the walls of the chamber:

$$\frac{dm}{dt} = \left(\frac{dm}{dt}\right)_{nucleation} + \left(\frac{dm}{dt}\right)_{condensation} - \left(\frac{dm}{dt}\right)_{evaporation} - \left(\frac{dm}{dt}\right)_{wall\ deposition}$$
$$(2.4)$$

Tracking of the change in the aerosol size distribution is achieved through mass balances of suspended particles based on their diameter D_p that, together, amount to the mass balance of the total suspended particle population. Whereas vapor condensation leads to an overall increase in the total mass of the aerosol population,

it can result in either an increase or a decrease in the mass of particles of a specific size: e.g., if particles in a population, of size D_p, all grow to size $D_p + \delta$ over an increment of time, then the mass of particles with diameter D_p will decrease even as the total aerosol mass is increasing.

Transforming this mass balance into a particle number concentration balance by assuming a constant density yields the component terms in the aerosol general dynamic equation (GDE), which describes the particle processes that occur within an environmental chamber (Gelbard and Seinfeld, 1979):

$$\frac{dn(D_p,t)}{dt} = \left[\frac{dn(D_p,t)}{dt}\right]_{evaporation/condensation} + \left[\frac{dn(D_p,t)}{dt}\right]_{coagulation}$$
$$+ \left[\frac{dn(D_p,t)}{dt}\right]_{nucleation} + \left[\frac{dn(D_p,t)}{dt}\right]_{wall\ deposition}$$

(2.5)

where $n(D_p,t)$ is the number concentration distribution of particles of diameter D_p at time t. Provided that the volume removed for sampling throughout the experiment is sufficiently small, the chamber volume can be assumed constant (and at constant pressure); if this is not the case and makeup air is required to account for that removed by sampling, a dilution term is added to Equation 2.5.

2.2.3 Gas-Phase Dynamics

Gas-phase VOC oxidation causes coupling between the aerosol and gas phases. A gas-phase species can condense onto particles suspended in the chamber, condense onto particles deposited onto the chamber walls, deposit directly onto the chamber walls, react chemically, or become incorporated into nucleated particles. The mass m_i of a gas-phase species can increase due to evaporation from particles or the wall or from generation by chemical reaction:

$$\frac{dm_i}{dt} = \left(\frac{dm_i}{dt}\right)_{evap/cond\ (suspended\ particles)} + \left(\frac{dm_i}{dt}\right)_{evap/cond\ (deposited\ particles)}$$
$$+ \left(\frac{dm_i}{dt}\right)_{vapor-wall\ deposition} + \left(\frac{dm_i}{dt}\right)_{evap\ from\ wall} + \left(\frac{dm_i}{dt}\right)_{nucleation}$$
$$+ \left(\frac{dm_i}{dt}\right)_{reaction\ of\ i} + \left(\frac{dm_i}{dt}\right)_{reaction\ to\ i}$$

(2.6)

Molecular condensation onto a particle surface involves two steps: a vapor molecule has to diffuse from the gas phase to the particle surface, followed by surface uptake. The parameter that describes the probability of uptake of a vapor molecule at the surface of a particle is the *mass accommodation coefficient*, α_p ($0 \leq \alpha_p \leq 1$) (Julin et al., 2014; Kolb et al., 2010; Sunol, Charan, and Seinfeld, 2018). Note that the parameter α_p incorporates the accommodation of a vapor molecule both to the surface of and the bulk of a particle.

For a liquid-phase particle, accommodation of an impinging gas-phase molecule into the particle phase is assumed to be efficient and rapid (Shiraiwa and Seinfeld, 2012). However, when the particle is sufficiently viscous and acts as a solid or semisolid or when there is significant particle-phase chemistry controlling vapor uptake, accommodation may not occur instantaneously. In the absence of experimental data, it is difficult to predict α_p for a specific vapor-particle system from first-principles; thus, the value of α_p is generally determined empirically by fitting of aerosol growth rates. These fits of particle growth rates for oxidation products of various volatile compounds show values of α_p from 10^{-3} to 1,(McVay, Cappa, and Seinfeld, 2014) and a recent study reveals through direct measurements that α_p is nearly unity for a wide range of semi-volatile organic compounds (Liu, Day, et al., 2019).

A related parameter, α_{pw}, is defined as the accommodation coefficient for particles deposited on the chamber wall: the probability that a bulk, gas-phase molecule will be taken up by a particle already on the wall. Strictly speaking, the accommodation coefficient of vapor molecules on a suspended particle compared to a particle deposited on the wall should be the same. However, the transport processes involved are different in the two cases; for a particle deposited on the wall of the chamber, a vapor molecule has to traverse the boundary layer at the wall before diffusing to the deposited particle, while for a suspended particle, the vapor molecule simply diffuses to the particle. Whereas the incorporation into the particle is essentially identical, the process of transport to the particle is different in the two cases. For deposited particles, the process depends on the rate of chamber mixing. For the purpose of generality, we assume that the accommodation coefficients can be distinct but that $\alpha_{pw} \leq \alpha_p$.

To describe the dynamics of particles in the size range of the mean free path of air (λ), one must account for non-continuum effects (Seinfeld and Pandis, 2016; Park and Lee, 2000). A widely-used correction factor for non-continuum effects is that

of Fuchs and Sutugin (1971):

$$f(\text{Kn}, \alpha_p) = \frac{0.75\alpha_p(1 + \text{Kn})}{\text{Kn}^2 + \text{Kn} + 0.283\alpha_p\text{Kn} + 0.75\alpha_p} \tag{2.7}$$

where Kn is the Knudsen number given by $\frac{2\lambda}{D_p}$. The net change in mass concentration m_i of a particle of diameter D_p due to molecular condensation and evaporation is:

$$\frac{dm_i}{dt} = \frac{2\pi D_p \mathcal{D}_{gi} M_i}{RT} f(\text{Kn}, \alpha_p)(p_i - p_{eq,i}) \tag{2.8}$$

where, for compound i, $\mathcal{D}_{gi}$ is the molecular diffusivity in air, M_i is molecular weight, T is the particle temperature (same as chamber temperature), R is the ideal gas constant, p_i is vapor pressure, and $p_{eq,i}$ is equilibrium vapor pressure. Note that, for sufficiently small particles, $p_{eq,i}$ must include the effect of the curved surface on vapor pressure (the so-called Kelvin effect). In this case, assuming an ideal solution,

$$p_{eq,i}(D_p) = \chi_i p_{eq,i}^o \exp\left(\frac{4\sigma M_i}{RT\rho_{p,i}D_p}\right) \tag{2.9}$$

where $p_{eq,i}^o$ is the equilibrium vapor pressure of the pure compound i, χ_i is its particle-phase mole fraction, $\rho_{p,i}$ is its density in the condensed phase, and σ is the surface tension of the particle. Pure component equilibrium vapor pressure can be predicted with a number of publicly available methods (Barley and McFiggans, 2010; O'Meara et al., 2014; Topping and Jones, 2016), but different methods used to estimate compound vapor pressure can yield different results for the same compound. This, therefore, is a source of uncertainty.

The equation comparable to (2.8) for particle diameter is:

$$\frac{dD_p}{dt} = \frac{4\mathcal{D}_{gi}M_i}{\rho_{p,i}RTD_p} f(\text{Kn}, \alpha_p)(p_i - p_{eq,i}). \tag{2.10}$$

Note that the condensation rate is proportional to $p_i - p_{eq,i}$, so that when these are equal the gas and particle phases are at equilibrium. If p_i, the ambient partial pressure of the compound, varies slowly with respect to the gas-particle equilibrium timescale, one can assume that gas-particle equilibrium is achieved in each computational timestep, since the aerosol grows or shrinks in a pseudo-equilibrium (Odum et al., 1996; Donahue, Robinson, et al., 2006). Under typical atmospheric conditions, the timescale needed for a steady-state profile of the vapor to be established around a growing or shrinking particle is $< 10^{-3}$ s (Seinfeld and Pandis, 2016).

The change in the size distribution of an aerosol population from condensation and evaporation is given by

$$\left[\frac{\partial n(D_p, t)}{\partial t}\right]_{evap/cond} + \frac{\partial \left[I_D(D_p, t)n(D_p, t)\right]}{\partial D_p} = 0 \tag{2.11}$$

where $n(D_p, t)$ is the particle number distribution and, for an individual particle, the particle diameter rate of change solely as a result of condensation and evaporation is $I_D(D_p, t) = dD_p/dt$.

2.2.4 Particle-Phase Diffusion

In the process of condensation, a gas-phase molecule (1) diffuses from the bulk vapor-phase to the particle surface, (2) becomes incorporated into the surface of the particle, and (3) diffuses into the bulk of the particle and (possibly) undergoes reaction with other particle-phase species. Analytic and numeric solutions of coupled diffusion and reaction between gas and particle phases have been developed to describe these processes (Vesala et al., 2001; Shiraiwa, Pfrang, et al., 2012; Zaveri, Easter, et al., 2014; Liu, Zaveri, and Seinfeld, 2014). If chemistry involving the condensed species does not occur in the particle phase, or if that chemistry conforms to first-order kinetics, a closed-form analytic solution of both the gas and particle phase dynamics can be obtained.

The rate of diffusion of a gas-phase molecule to the surface of a particle is governed by the molecular diffusion coefficient for the gas-phase species, $\mathcal{D}_{g,i}$, and the particle diameter, D_p. The timescale for which this process relaxes to steady state is typically of the order of 10^{-6} s: given by $\frac{D_p^2}{4\pi^2 \mathcal{D}_{g,i}}$ (Liu, Zaveri, and Seinfeld, 2014). Consequently, it is generally assumed that the gas-phase concentration surrounding a particle is at quasi-steady state.

The combined rate of uptake at the particle surface, followed by diffusion into the particle is determined by the timescale to establish equilibrium across the interface, τ_{ipe}, which is determined both by the uptake probability of the molecule onto the surface upon collision, α_p, and by the rate of diffusion from the surface of the particle into the bulk, $\mathcal{D}_b$: (Liu, Zaveri, and Seinfeld, 2014; Zaveri, Easter, et al., 2014; Seinfeld and Pandis, 2016)

$$\tau_{ipe} = \mathcal{D}_b \left(\frac{4}{\alpha_p \bar{c}}\right)^2 \tag{2.12}$$

For a typical liquid particle-phase diffusion coefficient $\mathcal{D}_b$ of order $\sim 10^{-5}$ cm^2 s^{-1}, τ_{ipe} lies in the range between $\sim 10^{-11}$ and $\sim 10^{-5}$ s, which implies that the interface is in quasi-equilibrium. Ambient organic aerosols tend to contain either inorganic salts or acids and water. These aqueous solutions of organic substances sometime develop into glassy or semi-solid phases under decreasing humidity conditions. In laboratory studies under various ambient-relevant conditions, different types of SOA have been observed to be liquid, semi-solid, or glassy (Renbaum-Wolff et al., 2013; Zhang, Schwantes, et al., 2015; Song et al., 2015; Mikhailov et al., 2009; Vaden, Imre, et al., 2011; Shiraiwa, Zuend, et al., 2013; Virtanen, Joutsensaari, et al., 2010; Saukko et al., 2012; Mai et al., 2015). The characteristic timescale for diffusion in aerosol particles varies from 10^{-6} to 10^{-3} s for liquids, to seconds to years for semi-solids. Customarily, one assumes that the gas-particle equilibrium partitioning of organics is instantly achieved; this assumption will not hold if particles are semi-solid or glassy. For semi-solid or glassy particles, τ_{ipe} may be relatively long, such that the timescale to establish interfacial equilibrium is competitive with those of other processes such as vapor-wall interactions or oxidation reactions (Shiraiwa and Seinfeld, 2012).

The diffusive flux of a species into a particle of radius a can be expressed as: (Liu, Zaveri, and Seinfeld, 2014)

$$\mathcal{D}_b \left(\frac{\partial C_{par}}{\partial r}\right)_{r=a} = \frac{1}{4}\alpha_p \bar{c} \left(C_g(a,t) - \frac{C_{par}(a,t)}{H'}\right) \tag{2.13}$$

where C_{par} is the particle-phase concentration, C_g is the vapor-phase concentration, and $H' = HRT$ (dimensionless, where H is an equilibrium partitioning constant for the condensing species that has the nature of a Henry's law coefficient for a dilute particle). Taking the gas-phase concentration, $C_g(r,t)$, to be that at steady state gives

$$C_g(r,t) = C_g^b(t) - \frac{a}{r}\left[C_g^b(t) - C_g(a,t)\right] \tag{2.14}$$

where $C_g^b(t)$ is the bulk gas-phase concentration of the species. Since the interface has no volume, fluxes at the air-particle interface must be equal:

$$\mathcal{D}_b \left(\frac{\partial C_{par}}{\partial r}\right)_{r=a} = \mathcal{D}_g \left(\frac{\partial C_g}{\partial r}\right)_{r=a} \tag{2.15}$$

Combining Equations 2.13–2.15:

$$\mathcal{D}_b \left(\frac{\partial C_{par}}{\partial r} \right)_{r=a} + \frac{\nu}{H'} C_{par}(a,t) = \nu C_g^b(t) \tag{2.16}$$

where $\nu = \left(\frac{4}{\alpha_p \bar{c}} + \frac{a}{\mathcal{D}_g} \right)^{-1}$.

For a constant bulk gas-phase concentration C_g^b, the dynamics of the particle phase, including first-order reaction, obey

$$\frac{\partial C_{par}(r,t)}{\partial t} = \mathcal{D}_b \left(\frac{\partial^2 C_{par}(r,t)}{\partial r^2} + \frac{2}{r} \frac{\partial C_{par}(r,t)}{\partial r} \right) - k C_{par}(r,t), \tag{2.17}$$

where k is the particle-phase first-order reaction rate constant. At $t = 0$,

$$C_{par}(r,0) = C_{par,0} \tag{2.18}$$

where $C_{par,0}$ is the initial concentration of the particle-phase species, and

$$\left(\frac{\partial C_{par}}{\partial r} \right)_{r=0} = 0. \tag{2.19}$$

$$-\mathcal{D}_{b,i} \left(\frac{\partial C_{par}}{\partial r} \right)_{r=a} = \nu \left[\frac{C_{par}(a,t)}{H'} - C_g^b \right] \tag{2.20}$$

Without any particle-phase reactions (i.e., $k = 0$), the solution to Equations 2.17-2.20 is

$$C_{k=0}(r,t) = H' C_g^b \left(1 - \frac{2a}{r} \sum_{n=1}^{\infty} \frac{L \sin \left(B_n \frac{r}{a} \right) e^{-\frac{\mathcal{D}_b B_n^2 t}{a^2}}}{\left[B_n^2 + L(L-1) \right] \sin (B_n)} \right) \tag{2.21}$$

where B_n are the roots of $B_n \cot (B_n) + L - 1 = 0$ and $L = \left(\frac{\nu}{H'} \right) / \left(\frac{\mathcal{D}_{b,i}}{a} \right)$.

The case in which $k \neq 0$ can be related to the pure-diffusion solution by (Liu, Zaveri, and Seinfeld, 2014):

$$C_{par}(r,t) = k \int_0^t C_{k=0}(r,t') e^{-kt'} dt' + C_{k=0}(r,t) e^{-kt} \tag{2.22}$$

From Equation 2.22, the full solution for $C_{par}(r,t)$ with first-order chemical reaction in the particle phase, in which the condensing species in the bulk gas phase, $C_g^b(t)$, is a constant, C_g^b, is:

$$C_{par}(r,t) = H'C_g^b \left\{ k \int_0^t \left[1 - \frac{2a}{r} \sum_{n=1}^{\infty} \frac{L \sin\left(B_n \frac{r}{a}\right) e^{-\frac{\mathcal{D}_b B_n^2 t'}{a^2}}}{\left[B_n^2 + L(L-1)\right] \sin(B_n)} \right] e^{-kt'} dt' \right.$$

$$\left. + \left[1 - \frac{2a}{r} \sum_{n=1}^{\infty} \frac{L \sin\left(B_n \frac{r}{a}\right) e^{-\frac{\mathcal{D}_b B_n^2 t}{a^2}}}{\left\{B_n^2 + L(L-1)\right\} \sin(B_n)} \right] e^{-kt} \right\} \tag{2.23}$$

When particle-phase processes are sufficiently faster than that of C_g^b, a quasi-steady-state approximation holds, and a balance on $C_g^b(t)$ can be coupled to the constant C_g^b in Equation 2.23; if condensation occurs on a monodisperse, identical particle population of total number concentration N, the balance for the condensing species is

$$\frac{dC_g^b(t)}{dt} = -4\pi a^2 N \mathcal{D}_b \left(\frac{\partial C_{par}}{\partial r} \right)_{r=a} \tag{2.24}$$

with initial concentration $C_g^b(0) = C_{g,0}^b$. Applying the boundary condition of Equation (2.20) to Equation (2.24), and assuming that a quasi-steady state holds, we obtain

$$\frac{dC_g^b(t)}{dt} = -4\pi a^2 N v \left[C_g^b(t) - \frac{C_{par}(a,t)}{H'} \right]. \tag{2.25}$$

From Equation 2.23, Equation 2.25 becomes

$$\frac{dC_g^b(t)}{dt} = -4\pi a^2 N v C_g^b(t) \left\{ 1 - k \int_0^t \left[1 - 2 \sum_{n=1}^{\infty} \frac{L e^{-\frac{\mathcal{D}_b B_n^2 t'}{a^2}}}{\left\{B_n^2 + L(L-1)\right\}} \right] e^{-kt'} dt' \right.$$

$$\left. - \left[1 - 2 \sum_{n=1}^{\infty} \frac{L e^{-\frac{\mathcal{D}_b B_n^2 t}{a^2}}}{\left\{B_n^2 + L(L-1)\right\}} \right] e^{-kt} \right\}. \tag{2.26}$$

Subject to the initial condition $C_g^b(0) = C_{g,0}^b$, the solution for $C_g^b(t)$ is

$$\frac{C_g^b(t)}{C_{g,0}^b} = \exp\left\{-4\pi a^2 N\nu\left(1 - k\int_0^t\left[1 - 2\sum_{n=1}^{\infty}\frac{Le^{-\frac{\mathcal{D}_b B_n^2 t'}{a^2}}}{\{B_n^2 + L(L-1)\}}\right]e^{-kt'}dt'\right.\right.$$

$$\left.\left. - \left[1 - 2\sum_{n=1}^{\infty}\frac{Le^{-\frac{\mathcal{D}_b B_n^2 t}{a^2}}}{\{B_n^2 + L(L-1)\}}\right]e^{-kt}\right)\right\}. \tag{2.27}$$

In summary, Equation 2.27 describes the dynamics of a vapor species diffusing to and undergoing first-order reaction in a particle, with H serving as an appropriate gas-particle equilibrium constant.

Figure 2.3 shows the range of timescales for achieving equilibration between the vapor and particle phases at varying values of α_p and $\mathcal{D}_b$, the vapor-particle accommodation coefficient and the particle-phase diffusion coefficient of the condensing species, respectively, for a particle of $D_p = 1000$ nm. The particle phase state regime is indicated on the $\mathcal{D}_b$ axis, proceeding from semi-solid to liquid. For $\alpha_p \gtrsim 10^{-1.5}$ and $\mathcal{D}_b \gtrsim 10^{-13}$ cm^2 s^{-1}, equilibration is *gas-diffusion limited*, whereas for $\alpha_p \gtrsim 10^{-1.5}$ and $\mathcal{D}_b \lesssim 10^{-13}$ cm^{-2} s^{-1}, equilibration is *particle-diffusion limited*. For $\alpha_p \lesssim 10^{-1.5}$, and $\mathcal{D}_b \gtrsim 10^{-13}$ cm^{-2} s^{-1}, equilibration is *interfacial-transport limited*. Figure 2.4 shows the timescale for equilibration as a function of particle diameter D_p and both the dimensionless equilibrium partition coefficient H' and the saturation mass concentration C^* and similarly delineates the limiting processes.

2.2.5 Particle-Particle Coagulation

Particle-particle coagulation is a ubiquitous process in an environmental chamber. Particle-particle coagulation rates depend on the total aerosol number concentration and the range of particle sizes. Upon particle-particle collision, the probability of sticking is represented by the accommodation coefficient, α. For particles significantly larger than the mean free path of air, the value of α has little effect on the rate of coagulation; for particles much smaller than the mean free path of air, the rate of coagulation is directly proportional to α. The coagulation rate is governed by the coagulation coefficient between particles i and j, $K_{i,j}$ (Fuchs, 1964):

$$K_{i,j} = 2\pi\left(\mathcal{D}_{par,i} + \mathcal{D}_{par,j}\right)\left(D_{p,i} + D_{p,j}\right)\left[\frac{D_{p,i} + D_{p,j}}{D_{p,i} + D_{p,j} + 2\left(g_i^2 + g_j^2\right)^{1/2}}\right.$$

$$\left. + \frac{8\left(\mathcal{D}_{par,i} + \mathcal{D}_{par,j}\right)}{\alpha\left(\bar{c}_i^2 + \bar{c}_j^2\right)^{1/2}\left(D_{p,i} + D_{p,j}\right)}\right]^{-1} \tag{2.28}$$
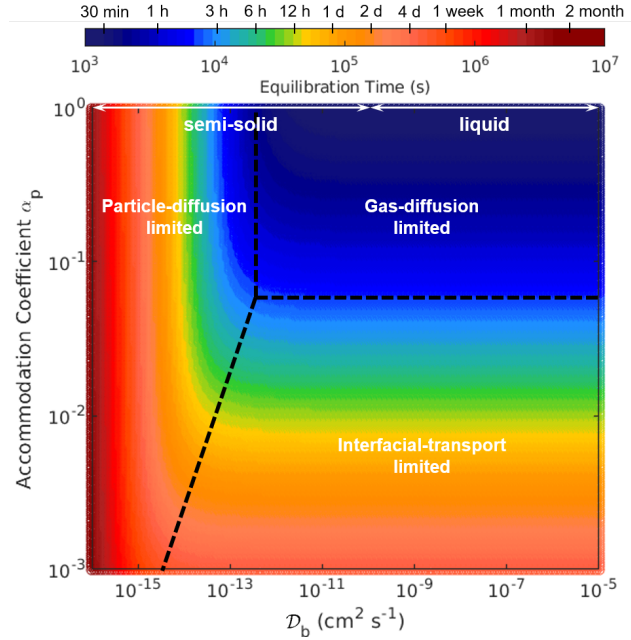
Figure 2.3: Equilibration timescales between vapor and particle phases as a function of the particle-phase diffusion coefficient of the condensing species, $\mathcal{D}_b$, and the vapor-particle accommodation coefficient, α_p. Particle diameter is fixed at 1000 nm, vapor molecular weight is 200 g mol^{-1}, $\mathcal{D}_g = 0.1$ cm^2 s^{-1}, and $H' = 10^{11}$. An equilibration timescale longer than about a week (the typical lifetime of aerosols in the atmosphere), indicative of low particle-phase diffusivity, implies that the particle will not achieve equilibrium with the gas phase during its time in the atmosphere. In this case, the extent of gas-particle partitioning is mostly determined by gas-phase diffusion and interfacial accommodation.

where $\mathcal{D}_{par}$ is particle diffusivity (which is a function of the particle size), $\bar{c}$ is the root-mean-square velocity of the particle, and g_i is the mean distance from the surface of a sphere covered by a particle after moving one mean free path, accounting for relative motion, given by

$$g_i = \frac{\sqrt{2}\pi\bar{c}_i}{24\mathcal{D}_{par,i}D_p}\left[\left(D_{p,i} + \frac{8\mathcal{D}_{par,i}}{\pi\bar{c}_i}\right)^3 - \left(D_{p,i}^2 + \frac{64\mathcal{D}_{par,i}^2}{\pi^2\bar{c}_i^2}\right)^{3/2}\right] - D_{p,i} \quad (2.29)$$

Equation 2.28 does not necessarily assume that the resulting particle is a sphere. However, to be consistent with the general dynamic equation, the volume of coagulated particles is conserved. To simplify the calculation, we use a volume-equivalent spherical diameter as the size of a newly formed particle through coagulation, though this particle could exist in any shape with sufficiently high viscosity. The rate of
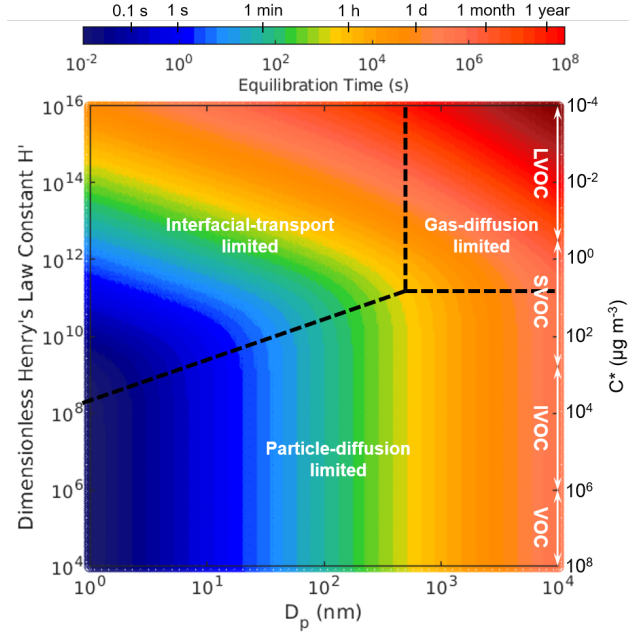
Figure 2.4: Equilibrium timescales between vapor and particle phases as a function of particle diameter, D_p, and dimensionless equilibrium partition coefficient, H'. The three regimes of interfacial transport limited, gas-diffusion limited, and particle-diffusion limited are delineated. Particle-phase diffusivity $\mathcal{D}_b$ is fixed at 10^{-13} cm^2 s^{-1}, vapor molecular weight is 200 g mol^{-1}, $\mathcal{D}_g = 0.1$ cm^2 s^{-1}, particle density $\rho_p = 1$ g cm^{-3}, and accommodation coefficient $\alpha_p = 1$. Saturation mass concentration C^* spans the range from that of a low-volatility organic compound (LVOC) to that that of a semivolatile organic compound (SVOC), intermediate volatility organic compound (IVOC), and a volatile organic compound (VOC).

change of the particle size distribution function, $n(D_p, t)$, owing to coagulation is given by

$$\left(\frac{\partial n(D_p, t)}{\partial t} \right)_{coagulation} = \frac{1}{2} \int_0^v K(v - q, q) n(v - q, t) n(q, t) dq \\ - n(v, t) \int_0^\infty K(q, v) n(q, t) dq \tag{2.30}$$

where $v = \frac{\pi}{6} D_p^3$, q is a dummy volume, and $K(a, b) = K_{i,j}$ where $a = \frac{\pi}{6} D_{p,i}^3$ and $b = \frac{\pi}{6} D_{p,j}^3$. In discrete form, the integrals in Equation 2.30 become sums and the sums are performed over the available bin sizes.

In an SOA-forming system, there will generally be multiple vapor compounds condensing (i.e., different VOC oxidation products) and, so, since the rate of condensation is particle diameter dependent, differently sized particles may have different compositions. Since differently sized particles coagulate, particle composition must

also be tracked in the coagulation process, subject to the constraint that the mass of each component is conserved. One method to accomplish this is to assume that the particle populations remain distinct within each size bin. Since particle populations from different sources tend to be differentiated in composition by size (e.g., smaller particles tend to be of one composition and larger particles of another), and since externally mixed particle populations become internally mixed as coagulation occurs, this is a reasonable approximation.

2.2.6 Deposition of Particles onto Chamber Walls

The rate at which particles deposit onto the walls of an environmental chamber depends on the chamber design parameters. This rate is experimentally evaluated by injecting inert particles with determinable diameters into the chamber and subsequently measuring the size-dependent particle-loss rate by wall deposition. The suspended particle number concentration distribution changes at a rate of

$$\left(\frac{\partial n\left(D_p, t\right)}{\partial t}\right)_{wall\ deposition} = -\beta\left(D_p\right) n\left(D_p, t\right) \tag{2.31}$$

where $\beta(D_p)$, the particle wall deposition coefficient, is a size-dependent parameter experimentally derived for each chamber.

Particle wall deposition results from a combination of gravitational settling and Brownian diffusion (wall deposition can also result from particle charging; we will address this later). The combination of these two processes produces a functional form of $\beta(D_p)$ that for the smallest diameters is dominated by Brownian diffusion, and so decreases as particles get larger. Then, $\beta(D_p)$ reaches a minimum before increasing due to the dominance of particle settling, which increases as particles get larger. See Box 2.3.2. As noted above, the parameters that describe $\beta(D_p)$ are different for each chamber (Charan et al., 2018): a common method for determining $\beta(D_p)$ is to fit the observed $n(D_p, t)$ to the solution of Equation 2.31 (Figure 2.5).

2.2.7 Simultaneous Coagulation and Wall Deposition

Wall deposition and coagulation of particles occur simultaneously in a chamber. Figure 2.6 shows the results of a computational simulation of the dynamics of particle number concentration (panels A-C), surface area concentration (panels D-F), and volume concentration (panels G and H) when considering wall deposition only, coagulation only, and simultaneous coagulation and wall deposition. For wall deposition alone, the fractional change of the particle number concentration
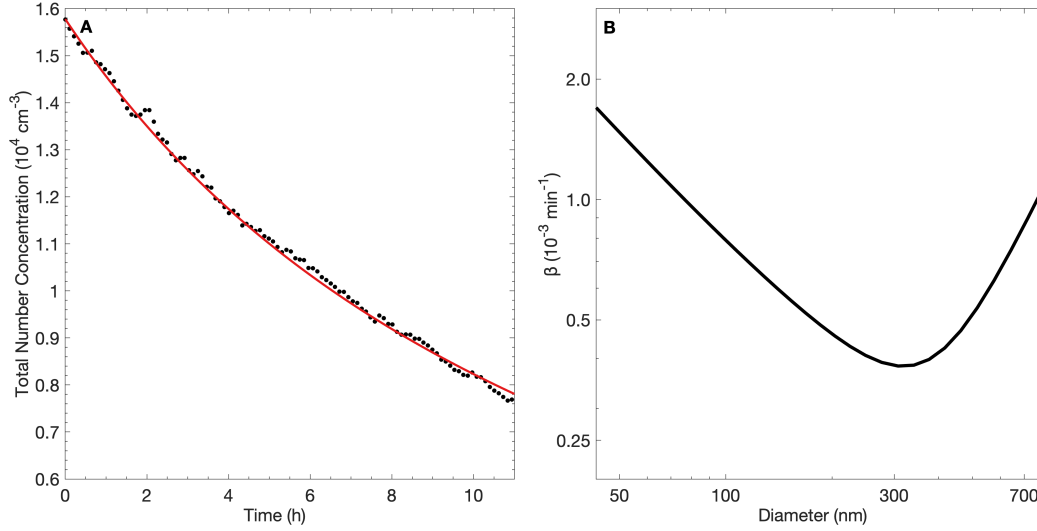
Figure 2.5: Fitting of total particle number concentration decay owing to wall deposition from which to infer the particle wall deposition coefficient $\beta(D_p)$ (panel A). Optimal $\beta(D_p)$ inferred by fitting the decay of particle number concentration with respect to particle diameter D_p (panel B). For this case, in the particle diameter range $\lesssim 3 \times 10^2$ nm, wall deposition is controlled largely by Brownian diffusion, whereas in the range $\gtrsim 3 \times 10^2$ nm, wall deposition is controlled largely by particle settling under gravity.

is independent of the total aerosol number concentration since loss to the wall occurs by first-order decay; thus, panels A, D, and G are independent of the initial particle number concentration. The wall deposition rate does, however, depend on the particle size (for which D_{pg} is a proxy) and is most rapid in the limits of very large and very small particles. For the same initial number concentration (panel B), coagulation generally is more efficient than wall deposition at decreasing the number concentration of small particles. When wall deposition and coagulation occur simultaneously, however, the result is not simply a sum of their individual contributions; as particles coagulate, their numbers decrease but sizes increase, both of which affect the rate of wall deposition in a nonlinear fashion.

2.2.7.1 Determining Parameters in the Presence of Simultaneous Processes

If the only process that changes the suspended aerosol number concentration occurring within the chamber is the deposition of particles onto the chamber walls, one can determine $\beta(D_p)$ from the evolution of the particle size distribution by fitting the solution of Equation 2.31 to the observed decay rate. However, if particle number concentrations are sufficiently high that coagulation is significant, one must

Box 2.2.2: Theoretical Prediction of $\beta(D_p)$ in a Well-Mixed Spherical Chamber

For a well-mixed spherical chamber, an analytic expression for $\beta(D_p)$ is given by (Crump and Seinfeld, 1981):

$$\beta(D_p) = \frac{6\sqrt{k_e \mathcal{D}_{par}}}{\pi r} D_1\left(\frac{\pi v_s}{2\sqrt{k_e \mathcal{D}_{par}}}\right) + \frac{3v_s}{4r} \tag{2.32}$$

where k_e is the eddy-diffusion coefficient of the chamber, r is a characteristic lengthscale for the chamber taken to be the spherical equivalent radius, $r = \left(\frac{3V}{4\pi}\right)^{1/3}$. The particle Brownian diffusivity, $\mathcal{D}_{par}$, is calculated with the slip-corrected Stokes-Einstein-Sutherland relation: $\mathcal{D}_{par} = \frac{kTC_C}{3\pi\mu D_p}$, where k is the Boltzmann constant, and C_C is the Cunningham slip-correction factor:

$$C_C = 1 + \frac{2\lambda}{D_p}\left[1.257 + 0.4\exp\frac{-1.1D_p}{2\lambda}\right] \tag{2.33}$$

with the mean free path of air, λ, given by

$$\lambda = \frac{\mu}{p}\sqrt{\frac{\pi RT}{2M_{air}}} \tag{2.34}$$

where p is the pressure within the chamber, and M_{air} is the molecular weight of air. The first-order Debye function D_1 is

$$D_1(z) = \frac{1}{z}\int_0^z \frac{t}{e^t - 1}dt. \tag{2.35}$$

The terminal particle settling velocity is given by:

$$v_s = \frac{D_p^2 \rho_p g C_C}{18\mu} \tag{2.36}$$

where ρ_p is the density of the particle, g is the gravitational constant, and μ is the viscosity of air. Note that while most chambers are not actively mixed, air currents inside the chamber itself are generally sufficient to maintain a relatively well-mixed state.
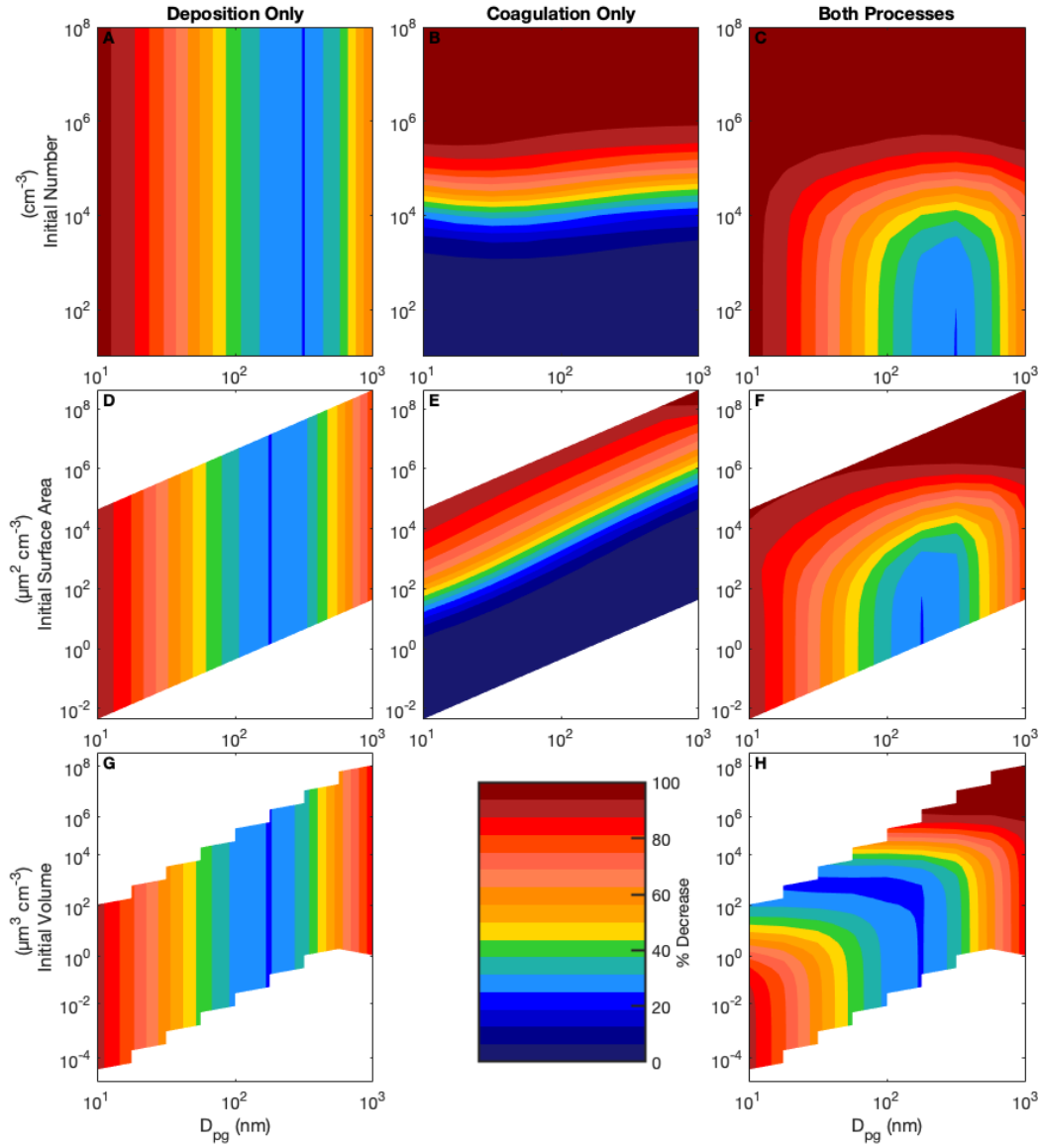
Figure 2.6: Percent decrease in suspended particle number concentration after 10 h of the simulation of wall deposition only, coagulation only, and combined wall deposition and coagulation in particle number (A-C), surface area (D-F), and volume (G and H) concentrations at different initial concentrations and different initial size distributions. D_{pg} (the horizontal axis) is the median diameter of the lognormal distribution simulated. For all distributions, the geometric standard deviation, σ_g, is taken to be 1.5. All simulations were performed with 250 size bins lognormally distributed between 1 and 10^4 nm, $T = 300$ K, and $\rho_p = 1770$ kg m^{-3}. Wall-deposition parameters are those for a 19 m^3 spherical chamber with an eddy-diffusion coefficient of 0.19 s^{-1}.

carefully include the effect of simultaneous coagulation on the measured evolution of the particle distribution evolution when determining $\beta(D_p)$. For example, as shown in Figure 2.6, with an initial number concentration of 10^4 cm^{-3} at $D_{pg} = 100$ nm, the predicted percent change in number concentration over a period of 10 h from wall deposition alone is 39%, from coagulation alone is 30%, whereas from simultaneous coagulation and wall deposition is 53%. When the initial number concentration is 10^3 cm^{-3}, wall deposition alone still leads to a 39% decrease in number concentration over 10 h, whereas coagulation alone causes a 4% decrease; combined, there is a 41% decrease in number concentration.

Combining Equations 2.30 and 2.31 gives the equation governing the evolution of the suspended aerosol size distribution in the absence of condensation, evaporation, or nucleation:

$$
\begin{aligned}
\frac{\partial n(D_p, t)}{\partial t} = {} & \frac{1}{2} \int_0^{D_p} K\left(\left[D_p^3 - q^3\right]^{1/3}, q\right) n\left(\left[D_p^3 - q^3\right]^{1/3}, t\right) n\left(q, t\right) dq \\
& - n\left(D_p, t\right) \int_0^{\infty} K\left(q, D_p\right) n(q, t) dq \\
& - \beta\left(D_p\right) n\left(D_p, t\right)
\end{aligned}
\tag{2.37}
$$

where $K(D_{p,i}, D_{p,j})$ is the coagulation coefficient between particles of diameter $D_{p,i}$ and $D_{p,j}$. $\beta(D_p)$ has a characteristic V-shape in log-log space (Figure 2.5) with a theoretical functional form for a well-mixed spherical chamber given by Equation 2.32. However, since $\beta(D_p)$ depends on the chamber conditions for which its parametric form cannot be derived *a priori*, and since empirical data on wall-deposition rates include the presence of coagulation effects, determining $\beta(D_p)$ requires accounting for coagulation as described in Equation 2.37 subject to the initial condition $n(D_p, 0)$. This determination is achieved by fitting the observed rate of change of $n(D_p, t)$ to the numerical solution of Equation 2.37 such that the objective function (Pierce et al., 2008; Nah, McVay, Pierce, et al., 2017)

$$
J = \int_0^{t_f} \int_{D_{p,lower}}^{D_{p,upper}} \left[n_{obs}(D_p, t) - n_{pred}(D_p, t; k_e)\right]^2 dD_p dt
\tag{2.38}
$$

is minimized, where $n_{obs}(D_p, t)$ is the observed size distribution of suspended particles and $n_{pred}(D_p, t)$ is the predicted size distribution calculated with the assumed $\beta(D_p)$. Minimization functions other than Equation 2.38 can be used to prioritize, for example, aerosol size bins with a smaller error in counting statistics (Charan et al., 2018; Schwantes, Charan, et al., 2019).

The particle wall deposition function $\beta(D_p)$ has been determined using other methods than that described above. Pierce et al. (2008) solved for wall deposition at each computational timestep, providing a time-dependent β parameter. Wang et al. (2018) used an adapted version of this model from Nah, McVay, Pierce, et al. (2017) that explicitly accounts for coagulation to represent deposition both before and after an experiment and evaluated the change in wall deposition rates for a particular chamber over a period of years. Loza, Chhabra, et al. (2012) and Hildebrandt, Donahue, and Pandis (2009) assumed that wall-deposition and condensation rates are independent of particle size, and used the measured organic to inorganic ratio in the bulk particle phase to determine overall wall loss.

2.2.7.2 Bounds on Interactions of Vapor Molecules with Particles Deposited on the Chamber Walls

During a chamber experiment, every particle depositing on the chamber wall carries with it the organic oxidation products that have condensed on it from the beginning of oxidation. When calculating the overall SOA yield, one must track these particle-borne organic oxidation products that have been taken up by the chamber wall to avoid underestimating the yield. Wall-deposited particles may also continue to serve as condensation sinks for oxidation products in the bulk of the chamber. Since the magnitude of this interaction is unclear, the contribution of wall-deposited particles as a condensation sink is understood to fall between two limiting assumptions (Hildebrandt, Donahue, and Pandis, 2009; Loza, Chan, et al., 2010). In the *lower bound*, as soon as a particle deposits on the chamber wall, it no longer interacts with the gas-phase bulk species. In the *upper bound*, a wall-deposited particle acts exactly like a suspended particle and continues to take up bulk gas-phase species at the same rate. It is as if, in the upper limit, deposited and suspended particles are identical, since one also assumes that after deposition a spherical particle remains spherical and, therefore, maintains its surface area.

Figure 2.7 shows the effect of the mass accommodation coefficient α_{pw} on the partitioning of organic matter to particles inside the chamber; that is, the extent to which organic aerosol is located on suspended versus deposited particles. Even at the end of an experiment in the lower bound case ($\alpha_{pw} = 0$), SOA will exist on some deposited particles ($\Delta SOA_{dep} \neq 0$). This SOA is that formed on suspended particles before those particles deposited onto the wall. Simulated experiments can provide limits on the SOA yield based on limits of α_{pw} (Trump et al., 2016).

Table 2.1: Nominal values of parameters used in simulations.

Parameter	Value	Units
α_p	10^{-3}	
α_{pw}	0	
α_w	10^{-7}	
C_w	10	mg m^{-3}
$C_A^*, C_B^*, C_C^*, C_D^*$	10^2, 10, 1, 10^{-1}	µg m^{-3}
D_{pg}	150	nm
$k_{A,OH}, k_{B,OH}, k_{C,OH}$	1, 5, 25	10^{-4} s^{-1}
k_e	0.2	s^{-1}
N	10^4	cm^{-3}
σ	28.21	dyn cm^{-1}
σ_g	1.5	
Δt	60	s
T	25	°C
p	10^5	Pa
ρ_p	1770	kg m^{-3}

2.2.8 Deposition of Vapor Molecules onto Chamber Walls

Molecular and turbulent diffusion both contribute to the transport of gas-phase species from the well-mixed bulk of the chamber to the wall's boundary layer; when a vapor molecule finally arrives at the wall, the probability that it is taken up is given by α_w (denoted as α_w as distinct from α_p), which is a function of the wall surface as well as of the chemical properties of the vapor. FEP Teflon, a polymer film commonly used for chambers, can be treated as an infinite medium for the dissolution of vapor molecules (Vieth, Howell, and Hsieh, 1976; Frisch, 1980). Matsunaga and Ziemann (2010) first proposed the concept of C_w, that governs the vapor-wall partitioning equilibrium in a similar manner to the way that gas-particle partitioning is governed. Equilibrium vapor-wall partitioning of organic substances has been verified by a number of studies (Loza, Chan, et al., 2010; Matsunaga and Ziemann, 2010; Zhang, Cappa, et al., 2014; Krechmer, Pagonis, et al., 2016; Ye, Zhao, et al., 2018; Kokkola et al., 2014) and facilitates the description of the competitive sinks of vapor molecules in chamber experiments (McVay, Cappa, and Seinfeld, 2014; Yeh and Ziemann, 2014; Bian et al., 2015; Krechmer, Coggon, et al., 2015; Zhang, Schwantes, et al., 2015; Cappa, Jathar, et al., 2016; La et al., 2016; Nah, McVay, Zhang, et al., 2016; Trump et al., 2016). If $C_w \rightarrow \infty$, the wall presents essentially a perfectly absorbing medium. Note that C_w might be a characteristic of the chamber wall material (e.g., FEP Teflon) or of organic material
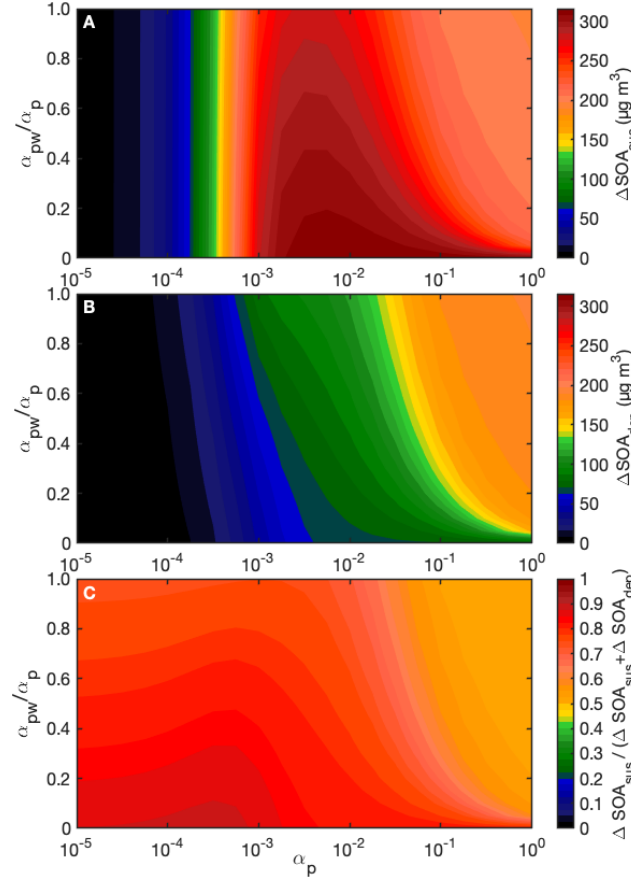
Figure 2.7: SOA on particles suspended in the bulk of the chamber (A), on particles deposited onto the chamber walls (B), and the fraction of SOA on suspended particles (C) shown as a function of α_p itself and of the ratio between the mass accommodation coefficient of a vapor molecule to a wall-deposited particle (α_{pw}) and that to a suspended particle (α_p). Due to the boundary layer at the chamber wall, $\alpha_{pw} \leq \alpha_p$; in the absence of a boundary layer, $\alpha_{pw} = \alpha_p$. So, limits on calculated yields can be determined by evaluating the difference between ΔSOA_{sus} at $\alpha_{pw} = 0$ and at $\alpha_{pw} = \alpha_p$. All parameters match those in Table 2.1 unless otherwise noted. Simulations carried out for 10 h. Because of competition with vapor-wall deposition, the total SOA formed is small for $\alpha_p \ll 1$, but the fraction of the aerosol that is on suspended particles is large in this region.

already accumulated on the wall. Efforts have been made to quantify the value of C_w and the corresponding timescale to reach vapor-wall equilibrium, τ_{vwe} (Zhang, Cappa, et al., 2014; Yeh and Ziemann, 2015; Krechmer, Pagonis, et al., 2016; Ye, Ding, et al., 2016). Within the temperature range that chamber experiments are carried out, FEP Teflon exists in a glassy state for which kinetic dissolution describes the slow molecular diffusion inside the polymer, a process that depends on the chemical nature of the vapor molecules (Crank, 1953). The challenge then
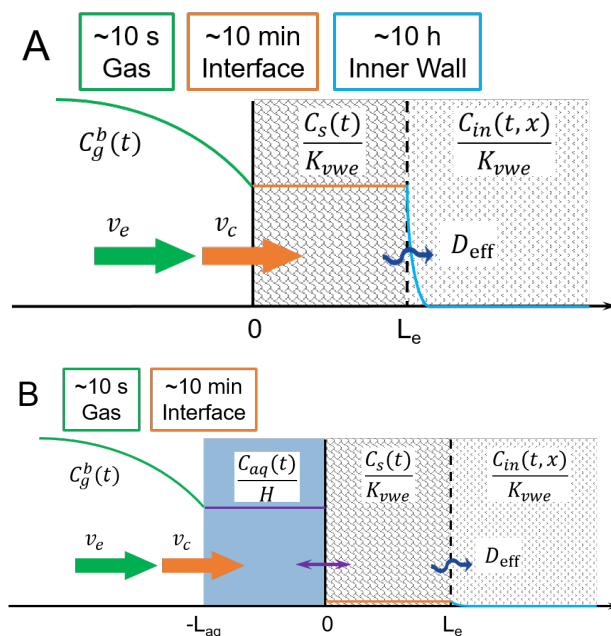
Figure 2.8: Models of vapor uptake into Teflon film in (A) a dry, two-layer system and (B) a moist, three-layer laboratory chamber wall. The boundary layer mass transport by eddies and surface accommodation velocities are v_e and v_c, respectively. The bulk gas-phase concentration is $C_g^b(t)$; $C_s(t)$ and $C_{aq}(t)$ are the (rapidly achieved) uniform concentrations within the surface layer of thickness L_e and the aqueous film of thickness L_{aq}, respectively. C_{in} is the transient inner-layer concentration.

arises of quantifying a compound-dependent C_w and the associated equilibration timescale.

Huang et al. (2018) proposed a unified theory to reconcile the observed dissolution timescale τ_{vwe} with the conventional concept of C_w, leading to a two-layer kinetic sorption model (Figure 2.8). Vapor molecules that have passed through the boundary layer between the bulk and chamber wall gas-phases first encounter an interfacial region of the wall, where the Teflon polymer is swollen and, therefore, nearly stress-free. In this region, the timescale for vapor-wall equilibrium is quite short. From this outer region, the molecules slowly diffuse further into the polymer by breaking inter-molecular forces between poly-molecular chains, but are impeded by the polymer network. In the outer region of the wall, the estimated timescale for a pseudo-steady-state profile is just 10 s; the dissolution timescale in the inner wall layer is 10 min (Huang et al., 2018; Krechmer, Pagonis, et al., 2016).

The process of partitioning as dominated by the parameter C_w corresponds to absorption of vapor molecules by surface layer. The compound-dependent version

of this parameter, defined as $C'_w = \dfrac{C_w}{\gamma^\infty}$ incorporates a specific compound's activity in an FEP Teflon wall, where γ^∞ is the solute activity coefficient in Teflon. The empirical expression relating γ^∞ and vapor saturation concentration C^* estimated by the EVAPORATION parameterization is (Tropo, 2014; Compernolle, Ceulemans, and Müller, 2011)

$$\log_{10}(\gamma^\infty) = a_1 \log_{10}(C^*) + b_1 \tag{2.39}$$

where $a_1 = -6.407 \pm 0.0375$ and $b_1 = 3.299 \pm 0.147$ (Huang et al., 2018). For most organic compounds, $\gamma^\infty > 1$, indicating a preference for the gas phase.

By introducing γ^∞, the compound dependence of C_w is removed, and thus C_w can be represented in terms of the surface layer thickness L_e, the density of FEP material $\rho_w = 2150$ kg m^{-3} (Boedeker, 2017), and the surface-to-volume ratio of the chamber $\dfrac{A}{V}$. Based on measurements of C_w (Matsunaga and Ziemann, 2010; Yeh and Ziemann, 2015; Krechmer, Pagonis, et al., 2016), a value of $L_e = 5$ nm can be assumed corresponding to a $C_w = L_e \rho_w \dfrac{A}{V} = 32.2$ mg m^{-3} for $\dfrac{A}{V} = 3$ m^{-1} (Krechmer, Pagonis, et al., 2016; Yeh and Ziemann, 2015). The surface layer is swollen and stress-free so that the diffusivity of molecules is of order 10^{-13} m^2 s^{-1} (Tokarev et al., 2006), determining a timescale for uniform concentration within the surface layer of ~1 ms. This is consistent with the assumption of equilibrium absorption in the surface layer.

The dimensionless equilibrium constant between vapor and wall, K_{vwe}, is analogous to a Henry's law constant and given by $K_{vwe} = \dfrac{\rho_w}{\gamma^\infty C^*} \dfrac{M_{voc}}{M_w}$, where C^* represents the saturation vapor mass concentration, M_{voc} is the molecular weight of the VOC and $M_w = 200$ g mol^{-1} is the molecular weight of the FEP film (Matsunaga and Ziemann, 2010), respectively. Equation 2.39 estimates γ^∞, the compound activity coefficient in Teflon.

The mass transport coefficient within the gas-phase boundary layer is given by $v_e = \dfrac{2}{\pi}\sqrt{k_e \mathcal{D}_g}$, where $\mathcal{D}_g$ is the diffusivity of vapor molecules in air and k_e is the chamber eddy-diffusion coefficient. Estimates of k_e for actively mixed chambers are between 0.02 and 0.12 s^{-1}; for those chambers without active mixing, k_e is between 0.015 and 0.075 s^{-1} (Zhang, Cappa, et al., 2014). The vapor-Teflon transport coefficient is $v_c = \dfrac{\alpha_w v}{4}$, where v is the average velocity of vapor molecules, and α_w is the accommodation coefficient of vapor molecules to the Teflon wall. An empirical relationship has been established between α_w and C^* for FEP Teflon

(Huang et al., 2018):

$$\log_{10}(\alpha_w) = a_2 \log_{10}(C^*) + b_2 \tag{2.40}$$

where $a_2 = -0.6566 \pm 0.2514$ and $b_2 = -2.744 \pm 1.233$.

The overall mass transport coefficient, then, from the bulk chamber into the outer layer, is $v_l = \left(\dfrac{1}{v_e} + \dfrac{1}{v_c}\right)^{-1}$ (Seinfeld and Pandis, 2016). The mass balance for the bulk gas-phase concentration, C_g^b, including both the mass transfer from the bulk to the wall and the gas-phase chemical reactions is:

$$\frac{dC_g^b(t)}{dt} = -k_{vw} C_g^b(t) + k_{wv} C_s(t) + \sum^i R_i \tag{2.41}$$

where $k_{vw} = \left(\dfrac{A}{V}\right) v_l$ is the transfer rate coefficient from gas phase to the wall, $k_{wv} = \left(\dfrac{A}{V}\right) v_l \dfrac{\gamma^\infty C^*}{\rho_w} \dfrac{M_w}{M_{voc}}$ is the transfer rate coefficient from wall to gas phase, C_s is the concentration of dissolved vapor in the wall surface layer, and $\sum^i R_i$ is the net accumulation rate of the species through chemical reaction and vapor-particle partitioning.

The mass balance for C_s is given by:

$$\frac{dC_s(t)}{dt} = k_{vw} C_g^b(t) - k_{wv} C_s(t) + \frac{1}{A L_e} J_d|_{x=L_e} \tag{2.42}$$

where $J_d|_{x=L_e} = -A \mathcal{D}_{\text{eff}} \left.\dfrac{\partial C_{in}(x,t)}{\partial x}\right|_{x=L_e}$ is the diffusive flux from the surface layer to the inner layer at the boundary between them, and $\mathcal{D}_{\text{eff}}$ is the effective diffusivity of vapor molecules in the inner layer (Figure 2.8). For long experiments (on the order of hours), $\mathcal{D}_{\text{eff}}$ is the key parameter in determining the bulk gas-phase concentration, $C_g^b(t)$. $\mathcal{D}_{\text{eff}}$ depends on the state of the Teflon film, which is typically either partially liquid and partially solid (and composed of immobile micro-voids) or glassy (Frisch, 1980). According to dual sorption theory, unlike in a liquid, diffusion occurs after Langmuir adsorption equilibrium on the local micro-voids inner surface is established (Vieth, Howell, and Hsieh, 1976), which makes the diffusion of molecules in a polymer smaller than that in a liquid (10^{-13} to 10^{-9} m^2 s^{-1}) (Shiraiwa, Ammann, et al., 2011). Therefore, the inner-layer $\mathcal{D}_{\text{eff}}$ of molecules is of order 10^{-22} to 10^{-17} m^2 s^{-1}, corresponding to semi-solid diffusivities (Shiraiwa, Yee, et al., 2013). Huang et al. (2018) created an empirical expression relating $\mathcal{D}_{\text{eff}}$

and C^* through fitting $\mathcal{D}_{\text{eff}}$ with the time-dependent decay of a variety of species in a Teflon chamber due to wall uptake: the third term on the right side of Equation 2.42 can be approximated as a first-order decay of $C_s(t)$, with decay rate k_{si} (s^{-1}), the value of which is based on the empirical expression:

$$\log_{10}(k_{si}) = a_3 \log_{10}^2(\mathcal{D}_{\text{eff}}) + b_3 \log_{10}(\mathcal{D}_{\text{eff}}) + c_3 \tag{2.43}$$

where $a_3 = -0.055 \pm 0.040$, $b_3 = 2.574 \pm 1.568$, and $c_3 = 24.43 \pm 15.33$. If $\mathcal{D}_{\text{eff}}$ is small enough that there is minimal diffusion into the inner layer of the chamber wall over the course of an experiment, one can assume a single-layer sorption model with a vapor-wall equilibrium timescale (τ_{vwe}) of:

$$\tau_{vwe} = \left(\frac{A}{V}\right)^{-1} \left(1 + \frac{1}{K_w L_e} \frac{V}{A}\right)^{-1} v_l^{-1} \tag{2.44}$$

If the compound in question is injected into the chamber, the initial conditions for Equations 2.41 and 2.42 are $C_g^b(0) = C_{g0}^b$ and $C_s(0) = C_{g0}^b \dfrac{k_{vw}}{k_{wv}}$; the initial conditions are $C_g^b(0) = C_s(0) = 0$ if generated *in situ*.

As the relative humidity (RH) in the chamber becomes sufficiently high (e.g., RH > 90%), a film of water forms on the wall of the chamber (Figure 2.8B, assuming the film thickness is L_{aq}). The molecular diffusivity in the aqueous phase $\mathcal{D}_{aq}$ is ~10^{-9} m^2 s^{-1} (Schwarzenbach, Gschwend, and Imboden, 2005), thus the timescale $\left(\dfrac{L_{aq}^2}{\mathcal{D}_{aq}}\right)$ to obtain a uniform dissolved vapor concentration in the thin water layer is small (e.g., ~10^{-1} s when $L_{aq} = 10$ μm) such that the vapor uptake rate at high RH is no longer limited by condensed-phase diffusion. γ^∞ of oxidized vapors in the water layer is usually smaller than that in Teflon film since oxidized molecules are polar, such that partitioning to the water layer is more favorable than to the Teflon film. Thus, it is reasonable to assume that at high RH, vapors exclusively partition to the aqueous layer on the Teflon surface. This case then can be described by a single-layer model, which uses Equation 2.44 with L_e and K_{vwe} replaced by L_{aq} and the Henry's law constant H, respectively.

2.2.9 Charge Effects in the Environmental Chamber

2.2.9.1 Particle Charging

The atmosphere as well as the laboratory are constantly affected by the omnipresence of small air ions, termed cluster ions. Cluster ions arise from a number of sources, including galactic cosmic rays, radioactive decay in soil, and splashing

water (Hirsikko, Nieminen, et al., 2011). Cluster ions can serve as sites for vapor nucleation (Laakso, Kulmala, and Lehtinen, 2003), but they also diffuse quickly to suspended particles and impart their charge onto them.

Field charging occurs when cluster ions drift along electric field lines and impinge on particles. *Diffusion charging* results from thermal collisions between ions and particles. Diffusion charging can be delineated into *bipolar charging*, in which positive and negative ions impact the particle and *unipolar charging*, where particles are exposed to ions of a single charge. Diffusion charging is the dominant atmospheric mechanism involving particles of diameter $\lesssim$ 400 nm. Unipolar and bipolar diffusion charging between ions and particles can be described analogously to particle-particle coagulation, with the collision mechanism governed by the magnitude of the Knudsen number, Kn= $2\lambda_{ion}/D_p$ (λ_{ion} is the ion mean free path). In the continuum and slip flow regimes (Kn $\leq$ 0.25 or $D_p \geq$ 500 nm), ions move to the surface by Brownian diffusion. In the free molecule regime, the ion mean free path considerably exceeds typical particle diameters. As in the transition regime of molecular diffusion to particles, the ion collision probability is a combination of free molecule and continuum mechanisms. When the bipolar ion concentration greatly exceeds the particle number concentration, the particle charge distribution attains an equilibrium state.

Most aerosol particles are electrically charged; some are charged during generation and others by contact with ions. Particles generated by condensation following evaporation tend to reach a Boltzmann charge distribution, whereas the charge state of aerosols generated by drying after atomization depends on the atomization solution and the charge conditioner (also called a neutralizer). Charge conditioners typically employ soft x-rays or radiation sources that subject particles to bombardment with ions.

Diffusion charging of particles by bipolar ions plays an important role in determination of aerosol size distributions based on their electrical mobility. In bipolar charging, both equal and unequal concentrations of positive and negative ions can be used. For particles with $D_p \lesssim$ 100 nm, diffusion of ions to particles is the predominant charging mechanism. In general, when particles are charged in an environment of unequal concentrations of bipolar ions, the charge attained on the particles depends on the ratio of the product of number concentrations and ion mobilities of negative and positive ions. The charge distribution in equal bipolar charging attains a steady state that does not depend on the initial particle charge for

a sufficiently large ion number concentration.

Typical ion concentrations in an indoor urban environment are on the order of 10^3 cm^{-3} for both negatively and positively charged ions (Hirsikko, Yli-Juuti, et al., 2007). In theory, a statistical charge distribution can be calculated if the rate of cluster ion production is known (López-Yglesias and Flagan, 2013b). However, since cluster ions are produced by galactic cosmic rays, it is difficult to ensure a constant, reproducible ion concentration in the laboratory. Moreover, such calculations can be computationally intensive and require assumptions about the ion mobilities that may not always be uniform.

A rich body of literature exists addressing the charge distribution of particles at steady-state exposed to an atmosphere of abundant cluster ions (Hoppel and Frick, 1986). Neutral particles obtain charge upon collision with the almost equal numbers of abundant positive and negative clusters, whereas charged particles attract clusters of opposite polarity and are neutralized. With these processes, the collection of particles and ion clusters eventually reaches a stationary equilibrium charge state (Fuchs, 1963; Hoppel and Frick, 1986; Hoppel and Frick, 1990). This steady-state equilibrium has been parameterized by Wiedensohler (1988) for radioactive sources (Figure 2.9) and by Tigges, Jain, and Schmid (2015) for soft X-ray irradiation in dry ambient air.

The probability of an individual particle having a charge increases with its size; there is a <10% chance that particles with diameters smaller than 155 nm have charge more negative than $-1e$ and that particles with diameters smaller than 255 nm have a charge more positive than $+1e$. Cluster ions are usually produced in pairs. The negatively charged cluster ions are smaller (since they are often just an electron); consequently, the negatively charged cluster ions have a higher mobility. Thus the steady-state distribution comprises slightly more negatively charged than positively charged particles. Note that, at steady-state, particles are constantly exchanging charges as they coagulate with other charged or uncharged particles and are hit by fresh cluster ions.

To achieve reproducibility between experiments and to ensure that particle atomization does not lead to a pronounced ion preference, seed particles are customarily flowed through a charge conditioner device prior to introduction into the chamber. Nevertheless, it cannot necessarily be assumed that particles in the chamber maintain a steady-state charge distribution. Cluster ions present in environmental chambers in lower concentrations than those required for steady state or preferential
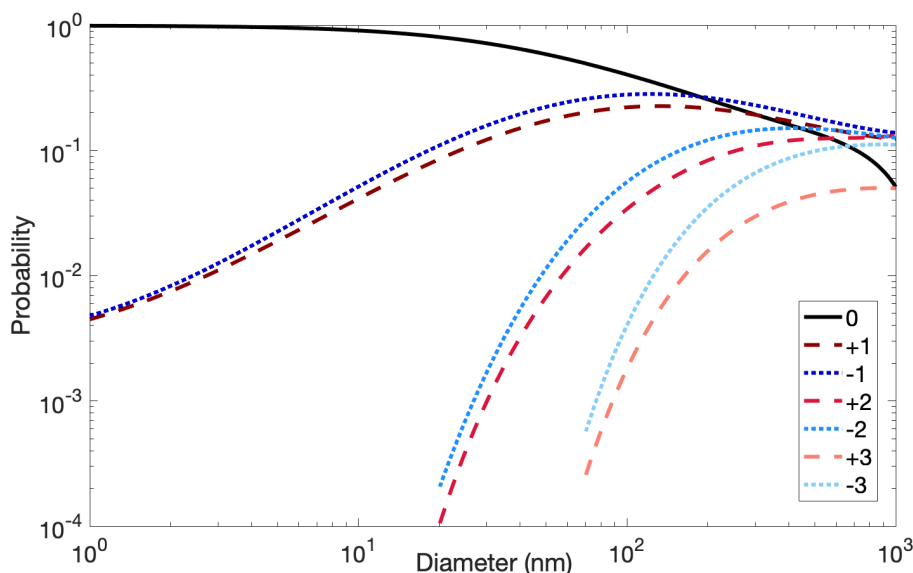
Figure 2.9: Approximate steady-state charge distribution derived from an empirical fit to theoretical cluster ion diffusion rates from Wiedensohler (1988) after a particle population encounters a high ion concentration (as in a diffusion charger). In steady-state, the probability of a particle having one or multiple charges is dependent on the particle size. An evaluation of the accuracy of this model and of other charge-distribution approximations is provided by López-Yglesias and Flagan (2013a).

loss of charged particles may change the charge distribution over time. In this way, the particle charge distribution can be affected by the presence of an electric field, for instance that induced by Teflon chamber walls. See Box 2.2.3.

2.2.9.2   Chamber Charge

Chambers acquire charge in much the same way that latex balloons do: via contact with non-conductive objects in their environment. The presence of charge on chamber walls can induce additional particle deposition beyond that arising from purely dynamical effects. A small ($\sim$0.25 m^3) charged Teflon chamber was estimated by McMurry and Rader (1985) to exhibit a mean electric field within the chamber of $\sim$ 45 V cm^{-1}. The presence of such an electric field over a period of 20 h has been shown to lead to a final particle number concentration < 50% of that in the absence of the electric field (Charan et al., 2018).

Typical charging from interactions with cloth for fewer than 5 min can lead to estimated electric fields on larger (19 m^3) Teflon chambers of 26 to 55 m V cm^{-1} (Charan et al., 2018). Incidental interactions (e.g., adjustments of sample lines)

Box 2.2.3: Measuring Particle Size and Charge Distribution

Instead of directly measuring the particle size distribution, instruments actually measure the particle electrical mobility distribution from the electrical migration velocity in an electric field (Flagan, 2014). The overall measurement process involves charging the particles by flowing them through a charge conditioner to achieve a known charge distribution (see Figure 2.9), separating the charged particles in an electric field orthogonal to the fluid field (in the so-called differential mobility analyzer, DMA), and counting the separated particles with a condensation particle counter. Depending on the purpose of measurement, the entire setup of the instruments can be called a differential mobility particle sizer (DMPS, DMA in stepping mode) or a scanning mobility particle sizer (SMPS, DMA in scanning mode) (Wiedensohler, Wiesner, et al., 2018).

A diffusion charger is usually employed to change the charge states of the particles. This can involve radioactive sources (^{85}K, ^{210}Po, ^{241}Am, etc.), soft X-ray irradiation, or corona discharge (unipolar) (Kallinger and Szymanski, 2015). Inside the diffusion charger, primary ions (e^-, N_2^+, O_2^+), generated from ionization of the carrier gas molecules, cluster with the most abundant species in the carrier gas (based on their proton affinity and polarity) to form large clusters (Steiner and Reischl, 2012). This actively charging process can be predicted theoretically, which can be applied for particle size measurement.

In the ambient atmosphere, because of the existence of ubiquitous ions (e.g., induced by galactic cosmic rays), many particles are charged. To determine the ambient particle charge distribution, one measures and compares the particle mobility distribution in the presence and absence of a diffusion charger (Buckley, Wright, and Henshaw, 2008): a known charge distribution is obtained with the diffusion charger and then the charge distribution can be obtained by the difference between the particle counts measured with and without the charger.

have been observed to generate a sustained electric field on the walls (Wang et al., 2018). Importantly, it is possible to reduce, or even eliminate, the charge on Teflon walls by limiting interactions of the chamber with its surroundings, achieved for example, by maintaining a chamber that is always filled, suspended, and isolated from interactions with its environment.

2.2.9.3 Effect of Particle Charge on Particle Dynamics

The presence of particle charge can affect each of the processes of evaporation/condensation, coagulation, nucleation, and wall deposition. Although the presence of particle charge may also affect particle growth rates, this effect is
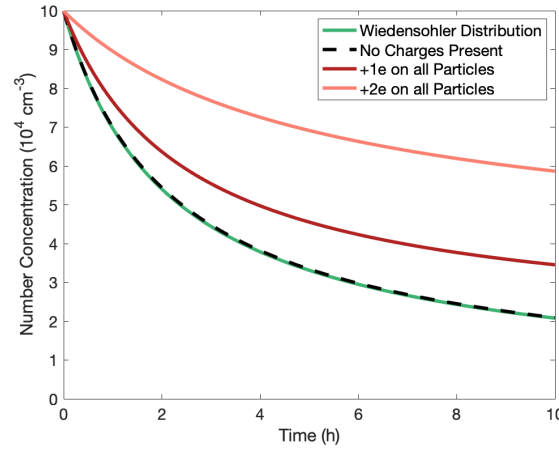
Figure 2.10: Effect of particle charge on decay of particle number concentration by coagulation. When the absolute value of the net charge on the particle population is substantial, particle charge can significantly affect coagulation rates. In a steady-state charge distribution, such as that given by Wiedensohler (1988), there is little difference in the total coagulation rate over the entire particle population than that in the absence of charges. Conditions for the simulation are a computational timestep of 1 min, simulation for 10 h, 50 size bins log-normally distributed between 30 and 800 nm, D_{pg} = 100 nm, and σ_g = 1.5. In this simulation, there is no wall deposition or condensation. To demonstrate the effect of the initial particle charge distribution, small air ions are assumed not to be present.

small for particles larger than the nucleation range. Thus, charge-induced effects on condensation/evaporation in chambers are generally negligible in the presence of seed particles (Laakso, Kulmala, and Lehtinen, 2003).

Particle-Particle Coagulation In the presence of a substantially uneven charge distribution over the particle population, particle charge can exert a significant effect on coagulation rate (Figure 2.10) (Charan et al., 2018; Ghosh et al., 2017). The effect of particle charge on the rate of coagulation is mathematically represented with a correction factor of $\frac{\kappa}{e^\kappa - 1}$ to the Brownian coagulation kernel (Equation 2.28). κ is given by

$$\kappa = \frac{n_{c,i} n_{c,j} e^2}{2\pi \epsilon_0 \epsilon (D_{p,i} + D_{p,j}) k_B T} \tag{2.45}$$

where ϵ is the dielectric constant of air and ϵ_0 is the permittivity of free space (Seinfeld and Pandis, 2016; Charan et al., 2018).

Figure 2.10 shows the simulated total particle number concentration evolution un-

dergoing solely coagulation over a period of 10 h beginning with an identical size distribution and number concentration but with different initial charge distributions. When the charge on all particles has the same sign (+1 or +2, shown in dark and light red, respectively), then, owing to repulsive forces, coagulation is slowed as compared to the case of the absence of charges (shown as a dashed, black curve).

In a steady-state charge distribution, that which is assumed to result from passing particles through a charge conditioner (Kallinger and Szymanski, 2015), both polarities are present in proportions dependent on the particle size (Figure 2.9), as discussed above. In this distribution, similarly charged particles repel one another, and oppositely charged particles attract, the result of which is that the effect of charge on coagulation is essentially nullified. Consequently, the total particle number concentration evolution that begins with the Wiedensohler distribution (dark green curve in Figure 2.10) closely follows that in the absence of charges.

In general, as long as positively and negatively charged small air ions are present at essentially similar concentrations, which is usually the case under chamber conditions in which ions are not actively produced (Hirsikko, Yli-Juuti, et al., 2007), the effect of particle charge on coagulation can be neglected (e.g., $< 1\%$ difference in number concentration over 20 h for an initial concentration of 2×10^4 cm^{-3}) (Charan et al., 2018).

Particle Wall Deposition For a spherical chamber with a mean electric field as experienced within the chamber of $\bar{E}$, and assuming a symmetry of positive and negatively charged particles, the first-order particle wall deposition coefficient for a particle carrying net n_c charges is (McMurry and Rader, 1985)

$$\beta_{n_c}(D_p) = \frac{3\sqrt{k_e \mathcal{D}_{par}}}{\pi r x} \left\{ \frac{(x+y)^2}{2} + (x+y)D_1(x+y) + (x-y)D_1(x-y) \right\} \quad (2.46)$$

where $x = \frac{\pi v_s}{2\sqrt{k_e \mathcal{D}_{par}}}$, $y = \frac{\pi \bar{v}_e}{2\sqrt{k_e \mathcal{D}_{par}}}$, and the electrostatic migration velocity ($\bar{v}_e$) has magnitude

$$\bar{v}_e = \left| \frac{n_c e C_C \bar{E}}{3\pi\mu D_p} \right| \quad (2.47)$$

where e is the elementary charge, and all other parameters are defined in Section 2.2.6.

The coefficient of particle deposition rate, $\beta_{n_c}(D_p)$, in a given chamber with approximately constant $\bar{E}$ is a function only of particle size and charge (see Figure 2.11A).

If the particle charge distribution for each particle size remains the same throughout an experiment, the rate of wall deposition is a function only of diameter. For example, if each suspended particle maintains a zero charge throughout an experiment, the rate of particle wall deposition will not change in time and is represented by the black curves in both panels of Figure 2.11 for the given parameters; if $n = 0$, then $\bar{v}_e = 0$, so $\beta_{n_c}(D_p)$ for fixed k_e is a function only of v_s, which is a function only of D_p. Similarly, in the absence of a mean electric field on the chamber walls ($\bar{E} = 0$), then $\bar{v}_e = 0$ and $\beta_{n_c}(D_p)$ is again a function only of particle diameter.

The charge distribution of a particle population may change over time, in which case the wall deposition rate depends upon both particle diameter and particle charge. Since particle charge changes upon coagulation or collision with cluster ions and is generally not tracked, the size-resolved charging probability likely changes with time. If so, $\beta(D_p)$ would appear to change with time; in reality, this behavior is merely the result of the evolution of the charge distribution. Figure 2.11B shows the effect of a changing charge distribution on the rate of wall deposition in the absence of cluster ions.

The effect of charge on particle wall deposition can be addressed in one of three ways (Charan et al., 2018): (1) $\bar{E}$ can be reduced by minimizing physical interactions between the Teflon chamber and its surroundings so that the wall-deposition coefficient, $\beta_{n_c}(D_p)$, is, as closely as possible, a function only of particle size. In this case, the procedure described in Section 2.2.6 can be carried out, in which the the minimization function (Equation 2.38) depends only on the single-parameter k_e. If charge effects are non-negligible, in procedure (2) ideally one must measure both the particle charge distribution and the particle size distribution.

The optimization procedure described in Section 2.2.6 can then be carried out with $\beta_{n_c}(D_p)$ in Equation 2.46 replacing $\beta(D_p)$. Because Equation 2.46 depends on both the size and charge of each particle, these quantities are varied in the minimization procedure. The objective function is then

$$J = \int_0^{t_f} \int_{D_{p,lower}}^{D_{p,upper}} \int_{-\infty}^{\infty} \left[n_{obs}(D_p, n_c, t) - n_{pred}(D_p, n_c, t; k_e, \bar{E}) \right]^2 dn_c dD_p dt$$

(2.48)

where n_c is the number of elementary charges on a particle. The two-parameter minimization is carried out to determine both k_e and $\bar{E}$. It is reasonable to assume that $\bar{E}$ is relatively constant over the course of an experiment, since electric fields
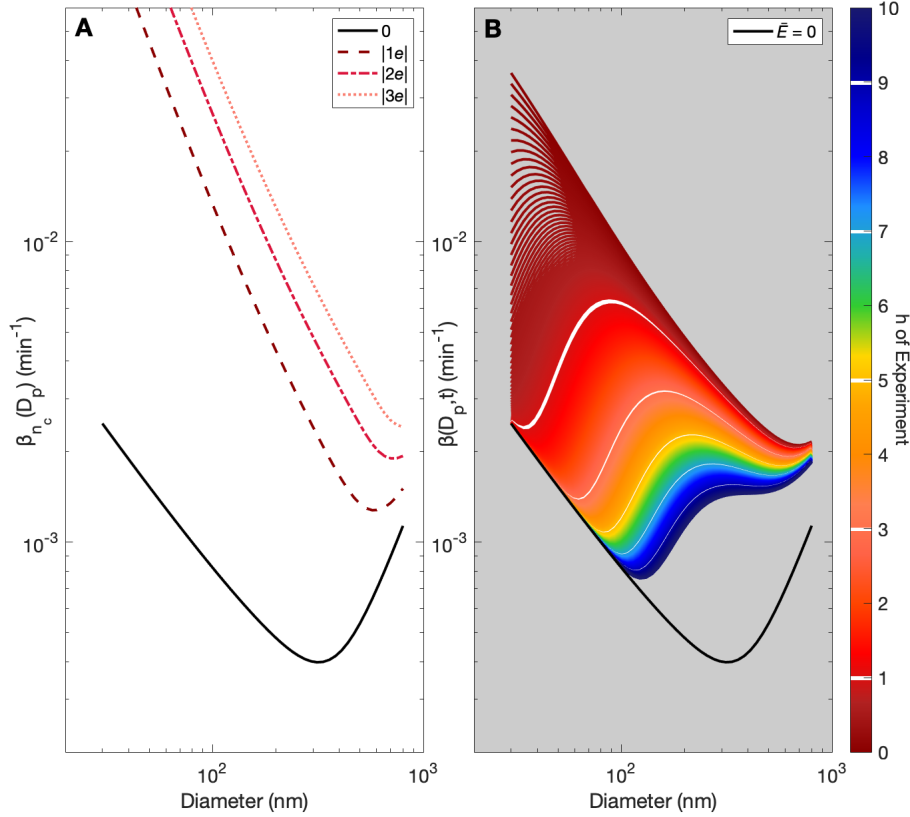
Figure 2.11: Wall-deposition parameter $\beta_{n_c}(D_p)$ in the presence of a mean electric field of $\bar{E} = -45$ V cm^{-1} for different values of numbers of elementary charges on a particle, n_c (panel A). Note that in the derivation of Equation 2.46, equivalent mobilities of positively and negatively charged particles are assumed so that $\beta_{-n_c}(D_p) = \beta_{n_c}(D_p)$. Panel B shows the transformation of $\beta_{n_c}(D_p)$ to $\beta(D_p, t)$ where an initial charge distribution that matches the approximation from Wiedensohler (1988) is assumed (see Figure 2.9) with no cluster ions present. For this simulation, the chamber volume is taken to be 19 m^3, $k_e = 0.2$ s^{-1}, 300 K, simulation for 10 h. Other conditions are: 50 size bins, lognormally distributed between 30 and 800 nm, an initial number concentration of 10^4 cm^{-3}, $D_{pg} = 100$ nm, and $\sigma_g = 1.5$. Note that the black curve in panel A represents an uncharged particle and the black curve in panel B represents an uncharged chamber wall.

on Teflon chamber walls have been observed to be remarkably stable (Wang et al., 2018). Similarly, since the cluster ion concentration affects the charge distribution, which affects the rate of wall deposition, the cluster ion concentration must be either measured or assumed in order to predict the particle number concentration distribution.

If it is not possible to reduce $\bar{E}$ to ~0 experimentally, and if direct measurement of the particle charge distribution is not available, then, in approach (3), one uses

the minimization procedure with $\beta_{n_c}(D_p)$ (Equation 2.46) in place of $\beta(D_p)$, as in method (2). Again, a constant $\bar{E}$ is assumed to exist throughout the experiment. An initial charge distribution and a constant small air ion concentration must also be assumed. Then, the values of $\bar{E}$ and k_e can be determined from the two-parameter minimization of the function

$$J = \int_0^{t_f} \int_{D_{p,lower}}^{D_{p,upper}} \left[n_{obs}(D_p, t) - \int_{-\infty}^{\infty} n_{pred}(D_p, n_c, t; k_e, \bar{E}) dn_c \right]^2 dD_p dt.$$

(2.49)

Application of method (1) is shown in Charan et al. (2018), whereas Method (3) is described in Schwantes, Charan, et al. (2019)

2.2.10 The Continuously Mixed Flow Reactor

In a continuously mixed flow reactor (CMFR), organic vapors and seed particles (if seed particles are used) are continuously fed into and sampled from the reactor. The contents of the CMFR, which ordinarily is several cubic meters in volume, are assumed to be well-mixed, so that the concentrations of vapor and particles in the outflow represent those in the bulk of the chamber. Note that some flow reactors incorporate active mixing of the reactor contents, whereas others achieve a mixed state as a result of the mixing that takes place from the flows of gas-phase streams into and out of the reactor. Following a start-up period, the concentrations of vapors and the particle size distribution in the reactor eventually reach a steady state. Once a steady state has been achieved, the reactor outflow can be sampled over a length of time sufficient to obtain accurate data. Just as in batch chambers, low-volatility vapors generated in the process of oxidation in chambers operated in steady-state mode deposit on the the chamber walls as well as on growing particles. For CMFRs, therefore, it is also necessary to account for competing processes.

In this section, we highlight the governing equations for a CMFR with reference to those given for a batch reactor. Particle growth in a CMFR has been derived analytically by Seinfeld, Kleindienst, et al. (2003), Kuwata and Martin (2012), and Martin, Kuwata, and Smith (2014).

As noted above, in order to operate a CMFR in steady-state mode, a start-up period is required during which the entire gas-particle system comes to a steady state, and in which all the variables of the system are independent of time. The duration of the required start-up period is usually measured in terms of the number of residence times in the reactor, which is determined by the chamber volume and the influent/effluent volumetric flow rate. Usually several residence times are required

for the reactor to achieve a steady state.

Compared with Equation 2.6 in a batch reactor, the physical and chemical processes are essentially the same, except that there are two additional flux terms for vapor molecules and suspended particles: the influent and effluent fluxes. The dynamic equation for the concentration of gas-phase species i becomes:

$$
\begin{aligned}
\frac{dC_{g,i}^b}{dt} &= \left(\frac{C_{g,i}^0}{\tau_{\text{CMFR}}}\right)_{influent\ flux} - \left(\frac{C_{g,i}^b}{\tau_{\text{CMFR}}}\right)_{effluent\ flux} \\
&+ \left(\frac{dC_{g,i}^b}{dt}\right)_{evap/cond\ (suspended\ particles)} + \left(\frac{dC_{g,i}^b}{dt}\right)_{evap/cond\ (deposited\ particles)} \\
&+ \left(\frac{dC_{g,i}^b}{dt}\right)_{vapor-wall\ deposition} + \left(\frac{dC_{g,i}^b}{dt}\right)_{evap\ from\ wall} + \left(\frac{dC_{g,i}^b}{dt}\right)_{nucleation} \\
&+ \left(\frac{dC_{g,i}^b}{dt}\right)_{reaction\ of\ i} + \left(\frac{dC_{g,i}^b}{dt}\right)_{reaction\ to\ i}
\end{aligned}
$$

(2.50)

the general dynamic equation for suspended particle number concentration becomes:

$$
\begin{aligned}
\frac{dn\left(D_p,t\right)}{dt} &= \left[\frac{n^0(D_p)}{\tau_{\text{CMFR}}}\right]_{influent\ flux} - \left[\frac{n(D_p,t)}{\tau_{\text{CMFR}}}\right]_{effluent\ flux} \\
&+ \left[\frac{dn\left(D_p,t\right)}{dt}\right]_{evaporation/condensation} + \left[\frac{dn\left(D_p,t\right)}{dt}\right]_{coagulation} \\
&+ \left[\frac{dn\left(D_p,t\right)}{dt}\right]_{nucleation} + \left[\frac{dn\left(D_p,t\right)}{dt}\right]_{wall\ deposition}
\end{aligned}
$$

(2.51)

and the dynamic equation for particle-phase organic mass becomes:

$$
\begin{aligned}
\frac{dC_{par,i}}{dt} &= -\left(\frac{C_{par,i}}{\tau_{\text{CMFR}}}\right)_{effluent\ flux} \\
&+ \left(\frac{dC_{par,i}}{dt}\right)_{nucleation} + \left(\frac{dC_{par,i}}{dt}\right)_{condensation} \\
&- \left(\frac{dC_{par,i}}{dt}\right)_{evaporation} - \left(\frac{dC_{par,i}}{dt}\right)_{wall\ deposition}
\end{aligned}
$$

(2.52)

where $C_{g,i}^0$ and $n^0(D_p)$ are the concentration of gas-phase species i and particle number concentration with diameter D_p in the influent flow and τ_{CMFR} is the average residence time of CMFR. Each dynamic term on the right-hand side of Equations 2.50-2.52 is the same as that for a batch reactor.

Gas-particle partitioning equilibrium is never reached in a CMFR at steady state; that is, the condensation-driving force in Equation 2.10 must always be non-zero. This is the fundamental difference between the time-dependent batch chamber and the steady-state CMFR: whereas gas-particle equilibrium partitioning can be achieved in the batch chamber given a sufficiently long time, equilibrium cannot be achieved in the CMFR, as a driving force for gas-to-particle condensation must be maintained regardless of the mean residence time in the chamber.

The total SOA yield at steady state in the CMFR is still defined as the ratio of the mass concentrations of particle-phase oxidation products to the overall reacted concentration of the parent compound (Equation 2.1). When the CMFR is at steady state, the correction for particle-wall deposition is:

$$Y = \frac{\Delta \text{SOA}_{\text{sus}}}{\Delta \text{VOC}} \left(1 + \bar{\beta} \tau_{\text{CMFR}}\right) \tag{2.53}$$

where $\bar{\beta}$ is the particle-volume-weighted particle-wall loss rate (see Box 2.2.2):

$$\bar{\beta} = \frac{\int_0^\infty D_p^3 \beta(D_p) dD_p}{\int_0^\infty D_p^3 dD_p} \tag{2.54}$$

When vapor wall deposition is a reversible process, steady state is achieved only when the vapor and wall concentrations have established equilibrium. However, if vapor wall deposition is irreversible and constant, steady state may be established sooner because the walls do not first have to saturate. In this case, however, vapor wall deposition diminishes the measured SOA yield even at steady state, because a non-zero amount of condensable oxidation products are continually removed from the chamber through the walls; this contrasts with the case of reversible vapor wall deposition, in which vapor wall deposition does not depress the yield at steady state (see Section 2.2.8).

2.3 Computational Simulation of Environmental Chamber Dynamics

Simulation of environmental chamber dynamics requires tracking of the aerosol size-composition distribution as a function of time. Several approaches exist to represent the evolution of this distribution. The two most common are depicted in Figure 2.12: the modal representation and the sectional representation. In the *modal* representation, size-composition distributions are prescribed in a given form, usually superimposed lognormal distribution, that shifts over time, to track the change in size and composition. In the *sectional* representation, the particle population is
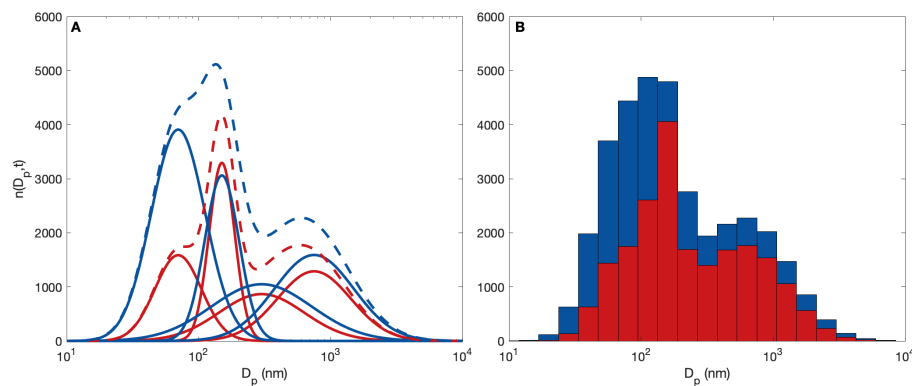
Figure 2.12: Representation of aerosol size and composition. Panel A shows a modal representation; panel B a sectional representation. In each representation, two components are presumed to be present, given by the blue and red distributions. The modal representation comprises a distribution with four modes. The modes are generally represented by lognormal distributions. In the sectional distribution, the particle population is divided into discrete bins of fixed sizes. The distributions shown represent those at a particular time in the course of a chamber experiment. For each representation, the evolution of the size-dependent distribution of particle phase composition is tracked as a function of time. The computational approach that we utilize here is the sectional distribution (panel B), in which the particle population is divided into discrete, fixed-size (diameter) bins and for which the change in concentration and composition of each bin is computed as a function of time.

divided into discrete bins of fixed sizes, for which the change in concentration and composition of each bin is computed as a function of time. A *moving-bin* model is a computational option, in which the mean diameter of each size bin is allowed to change as the particles within the bin grow or shrink. A drawback of the moving-bin model is that it is computationally challenging to account for the effect of particle-particle coagulation on the bin dynamics. As with the moving-bin model, accounting for coagulation in the modal model poses computational challenges, especially in tracking aerosol composition. Laboratory chambers, in general, have volumes of the order of 10^4 L with particle concentrations of ~10^4 particles cm^{-3}. The sheer number of particles precludes resolving individual particles. We employ here the fixed-bin sectional model to represent aerosol size-composition evolution. As particles grow, they must be apportioned between different particle size bins, which is a source of uncertainty (see Box 2.3.1).

Box 2.3.1: Particle Apportionment in a Fixed-Bin Model

In the fixed-bin computational model, as particles grow, the particle number concentration must be apportioned between different particle size bins. For example, in a bin containing 100 particles, if particle growth rate $\frac{dD_p}{dt} = 2$ nm s^{-1} and the size bin in question (e.g., bin 1) has a mean diameter of $D_p = 10$ nm, then over a timestep of 1 s, all 100 particles would move from the bin with $D_p = 10$ nm to the bin with $D_p = 12$ nm. If, on the other hand, the mean diameter of the next size bin were $D_p = 14$ nm, then only a fraction of the particles would move into that bin in the timestep. With a linear (by mass or volume) apportionment, of the 100 particles, 58 would remain in the 10 nm bin and 42 would move to the 14 nm bin over the timestep. More generally, if all the particles in a bin with number concentration n_k grow to an average diameter of $D_{p,k}$, where $D_{p.i}$ is the size bin immediately smaller and $D_{p,i+1}$ is the size bin immediately larger, the apportionment factor, f_c is:

$$f_c = \frac{D_{p.k}^3 - D_{p.i}^3}{D_{p,i+1}^3 - D_{p,i}^3} \tag{2.55}$$

where $f_c n_k$ particles are added to bin $i+1$ and $(1 - f_c)\, n_k$ particles are added to bin i. The first term of Equation 2.5, then, can be calculated by subtracting all the particles that leave a size bin in a given timestep, which is $\left(\frac{\partial D_p}{\partial t}\right)_{cond/evap} (\Delta t) n(D_p, t)$ multiplied by the appropriate f_c if not all particles grow/shrink enough to completely depart from the section in question. Adding all particles that enter the size bin from all smaller bins (if $\frac{\partial D_p}{dt} > 0$, condensation) or from all larger bins (if $\frac{\partial D_p}{dt} < 0$, evaporation) completes the computational timestep. Note that the discretization of the size bins has the effect of spreading the size distribution (called *numerical diffusion*) because, in the example given above, it would appear as if there are particles of two sizes ($D_p = 10$ or 14 nm) in the next timestep instead of all particles of the same size ($D_p = 12$ nm).

2.3.1 Computational Simulation of Idealized SOA Formation

If the chemical mechanism leading from the parent VOC to low-volatility condensable products is available with appropriate reaction rate constants, then computational simulation of oxidation of the parent compound to generate SOA can be carried out explicitly. However, the extent to which a complete VOC oxidation mechanism is available will vary from system to system. For example, straight-chain alkenes and alcohols (Figure 2.13) exemplify systems for which the full OH radical-induced oxidation mechanisms leading to low volatility products are relatively well established (see Box 2.3.2).

The gas-phase mechanism by which a parent VOC is oxidized to produce low-
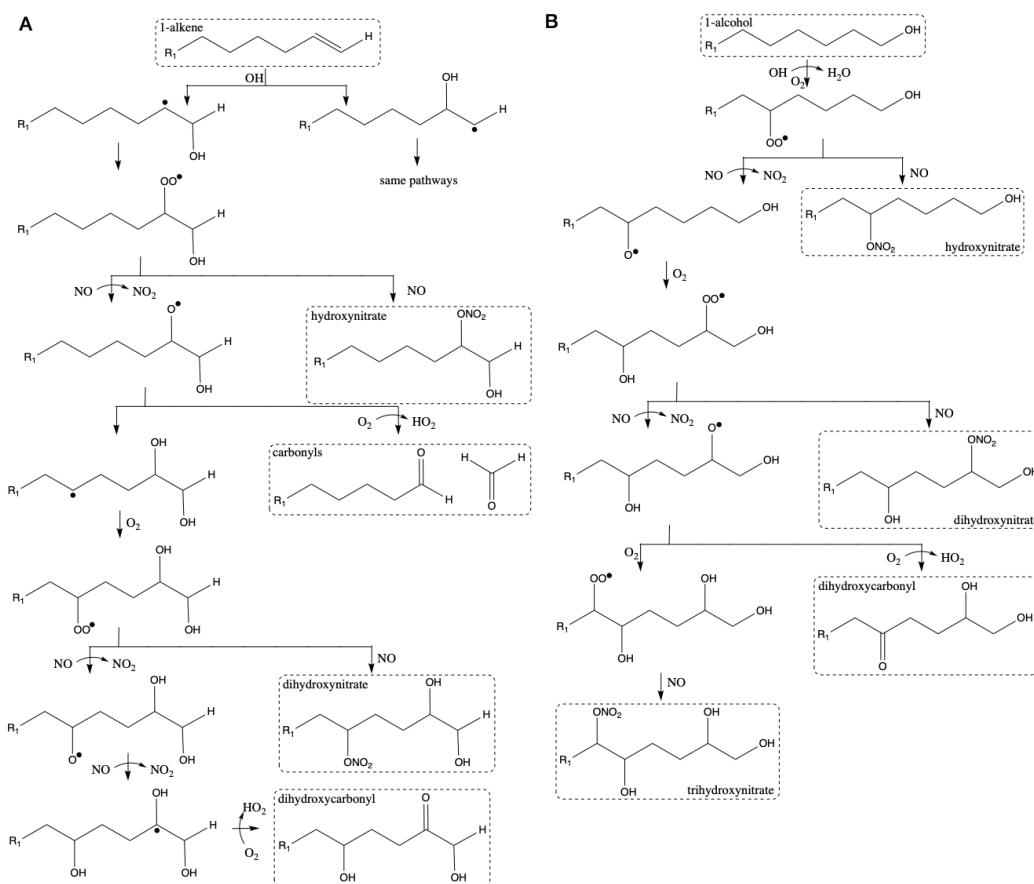
Figure 2.13: Generic reaction of a linear alkene (panel A) and a linear alcohol (panel B) with the hydroxyl radical in the presence of NO_x (Ziemann, 2011).

volatility products is generally complex. The present review does not focus explicitly on the gas-phase mechanisms by which condensable products are formed.

In simulating the generation and consumption of each species, it is possible to follow the progression of oxidation. Consequently, we represent gas-phase VOC oxidation by the idealized first-order kinetic scheme (McVay, Cappa, and Seinfeld, 2014)

$$ A \xrightarrow{k_{OH,1}} B \xrightarrow{k_{OH,2}} C \xrightarrow{k_{OH,3}} D $$
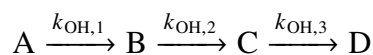
where A represents the parent compound, and B, C, and D represent oxidation products of progressively decreasing volatility.

Actual oxidation pathways tend to be considerably more complex than this basic mechanism. Such a mechanism can include bond scission, leading to products of higher volatility. Or, the successive addition of function groups in each oxidation

---

Box 2.3.2: Explicit Chemical Mechanisms

In the general reaction of a 1-alkene with OH in the presence of NO_x (Figure 2.13A) (Ziemann, 2011), initially there is an OH addition to the double bond and then an addition of O_2 to form a hydroxy-peroxy alkyl radical. The subsequent reaction of this radical with NO leads, via a minor branch (fraction 0.14), to a hydroxy-nitrate and, via a major branch (0.86), to the corresponding alkoxy radical. The alkoxy radical undergoes subsequent decomposition (0.45) and reaction with O_2 to yield formaldehyde and an aldehyde. The second pathway (0.55) involves isomerization to yield a dihydroxy alkyl radical that rapidly adds O_2. In the dominant pathway (0.92), the resulting peroxy radical reacts with NO to yield the corresponding alkoxy radical that can undergo isomerization to produce a dihydroxycarbonyl.

As a second mechanistic example, we consider a straight chain 1-alcohol initiated by the OH radical under high NO conditions (Figure 2.13B). The tri-hydroxy nitrate product after six generations of reaction is, as well, of sufficiently low volatility to condense as SOA: three -OH groups and one nitrate group serve to lower the saturation vapor pressure of the molecule by an estimated factor of 10^{-10}.

---

reaction, or the very rapid addition of many groups in a single oxidation step due to autoxidation, might lead to the formation of less volatile compounds.

In autoxidation, a compound initially reacts with OH and then the peroxy radical (RO_2) undergoes a unimolecular isomerization reaction that forms an alkyl radical and a hydroperoxide functional group (Crounse et al., 2013). This alkyl radical can then react with oxygen to regenerate another RO_2 in a process whereby functional groups are rapidly added to the molecule.

Because our principal goal in this section is to illustrate how an oxidation mechanism can interface with a full-scale numerical computation, we have selected this rudimentary mechanism involving species A, B, C, and D. By contrast, Figure 2.13 shows a realistic mechanism of oxidation of a linear alkene (panel A) and a linear alcohol (panel B) by the hydroxyl radical in the presence of NO_x.

The first-order oxidation rate constants of vapor species A, B, and C are $k_{OH,1}$, $k_{OH,2}$, and $k_{OH,3}$, respectively. These rate constants determine the overall system reaction timescale, since we assume that no particle-phase chemistry occurs. They are chosen here for purpose of computational illustration to increase successively by a factor of five: $k_{OH,1} = 10^{-4}$ s^{-1}, $k_{OH,2} = 5 \times 10^{-4}$ s^{-1}, and $k_{OH,3} = 2.5 \times 10^{-3}$ s^{-1}. The oxidation product volatilities are given by the saturation mass concentrations: C_B^*, C_C^*, and C_D^*.

We choose, for simplicity, to use the lower-bound assumption for α_{pw}, in which vapor condensation halts once a particle is removed from the bulk chamber (i.e., $\alpha_{pw} = 0$). Vapor wall deposition is controlled by C_w, the wall equivalent organic mass concentration, and by α_w, the accommodation coefficient of vapor species condensing on the wall. For all species, the nominal value of α_w used for computation is 10^{-7}, though α_w can be calculated by Equation 2.40 based on a compound's C^* value. Nominal values and units of parameters used in the computations are given in Table 2.1.

To minimize particle wall deposition, seed particle size-distributions are usually chosen such that the mean diameter of the distribution falls in a range where $\beta(D_p)$ is near its minimum; a representative value of which is $D_{pg} \approx 150$ nm. Here, we assume a log-normal initial seed aerosol size distribution with mean diameter $D_{pg} = 150$ nm and geometric standard deviation $\sigma_g = 1.5$. The nominal initial seed aerosol number concentration is 10^4 cm^{-3}.

The computation tracks the gas-phase concentrations of and the physical and locational state of each compound (A, B, C, and D) for an experimental duration of 10 h. Since for this idealized case, the stoichiometric coefficients are all 1 and, for simplicity, all compounds have the same molecular weight,the theoretical maximum SOA yield is 1.

Using these nominal values, the effect of different processes, both individually and in concert, is shown in Figures 2.14 and 2.15. As in Figure 2.2, the effect of competing physical processes on SOA yield is shown. For $\alpha_p = 10^{-3}$, vapor deposition on the wall (Figure 2.14, panel G) is seen to have a small effect on the aerosol size distribution evolution (panel F vs. panel G), but a modest fraction of species D is wall-deposited vapor at the end of 10 h (panel Q). Particle deposition on the chamber wall has an appreciable effect on the aerosol size distribution (panel H) and on the amount of species D incorporated into wall-deposited particles (panel R). Coagulation alone has an effect somewhat more influential than that of wall deposition of particles on the particle size distribution (panel I vs. H), but very little effect on the final distribution of species D between phases (panel S vs. P). For the set of parameters chosen, after 10 h of reaction, the gas-phase system has evolved largely into species D, the least volatile of the species. Note that we have assumed that D cannot be further oxidized. In the absence of wall deposition and coagulation (panel P), most of D is on suspended particles. The predominant amount of D exists on suspended particles. The idealized SOA yield is that given in panel P by the ratio

of the sum of the masses of species B, C, and D on suspended particles to the mass of A reacted in panel K.

With an accommodation coefficient of unity (Figure 2.15), condensation occurs very quickly. Since there are no particle-phase reactions, more of the earlier oxidation products (Species B and C) condense onto particles than in the case where $\alpha_p = 10^{-3}$ (panel Q, Figure 2.14 vs. 2.15). Due to rapid condensation, the SOA yield increases rapidly at the beginning of the experiment, since there is a minimal delay in the SOA formed once species A has reacted (panels K-O). Particle deposition continues to influence the system even after all the vapor has condensed, but vapor deposition does not have much of an effect because the condensational sink is so large (panels P vs. Q). Coagulation affects the particle size distribution (shifting the particles to larger sizes, panels I and J vs. F), but minimally affects the condensation rate since condensation is sufficiently fast not to be influenced by particle size (panel S vs. P).

The effect on yield after a 10 h simulation of α_w, C_w, C^*, and k_{OH} as a function of α_p is shown in Figure 2.16, demonstrating that the effect of each variable is dependent on the values of other variables because the limiting process for aerosol formation changes as different variables change.

2.3.2 Kinetic versus Quasi-Equilibrium Particle Growth

The traditional approach to describing the rate of aerosol growth as a result of condensation of low volatility VOC oxidation products is to assume that gas-particle partitioning equilibrium is established instantaneously: this results in a so-called *quasi-equilibrium* growth state. This growth state is, however, not always attained. Recent work has shown that aerosol sometimes exhibits properties of semisolid material, in which case the timescale for vapor-particle equilibrium is quite long and molecules that enter the aerosol phase rarely escape back into the gas-phase (Shiraiwa, Zuend, et al., 2013; Shiraiwa, Yee, et al., 2013; Vaden, Song, et al., 2010; Virtanen, Kannosto, et al., 2011). In this situation, particle growth is *diffusion-limited*, also referred to as *kinetically-limited* since particle growth is affected not just by the gas-phase concentration of a species but also by the duration of time over which the particle interacts with that gas-phase species (Zhang, Pandis, and Seinfeld, 2012; Shiraiwa and Seinfeld, 2012; Zhou et al., 2013).

In the absence of other loss terms for gas and particle phase species, the time required to establish equilibrium between the suspended gas and particle phases should not influence the final observed yield. In reality, however, processes competitive
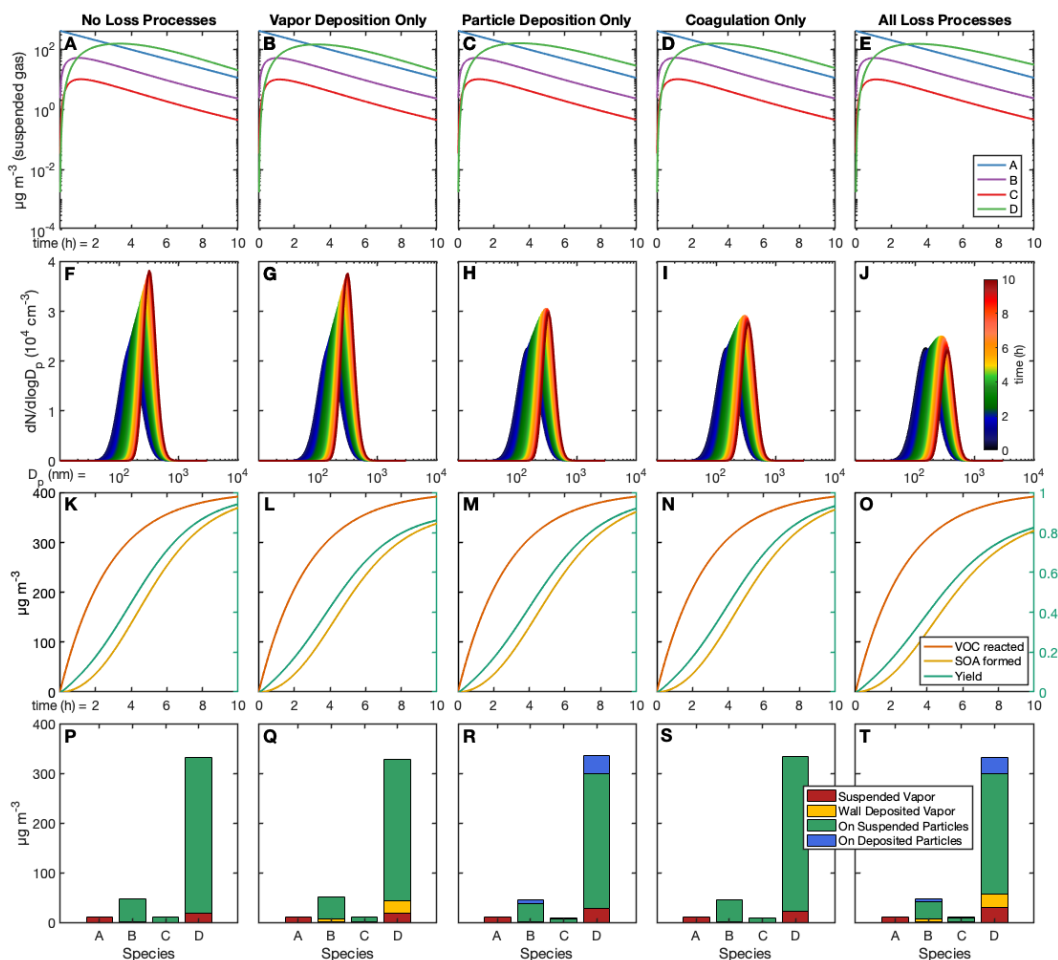
Figure 2.14: Simultaneous solutions of Equations 2.5 and 2.6 that account for different loss processes provide the theoretical evolution of a batch reactor system. Nominal values listed in Table 2.1 are used for the simulation, where the accommodation coefficient is $\alpha_p = 10^{-3}$. Panels A-E show the dynamics of the A → B → C → D chemical system. Since the aerosol dynamics minimally feed back into the gas-phase dynamics, each of the panels is nearly identical. Panels F-J show the evolution of the aerosol size distribution over the course of the experiment, where panel F shows the aerosol size distribution evolving without wall interaction and particle-particle coagulation. The combined effect of processes shown individually in panels G, H, I is shown in panel J. Panels K-O show the effect of each of the processes on SOA formed and on SOA yield. As expected, these aerosol processes have no effect on VOC reacted. Finally, panels P-T show the distribution of chemical species A, B, C, and D after 10 h of oxidation between the suspended gas-phase, vapor deposited on the chamber wall, the suspended particle-phase, and the deposited particle-phase. Panel T shows the combined effect of all the processes on the distribution of the four species.
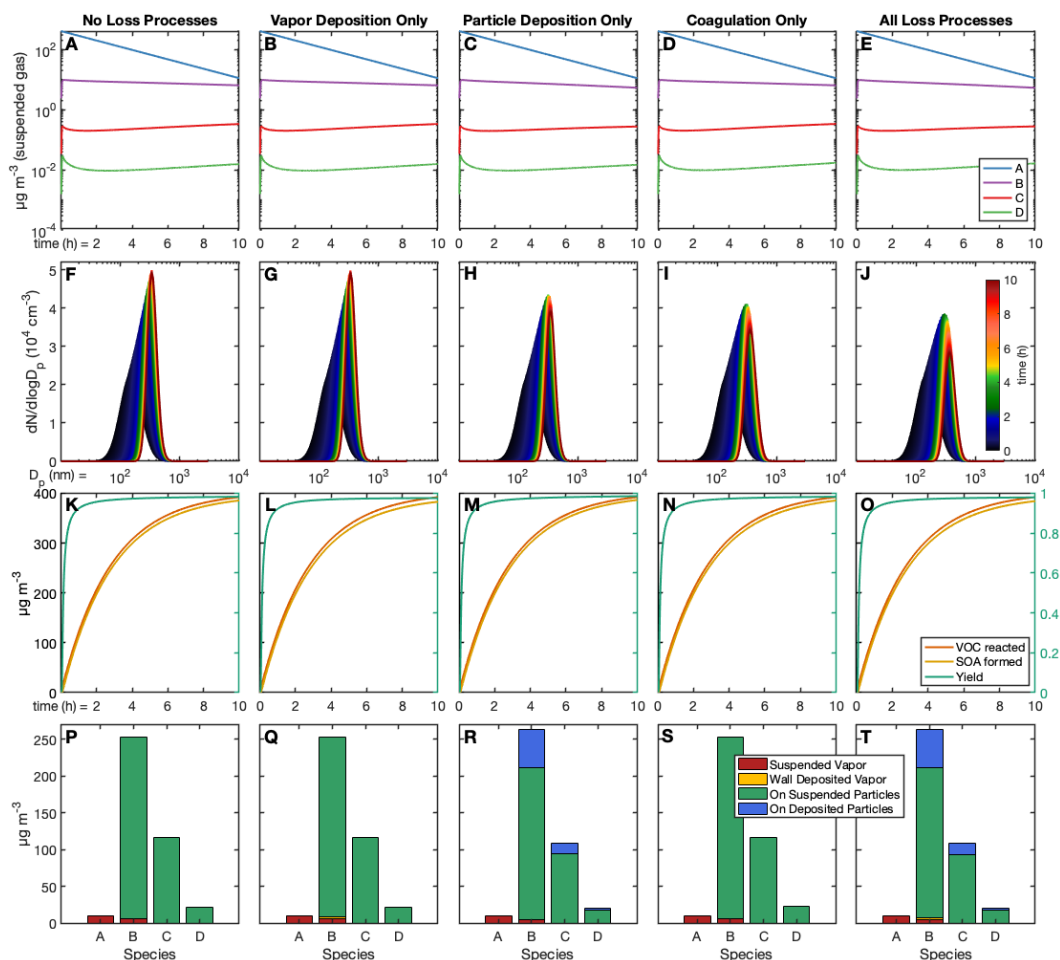
Figure 2.15: The same simulations as shown in Figure 2.14, except with $\alpha_p = 1$. As above, panels A-E show the gas-phase species, panels F-J show the aerosol-size-distribution evolution, panels K-O show the net amount of species A reacted and of SOA condensed onto particles, and panels P-T show phase-distributions of each of the species after 10 h of simulation. Panels A, F, K, and P show the ideal case, where only condensation occurs. Panels B, G, L, and Q include just condensation and vapor-wall deposition. In panels C, H, M, and R, only particle-wall deposition is included with condensation. The effect of coagulation in the presence of condensation only is shown in panels D, I, N, and S. All these processes are included for panels E, J, O, and T, which is what would be observed in a real chamber system. Since condensation is faster than in Figure 2.14, more of species B and C ends up on particles than in Figure 2.14.
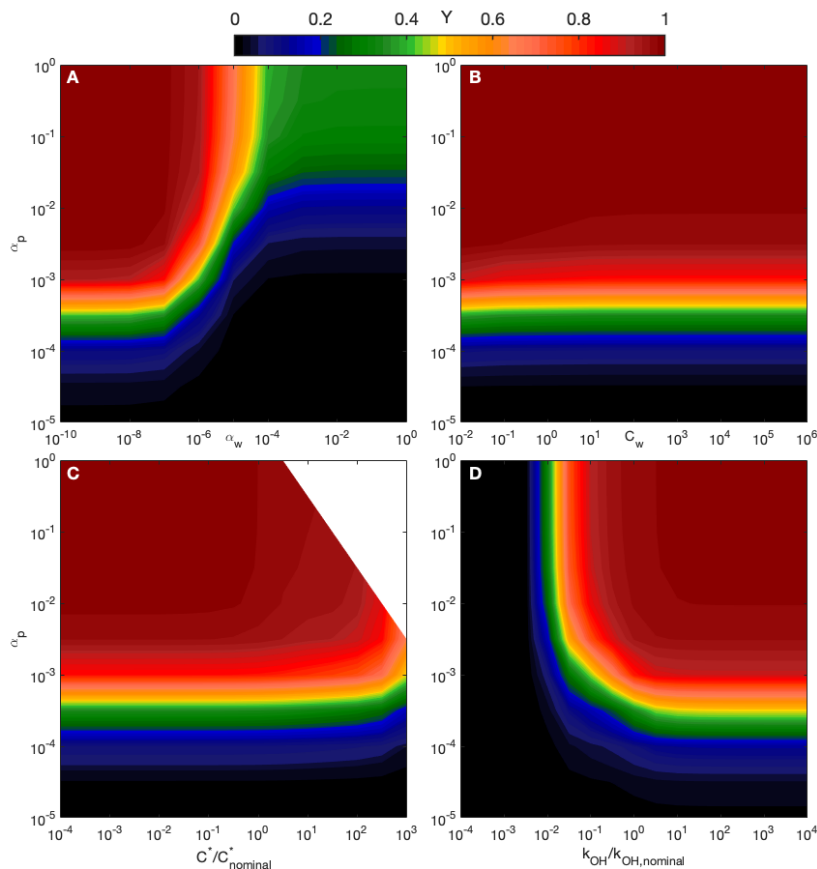
Figure 2.16: Effect on SOA yield of parameters for a range of vapor-to-suspended particle mass accommodation coefficients, α_p, of (A) α_w, the vapor-to-wall accommodation coefficient, (B) C_w, the equivalent absorbing mass of the wall, (C) $C^*/C^*_{nominal}$, the saturation mass concentration of each of the simulated compounds (A, B, C, and D) compared to their nominal values in Table 2.1 and (D) $k_{OH}/k_{OH,nominal}$, the ratio of the first-order oxidation rate coefficients to their nominal value (also given in Table 2.1). Panel A demonstrates the trade-off between vapor condensation and vapor-wall deposition: the observed yield is greatest when the vapor condensation pathway is most rapid, which occurs for larger values of α_p and smaller values of α_w. Panel B shows that as C_w increases, increasing the wall capacity to uptake organics, the propensity for vapor-wall deposition also slightly increases (seen as the increase in Y for $\alpha_p \approx 10^{-2.5}$). Panel C demonstrates that, for the nominal value of C^* and for less volatile species, the SOA yield Y is limited by the rate of condensation. However, for sufficiently large values of α_p and more volatile C^* compounds, the SOA yield Y is volatility-limited. Panel D also represents two distinct regimes: a reaction-rate limited region ($k_{OH} \lesssim k_{OH,nominal}$ and $\alpha_p \gtrsim 10^{-3}$) and a condensation-rate limited region ($k_{OH} \gtrsim 10^{-1} \times k_{OH,nominal}$ and $\alpha_p \lesssim 10^{-2}$). However, for considerably more volatile compounds than those shown here, the volatility is more influential than the accommodation coefficient for gas-particle uptake. All parameters match those in Table 2.1 unless otherwise noted. Simulations carried out for 10 h by solving Equations 2.5 and 2.6.

with condensation onto suspended particles siphon away the condensable gas-phase species: vapor-wall deposition and oxidation are the most directly competitive. Note, however, that faster oxidation rates can actually lead to a more rapid rate of condensation if lower volatility compounds are formed and these products do not have other available pathways.

Two parameters are the most influential for establishing the gas-particle phase equilibration time: α_p and the total seed surface area concentration C_{sa}. Since α_p is the probability that a gas-phase molecule transitions to the particle phase upon contact, as α_p increases, particle-gas phase equilibration time decreases (see Equations 2.7-2.8). Similarly, the probability that a gas-phase molecule will impinge upon a particle at all is determined by the total available surface area (or, relatedly, number) concentration, because as the area of the gas-particle interface increases, the rate of exchange between the phases will also increase.

As shown in Figure 2.17, for $\alpha_p \approx 0.1$ to 1.0, the oxidation rate determines the overall timescale, and Y grows larger as the VOC oxidation rate does (see Figure 2.16D). In this case, seed aerosol surface area barely affects Y. For values of $\alpha_p \sim 0.001$, on the other hand, both oxidation rate and seed surface area effects are important. At slow rates of oxidation and high concentrations of seed surface area, the oxidation rate governs the value of Y, whereas seed surface area governs Y when seed surface area is low and oxidation rates are fast. The effect of α_p on the size distribution evolution is evident in Figure 2.18.

Figure 2.16A shows the effect on SOA yield Y of the competition between α_w and α_p; Figure 2.19 shows the effect between α_w and total initial seed aerosol number concentration. For a fixed initial seed aerosol number concentration, Figures 2.20 and 2.21, respectively, show the effect of this competition on the particle size distribution evolution and on the distribution of the gas-phase mass within the chamber. For values of α_w approaching unity, the wall is the major sink of gas-phase species (Figure 2.21C) and the condensational growth of the suspended particles is severely retarded, whereas particles continue to deposit on the wall and undergo coagulation (Figure 2.20C). For small values of α_w, the opposite is the case (Figures 2.20A and 2.21A).

It is possible to formulate a dimensionless group Ki that measures the extent that kinetic versus quasi-equilibrium growth governs oxidation:
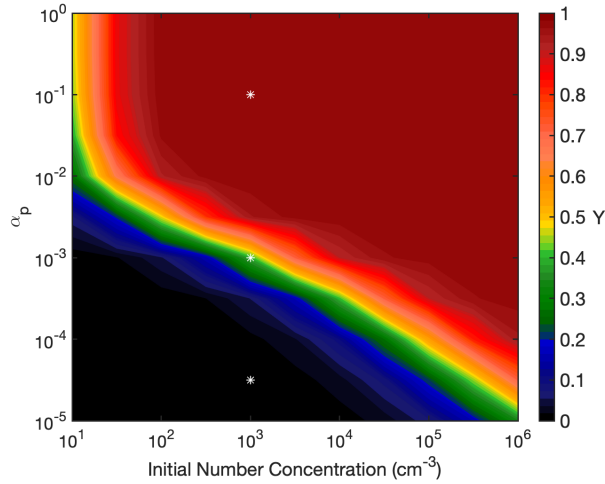
Figure 2.17: Effect of kinetically-limited versus quasi-equilibrium growth on SOA yields after 10 h of oxidation determined by solving Equations 2.5 and 2.6. All parameter values are the nominal values in Table 2.1, except for α_p, the accommodation coefficient of vapors to suspended particles, N, the number concentration of the seed aerosol, and α_w (which is set here to 0), the accommodation coefficient of vapors to the chamber wall. At high initial concentrations of seed aerosol and large values of α_p, the predominance of particle surface area leads to equilibrium growth. When the accommodation coefficient $\alpha_p \ll 1$, however, growth is limited by the rate at which vapor species are taken up into particles and, therefore, the seed surface area has an effect on the rate of condensation and, consequently, the SOA yield. Size distribution evolution is shown in Figure 2.18 for the conditions corresponding to the white stars.

$$\text{Ki} = \frac{\alpha_p v C_{sa}}{4(k_{\text{OH}} + k_{vwe})} \tag{2.56}$$

where v is the gas molecule velocity, $C_{sa} = \int_0^\infty \pi D_p^2 n(D_p) dD_p$ is the total particle surface area, k_{OH} is the pseudo-first-order reaction rate constant of gas-phase species with OH, and k_{vwe} is the inverse of the vapor-wall equilibration time (τ_{vwe}) given by Equation 2.44. Note that k_{vwe} is a function of the environmental chamber design parameters (surface area to volume ratio and k_e) and of α_w. For either large values of α_p or high aerosol number concentrations, and hence large C_{sa} (i.e., Ki $\gg$ 1), vapor condensation onto growing particles is highly preferred over wall deposition and the system is in the quasi-equilibrium growth regime. For large α_w values or, e.g., large chamber surface area to volume ratios, Ki $\ll$ 1 and the system is in the kinetically-limited growth regime.
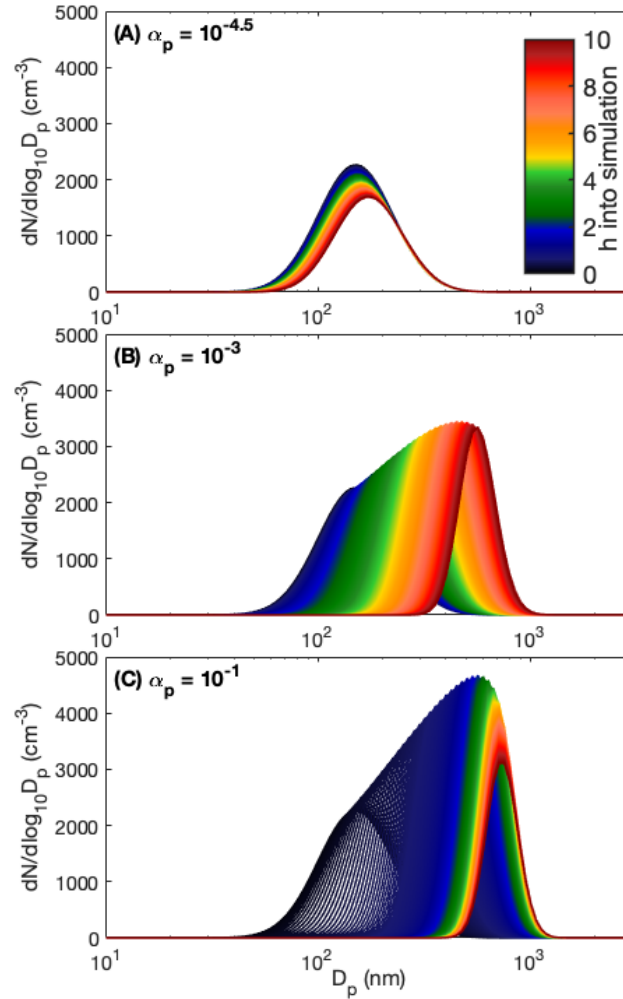
Figure 2.18: Effect of kinetically-limited versus quasi-equilibrium growth on the size distribution evolution of particles over a duration of 10 h. All parameters used are listed in Table 2.1 except for the vapor-to-suspended particle mass accommodation coefficient (α_p, shown in the upper left corner of each panel), the seed aerosol number concentration ($N = 10^3$ cm^{-3}), and no vapor-wall loss ($\alpha_w = 0$). Each of these three panels represents different regimes designated as white stars in Figure 2.17.
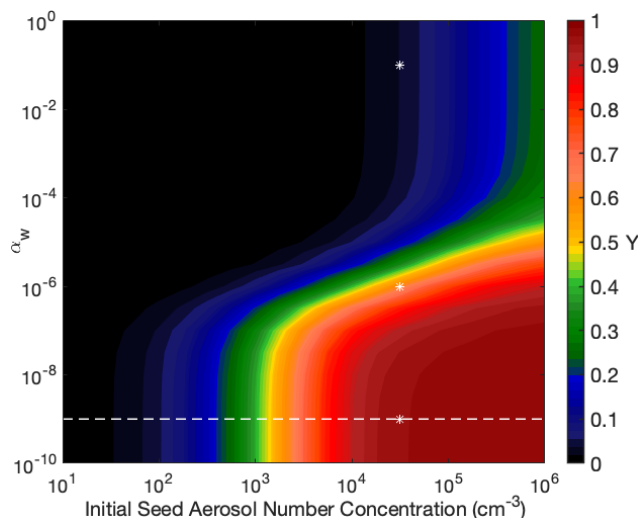
Figure 2.19: Joint effect of initial seed aerosol surface area (expressed in terms of initial seed aerosol number concentration) and accommodation coefficient of wall deposition of vapor oxidation products, α_w, on yield Y determined by simultaneously solving Equations 2.5 and 2.6 for a simulated 10 h. All parameters values used are listed in Table 2.1 except for the accommodation coefficient of the wall, α_w, and the initial number concentration of the seed, N. At high initial concentrations of seed aerosol and small values of α_w, there is essentially no change in yield as seed surface area increases, owing to the small rate of uptake of vapors on the chamber wall. At initial seed aerosol number concentrations of $\gtrsim 10^2$ cm^{-3} and intermediate values of α_w ($\sim 10^{-7}$ to $\sim 10^{-4}$), a large change occurs in observed yield as α_w varies.

2.3.3 Seed Surface Area Effect

Use of increasing concentrations of seed aerosol has been shown in certain cases to promote increased SOA yield. The intensity of this effect depends on the propensity for the precursors and products to be taken up by the chamber walls as well as the key parameters characterizing the chamber system. For example, the seed surface area effect is seen in the toluene-OH system, where Y increases dramatically with seed aerosol surface area, but not in the α-pinene-ozone system, where Y shows no dependence on the amount of seed used in the experiment (Zhang, Cappa, et al., 2014; Nah, McVay, Zhang, et al., 2016). McVay, Cappa, and Seinfeld (2014) demonstrated that the relevant timescales to see the effect of surface area on condensation rates and on observed SOA yield are that for gas-particle equilibrium, precursor oxidation, and vapor-wall deposition: only when the gas-particle equilibrium is longer than or of the same order of magnitude as either of the other two. This is a result of the competition for condensable oxidation products between the chamber wall and existing particles. The condensation rate is determined by the propensity for an oxidation
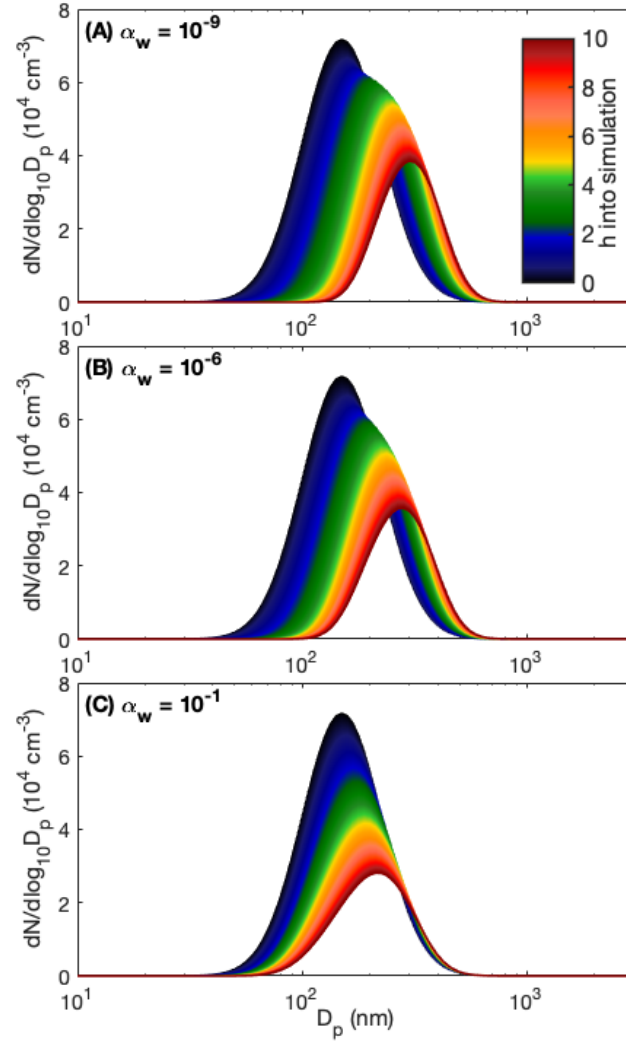
Figure 2.20: Seed surface area effect on the chamber size distribution evolution. All parameters match those in Figure 2.19, where the three size distributions correspond to the white stars in Figure 2.19. The assumed initial seed aerosol concentration is $N = 10^{4.5}$ cm^{-3}.
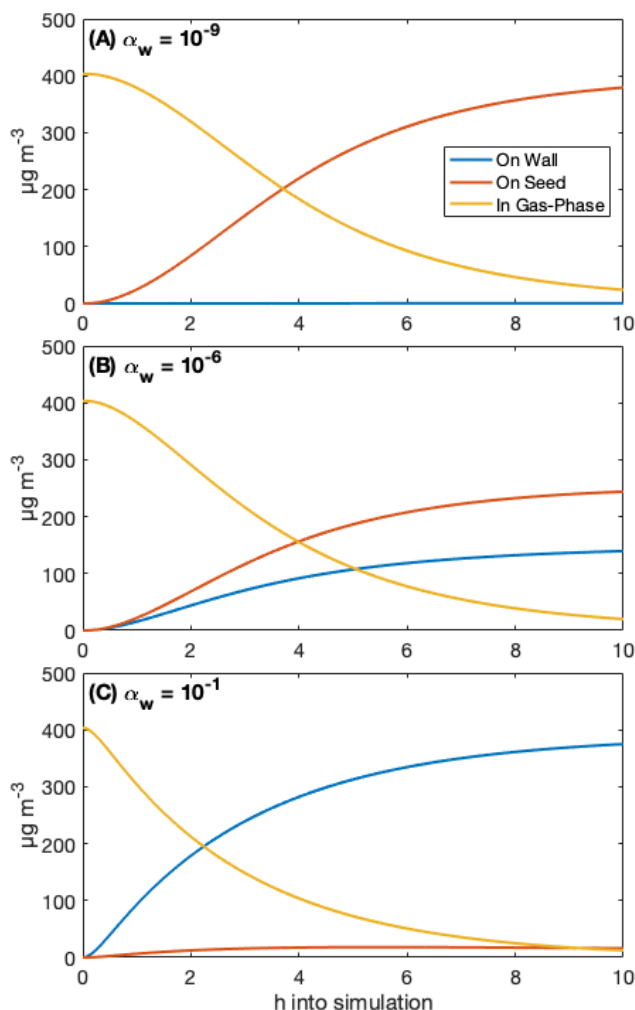
Figure 2.21: Seed surface area effect on fate of species in the chamber system, for the chemical mechanism $A \to B \to C \to D$. All parameters match those in Figure 2.19, in which the displayed concentrations are marked as white stars. The assumed initial seed aerosol concentration is $N = 10^{4.5}$ cm^{-3}.

product to condense onto a particle when the vapor and particle collide (determined by α_p), the likelihood of a collision (determined by the seed aerosol surface area), and the amount of vapor available to condense (determined by the VOC oxidation rates). Generally, when α_p is between ~0.1 and 1, the oxidation rate determines Y; the faster the VOC gets oxidized, the higher Y is. For $\alpha_p \approx 0.001$, however, both oxidation rate and seed surface area matter: when oxidation is slow, its rate dominates Y, but when oxidation is fast and there is little seed surface area, this seed surface area is the most important for determining Y. That is, at large values of α_p or N_t, the oxidation rate is not limiting the condensation rate, so changes in either variable does not have a substantial effect on Y.
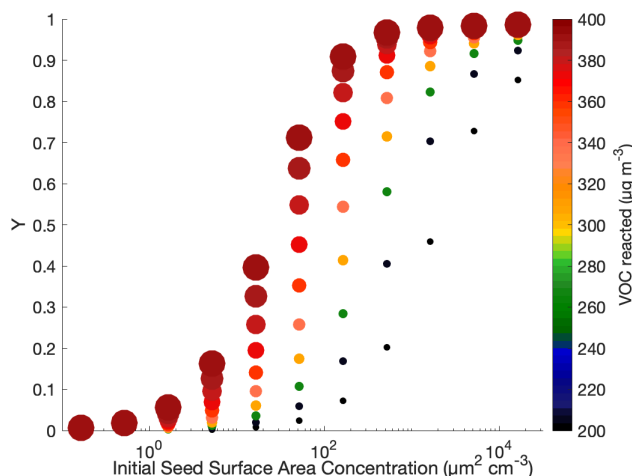
Figure 2.22: Effect of seed surface area (in terms of initial seed aerosol number concentration) on SOA yield in the chamber system of A → B → C → D. All parameters match those in Figure 2.19, where the range of concentrations is marked as a white dashed line. The measured SOA yield is shown every simulated hour (for 10 h), where the size of the circle increases with the time into the experiment. In the regime where the seed surface area effect is pronounced (initial surface area concentrations $\lesssim 10^3$ μm^2 cm^{-3}), the observed yield increases with increasing seed surface area. Above this regime (initial surface area concentrations $\gtrsim 10^3$ μm^2 cm^{-3}), the observed yield approaches the true mechanistic yield.

Experimentally, the seed surface area can be modulated to affect the gas-particle equilibration time and move the system away from one that is competitive with vapor wall loss (i.e., to move the system into a quasi-equilibrium growth regime). The effect of changing the seed number concentration on the observed yield has been termed the *seed surface area effect* and is demonstrated by the dashed line in Figure 2.19 and the yields in Figure 2.22. The true yield that would be achieved in the absence of walls, is observed only at sufficiently high surface area concentration, where the actual required surface area concentration is determined by α_p and α_w.

Whereas increasing concentrations of seed aerosol provide increasing surface area for condensation of vapor oxidation products, higher aerosol number concentrations promote increased coagulation, therefore shifting the particle size distribution toward larger sizes, while simultaneously causing the overall suspended particle surface area to decrease. If coagulation serves to shift the aerosol size distribution toward the regime of diameters in which $\beta(D_p)$ increases with increasing D_p, the corresponding decrease in aerosol surface area may limit the effectiveness of increasing overall aerosol surface area that is supposed to facilitate the condensation of vapor oxidation products on seed particles. The competition between increased

condensational growth of seed aerosol and increased rate of particle wall deposition can be assessed *a priori* by computational simulation in which seed aerosol concentrations are systematically varied (e.g., as in Figure 2.22).

2.3.4 Effect of Viscous Secondary Organic Aerosol Particles on Dynamics of the Aerosol Size Distribution

Without ample conflicting evidence, it has generally been assumed that the particulate organic SOA phase acts like a liquid and, therefore, has relatively rapid intraparticle diffusion. This situation would correspond to particle-phase diffusivity, $\mathcal{D}_b$, exceeding 10^{-10} cm^2 s^{-1} (Zaveri, Shilling, et al., 2018). Section 2.2.4 presents a general solution to transient diffusion to and uptake into a particle in which first-order chemical conversion is occurring. Rapid particle-phase reaction can occur that in some cases can produce highly viscous low-volatility products. The timescale for intraparticle diffusion scales as D_p^2, whereas the mass of the particle varies as D_p^3. For $\mathcal{D}_b = 10^{-15}$ cm^2 s^{-1}, a particle of diameter 20 nm has a particle-phase timescale of ~1 min, while a particle of diameter 200 nm has a timescale of ~100 min. For these particles, the same mass is required to increase the diameter of 100 particles of diameter 20 nm by 20 more nm as to grow a single particle from a diameter of 200 nm to 240 nm (Zaveri, Shilling, et al., 2018). Thus, as the uptake rate of oxidation products by large semi-solid particles decreases slightly, condensable organics are preferentially taken up by smaller particles with shorter diffusion timescales. In addition, if the condensing oxidation products undergo particle-phase chemistry to form lower volatility products, the uptake of these products by smaller particles will continue to dominate at the expense of the larger particles.

2.4 Summary and Perspectives

Data from laboratory chambers serve as the basis of our understanding of secondary organic aerosol and its formation. Extrapolation of chamber results to the atmosphere requires careful quantification of the processes unique to the laboratory chamber. Computational simulations can play an important role in this quantification and in experimental design.

The present review develops the fundamental foundation for computational simulation of laboratory chamber studies. We have addressed chamber processes: gas-phase dynamics, particle-particle coagulation, particle-wall deposition, vapor-wall deposition, and particle-phase dynamics. The rates and importance of each of these processes depend on various chamber parameters (e.g., chamber size, charge-state,

rate of mixing), particle parameters (e.g., particle size, charge-state, viscosity), and chemical parameters (e.g., volatility, concentration, affinity for the chamber wall).

We have presented here a number of illustrative computational simulations of chamber experiments in order to demonstrate predictions of outcomes sans experimental data. With specified parameter ranges, the result of the computational simulations is an ideal time-dependent SOA yield, for which individual processes can be isolated. The computational procedure can inform chamber and *a priori* experimental design: for example, to optimize for parameters that may be most relevant for the specific aspect of SOA studied. Another powerful attribute of simulation is that one can elucidate components that are difficult (or impossible) to measure; such as the concentration and composition of particles on the chamber walls. Computational models also have the potential to assist in the quantification of experimental uncertainty (Charan et al., 2018; Wiedensohler, Birmili, et al., 2012; Pierce et al., 2008).

To determine parameters necessary for simulation, computational models can be run in an inverse manner. We have given examples of this method in the determination of the wall deposition parameter k_e in Section 2.2.7.1: it is demonstrated here using an optimization procedure based on simulated data. There is significant opportunity for applying computational models to determine parameters relevant for understanding chamber processes and to evaluate chamber/experiment design trade-offs.

In all respects, the most important process occurring in the laboratory chamber is the detailed step-by-step oxidation chemistry that eventually converts a volatile organic species into a spectrum of high- and low-volatility organic molecules. Discerning the molecular routes by which VOC oxidation occurs for a given volatile organic compound lies at the heart of understanding SOA formation. In the present review, in order to illustrate the computational aspects, we have represented gas-phase oxidation by the generic reaction mechanism A → B → C → D, in which the volatility of each successive species decreases by a prescribed amount. For real systems, the understanding of chamber processes achieved via computational simulation can assist in analysis of chemical oxidation data.

The core of the chamber model is the dynamic balance on vapor molecules: production by VOC oxidation, loss by condensation on growing particles, and loss by deposition on the chamber wall. The vapor balance is coupled to a representation of the chemistry of VOC oxidation leading to SOA formation. While in a few instances, an explicit oxidation mechanism for a VOC has been determined, in many

cases such a mechanism is not available. Models of the evolution of volatility and oxidation state of the VOC oxidation product, used to simulate the SOA formation in the absence of an explicit chemical mechanism, have recently emerged.

Two widely used models are the Volatility Basis Set (VBS) (Donahue, Epstein, et al., 2011; Donahue, Kroll, et al., 2012) and the Statistical Oxidation Model (SOM) (Cappa and Wilson, 2012). Each of these models tracks the evolution of oxidation products on a two-dimensional space, with coordinates representing the volatility of the aerosol, such as saturation mass concentration, C^*, and oxygen content, expressed either as O:C ratio, oxidation state OS_c, or explicit numbers of O and C atoms. The Statistical Oxidation Model, for example, describes the many generations from gas-phase reactions that drive production of low volatility vapors as a trajectory through a space of the number of C and O atoms comprising a "species" and calculates the time-varying gas-particle partitioning of these species. The SOM uses six parameters to describe the extent of functionalization (i.e., the number of O atoms added) and fragmentation and the mean vapor pressure decrease per functional group (oxygen) added. These parameters are empirically determined for a given system by fitting the model to experimentally generated time-dependent SOA formation profiles. In short, models that employ either the Volatility Basis Set or the Statistical Oxidation Model simulate SOA evolution with regard to the change in the vapor volatility, the ratio of oxygen atoms to carbon atoms in oxidation products, and the degree of functionalization versus fragmentation during gas-phase reactions.

Historically, detailed analysis of wall effects, particle-particle coagulation, etc. was not carried out in the interpretation of data from SOA chamber experiments. Those historical data form the basis for the representation of SOA formation in large-scale atmospheric chemistry and air quality models. Given initial conditions for past experiments, in principle it is now possible to re-simulate prior experiments, given that VOC oxidation chemistry had been represented by an explicit mechanism or a model such as the Volatility Basis Set or the Statistical Oxidation Model. That re-simulation could provide a revised estimate of SOA yield. For example, Cappa, Jathar, et al. (2016) re-analyzed SOA chamber data by SOM with and without accounting for vapor wall loss, concluding that simulated SOA concentrations can be underestimated significantly.

A number of areas relating to aerosol behavior have not been addressed in this review. Organic particles, in the atmosphere, as well as in the laboratory chamber, may

contain inorganic salts and water as well. Mixtures of organics, inorganic salts, and water are generally complex and non-ideal solutions that involve phase separation (e.g., liquid-liquid or liquid-solid), depending on the presence of hydrophobic and hydrophilic organic compounds. This behavior, which can now be predicted by thermodynamic models, has been observed in both the lab and the field (Zuend, Marcolli, et al., 2010; Zuend and Seinfeld, 2012; Zuend and Seinfeld, 2013; Topping, Barley, and McFiggans, 2013; Chang and Pankow, 2006; You et al., 2014; Smith et al., 2013). The effective mass saturation concentration of the mixture in a particle depends on the non-ideal thermodynamic behavior of the mixture. Moreover, as noted earlier, the phase state of an organic-containing aerosol can be liquid, semi-solid, or solid, depending on its chemical composition and ambient conditions. This range of behavior has been confirmed in laboratory studies, where, under low humidity conditions, organic-containing particles bounce off inertial impaction device surfaces (Reid et al., 2018). Particle viscosity is directly related to its bulk diffusion coefficient. As shown in Figures 2.3 and 2.4, the corresponding characteristic time for molecular diffusion in the particle phase can vary from microseconds to milliseconds for liquid-phase particles, and seconds to years for semi-solids. Consequently, the rate of diffusion in particles may limit rates of mass transport and chemical reactions.

Traditionally, one assumes that the gas-particle equilibrium partitioning of organics is sufficiently fast to be nearly instantaneous. This assumption may not hold if particles are fully or partially semi-solid. The extent to which quasi-equilibrium versus non-equilibrium secondary organic aerosol growth prevails is a key issue in SOA formation. In short, the extent to which SOA phase state, non-ideal thermodynamic mixing, and morphology influence formation, growth, and partitioning must be addressed with each SOA system. Moreover, particle-phase chemistry can play a role as the SOA size distribution and its mass concentration evolve. When multiphase reactions are important, they tend to be important either at or near the particle surface. In this situation, coupling particle-phase chemistry and size distribution dynamics becomes important.

Overall, one or many generations of gas-phase oxidation products condense into or onto particles to form secondary organic aerosol. Particle growth is governed by the rate of these reactions involving sequential and parallel reaction pathways, as well as the chemical kinetics that can be limited by gas-, interfacial, and particle-phase mass transport. Computational simulation provides a means to reveal the roles of

these various processes and to differentiate, for each chemical system, the different limiting factors.

APPENDIX

2.A Variables and Abbreviations

Table 2.A.1: Variables and Typical Units. Some symbols may differ from their primary references; each was chosen for convenience. For variables that are unitless, the units column is left blank.

Variable	Units	Description
a	m	particle radius
A	m^2	chamber surface area
α		probability of two particles sticking together upon collision
α_p		mass accommodation coefficient of vapor molecules to particles suspended in the bulk chamber
α_{pw}		mass accommodation coefficient of vapor molecules to particles deposited on the chamber wall
α_w		mass accommodation coefficient of vapor molecules to the chamber wall itself
B_n		roots of $B_n \cot(B_n) + L - 1 = 0$
$\beta(D_p)$	min^{-1}	first-order particle wall deposition coefficient for a particle with diameter D_p
$\beta_{n_c}(D_p)$	min^{-1}	first-order particle wall deposition coefficient for a particle with diameter D_p and charge $n_c e$
$\bar{\beta}$	min^{-1}	particle-volume-weighted first-order particle wall deposition coefficient
$\bar{c}$	$m\,s^{-1}$	root-mean-square velocity of particles
C^*	$\mu g\,m^{-3}$	saturation mass concentration
C_{aq}	$\mu g\,m^{-3}$	vapor concentration in aqueous phase
C_g^b	$\mu g\,m^{-3}$	gas-phase concentration in the bulk chamber
$C_{g,0}^b$	$\mu g\,m^{-3}$	initial gas-phase concentration in the bulk chamber
C_g^0	$\mu g\,m^{-3}$	influent gas-phase concentration to the CMFR
C_C		Cunningham slip-correction factor
C_{in}	$\mu g\,m^{-3}$	transient concentration of the inner layer

C_{par}	µg m^{-3}	concentration of a species in the particle
C_s	µg m^{-3}	vapor concentration dissolved in the surface layer of the wall
C_{sa}	µm^2 cm^{-3}	total particle surface area concentration
C_w	mg m^{-3}	equivalent absorbing mass of the wall
C_w'	mg m^{-3}	activity-corrected equivalent absorbing mass of the wall
$\mathcal{D}_b$	cm^2 s^{-1}	diffusivity inside a particle
$\mathcal{D}_{eff}$	m^2 s^{-1}	effective diffusivity of vapor molecules in the inner layer
$\mathcal{D}_g$	m^2 s^{-1}	molecular diffusion coefficient
$\mathcal{D}_{par}$	cm^2 s^{-1}	particle Brownian diffusivity
D_p	nm	particle diameter
D_{pg}	nm	median particle diameter of a lognormal distribution
ΔSOA	µg m^{-3}	change in mass of SOA
ΔSOA$_{dep}$	µg m^{-3}	change in mass of SOA that is on wall-deposited particles
ΔSOA$_{sus}$	µg m^{-3}	change in mass of SOA that is on suspended particles
Δt	s	timestep
ΔVOC	µg m^{-3}	change in mass of reacted precursor
e	C	elementary charge
$\bar{E}$	V cm^{-1}	mean electric field experienced by particles suspended in the chamber
ϵ		dielectric constant of air
ϵ_0	F m^{-1}	permittivity of free space
f_c		particle apportionment factor
$f(\text{Kn}, \alpha_p)$		Fuchs-Sutugin correction factor
g	m s^{-2}	gravitational constant
g_i	nm	mean distance of one mean free path from the surface of a sphere
γ^∞		activity coefficient of a compound in a dilute Teflon film solution
H	mol m^{-3} Pa^{-1}	Henry's law constant between gas and particle phases

H'		dimensionless Henry's law constant between gas and particle phases
$I_D(D_p, t)$	nm s^{-1}	rate of change of particle diameter due to condensation or evaporation
J	nm s cm^{-6}	minimization function
$J_d\|_{x=L_e}$	µg s^{-1}	interfacial diffusive flux from the surface layer to the inner layer
k_B	m^2 kg s^{-2} K^{-1}	Boltzmann constant
k	s^{-1}	first-order rate constant for particle-phase reaction
k_e	s^{-1}	eddy-diffusion coefficient
$K_{i,j}$ or $K(i,j)$	cm^3 s^{-1}	coagulation kernel between particles i and j
k_{OH}	s^{-1}	first-order rate constant of reaction with the hydroxyl radical
k_{si}	s^{-1}	first-order decay rate of C_s
k_{vw}	s^{-1}	vapor to wall transfer rate
k_{vwe}	s^{-1}	pseudo-first-order rate coefficient for vapor wall equilibrium
k_{wv}	s^{-1}	wall to vapor transfer rate
K_{vwe}		vapor-wall equilibrium constant
κ		correction to the coagulation coefficient due to charging
L		ratio of gas-particle mass transport rate to particle-phase diffusion velocity
L_{aq}	nm	aqueous film thickness
L_e	nm	surface layer thickness of the wall
λ	nm	mean free path of air
m	µg m^3	mass concentration
M_i	g mol^{-1}	molecular weight of species i
μ	kg m^{-1} s^{-1}	viscosity of air
N	cm^{-3}	total number concentration
n_c		number of elementary charges on a particle
$n(D_p, t)$	nm^{-1} cm^{-3}	particle number concentration distribution at time t
$n^0(D_p)$	nm^{-1} cm^{-3}	particle number concentration distribution in the influent flow of a CMFR

n_{obs}	cm^{-3}	measured particle number concentration
n_{pred}	cm^{-3}	particle number concentration predicted using the given parameters
v	m s^{-1}	overall mass transfer coefficient between the bulk gas-phase and the particle surface
v_c	m s^{-1}	mass transfer coefficient through the vapor-Teflon interface
v_e	m s^{-1}	mass transfer coefficient across the gas-phase boundary layer
$\bar{v}_e$	m s^{-1}	electrostatic migration velocity
v_l	m s^{-1}	mass transfer coefficient through the gas-phase boundary and the vapor-Teflon interface
v_s	m s^{-1}	terminal particle settling velocity
p	Pa	total pressure
$p_{eq,i}$	Pa	equilibrium vapor pressure of species i, accounting for the Kelvin effect
$p^{\circ}_{eq,i}$	Pa	equilibrium vapor pressure of the pure species i
p_i	Pa	vapor pressure of species i
r	m	characteristic lengthscale for the chamber
R	J mol^{-1} K^{-1}	ideal gas constant
R_i	µg m^{-3}	net accumulation rate of species i through chemical reaction and vapor-particle partitioning
ρ_p	g cm^{-3}	density of the particle-phase
ρ_w	g cm^{-3}	density of the wall material
σ	dyn cm^{-1}	surface tension of the particle phase
σ_g		standard deviation of a lognormal distribution
t	s	time
t_f	s	total time
T	K or °C	temperature
τ_{CMFR}	s	average residence time of a CMFR
τ_{ipe}	s	timescale for interfacial particle equilibrium
τ_{vwe}	s	timescale for vapor-wall equilibrium
v	m s^{-1}	vapor molecular mean speed

χ_i		mole fraction of the species i in the particle phase
V	m^3	volume of the chamber
Y		SOA yield
Z	$s\ m^2\ V^{-1}$	electrical mobility

Table 2.A.2: A list of abbreviations from this chapter.

Abbreviation	Description
CMFR	continuously mixed flow reactor
D_1	first-order Debye function
δ	a small change of the relevant value
FEP	fluorinated ethylene propylene
GDE	aerosol general dynamic equation
IVOC	intermediate-volatility organic compound
Ki	kinetic growth versus quasi-equilibrium dimensionless number
Kn	Knudsen number
LVOC	low-volatility organic compound
NO_x	oxides of nitrogen
OH	hydroxyl radical
POA	primary organic aerosol
RH	relative humidity
RO_2	peroxy radicals
SOA	secondary organic aerosol
SOM	Statistical Oxidation Model
SVOC	semivolatile organic compound
VBS	Volatility Basis Set
VOC	volatile organic compound

References

Abbatt, Jon, Christian George, Megan Melamed, Paul Monks, Spyros Pandis, and Yinon Rudich (Feb. 2014). "New directions: fundamentals of atmospheric chemistry: keeping a three-legged stool balanced." In: *Atmos. Environ.* 84, pp. 390–391. ISSN: 13522310. DOI: 10.1016/j.atmosenv.2013.10.025.

Barley, M. H. and G. McFiggans (Jan. 2010). "The critical assessment of vapour pressure estimation methods for use in modelling the formation of atmospheric organic aerosol." In: *Atmos. Chem. Phys.* 10.2, pp. 749–767. ISSN: 1680-7324. DOI: 10.5194/acp-10-749-2010.

Bian, Q., A. A. May, S. M. Kreidenweis, and J. R. Pierce (2015). "Investigation of particle and vapor wall-loss effects on controlled wood-smoke smog-chamber experiments." In: *Atmos. Chem. Phys.* 15.19, pp. 11027–11045. DOI: `10.5194/acp-15-11027-2015`.

Boedeker (2017). *PTFE, FEP, and PFA Specifications*. URL: `http://www.boedeker.com/feppfa_p.htm` (visited on 01/23/2017).

Buckley, Alison J., Matthew D. Wright, and Denis L. Henshaw (2008). "A technique for rapid estimation of the charge distribution of submicron aerosols under atmospheric conditions." In: *Aerosol Sci. Technol.* 42.12, pp. 1042–1051. ISSN: 02786826. DOI: `10.1080/02786820802400645`.

Burkholder, James B. et al. (2017). "The essential role for laboratory studies in atmospheric chemistry." In: *Environ. Sci. Technol.* 51.5, pp. 2519–2528. ISSN: 0013-936X. DOI: `10.1021/acs.est.6b04947`.

Bzdek, Bryan R. and Jonathan P. Reid (2017). "Perspective: aerosol microphysics: from molecules to the chemical physics of aerosols." In: *J. Chem. Phys.* 147.22, p. 220901. DOI: `10.1063/1.5002641`.

Cappa, C. D. and K. R. Wilson (2012). "Multi-generation gas-phase oxidation, equilibrium partitioning, and the formation and evolution of secondary organic aerosol." In: *Atmos. Chem. Phys.* 12.20, pp. 9505–9528. DOI: `10.5194/acp-12-9505-2012`.

Cappa, Christopher D., Shantanu H. Jathar, Michael J. Kleeman, Kenneth S. Docherty, Jose L. Jimenez, John H. Seinfeld, and Anthony S. Wexler (2016). "Simulating secondary organic aerosol in a regional air quality model using the statistical oxidation model - Part 2: Assessing the influence of vapor wall losses." In: *Atmos. Chem. Phys.* 16.5, pp. 3041–3059. ISSN: 16807324. DOI: `10.5194/acp-16-3041-2016`.

Chang, Elsa I. and James F. Pankow (2006). "Prediction of activity coefficients in liquid aerosol particles containing organic compounds, dissolved inorganic salts, and water-Part 2: Consideration of phase separation effects by an X-UNIFAC model." In: *Atmos. Environ.* 40.33, pp. 6422–6436. DOI: `10.1016/j.atmosenv.2006.04.031`.

Charan, Sophia M., Weimeng Kong, Richard C. Flagan, and John H. Seinfeld (2018). "Effect of particle charge on aerosol dynamics in Teflon environmental chambers." In: *Aerosol Science and Technology* 52.8, pp. 854–871. DOI: `10.1080/02786826.2018.1474167`.

Compernolle, S., K. Ceulemans, and J.-F. Müller (2011). "EVAPORATION: a new vapour pressure estimation method for organic molecules including non-additivity and intramolecular interactions." In: *Atmos. Chem. Phys.* 11.18, pp. 9431–9450. DOI: `10.5194/acp-11-9431-2011`.

Crank, J. (1953). "A theoretical investigation of the influence of molecular relaxation and internal stress on diffusion in polymers." In: *J. Polym. Sci.* 11.2, pp. 151–168. DOI: 10.1002/pol.1953.120110206.

Crounse, John D., Lasse B. Nielsen, Solvejg Jørgensen, Henrik G. Kjaergaard, and Paul O. Wennberg (2013). "Autoxidation of organic compounds in the atmosphere." In: *J. Phys. Chem. Lett.* 4.20, pp. 3513–3520. DOI: 10.1021/jz4019207.

Crump, James G. and John H. Seinfeld (1981). "Turbulent deposition and gravitational sedimentation of an aerosol in a vessel of arbitrary shape." In: *Journal of Aerosol Science* 12.5, pp. 405–415. ISSN: 00218502. DOI: 10.1016/0021-8502(81)90036-7.

Donahue, N. M., S. A. Epstein, S. N. Pandis, and A. L. Robinson (2011). "A two-dimensional volatility basis set: 1. organic–aerosol mixing thermodynamics." In: *Atmos. Chem. Phys.* 11.7, pp. 3303–3318. DOI: 10.5194/acp-11-3303-2011.

Donahue, N. M., K. M. Henry, et al. (2012). "Aging of biogenic secondary organic aerosol via gas-phase OH radical reactions." In: *Proc. Natl. Acad. Sci. U.S.A.* 109.34, pp. 13503–13508. ISSN: 0027-8424. DOI: 10.1073/pnas.1115186109.

Donahue, N. M., J. H. Kroll, S. N. Pandis, and A. L. Robinson (2012). "A two-dimensional volatility basis set: 2. diagnostics of organic-aerosol evolution." In: *Atmos. Chem. Phys.* 12.2, pp. 615–634. DOI: 10.5194/acp-12-615-2012.

Donahue, N. M., A. L. Robinson, C. O. Stanier, and S. N. Pandis (2006). "Coupled partitioning, dilution, and chemical aging of semivolatile organics." In: *Environ. Sci. Technol.* 40.8, pp. 2635–2643. DOI: 10.1021/es052297c.

Flagan, Richard C. (2014). "Continuous-flow differential mobility analysis of nanoparticles and biomolecules." In: *Annu. Rev. Chem. Biomol. Eng.* 5.1, pp. 255–279. ISSN: 1947-5438. DOI: 10.1146/annurev-chembioeng-061312-103316.

Frisch, H. L. (1980). "Sorption and transport in glassy polymers - a review." In: *Polym. Eng. Sci.* 20.1, pp. 2–13. DOI: 10.1002/pen.760200103.

Fuchs, N. A. (Sept. 1963). "On the stationary charge distribution on aerosol particles in a bipolar ionic atmosphere." In: *Geofis. Pura Appl. (Engl. Transl.)* 56.1, pp. 185–193. ISSN: 0033-4553. DOI: 10.1007/BF01993343.

– (1964). *The mechanics of aerosols*. Oxford: Pergamon Press. ISBN: 0-486-66055-9.

Fuchs, N. A. and A. G. Sutugin (1971). "High-dispersed aerosols." In: *Topics in Current Aerosol Research*. Ed. by G. M. Hidy and J. R. Brock. Oxford: Pergamon Press. Chap. High-dispersed aerosols, pp. 1–60. DOI: 10.1016/B978-0-08-016674-2.50006-6.

Gelbard, F. and J. H. Seinfeld (1979). "The general dynamic equation for aerosols." In: *J. Colloid Interface Sci.* 68.2, pp. 363–382.

Ghosh, K., S.N. Tripathi, Manish Joshi, Y.S. Mayya, Arshad Khan, and B.K. Sapra (Mar. 2017). "Modeling studies on coagulation of charged particles and comparison with experiments." In: *Journal of Aerosol Science* 105, pp. 35–47. ISSN: 00218502. DOI: 10.1016/j.jaerosci.2016.11.019.

Goldstein, Allen H. and Ian E. Galbally (Mar. 2007). "Known and unexplored organic constituents in the Earth's atmosphere." In: *Environ. Sci. Technol.* 41.5, pp. 1514–1521. ISSN: 0013-936X. DOI: 10.1021/es072476p.

Hallquist, M. et al. (July 2009). "The formation, properties and impact of secondary organic aerosol: current and emerging issues." In: *Atmos. Chem. Phys.* 9.14, pp. 5155–5236. ISSN: 1680-7324. DOI: 10.5194/acp-9-5155-2009.

Han, Yuemei, Zhaoheng Gong, Pengfei Liu, Suzane S. de Sá, Karena A. McKinney, and Scot T. Martin (2019). "Influence of particle surface area concentration on the production of organic particulate matter in a continuously mixed flow reactor." In: *Environ. Sci. Technol.* 53.9, pp. 4968–4976. DOI: 10.1021/acs.est.8b07302.

Hildebrandt, L., N. M. Donahue, and S. N. Pandis (2009). "High formation of secondary organic aerosol from the photo-oxidation of toluene." In: *Atmos. Chem. Phys.* 9.9, pp. 2973–2986. ISSN: 16807316. DOI: 10.5194/acp-9-2973-2009.

Hirsikko, A., T. Nieminen, et al. (Jan. 2011). "Atmospheric ions and nucleation: a review of observations." In: *Atmospheric Chemistry and Physics* 11.2, pp. 767–798. ISSN: 1680-7324. DOI: 10.5194/acp-11-767-2011.

Hirsikko, Anne, Taina Yli-Juuti, Tuomo Nieminen, Eija Vartiainen, Lauri Laakso, Tareq Hussein, and Markku Kulmala (2007). "Indoor and outdoor air ions and aerosol particles in the urban atmosphere of Helsinki: characteristics, sources and formation." In: *Boreal Environment Research* 12, 295–310. ISSN: 12396095. URL: http://www.borenv.net/BER/archive/pdfs/ber12/ber12-295.pdf.

Hoppel, W. A. and G. M. Frick (1990). "The nonequilibrium character of the aerosol charge distributions produced by neutralizers." In: *Aerosol Sci. Technol.* 12.3, pp. 471–496. ISSN: 15217388. DOI: 10.1080/02786829008959363.

Hoppel, William A. and Glendon M. Frick (Jan. 1986). "Ion–aerosol attachment coefficients and the steady-state charge distribution on aerosols in a bipolar ion environment." In: *Aerosol Sci. Technol.* 5.1, pp. 1–21. ISSN: 0278-6826. DOI: 10.1080/02786828608959073.

Huang, Yuanlong, Ran Zhao, Sophia M. Charan, Christopher M. Kenseth, Xuan Zhang, and John H. Seinfeld (2018). "Unified theory of vapor–wall mass transport in Teflon–walled environmental chambers." In: *Environ. Sci. Technol.* 52.4, pp. 2134–2142. DOI: 10.1021/acs.est.7b05575.

Isaacman-VanWertz, Gabriel et al. (Apr. 2018). "Chemical evolution of atmospheric organic carbon over multiple generations of oxidation." In: *Nat. Chem.* 10.4, pp. 462–468. ISSN: 1755-4330. DOI: 10.1038/s41557-018-0002-2.

Julin, Jan, Paul M. Winkler, Neil M. Donahue, Paul E. Wagner, and Ilona Riipinen (Oct. 2014). "Near-unity mass accommodation coefficient of organic molecules of varying structure." In: *Environ. Sci. Technol.* 48.20, pp. 12083–12089. ISSN: 0013-936X. DOI: 10.1021/es501816h.

Kallinger, Peter and Wladyslaw W. Szymanski (Apr. 2015). "Experimental determination of the steady-state charging probabilities and particle size conservation in non-radioactive and radioactive bipolar aerosol chargers in the size range of 5–40 nm." In: *J. Nanopart. Res.* 17.4, pp. 1–12. ISSN: 1388-0764. DOI: 10.1007/s11051-015-2981-x.

Kanakidou, M. et al. (Mar. 2005). "Organic aerosol and global climate modelling: a review." In: *Atmos. Chem. Phys.* 5.4, pp. 1053–1123. ISSN: 1680-7324. DOI: 10.5194/acp-5-1053-2005.

Kokkola, H., P. Yli-Pirila, M. Vesterinen, H. Korhonen, H. Keskinen, S. Romakkaniemi, L. Hao, A. Kortelainen, J. Joutsensaari, D. R. Worsnop, A. Virtanen, and K. E.J. Lehtinen (2014). "The role of low volatile organics on secondary organic aerosol formation." In: *Atmos. Chem. Phys.* 14.3, pp. 1689–1700. ISSN: 16807316. DOI: 10.5194/acp-14-1689-2014.

Kolb, C. E. et al. (2010). "An overview of current issues in the uptake of atmospheric trace gases by aerosols and clouds." In: *Atmos. Chem. Phys.* 10.21, pp. 10561–10605. ISSN: 16807316. DOI: 10.5194/acp-10-10561-2010.

Krechmer, Jordan E., Matthew M. Coggon, et al. (2015). "Formation of low volatility organic compounds and secondary organic aerosol from isoprene hydroxyhydroperoxide low-NO oxidation." In: *Environ. Sci. Technol.* 49.17, pp. 10330–10339. DOI: 10.1021/acs.est.5b02031.

Krechmer, Jordan E., Demetrios Pagonis, Paul J. Ziemann, and Jose L. Jimenez (June 2016). "Quantification of gas-wall partitioning in Teflon environmental chambers using rapid bursts of low-volatility oxidized species generated in situ." In: *Environ. Sci. Technol.* 50.11, pp. 5757–5765. ISSN: 15205851. DOI: 10.1021/acs.est.6b00606.

Kroll, Jesse H. and John H. Seinfeld (May 2008). "Chemistry of secondary organic aerosol: formation and evolution of low-volatility organics in the atmosphere." In: *Atmos. Environ.* 42.16, pp. 3593–3624. ISSN: 13522310. DOI: 10.1016/j.atmosenv.2008.01.003.

Kuwata, Mikinori and Scot T. Martin (2012). "Particle size distributions following condensational growth in continuous flow aerosol reactors as derived from residence time distributions: theoretical development and application to secondary organic aerosol." In: *Aerosol Sci. Technol.* 46.8, pp. 937–949. DOI: 10.1080/02786826.2012.683204.

La, Y. S., M. Camredon, P. J. Ziemann, R. Valorso, A. Matsunaga, V. Lannuque, J. Lee-Taylor, A. Hodzic, S. Madronich, and B. Aumont (2016). "Impact of chamber wall loss of gaseous organic compounds on secondary organic aerosol formation:

explicit modeling of SOA formation from alkane and alkene oxidation." In: *Atmos. Chem. Phys.* 16.3, pp. 1417–1431. DOI: `10.5194/acp-16-1417-2016`.

Laakso, Lauri, Markku Kulmala, and Kari E. J. Lehtinen (2003). "Effect of condensation rate enhancement factor on 3–nm (diameter) particle formation in binary ion–induced and homogeneous nucleation." In: *J. Geophys. Res.* 108.D18. DOI: `10.1029/2003JD003432`.

Liu, Albert Tianxiang, Rahul A. Zaveri, and John H. Seinfeld (June 2014). "Analytical solution for transient partitioning and reaction of a condensing vapor species in a droplet." In: *Atmos. Environ.* 89, pp. 651–654. ISSN: 13522310. DOI: `10.1016/j.atmosenv.2014.02.065`.

Liu, Xiaoxi, Douglas A. Day, Jordan E. Krechmer, Wyatt Brown, Zhe Peng, Paul J. Ziemann, and Jose L. Jimenez (2019). "Direct measurements of semi-volatile organic compound dynamics show near-unity mass accommodation coefficients for diverse aerosols." In: *Communications Chemistry* 2.98, pp. 1–9. DOI: `10.1038/s42004-019-0200-x`.

López-Yglesias, Xerxes and Richard C. Flagan (2013a). "Ion-aerosol flux coefficients and the steady-state charge distribution of aerosols in a bipolar ion environment." In: *Aerosol Sci. Technol.* 47.6, pp. 688–704. ISSN: 02786826. DOI: `10.1080/02786826.2013.783684`.

– (2013b). "Population balances of micron–sized aerosols in a bipolar ion environment." In: *Aerosol Sci. Technol.* 47.6, pp. 681–687. DOI: `10.1080/02786826.2013.783683`.

Loza, C. L., P. S. Chhabra, L. D. Yee, J. S. Craven, R. C. Flagan, and J. H. Seinfeld (2012). "Chemical aging of m-xylene secondary organic aerosol: Laboratory chamber study." In: *Atmosp. Chem. Phys.* 12.1, pp. 151–167. ISSN: 16807316. DOI: `10.5194/acp-12-151-2012`.

Loza, Christine L., Arthur W. H. Chan, Melissa M. Galloway, Frank N. Keutsch, Richard C. Flagan, and John H. Seinfeld (2010). "Characterization of vapor wall loss in laboratory chambers." In: *Environ. Sci. Technol.* 44.13, pp. 5074–5078. DOI: `10.1021/es100727v`.

Mai, Huajun, Manabu Shiraiwa, Richard C. Flagan, and John H. Seinfeld (Oct. 2015). "Under what conditions can equilibrium gas–particle partitioning be expected to hold in the atmosphere?" In: *Environ. Sci. Technol.* 49.19, pp. 11485–11491. ISSN: 0013-936X. DOI: `10.1021/acs.est.5b02587`.

Martin, Scot T., Mikinori Kuwata, and Mackenzie L. Smith (2014). "An analytic equation for the volume fraction of condensationally grown mixed particles and applications to secondary organic material produced in continuously mixed flow reactors." In: *Aerosol Sci. Technol.* 48.8, pp. 803–812. DOI: `10.1080/02786826.2014.931564`.

Matsunaga, Aiko and Paul J. Ziemann (Aug. 2010). "Gas-wall partitioning of organic compounds in a Teflon film chamber and potential effects on reaction product and aerosol yield measurements." In: *Aerosol Sci. Technol.* 44.10, pp. 881–892. ISSN: 0278-6826. DOI: `10.1080/02786826.2010.501044`.

McMurry, P. H. and D. J. Rader (Jan. 1985). "Aerosol Wall Losses in Electrically Charged Chambers." In: *Aerosol Science and Technology* 4.3, pp. 249–268. ISSN: 0278-6826. DOI: `10.1080/02786828508959054`.

McVay, Renee C., Christopher D. Cappa, and John H. Seinfeld (Sept. 2014). "Vapor-wall deposition in chambers: Theoretical considerations." In: *Environ. Sci. Technol.* 48.17, pp. 10251–10258. ISSN: 15205851. DOI: `10.1021/es502170j`.

Mikhailov, E., S. Vlasenko, S. T. Martin, T. Koop, and U. Pöschl (Dec. 2009). "Amorphous and crystalline aerosol particles interacting with water vapor: conceptual framework and experimental evidence for restructuring, phase transitions and kinetic limitations." In: *Atmos. Chem. Phys.* 9.24, pp. 9491–9522. ISSN: 1680-7324. DOI: `10.5194/acp-9-9491-2009`.

Nah, T., R. C. McVay, X. Zhang, C. M. Boyd, J. H. Seinfeld, and N. L. Ng (2016). "Influence of seed aerosol surface area and oxidation rate on vapor wall deposition and SOA mass yields: a case study with α-pinene ozonolysis." In: *Atmos. Chem. Phys.* 16.14, pp. 9361–9379. DOI: `10.5194/acp-16-9361-2016`.

Nah, Theodora, Renee C. McVay, Jeffrey R. Pierce, John H. Seinfeld, and Nga L. Ng (Feb. 2017). "Constraining uncertainties in particle-wall deposition correction during SOA formation in chamber experiments." In: *Atmospheric Chemistry and Physics* 17.3, pp. 2297–2310. ISSN: 1680-7324. DOI: `10.5194/acp-17-2297-2017`.

O'Meara, Simon, Alastair Murray Booth, Mark Howard Barley, David Topping, and Gordon McFiggans (2014). "An assessment of vapour pressure estimation methods." In: *Phys. Chem. Chem. Phys.* 16.36, pp. 19453–19469. ISSN: 1463-9076. DOI: `10.1039/C4CP00857J`.

Odum, Jay R., Thorsten Hoffmann, Frank Bowman, Don Collins, Richard C. Flagan, and John H. Seinfeld (1996). "Gas–particle partitioning and secondary organic aerosol yields." In: *Environ. Sci. Technol.* 30.8, pp. 2580–2585. ISSN: 0013-936X. DOI: `10.1021/es950943+`.

Park, S. H. and K. W. Lee (Sept. 2000). "Condensational growth of polydisperse aerosol for the entire particle size range." In: *Aerosol Sci. Technol.* 33.3, pp. 222–227. ISSN: 0278-6826. DOI: `10.1080/027868200416213`.

Pierce, J. R., G. J. Engelhart, L. Hildebrandt, E. A. Weitkamp, R. K. Pathak, N. M. Donahue, A. L. Robinson, P. J. Adams, and S. N. Pandis (Oct. 2008). "Constraining particle evolution from wall losses, coagulation, and condensation-evaporation in smog-chamber experiments: Optimal estimation based on size distribution measurements." In: *Aerosol Sci. Technol.* 42.12, pp. 1001–1015. ISSN: 0278-6826. DOI: `10.1080/02786820802389251`.

Pöschl, Ulrich and Manabu Shiraiwa (2015). "Multiphase chemistry at the atmosphere-biosphere interface influencing climate and public health in the anthropocene." In: *Chem. Rev.* 115.10, pp. 4440–4475. DOI: `10.1021/cr500487s`.

Reid, Jonathan P., Allan K. Bertram, David O. Topping, Alexander Laskin, Scot T. Martin, Markus D. Petters, Francis D. Pope, and Grazia Rovelli (Dec. 2018). "The viscosity of atmospherically relevant organic particles." In: *Nat. Commun.* 9.1, pp. 1–14. ISSN: 2041-1723. DOI: `10.1038/s41467-018-03027-z`.

Renbaum-Wolff, L., J. W. Grayson, A. P. Bateman, M. Kuwata, M. Sellier, B. J. Murray, J. E. Shilling, S. T. Martin, and A. K. Bertram (May 2013). "Viscosity of α-pinene secondary organic material and implications for particle growth and reactivity." In: *Proc. Natl. Acad. Sci. U.S.A.* 110.20, pp. 8014–8019. ISSN: 0027-8424. DOI: `10.1073/pnas.1219548110`.

Saleh, Rawad, Neil M. Donahue, and Allen L. Robinson (June 2013). "Time scales for gas-particle partitioning equilibration of secondary organic aerosol formed from alpha-pinene ozonolysis." In: *Environ. Sci. Technol.* 47.11, pp. 5588–5594. ISSN: 0013-936X. DOI: `10.1021/es400078d`.

Saukko, E., A. T. Lambe, P. Massoli, T. Koop, J. P. Wright, D. R. Croasdale, D. A. Pedernera, T. B. Onasch, A. Laaksonen, P. Davidovits, D. R. Worsnop, and A. Virtanen (Aug. 2012). "Humidity-dependent phase state of SOA particles from biogenic and anthropogenic precursors." In: *Atmos. Chem. Phys.* 12.16, pp. 7517–7529. ISSN: 1680-7324. DOI: `10.5194/acp-12-7517-2012`.

Schwantes, Rebecca H., Sophia M. Charan, Kelvin H. Bates, Yuanlong Huang, Tran B. Nguyen, Huajun Mai, Weimeng Kong, Richard C. Flagan, and John H. Seinfeld (2019). "Low-volatility compounds contribute significantly to isoprene secondary organic aerosol (SOA) under high-NO_x conditions." In: *Atmospheric Chemistry and Physics* 19.11, pp. 7255–7278. DOI: `10.5194/acp-19-7255-2019`.

Schwantes, Rebecca H., Renee C. McVay, Xuan Zhang, Matthew M. Coggon, Hanna Lignell, Richard C. Flagan, Paul O. Wennberg, and John H. Seinfeld (2017). In: *Advances in Atmospheric Chemistry Volume I*. Ed. by J.R. Barker, A.L. Steiner, and T.J. Wallington. Singapore: World Scientific. Chap. Science of the environmental chamber, pp. 1–93. ISBN: 978-981-3147-34-8.

Schwarzenbach, Rene P., Philip M. Gschwend, and Dieter M. Imboden (2005). *Environmental organic chemistry*. 2nd. Hoboken, New Jersey: John Wiley & Sons, Inc. ISBN: 9780471350538. DOI: `10.1002/0471649643`.

Seinfeld, John H., Tadeusz E. Kleindienst, Edward O. Edney, and Jason B. Cohen (2003). "Aerosol growth in a steady-state, continuous flow chamber: application to studies of secondary aerosol formation." In: *Aerosol Sci. Technol.* 37.9, pp. 728–734. DOI: `10.1080/02786820300915`.

Seinfeld, John H. and Spyros N. Pandis (2016). *Atmospheric Chemistry and Physics: From Air Pollution to Climate Change*. 3rd. Hoboken: John Wiley & Sons. ISBN: 978-1118947401.

Shiraiwa, M., C. Pfrang, T. Koop, and U. Pöschl (Mar. 2012). "Kinetic multi-layer model of gas-particle interactions in aerosols and clouds (KM-GAP): linking condensation, evaporation and chemical reactions of organics, oxidants and water." In: *Atmos. Chem. Phys.* 12.5, pp. 2777–2794. ISSN: 1680-7324. DOI: `10.5194/acp-12-2777-2012`.

Shiraiwa, Manabu, Markus Ammann, Thomas Koop, and Ulrich Pöschl (2011). "Gas uptake and chemical aging of semisolid organic aerosol particles." In: *Proc. Natl. Acad. Sci. U.S.A.* 108.27, pp. 11003–11008. DOI: `10.1073/pnas.1103045108`.

Shiraiwa, Manabu and John H. Seinfeld (2012). "Equilibration timescale of atmospheric secondary organic aerosol partitioning." In: *Geophys. Res. Lett.* 39.24, pp. 1–6. ISSN: 00948276. DOI: `10.1029/2012GL054008`.

Shiraiwa, Manabu, Lindsay D. Yee, Katherine A. Schilling, Christine L. Loza, Jill S. Craven, Andreas Zuend, Paul J. Ziemann, and John H. Seinfeld (July 2013). "Size distribution dynamics reveal particle-phase chemistry in organic aerosol formation." In: *Proc. Natl. Acad. Sci. U.S.A.* 110.29, pp. 11746–11750. ISSN: 0027-8424. DOI: `10.1073/pnas.1307501110`.

Shiraiwa, Manabu, Andreas Zuend, Allan K. Bertram, and John H. Seinfeld (2013). "Gas–particle partitioning of atmospheric aerosols: interplay of physical state, non-ideal mixing and morphology." In: *Phys. Chem. Chem. Phys.* 15.27, pp. 11441–11453. ISSN: 1463-9076. DOI: `10.1039/c3cp51595h`.

Shrivastava, Manish et al. (2017). "Recent advances in understanding secondary organic aerosol: implications for global climate forcing." In: *Rev. Geophys.* 55.2, pp. 509–559. DOI: `10.1002/2016RG000540`.

Smith, Mackenzie L., Yuan You, Mikinori Kuwata, Allan K. Bertram, and Scot T. Martin (2013). "Phase transitions and phase miscibility of mixed particles of ammonium sulfate, toluene-derived secondary organic material, and water." In: *J. Phys. Chem. A* 117.36, pp. 8895–8906. DOI: `10.1021/jp405095e`.

Song, M., P. F. Liu, S. J. Hanna, Y. J. Li, S. T. Martin, and A. K. Bertram (May 2015). "Relative humidity-dependent viscosities of isoprene-derived secondary organic material and atmospheric implications for isoprene-dominant forests." In: *Atmos. Chem. Phys.* 15.9, pp. 5145–5159. ISSN: 1680-7324. DOI: `10.5194/acp-15-5145-2015`.

Steiner, Gerhard and Georg P. Reischl (Dec. 2012). "The effect of carrier gas contaminants on the charging probability of aerosols under bipolar charging conditions." In: *J. Aerosol Sci.* 54, pp. 21–31. ISSN: 00218502. DOI: `10.1016/j.jaerosci.2012.07.008`.

Sunol, A. M., S. M. Charan, and J. H. Seinfeld (2018). "Computational simulation of the dynamics of secondary organic aerosol formation in an environmental chamber." In: *Aerosol Science and Technology* 52.4, pp. 470–482. ISSN: 15217388. DOI: `10.1080/02786826.2018.1427209`.

Tian, J., B. T. Brem, M. West, T. C. Bond, M. J. Rood, and N. Riemer (July 2017). "Simulating aerosol chamber experiments with the particle-resolved aerosol model PartMC." In: *Aerosol Sci. Technol.* 51.7, pp. 856–867. ISSN: 0278-6826. DOI: `10.1080/02786826.2017.1311988`.

Tigges, L., A. Jain, and H.-J. Schmid (Oct. 2015). "On the bipolar charge distribution used for mobility particle sizing: Theoretical considerations." In: *J. Aerosol Sci.* 88, pp. 119–134. ISSN: 00218502. DOI: `10.1016/j.jaerosci.2015.05.010`.

Tokarev, A., K. Friess, J. Machkova, M. Šipek, and Yu. Yampolskii (2006). "Sorption and diffusion of organic vapors in amorphous Teflon AF2400." In: *J. Polym. Sci. Pol. Phys.* 44.5, pp. 832–844. ISSN: 1099-0488. DOI: `10.1002/polb.20725`.

Topping, David, Mark Barley, and Gordon McFiggans (2013). "Including phase separation in a unified model to calculate partitioning of vapours to mixed inorganic-organic aerosol particles." In: *Faraday Discuss.* 165.0, pp. 273–288. DOI: `10.1039/C3FD00047H`.

Topping, David and Dave Jones (2016). *UManSysProp*. URL: `http://umansysprop.seaes.manchester.ac.uk/tool/vapour_pressure`.

Tropo (2014). *Vapour pressure of pure liquid organic compounds*. URL: `http://tropo.aeronomie.be/models/evaporation_run.htm` (visited on 06/11/2014).

Trump, Erica R., Scott A. Epstein, Ilona Riipinen, and Neil M. Donahue (Nov. 2016). "Wall effects in smog chamber experiments: a model study." In: *Aerosol Sci. Technol.* 50.11, pp. 1180–1200. ISSN: 0278-6826. DOI: `10.1080/02786826.2016.1232858`.

Vaden, T. D., D. Imre, J. Beranek, M. Shrivastava, and A. Zelenyuk (Feb. 2011). "Evaporation kinetics and phase of laboratory and ambient secondary organic aerosol." In: *Proc. Natl. Acad. Sci. U.S.A.* 108.6, pp. 2190–2195. ISSN: 0027-8424. DOI: `10.1073/pnas.1013391108`.

Vaden, T. D., C. Song, R. A. Zaveri, D. Imre, and A. Zelenyuk (Apr. 2010). "Morphology of mixed primary and secondary organic particles and the adsorption of spectator organic gases during aerosol formation." In: *Proc. Natl. Acad. Sci. U.S.A.* 107.15, pp. 6658–6663. ISSN: 0027-8424. DOI: `10.1073/pnas.0911206107`.

Vesala, T., A.U. Hannemann, B.P. Luo, M. Kulmala, and Th Peter (July 2001). "Rigorous treatment of time-dependent trace gas uptake by droplets including bulk diffusion and surface accommodation." In: *J. Aerosol Sci.* 32.7, pp. 843–860. ISSN: 00218502. DOI: `10.1016/S0021-8502(00)00115-4`.

Vieth, W. R., J. M. Howell, and J. H. Hsieh (1976). "Dual sorption theory." In: *J. Membr. Sci.* 1, pp. 177–220. DOI: `http://dx.doi.org/10.1016/S0376-7388(00)82267-X`.

Virtanen, A., J. Kannosto, et al. (Aug. 2011). "Bounce behavior of freshly nucleated biogenic secondary organic aerosol particles." In: *Atmos. Chem. Phys.* 11.16, pp. 8759–8766. ISSN: 1680-7324. DOI: `10.5194/acp-11-8759-2011`.

Virtanen, Annele, Jorma Joutsensaari, Thomas Koop, Jonna Kannosto, Pasi Yli-Pirilä, Jani Leskinen, Jyrki M. Mäkelä, Jarmo K. Holopainen, Ulrich Pöschl, Markku Kulmala, Douglas R. Worsnop, and Ari Laaksonen (Oct. 2010). "An amorphous solid state of biogenic secondary organic aerosol particles." In: *Nature* 467.7317, pp. 824–827. ISSN: 0028-0836. DOI: `10.1038/nature09455`.

Wang, N., S. D. Jorga, J. R. Pierce, N. M. Donahue, and S. N. Pandis (2018). "Particle wall-loss correction methods in smog chamber experiments." In: *Atmos. Meas. Tech.* 11.12, pp. 6577–6588. DOI: `10.5194/amt-11-6577-2018`.

Wiedensohler, A. (June 1988). "An approximation of the bipolar charge distribution for particles in the submicron size range." In: *Journal of Aerosol Science* 19.3, pp. 387–389. ISSN: 00218502. DOI: `10.1016/0021-8502(88)90278-9`.

Wiedensohler, A., W. Birmili, et al. (2012). "Mobility particle size spectrometers: Harmonization of technical standards and data structure to facilitate high quality long-term observations of atmospheric particle number size distributions." In: *Atmos. Meas. Tech.* 5.3, pp. 657–685. DOI: `10.5194/amt-5-657-2012`.

Wiedensohler, A., A. Wiesner, et al. (2018). "Mobility particle size spectrometers: Calibration procedures and measurement uncertainties." In: *Aerosol Sci. Technol.* 52.2, pp. 146–164. ISSN: 15217388. DOI: `10.1080/02786826.2017.1387229`.

Ye, Penglin, Xiang Ding, Jani Hakala, Victoria Hofbauer, Ellis S. Robinson, and Neil M. Donahue (Aug. 2016). "Vapor wall loss of semi-volatile organic compounds in a Teflon chamber." In: *Aerosol Sci. Technol.* 50.8, pp. 822–834. ISSN: 0278-6826. DOI: `10.1080/02786826.2016.1195905`.

Ye, Penglin, Yunliang Zhao, Wayne K. Chuang, Allen L. Robinson, and Neil M. Donahue (May 2018). "Secondary organic aerosol production from pinanediol, a semi-volatile surrogate for first-generation oxidation products of monoterpenes." In: *Atmos. Chem. Phys.* 18.9, pp. 6171–6186. ISSN: 1680-7324. DOI: `10.5194/acp-18-6171-2018`.

Yeh, Geoffrey K. and Paul J Ziemann (Sept. 2014). "Alkyl nitrate formation from the reactions of C_8-C_{14} n-Alkanes with OH radicals in the presence of NO_x: Measured yields with essential corrections for gas-wall partitioning." In: *J. Phys. Chem. A* 118.37, pp. 8147–8157. ISSN: 15205215. DOI: `10.1021/jp500631v`.

– (Sept. 2015). "Gas-wall partitioning of oxygenated organic compounds: measurements, structure—activity relationships, and correlation with gas chromatographic retention factor." In: *Aerosol Sci. Technol.* 49.9, pp. 727–738. ISSN: 0278-6826. DOI: `10.1080/02786826.2015.1068427`.

You, Yuan, Mackenzie L. Smith, Mijung Song, Scot T. Martin, and Allan K. Bertram (2014). "Liquid-liquid phase separation in atmospherically relevant particles consisting of organic species and inorganic salts." In: *Int. Rev. Phys. Chem.* 33.1, pp. 43–77. DOI: 10.1080/0144235X.2014.890786.

Zaveri, R. A., R. C. Easter, J. E. Shilling, and J. H. Seinfeld (May 2014). "Modeling kinetic partitioning of secondary organic aerosol and size distribution dynamics: Representing effects of volatility, phase state, and particle-phase reaction." In: *Atmos. Chem. Phys.* 14.10, pp. 5153–5181. ISSN: 1680-7324. DOI: 10.5194/acp-14-5153-2014.

Zaveri, Rahul A., John E. Shilling, et al. (2018). "Growth kinetics and size distribution dynamics of viscous secondary organic aerosol." In: *Environ. Sci. Technol.* 52.3, pp. 1191–1199. DOI: 10.1021/acs.est.7b04623.

Zhang, Xi, Spyros N. Pandis, and John H. Seinfeld (Aug. 2012). "Diffusion-limited versus quasi-equilibrium aerosol growth." In: *Aerosol Sci. Technol.* 46.8, pp. 874–885. ISSN: 0278-6826. DOI: 10.1080/02786826.2012.679344.

Zhang, Xuan, Christopher D. Cappa, Shantanu H. Jathar, Renee C. McVay, Joseph J. Ensberg, Michael J. Kleeman, and John H. Seinfeld (2014). "Influence of vapor wall loss in laboratory chambers on yields of secondary organic aerosol." In: *Proc. Natl. Acad. Sci. U.S.A.* 111.16, pp. 5802–5807. DOI: 10.1073/pnas.1404727111.

Zhang, Xuan, John Ortega, Yuanlong Huang, Stephen Shertz, Geoffrey S. Tyndall, and John J. Orlando (2018). "A steady-state continuous flow chamber for the study of daytime and nighttime chemistry under atmospherically relevant NO levels." In: *Atmos. Meas. Tech.,* 11.5, pp. 2537–2551. DOI: 10.5194/amt-11-2537-2018.

Zhang, Xuan, R. H. Schwantes, R. C. McVay, H. Lignell, M. M. Coggon, R. C. Flagan, and J. H. Seinfeld (Apr. 2015). "Vapor wall deposition in Teflon chambers." In: *Atmos. Chem. Phys.* 15.8, pp. 4197–4214. ISSN: 1680-7324. DOI: 10.5194/acp-15-4197-2015.

Zhou, Shouming, Manabu Shiraiwa, Robert D. McWhinney, Ulrich Pöschl, and Jonathan P.D. Abbatt (2013). "Kinetic limitations in gas–particle reactions arising from slow diffusion in secondary organic aerosol." In: *Faraday Discuss.* 165, pp. 391–406. ISSN: 13596640. DOI: 10.1039/c3fd00030c.

Ziemann, P. J. (Apr. 2011). "Effects of molecular structure on the chemistry of aerosol formation from the OH-radical-initiated oxidation of alkanes and alkenes." In: *Int. Rev. Phys. Chem.* 30.2, pp. 161–195. ISSN: 0144-235X. DOI: 10.1080/0144235X.2010.550728.

Ziemann, Paul J. and Roger Atkinson (2012). "Kinetics, products, and mechanisms of secondary organic aerosol formation." In: *Chem. Soc. Rev.* 41.19, pp. 6582–605. ISSN: 0306-0012. DOI: 10.1039/c2cs35122f.

Zuend, A., C. Marcolli, T. Peter, and J. H. Seinfeld (2010). "Computation of liquid-liquid equilibria and phase stabilities: implications for RH-dependent gas/particle partitioning of organic-inorganic aerosols." In: *Atmos. Chem. Phys.* 10.16, pp. 7795–7820. DOI: `10.5194/acp-10-7795-2010`.

Zuend, A. and J. H. Seinfeld (2012). "Modeling the gas-particle partitioning of secondary organic aerosol: the importance of liquid-liquid phase separation." In: *Atmos. Chem. Phys.* 12.9, pp. 3857–3882. DOI: `10.5194/acp-12-3857-2012`.

Zuend, Andreas and John H. Seinfeld (2013). "A practical method for the calculation of liquid-liquid equilibria in multicomponent organic-water-electrolyte systems using physicochemical constraints." In: *Fluid Phase Equilib.* 337, pp. 201–213. ISSN: 0378-3812. DOI: `10.1016/j.fluid.2012.09.034`.

Chapter 3

FREE OF CHARGE? EFFECT OF PARTICLE CHARGE ON AEROSOL DYNAMICS IN TEFLON ENVIRONMENTAL CHAMBERS

Abstract

The contribution of particle charge to the rate of particle wall deposition has been a persistent source of uncertainty for experiments performed in environmental chambers. By tracking the preferential deposition of positively charged particles; by comparing experiments carried out under standard, humid, and highly statically charged conditions; and by performing two-parameter optimizations for the chamber eddy-diffusion coefficient (k_e) and the average magnitude of the electric field ($\bar{E}$), the effect of charge on the rate of particle wall deposition is isolated. A combined experimental and computational method is also developed for determining values for k_e and $\bar{E}$ within a FEP Teflon chamber. To fully account for the effects of charge on particle dynamics in environmental chambers, studies of the effect of air ion concentration on the rate of particle coagulation over a typical 20 h experiment are performed and demonstrate, in general, that particle charge is negligible for characteristic chamber ion concentrations. Whereas the effect of particle charge on aerosol dynamics in an environmental chamber must be addressed for each specific chamber, we demonstrate experimentally that for the Caltech 19 m^3 Environmental Chamber, charge effects on the rate of particle wall deposition are negligible.

3.1   Introduction

Data from environmental chambers are instrumental to understanding the chemistry of the atmosphere and aerosol formation. A common experiment in atmospheric chambers involves determination of the secondary organic aerosol (SOA) yield, the ratio of the mass of aerosol formed to that of a precursor vapor reacted. SOA yields are determined predominantly from experiments carried out in Teflon chambers.

Since measurements of the amount of aerosol formed in such an experiment can be carried out only on suspended particles, one must account for particles deposited onto the chamber walls throughout the duration of an experiment to obtain an accurate assessment of SOA yield.

Particle charge has long been recognized as a possible factor in the rate of particle wall deposition. McMurry and Rader (1985) determined empirical parameters describing the rate of wall deposition of charged particles by extrapolating the average electric field ($\bar{E}$) from a small Teflon bag to a much larger chamber, obtaining a characteristic value of ~45 V cm^{-1}. Since 1985, however, experimental chamber procedures have evolved, but questions of the strength of the average electric field in standard Teflon environmental chambers have remained. Currently, chambers are constructed so as to avoid the build-up of static charge on the walls. While it has long been assumed that some electric field remains within a Teflon chamber, the strength of the field or of its effect on particle wall deposition is largely unknown (Pierce et al., 2008; Nah et al., 2017; Tian et al., 2017).

In this paper, we explore the effect of particle charge on aerosol-formation and aerosol-growth experiments carried out in Teflon-walled environmental chambers. Particle charge can influence both the rate of particle wall deposition and the rate of particle-particle coagulation. Theoretical treatments of particle wall deposition (Crump and Seinfeld, 1981; McMurry and Rader, 1985) and of the effect of particle charge on the rate of coagulation (Seinfeld and Pandis, 2016) exist. We present here a combined experimental-modeling study of the effect of charge on particle dynamics in a Teflon-walled environmental chamber with the goal of providing guidance as to its potential importance in chamber experiments.

We begin with derivations of the effect of particle charge on coagulation rates and of the effect of a statically-charged wall on the rate of particle wall deposition. Then, we investigate the effects of charge and air ion concentration on coagulation using a dynamic chamber model. Next, we probe the strength of the mean electric field and its effect on wall deposition with three methods: (1) an experimental procedure that tracks positive charges, (2) a related experimental procedures that compares particle wall deposition for a chamber operated under standard and humid conditions, and (3) an optimization method that relies upon the prior experiments and the chamber model previously used for coagulation. Finally, we discuss those effects that can be neglected.

3.2 Theory of Charge Effects on Particle Dynamics in Teflon Chambers

3.2.1 Effect of Particle Charge on Coagulation

As experiments to determine the rate of particle wall deposition are performed, the number concentration of the non-volatile particles in the chamber is measured as a function of time. Since coagulation decreases the number concentration throughout these experiments, particles in each size bin are subject to both wall deposition and coagulation (e.g., Nah et al., 2017). Moreover, it is necessary to account for the dynamics of particles in each size bin, since the rate of particle deposition to the wall is dependent on particle size.

In theory, the rate of coagulation is affected by the presence of particle charge. Indeed, calculations reported by Ghosh et al. (2017) indicate that charging particles significantly beyond their steady-state charge distribution leads to a demonstrable effect on their rate of coagulation. However, approximations cited by Seinfeld and Pandis (2016) indicate this effect for atmospheric aerosols is small.

For two particles with charge numbers n_1 and n_2 and diameters D_{p1} and D_{p2}, respectively, the Brownian coagulation kernel is adjusted by a factor of

$$\frac{\kappa}{e^\kappa - 1} \tag{3.1}$$

to account for Coulomb forces, where $\kappa = \frac{n_1 n_2 e^2}{2\pi \epsilon_0 \epsilon (D_{p1} + D_{p2}) kT}$, ϵ is the dielectric constant of air, and ϵ_0 is the permittivity of free space (Seinfeld and Pandis, 2016). Unlike Ghosh et al. (2017), we ignore electrostatic dispersion effects because, while charges are present, they should not be far from the steady-state bipolar charge distribution and there should not be significantly more charges of one polarity than of the other.

3.2.2 Effect of Particle Charge on Wall Deposition

Assuming symmetry of the wall deposition of positively and negatively charged particles, McMurry and Rader (1985) developed the following equation for the first-order particle-wall-deposition coefficient $\beta_n(D_p)$ of particles that carry an average of n charges in a spherical chamber in the presence of an average electric field $\bar{E}$:

$$\beta_n(D_p) = \frac{3\sqrt{k_e D}}{\pi R x} \left\{ \frac{(x+y)^2}{2} + (x+y)D_1(x+y) + (x-y)D_1(x-y) \right\}, \tag{3.2}$$

where k_e is the chamber eddy-diffusion coefficient, D is the particle Brownian diffusivity; R is the spherical equivalent radius of the chamber; and D_1 is the

first-order Debye function, defined as

$$D_1(z) = \frac{1}{z} \int_0^z \frac{t}{e^t - 1} dt.$$ (3.3)

The terminal particle settling velocity is given by:

$$v_s = \frac{D_p^2 \rho g C_C}{18\mu};$$ (3.4)

where ρ is the density of the particle, g is the gravitational constant, C_C is the Cunningham slip-correction factor, and μ is the viscosity of air (Seinfeld and Pandis, 2016). The magnitude of the electrostatic migration velocity, $\bar{v}_e$, where e is the elementary charge, is

$$\bar{v}_e = \left| \frac{neC_C\bar{E}}{3\pi\mu D_p} \right|.$$ (3.5)

D is given by the slip-corrected Stokes-Einstein-Sutherland relation:

$$D = \frac{kTC_C}{3\pi\mu D_p},$$ (3.6)

where k is the Boltzmann constant and T is the chamber temperature. The Cunningham slip-correction factor is:

$$C_C = 1 + \frac{2\lambda}{D_p} \left[1.257 + 0.4 \exp \frac{-1.1D_p}{2\lambda} \right],$$ (3.7)

where λ is the mean free path of air equal to $\frac{\mu}{p}\sqrt{\frac{\pi RT}{2MW_{air}}}$, p is pressure within the chamber, R is the ideal gas constant, and MW_{air} is the molecular weight of air (Seinfeld and Pandis, 2016).

When the particle charge distribution (i.e., the number concentration of particles in each size interval with a given charge number) is known, the remaining parameters to be determined are the chamber eddy-diffusion coefficient, k_e, and the average electric field within the chamber, $\bar{E}$. Since neither k_e nor $\bar{E}$ can be easily and reliably measured, these parameters must be determined by optimal fitting of experimental data.

3.3 Dynamic Chamber Model

A particle-mass-conserving computational model accounts for the effects of coagulation and particle wall deposition due to Brownian motion and to electrostatic effects. The model is based on the numerical solution of the aerosol dynamic equation (see, for example, Sunol, Charan, and Seinfeld, 2018). For all simulations except those

involving small air ions, numerical solutions are obtained over 40 fixed-particle-size bins with mean diameters extending from 23 to 804 nm (chosen to match the range of the SMPS); when ions are considered (Section 3.4), 80 fixed-particle-size bins with mean diameters from 1.6 to 1631 nm are used. In both cases, these size bins are further differentiated into 13 charge bins, ranging from -6 to 6 elementary charges. Since particles in the size range typical of chamber experiments tend not to be highly charged, any particle predicted to have charges outside the range -6e to 6e are assumed to have saturated at -6e or 6e, respectively. Any positive or negative ions added are placed into the 1.6 nm diameter +1e or -1e bins, respectively. When the ion concentration is held constant, the values in these bins are not changed for the duration of the simulation; when the ion concentration is only an initial value, the particles in the 1.6 nm +1e and -1e bins are not replenished throughout the experiment. For calculations comparing number or surface area concentrations between cases with and without ions present, only particles with diameters above 20 nm are compared. All particles used in the particle-wall-deposition experiments, to be described subsequently, are non-volatile. Parameter values and variables are given in Tbl. 3.1.

As the particle population undergoes wall deposition, coagulation occurs continuously in the chamber. It is assumed that each coagulation event results in a new particle with a mass that is the sum of the masses of the two colliding particles and a charge equal to the sum of the charges of the two particles. Suspended particles are assumed to maintain their charge.

To perform these simulations, we assume an initial charge distribution. In typical environmental chamber experiments, aerosols are injected into the chamber and allowed to mix prior to the beginning of data collection. It is standard procedure to use a neutralizer, also called a charge conditioner, to establish a particle charge distribution immediately after particle generation. The neutralizer upstream of the chamber contains a soft x-ray source that produces a charge distribution that is a function of particle diameter. By comparing the distribution of particles that flow through the upstream neutralizer in the presence and absence of a downstream, polonium neutralizer, we confirmed that the outputs from the two neutralizers are the same and, therefore, likely close to the charge distribution given by Wiedensohler (1988); however, the particles may not be at their steady-state distribution at the beginning of the experiment if $\bar{E}$ is large or if a significant number of ions is present. Nevertheless, we assume a charge distribution computed with the Wiedensohler

Table 3.1: Chamber and particle parameters

Parameter	Symbol	Value
General		
Boltzmann constant	k	1.38×10^{-23} J K^{-1}
dielectric constant of air	ϵ	1.0005
elementary charge	e	1.602×10^{-19} C
gravitational constant	g	9.8 kg m^{-1} s^{-1}
molecular weight of air	MW_{air}	29.0 g mol^{-1}
particle density	ρ	1700 kg m^{-3}
permittivity of free space	ϵ_0	8.854×10^{-12} F m^{-1}
viscosity of air	μ	1.81×10^{-5} kg m^{-1} s^{-1}
Caltech Chamber Parameters		
pressure	p	745 Torr
temperature	T	19.6°C
volume of chamber	V	19.0 m^3
Definitions of Variables		
average electric field within the chamber	$\bar{E}$	
Brownian diffusivity of a particle	D	
Cunningham slip-correction factor	C_C	
diameter (general)	D_p	
diameter of particle i	D_{pi}	
eddy-diffusion coefficient	k_e	
electrostatic migration velocity	$\bar{v}_e$	
elementary charges on particle i	n_i	
equivalent radius of the chamber	R	
mean free path of air	λ	
optimization function	J	
particle number concentration	N	
positively charged particles directly from the chamber	$n^+_{chamber}$	
positively charged particles that are charge-conditioned	$n^+_{conditioned}$	
particle surface area concentration	SA	
particle-wall-deposition coefficient (general)	β	
particle-wall-deposition coefficient with n charges	β_n	
terminal particle settling velocity	v_s	

(1988) formula and provided in Tbl. 1-1 of TSI (2013).

The form of the particle-wall-deposition function $\beta(D_p)$ depends, in principle, on the geometry of the chamber. As chambers with flexible walls are generally neither perfect spheres nor perfect cubes, we carried out the optimization procedure for these two limiting shape assumptions: for the spherical chamber, the equivalent radius is $R = \left(\frac{3V}{4\pi}\right)^{1/3}$; for the cubic chamber, the characteristic length is $R = V^{1/3}$, where V is the volume of the chamber. Assuming the absence of an electric field ($\bar{E} = 0$) and focusing on experiments performed under standard operating conditions ("A"-"F"), optimal values of k_e were determined by minimizing J, as defined subsequently

by Eq. (3.8), for the spherical chamber assumption and according to the derived $\beta(D_p)$ from Crump and Seinfeld (1981) for the cubic chamber. Figure 3.1 shows a comparison of the results of the two minimizations to the total measured number concentration; Fig. 3.2 compares the optimal wall-deposition curves obtained for the two chamber shape assumptions. In each case, a negligible difference exists between the results based on the two limiting chamber shapes. We, therefore, confidently use the spherical assumption for the duration of this work.
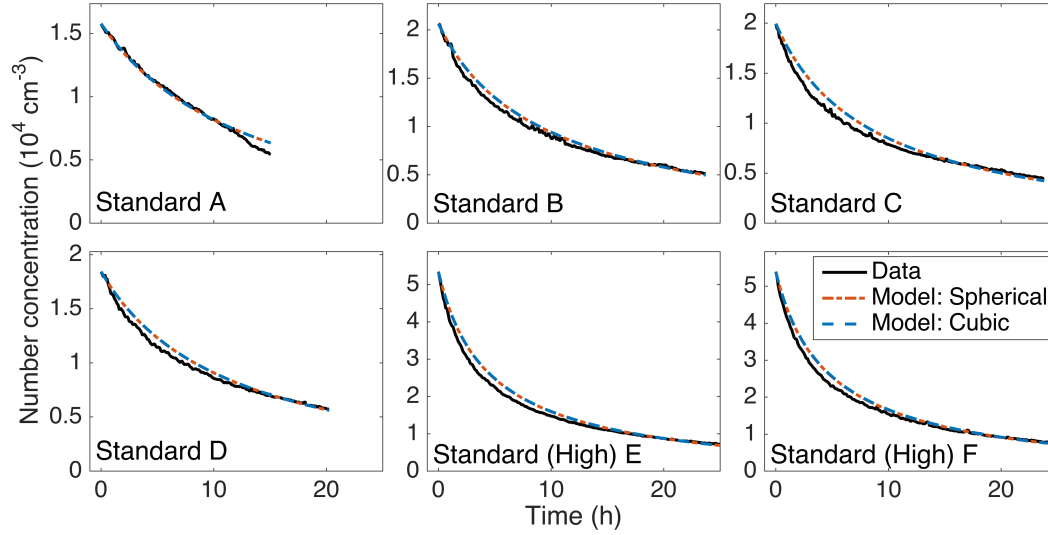
Figure 3.1: Aerosol number concentration evolution for the six "Standard" experiments (Tbl. 3.3), as compared to a computational model that assumes the 19.0 m^3 chamber is spherical (red) or cubic (blue). As model predictions are compared to data, the simulated number concentrations include contributions from coagulation and from wall deposition. The parameter k_e, which represents the effect of turbulent mixing in the chamber on the rate of particle wall deposition, was found through the optimization procedure described in the text, where particle charge is neglected ($\bar{E} = 0$). The optimized results for a spherical and a cubic chamber are essentially identical.

3.4 Coagulation: Effect of Charge and Ions

Using the Brownian coagulation kernel with the factor given in Eq. (3.1) and neglecting, for the moment, particle wall deposition (setting $\beta_n(D_p) = 0$ for all diameters and all charges), we simulated a 20 h experiment with an initial number concentration of 2.1×10^4 cm^{-3} and a distribution corresponding to the beginning of an experiment described in Section 3.5.3 ("Standard B") with either uncharged particles or those having an initial charge distribution corresponding to the Wiedensohler formula. The final predicted number concentrations for the two cases are within
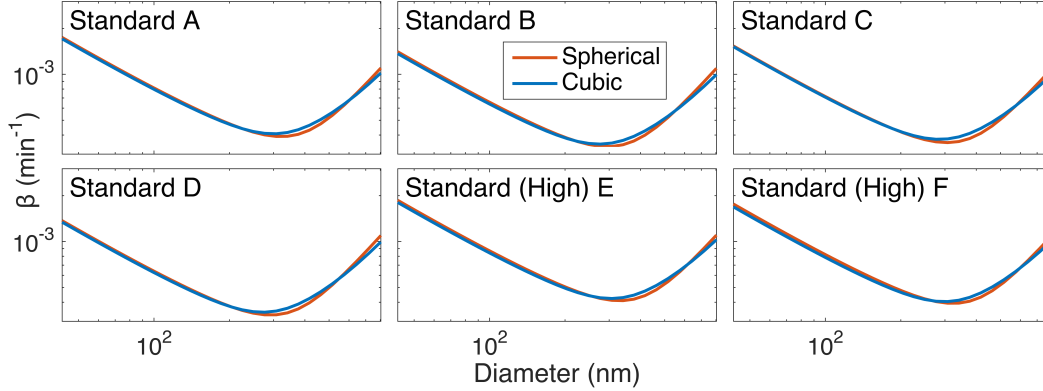
Figure 3.2: The size-dependent, wall-deposition parameter $\beta(D_p)$ for a spherical (red) and a cubic (blue) chamber of the same volume are compared for the six experiments performed under standard operating conditions. These curves were determined by minimizing J with respect to k_e (see Section 3.5.4), thereby fitting observations to simulated predictions. It was assumed that neither an electric field ($\bar{E} = 0$) nor any air ions were present. Due to the similarity of these curves, it is sufficient to represent the chamber as a sphere in this work.

0.4% of one another (Fig. 3.3).

In any laboratory, there are naturally occurring small air ions, also called cluster ions. These originate from, amongst other sources, galactic cosmic rays, radon decay in soil, splashing water, and nearby power lines (Hirsikko, Nieminen, et al., 2011). While charge effects on coagulation may be negligible when particles are close to their steady-state charge distribution, this may not be the case in a standard laboratory setting.

To simulate the presence of ions, we assume the ions are particles with a diameter of 1.6 nm and a unit positive or negative charge. This diameter was chosen based on the size at which small air ions are defined by Hirsikko, Nieminen, et al. (2011) but it is only an approximation, since different ion polarities may have different mobilities or diameters depending on the environment. Here, we consider only small air ions because ions larger than cluster ions are not produced within a chamber. We have verified, for example, that Caltech Environmental Chamber experiments are clear of particles of ≥ 1.7 nm diameter (personal communication, H. Mai, 2017).

Simulated 1.6 nm ions at a chosen concentration were added to the initial distribution corresponding to that of the "Standard B" experiment. Then, in the absence of wall deposition, we allow the particles and ions to coagulate for 20 h. We consider ion concentrations between 0 and 5000 cm^{-3} at different polarity ratios, noting that 5000
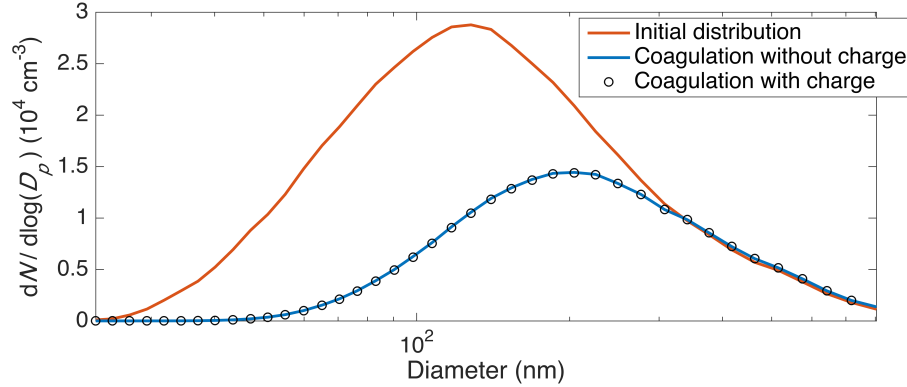
Figure 3.3: Simulated number-concentration size distributions in the presence of coagulation only (no wall deposition) after 20 h. The initial distribution, shown in red, matches the initial condition for the "Standard B" experiment and has a total number concentration of $\sim 2 \times 10^4$ cm^{-3}. Simulations were performed both under the assumption that particles have no initial charge (blue line) and with the assumption that the initial charge distribution satisfies the Wiedensohler formula (black circles). Since the size distributions under these assumptions coincide almost exactly (number concentrations are <0.4% different), one can conclude that the effect of particle charge on the rate of coagulation is negligible for chamber experiments similar to those considered here when there are no ions present.

cm^{-3} per polarity is an extreme ambient ion concentration (Hirsikko, Nieminen, et al., 2011; Vartiainen et al., 2007). Adding these particles to the simulation increases particle volume in the chamber by <0.01%. Particle volume is, therefore, still considered conserved in the absence of wall deposition.

When we consider ions, we account for the presence of charge in the coagulation calculations. In order to determine the extent to which charge effects can be neglected, we must compare the result of these simulations to ones that do *not* account for charge or for ions, which we call the Reference Case. Relative charges in the total aerosol number or surface area concentrations after 20 h of simulated coagulation are compared to what those concentrations would have been in the absence of ions and of charge (the Reference Case).

Even when the ion concentrations are high and are held constant, the effect of charge on coagulation is minimal for equal concentrations of positive and negative ions, as shown in Case 5 (Figs. 3.4 and 3.5, Tbl. 3.2): there is only a 0.88% difference in number concentrations after 20 h between the Reference Case and a simulation with positive and negative ion concentrations of 5000 cm^{-3} each. In the absence of an ion production source, i.e., when there is nothing maintaining the ion concentration and so ion concentration is not held constant, the charge effect on the rate of coagulation
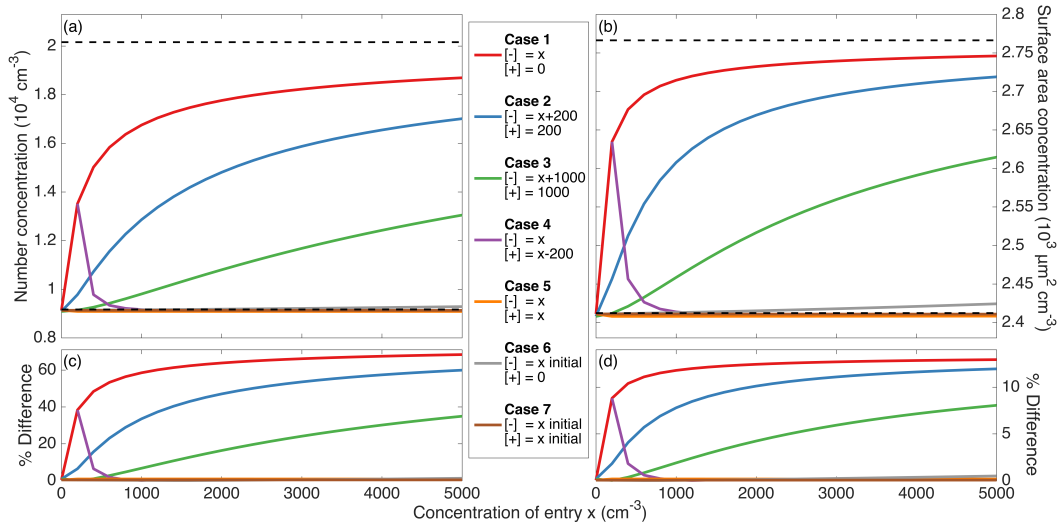
Figure 3.4: Total number and surface area concentrations after 20 h of coagulation (neglecting wall deposition) at different ion concentrations according to the 7 cases described in Tbl. 3.2 are shown in Panels (a) and (b), respectively. The initial number concentration and surface area concentration of 2.0×10^4 cm^{-3} and 2.8×10^3 µm^2 cm^{-3} are displayed as the top dashed line in these panels. These concentrations – excluding the variable concentration of ions present – correspond to the initial condition for the simulations taken from the initial particle distribution of the "Standard B" experiment, which is shown in red in Fig. 3.3. The final number and surface area concentrations when no ions are present and each particle has a neutral charge (the Reference Case), shown as the bottom dashed line in the same panels, are 9.2×10^3 cm^{-3} and 2.4×10^3 µm^2 cm^{-3}; the percent difference of the final number and surface area concentrations from these values are shown in Panels (c) and (d), respectively. When there is a large difference between the concentrations of the two ion polarities (Case 1-3), the rate of coagulation is dramatically decreased and, therefore, the difference between the coagulated concentrations with and without considering ions and charge is fairly significant. When the difference in concentrations of the two ion polarities are maintained but the absolute concentrations increase, the difference from the Reference Case decreases (Case 4 and Cases 1-3 for the same x). Values for Cases 4 through 7 are shown more clearly in Fig. 3.5.

Table 3.2: Coagulation of the "Standard B" initial particle size distribution with 1.6 nm diameter ions over 20 h. Wall deposition was neglected ($\beta=0$ for all diameters and all charges). Entry x in the table varies from 0 to 5000 cm^{-3} (except for when this leads to a negative ion concentration). Percent differences were calculated as the difference between the number or surface area concentrations calculated after 20 h of the condition considered and the number and surface area concentrations of the Reference Case. The Reference Case is a 20 h simulation of coagulation where the ion concentrations are 0 and all particles are assumed to have a neutral charge: this gives a final number concentration of 9.2×10^3 cm^{-3} and a final surface area concentration of 2.4×10^3 μm^2 cm^{-3}. If the concentration is not held constant ("no" for column "Held Constant?"), then ions are added at the beginning of the simulation only; if they are held constant, any ions that disappear by coagulation are replaced so that a constant ion concentration is maintained. Figures 3.4 and 3.5 show these values in graphical form.

Case	Description	Negative Ion Conc (cm^{-3})	Positive Ion Conc (cm^{-3})	Held Constant?	% Difference of Number Concentration x equal to		% Difference of Surface Area Concentration x equal to	
					200 cm^{-3}	5000 cm^{-3}	200 cm^{-3}	5000 cm^{-3}
1	[-] varies, [+] = 0	x	0	yes	38%	68%	8.8%	13%
2	[-] varies, [+] = 200	x+200	200	yes	0.88%	59%	0.18%	12%
3	[-] varies, [+] = 1000	x+1000	1000	yes	0.32%	35%	0.014%	8.1%
4	[+] - [-] = 200	x	x-200	yes	38%	0.86%	8.8%	0.15%
5	[-] = [+]	x	x	yes	0.88%	0.89%	0.18%	0.16%
6	[-]$_{initial}$ varies, [+] = 0	x	0	no	0.34%	1.3%	0.037%	0.50%
7	[-]$_{initial}$=[+]$_{initial}$	x	x	no	0.38%	0.40%	0.051%	0.057%

is also negligible (Cases 6 and 7).

However, holding the positive ion concentration constant while varying that of the negative ions leads to a significant effect of charge on coagulation, as given by Cases 1 through 3 (Fig. 3.4, Tbl. 3.2). Note that as the value of the constant positive ion concentration is increased, while maintaining the absolute difference in polarity concentrations, the final distributions from coagulation approach that of the Reference Case. We see this when comparing Case 2 to 1 and Case 3 to 2. Case 4 shows this more directly; the absolute difference between ion polarity concentrations is maintained at 200 cm^{-3} as the concentrations increase.

In what are seemingly symmetric simulations, there is a slight difference when the concentrations of the ion polarities are switched (e.g., if we compare the case of positive ions at 200 cm^{-3} and negative ions at 0 cm^{-3} to the case of positive ions at 0 cm^{-3} and negative ions at 200 cm^{-3}), because the Wiedensohler distribution exhibits a slight preference for negatively-charged particles over positively charged ones. However, these differences are sufficiently small that we, simply and conservatively, report values for the simulation that, in general, gives a higher percent difference
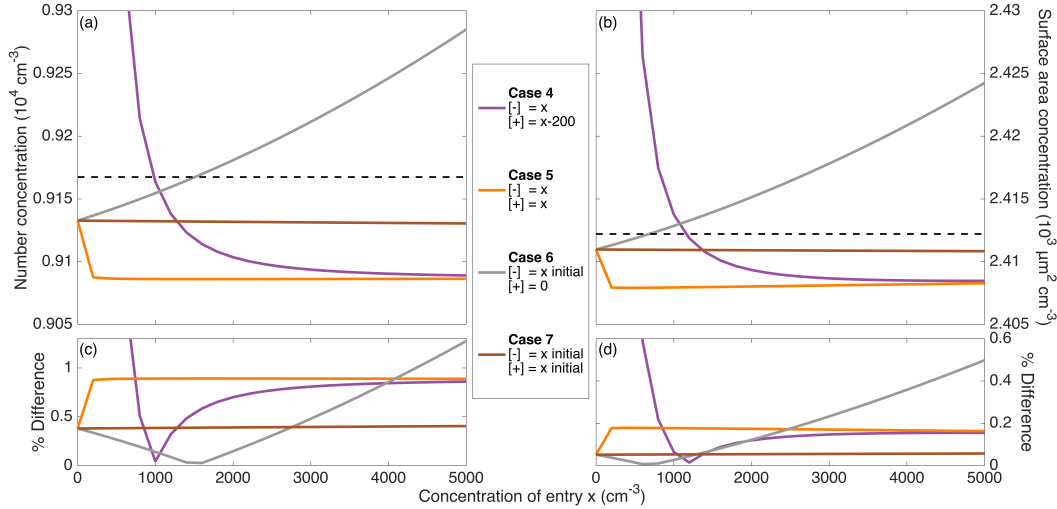
Figure 3.5: A magnified version of Fig. 3.4 that more clearly displays Cases 4 through 7 (defined in Tbl. 3.2). Panels (a) and (b) show the total simulated number and surface area concentrations after 20 h of simulated coagulation. The initial distribution corresponds to the beginning of experiment "Standard B," but with ions present. In Panels (c) and (d), the final number and surface area concentrations for Case 4 through 7 are compared to 9.2×10^3 cm^{-3} and 2.4×10^3 μm^2 cm^{-3}, which are the final total number and surface area concentrations for the Reference Case. When no ion production source is present, as approximated in Cases 6 and 7, there is a negligible effect of the ion concentrations and of charge on coagulation. Even for high ion concentrations, when the two polarities are of equal concentrations (Case 5), there is a small effect of charge. Only when there is a difference between the positive and negative ion concentrations (Cases 1 through and 3), does much of an effect of charge exist. When the difference between the two polarity concentrations remains constant, the effect of charge on coagulation decreases as the absolute concentrations of ions increases (Case 4).

instead of reporting nearly identical simulations.

Ion production within the chamber by cosmic rays or other energetic particles result in ion pairs with negative charges initially present as free electrons that later attach to gas molecules. However, differing ion mobilities may lead to different ion polarity concentrations (Reiter, 1985; Harrison and Aplin, 2007; Hirsikko, Nieminen, et al., 2011). Thus, while the ratio of positive and negative ions tends to be close to 1, it is not always exactly 1. Nonetheless, Hirsikko, Yli-Juuti, et al. (2007) found that, in an urban environment, the difference in concentration between positive and negative small air ions was minimal, both indoors and outdoors. For example, the median positive and negative ion concentrations indoors were 966 and 1065 cm^{-3} on a weekday and 1357 and 1376 cm^{-3} on a weekend, respectively. When we

repeat the simulations described above with these ion concentrations, we find that the charge effect on coagulation rates is still minimal: a 0.72% and 0.13% difference indoors on weekdays in number and surface area concentrations, respectively. On the weekends, there is a 0.89% and 0.17% difference. Therefore, though charge *can* have a significant effect on the rate of coagulation, we do not expect it will for typical environmental chamber experiments.

3.5 Particle Wall Deposition: Effect of Charge Probed Three Ways

We turn now to the effect of charge on the rate of particle wall deposition. Using the chamber model, Fig. 3.6 shows the simulated effect of the average electric field ($\bar{E}$) on the rate of particle wall deposition. Both coagulation and wall deposition are accounted for; a simulation with coagulation alone is shown for comparison. Beginning with an initial distribution corresponding to that of an experiment described below ("Standard B") and simulated for 20 h, values of $\bar{E} = 2.5$ V cm^{-1} and $\bar{E} = 100$ V cm^{-1} lead to final number concentrations that are 86% and 44%, respectively, of that when $\bar{E} = 0$. Therefore, the presence of a surface charge will have an effect on particle wall deposition.
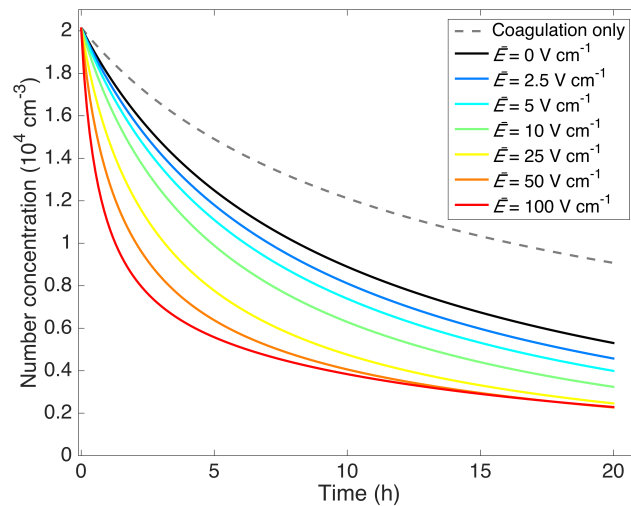
Figure 3.6: Simulated particle-number-concentration evolution subject to coagulation and wall deposition for a 20 h experiment. The initial number distribution matches that of the "Standard B" experiment (see Fig. 3.3). The effect of assumed electric field strength $\bar{E}$ is shown, based on $k_e = 0.19$ s^{-1}. The results indicate that the strength of the electric field is influential, even when relatively small. The black curve shows the number concentration evolution in the absence of an electric field. The gray, dashed curve shows the sole contribution of coagulation to the particle-number-concentration evolution.

If there is a charge present on the walls of a Teflon chamber, it would likely be a

negative charge, because FEP Teflon film is often observed to be negatively charged and because PTFE Teflon, which is similar in structure to FEP Teflon, has been shown to have a large negative charge affinity (Sessler, Alquié, and Lewiner, 1992; Chen and Wang, 2017). If there is no additional ion source, a negatively-charged wall would lead to preferential depletion of the positively charged particles in the chamber. Since there are a finite number of positively charged ions, if one does not account for the electric field and simply attempts to determine $\beta(D_p)$, it would appear as if $\beta(D_p)$ is a function of time.

If it can be shown that no electric field is present, then one can justify the use of a $\beta(D_p)$ that is independent of time and is valid in multiple experiments. We provide here three methods for making this determination: the *SMPS method*, the *humidity method*, and the *parameter optimization method*. If one seeks to determine the extent to which an electric field exists in a laboratory chamber, we suggest the experiments and optimizations described below. If it is established that a chamber is free of surface charge, one need not account for a time-dependent $\beta(D_p)$. Alternatively, with these verification methods, one will be able to adjust the conditions of a chamber so that it does not exhibit an average electric field.

3.5.1 Experimental Protocol

All particle dynamics experiments were performed in the Caltech 19 m^3 Environmental Chamber that has 2 mil FEP Teflon walls. Before each experiment, the chamber is flushed with clean, dry air for >24 h, and contact with the chamber surface is minimized. Experimental conditions are summarized in Tbl. 3.3. In "Humid" experiments, the chamber enclosure (the area outside of the environmental chamber) had a relative humidity of >40% at an average temperature of ~20°C; for the rest of the experiments ("Standard" and "Static Charge"), the enclosure temperature was also ~20°C but had a relative humidity <30% (usually ~25%). For experiments that required a static charge ("Static Charge" experiments) on the chamber walls, charge was induced by rubbing cloth against the external walls prior to or during an experiment. While "Static Charge" experiments are characterized by a greater value of $\bar{E}$ than either the "Standard" or the "Humid" experiments, the value of $\bar{E}$ in an individual experiment likely varied due to the uncontrolled duration and vigor of charge inducement between or during experiments.

Experiments were performed over a range of initial particle concentrations (Tbl. 3.3). Particles were injected into the chamber by atomizing an aqueous $(NH_4)_2SO_4$

Table 3.3: Conditions for experiments performed

Label	Relative Humidity	Induced Static Charge?	Initial Number Conc (cm^{-3})	Initial Surface Area Conc (μm^2 cm^{-3})	Experiment Duration (h)
SMPS	< 30%	Partway[a]	3.4×10^4	3.5×10^3	4.1 + 2.2[b]
Standard A	< 30%	no	1.6×10^4	2.6×10^3	15.1
Standard B	< 30%	no	2.1×10^4	2.7×10^3	23.7
Standard C	< 30%	no	2.0×10^4	1.9×10^3	23.8
Standard D	< 30%	no	1.8×10^4	2.4×10^3	20.3
Standard (High) E	< 30%	no	5.3×10^4	6.6×10^3	25.1
Standard (High) F	< 30%	no	5.4×10^4	7.0×10^3	24.2
Humid G	> 40%	no	1.9×10^4	2.2×10^3	19.4
Humid H	> 40%	no	3.0×10^4	3.5×10^3	17.0
Static Charge I	< 30%	yes	1.8×10^4	1.9×10^3	23.9
Static Charge J	< 30%	yes	1.3×10^4	1.8×10^3	23.2

a. In the "SMPS" experiment, a static charge was induced partway through the experiment.

b. The "SMPS" experiment began 4.1 h before a static charge was induced and then proceeded to run for an additional 2.2 h.

solution at a flow rate of 2.6 L min^{-1}. So as to obtain a sufficiently broad size distribution, a 0.6 M solution was atomized for roughly half of the injection duration and a 0.006 M solution was atomized for the remaining time. After atomization, the particles were dried and then charge conditioned with a soft x-ray neutralizer (TSI Advanced Aerosol Neutralizer Model 3088) before entering the chamber. The injection time varied based on the desired initial chamber particle number concentration. After a few minutes of mixing, the time- and size-resolved number concentration in the chamber was recorded using a custom-built scanning mobility particle sizer (SMPS) comprised of a coupled differential mobility analyzer (DMA) employing recirculating flow, and butanol-based condensation particle counter (CPC), models TSI 3081 and TSI 3010, respectively. The SMPS was operated with an aerosol flow rate of 0.515 L min^{-1} and a 2.67 L min^{-1} sheath and excess flow. Voltage scans (from 15 to 9850 V) were carried out with measurements made during a 240 s increasing voltage ramp. For experiments "A"-"J," the aerosol flowed through a ^{210}Po source neutralizer prior to entering the DMA. For the "SMPS" experiment, the aerosol flow path was switched at the end of each scan between two pathways of nearly identical length and geometry, each of which led to the DMA after passing through a charge conditioner holder. One of these holders contained ^{210}Po sources, while the other did not (see Fig. 3.7). This made it possible to contrast measurements of the charge state in the chamber against that of a freshly neutralized aerosol.

3.5.2 Wall Deposition Method 1: Using the SMPS

A scanning mobility particle sizer (SMPS) with a negative voltage source measures positive particles based on their electrical mobility, which increases with decreasing
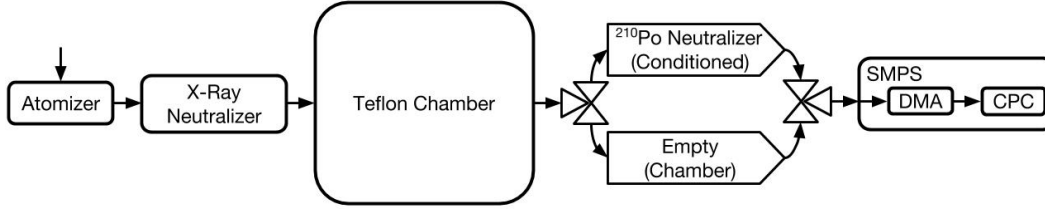
Figure 3.7: Experimental setup for the scanning mobility particle sizer (SMPS) experiment to determine the ratio of positively charged particles of a specific electrical mobility actually in the chamber ($n^+_{chamber}$) to what the steady-state distribution of positively charged particles in the chamber would be ($n^+_{conditioned}$). Those that pass through the "Chamber" pathway are counted as $n^+_{chamber}$, while those that pass through the "Conditioned" pathway are counted as $n^+_{conditioned}$. The SMPS comprises a differential mobility analyzer (DMA) and a condensation particle counter (CPC).

mass to charge (m/z) ratio. At the beginning of a voltage scan, particles with the largest mobility (smallest m/z ratio) successfully travel through a column and are then counted. As the voltage increases, the column selects for larger m/z ratios. Therefore, as the time into the voltage scan increases, the electrical mobility of the positively charged particles transmitted decreases.

Under general operation, in order to obtain the particle size distribution from SMPS data, aerosol is passed through a charge condition that produces a known, steady-state charge distribution before entering the DMA. Only a small fraction of particles acquire charge, and so the concentrations of charged particles transmitted through the SMPS at a particular time in the scan is divided by the probability that a particle of the corresponding size has acquired a positive charge. That probability is estimated using the Wiedensohler (1988) charge distribution.

To determine the charge state of the aerosol within the chamber, we have added a second path for the aerosol to enter the DMA, as shown in Fig. 3.7. This pathway is identical to the first one except that the ^{210}Po elements have been removed from the charge conditioner. Thus, the aerosol enters the DMA without altering the charge state from that within the chamber, while being subjected to the same losses within the instrument.

The differences between charge states obtained by these two methods can be seen by comparing the number of charged particles detected using the charge conditioner, $n^+_{conditioned}$, with that obtained directly from the chamber, $n^+_{chamber}$. Unlike under general operation, no correction is made for the charging probability in this com-

parison as that for the latter ($n^+_{chamber}$) is unknown. In other words, $n^+_{chamber}$ is the concentration of positively charged particles in the chamber, while $n^+_{conditioned}$ is the concentration of positively charged particles in the chamber if the particles within the chamber are in charge steady-state.

The standard notation of n^+ is usually used to symbolize the particle number concentration per particle diameter and has units of number per volume per length (Seinfeld and Pandis, 2016). Since we cannot accurately convert from electrical mobility to particle diameter, we instead allude to the standard notation but use n^+ to represent the number concentration of particles transmitted to the CPC integrated over 0.5 s of the voltage scan (20.5 V). So, here the units of n^+ are number per volume in 0.5 s of the voltage scan. Technically, then, n^+ must be integrated over an electrical mobility range, not a diameter range, to get the total number of positively charged particles. However, since most positively charged particles of the sizes we consider will have no more than a single charge, electrical mobility is analogous to diameter. However, a decreasing electrical mobility corresponds to an increase in particle diameter. As a voltage ramp proceeds, the diameter of a singly charged particle that is counted by the CPC will increase.

For a specific voltage, if $n^+_{conditioned} = n^+_{chamber}$, then the charge distribution entering the SMPS system is close to the Wiedensohler distribution at the particle diameter generally corresponding to the electrical mobility transmitted at that voltage. If $n^+_{conditioned} < n^+_{chamber}$, more positive particles of that size exist than in the Wiedensohler distribution, and if $n^+_{conditioned} > n^+_{chamber}$, there are fewer. We, therefore, track $\frac{n^+_{chamber}}{n^+_{conditioned}}$.

More important than the exact value of $\frac{n^+_{chamber}}{n^+_{conditioned}}$ is the extent to which this ratio is constant, since a constant ratio indicates the absence of forces acting preferentially on positively charged particles over negatively-charged particles. That is, if $\frac{n^+_{chamber}}{n^+_{conditioned}}$ is constant, there is no electric field effect on the rate of wall deposition and, therefore, $\beta(D_p)$ is not a function of time.

Figure 3.8 shows the number concentration of positively charged particles that passed through the charge-conditioned pathway (Panel (a), called "Conditioned") and through a direct, non-neutralized pathway (Panel (b), called "Chamber") shown in Fig. 3.7. When the chamber is operated in a standard condition (-4.1 to 0 h), wall deposition and coagulation both gradually decrease the number concentration. Coagulation also shifts the peak in transmitted particles to a lower electrical mobility

(for singly-charged particles, to a larger diameter). Experimental conditions are shown in Tbl. 3.3 ("SMPS").

When a static charge is induced, positively charged particles with the highest electrical mobility disappear first. This matches intuition: if there is a large negative charge on the chamber walls, positively charged particles will be lost preferentially and the ones that will be lost most quickly are those with the highest electrical mobility.
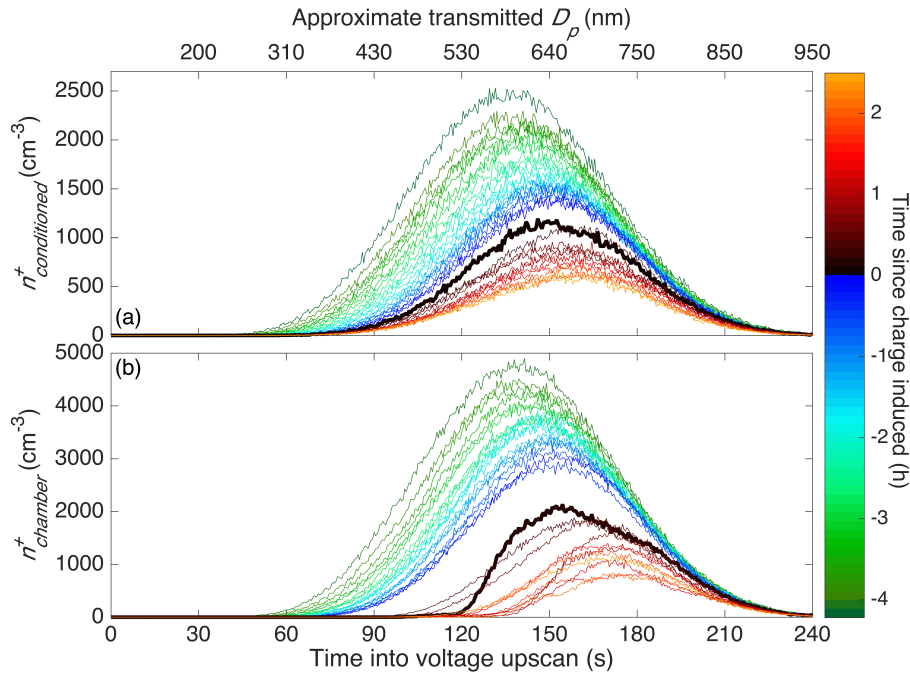
Figure 3.8: Concentration of positively charged particles that reach the CPC through the "Conditioned" (Panel (a)) and through the "Chamber" (Panel (b)) pathway, as shown in Fig. 3.7. Both $n^+_{conditioned}$ and $n^+_{chamber}$ have units of particle number per cm^3 per 0.5 s of the voltage scan. The top axis labels the approximate diameter of transmitted singly and positively charged particles, found using analytical methods (Stolzenburg, 1988). Since most, but not all, transmitted particles are singly charged, this corresponds only roughly to the size of the particles that reach the CPC. Prior to charge inducement, the chamber was run under standard operating conditions. After 4.1 h of operation, i.e., at 0 h, a static charge was induced on the chamber walls. The first scans after charge inducement are shown in bold. The curves in each panel are separated by 13 min except for those immediately after charge inducement: these are 6.5 min in Panel (a) and 19.5 min in Panel (b).

In Fig. 3.9, the ratio of positively charged particles that flow through an empty pathway to those that flow through the charge-conditioned pathway ($\frac{n^+_{chamber}}{n^+_{conditioned}}$) is shown for the same experiment as in Fig. 3.8. After a static charge was applied to
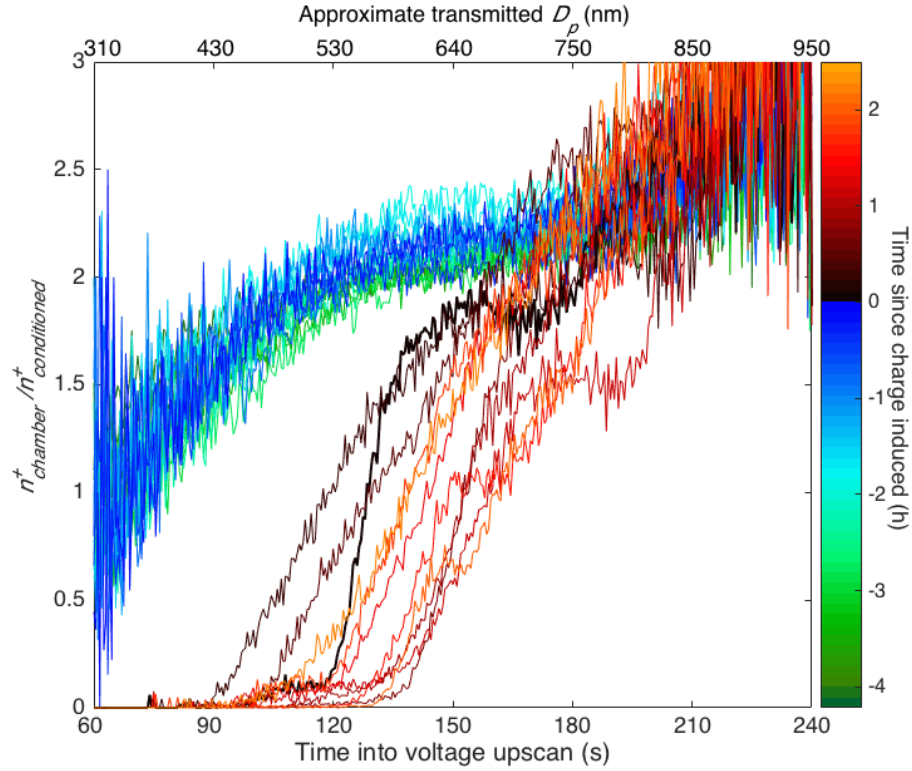
Figure 3.9: The absence or presence of an electric field within the chamber is discerned by the concentration of positively charged particles that are in the chamber at a given time ($n^+_{chamber}$) as compared to the concentration of positively charged particles from a charge-conditioned version of the same sample ($n^+_{conditioned}$). Since the same SMPS system was used to measure the concentrations from both pathways, the ratio is calculated as $n^+_{chamber}$ divided by the average of the two $n^+_{conditioned}$ closest in time. Curves are, therefore, 13 min apart except for the curve immediately after charge inducement (shown in bold), which is 19.5 min apart from the previous one so as to give the most accurate ratio between the before and after inducement cases. As in Fig. 3.8, the top axis shows the approximate diameter of transmitted singly and positively charged particles, which only inexactly corresponds to the size of the particles that reach the CPC.

the walls at 0 h, the ratio decreased rapidly, indicating that when the wall is charged, a preferential loss of positively charged particles does occur as expected. When the chamber was operating in a standard condition (-4.1 to 0 h), there was no change in $\frac{n^+_{chamber}}{n^+_{conditioned}}$, indicating that no charge was present on the chamber walls.

Immediately after charge inducement, the concentration of the smallest positively charged particles nearly disappears. Within about half an hour, there is still a preferential depletion of positively charged particles, but the smallest ones begin reappearing. This is likely because of the air ions which, if there were no polar-preferential wall losses, would re-establish a steady charge distribution within this time frame (for characteristic ion concentrations). Since $\frac{n^+_{chamber}}{n^+_{conditioned}} < \left(\frac{n^+_{chamber}}{n^+_{conditioned}}\right)_{before\ 0\ h}$ even 2 h after charge inducement, we conclude that the effects of the static charge on the chamber remain long after the charge is initially induced. While the discharge time likely depends on the initial strength of the electric field and on the concentration of air ions, we have observed static charges that remain for >8 h and we assume they remain for much longer.

As mentioned above, a constant $\frac{n^+_{chamber}}{n^+_{conditioned}}$ is sufficient to establish that the rate of wall deposition is not dependent on the surface charge of the Teflon walls, which indicates that $\beta(D_p)$ will not change with time. Intuitively, however, one would expect $\frac{n^+_{chamber}}{n^+_{conditioned}} = 1$ if the particles within the chamber are at their steady-state charge distribution. We see in Fig. 3.9, however, that $\frac{n^+_{chamber}}{n^+_{conditioned}} > 1$ (this was confirmed in other, identical, standard experiments). This suggests that, either there is an unintended experimental difference between the two pathways, there is a preference for *negatively* charged particles to deposit to the wall, or the air ions are affecting this ratio.

We confirmed that the two pathways ("Conditioned" and "Chamber") shown in Fig. 3.7 have approximately the same transmission efficiency. We also confirmed that, when measured directly from the upstream x-ray neutralizer, $\frac{n^+_{chamber}}{n^+_{conditioned}} = 1$. This indicates that particles that enter the chamber are at a steady-state charge distribution. If there is an electric field caused by a static charge on the chamber walls, we would expect it to be negatively charged because Teflon has a high negative-charge affinity, as discussed at the beginning of Section 3.5. A negatively-charged wall would lead to the preferential loss of *positively* charged particles (not negatively-charged particles, as we see here). So, it is unlikely that the presence of excess positively charged particles is a result of a surface charge on the Teflon walls.

The observed values of $\frac{n^+_{chamber}}{n^+_{conditioned}} > 1$, then, can be attributed to air ions. When, in the absence of wall deposition, we simulate coagulation as described in Section 3.2.1, we compare simulations in the presence and absence of ions. For the same charge and diameter, in general there were more positively charged particles when ions were present as long as the negative ion concentration did not greatly exceed the positive ion concentration. This was true even for cases in which the charge effects on the rate of coagulation were minimal. In the simulations, the time required to reach an approximate steady $\frac{n^+_{chamber}}{n^+_{conditioned}}$ was less than the particle injection and mixing time. We conclude, then, that $\frac{n^+_{chamber}}{n^+_{conditioned}} \neq 1$ owing to the production of air ions with different properties than those generated in the charge conditioner; the conclusion from this experiment that charge does not alter the rate of wall deposition remains.

3.5.3 Wall Deposition Method 2: Humidity Effects on Static Charge

The second method for determining the effect of charge on wall deposition relies on the assumption that, as the relative humidity of the air surrounding an environmental chamber increases, there is a corresponding decrease in the static charge on the chamber walls.

A study of the effect of humidity on the corona charging of polyvinylidenefluoride (PVDF) films, similar in structure to FEP Teflon, shows a linear decrease in the maximum voltage generated with an increase in relative humidity and, furthermore, that increasing the relative humidity decreases the surface potential even for a film that is already charged (Ribeiro et al., 1992). Ribeiro et al. (1992) postulate this is a result of dissociated absorbed water on the film surface.

According to Funer and James (1993), typically PVDF film shows an absorption of water of 0.02%, while polytetrafluorethylene (PTFE) Teflon shows an absorption of < 0.01% water when immersed at 23°C, which are both infinitesimally small. Another study of the amorphous version of PTFE films (Teflon AF) showed no measurable absorption of water until 75% relative humidity was reached (Vetelino et al., 1997). PTFE Teflon has fluoride atoms bound to carbon atoms; FEP Teflon has both fluoride atoms and trifluoromethyl groups bound to carbon atoms, whereas PVDF films consist of hydrogen and fluoride atoms bound to carbon atoms. Therefore, while it is possible that the relative humidity effect is unique to PVDF films, the Ribeiro et al. (1992) study suggests that it is possible, if not probable, that increasing the relative humidity surrounding a chamber will decrease the chamber's surface

charge.
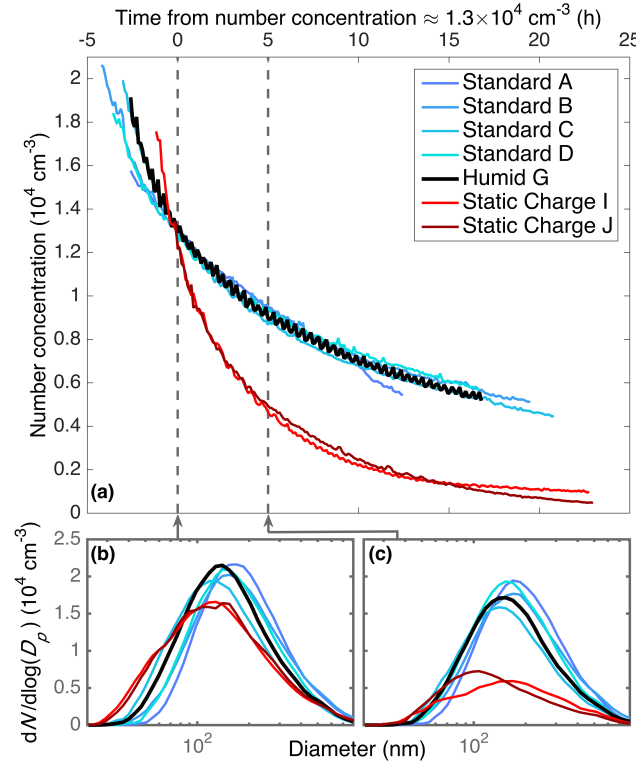
Figure 3.10: Particle-number-concentration evolution for experiments with approximately the same initial number concentration and size distribution. For humid and standard conditions, the number-concentration evolutions overlap. When a static charge is present, wall deposition occurs much faster and the number concentration decreases more quickly (Panel (a)). The particle size distribution aligned at a time when all the experiments shown have an approximate number concentration of 1.3×10^4 cm^{-3} (Panel (b)) is compared to that distribution about 5 h later (Panel (c)). All distributions begin similarly, but the particles under static charge conditions deposit much faster. Thus, the evolution in total number concentration, shown in Panel (a), is not a result of the difference in the rate of coagulation or in the diameter-dependence of the wall-deposition rate. The difference in the number-concentration evolution, then, is a result only of the electric field strength. Since in a humid experiment the static charge on the chamber walls is reduced, and therefore decreases any electric field that may be on the chamber, the similarity in wall-deposition rates between the "Humid" and "Standard" experiments indicates that any electric field present in the standard experiments has a negligible effect.

Figure 3.10(a) shows dynamics of the total number concentration of inorganic particles subject to simultaneous coagulation and wall deposition for experiments that began with approximately the same number distribution and are aligned at a common number concentration (as verified in the displayed size distribution in

Fig. 3.10(b)). The "Standard" experiments align with each other, as expected, but also with the "Humid" experiments. The "Static Charge" experiments, although they begin with approximately the same number concentration and size distribution, exhibit much faster wall deposition than either the "Standard" or the "Humid" experiments. The electric field on the chamber walls affects only wall deposition, so the sole difference between these experiments is the average electric field. Since the number concentration evolution in the "Standard" and the "Humid" experiments overlap, they likely are subject to the same $\bar{E}$; Fig. 3.10(a) verifies that the total number concentration evolutions align, and Fig. 3.10(c) shows that the number distribution does as well.

The number concentration evolution is sensitive to the electric field, as shown both from the number concentration evolution in Fig. 3.6 and from the fact that an increase in static charge from the standard conditions *does* lead to an increase in the rate of wall deposition (demonstrated by the increase in deposition for the "Static Charge" experiments).

If higher humidity conditions do reduce the electric field strength, the "Humid" experiments should show less of a static charge on the chamber walls compared to the "Standard" experiments, if such a charge exists. Since the "Humid" experiment matches the "Standard" experiments, any difference in average electric fields can be considered to be negligible. Thus, since it is possible that any charge on the chamber walls would decrease when the enclosure is at a higher humidity, this is additional evidence that the charge on the chamber walls is negligibly small, even when operated under standard conditions.

3.5.4   Optimal Parameter Estimation

The basic experimental procedure to determine k_e and $\bar{E}$ is centered on the measurement of the dynamics of the size distribution of particles introduced into the chamber. We compare the observed dynamics to those predicted by a numerical solution to the aerosol dynamics equation. The numerical solution includes contributions from coagulation and wall deposition, the latter in the form of undetermined parameters, k_e and $\bar{E}$, which govern the rate of particle wall deposition owing to mixing in the chamber and to electrostatic effects, respectively.

Seemingly, a complicated optimization procedure could be avoided by directly measuring the electric field on a Teflon surface. However, it cannot be assumed that the electric field immediately adjacent to the Teflon walls is the same as the

average electric field $\bar{E}$ within the chamber (McMurry and Rader, 1985). Moreover, neither $\bar{E}$ nor k_e can be measured empirically. Therefore, both parameters must be determined by optimal fitting of time-dependent chamber particle-wall-deposition data.

The general optimization method is as follows: we begin with an initial size-resolved number concentration distribution that matches that from the first SMPS scan of the experiment considered, then we assign to it a charge distribution corresponding to the Wiedensohler (1988) formula, as detailed in Section 3.3. Next, we iteratively minimize the objective function J by determination of the parameters k_e and $\bar{E}$, where

$$ J = \int_0^{t_{final}} \sum_{D_p} \left(N\left(D_p, t\right)_{observed} - \sum_{charges} N\left(D_p, t; k_e, \bar{E}\right)_{simulated} \right)^2 dt. \quad (3.8) $$

Note that when $\bar{E} = 0$, particle charge is not a factor, and J is a function only of k_e. Minimization of J is performed with the Matlab *fminsearch* function, which uses a Nelder-Mead simplex algorithm (Lagarias et al., 1998).

3.5.5 Wall Deposition Method 3: Determining the Electric Field Through Optimization

The final method for determining the charge effect on wall deposition rates has the additional benefit of providing necessary parameters for representing wall deposition, whether or not there is a static charge present on the chamber walls. We use the optimal parameter procedure from Section 3.5.4 and the experimental data from Section 3.5.3 to carry out an optimization simultaneously for k_e and for $\bar{E}$. The results are shown in Fig. 3.11 and discussed below.

Determining an optimal value for k_e while assuming that there is a negligible electric field present on the chamber walls ($\bar{E} \cong 0$) is equivalent to assuming that the particles within the chamber are essentially charge-free. This is supported by the fact that coagulation is affected minimally by the presence of charge under characteristic indoor ion concentrations and, when $\bar{E} = 0$, particle charge has no effect on the rate of wall deposition. When this optimization is carried out, the "Humid" and "Standard" experiments are characterized by similar k_e values and produce similar wall-deposition curves (as shown in Fig. 3.12). This corroborates that the "Humid" and "Standard" experiments are nearly indistinguishable and, therefore, reflect nearly identical $\bar{E}$ values.
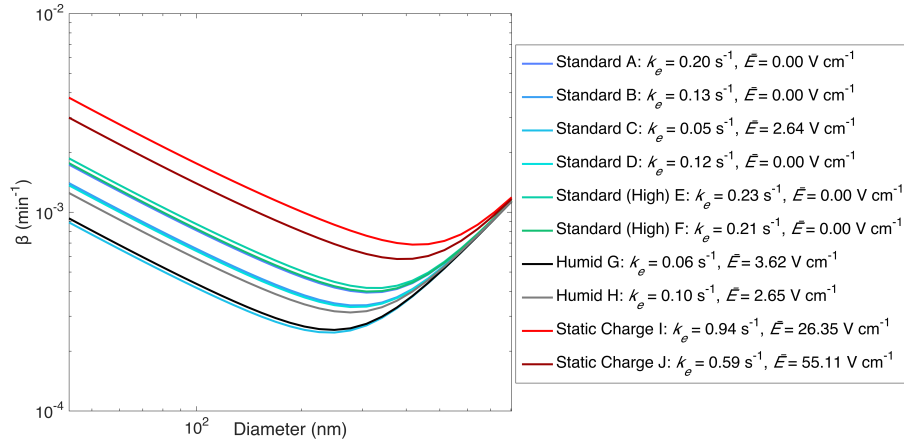
Figure 3.11: Optimal estimated $\beta_{n=0}(D_p)$ based on the values of k_e and $\bar{E}$ (given in the legend) when particles are assumed to have an initial charge. Optimized values of $\bar{E}$ for the experiments performed under standard conditions are close to 0; those for the "Static Charge" experiments are much larger than those for the "Standard" and "Humid" experiments.
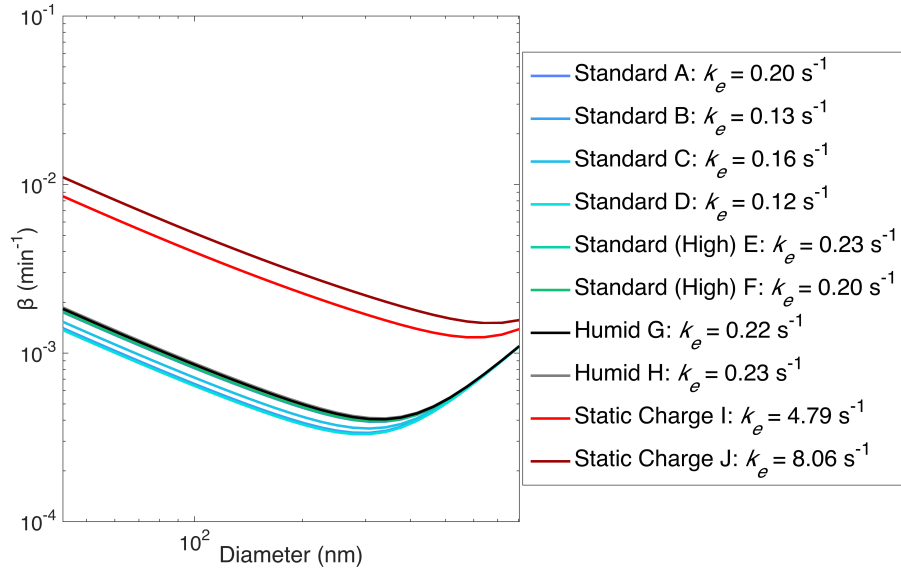
Figure 3.12: Optimal estimated $\beta(D_p)$ based on values of k_e when particles are assumed to be charge-free. Optimal values of k_e are shown in the legend. Note that particles within the chamber may have significant charge, but that this affects the β-curve only when static charge is induced on the chamber walls prior to or during an experiment.

The "Static Charge" experiments, on the other hand, lead to very different $\beta(D_p)$ curves and significantly larger k_e values. Since, for these experiments, $\bar{E} \neq 0$, these larger optimal values of k_e, in effect, attempt to compensate for the charge contribution to wall deposition.

With a two-parameter optimization, small $\bar{E}$ values for the "Humid" and "Standard" experiments are attained. Figure 3.11 shows the optimized k_e and $\bar{E}$ values and the corresponding $\beta_{n=0}(D_p)$ curves: $\bar{E}$ is small for all but the "Static Charge" experiments. We show $\beta_{n=0}(D_p)$, which is the $\beta(D_p)$ for particles with a charge of 0, because most particles are neutrally charged and so, when comparing wall-deposition rates, it is most informative to consider the wall-deposition rate of neutrally charged particles.

To demonstrate further that, when $\bar{E} \neq 0$, there is an increased rate of wall deposition, especially for smaller particles, we include Fig. 3.13, which is a transformation of $\beta_n(D_p)$ to $\beta(D_p, t)$ for the "Static Charge I" experiment. Figure 3.13 is similar to a figure in Pierce et al. (2008), which also shows that an electric field caused by surface charge affects the rate of wall deposition.
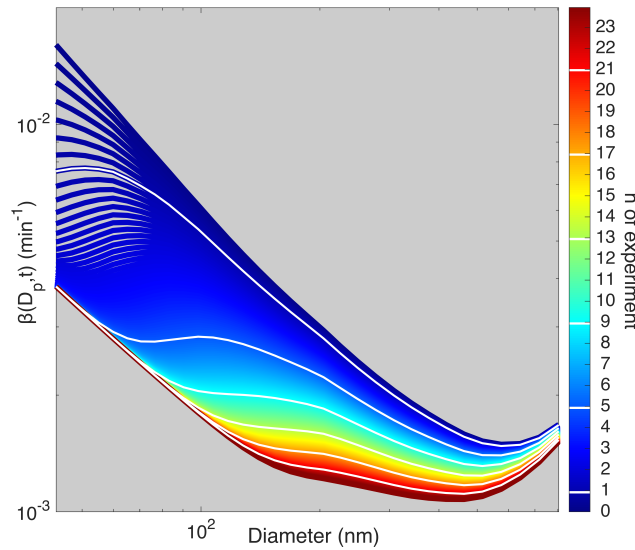
Figure 3.13: Transformation of $\beta_n(D_p)$ to $\beta(D_p, t)$ for the "Static I" experiment using the parameters optimized for that experiment ($k_e = 0.94$ s^{-1} and $\bar{E} = 26.35$ V cm^{-1}). $\beta(D_p, t)$ was determined every 6.5 min. At the beginning of the experiment, $\beta(D_p, t)$ is much larger than that towards the end of the experiment. This difference is particularly pronounced for small particles.

The fact that the majority of the "Standard" experiments (five of the six) lead to an optimal value of $\bar{E} = 0$ further reinforces the essential absence of an electric field

for experiments performed under the standard conditions.

3.6 Further Optimization: Finding the Empirical k_e Parameter

Once one has verified the lack of a charge effect on the rate of particle wall deposition, one can reduce the optimization of the wall-deposition coefficient to one parameter. Note that the $\beta_{n=0}(D_p)$ curves in Fig. 3.11 are less tightly clustered than those in Fig. 3.12 because a two-parameter fit allows a trade-off between the two parameters to account for the number concentration evolution, producing local minima instead of an absolute minimum.

If a local minimum is found, two possibilities exist: either the minimization procedure converged to a local minimum because of the initial guess chosen, or the data – which are subject to random error – give an absolute minimum at a point that (if the data are completely accurate) corresponds to what is actually a local minimum. To address the former possibility, we reanalyzed experiments "Standard C" and "Static Charge I" with initial guesses of k_e between 0.015 and 1.5 s^{-1} and of $\bar{E}$ between 5 and 500 V cm^{-1}. Each optimization returned the originally reported minimum.

Because of the trade-offs in parameter values, optimizing solely for k_e, while setting $\bar{E}$ to 0, or optimizing for both parameters gives good agreement to the data; see Figs. 3.14 and 3.15, where the former is shown in green, the latter is shown in blue, and data are shown in black. The wall-deposition curves for each experiment, which are similar for the "Standard" and "Humid" experiments but quite different for the static one, are shown in Fig. 3.16.

Since it has been established that one can assume $\bar{E} = 0$, we performed a one-parameter optimization of all the "Standard" experiments together and obtained $k_e = 0.19$ s^{-1}. This optimal set of parameters fits the data well (shown in red in Figs. 3.14 and 3.15) for all except the "Static Charge" experiments, in which the substantial charge on the chamber walls precludes such a fit. These parameters also fit well to the wall-deposition curves optimized for each individual experiment, shown in red in Fig. 3.16 (again, all except for the "Static Charge" experiments, as expected).

In application to SOA experiments, the fit to the total surface area concentration (Fig. 3.15) is especially important because, since the transport of vapor molecules to particles depends on particle surface area, SOA yield depends on the aerosol surface area concentration.
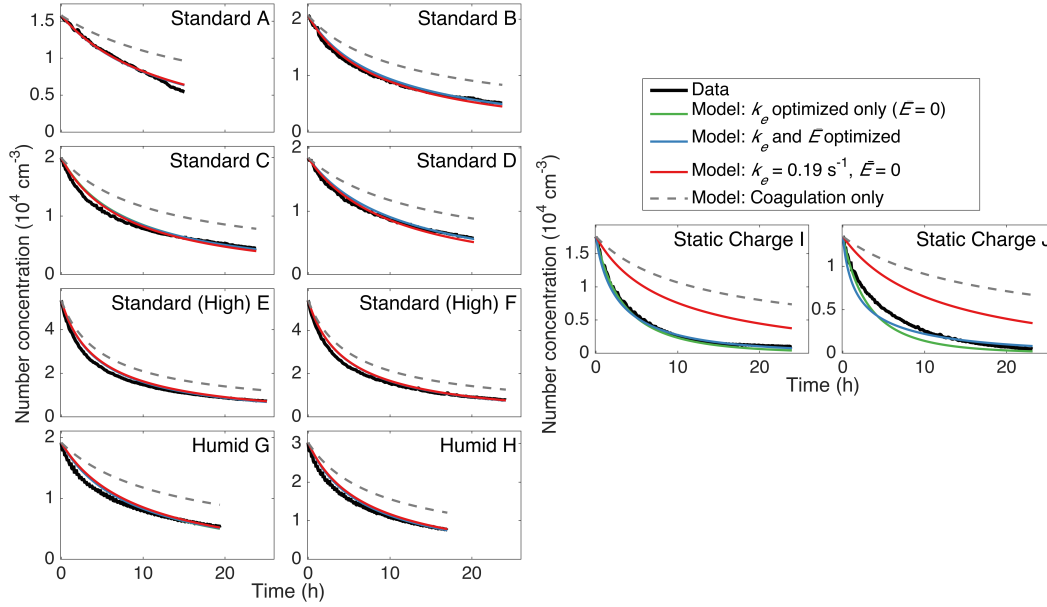
Figure 3.14: Particle-number-concentration evolution throughout the duration of experiments under standard, humid, and static charge conditions. Data are compared to the simulated number concentration calculated with parameters found from different forms of optimization. Data are given in black, and a model with only coagulation included (no wall deposition) is the dashed, gray curve shown to demonstrate that a significant amount of the loss in number concentration is the result of particle wall deposition. For experiments "A"-"H," the final selected k_e and $\bar{E}$ values of 0.19 s^{-1} and 0 V cm^{-1} (red), respectively, match well with the number concentrations found by optimizing for only k_e while holding $\bar{E} = 0$ (green) and with that found by optimizing over both k_e and $\bar{E}$ (blue). In experiments "I" and "J," the static charge cases, the final selected k_e and $\bar{E}$ values do not match the data well, as expected, because of the strong effect of the electric field on the rate of particle wall deposition. The simulated number concentrations found from optimizing only k_e and found from simultaneously optimizing k_e and $\bar{E}$ each match the data well. When $\bar{E}$ is set to 0, the value of k_e compensates until the fit matches the data. This demonstrates the difficulty associated with multiple parameters, especially when each parameter must be determined in the same experiment and may not be extrapolated from one experiment to the next: optimized parameters compensate for one another and lead to much greater uncertainty.
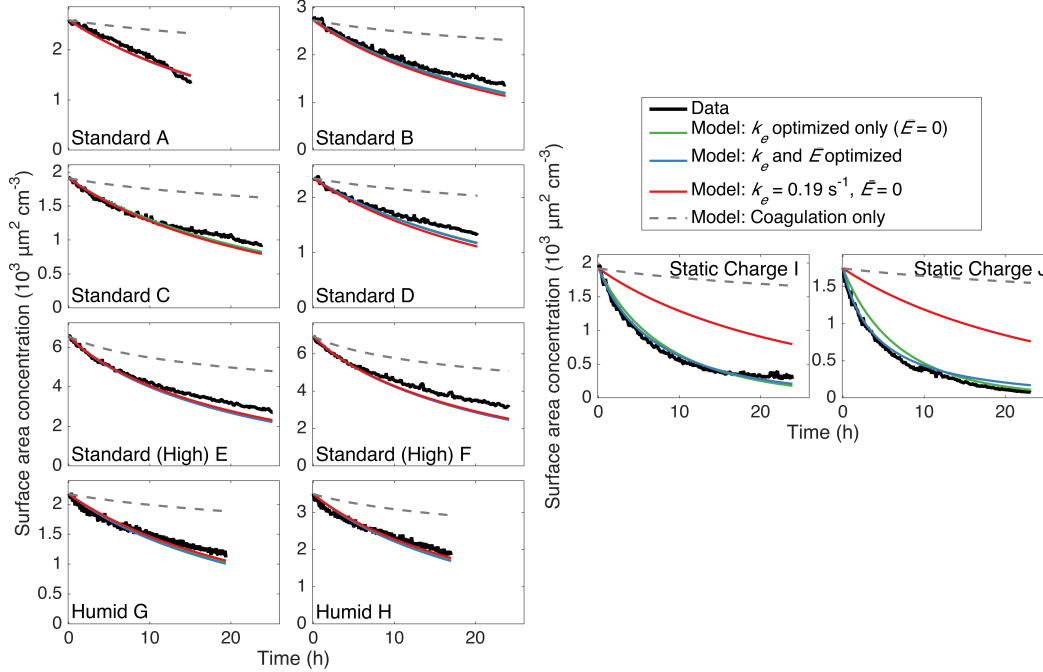
Figure 3.15: Particle surface area concentration throughout the duration of experiments. The same conclusions as in Fig. 3.14 are drawn here. For all the cases, the optimized models match the data well. Again, for experiments "A"-"H," the final selected parameters lead to a surface-area-concentration evolution that matches the data but for experiments "I" and "J," the static charge experiments, these parameters do not lead to a good fit. Since surface area concentration is used for calculating the rate of vapor uptake in SOA formation experiments, fits of the surface area concentrations using the final selected values of k_e and $\bar{E}$ are highly relevant.

3.7 Conclusion

Despite the early recognition that aerosol dynamic experiments carried out in Teflon chambers may be subject to particle charging effects, no comprehensive evaluation of the role of particle charge in such experiments has previously been available. Here, using observed chamber dynamics and computational simulations, we show that the dynamics of particle-particle coagulation are essentially unaffected by particle charge under typical chamber operating conditions as long as the positive and negative ions in the surrounding area are of about equal concentration, as is the case when characteristic urban indoor ion concentrations are taken.

The ratio of positively charged particles taken directly from the chamber to those that reached the Wiedensohler distribution after leaving the chamber is constant for a typical experiment (Fig. 3.9), the number-concentration evolution for the humid experiments does not differ significantly from that of the standard experiments (Fig.
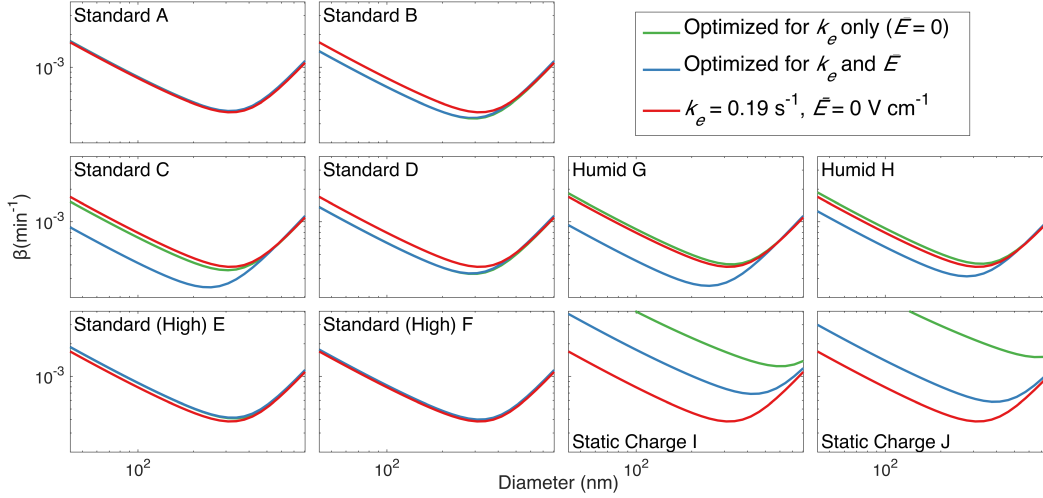
Figure 3.16: Resulting wall-deposition curves for the final selected parameters (k_e = 0.19 s^{-1} and $\bar{E}$ = 0) are compared to that determined by minimizing J for each experiment when only k_e is allowed to vary ($\bar{E}$ set to 0) and when both k_e and $\bar{E}$ are subject to optimization. The former represents an uncharged chamber in which the electric field has no effect on the wall deposition. Note that, rigorously speaking, all curves are $\beta_{n=0}(D_p)$, the wall-deposition parameter for neutrally charged particles. Except for the static charge experiments, in which one would expect the charges on particles to be influential, the wall-deposition curve obtained is similar to both the curve found from assuming there is zero charge and from that found assuming charge is present. As in Figs. 3.14 and 3.15, the final selected wall-deposition curve fits well for all but the static charge cases.

3.10), a two-parameter optimization procedure gives $\bar{E}$=0 for most of the "Standard" experiments (Fig. 3.11), and the assumption of an average electric field of 0 gives good fits for both humid and standard operating condition experiments (Fig. 3.14). We are able to conclude, therefore, that the standard experiments are subject to a negligible electric field, and that any electric field present is insignificant for the analysis of particle wall deposition. Furthermore, since the wall-deposition curves $\beta(D_p)$, as individually optimized, do not vary noticeably from those based on the optimal k_e value of 0.19 s^{-1} (Fig. 3.16), one can use the wall-deposition curve produced by assuming k_e = 0.19 s^{-1} and $\bar{E}$ = 0 for all experiments performed under standard operating conditions in the Caltech Environmental Chamber.

Ideally, there would be no static charge on the walls of environmental chambers. This would allow the use of a constant $\beta(D_p)$ from experiment to experiment and, by preventing any charge preference for particles within the chamber, minimally affect the rate of coagulation. Unfortunately, charge is too easily induced on Teflon walls: simply brushing one's clothes or hair against a chamber is enough to induce

a measurable static charge. We provide here three methods for discerning the state of a static charge on Teflon chamber walls that can be applied to other chambers.

References

Chen, Jun and Zhong Lin Wang (Nov. 2017). "Reviving vibration energy harvesting and self-powered sensing by a triboelectric nanogenerator." In: *Joule* 1.3, pp. 480–521. ISSN: 25424351. DOI: 10.1016/j.joule.2017.09.004.

Crump, James G. and John H. Seinfeld (1981). "Turbulent deposition and gravitational sedimentation of an aerosol in a vessel of arbitrary shape." In: *Journal of Aerosol Science* 12.5, pp. 405–415. ISSN: 00218502. DOI: 10.1016/0021-8502(81)90036-7.

Funer, Rolf E. and David B. James (1993). "New Thermoplastics and Their Properties." In: *Polymers for Electronic and Photonic Applications*. Ed. by C.P. Wong. San Diego: Academic Press, Inc. Chap. Advances in Thermoplastics for Electronic Applications, pp. 339–362. ISBN: 0-12-762540-2.

Ghosh, K., S.N. Tripathi, Manish Joshi, Y.S. Mayya, Arshad Khan, and B.K. Sapra (Mar. 2017). "Modeling studies on coagulation of charged particles and comparison with experiments." In: *Journal of Aerosol Science* 105, pp. 35–47. ISSN: 00218502. DOI: 10.1016/j.jaerosci.2016.11.019.

Harrison, R.G. and K.L. Aplin (Aug. 2007). "Water vapour changes and atmospheric cluster ions." In: *Atmospheric Research* 85.2, pp. 199–208. ISSN: 01698095. DOI: 10.1016/j.atmosres.2006.12.006.

Hirsikko, A., T. Nieminen, et al. (Jan. 2011). "Atmospheric ions and nucleation: a review of observations." In: *Atmospheric Chemistry and Physics* 11.2, pp. 767–798. ISSN: 1680-7324. DOI: 10.5194/acp-11-767-2011.

Hirsikko, Anne, Taina Yli-Juuti, Tuomo Nieminen, Eija Vartiainen, Lauri Laakso, Tareq Hussein, and Markku Kulmala (2007). "Indoor and outdoor air ions and aerosol particles in the urban atmosphere of Helsinki: characteristics, sources and formation." In: *Boreal Environment Research* 12, 295–310. ISSN: 12396095. URL: http://www.borenv.net/BER/archive/pdfs/ber12/ber12-295.pdf.

Lagarias, Jeffrey C., James A. Reeds, Margaret H. Wright, and Paul E Wright (Jan. 1998). "Convergence Properties of the Nelder-Mead Simplex Method in Low Dimensions." In: *SIAM Journal on Optimization* 9.1, pp. 112–147. ISSN: 1052-6234. DOI: 10.1137/S1052623496303470.

McMurry, P. H. and D. J. Rader (Jan. 1985). "Aerosol Wall Losses in Electrically Charged Chambers." In: *Aerosol Science and Technology* 4.3, pp. 249–268. ISSN: 0278-6826. DOI: 10.1080/02786828508959054.

Nah, Theodora, Renee C. McVay, Jeffrey R. Pierce, John H. Seinfeld, and Nga L. Ng (Feb. 2017). "Constraining uncertainties in particle-wall deposition correction

during SOA formation in chamber experiments." In: *Atmospheric Chemistry and Physics* 17.3, pp. 2297–2310. ISSN: 1680-7324. DOI: `10.5194/acp-17-2297-2017`.

Pierce, J. R., G. J. Engelhart, L. Hildebrandt, E. A. Weitkamp, R. K. Pathak, N. M. Donahue, A. L. Robinson, P. J. Adams, and S. N. Pandis (Oct. 2008). "Constraining Particle Evolution from Wall Losses, Coagulation, and Condensation-Evaporation in Smog-Chamber Experiments: Optimal Estimation Based on Size Distribution Measurements." In: *Aerosol Science and Technology* 42.12, pp. 1001–1015. ISSN: 0278-6826. DOI: `10.1080/02786820802389251`.

Reiter, R. (Sept. 1985). "Part B: Frequency Distribution of Positive and Negative Small Ion Concentrations, Based on Many Years' Recordings at Two Mountain Stations Located at 740 and 1780 m ASL." In: *International Journal of Biometeorology* 29.3, pp. 223–231. ISSN: 0020-7128. DOI: `10.1007/BF02189654`.

Ribeiro, P.A., M. Raposo, J.N. Marat-Mendes, and J.A. Giacometti (1992). "Constant-current Corona Charging of Biaxially Stretched PVDF Films in Humidity-Controlled Atmospheres." In: *IEEE Transactions on Electrical Insulation* 27.4, pp. 744–750. ISSN: 00189367. DOI: `10.1109/14.155791`.

Seinfeld, John H. and Spyros N. Pandis (2016). *Atmospheric Chemistry and Physics: From Air Pollution to Climate Change*. 3rd. Hoboken: John Wiley & Sons. ISBN: 978-1118947401.

Sessler, G. M., C. Alquié, and J. Lewiner (Mar. 1992). "Charge distribution in Teflon FEP (fluoroethylenepropylene) negatively corona-charged to high potentials." In: *Journal of Applied Physics* 71.5, pp. 2280–2284. ISSN: 0021-8979. DOI: `10.1063/1.351127`.

Stolzenburg, Mark R. (1988). "An Ultrafine Aerosol Size Distribution Measuring System." PhD thesis. University of Minnesota.

Sunol, A. M., S. M. Charan, and J. H. Seinfeld (2018). "Computational simulation of the dynamics of secondary organic aerosol formation in an environmental chamber." In: *Aerosol Science and Technology* 52.4, pp. 470–482. ISSN: 15217388. DOI: `10.1080/02786826.2018.1427209`.

Tian, J., B. T. Brem, M. West, T. C. Bond, M. J. Rood, and N. Riemer (July 2017). "Simulating aerosol chamber experiments with the particle-resolved aerosol model PartMC." In: *Aerosol Science and Technology* 51.7, pp. 856–867. ISSN: 0278-6826. DOI: `10.1080/02786826.2017.1311988`.

TSI (2013). *Advanced Aerosol Neutralizer Model 3088: Operation and Service Manual*. Shoreview: TSI Incorporated.

Vartiainen, Eija et al. (2007). "Ion and particle number concentrations and size distributions along the Trans-Siberian railroad." In: *Boreal Environment Research* 12, pp. 375–396. ISSN: 12396095. URL: `http://www.borenv.net/BER/archive/pdfs/ber12/ber12-375.pdf`.

Vetelino, Kevin A., Patrick R. Story, Russell D. Mileham, Claudius Feger, and David Galipeau (1997). "A novel surface acoustic wave microsensor technique for polymer surface characterization." In: *Polymer Surfaces and Interfaces: Characterization, Modification and Application*. Ed. by K. L. Mittal and K.-W. Lee. Utrecht: VSP BV. Chap. Part 1. Polymer Surface Modification and Characterization, pp. 101–108. ISBN: 90-6764-217-7.

Wiedensohler, A. (June 1988). "An approximation of the bipolar charge distribution for particles in the submicron size range." In: *Journal of Aerosol Science* 19.3, pp. 387–389. ISSN: 00218502. DOI: 10.1016/0021-8502(88)90278-9.

Chapter 4

SECONDARY ORGANIC AEROSOL YIELDS FROM THE OXIDATION OF BENZYL ALCOHOL

Abstract

Recent inventory-based analysis suggests that emissions of volatile chemical products in urban areas are competitive with those from the transportation sector. Understanding the potential for secondary organic aerosol formation from these volatile chemical products is, therefore, critical to predicting levels of aerosol and for formulating policy to reduce aerosol exposure. Experimental and computationally simulated environmental chamber data provide an understanding of aerosol yield and chemistry under relevant urban conditions (5–200 ppb NO and 291–312 K) and give insight into the effect of volatile chemical products on the production of secondary organic aerosol. Benzyl alcohol, one of these volatile chemical products, is found to have a large secondary organic aerosol formation potential. At NO concentrations of ~80 ppb and 291 K, secondary organic aerosol mass yields for benzyl alcohol can reach 1.

4.1 Introduction

A major component of ambient fine particulate matter is secondary organic aerosol (SOA), the precursors of which are originally emitted into the atmosphere in the gas-phase (Shrivastava et al., 2017; Goldstein and Galbally, 2007). Through single or multiple generations of oxidation, emitted vapors can become progressively less volatile and eventually condense into the particle phase to form this SOA (Seinfeld and Pandis, 2016).

Understanding the formation of particulate matter is of critical importance. Exposure to particulate matter causes respiratory and cardiovascular disease (Mannucci et al., 2015), and yet particulate matter has remained stubbornly high despite regulation: over 20 million people in the U.S. live in regions with larger concentrations

of PM$_{2.5}$ than deemed safe (EPA, 2012). Additionally, SOA-containing particles can serve as cloud condensation nuclei; the interaction between particulate matter and cloud formation is one of the most important processes in the Earth's radiative budget and, therefore, in climate predictions (IPCC, 2014).

However, accurately predicting the mass of secondary organic aerosol formed from the oxidation of volatile chemical products (VCPs) poses a major challenge. A mass-balance analysis of VCPs in the Los Angeles atmosphere indicates that VCPs could account for around half of the SOA in that area (McDonald et al., 2018). This analysis was based on estimating secondary organic aerosol yields for a number of these oxygenated compounds that have traditionally not been studied for their SOA formation potential. Direct measurements of the SOA yields of these compounds is paramount to constraining estimates and formulating policy to reduce secondary organic aerosol formation (Burkholder et al., 2017).

This study focuses on one of these volatile chemical products, benzyl alcohol. Benzyl alcohol is a widely used compound in consumer products that can be found in soaps, inks, paints and, correspondingly, indoor air (Wang, 2015; Harrison and Wells, 2009). It is also emitted from biogenic sources, such as fruits and flowers (Baghi et al., 2012; Bernard et al., 2013; Horvat et al., 1990). The emission inventory-based analysis by McDonald et al. (2018) of the production rates of volatile chemical products estimated that benzyl alcohol comprised 0.06% of the total volatile organic compounds (VOCs) in the Los Angeles basin in 2010. Using the Statistical Oxidation Model, they calculated that for half a day of oxidation under high ambient NO$_x$ conditions, benzyl alcohol will have a SOA yield of 0.09. Based on this value, it was further estimated that benzyl alcohol contributes 0.14% of the total atmospheric secondary organic aerosol in the Los Angeles basin.

Whereas the SOA yield of benzyl alcohol oxidation estimated in the McDonald et al. (2018) analysis was relatively low, in a laboratory chamber study, Carter et al. (2005) measured the SOA yield of benzyl alcohol to be ~0.3 in a mixture of reactive compounds and 25–30 ppb of NO$_x$. This reactive compound mixture comprised compounds that one would not expect to form significant SOA yield, but that may influence the fate of RO$_2$ radicals that could be formed from benzyl alcohol oxidation. That study also estimated the reaction rate constant of benzyl alcohol with OH as 2.56×10^{-11} cm^3 molec^{-1} s^{-1}. An extension of the study (Li et al., 2018), which also used a base mixture of reactive compounds, determined a benzyl alcohol SOA yield of 0.41.

The goal of determining SOA formation in an environmental chamber is to extrapolate the SOA yields to the atmosphere. Since at different times or in disparate places, different temperatures or NO_x mixing ratios may be most relevant, it is important to study SOA formation in a wide parameter-space. Studies performed under varying conditions can also assist in teasing out which data result from the atmospheric chamber itself and how these data ought to be corrected for the atmosphere. For example, for toluene, a compound for which benzyl alcohol is a major photooxidation product (Hamilton et al., 2005), Zhang, Cappa, et al. (2014) found a SOA yield 70% higher at low NO_x concentrations than at high NO_x concentrations and found that the true SOA yield was a factor of 4 higher than that calculated without accounting for the chamber-process of vapor wall deposition.

While the experiments described here were performed under conditions that minimize corrections required to extrapolate SOA yields to the atmosphere, historically these corrections could be quite significant (Zhang, Cappa, et al., 2014). As a result, we devote Sect. 4.3 to a detailed discussion of the SOA yield calculation including possible corrections. Understanding these corrections is critical to ensuring that the SOA yields calculated are atmospherically relevant.

4.2 Instruments and Procedure

4.2.1 Experimental Method and Chamber Description

All experiments were performed in batch mode in the Caltech 17.9 m^3 FEP Teflon-walled Environmental Chamber, which hangs in a temperature-controlled enclosure. The chamber volume was characterized according to the procedure outlined in Schwantes, McVay, et al. (2017). While the chamber pressure remains constant throughout the duration of an experiment, the volume decreases as air is sampled by various instruments; the fraction of the volume at the end of the experiment compared to the beginning of it is given in Table 5.1. Before each experiment, the chamber was flushed for > 24 h with clean air (compressed air with ozone, nitrogen oxides, water vapor, and organic carbon removed). The radical source H_2O_2 was injected at 42°C and 5 Lpm into the chamber, followed by the injection of benzyl alcohol (Sigma Aldrich ReagentPlus, ≥99%) with gentle heating (60°C) at 2 Lpm (5 Lpm for experiments S1–3 and E1) for >50 min. The purity of the benzyl alcohol was verified with Nuclear Magnetic Resonance (NMR) spectroscopy. Meanwhile, a 0.06 M $(NH_4)_2SO_4$ solution (0.15 M for experiments S2 and E1) was atomized and the resulting particles dried, charge-conditioned with a TSI Model 3088 soft x-ray neutralizer, and then injected into the chamber for varying lengths of

time (depending on the desired initial seed concentration; note that no particles were injected for experiment S1). The solution was sonicated before each injection. Then, NO (506.9 ppm ± 2%, Airgas Specialty Gases, Certified Standard) or, for experiment E1, NO_2 (488 ppm, Air Liquide) was injected into the chamber at 5 Lpm to achieve the desired initial NO or NO_2 concentration. Ultraviolet broadband lights centered around 350 nm were used to photolyze H_2O_2 with a rate of $j_{H_2O_2} \approx 4.7 \times 10^{-6}$ s^{-1}, calculated using the measured variation in irradiance with wavelength and the NO_2 photolysis rate ($j_{NO_2} = 6.2(\pm0.1) \times 10^{-3}$ s^{-1}) found using a 0.29 L quartz tube and the procedure outlined in Zafonte, Rieger, and Holmes (1977). Experiment L1 was performed at 8% of the light strength of the other experiments ($j_{H_2O_2} \approx 3.7 \times 10^{-7}$ s^{-1}).

A Vaisala HMM211 probe was used to measure the temperature and humidity of the chamber. Humidity was calibrated for RH from 11 to 95% (using LiCl, KNO_3, $Mg(NO_3)_2$, and $MgCl_2$ salts). A Teledyne Nitrogen Oxide Analyzer (Model T200) was used to measure the NO and NO_2 concentrations throughout the experiments; note that this instrument measures the contribution of NO_y compounds (e.g., organic nitrates) as NO_2. Owing to some drift between experiments, linear fits were performed on the slope and offset calibrations, except for experiments S2–3 and U5, due to a calibration problem. Ozone was measured with a Horiba Ambient Monitor. NO, NO_2, and O_3 measurements were recorded every 30 s. Humidity and temperature uncertainties were calculated as standard deviations from the mean value, where measurements were taken every 30 s throughout the experiment. Initial NO and NO_2 mixing ratios were determined (as well as their standard deviations) prior to irradiation during the background collection period (usually $\gtrsim$60 min). For experiments N1–6 and U6, NO was continuously injected during oxidation to maintain a stable NO mixing ratio.

4.2.2 Gas-Phase Measurements

A CF_3O^- chemical ionization mass spectrometer (CIMS) measured oxidation products and the benzyl alcohol concentration by scanning m/z ratios between 50 and 330. The CIMS is equipped with a Varian 1200 triple quadrupole mass analyzer. A custom-built inlet was used to ensure that the sample was taken at a constant temperature (the top of the inlet was 25°C). To reduce loss of vapor to the tubing prior to analysis, the CIMS sampled off of a bypass flow that was accelerated using a mechanical pump.

Table 4.1: Experiments analyzed for this chapter.

Label/Date	[BnOH]$_0$ (ppb) (% Reacted at Experiment End)	T (K)	Initial Seed Surface Area† (10^3 μm² cm⁻³)	[NO]‡ (ppb)	Wall-Loss Slope (μm³ cm⁻³ s⁻¹)	$k_{\mathrm{BnOH+OH}}$[OH]⊤ (10^{-4} s⁻¹)	Length (h) (% of Total Volume at Experiment End)	uncorrected SOA Y (% of SOA Y with ω = 0)	SOA Y (ω = 0)	SOA Y (ω = 1)
R1/190321	199±32 (82%)	291.0±0.3	1.74±0.17	77.3±0.9	0.048±0.050	1.10 ± 0.06	6.1 (86%)	0.68 (89%)	0.76±0.16	0.79±0.16
R2/190323	160±18 (88%)	290.9±0.3	1.98±0.18	77.4±0.8	-0.041±0.145	1.03 ± 0.06	6.5 (85%)	0.87 (88%)	0.99±0.16	1.04±0.16
R3/190312	202±24 (95%)	291.1±0.2	1.50±0.16	72.6±0.7	-0.027±0.042	0.86 ± 0.04	12.0 (73%)	0.54 (77%)	0.70±0.13	0.75±0.13
R4/190319	199±28 (85%)	291.0±0.2	1.97±0.18	74.0±1.0	-0.009±0.076	1.03 ± 0.06	6.3 (85%)	0.70 (88%)	0.79±0.15	0.83±0.15
R5/190128	222±27 (78%)	291.2±0.2	2.19±0.21	93.7±0.7	-0.017±0.059	0.71 ± 0.03	8.8 (80%)	0.58 (81%)	0.72±0.13	0.78±0.13
S1/191219	455±29 (60%)	291.3±0.2	0.00±0.00	72.4±0.6		0.49 ± 0.03	5.3 (90%)	0.41 (91%)	0.45±0.06	0.47±0.06
S2/191002	252±16 (85%)	291.2±0.2	0.33±0.07	~96	-0.008±0.013	0.99 ± 0.04	6.3 (88%)	0.34 (87%)	0.39±0.04	0.41±0.04
S3/190930	174±15 (83%)	291.0±0.2	0.64±0.10	~90	0.016±0.017	1.17 ± 0.05	4.5 (91%)	0.48 (88%)	0.52±0.06	0.54±0.06
S4/190325	153±27 (82%)	291.0±0.3	5.47±0.32	77.8±0.8	0.010±0.213	1.08 ± 0.09	5.1 (88%)	0.81 (84%)	0.96±0.25	1.04±0.25
T1/190419	216±30 (86%)	296.7±0.4	2.33±0.21	75.6±0.9	-0.069±0.062	1.44 ± 0.07	5.0 (91%)	0.54 (89%)	0.60±0.11	0.63±0.11
T2/190417	193±23 (89%)	301.6±0.4	1.93±0.19	71.7±0.9	-0.012±0.060	1.44 ± 0.08	5.0 (91%)	0.48 (88%)	0.54±0.09	0.57±0.09
T3/190422	212±34 (91%)	306.6±0.4	2.76±0.23	76.9±0.7	0.070±0.144	1.13 ± 0.09	6.3 (89%)	0.53 (84%)	0.63±0.13	0.67±0.13
T4/190410	266±43 (87%)	311.6±0.5	2.12±0.2	80.4±0.8	-0.013±0.114	1.18 ± 0.08	5.5 (90%)	0.32 (87%)	0.37±0.08	0.39±0.08
N1/190408*	191±27 (92%)	291.1±0.3	2.00±0.19	4.8 (0.7–8)	0.056±0.101	1.27 ± 0.05	5.0 (91%)	0.63 (91%)	0.70±0.12	0.73±0.12
N2/190403*	190±35 (86%)	290.9±0.3	2.09±0.19	14.3 (8–18)	0.003±0.094	1.02 ± 0.11	5.0 (88%)	0.61 (90%)	0.68±0.16	0.71±0.16
N3/190426*	166±32 (79%)	290.9±0.3	2.71±0.23	64.0 (56–69)	0.027±0.070	0.77 ± 0.06	6.0 (90%)	0.56 (84%)	0.66±0.17	0.70±0.17
N4/190401*	183±17 (73%)	291.0±0.3	1.84±0.18	76.2 (52–106)	0.008±0.05	0.86 ± 0.05	5.0 (88%)	0.54 (90%)	0.60±0.09	0.63±0.09
N5/190424*	167±19 (76%)	290.9±0.3	2.84±0.23	111.7 (103–118)	0.027±0.186	0.77 ± 0.05	5.0 (91%)	0.46 (85%)	0.54±0.10	0.58±0.10
N6/190405*	189±18 (76%)	290.9±0.1	1.78±0.18	200.6 (194–208)	0.000±0.082	0.76 ± 0.03	5.0 (88%)	0.42 (89%)	0.47±0.08	0.50±0.08
E1/200109⊥	295±18 (78%)	291.1±0.2	2.83±0.22	1.4±1.0	0.091±0.093	0.83 ± 0.02	5.5 (89%)	0.29 (82%)	0.35±0.05	0.38±0.05
L1/190110	135±12 (52%)	285.78±0.03	2.58±0.21	80.4±1.1	0.033±0.009	0.115 ± 0.002	16.7 (58%)	0.10 (27%)	0.37±0.18	0.51±0.18
U1/190327	189±22	290.9±0.2	~4.03	81.1±0.7		2.09±0.25	5.2 (88%)			
U2/190430	136±20	291.1±0.2	1.36±0.13	71.0±0.9		1.16±0.07	5.2 (91%)			
U3/190628		291.2±0.4	~1.48	77.7±0.9			5.0 (91%)			
U4/190529	139±26	291.1±0.3	~5.40	70.7±0.7			5.5 (90%)			
U5/190828	325±20	284.5±0.1	1.70±0.14	~69		1.10±0.06	5.4 (86%)			
U6/190428*	152±25	291.1±0.2	3.11±0.23	137.8 (133–144)		0.19±0.01	5.9 (90%)			
U7/190225		290.9±0.2	~2.2	71.6±1.0		0.74± 0.06	6.6 (84%)			
U8/190227		290.9±0.3		76.9±0.9			9.6 (78%)			

*For these experiments, N1–6 and U6, [NO] was held constant through a continuous injection.

†Experiments with particles outside the range of the SMPS used for particle measurement or those with other measurement issues are reported without uncertainties and should be taken as approximate values. This applies to experiments U1, U3–4, and U7–8.

‡For constant [NO] experiments, the average [NO] is reported along with the range of [NO] throughout the experiment. For all other experiments, the initial [NO] is given with the standard deviation during the background collection period. For experiments with NO$_x$ measurement problems, an approximate value is given.

⊥Experiment E1 had an initial NO$_2$ mixing ratio of 71.0±0.8 ppb. All other experiments began with no initial NO$_2$.

⊤The reported value is from a first-order exponential fit of the benzyl alcohol decay.

The 193 m/z signal (the mass of benzyl alcohol $+ \, CF_3O^-$), which was measured every 162 to 172 s, was normalized to the 86 m/z signal (the M+1 peak for CF_3O^-) and used to measure the benzyl alcohol concentration. This signal was calibrated using dilutions of an 800 L Teflon bag of ~44 ppb benzyl alcohol. The concentration in this bag was verified using Fourier transform infrared absorption (FT-IR) spectroscopy with a 19 cm path length and absorption cross sections from the Pacific Northwest National Laboratory (PNNL) database. In this way, any wall or sampling loss was accounted for since the CIMS sampled from the same volume as the FT-IR. Multiple FT-IR samples were taken in succession until there were consistent spectra; this was to ensure a minimal effect from any compound deposited on the FT-IR instrument walls or sampling lines.

For the experiments labeled U3 and U7–8, there were errors with the CIMS measurements. Correspondingly, Table 4.1 does not report an initial benzyl alcohol concentration, a first-order exponential fit to the benzyl alcohol decay, or any SOA yields. The experiments are still included in Table 4.1 because their results are used to understand differences in chemical composition.

During the background collection period of ~1 h for each experiment, the standard deviation of the benzyl alcohol mixing ratio, along with the uncertainty in the calibration, was used to estimate the uncertainty of the initial benzyl alcohol mixing ratio (see Table 4.1). This combined standard deviation was also considered as the uncertainty in the measurement of the time-resolved gas-phase mixing ratio throughout the experiment. The SOA yield is determined from the reacted benzyl alcohol, which is the difference between the measured benzyl alcohol concentration at any given time and the initial benzyl alcohol concentration. The variance of the reacted benzyl alcohol is the sum of the variances of the initial and measured benzyl alcohol mixing ratios. The uncertainty reported in Table 4.1 is, then, the square root of the reacted benzyl alcohol mixing ratio variance.

The conversion from mixing ratio to mass concentration of reacted benzyl alcohol was performed assuming a constant pressure of 1 atm. Note that the chamber is located three floors from a weather station, which reported an average atmospheric pressure of 0.97 atm in the year 2019 (TCCON Weather Data, 2020); thus, 1 atm is a reasonable estimate of the pressure in the experiments.

4.2.3   Particle-Phase Measurements

To measure the particle size distribution, a custom-built scanning mobility particle sizer (SMPS) with a 3081 TSI Differential Mobility Analyzer (DMA) and a TSI 3010 butanol condensation particle counter (CPC) was used with a sheath flow rate of 2.64 Lpm, an aerosol flow rate from the chamber of 0.515 Lpm, and a dilution flow of 0.485 Lpm. A full size-scan was collected every 5.5 minutes (for experiments S1–3 and E1 scans were performed every 6 min), and the voltage was scanned over 4 min from 15 to 9875 V. Data inversion was performed using the method described in Mai et al. (2018). Total number, volume, and surface area concentrations were determined assuming 431 size bins between 22 and 847 nm. When the sample flow was <0.515 Lpm, an adjustment to the total number concentration was performed to account for the sampled flow. Particles were charged with a 500 microcurie Po-210 source, except for experiments S1–3 and E1, which used an X-ray source.

When the aerosol size distribution was close to the edges of the measurable range, a logarithmic fit of the distribution tail was performed on the edges of the distribution: diameters of 382 to 600 nm were used to fit particles above 600 nm, and those with diameters 35 to 200 nm were used to fit particles with diameters smaller than 35 nm. Fits of the tail distribution were performed on the upper end of the size distribution for experiment N5, which produced an average of a 3.4% decrease from the raw measurement in the volume concentration; the lower end of the size distribution for experiment S2, which led to a volume concentration adjustment of <0.1%; and on both the upper and lower ends of the size distribution for the nucleation experiment S1, which (for those points after at least 100 min of oxidation) led to a volume concentration difference of <1% from that measured in the absence of any adjustment. Particle volume was converted to particle mass with a SOA density of 1.4 g cm^{-3}, consistent with past work on isoprene (Dommen et al., 2006; Kroll et al., 2005; Kroll et al., 2006) and on benzyl alcohol (Li et al., 2018).

Uncertainty in the particle size was assumed not to exceed 2 nm, as is typical. For the CPC-associated margin of error, according to approximate Poisson statistics, the uncertainty of the number in each particle size bin was taken as the square root of the number concentration in that bin and that value of uncertainty was propagated into surface area and volume measurements both by bin and, eventually, for the total number concentration. Additionally, an uncertainty in the measured volume concentration due to sample noise was added from the uncertainty of the wall-loss corrected volume concentrations in the background collection period prior to lights

on (see Sect. 4.3.2.1).

For experiments U1–8, there were issues with the particle-volume measurements or with the particle-wall-deposition correction (see Sect. 4.3.2.1). While these experiments were used for the analysis of chemical composition, no SOA yields or wall-loss slopes are reported. Additionally, experiments U1, U3–4, and U7 report approximate initial seed surface area concentrations. There is no initial measured seed surface area concentration for experiment U8.

Aerosol-phase bulk composition was determined using an in situ high-resolution time-of-flight aerosol mass spectrometer (AMS, Aerodyne Research) in the high-sensitivity V-mode. Data were analyzed with Igor Pro (version 6.37) and the Squirrel (1.57l) and Pika (1.16l) toolkits. Elemental composition was determined following the improved-ambient method from Canagaratna et al. (2015) and Aiken et al. (2008). Absolute uncertainties of O:C and H:C ratios are ±28% and ±13%, respectively (Canagaratna et al., 2015).

Measurements from the AMS can be utilized to determine the mass fraction of organonitrates ($RONO_2$) in the aerosol-phase following the method described by Farmer et al. (2010). Both inorganic and organic nitrates fragment to an m/z of 30 (NO^+) and an m/z of 46 (NO_2^+), but the ratio of these two fragments for organonitrates (including those derived from aromatic hydrocarbons) and for ammonium nitrate is quite different and this difference can be utilized to determine the contribution of organonitrates to the nitrate signal in the AMS (Farmer et al., 2010; Fry et al., 2013; Kiendler-Scharr et al., 2016; Sato et al., 2010). The measured mass ratio of NO/NO_2 (called the NO_x^+ ratio) is used to show the contribution of organonitrates to aerosol mass (see Appendix 4.A.2). Note that fragments of the form $C_xH_yN_z^+$ are sufficiently scarce that they are neglected: the N:C ratio was never more than 0.026 for the experiments considered here.

For experiments N1–3 and U1–6, the chemical composition of particle-phase compounds was further analyzed using offline ultra-high performance liquid chromatography electrospray ionization quadruple time of flight mass spectrometry (UPLC/ESI-Q-ToFMS) (Zhang, Dalleska, et al., 2016). This method is described in Appendix 4.A.1.

4.3 Calculations of SOA Yield

4.3.1 Method

The secondary organic aerosol yield (SOA Y) is given by

$$Y = \frac{\Delta SOA_{meas}}{\Delta BnOH_{meas}} \tag{4.1}$$

where $\Delta BnOH_{meas}$ is the reacted mass of benzyl alcohol; that is, the difference between the initial concentration and the measured concentration at a given time. ΔSOA_{meas} is the difference between the measured and wall-deposition-corrected aerosol mass concentration at a given time and the aerosol concentration prior to the beginning of oxidation. The wall-deposition correction assumes that once a particle deposits on the wall, suspended gas-phase molecules no longer condense onto it; its growth ceases. This corresponds to the technical assumption that $\omega = 0$, where ω is a proportionality factor that describes the degree to which vapor condenses onto particles already deposited on the chamber walls compared to those suspended in the bulk of the chamber: if $\omega = 0$, once a particle deposits on the chamber wall it is lost to the system and no longer acts as a condensation sink; if $\omega = 1$, a particle deposited on the chamber wall acts as a condensation sink identically to that of a suspended particle (Trump et al., 2016; Weitkamp et al., 2007).

The SOA yield is bounded by the assumptions that $\omega = 0$ and $\omega = 1$. The extent of difference between these cases is dependent on characteristics of the chamber (e.g., the rate of particle-wall-deposition) and of the chemical system (e.g., the amount of kinetic vs. equilibrium particle growth that occurs) (Trump et al., 2016). Appendix 4.B describes the calculation of $\Delta SOA_{meas,\omega=1}$ and the corresponding assumptions.

Table 4.1 shows the SOA yields calculated with uncertainties for the $\omega = 0$ and the $\omega = 1$ assumption. The SOA yield calculation with both $\omega = 0$ and $\omega = 1$ is shown for experiment R1 in Fig. 4.1. Since the difference between the SOA yield calculated with $\omega = 1$ and with $\omega = 0$ is dependent on the amount of organic aerosol that deposits onto the chamber walls, experiments with a higher initial aerosol concentration or that simply last for a longer period tend to have a greater disparity between SOA yields calculated with the $\omega = 0$ assumption and those calculated with the $\omega = 1$ assumption. Even so, for all the experiments considered here, the $\omega = 1$ calculated SOA yield is within the uncertainty of the SOA yield found assuming that $\omega = 0$. Furthermore, optimization of chamber parameters indicates that the $\omega = 0$ case is closer to reality than the $\omega = 1$ case (see Table 4.2 and the discussion in Appendix 4.C.4).
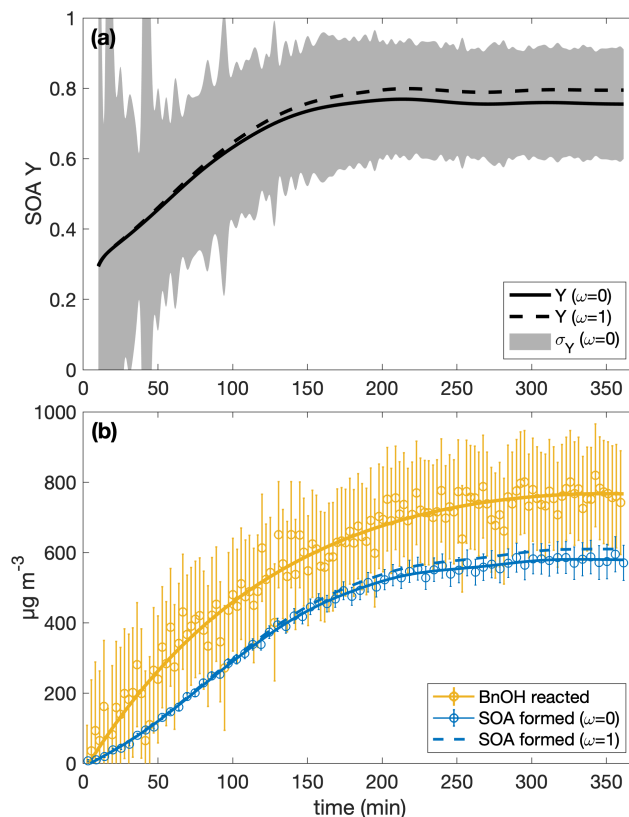
Figure 4.1: (a) The SOA yield for experiment R1 calculated with the assumption that $\omega = 0$ is shown as a solid curve and with $\omega = 1$ as a dashed one. The shaded region is the associated uncertainty for the $\omega = 0$ case. Due to low signal at the beginning, the first 10 min of the experiment are not shown. Panel (b) shows the wall-deposition-corrected mass concentration of SOA formed assuming $\omega = 0$ (blue solid curve fitted to the circles and error bars) and $\omega = 1$ (dashed blue curve). The measured mass concentration of benzyl alcohol is the yellow circles with associated error bars, to which the yellow curve is fit.

Table 4.2: Optimization of parameters. The equivalent saturation mass concentration of the Teflon wall, C_w, has units of μg m^{-3}. The accommodation coefficient of vapor to suspended particles (α_p) and of vapor to deposited particles (α_{pw}) are unitless. For all optimizations, starting conditions were $\alpha_p = 1$, $\alpha_{pw} = 0$, and $C_w = 10^4$. When not optimized, $\alpha_{pw} = 0$, $C_w = 10^4$, and α_p is given in parentheses.

Experiments Used for Optimization	α_p Optimized	α_p and α_{pw} Optimized		α_p, α_{pw}, and C_w Optimized			C_w Optimized			α_p and C_w Optimized	
	α_p	α_p	α_{pw}	α_p	α_{pw}	C_w	C_w ($\alpha_p = 1$)	C_w ($\alpha_p = 10^{-1}$)	C_w ($\alpha_p = 10^{-2}$)	α_p	C_w
N1–3	2.2×10^{-2}	2.2×10^{-2}	6.2×10^{-9}	2.2×10^{-2}	4.0×10^{-8}	1.7×10^4	4.0×10^8	1.2×10^8	6.8×10^2	2.2×10^{-2}	1.9×10^4
N4–6	7.3×10^{-3}	7.3×10^{-3}	4.1×10^{-9}	7.5×10^{-3}	7.1×10^{-9}	1.7×10^4	2.0×10^8	2.8×10^8	2.2×10^7	7.6×10^{-3}	1.9×10^4
R1–4	5.7×10^{-2}	5.7×10^{-2}	3.1×10^{-8}	6.0×10^{-2}	3.2×10^{-8}	1.7×10^4	7.9×10^8	2.9×10^8	1.5×10^2	6.0×10^{-2}	1.8×10^4
S2–4 and R1	1.5×10^{-2}	1.5×10^{-2}	8.4×10^{-9}	1.5×10^{-2}	2.9×10^{-8}	1.7×10^4	8.2×10^7	6.6×10^7	2.3×10^3	1.5×10^{-2}	1.9×10^4
S2–4 and R1–4	2.2×10^{-2}	2.2×10^{-2}	1.3×10^{-8}	2.2×10^{-2}	2.0×10^{-8}	1.7×10^4	6.6×10^7	6.6×10^7	7.5×10^2	2.3×10^{-2}	1.8×10^4

4.3.2 Corrections

The chamber walls have, primarily, two effects on the SOA yield results: particles with organic mass on them may deposit on the chamber walls and not be detected (called particle wall deposition) or low-volatility compounds that, in the atmosphere, would condense onto suspended particles and form secondary organic aerosol mass instead deposit directly onto the chamber walls (called vapor wall deposition).

Since vapor wall deposition can involve loss to the wall of the oxidation products and not just the precursor compound, it is difficult to directly correct for the effect of vapor-wall deposition on the observed SOA yield. This is because, often, as is the case here, not all the oxidation products are fully measured and characterized. Instead, one can minimize its effect by increasing the presence of the suspended aerosol surface area concentration so that the suspended aerosol outcompetes the chamber wall as a condensation sink. To do so, however, increases the effect of particle wall deposition because as there are more particles in the chamber, a greater fraction will generally deposit onto the chamber walls (due to a nonlinear decay) (Charan, Huang, and Seinfeld, 2019).

Noting that one must always account for particle wall deposition, since even a nucleation experiment will produce particles that may deposit on the chamber walls while one is attempting to measure them, we take this approach of correcting for particle wall deposition and operating our experiments in a regime that minimizes the effect of vapor wall deposition.

4.3.2.1 Particle-Wall Deposition

To determine the particle-wall-deposition correction parameters for the 17.9 m^3 chamber, two-parameter fits to the eddy-diffusivity coefficient (k_e) and the mean electric field experienced within the chamber ($\bar{E}$), following the protocol in Charan, Flagan, and Seinfeld (2018), were performed on dry, ammonium sulfate experiments with an assumed density of 1770 kg m^{-3}. For this study, two experiments were carried out for 8 h in the dark with only ammonium sulfate seed present, one was a 6 h experiment under irradiation, and an additional four were 4 h dark experiments with the precursors of a VOC oxidation experiment. All dark experiments were carried out at 25.6°C and that in the presence of light was performed at 28.6°C. Analysis began 30 min after initial mixing and used 15 size bins to improve the counting statistics. All bins were included in analysis.

When a two-parameter minimization on k_e and $\bar{E}$ for each experiment was performed

following the protocol described in Charan, Huang, and Seinfeld (2019), initial guesses of k_e were varied between 0.15 and 5 s^{-1} and of $\bar{E}$ between 0 and 50 V cm^{-1}. Three of the seven experiments gave $\bar{E} < 0.1 \times 10^{-9}$ V cm^{-1}, and the other four gave $\bar{E} = 2.1, 2.3, 3.9$, and 5.1 V cm^{-1}. Note that this is small: over 20 h of solely particle wall deposition and coagulation for an initial surface area concentration of 2.7×10^3 μm^2 cm^{-3} and a lognormal distribution centered around ~125 nm, an $\bar{E} = 2.5$ V cm^{-1} gave a number concentration 86% of that when $\bar{E} = 0$ (Charan, Flagan, and Seinfeld, 2018); a characteristic value for a chamber with charge is ~ 45 V cm^{-1} (McMurry and Rader, 1985). This chamber, unlike many with larger values of $\bar{E}$, is constantly suspended and does not touch the enclosure walls.

When all the experiments were analyzed together, with an initial guess of k_e varying between 0.001 and 10 s^{-1}, the minimization function converged with $k_e = 0.0769$ s^{-1}. Even for those experiments that gave $\bar{E} \neq 0$ when optimized, all fit approximately as well to their one-parameter minimization and to the all-experiment optimized value ($k_e = 0.0769$ s^{-1}) as to their individually optimized values. One-parameter optimization (optimizing only for k_e, while assuming $\bar{E} = 0$) was also performed for each of the 7 experiments. Uncertainty in wall-loss was determined by taking the smallest k_e value found from each of these experiments (0.0004 s^{-1}) as a lower bound and the largest k_e value (0.5 s^{-1}) as an upper bound. The total mass concentration of SOA formed, which was used to calculate the SOA yield, was found from a smoothing spline fit of the particle-wall-deposition-corrected volume concentration ($R^2 \geq 0.994$). Wang, Jorga, et al. (2018) have shown, for a similarly configured chamber to those used here, that neither UV lights, nor flushing of the chamber, nor gas-phase injections had an effect on particle wall deposition.

As additional verification, for three experiments performed under the standard replication conditions for this study, the contents of the chamber were allowed to sit undisturbed for 4 h prior to the lights being turned on. During these 4 h, the wall loss correction was performed using the parameters $k_e = 0.0769$ s^{-1} and $\bar{E} = 0$, for which it was verified that these values gave constant volume concentrations.

Prior to the commencement of oxidation, all experiments were mixed and then allowed to sit undisturbed for ≥ 1 h. During this background-collection period, during which we assume no aerosol growth took place, the wall-deposition-corrected volume concentration was calculated using the k_e and $\bar{E}$ parameters given above. To quantify the degree to which this volume concentration was properly wall-deposition corrected, the slope of a linear fit of the volume concentration as a function of the time

(with a 95% confidence interval) during this background period is reported in Table 4.1. Since experiment S1 was performed in the absence of initial seed, the aerosol volume concentration during the background collection time was 0 and no slope is reported. For all 20 experiments in which a SOA yield is reported (excluding S1), the wall-deposition-corrected volume concentration during the background collection time was relatively constant: the absolute value of the slopes for all experiments was < 0.1 μm^3 cm^3 s^{-1} and the mean was 0.03 μm^3 cm^{-3} s^{-1}.

The initial particle surface area concentration was taken to be the average of the wall-loss corrected values of the seed volume during the background-collection period.

4.3.2.2 Vapor-Wall Deposition

Based on three periods of vapor wall loss prior to experiment S3, each >100 min, the timescale of the loss of benzyl alcohol to the Teflon chamber walls is on the order of days (~2 to 5 days). While benzyl alcohol itself may be lost slowly, benzyl alcohol oxidation products might partition to the wall. The accommodation coefficient of vapor to suspended particles (α_p) was derived to be on the order of 10^{-2} (see Appendix 4.C). This also implies the presence of a seed surface area effect because the slower the gas-particle equilibration, the more likely that the chamber wall is an attractive condensation sink. Indeed, this value of α_p corresponds to competitive kinetic and quasi-equilibrium growth for the parameters of the chamber and predicted oxidation products (see the dimensionless group Ki in Charan, Huang, and Seinfeld, 2019).

To understand the extent to which the chamber wall is competitive with the suspended aerosol as a condensation sink, the initial seed surface area concentration was varied for otherwise identical experimental conditions. Figure 4.2 shows this observed SOA yield, where no vapor-wall-deposition corrections are performed, for a range of initial seed surface area concentrations. Above ~1800 μm^2 cm^{-3}, there appears to be little change in the observed SOA yield; thus, we assume that the effect of vapor wall deposition is minimal.

For each chamber and each chemical system, the initial seed surface area concentration at which the effect of vapor wall deposition is no longer significant is different: this is a function of, among other factors, the particle-vapor equilibration time, the accommodation coefficient of the gas-phase product to the chamber walls, the
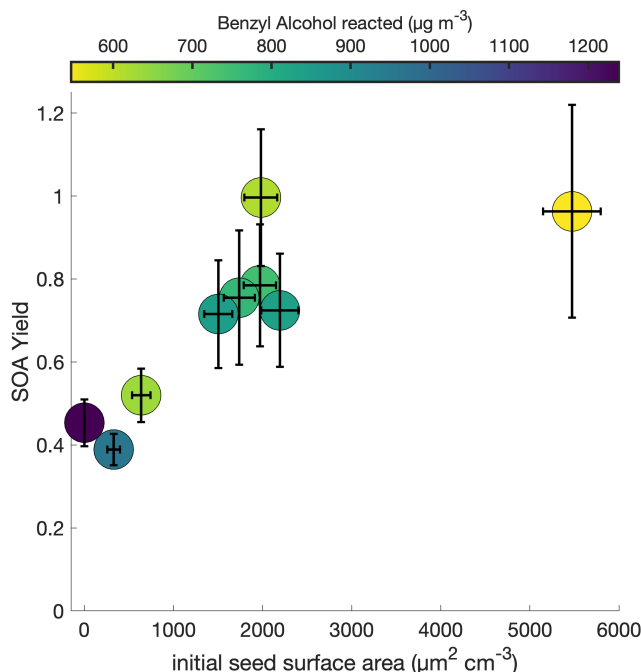
Figure 4.2: Variation in observed benzyl alcohol SOA yield with an initial NO mixing ratio of 80 ppb at 291 K as a function of the amount of benzyl alcohol reacted and the initial aerosol seed surface area. The lack of a difference in the yield over differing seed surface areas above ~1800 μm^2 cm^{-3} indicates that the experiments lie within a regime where the seed surface area does not affect the measured SOA yield.

chamber dimensions, and the initial precursor concentration (Charan, Huang, and Seinfeld, 2019; Zhang, Schwantes, et al., 2015).

In theory, the fact that we can neglect the effects of vapor wall deposition on SOA yield at a temperature of 291 K and an initial NO mixing ratio of ~80 ppb (as is the case for experiments R1–5 and S1–4, which are shown in Fig. 4.2), does not mean that we can neglect the effects for all temperatures and all NO mixing ratios, since different experimental conditions may change the chemistry of the system. However, while the identities and relative ratios of gas-phase products may differ for the different experiments explored in this paper, and hence the propensity to partition into the wall may vary, it is assumed that the products are sufficiently similar that the range at which vapor-wall deposition is considered insignificant remains the same. And, so, we apply the assumption that vapor wall deposition minimally affects the observed SOA yield at initial seed surface area concentrations above ~ 1800 μm^2 cm^{-3} to all experiments in this paper.

4.3.3 Uncertainties in Measured SOA Yields

The SOA yield is defined as the ratio of the mass of aerosol formed to the mass of precursor reacted (see Eq. 4.1). One may overestimate the yield by underestimating the amount of benzyl alcohol reacted or by overestimating the amount of aerosol formed. If the particle-wall-deposition adjustment overcorrects the aerosol formed, it would seem as if a higher yield exists than that in actuality. Table 4.1 shows the SOA yield that would be calculated assuming that no particles were lost to the chamber walls during the experiment: this is simply the difference between the measured aerosol mass at the end of the experiment and that at the beginning, divided by the total reacted benzyl alcohol mass. Except for experiment R3 and L1, which ran for 12 h and 17 h, respectively, the raw particle volumes at the end of the experiments were > 80% of the wall-deposition-corrected volumes. So, even if there are errors in the particle-wall-deposition correction, the SOA yields will still be quite large. For experiment R1, the assumed uncertainty that comes from particle-wall-deposition is $\sim 8\%$. This dominates, for ΔSOA_{meas}, the random and counting error. The total uncertainty in ΔSOA_{meas} for experiment R1 is, including the uncertainty in the aerosol density, the wall-deposition, and the random error, $\sim 9\%$.

Most of the reported uncertainty in the SOA yield comes not from the wall-deposition correction, but from the uncertainty in the benzyl alcohol concentration. For experiment R1, the random error in the benzyl alcohol signal, measured during the background collection period, was 15%. Combined with the uncertainty of the calibration (6%), this was a 16% uncertainty. This same error was applied to the concentration of benzyl alcohol measured at the end of the experiment. Since $\Delta[BnOH]_{meas} = [BnOH]_0 - [BnOH]_{t=end}$, the uncertainty of $\Delta[BnOH]_{meas}$ is 19.5%.

With the 9% and 19.5% uncertainties in ΔSOA_{meas} and $\Delta[BnOH]_{meas}$, respectively, we get a 21% uncertainty in the final calculated SOA yield. Most of this comes from the precursor concentration.

Uncertainty from vapor-wall deposition is not included in the calculated error, but any vapor-wall deposition would only decrease the fraction of organic aerosol observed. That is, the true ΔSOA_{meas} would be larger than the calculated ΔSOA_{meas}. If experiments were not run at a sufficiently large aerosol surface area concentration to neglect the loss of gas-phase products to the chamber walls, the true SOA yield will only be larger than what is reported here.

4.4 SOA Yields

4.4.1 Adsorptive and Absorptive Aerosol Growth

The uptake and growth of aerosol can occur either through adsorption or absorption of oxidation products. Generally, we think of secondary organic aerosol growth as governed by absorption, though adsorption is also possible, especially at the large surface area concentrations used in this study to reduce the effect of vapor-wall deposition. To estimate the relative effects of these two processes, we use the gas-particle partitioning coefficient given by (Pankow, 1994; Pankow, 1987):

$$K_p = \frac{1}{p_L^0} \left[N_s A_{tsp} RT e^{\Delta Q/RT} + \frac{f_{om} RT}{MW_{om} \gamma} \right] \tag{4.2}$$

where the first term comes from adsorption and the second from absorption. The absorbent vapor pressure, p_L^0 is in units of atm. If we assume that the molecular weight of the organic material $MW_{om} = 188 \text{ g mol}^{-1} = 1.88 \times 10^8 \text{ μg mol}^{-1}$, which is the molecular weight of the major low-volatility oxidation product of benzyl alcohol calculated by Wang (2015); the activity coefficient of a compound in the organic phase is $\gamma = 1$; and the temperature is $T = 291$ K (matching that in experiment R1), the absorptive term is $\sim (1.3 \times 10^{-10}) f_{om} \text{ m}^3 \text{ atm μg}^{-1}$, where f_{om} is the mass fraction of absorbing organic in the aerosol phase.

The specific surface area of the particulate matter, A_{tsp}, changes little throughout experiment R1. At the beginning of the experiment, when particles are the smallest, $A_{tsp} \approx 0.14 \text{ cm}^2 \text{ μg}^{-1}$. Using Eq. 60 from Pankow (1987), the surface concentration of sorption sites on an adsorbing surface is $N_{s,om} \approx 4.5 \times 10^{-10} \text{ mol cm}^{-2}$ for the organic phase and $N_{s,amm \ sulf} \approx 6.7 \times 10^{-10} \text{ mol cm}^{-2}$ for ammonium sulfate. Note that the calculation for the organic phase uses $\rho_{om} = 1.4 \text{ g cm}^{-3}$. To get an upper-bound estimate of adsorption, if we take $N_s = N_{s,amm \ sulf}$, the adsorptive term is $\sim (2.2 \times 10^{-12}) e^{1.7 \Delta Q} \text{ m}^3 \text{ atm μg}^{-1}$, where ΔQ is the enthalpy difference between desorption from the particle surface and vaporization of the pure liquid and has units of kcal mol^{-1}.

To determine the relative importance of adsorption and absorption, we need ΔQ and f_{om}. For liquid-like adsorption, $\Delta Q \approx 0$, but for SOA from polycyclic aromatic hydrocarbons rings and organochlorines, $\Delta Q \approx 2$–4 kcal mol^{-1} and $\Delta Q \approx 1$–2 kcal mol^{-1}, respectively (Pankow, 1987; Yamasaki, Kuwata, and Miyamoto, 1982). For experiment R1, f_{om} is 0.1 by 10 min and 0.5 by 1 h. At the end of the experiment, $f_{om} = 0.8$.

Depending on the value of ΔQ, the length into the experiment at which adsorption is insignificant changes. If $\Delta Q \approx 0$, adsorption will be responsible for $< 15\%$ partitioning 10 min into the experiment. If $\Delta Q \lesssim 0.9$ kcal mol^{-1}, adsorption will be responsible for $< 15\%$ partitioning 1 h into the experiment, and if $\Delta Q \lesssim 1.2$ kcal mol^{-1}, adsorption will be responsible for $< 15\%$ partitioning at the end of the experiment. Note that, since prior to the commencement of oxidation, no aerosol growth is observed, the seed aerosol neither adsorbs nor absorbs benzyl alcohol.

4.4.2 Absorptive Particle Partitioning

If absorption dominates gas-particle partitioning, the SOA yield would depend on the amount of organic material in the aerosol phase (ΔSOA_{meas}, which varies with f_{om}) if equilibrium growth occurs, as is shown in Fig. 4.3 (Pankow, 1994; Odum et al., 1996). Traditionally, this partitioning is given by

$$Y = \Delta SOA_{meas} \sum_{i=1}^{n} \left(\frac{\alpha_i K_{om,i}}{1 + K_{om,i} \Delta SOA_{meas}} \right) \tag{4.3}$$

where a one-product model has $n = 1$ and a two-product model has $n = 2$ (Pankow, 1994; Odum et al., 1996; Ng et al., 2007). The stoichiometric fraction of product i in mass units is α_i. $K_{om,i}$ is the absorptive partitioning coefficient for the organic phase for species i, which is $\frac{K_{p,i}}{f_{om}}$ from Eq. 4.2 (Odum et al., 1996).

The two-product model does not improve from the one-product model (dotted curve in Fig. 4.3a), but only creates a very large non-volatile compound ($K_{om} >> 1$) that is formed in very small quantities ($\alpha << 1$) and the other compound nearly matches the compound found in the one-product optimization. The one-product optimization gives $\alpha = 0.97$ and $K_{om} = 0.009$ if all points are equally weighted. If we only include the end points, this gives $\alpha = 1.05$ and $K_{om} = 0.005$.

At $\gtrsim 500$ µg m^{-3}, the SOA yield flattens out. This indicates that, above this ΔSOA_{meas}, the partitioning coefficients for the oxidative products are sufficiently large (that is, the products are sufficiently non-volatile), that Y approaches α, the gas-phase stoichiometric fraction in mass units for the oxidation products (Ng et al., 2007).

4.4.3 Time Dependence

While, usually, the SOA yield is reported as a single number at the end of an experiment, it can also be understood as a function of time since multiple generations of oxidation products usually exist (Cappa et al., 2013). For example, in the α-
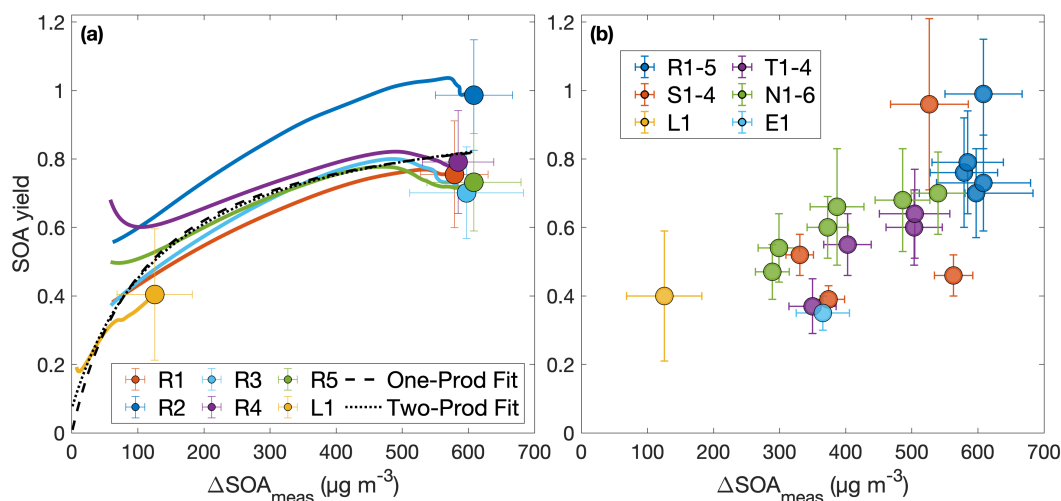
Figure 4.3: Secondary organic aerosol yields as a function of organic aerosol formed (a) throughout experiments performed under similar initial conditions (R1–5 and L1) and (b) at the end of oxidation for experiments with quantitative SOA yields. In panel (a), the first 30 min of oxidation are removed due to low signal and large uncertainties in SOA yield. Note that the experiment run at a lower oxidation rate (L1) nearly matches the outcomes of those run under otherwise similar conditions (R1–5), though the discrepancy may be due to the slightler lower temperature of experiment L1 (286 K compared to 291 K). The measured SOA yield appears to depend on the organic aerosol mass concentration, ΔSOA_{meas}, which indicates that particle partitioning is important for SOA yield determination. Panel (a) also includes a one-product and two-product fit to the data.

pinene system, the SOA yield has been shown to depend on the total hydroxyl radical exposure (Donahue et al., 2012; Wang, Kostenidou, et al., 2018). Figure 4.4 shows, for each experiment, the terminal SOA yield and the bands indicating at which times each of the experiments lie within 10%, 5%, and 1% of the final reported yield. The most atmospherically representative value of α is that to which the experiments converge. For almost all the experiments, the yields appear to have converged sufficiently to justify the reporting of the final yield, though the benzyl alcohol concentration may not yet have all reacted (see Table 4.1); as more reacts, more aerosol is formed but the SOA yield levels out. Experiments R3 and R5, which were run for considerably longer than other experiments, show that the final SOA yield changed little from earlier in oxidation, when the other experiments were terminated.

Note that for experiment L1, also run for considerably longer than the other experiments, the light strength was ~8% of that in all the other experiments. At this lower oxidation rate, the SOA yield takes much longer to converge but does
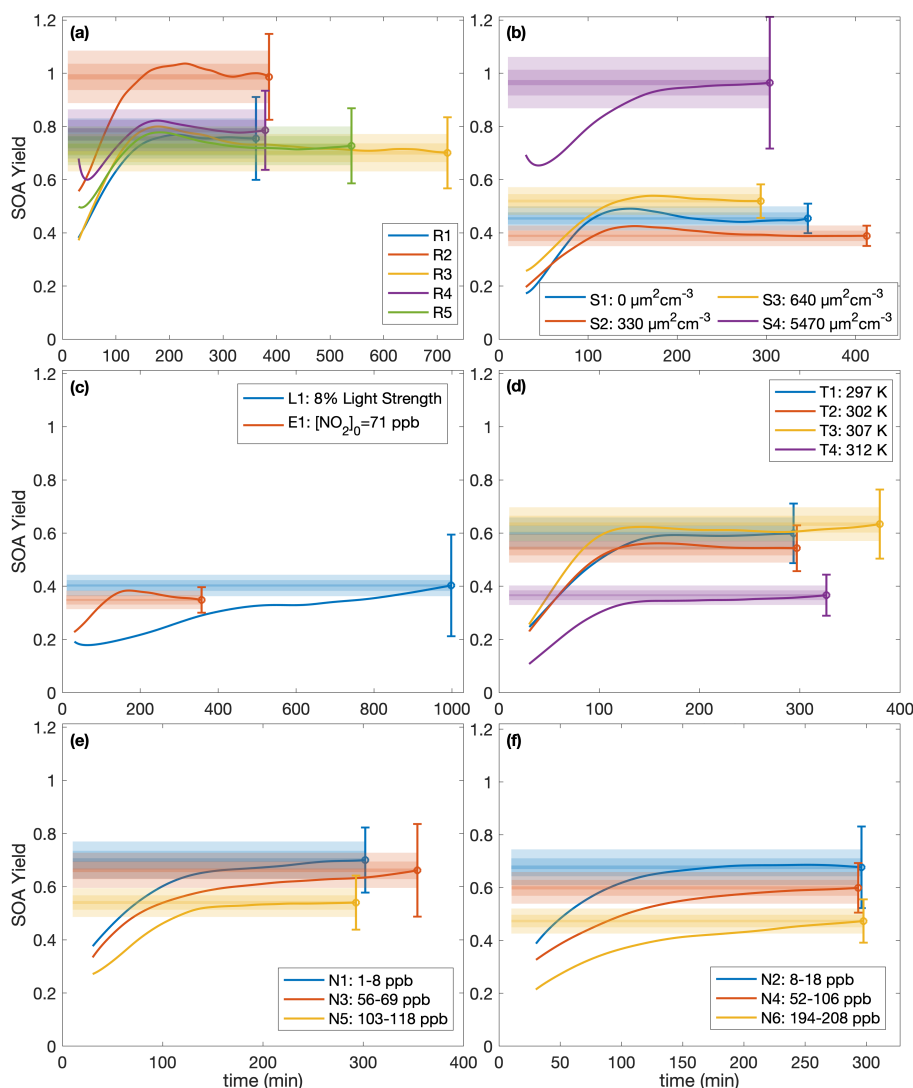
Figure 4.4: SOA yield calculated assuming $\omega = 0$ as a function of time for (a) experiments run under approximately identical conditions, (b) different initial surface area experiments, (c) the low light strength experiment (L1) and the initial NO_2 experiment (E1), (d) different temperature experiments, and (e–f) variable constant NO mixing ratio experiments. The measured SOA yields are the solid line and the reported end yield is the circle with the reported error bars. The lightest shaded region is $\pm 10\%$ of the reported end yield, the medium-shared region is $\pm 5\%$, and the darkest shaded region is $\pm 1\%$. The first 30 min of oxidation are omitted due to low signal and large noise at the beginnings of the experiments.

appear to be a function of ΔSOA_{meas} (Fig. 4.3). This shows that the convergence time depends on the rate of oxidation. Table 4.1 includes the amount of benzyl alcohol that reacted by the end of the experiment and a first-order exponential fit to the decay ($k_{BnOH+OH}[OH]$): for all except experiment L1, the $k_{BnOH+OH}[OH]$ is similar, indicating a similar decay. Note that since the exact [OH] is not calculated, $k_{BnOH+OH}[OH]$ is reported assuming that [OH] is constant throughout the experiment.

4.4.4 Temperature Dependence

Figure 4.5 shows the SOA yield of benzyl alcohol over a range of temperatures, all corresponding to approximately the same initial surface area range (1500–2800 μm^2 cm^{-3}) and the same initial NO mixing ratio of ∼ 80 ppb (see R1–5 and T1–4 in Table 4.1). In general, a lower yield of benzyl alcohol exists at higher temperatures; this is expected due to the decreased volatility of oxidation products at lower temperatures and to the increased rapidity of second-generation reactions, which may potentially form high volatility fragments before the lower volatility first-generation products have time to partition into the particle phase.

At the lowest temperature measured, where one would expect the greatest seed surface area effect (that is, the most competition between the wall and suspended aerosol condensation sinks), we have already determined that we are outside the range of the seed surface area effect (Fig. 4.2). So, one would not expect that the difference in SOA yield is related to competition with the chamber wall.

A higher SOA yield at lower temperatures is also supported by Fig. 4.6, which shows how the chemical makeup of the aerosol is different for aerosol formed at different temperatures: the O:C ratio is higher and the H:C ratio is lower on aerosol formed at higher temperatures, meaning that more volatile compounds that might condense at lower temperatures (and have a smaller O:C ratio and a lower H:C ratio) do not condense at the higher temperature (panels a and c). Though the difference is slight, there is a trend for a larger NO_x^+ ratio (panel b) and, correspondingly, a larger mass fraction of organonitrates at higher temperatures. The former indicates that the organonitrates may be less volatile than other nitrogen-containing compounds that may condense into the aerosol phase (including, potentially, inorganic ammonium nitrate). The latter suggests that the gas-phase branching may be different. It may be that fewer organonitrates are formed at lower temperatures.

If Eq. 4.3 governs the SOA yield curve, then one would expect the curve to asymp-
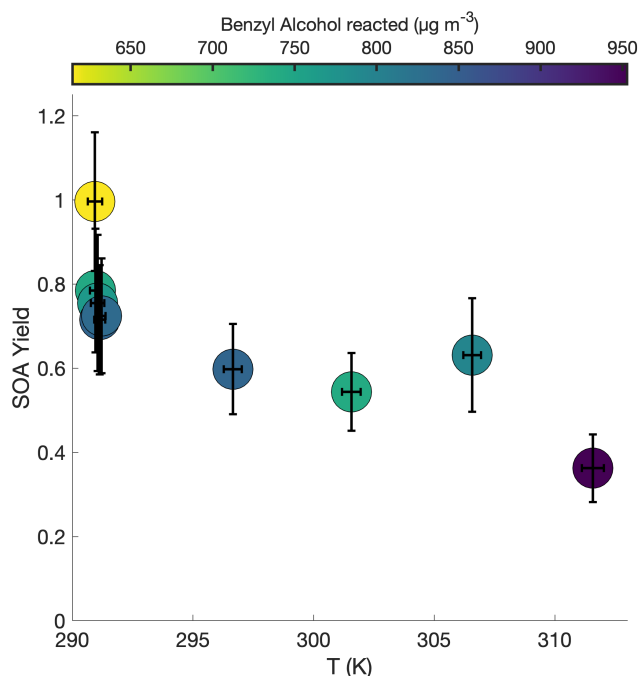
Figure 4.5: Variation in SOA yield over several hours of benzyl alcohol oxidation as a function of temperature with an initial NO mixing ratio of 72 to 81 ppb as a function of the amount of benzyl alcohol reacted for experiments R1–3 and T1–4. The color is proportional to the amount of benzyl alcohol that has reacted at the end of the experiment. Experiments began with between 78 and 102 ppb of benzyl alcohol and initial seed surface area concentrations of 1800 to 2900 μm^2 cm^{-3}. Error bars are given for the yields at the end of each experiment (experiment lengths are given in Table 4.1).

totically approach α as ΔSOA_{meas} increases. The partitioning coefficient K_{om} is explicitly temperature dependent, but α is temperature-dependent only insofar as the oxidation products preferred for formation change with temperature. In Fig. 4.7, the flattening out of the SOA yield curves indicates that it is α (and not just K_{om}) that changes with temperature. This points to a change in chemistry accounting for the difference in SOA yields at different temperatures.

This difference in chemistry accounting for the difference observed in the SOA yield is also supported by observations in the gas phase. The gas-phase concentration of hydroxybenzyl alcohol (HOBnOH) has a molar mass of 124 g mol^{-1} and is detected at M+19, corresponding to the addition of F^- (Schwantes, Schilling, et al., 2017). This signal normalized to the reactant ion signal by the initial benzyl alcohol concentration (expressed in signal normalized to reactant ion signal) for each of the experiments described here is given in Fig. 4.8. Note that this is, essentially, the HOBnOH concentration divided by the initial benzyl alcohol concentration. The
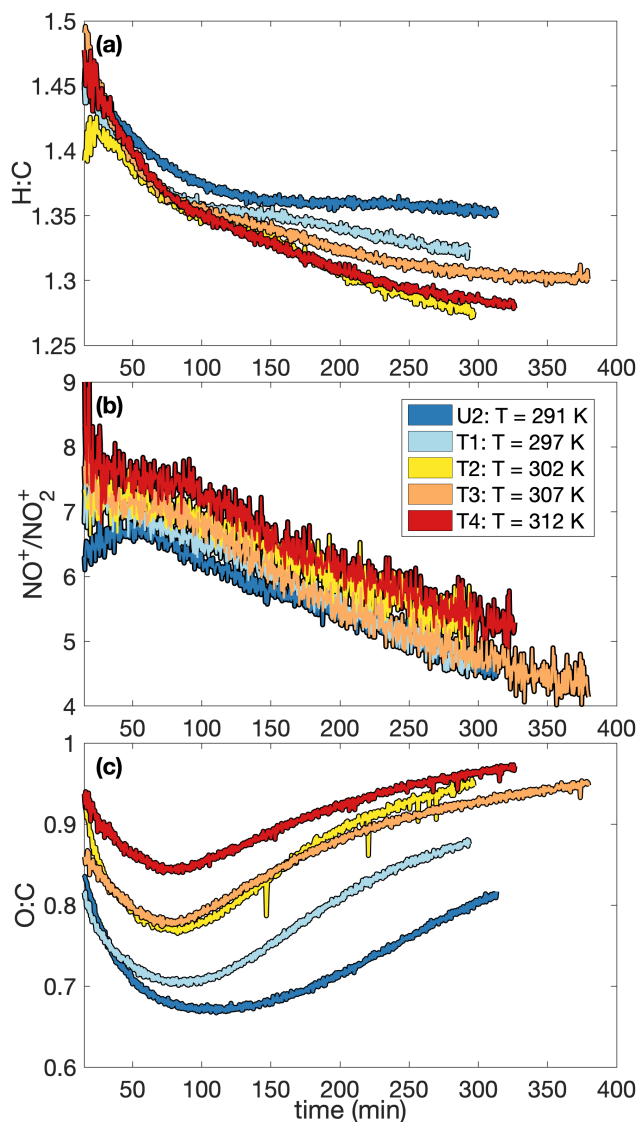
Figure 4.6: Variation in (a) the hydrogen to carbon atomic ratio, (b) the NO$_x^+$ ratio, and (c) the oxygen to carbon atomic ratio indicate that the difference in SOA yield observed at different temperatures might be a result of chemical differences in the aerosol formed. At higher temperatures, O:C ratios are larger and H:C ratios tend to be smaller. There is also a slight increase in the NO$_x^+$ ratio with temperature. Absolute uncertainties are 13% and 28% for the H:C and O:C ratios, respectively. Since the ratios are relevant only when there is a sufficient amount of aerosol present, the first 15 min after oxidation are not shown. A SOA yield is not calculated for experiment U2 due to uncertainties in the rate of particle-wall deposition, but that should not affect the chemical composition of the aerosol.
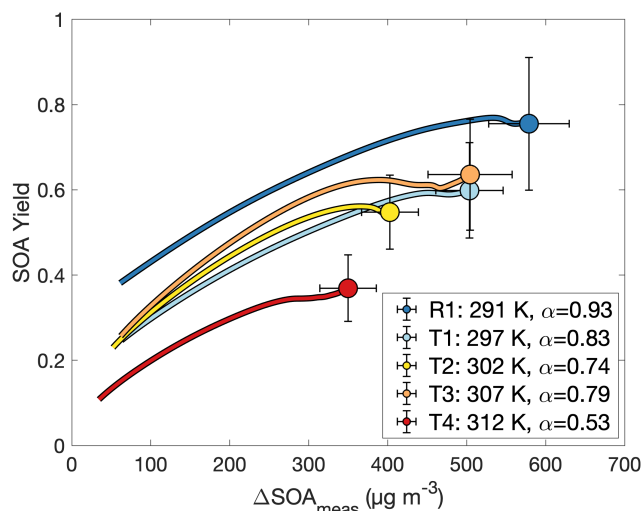
Figure 4.7: Secondary organic aerosol yields as a function of organic aerosol formed for experiments R1 and T1–T4, all run at different temperatures and otherwise similar initial conditions. The value of α is from a two-parameter fit to Eq. 4.3 (K_{om} is not shown). Data are shown only after 30 min into the experiment to minimize the error from noise at the beginning of oxidation.

temporal evolution of HOBnOH for nearly identical experiments is fairly reproducible, as shown in panel a. The formation of HOBnOH or the rate at which it reacts away seems to increase slightly at higher temperatures (Fig. 4.8d), which also indicates that it is a change in chemical composition that accounts for changes in the SOA yield.

4.4.5 Nitric Oxide Mixing Ratio Dependence

To probe the different chemical pathways that form, the SOA yield dependence on variable NO concentrations was investigated (Fig. 4.9). NO mixing ratios were maintained throughout experiments N1–6 and U6, leading to an increase in the total NO_x in the system. NO_x increased by ~60 ppb for experiment N1 and ~100–200 ppb for experiments N2–6 and U6. Generally, the SOA yield seems to decrease with increased NO concentration.

As shown in Fig. 4.10c, there are also larger O:C ratios after ~2 h of oxidation for the lower NO mixing ratios (N1, N2, and N4). Note that experiment N4 appears to behave more similarly to N1–2 than to N5–6 and U6; the control on the NO mixing ratio for N4 was much less successful than for the other constant NO experiments (see the error bars in Fig. 4.9). While the [NO] throughout experiment N4 was, on average, 74 ppb, it was only 62 ppb on average during the first 3 h of oxidation
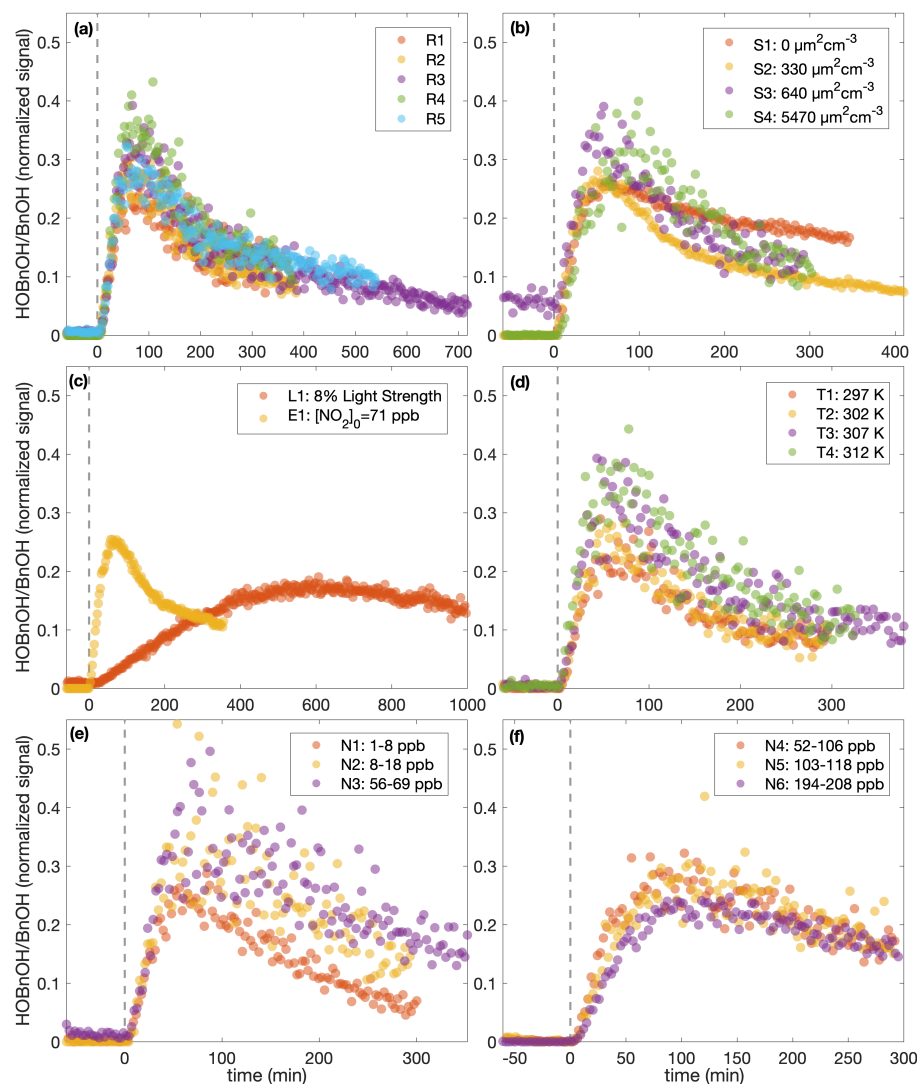
Figure 4.8: The normalized hydroxybenzyl alcohol (HOBnOH) signal divided by the initial normalized benzyl alcohol signal (as calculated during the background collection period) for (a) similar experiments, R1–5, (b) different initial surface are experiments, S1–4, (c) the low light strength experiment, L1, and the initial NO_2 experiment, E1, (d) different temperature experiments, T1–4, (e) low constant NO mixing ratio experiments, N1–3, and (f) high constant NO mixing ratio experiments, N4–6. The horizontal axis is the time since the beginning of oxidation. For all except experiment L1, the light strength was identical. Note that the random error in the initial benzyl alcohol mixing ratio is on the order of 10%.
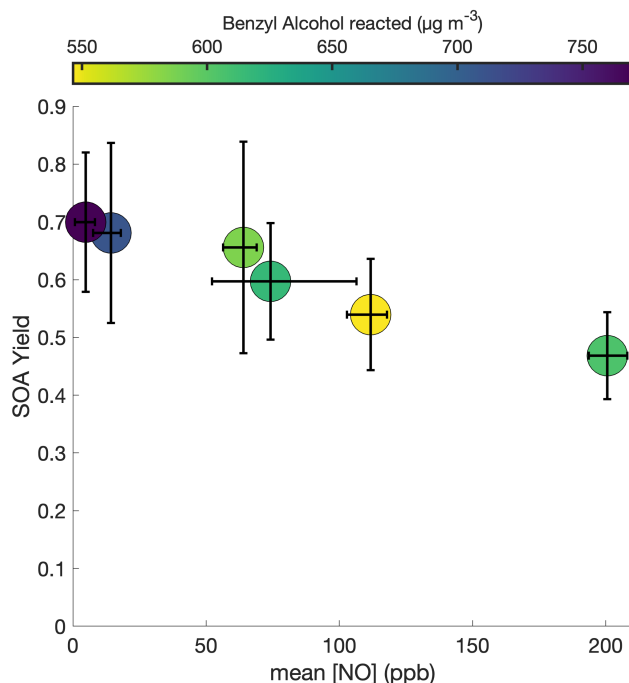
Figure 4.9: SOA yield under different constant NO conditions for experiments N1–6. To maintain the desired NO mixing ratio, NO was injected throughout these experiments at varying rates. All experiments were performed at 291 K, with initial benzyl alcohol mixing ratios between 70 and 82 ppb, and with initial seed surface area concentrations of 1800 to 2900 μm^2 cm^{-3}. The x-axis error bars show the full range of NO concentrations experienced throughout the experiment.

(experiment N3 had an average [NO] of 62 ppb during the first 3 h of oxidation).

Figure 4.8e shows a difference in the gas-phase chemistry at different NO mixing ratios for the lower constant NO experiments (N1–3), but there appears to be little difference in the HOBnOH concentration for the higher constant NO experiments (Fig. 4.8f). This also matches the observed change in O:C ratios (indicating a change in chemical composition) between experiments N1, N2, and N3 (but not between N5, U6, and N6).

This change in chemical composition could be in the prevalence of organonitrates. It appears that at the beginning of each experiment, the first secondary organic aerosol formed comprised a significant portion of organonitrates (as much >20% by mass), as shown in Fig. 4.A.1. While the mass fraction of organonitrates is not reported for the experiments shown in Figs. 4.6 and 4.10 (due to calibration issues), the NO_x^+ ratio trend is the same as that for the experiments shown in Fig. 4.A.1, where the mass fraction can be reported. Note that one pathway to form organonitrates is by reaction with the nitrate radical; since all our analysis from
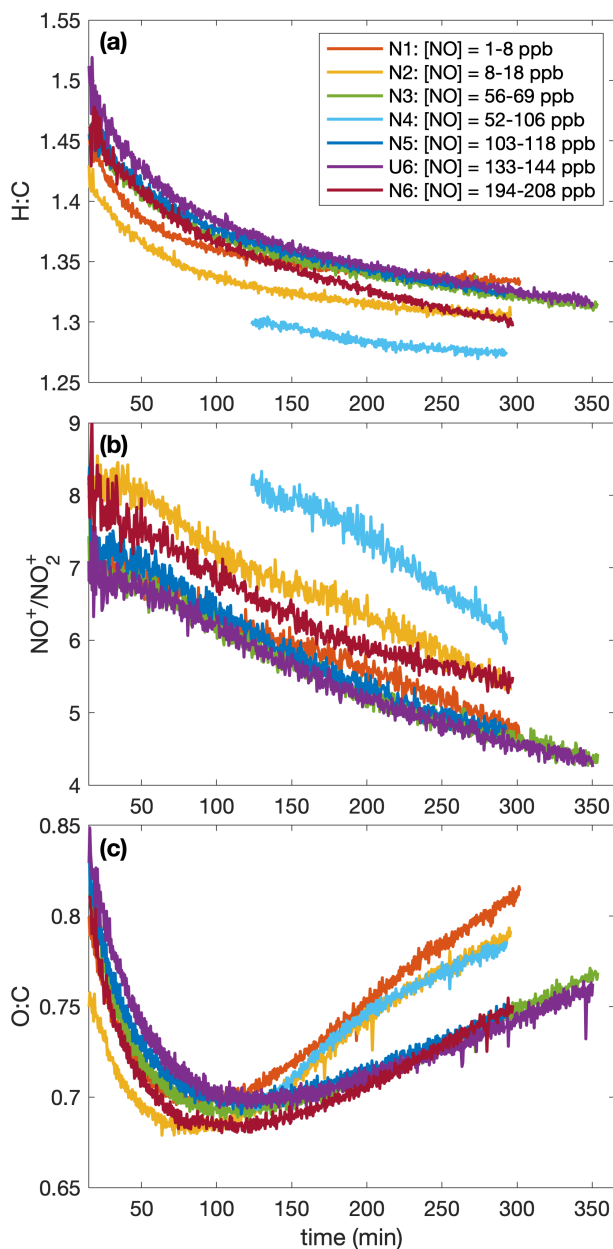
Figure 4.10: Variation in the (a) hydrogen to carbon atomic ratio, the (b) NO to NO$_2$ signal mass ratio, and the (c) oxygen to carbon atomic ratio indicate that the difference in SOA yield observed at different NO mixing ratios is a result of chemical differences in the aerosol formed. The lower NO experiments have a higher O:C ratio later in the experiment than the high NO ones; no trend is obvious in H:C ratios. Absolute uncertainties are 13% and 28% for the H:C and O:C ratios, respectively. Since the ratios are relevant only when there is a sufficient amount of aerosol present, the first 15 min after oxidation are not shown. Data were collected only after ~2 h of oxidation for experiment N4. A SOA yield is not calculated for experiment U6 due to uncertainties in the rate of particle-wall deposition, but that should not affect the chemical composition of the aerosol.

the AMS is of experiments with the ultraviolet lights on, one does not expect a significant concentration of nitrate radicals (Seinfeld and Pandis, 2016). Instead, we expect the organonitrates to have been formed by a $RO_2 \cdot +NO$ reaction; this reaction has a high gas-phase yield for organonitrates for large compounds (Arey et al., 2001; Rollins et al., 2010). Nitroaromatics could also form from the addition of NO_2 to a radical intermediate, as has been suggested as the formation mechanism for nitrocatechols from laboratory studies of *m*-cresol (Iinuma, Böge, and Herrmann, 2010).

Indeed, UPLC analysis found a high prevalence of RNO_2 compounds (see Table 4.A.1), which likely will not lead to the same NO_x^+ ratios as organonitrates and might contribute NO_2^+ fragments that could lower the NO_x^+ ratio. For all experiments with filters collected (N1–3 and U1–6), nearly all compounds detected with UPLC analysis were nitroaromatics. This indicates that the low-volatility products that condense into the aerosol phase retain their aromatic rings. Some of the ring-retaining compounds have C_7 structures, as does benzyl alcohol. However, several of the compounds detected are C_6 structures, indicating the possible loss of the methanol group. In particular, UPLC analysis showed a particularly high concentration of nitrocatechol in the aerosol. The atomic ratios of oxygen to carbon atoms (O:C) are quite large: between 0.6 and 1.0, which matches that of very oxygenated rings (Fig. 4.C.1), but could also match nitrocatechol (O:C of 0.67).

As oxidation continued, more non-nitrogenated organic compounds condensed into the particle phase decreasing the mass concentration of organonitrates. Simultaneously, the NO_x^+ ratio decreased, which could have been caused by nitric acid, formed from $OH + NO_2$, partitioning into the aerosol phase and forming nitrate ions. Partitioning of HNO_3 into secondary organic aerosol has been observed by Ranney and Ziemann (2016). Another possibility is that other compounds, such as organonitrites, might produce NO_2^+ fragments that lower the NO_x^+ ratio throughout the experiment.

It is possible, however, that there are non-ring retaining compounds which condense onto SOA that are simply not detectable by the UPLC. Additionally, the prevalence of nitroaromatics may be a result of the UPLC analysis method that is particularly sensitive to nitroaromatics: the detection of aerosol phase compounds via the UPLC/MS method is limited to detecting compounds that are water soluble and lie within the detection limits of the instrument. Though filters were stored at low temperatures, on-filter chemistry or hydrolysis in the aqueous phase could occur.

This could alter the molecular weight of the original compounds collected in the particle phase (Zhang, Dalleska, et al., 2016).

Nevertheless, the presence of many nitrogen-containing compounds in the particle phase is clear. This is supported by other studies: nitroaromatic hydrocarbons have been observed from daytime oxidation, sourced from anthropogenic sources, and attributed to the particle phase (Ikemori, Nakayama, and Hasegawa, 2019). These compounds have been observed in toluene chamber oxidation studies run at constant 15–20 ppb NO_x mixing ratios, for which benzyl alcohol was one of the measured oxidation products (Hamilton et al., 2005).

Perhaps at higher NO concentrations there are more nitroaromatics, and these compounds are more volatile than the nitrogen-free oxidation products (such as the very oxygenated rings). Though the differences in H:C and O:C ratios are slight, the larger O:C ratios—corresponding to the very oxygenated rings—that are seen at lower NO concentrations support the theory that the compounds formed differ (see Fig. 4.10).

Experiment E1, which is similar to experiments R1–5 except that, prior to the beginning of oxidation, it begins with 71.0±0.8 ppb of NO_2 and no NO, shows a much lower SOA yield than that from experiments R1–5. This suggests that it is the NO that is the relevant reactant that causes initially high SOA formation. This is supported by the significant mass fraction of organonitrates at the beginning of the experiments; organonitrates are formed by $RO_2 \cdot$ reaction with NO.

4.4.6 SOA Bulk Properties

Throughout all the experiments, the O:C ratio also first decreases and then increases. If particle growth is kinetically controlled (supported by a modeled $\alpha_p \sim 10^{-2}$, see Appendix 4.C), the change in O:C ratio throughout the experiment might simply be a result of the greater abundance of higher volatility oxidation products at the beginning of the experiment. Only the lowest volatility (which are, presumably, compounds with the highest O:C ratios) condense initially, but as higher volatility compounds build up, they may eventually partition into the aerosol phase, decreasing the O:C ratio. As lower volatility second- and third-generation compounds are formed, these might then increase the O:C ratio observed. There may also be particle-phase chemical reactions, such as oligimerization (Gao et al., 2004), that lead to the change in O:C ratio throughout the experiment. Or, the observed change could result from a change in the nitrogen-containing compounds in the aerosol-

phase. Note that, when there is a large contribution of organonitrates to the aerosol, the O:C ratio will be an underestimate (Aiken et al., 2008).

4.5   Conclusion

The secondary organic aerosol yields of benzyl alcohol determined in this study range from 0.35 to 0.99. McDonald et al. (2018), who found that volatile chemical products might contribute very significantly to SOA formation in cities like Los Angeles, estimated a SOA yield of 0.090 ± 0.023 for benzyl alcohol. Even in its upper limit, this is less than a third of the SOA yields found in this study. While benzyl alcohol is one of a number of volatile chemical products in the atmosphere, estimates of its atmospheric SOA level based on accounting studies lie significantly below those predicted by experimental chamber studies such as that presented here.

The one-product absorptive partitioning model predicted a mass-based stoichiometric coefficient of $\alpha \approx 0.97$ for oxidation products that partitioned into the aerosol phase. If we assume that these oxidation products can be described by very oxygenated rings with a molecular weight of 188 g mol^{-1}, then this corresponds to a mole-based branching ratio of 0.56. This exceeds modestly the value of 0.41 calculated by Wang (2015) for the formation of very oxygenated rings from benzyl alcohol oxidation (see Fig. 4.C.1 and Appendix 4.C.2). While the SOA yields calculated here appear high, they are not far from the those predicted in the gas-phase for the least volatile oxidation products.

A molecular weight of 188 g mol^{-1} for benzyl alcohol oxidation products also appears to be reasonable: these products would have an Oxygen-to-Carbon atom ratio of 0.86 (see Table 4.C.1), which is close to the ratios we see in Figs. 4.6 and 4.10 of as much as 0.95 and 0.83, respectively.

When extrapolating SOA yields to the atmosphere, one should note that all these experiments were conducted at < 9% relative humidity, which is far below the deliquescence point. Additionally, all experiments were conducted in the presence of NO$_x$. Care should be taken when extrapolating these conditions to humid and low-NO$_x$ environments.

The benzyl alcohol mixing ratios used in this study (>130 ppb) exceed substantially those in the atmosphere. Especially since we have suggested that, at least initially, SOA growth may proceed in a kinetically controlled (or mass-transfer-limited) regime, this could be a problem for extrapolating these results to the behavior of benzyl alcohol in the atmosphere. However, the long reaction time and
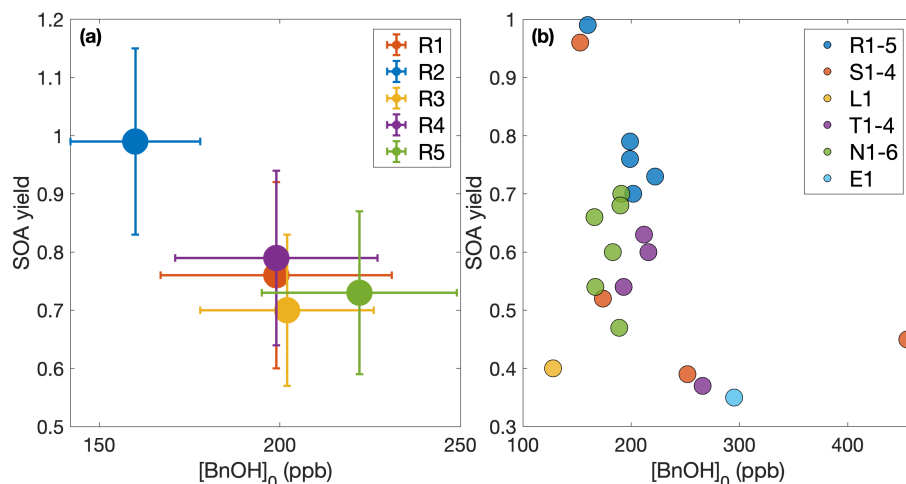
Figure 4.11: Effect of benzyl alcohol concentration on SOA yield. (a) Experiments R1–5, which are all run under approximately the same conditions, with uncertainties. (b) All the experiments where a quantitative SOA yield is calculated. In both panels, we assume that ω=0. No trend is discernible in either panel.

the asymptotic nature of the SOA yields (Figs. 4.4 and 4.3a) suggests that the SOA yield has reached equilibrium and would be the same regardless of the precursor concentration. Furthermore, Figs. 4.2, 4.5, and 4.9 all show the mass of benzyl alcohol reacted at the end of an experiment as a function of SOA yield and the relevant other variable (initial seed surface area concentration, temperatures, constant NO mixing ratio, respectively). In none of these figures does the amount of benzyl alcohol correlate to observed SOA yield.

This is seen more clearly in Fig. 4.11, where panel a shows the set of experiments carried out under approximately the same initial conditions and panel b shows all the experiments with a calculated SOA yield given in Table 4.1. Even for experiments R1–5, designed to be nearly identical, there are some differences in initial benzyl alcohol mixing ratios (panel a). But, these differences do not lead to a discernible trend in the observed SOA yield (in panel a nor panel b); if anything, there appears to be an increase in SOA yield as the initial benzyl alcohol ratio decreases and, if this trend were applied to extrapolation to the atmosphere, we would only expect to see larger SOA yields in the atmosphere than those reported here.

As the SOA formed from benzyl alcohol has a NO mixing ratio dependence, a temperature dependence, and exhibits vapor-wall-deposition effects, it seems likely that other oxygenated compounds emitted from volatile chemical products will have similar behavior.

APPENDIX

4.A   Organonitrates in the Aerosol Phase
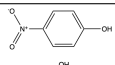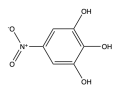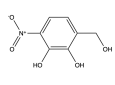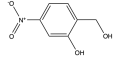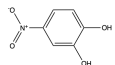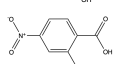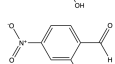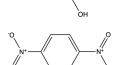
4.A.1   Offline Liquid Chromatography Analysis

Many nitroaromatics were observed in the aerosol phase using an offline ultra-high performance liquid chromatography electrospray ionization quadruple time of flight mass spectrometry (UPLC/ESI-Q-ToFMS). Post-oxidation samples were taken using 47 mm Pall Teflon filters, which were collected for ≥ 2 hours at 6.5 Lpm using an upstream activated carbon denuder. Additional Teflon filters were collected during photooxidation at 2 Lpm. This experimental set up is described by Kenseth et al. (2018).

The SOA collected was extracted by placing each filter sample into 6 mL of milliQ water and agitating the samples on an orbital shaker for 1 h. In an effort to prevent on-filter chemistry from occurring, samples were stored at -14°C after initial collection and before extraction. Analysis using UPLC-MS was carried out in negative mode (where the parent molecule is observed at M-H) which is sensitive to the nitroaromatics formed in the aerosol-phase. The 12 min eluent program for UPLC-MS and MS/MS fragmentation analysis required 4 µL of sample with gradient eluents between a 0.1% formic acid/99.9% water solution and a 100% acetonitrile solution. The total flow rate was 0.3 mLpm, and masses were scanned from m/z = 40 to 1000. The method was similar to that in Kenseth et al. (2018). MassLynx software was used to analyze the resulting spectra, which calculates possible chemical formulas based on masses quantified during analysis. Mass assignments were limited to carbon-, oxygen-, and nitrogen-containing formulas as these were the only chemically viable formulas for benzyl alcohol oxidation chemistry. The structures assigned to chemical formulas from MassLynx analysis were based on structures that corresponded to expected oxidation products and were confirmed based on MS/MS fragmentation analysis. Isomeric analysis was not conducted for these compounds, thus structures in Table 4.A.1 represent just one possible isomer. Several experiments with similar reaction conditions (U1–4; see Table 4.1) were analyzed to probe reproducibility of this technique; these experiments showed consistent results.

Other organic compounds may be present in the SOA collected that is insoluble in the extractant solvent, not able to elute from the chromatographic column, or not detectable in negative ion mode (Surratt et al., 2008). Additionally, the UPLC-MS exhibits different sensitivities to compounds depending on the polarizability

Table 4.A.1: Peak assignment for UPLC/ESI-Q-ToFMS analysis.

Retention Time (RT)	Mass	Error (mDa)	Molecular Formula	Compound
3.484, 5.384	138.0147	-3.9, -4.4	$C_6H_5NO_3$	
3.857	137.0195	-4.4	$C_7H_6O_3$	
3.956, 4.485, 4.653	170.0047/2/5	-4.2, -4.7, -4.4	$C_6H_5NO_5$	
4.165, 4.180	184.0199/7	-4.7/-5.0	$C_7H_7NO_5$	
4.279	148.0352	–	unassigned	
4.348	121.0245	-4.5	$C_7H_6O_2$	
4.561	168.0250	-4.7	$C_7H_7NO_4$	
4.759	154.0096	-4.4	$C_6H_5NO_4$	
4.820, 5.079, 5.346	182.0047	-3.9	$C_7H_5NO_5$	
5.673	166.0097	-4.3	$C_7H_5NO_4$	
5.719	198.9991	-4.2	$C_6H_4N_2O_6$	

of the compound as well as its ability to ionize. It is likely that the UPLC-MS is quite sensitive to the nitroaromatics reported in this work as compared to other compounds.

The prevalence of nitroaromatics in the constant NO concentration experiments is discussed in Sect. 4.4.5.

4.A.2 NO_x^+ Ratio

The measured mass ratio of NO/NO_2 (called the NO_x^+ ratio) is calibrated for ammonium nitrate for experiments R4 and U7–8 (3.20±0.04) and is assumed for organonitrates (7.2±1.1). The organonitrates ratio was calculated using the ammonium nitrate ratio and the correlation derived by Fry et al. (2013). From this NO_x^+ ratio, the time-resolved ratio of the fraction of the nitrate signal that comes from organonitrates for each experiment (x_{ON}) can be obtained using Eq. 1 in Farmer et al. (2010). With the mass concentration of nitrates (m_{NO_3}) and the mass concentration determined to be organics (m_{Org}), the time-resolved organonitrate mass fraction of

the aerosol is $\frac{x_{ON}*m_{NO_3}}{x_{ON}*m_{NO_3}+m_{Org}}$. This is plotted in Fig. 4.A.1.
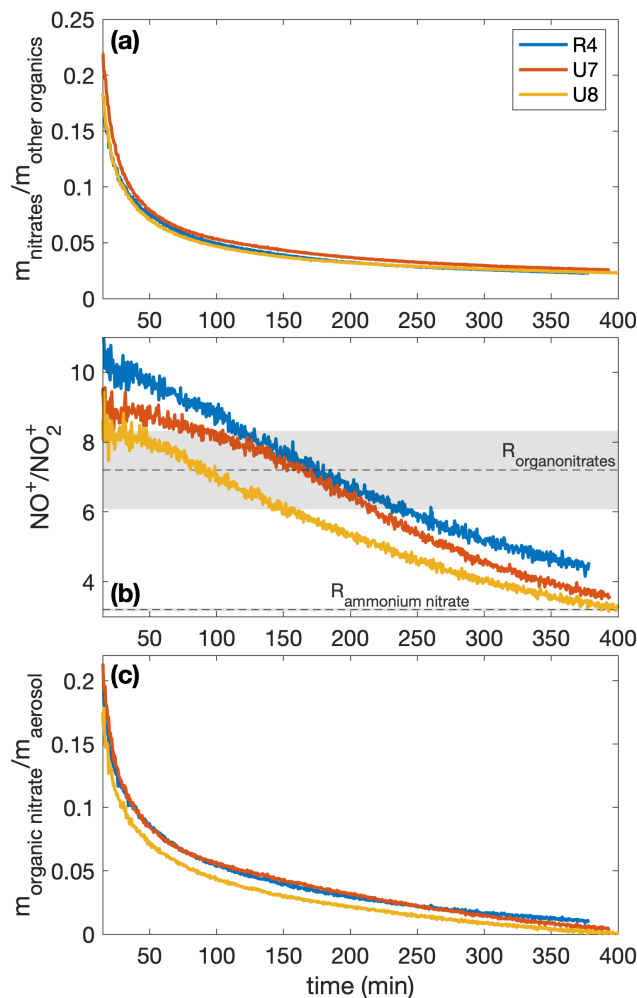
Figure 4.A.1: The mass ratios of (a) the nitrates to organics without nitrogen, (b) the NO^+ to the NO_2^+ signal from the AMS, and (c) the organonitrate to total organic aerosol mass for experiments R4, U7, and U8. All experiments were performed under similar initial conditions (291 K, $[NO]_0$ =71–77 ppb). Since the ratios are relevant only when there is a sufficient amount of aerosol present, the first 15 min after oxidation are not shown. In panel (b), the assumed organonitrate and ammonium nitrate NO to NO_2 ratios are shown as dashed lines with the uncertainty as the corresponding shaded region.

4.B Calculation of $\Delta SOA_{meas,\omega=1}$

To estimate the upper bound ($\omega = 1$) of the yield, we assumed that only particles that deposited after the onset of oxidation would take up vapor. That is, inorganic seed deposited during the background collection period of each experiment is not considered.

While different-sized particles both deposit to the wall and grow due to condensation at different rates, to simplify the calculation of the SOA yield upper bound, the volume-weighted mean diameter of the suspended size distribution was determined for each time point such that $D_{p,av,t} = \left(\frac{1}{N_{total,t}} \sum_{i=1}^{nbins} \left(D_{p,i}^3 N_{i,t} \right) \right)^{1/3}$, where $N_{total,t}$ is the total number concentration at time point t, *nbins* is the number of diameter size bins measured by the SMPS, $D_{p,i}$ is the mean diameter of each size bin, and $N_{i,t}$ is the number concentration of particles of diameter $D_{p,i}$ at time t. Then, the upper bound assumption of SOA mass formed during the experiment is given by

$$\Delta \text{SOA}_{\text{meas},\omega=1} = \Delta \text{SOA}_{\text{meas}} + \frac{\pi}{6}\rho \sum_{t=t_1}^{t_{end}} \left[\left(D_{p,av,t_{end}}^3 - D_{p,av,t}^3 \right) N_{lost,t} \right] \tag{4.4}$$

where ρ is the particle density, $N_{lost,t}$ is the number concentration of particles lost to the chamber wall between t_i and t_{i+1}, and t_{end} is the time in the experiment considered. This calculation was performed for 1 min time steps.

4.C Chamber Simulation

4.C.1 Important Parameters

To interpret the SOA yields and extrapolate them to the atmosphere, there are a few parameters that are useful. To understand the degree of kinetic vs. quasi-equilibrium growth, the accommodation coefficient to suspended particles, α_p, is useful; as α_p approaches 1, the system becomes closer to quasi-equilibrium growth.

While the difference in the assumed SOA yield between the case where gas-phase oxidation products produced in the chamber bulk readily partition onto particles deposited on the chamber wall ($\omega = 1$) and the case where the particles cease to participate in partitioning once deposited ($\omega = 0$) is slight, the general assumption is that $\omega = 0$ and any verification of that is useful for understanding chamber data. While we do not calculate ω here, if the accommodation coefficient to particles deposited on the chamber walls (α_{pw}) is ~ 0, that indicates that $\omega \approx 0$.

4.C.2 Gas-Phase Reactions

Oxidation of benzyl alcohol in the present system occurs predominantly via reaction with the hydroxyl radical (OH). The reaction with OH proceeds via H-abstraction from the CH_2 group or OH addition to the aromatic ring; its products may include benzaldehyde, hydroxybenzyl alcohol, 3-hydroxy-2-oxopropanal, butenedial, and glyoxal (Wang, 2015; Harrison and Wells, 2009). Measured rate constants for

reaction with the OH radical found using a relative-rate method are $(2.8\pm0.4)\times10^{-11}$ cm^3 $molecule^{-1}$ s^{-1} at 297 ± 3 K (Harrison and Wells, 2009; Bernard et al., 2013).

A chemical understanding of the gas-phase oxidation of benzyl alcohol is useful for modeling the system, which can aid in understanding the gas- and particle-phase dynamics. Note that while gas-phase dynamics affect the SOA formed, the assumptions made in this section do not affect the measured SOA yields and are only used for understanding the system.

The measured gas-phase yield of benzaldehyde from the reaction of benzyl alcohol with OH is 24±5% at 298 K (Harrison and Wells, 2009; Bernard et al., 2013), which also matches well with a calculated value of 29.6% (Wang, 2015). For gas-phase modeling and related optimization, we use branching ratios following the results of Wang (2015), which combine theoretical and experimental branching results: 0.25 to form benzaldehyde, 0.11 to form *o*-hydroxybenzyl alcohol (note that this differs somewhat from the measured yield of 0.22 Bernard et al. (2013)), 0.23 to high volatility fragments (including glyoxal and butanedial), and the remaining 0.41 to low volatility and ring-containing products. Since the intermediate reactions are theoretically much faster than the initial reaction of OH with benzyl alcohol (except for the reactions of benzaldehyde), we employ the mechanism given in Fig. 4.C.1, in which compounds of similar volatilities are grouped into the precursor (BnOH), benzaldehyde (BnAl), fragments (Frags), very oxygenated rings (VORings), and hydroxybenzyl alcohol (HOBnOH).

In Table 4.C.1, the molecular weights used for each compound class are the weighted values by component predicted by Wang (2015). For each compound class, the estimated vapor pressure is the component-weighted value found using the EVAPORATION method (Topping and Jones, 2016) at the mean temperature of the experiment under consideration; for reference, the saturation mass concentration C^* is given in Table 4.C.1 at 291 K. Note that using EVAPORATION gives results similar to the Nannoonal and Myrdal method. The Oxygen-to-Carbon ratio is also given for each compound class. Note that none of these predicted products are organonitrates or other nitrogen-containing organic compounds, as observed in the aerosol (see Sect. 4.4.6). The lack of nitrogen-containing products, especially at the very beginning of oxidation, could be responsible for some of the discrepancy between the observed and simulated results.
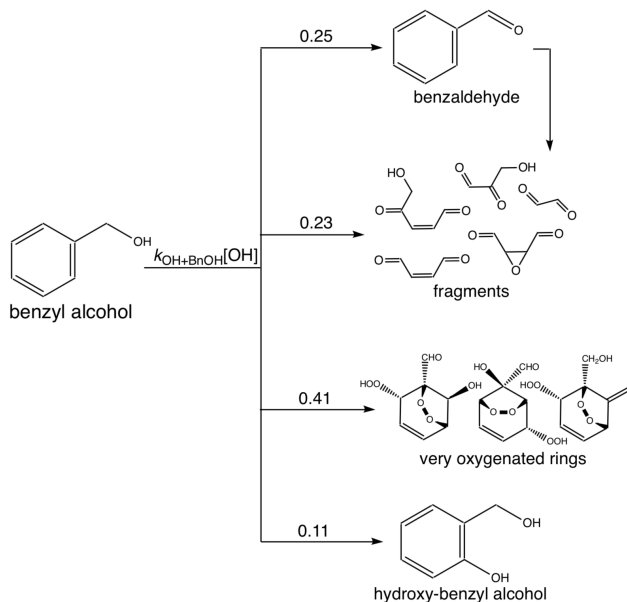
Figure 4.C.1: Benzyl alcohol reaction scheme used for simulations, roughly derived from Wang (2015).

Table 4.C.1: Compound class properties for simulating chamber experiments.

Compound Class	Abbreviation	MW (g mol^{-1})	O:C	$\log_{10} C^*$ at 291 K (µg m^{-3})	Initial Branching Ratio
benzyl alcohol	BnOH	108.14	0.14	5.73	
benzaldehyde	BnAl	106.12	0.14	6.88	0.25
fragments	Frags	87.84	0.75	7.25	0.23
very oxygenated rings	VORings	188.13	0.86	2.13	0.41
hydroxybenzyl alcohol	HOBnOH	124.13	0.29	5.79	0.11

4.C.3 Methodology

All optimization procedures and modeling are based on a fixed-bin model, as described in Charan, Huang, and Seinfeld (2019). A density of 1.4 g cm^{-3}, consistent with past work on similar compounds (Dommen et al., 2006; Kroll et al., 2005; Kroll et al., 2006; Brégonzio-Rozier et al., 2015), and a surface tension of 28.21 dyn cm^{-1}, that of benzene particles (Seinfeld and Pandis, 2016), are assumed for the particles with SOA. Wall accommodation coefficients are calculated using the saturation mass concentrations of each compound class (see Table 4.C.1) and the empirical fit described in Huang et al. (2018).

Modeling is carried out by fixing the decay of benzyl alcohol to the second-order exponential fit of the concentration. Since, in theory, $\frac{d[\text{BnOH}]}{dt} = -k_{\text{OH+BnOH}}[\text{OH}][\text{BnOH}]$, if [OH] were constant throughout the experiment then [BnOH] should follow a first-

order exponential decay in time (the decay constant for this fit is given in Table 4.1). A slightly better fit was found to a second-order exponential decay, which is used for modeling.

Note that the model is not designed for nucleation experiments, because seeding the model with small particles requires these particles to grow very quickly and, therefore, requires a much smaller time step. Hence, for the surface area experiments, we do not model experiment S1.

Because several of the simulation parameters are not constrained (the equivalent saturation concentration of the wall, C_w, the accommodation coefficient of vapor to suspended particles, α_p, the accommodation coefficient of vapor to deposited particles, α_{pw}, the accommodation coefficient of each product to the wall, $\alpha_{w,i}$), modeling of the system is associated with considerable uncertainty. If one is confident in the branching ratios under each condition, then one could determine α_w for each product and optimize α_p and C_w with experiments run under approximately identical conditions except for initial seed surface area concentrations (S2–4 and R1–4). Differences in products could then be determined at different temperatures (using experiments T1–4) and at different constant NO concentrations (using experiments N1–6).

4.C.4 Simulation Results

With the base assumption that $\alpha_p = 1$, $\alpha_{pw} = 0$, and $C_w = 1 \times 10^4$ µg m^3, the model reproduces experiments R1–4 fairly well, and most of the other experiments less successfully (see Fig. 4.C.2). Even for experiment R1, where the simulation captures the total organic mass well (Fig. 4.C.2A), the size distribution evolution is less successfully captured (Fig. 4.C.3).

Five experiment sets were chosen to optimize parameters, where the reproduction experiments are those performed under very similar initial conditions: low NO mixing ratios, high NO mixing ratios, reproduction experiments R1–4, surface area experiments S2–4 with one reproduction experiment R1, and surface area experiments S2–4 with reproduction experiments R1–4. Deriving the true α_p by first optimizing solely for α_p (with $\alpha_{pw} = 0$ and $C_w = 10^4$ µg m^{-3}) for each experiment set shows that α_p is on the order of 10^{-2}. This is the case for optimizations performed on all of the experiment sets. It is also the case if, instead of holding α_{pw} and C_w at constant values, they are also allowed to change during optimization. These results are shown in Table 4.2. Note that this is less than the general average for many
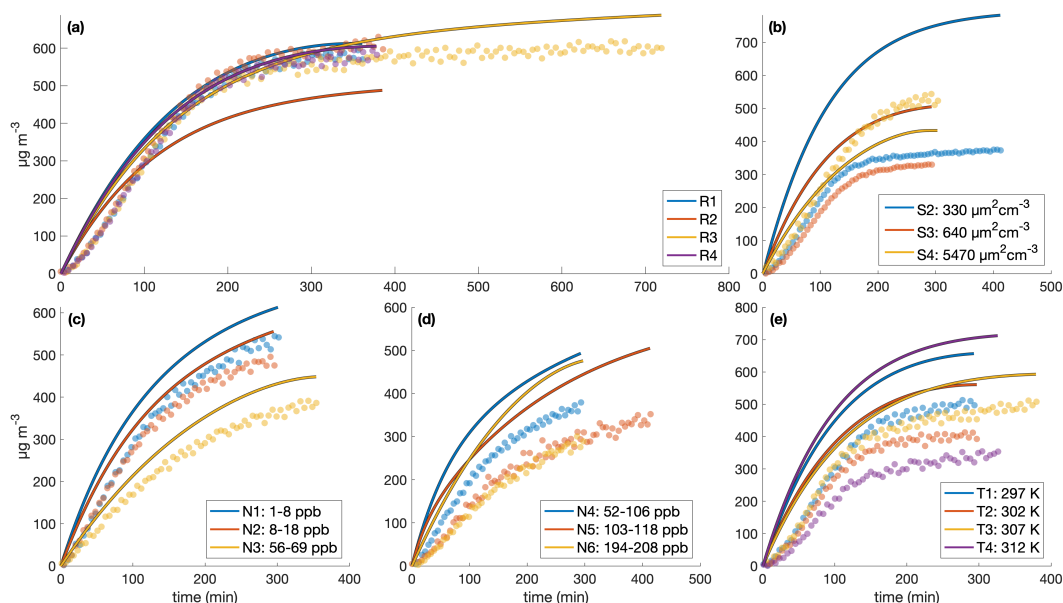
Figure 4.C.2: Comparison of measured (circles) and simulated (curves) secondary organic aerosol mass concentrations for different initial surface area concentrations assuming no vapor-wall deposition for the (a) similar experiments, (b) different surface area experiments, (c) low constant NO concentrations, (d) high constant NO concentrations, and (e) different temperature experiments. The decay of benzyl alcohol was simulated using a second-order exponential fit to the data. The accommodation coefficient of vapor to suspended particles $\alpha_p = 1$. Also, $\alpha_{pw} = 0$ and $C_w = 1 \times 10^4$ µg m^3. Simulation time steps were taken as 1 min.

studied aerosol ($\sim$0.9) and specifically for the similar compound toluene, which was determined to be $0.3 \leq \alpha_p \leq 0.6$ (Liu et al., 2019).

This suggests that mass-transfer limitations may be important for understanding the growth of SOA under these conditions. An accommodation coefficient close to 1 means that equilibrium between the gas- and particle-phase is quickly reached because there are few mass-transfer limitations. The smaller α_p found here indicates that the particles are highly viscous, i.e., that it takes some time for the particle-phase to equilibrate with the gas-phase. This is equivalent to saying that the system is kinetically controlled. For systems with lower values of α_p, one expects to see more of a seed surface area effect, which is discussed in Sect. 4.3.2.2.

Since any optimizations involving α_{pw} indicated very small values, for this chamber it appears that $\omega = 0$ is closer to reality than $\omega = 1$. This is because if $\alpha_{pw} \approx 0$, then effectively no gas-phase compounds are condensing onto particles that have already deposited on the chamber wall, which is the same as the assumption that $\omega \approx 0$.
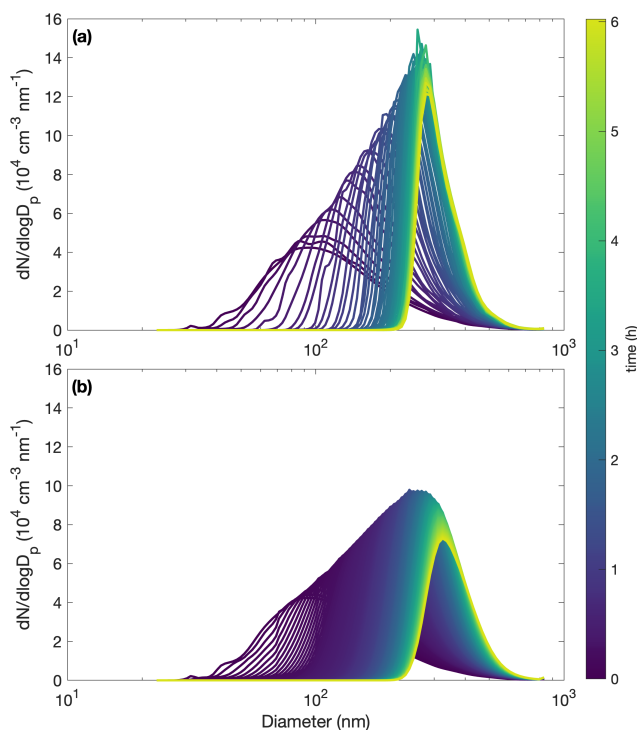
Figure 4.C.3: Comparison of measured (A) and simulated (B) particle size distributions throughout oxidation for experiment R1. The decay of benzyl alcohol is represented using a second-order exponential fit to the data. The accommodation coefficient of vapor to suspended particles $\alpha_p = 1$. Also, $\alpha_{pw} = 0$ and $C_w = 1 \times 10^4$ µg m^3. Computational time steps are taken as 1 min.

References

Aiken, Allison C. et al. (June 2008). "O/C and OM/OC Ratios of Primary, Secondary, and Ambient Organic Aerosols with High-Resolution Time-of-Flight Aerosol Mass Spectrometry." In: *Environ. Sci. Technol.* 42.12, pp. 4478–4485. ISSN: 0013-936X. DOI: 10.1021/es703009q.

Arey, Janet, Sara M. Aschmann, Eric S.C. Kwok, and Roger Atkinson (2001). "Alkyl Nitrate, Hydroxyalkyl Nitrate, and Hydroxycarbonyl Formation from the NO$_x$-Air Photooxidations of C$_5$–C$_8$ *n*-Alkanes." In: *J. Phys. Chem. A* 105.6, pp. 1020–1027. ISSN: 10895639. DOI: 10.1021/jp003292z.

Baghi, R., D. Helmig, A. Guenther, T. Duhl, and R. Daly (2012). "Contribution of flowering trees to urban atmospheric biogenic volatile organic compound emissions." In: *Biogeosciences* 9.10, pp. 3777–3785. ISSN: 17264170. DOI: 10.5194/bg-9-3777-2012.

Bernard, Francìois, Isabelle Magneron, Grégory Eyglunent, Véronique Daële, Timothy J. Wallington, Michael D. Hurley, and Abdelwahid Mellouki (2013). "Atmospheric chemistry of benzyl alcohol: Kinetics and mechanism of reaction with

OH radicals." In: *Environ. Sci. Technol.* 47.7, pp. 3182–3189. ISSN: 15205851. DOI: `10.1021/es304600z`.

Brégonzio-Rozier, L. et al. (2015). "Gaseous products and secondary organic aerosol formation during long term oxidation of isoprene and methacrolein." In: *Atmos. Chem. Phys.* 15.6, pp. 2953–2968. ISSN: 16807324. DOI: `10.5194/acp-15-2953-2015`.

Burkholder, James B. et al. (2017). "The essential role for laboratory studies in atmospheric chemistry." In: *Environ. Sci. Technol.* 51.5, pp. 2519–2528. ISSN: 0013-936X. DOI: `10.1021/acs.est.6b04947`.

Canagaratna, M. R. et al. (Jan. 2015). "Elemental ratio measurements of organic compounds using aerosol mass spectrometry: characterization, improved calibration, and implications." In: *Atmos. Chem. Phys.* 15.1, pp. 253–272. ISSN: 1680-7324. DOI: `10.5194/acp-15-253-2015`.

Cappa, C. D., X. Zhang, C. L. Loza, J. S. Craven, L. D. Yee, and J. H. Seinfeld (2013). "Application of the Statistical Oxidation Model (SOM) to Secondary Organic Aerosol formation from photooxidation of C12 alkanes." In: *Atmos. Chem. Phys.* 13.3, pp. 1591–1606. ISSN: 16807316. DOI: `10.5194/acp-13-1591-2013`.

Carter, William P. L., Irina L. Malkina, David R. Cocker III, and Chen Song (2005). *Environmental Chamber Studies Of VOC Species In Architectural Coatings And Mobile Source Emissions.* Tech. rep. Center for Environmental Research and Technology, University of California. URL: `http://citeseerx.ist.psu.edu/viewdoc/summary?doi=10.1.1.81.305`.

Charan, Sophia M., Yuanlong Huang, and John H. Seinfeld (2019). "Computational simulation of secondary organic aerosol formation in laboratory chambers." In: *Chemical Reviews.* DOI: `10.1021/acs.chemrev.9b00358`.

Charan Sophia M .and Kong, Weimeng, Richard C. Flagan, and John H. Seinfeld (2018). "Effect of particle charge on aerosol dynamics in Teflon environmental chambers." In: *Aerosol Sci. Technol.* 52.8, pp. 854–871. DOI: `10.1080/02786826.2018.1474167`.

Dommen, J., A. Metzger, J. Duplissy, M. Kalberer, M. R. Alfarra, A. Gascho, E. Weingartner, A. S.H. Prevot, B. Verheggen, and U. Baltensperger (2006). "Laboratory observation of oligomers in the aerosol from isoprene/NOx photooxidation." In: *Geophys. Res. Lett.* 33.13, pp. 1–5. ISSN: 00948276. DOI: `10.1029/2006GL026523`.

Donahue, N. M., J. H. Kroll, S. N. Pandis, and A. L. Robinson (2012). "A two-dimensional volatility basis set: 2. diagnostics of organic-aerosol evolution." In: *Atmos. Chem. Phys.* 12.2, pp. 615–634. DOI: `10.5194/acp-12-615-2012`.

EPA, United States (2012). *Green Book: PM-2.5 (2012) Designated Area/State Information with Design Values.* URL: `https://www3.epa.gov/airquality/greenbook/kbtcw.html`.

Farmer, D. K., A. Matsunaga, K. S. Docherty, J. D. Surratt, J. H. Seinfeld, P. J. Ziemann, and J. L. Jimenez (2010). "Response of an aerosol mass spectrometer to organonitrates and organosulfates and implications for atmospheric chemistry." In: *Proc. Natl. Acad. Sci. U.S.A.* 107.15, pp. 6670–6675. DOI: `10.1073/pnas.0912340107`.

Fry, J. L. et al. (Sept. 2013). "Observations of gas- and aerosol-phase organic nitrates at BEACHON-RoMBAS 2011." In: *Atmos. Chem. Phys.* 13.17, pp. 8585–8605. ISSN: 1680-7324. DOI: `10.5194/acp-13-8585-2013`.

Gao, Song, Nga L. Ng, Melita Keywood, Varuntida Varutbangkul, Roya Bahreini, Athanasios Nenes, Jiwen He, Kee Y. Yoo, J. L. Beauchamp, Robert P. Hodyss, Richard C. Flagan, and John H. Seinfeld (Dec. 2004). "Particle Phase Acidity and Oligomer Formation in Secondary Organic Aerosol." In: *Environ. Sci. Technol.* 38.24, pp. 6582–6589. DOI: `10.1021/es049125k`.

Goldstein, Allen H. and Ian E. Galbally (Mar. 2007). "Known and Unexplored Organic Constituents in the Earth's Atmosphere." In: *Environ. Sci. Technol.* 41.5, pp. 1514–1521. ISSN: 0013-936X. DOI: `10.1021/es072476p`.

Hamilton, Jacqueline F., Paul J. Webb, Alastair C. Lewis, and Montserrat M. Reviejo (2005). "Quantifying small molecules in secondary organic aerosol formed during the photo-oxidation of toluene with hydroxyl radicals." In: *Atmos. Environ.* 39.38, pp. 7263–7275. ISSN: 13522310. DOI: `10.1016/j.atmosenv.2005.09.006`.

Harrison, Joel C. and J. R. Wells (2009). "Gas-phase chemistry of benzyl alcohol: Reaction rate constants and products with OH radical and ozone." In: *Atmos. Environ.* 43.4, pp. 798–804. ISSN: 13522310. DOI: `10.1016/j.atmosenv.2008.11.001`.

Horvat, R. J., G. W. Chapman, J. A. Robertson, F. I. Meredith, R. Scorza, A. M. Callahan, and P. Morgens (1990). "Comparison of the Volatile Compounds from Several Commercial Peach Cultivars." In: *J. Agric. Food Chem.* 38.1, pp. 234–237. ISSN: 15205118. DOI: `10.1021/jf00091a051`.

Huang, Yuanlong, Ran Zhao, Sophia M. Charan, Christopher M. Kenseth, Xuan Zhang, and John H. Seinfeld (2018). "Unified theory of vapor–wall mass transport in Teflon–walled environmental chambers." In: *Environ. Sci. Technol.* 52.4, pp. 2134–2142. DOI: `10.1021/acs.est.7b05575`.

Iinuma, Yoshiteru, Olaf Böge, and Hartmut Herrmann (2010). "Methyl-nitrocatechols: Atmospheric tracer compounds for biomass burning secondary organic aerosols." In: *Environ. Sci. Technol.* 44.22, pp. 8453–8459. DOI: `10.1021/es102938a`.

Ikemori, Fumikazu, Tomoki Nakayama, and Hitomi Hasegawa (2019). "Characterization and possible sources of nitrated mono- and di-aromatic hydrocarbons containing hydroxyl and/or carboxyl functional groups in ambient particles in Nagoya, Japan." In: *Atmos. Environ.* 211.November 2018, pp. 91–102. DOI: `10.1016/j.atmosenv.2019.05.009`.

IPCC (2014). *Climate Change 2014: Synthesis report*. Tech. rep. Geneva, Switzerland: Intergovernmental Panel on Climate Change, p. 151. DOI: `10.1017/CB09781107415324`.

Kenseth, Christopher M., Yuanlong Huang, Ran Zhao, Nathan F. Dalleska, J. Caleb Hethcox, Brian M. Stoltz, and John H. Seinfeld (Aug. 2018). "Synergistic O_3 + OH oxidation pathway to extremely low-volatility dimers revealed in β-pinene secondary organic aerosol." In: *Proc. Natl. Acad. Sci. U.S.A.* 115.33, pp. 8301–8306. ISSN: 0027-8424. DOI: `10.1073/pnas.1804671115`.

Kiendler-Scharr, A. et al. (July 2016). "Ubiquity of organic nitrates from nighttime chemistry in the European submicron aerosol." In: *Geophys. Res. Lett.* 43.14, pp. 7735–7744. DOI: `10.1002/2016GL069239`.

Kroll, Jesse H., Nga L. Ng, Shane M. Murphy, Richard C. Flagan, and John H. Seinfeld (2005). "Secondary organic aerosol formation from isoprene photooxidation under high-NO_x conditions." In: *Geophys. Res. Lett.* 32.18, pp. 1–4. ISSN: 00948276. DOI: `10.1029/2005GL023637`.

– (2006). "Secondary organic aerosol formation from isoprene photooxidation." In: *Environ. Sci. Technol.* 40.6, pp. 1869–1877. ISSN: 0013936X. DOI: `10.1021/es0524301`.

Li, Weihua, Lijie Li, Chia Li Chen, Mary Kacarab, Weihan Peng, Derek Price, Jin Xu, and David R. Cocker (2018). "Potential of select intermediate-volatility organic compounds and consumer products for secondary organic aerosol and ozone formation under relevant urban conditions." In: *Atmos. Environ.* 178.February, pp. 109–117. ISSN: 18732844. DOI: `10.1016/j.atmosenv.2017.12.019`.

Liu, Xiaoxi, Douglas A. Day, Jordan E. Krechmer, Wyatt Brown, Zhe Peng, Paul J. Ziemann, and Jose L. Jimenez (Dec. 2019). "Direct measurements of semi-volatile organic compound dynamics show near-unity mass accommodation coefficients for diverse aerosols." In: *Commun. Chem.* 2.1, p. 98. ISSN: 2399-3669. DOI: `10.1038/s42004-019-0200-x`.

Mai, Huajun, Weimeng Kong, John H. Seinfeld, and Richard C. Flagan (Oct. 2018). "Scanning DMA Data Analysis II. Integrated DMA-CPC Instrument Response and Data Inversion." In: *Aerosol Sci. Technol.* 6826, pp. 1–35. ISSN: 0278-6826. DOI: `10.1080/02786826.2018.1528006`.

Mannucci, Pier Mannuccio, Sergio Harari, Ida Martinelli, and Massimo Franchini (2015). "Effects on health of air pollution: a narrative review." In: *Intern. Emerg. Med.* 10.6, pp. 657–662. ISSN: 19709366. DOI: `10.1007/s11739-015-1276-7`.

McDonald, Brian C. et al. (Feb. 2018). "Volatile chemical products emerging as largest petrochemical source of urban organic emissions." In: *Science* 359.6377, pp. 760–764. ISSN: 0036-8075. DOI: `10.1126/science.aaq0524`.

McMurry, P. H. and D. J. Rader (Jan. 1985). "Aerosol Wall Losses in Electrically Charged Chambers." In: *Aerosol Science and Technology* 4.3, pp. 249–268. ISSN: 0278-6826. DOI: `10.1080/02786828508959054`.

Ng, N. L., J. H. Kroll, A. W.H. Chan, P. S. Chhabra, R. C. Flagan, and J. H. Seinfeld (2007). "Secondary organic aerosol formation from m-xylene, toluene, and benzene." In: *Atmos. Chem. Phys.* 7.14, pp. 3909–3922. DOI: 10.5194/acp-7-3909-2007.

Odum, Jay R, Thorsten Hoffmann, Frank Bowman, Don Collins, C Flagan Richard, and H Seinfeld John (1996). "Gas particle partitioning and secondary organic aerosol yields." In: *Environ. Sci. Technol.* 30.8, pp. 2580–2585. DOI: 10.1021/es950943+.

Pankow, James F (Jan. 1987). "Review and comparative analysis of the theories on partitioning between the gas and aerosol particulate phases in the atmosphere." In: *Atmos. Environ.* 21.11, pp. 2275–2283. DOI: 10.1016/0004-6981(87)90363-5.

– (Jan. 1994). "An absorption model of gas/particle partitioning of organic compounds in the atmosphere." In: *Atmos. Environ.* 28.2, pp. 185–188. DOI: 10.1016/1352-2310(94)90093-0.

Ranney, April P. and Paul J. Ziemann (2016). "Kinetics of Acid-Catalyzed Dehydration of Cyclic Hemiacetals in Organic Aerosol Particles in Equilibrium with Nitric Acid Vapor." In: *J. Phys. Chem. A* 120.16, pp. 2561–2568. ISSN: 15205215. DOI: 10.1021/acs.jpca.6b01402.

Rollins, A. W., J. L. Fry, J. F. Hunter, J. H. Kroll, D. R. Worsnop, S. W. Singaram, and R. C. Cohen (2010). "Elemental analysis of aerosol organic nitrates with electron ionization high-resolution mass spectrometry." In: *Atmos. Meas. Tech.* 3.1, pp. 301–310. ISSN: 18678548. DOI: 10.5194/amt-3-301-2010.

Sato, Kei, Akinori Takami, Tasuku Isozaki, Toshihide Hikida, Akio Shimono, and Takashi Imamura (2010). "Mass spectrometric study of secondary organic aerosol formed from the photo-oxidation of aromatic hydrocarbons." In: *Atmos. Environ.* 44.8, pp. 1080–1087. ISSN: 1352-2310. DOI: 10.1016/j.atmosenv.2009.12.013.

Schwantes, Rebecca H., Renee C. McVay, Xuan Zhang, Matthew M. Coggon, Hanna Lignell, Richard C. Flagan, Paul O. Wennberg, and John H. Seinfeld (2017). In: *Advances in Atmospheric Chemistry Volume I*. Ed. by J.R. Barker, A.L. Steiner, and T.J. Wallington. Singapore: World Scientific. Chap. Science of the environmental chamber, pp. 1–93. ISBN: 978-981-3147-34-8.

Schwantes, Rebecca H., Katherine A. Schilling, Renee C. McVay, Hanna Lignell, Matthew M. Coggon, Xuan Zhang, Paul O. Wennberg, and John H. Seinfeld (2017). "Formation of highly oxygenated low-volatility products from cresol oxidation." In: *Atmos. Chem. Phys.* 17.5, pp. 3453–3474. ISSN: 16807324. DOI: 10.5194/acp-17-3453-2017.

Seinfeld, John H. and Spyros N. Pandis (2016). *Atmospheric Chemistry and Physics: From Air Pollution to Climate Change*. 3rd. Hoboken: John Wiley & Sons. ISBN: 978-1118947401.

Shrivastava, Manish et al. (2017). "Recent advances in understanding secondary organic aerosol: implications for global climate forcing." In: *Rev. Geophys.* 55.2, pp. 509–559. DOI: 10.1002/2016RG000540.

Surratt, Jason D. et al. (2008). "Organosulfate Formation in Biogenic Secondary Organic Aerosol." In: *J. Phys. Chem. A* 112.36, pp. 8345–8378. DOI: 10.1021/jp802310p.

TCCON Weather Data (2020). *Barometric Pressure*. URL: http://tccon-weather.caltech.edu/index.php.

Topping, David and Dave Jones (2016). *UManSysProp*. URL: http://umansysprop.seaes.manchester.ac.uk/tool/vapour_pressure.

Trump, Erica R., Scott A. Epstein, Ilona Riipinen, and Neil M. Donahue (Nov. 2016). "Wall effects in smog chamber experiments: a model study." In: *Aerosol Sci. Technol.* 50.11, pp. 1180–1200. ISSN: 0278-6826. DOI: 10.1080/02786826.2016.1232858.

Wang, Liming (May 2015). "The Atmospheric Oxidation Mechanism of Benzyl Alcohol Initiated by OH Radicals: The Addition Channels." In: *ChemPhysChem* 16.7, pp. 1542–1550. ISSN: 14394235. DOI: 10.1002/cphc.201500012.

Wang, N., S. D. Jorga, J. R. Pierce, N. M. Donahue, and S. N. Pandis (2018). "Particle wall-loss correction methods in smog chamber experiments." In: *Atmos. Meas. Tech.* 11.12, pp. 6577–6588. DOI: 10.5194/amt-11-6577-2018.

Wang, Ningxin, Evangelia Kostenidou, Neil M. Donahue, and Spyros N. Pandis (2018). "Multi-generation Chemical Aging of α-Pinene Ozonolysis Products by Reactions with OH." In: *Atmos. Chem. Phys.* 18.5, pp. 3589–3601. DOI: 10.5194/acp-18-3589-2018.

Weitkamp, Emily A., Amy M. Sage, Jeffrey R. Pierce, Neil M. Donahue, and Allen L. Robinson (Oct. 2007). "Organic Aerosol Formation from Photochemical Oxidation of Diesel Exhaust in a Smog Chamber." In: *Environ. Sci. Technol.* 41.20, pp. 6969–6975. ISSN: 0013-936X. DOI: 10.1021/es070193r.

Yamasaki, Hiroyasu, Kazuhiro Kuwata, and Hiroko Miyamoto (1982). "Effects of Ambient Temperature on Aspects of Airborne Polycyclic Aromatic Hydrocarbons." In: *Environ. Sci. Technol.* 16.4, pp. 189–194. DOI: 10.1021/es00098a003.

Zafonte, Leo, Paul L. Rieger, and John R. Holmes (1977). "Nitrogen Dioxide Photolysis in the Los Angeles Atmosphere." In: *Environ. Sci. Technol.* 11.5, pp. 483–487. ISSN: 15205851. DOI: 10.1021/es60128a006.

Zhang, X., N.F. Dalleska, D.D. Huang, K.H. Bates, A. Sorooshian, R.C. Flagan, and J.H. Seinfeld (Apr. 2016). "Time-resolved molecular characterization of organic aerosols by PILS + UPLC/ESI-Q-TOFMS." In: *Atmos. Environ.* 130, pp. 180–189. ISSN: 13522310. DOI: 10.1016/j.atmosenv.2015.08.049.

Zhang, Xuan, Christopher D. Cappa, Shantanu H. Jathar, Renee C. McVay, Joseph J. Ensberg, Michael J. Kleeman, and John H. Seinfeld (2014). "Influence of vapor wall loss in laboratory chambers on yields of secondary organic aerosol." In: *Proc. Natl. Acad. Sci. U.S.A.* 111.16, pp. 5802–5807. DOI: 10.1073/pnas.1404727111.

Zhang, Xuan, R. H. Schwantes, R. C. McVay, H. Lignell, M. M. Coggon, R. C. Flagan, and J. H. Seinfeld (Apr. 2015). "Vapor wall deposition in Teflon chambers." In: *Atmos. Chem. Phys.* 15.8, pp. 4197–4214. ISSN: 1680-7324. DOI: 10.5194/acp-15-4197-2015.

Chapter 5

IT ALL OH-DEPENDS: SECONDARY ORGANIC AEROSOL FORMATION FROM THE OXIDATION OF DECAMETHYLCYCLOPENTASILOXANE AT ATMOSPHERICALLY RELEVANT OH CONCENTRATIONS

Charan, Sophia M., Yuanlong Huang, Reina S. Buenconsejo, Qi Li, David R. Cocker III, and John H. Seinfeld (2021). "Secondary organic aerosol formation from the oxidation of decamethylcyclopentasiloxane at atmospherically relevant OH concentrations". [Submitted]. DOI: 10.5194/acp-2021-353.

Abstract

Decamethylcyclopentasiloxane (D5, $C_{10}H_{30}O_5Si_5$) is measured at ppt levels outdoors and ppb levels indoors. Primarily used in personal care products, its outdoor concentration is correlated to population density. Since understanding the aerosol formation potential of volatile chemical products is critical to understanding particulate matter in urban areas, the secondary organic aerosol yield of D5 was studied under a range of OH concentrations, OH exposures, NO_x concentrations, and temperatures. The secondary organic aerosol (SOA) yield from the oxidation of D5 is extremely dependent on the OH concentration, and differing measurements of the SOA yield from the literature are resolved in this study. Here, we compare experimental results from environmental chambers and flow tube reactors. Generally, there are high SOA yields (> 90%) at OH mixing ratios of 5×10^9 molec cm^{-3}. At atmospherically relevant OH concentrations, the SOA yield is largely <5% and usually ~1%. This is significantly lower than SOA yields used in emission and particulate matter inventories and demonstrates the necessity of OH concentrations similar to the ambient environment when extrapolating SOA yield data to the outdoor atmosphere.

5.1   Introduction

Present in outdoor mixing ratios as high as ~40 ppt, decamethylcyclopentasiloxane (D5, $C_{10}H_{30}O_5Si_5$) has been observed in cities, rural areas, and the Arctic (Buser, Kierkegaard, et al., 2013; Buser, Bogdal, et al., 2014; Ahrens, Harner, and Shoeib, 2014; McLachlan et al., 2010; Xu, Warner, et al., 2019). D5 is used in personal

care products, as well as for industrial purposes (Mackay et al., 2015); in 2004, over 17000 tons were used in the then European Union (Safron et al., 2015). Outdoor observations of D5 are population-dependent (Janechek, Hansen, and Stanier, 2017; Gkatzelis et al., 2021), and this dependence is sufficiently reliable to be used as a tracer to differentiate the effects of population from that of motor vehicles (Coggon et al., 2018). The impact of D5 does not stop at population centers; its long atmospheric lifetime means that it is found in areas with low population densities.

Likely more than 90% of the D5 used is emitted into the atmosphere (Balducci et al., 2012; Hughes et al., 2012), though much of this may be first emitted indoors and only later exchanged to the outdoors: in an engineering classroom in the U.S. in 2014, ~30% by mass of the total volatile organic compounds (VOCs) were D5 (Tang et al., 2015). In an athletic center in the morning, D5 mixing ratios exceeded 6 ppb and emissions were attributed to the humans in the room (Finewax et al., 2020). Even the international space station was found to contain D5 (Carter et al., 2015).

Given the abundance of D5 in the ambient atmosphere, it is important to understand its fate. The major loss source of D5 is reaction with the hydroxyl radical; losses by reaction with NO_3, O_3, and Cl are all negligible (Atkinson, 1991; Alton and Browne, 2020). The half-life of D5 outdoors is between 3.5 and 7 days, depending on the assumed global average OH concentration and the exact method used to calculate the reaction rate of OH with D5 (Safron et al., 2015; Xiao et al., 2015; Alton and Browne, 2020). Outside, both wet and dry deposition of D5 are negligible and methylsiloxanes do not photolyze in the actinic region (Hobson, Atkinson, and L., 1997). Previous studies by Janechek, Marek, et al. (2019) and Wu and Johnston (2017) measured secondary organic aerosol (SOA) yields, the ratios of the mass of organic aerosol formed to the mass of the precursor reacted, between 8 and 50%. This is a wide range and the conditions for these experiments were performed at OH concentrations much higher than those in the ambient atmosphere. By measuring the SOA formation potential of D5, we can better understand the contribution of volatile chemical products (VCPs) to aerosol levels in urban areas.

VCPs are a major (and perhaps majority) source of secondary organic aerosol in cities in the U.S., even urban areas that are not megacities (McDonald et al., 2018; Gkatzelis et al., 2021). Resolving uncertainties in the mass of SOA formed from VCPs is critical for refining SOA estimates and for creating policy to reduce SOA non-compliance in urban areas (Burkholder et al., 2017).

Researchers use both flow reactors and atmospheric chambers to measure the SOA

yields of various compounds. While many results agree between the two methods of analysis, different reactors have varying benefits and operating conditions (e.g., OH concentrations, experiment length, precursor concentrations, humidity values). One must account for the particular attributes of the different reactors when extrapolating to the atmosphere.

5.2 Methods

Chamber experiments were performed in a temperature-controlled $19\,m^3$ FEP Teflon Environmental Chamber run in batch mode. The chamber is hung in an enclosure, to reduce charge on the surface of the chamber, and is surrounded by ultraviolet lights centered at ~350 nm. Since the walls of the chamber are not rigid and data were collected continuously, the chamber decreased slightly in volume throughout the experiment, but never by more than 15%.

Prior to each chamber experiment, the contents of the chamber were flushed with air stripped of ozone, nitrogen oxides, water vapor, and organic carbon for > 24 h. H_2O_2, when used as an OH source, was injected by flowing air at 5 Lpm over liquid H_2O_2 in a ~42°C water bath to obtain an $[H_2O_2] \approx 2$ ppm. For the experiment that used methyl nitrite (CH_3ONO), a glass bulb was evacuated and then filled to the desired pressure to obtain ~600 ppb in the chamber. After bringing the bulb up to atmospheric pressure with nitrogen, it was flushed into the chamber with nitrogen. CH_3ONO forms OH as described in Schwantes et al. (2019).

D5 (99%, TCI America) was injected into the chamber for Experiments 1–8 at room temperature by flowing nitrogen through a glass bulb at 5 Lpm for > 60 min. To obtain the desired initial surface area concentration, a sonicated, 0.06 M (0.15 M for Experiment 2) $(NH_4)_2SO_4$ solution was atomized to create aerosol that was then dried, passed through a TSI Model 3088 soft x-ray neutralizer, and injected into the chamber. For Experiment 7, no aerosol was injected. For Experiments 5–7, NO (506.9 ppm ± 2%, Airgas Specialty Gases, Certified Standard) was injected prior to the beginning of the experiment to achieve initial NO mixing ratios between 80 and 100 ppb. During Experiments 5 and 6, 1 ppb min^{-1} of NO was injected from the inception of radiation to the end of the experiment.

Experiments at higher OH mixing ratios were conducted in the Caltech Photooxidation Flow Tube (CPOT, Huang, Coggon, et al., 2017) at a constant flow rate of 4.88 Lpm and 23.0±0.1°C. The mean residence time of the CPOT was 671 ± 15 s and the diffusivity was 15 ± 2 cm^2 s^{-1}, as calculated with a step injection of SO_2

using Equation 4 in Huang and Seinfeld (2019). For Experiments 9–15, clean air flowed through an ozone generator (UVP, 97-0067-01); for Experiments 16–19, O_2 flowed through the same generator to create higher concentrations of O_3. The 254 nm lights photolyze O_3 to form $O(^1D)$, which reacts with H_2O to form 2OH. After conditions were changed in the CPOT, no results were collected for at least 2 h. Data were averaged over between 1 and 11 h. D5 was injected through a syringe pump (Harvard Apparatus).

For all experiments, the concentration of D5 was measured with an HP 6890N gas chromatograph with a flame ionization detector (GC-FID) and a DB-5 column. Prior to the beginning of oxidation for the chamber experiments, all contents of the reactor were left to sit for 4 h (2.8 h for Experiment 7) and the initial concentration of D5 was taken as the mean concentration during this time. For the CPOT experiments, the initial concentration of D5 was calculated by measuring the outlet flow with lights off, no water source, and the absence of O_3. For Experiment 9, the change in D5 was sufficiently small that it was within the uncertainty. For calculating the SOA yield for this experiment, we used the OH exposure calculated from the change in SO_2 concentration to find the change in D5 (7 ppb).

To calibrate the GC-FID, a small Teflon bag was filled with 35 ppm of D5 and later diluted to 9 ppm. This bag was sampled using the GC-FID and the concentration was verified with a Fourier transform infrared absorption (FT-IR) spectrometer with a 19 cm path length and absorption cross sections from the Pacific Northwest National Laboratory (PNNL) database. To minimize vapor-wall-loss to the FT-IR enclosure, multiple samples were taken until a consistent spectrum was achieved.

Gas-phase oxidation products were evaluated with a CF_3O^- chemical ionization mass spectrometer (CIMS) equipped with a Varian 1200 triple quadrupole mass analyzer. Concentrations of NO and NO_2 were measured with a Teledyne Nitrogen Oxide Analyzer (Model T200) and O_3 was found with a Horiba Ambient Monitor. Temperature and humidity were determined using a Vaisala HMM211 probe.

Aerosol volume was measured by a custom-built scanning mobility particle sizer (SMPS) with a 3081 TSI Differential Mobility Analyzer (DMA) and a TSI 3010 butanol condensation particle counter (CPC). The sheath flow rate was 2.64 Lpm and the aerosol flow rate from the chamber was 0.515 Lpm. A voltage scan from 15 to 9875 V was performed in 240 s every 330 s. Aerosol from the chamber flowed through an x-ray source to provide a known charge distribution, and the size distributions were determined using the data inversion method described by

Mai et al. (2018). Experiment 2 required a logarithmic fit to the largest particles present, as described in Charan, Buenconsejo, and Seinfeld (2020), which is the source of the higher SOA yield uncertainty than in the other experiments (see Table 5.1). Conversions to mass concentration were performed by assuming that the aerosol density was 1.52 ± 0.04 g cm^{-3}, which was the density calculated at [OH] $\approx 9.4 \times 10^9$ molec cm^{-3} in a flow reactor (Xu and Collins, 2021) using an Aerosol Particle Mass Analyzer and a SMPS system as described in Malloy et al. (2009).

Uncertainty estimates for all the instruments used in this study were determined as described in Charan, Buenconsejo, and Seinfeld (2020). For the chamber experiments, particle-wall-deposition corrections were performed by calculating a diameter-independent first-order exponential fit (β =1–7×10^{-4} min^{-1}) to the particle volume concentration during the 3 h prior to the onset of oxidation and applying that correction to the rest of the experiment. This method was chosen because it aligns with a diameter-dependent fit as determined using the method in Charan, Flagan, and Seinfeld (2018) but is simpler and because, for the chamber experiments, minimal organic aerosol formed and so the particle diameters changed insignificantly throughout the duration of the experiment. For Experiment 7, in which no initial aerosol was present, no aerosol was generated throughout the experiment and so no correction was necessary to determine an apparent SOA yield of 0.

For the CPOT experiments, an upper estimate of the wall-deposition-corrected SOA mass was calculated with the inverse of the particle-size-dependent penetration efficiency of the flow-tube component of the reactor (data from Fig. 9d in Huang, Coggon, et al., 2017). Since particles nucleated in the CPOT, the penetration efficiency of only the flow-tube component (and not the static mixer prior to the region of reaction) was used. The penetration efficiency, however, is based on the entire flow tube and nucleated particles may not form immediately at the beginning of the flow-tube component; thus, the wall-deposition correction performed here is an upper bound of the correction. Note that this correction also neglects particle growth throughout the reactor and any particle-particle coagulation.

SOA yield (Y) is defined by $Y = \frac{\Delta\text{SOA}_{\text{corr}}}{\Delta\text{D5}}$, where $\Delta\text{SOA}_{\text{corr}}$ is the wall-deposition-corrected change in the aerosol mass concentration and ΔD5 is the mass concentration of reacted D5. Calculations were performed as described by Charan, Buenconsejo, and Seinfeld (2020) and with the assumption that a particle, once deposited on the reactor wall, no longer acts as a condensation sink (Trump et al., 2016). Note that since so little aerosol was formed during the chamber experiments,

this assumption had a negligible effect on the chamber results. For the CPOT experiments, any deviation from this assumption would have prevented the data from reaching steady-state.

While the vapor-wall-deposition lifetime of D5 to the chamber walls was estimated to be on the order of weeks, the propensity of vapor-wall-deposition of the oxidation products is not extensively investigated in this study. Even at high initial seed surface area concentrations, the SOA yield is still quite small (see Fig. 5.B.1). Alton and Browne (2020) estimated that, for their unseeded ~1 m^3 FEP Teflon chamber, 5% of the ester product of D5 oxidation might partition to the chamber walls during the reaction. The volume of the chamber used in this study is 19 m^3 and seed aerosol is introduced prior to the experiment (except for Experiment 7, which was performed in the absence of seed aerosol). Even if 5% of the oxidation products were lost to the chamber walls, the SOA yields would still be within the reported uncertainty and sufficiently small so as not to affect any conclusions. The CPOT reactor is operated at steady-state and, therefore, any oxidation products that are in equilibrium with the bulk flow (i.e., not lost permanently to the quartz walls) do not need a vapor-wall-deposition correction.

For chamber experiments that employed H_2O_2, the OH concentration was calculated by fitting the gas-phase D5 concentration to a first-order exponential, fixing the initial point of the fit as the initial D5 concentration (fits had $R^2 > 0.75$), and using the value for the reaction rate of OH with D5, $k = 2.1 \pm 0.1 \times 10^{-12}$ cm^3 $molec^{-1}$ s^{-1}, which was measured using the relative rate method at 297 ± 3 K (Alton and Browne, 2020). Note that other experimental evaluations of the reaction rate of OH with D5 that use the relative rates method vary by less than a factor of 2 (the reasons for this difference are not known), which would not affect the order of magnitude of the OH concentration estimate (Kim and Xu, 2017; Safron et al., 2015; Xiao et al., 2015). OH is the major loss source in the atmosphere and, we expect, in these experiments: losses to O_3, NO_3, and Cl are all negligible (Atkinson, 1991; Alton and Browne, 2020). The ozone concentration did not affect the SOA yield results: Experiments 7 and 9, which were performed at substantially different O_3 concentrations, still gave similar results for the SOA yield (0±0.1% and 0.8±0.8% with an upper wall-deposition-corrected bound of 1.4%, respectively). For Experiment 8, in which CH_3NO_2 served as the OH source, the sharp decrease in the D5 mixing ratio immediately after the commencement of radiation, followed by a gradual decrease in its concentration, indicates that two OH concentrations

are relevant for this experiment. Since the D5 concentration is measured every ~21 min, and the pulse with high OH concentrations occurs within the first 30 min of oxidation, the initial OH concentration is estimated with a two-point first-order exponential fit to the initial concentration and the first data point (12.3 min into radiation). The second OH concentration is estimated with a first-order exponential fit of the second point (33.3 min into radiation) to the end of the experiment.

OH exposure was calculated, for chamber experiments (Experiments 1–8) and experiments from Wu and Johnston (2017), as

$$[OH] * t = \frac{-1}{k_{OH+D5}} \ln\left(\frac{[D5]_{end}}{[D5]_0}\right), \tag{5.1}$$

where $k_{OH+D5} = 2.1 \times 10^{-12}$ cm^3 molec^{-1} s^{-1} (Alton and Browne, 2020). For the CPOT experiments (Experiments 9–19), OH exposure was calculated as

$$[OH] * t = \frac{-1}{k_{OH+SO_2}} \ln\left(\frac{[SO_2]_{end}}{[SO_2]_0}\right), \tag{5.2}$$

where $k_{OH+SO_2} = 9 \times 10^{-13}$ cm^3 molec^{-1} s^{-1} for an identical setup with SO$_2$ instead of D5 (Janechek, Marek, et al., 2019). The correlation between [H$_2$O] and OH exposure used to find the OH exposure for Experiments 9–19 is plotted in Fig. 5.B.2. Since the O$_3$ concentrations differed in Experiments 9–15 and 16–19, the correlation between the [H$_2$O] and the OH exposure is also different. Note that, for Experiments 9–19, the OH exposure calculated using Equation 5.2 is about twice that calculated using Equation 5.1. This effect may be due to the regeneration of OH during the oxidation of D5 or the absorption of OH into the aerosol particles. Ideally, we seek to report the OH exposure excluding any regeneration. So, for Experiments 9–19, the OH exposure is calculated with Equation 5.2. Experiments 1–8 and those from Wu and Johnston (2017) use Equation 5.1, but have a positive uncertainty equal to their calculated OH exposure. Note that, for Experiments 1–8, OH concentration is calculated independently of the OH exposure. For Experiments 9–19, OH concentration is the ratio of the OH exposure to the residence time of the reactor.

5.3   Results

SOA yields and experimental conditions are given in Table 5.1 with estimated uncertainties. These SOA yields vary from 0 to 110% (158% at the upper bound of the wall-deposition-corrected value), an even wider range than that reported by the literature of 8–50% (Janechek, Marek, et al., 2019; Wu and Johnston, 2017).

Table 5.1: Experimental conditions. All experiments began with $[NO_2]_0 = 0$ ppb. The estimated uncertainty of $[NO]_0$ is 5 ppb. Experiments in which NO was continuously injected maintained a rate of 1 ppb min^{-1}, starting at the inception of radiation. For Experiment 8, due to a pulse of OH when the CH_3NO_2 initially photolyzes followed by a steadier concentration, two OH mixing ratios are given: $[OH]=2 \times 10^8$ molec cm^{-3} at the beginning of the experiment and $[OH]=1 \times 10^6$ molec cm^{-3} at its end. The uncertainties associated with the chamber and CPOT temperature are $< 0.5°C$ and $0.1°C$, respectively. The uncertainty in the OH concentrations for the chamber and CPOT experiments are 5×10^5 molec cm^{-3} and 1×10^6 molec cm^{-3}, respectively. Uncertainties in the OH exposure for the CPOT experiments are 5×10^{10} molec s cm^{-3}. For the chamber experiments, the uncertainties in the negative direction are 4×10^{10} molec cm^{-3} and in the positive direction are the value of OH exposure reported for the experiment. For the CPOT experiments, the upper estimate of the wall-deposition-corrected SOA yield is shown in parentheses. The negative uncertainty in the SOA yields of the CPOT experiments is the reported uncertainty subtracted from the uncorrected Y and the positive uncertainty is the sum of the corrected Y and the reported uncertainty.

Label	Reactor	$[NO]_0$ (ppb)	Contin. NO Injection?	OH source	$[OH]$ (molec cm^{-3})	$[OH]$ exposure (molec s cm^{-3})	T (°C)	$[D5]_0$ (ppb)	$[Surf\ Area]_0$ (10^3 μm^2 cm^{-3})	SOA Yield
1	Chamber	0	No	H_2O_2	4.5×10^6	9×10^{10}	26.6	497 ± 5	3.6 ± 0.3	$1.5 \pm 1.5\%$
2	Chamber	0	No	H_2O_2	3.8×10^6	8×10^{10}	26.5	298 ± 3	5.1 ± 0.3	$5.7 \pm 8.0\%$
3	Chamber	0	No	H_2O_2	2.2×10^6	6×10^{10}	27.6	30 ± 1	0.8 ± 0.1	$0 \pm 0.3\%$
4	Chamber	0	No	H_2O_2	1.6×10^6	3×10^{10}	17.7	580 ± 5	2.4 ± 0.2	$2.6 \pm 4.0\%$
5	Chamber	82	Yes	H_2O_2	5.0×10^6	1.3×10^{11}	26.6	696 ± 9	3.9 ± 0.3	$0.7 \pm 0.7\%$
6	Chamber	86	Yes	H_2O_2	4.3×10^6	9×10^{10}	26.6	650 ± 6	1.1 ± 0.1	$0.2 \pm 0.3\%$
7	Chamber	76	No	H_2O_2	5.5×10^6	1.3×10^{11}	23.6	591 ± 2	0	$0 \pm 0.1\%$
8	Chamber	84	No	CH_3NO_2	$10^6 - 10^{8.3}$	2.3×10^{11}	26.6	603 ± 5	0.6 ± 0.1	$0 \pm 0.1\%$
9	CPOT	0	No	O_3	2.0×10^7	1.4×10^{10}	23.0	262 ± 10	0	$1.1(1.9) \pm 1.1\%$
10	CPOT	0	No	O_3	2.3×10^8	1.5×10^{11}	23.0	262 ± 10	0	$1.8(2.9) \pm 0.2\%$
11	CPOT	0	No	O_3	5.0×10^8	3.3×10^{11}	23.0	262 ± 10	0	$6.0(9.2) \pm 0.6\%$
12	CPOT	0	No	O_3	2.3×10^8	1.5×10^{11}	23.0	262 ± 10	0	$4.6(6.7) \pm 0.4\%$
13	CPOT	0	No	O_3	1.2×10^9	7.8×10^{11}	23.0	262 ± 10	0	$14(19) \pm 1\%$
14	CPOT	0	No	O_3	1.5×10^9	1.0×10^{12}	23.0	262 ± 10	0	$24(32) \pm 2\%$
15	CPOT	0	No	O_3	1.6×10^9	1.1×10^{12}	23.0	262 ± 10	0	$35(49) \pm 2\%$
16	CPOT	0	No	O_3	4.7×10^9	3.2×10^{12}	23.0	246 ± 3	0	$109(157) \pm 7\%$
17	CPOT	0	No	O_3	4.8×10^9	3.2×10^{12}	23.0	246 ± 3	0	$110(158) \pm 7\%$
18	CPOT	0	No	O_3	4.7×10^9	3.1×10^{12}	23.0	82 ± 3	0	$102(138) \pm 6\%$
19	CPOT	0	No	O_3	4.9×10^9	3.3×10^{12}	23.0	82 ± 3	0	$94(128) \pm 6\%$

Between the experiments performed here and those in the literature, the OH concentrations and OH exposures vary widely. Determining which of these is the relevant parameter is critical to extrapolating the SOA yield data to the atmosphere: environmentally relevant OH concentrations are on the order of 10^6 molec cm^{-3}, but since D5 is primarily lost to OH and has a half life of 3.5–7 days, OH exposures on the order of 10^{12} molec s cm^{-3} are also relevant. Due to experimental limitations, in particular an inability to perform experiments for multiple days without diluting the sample and otherwise changing the conditions, these two variables are often correlated.

Nonetheless, differentiating the effects of these two variables is possible. If a chemical process occurs in which the reaction of D5 and OH forms an intermediate or a second-generation product that then either reacts with OH or fragments, then the competition between the two outcomes is moderated by the relative time required for self-reaction or reaction with OH. This means that, as the OH concentration increases, the OH-reaction product will predominate. If this is the chemistry that D5 undergoes, then we would expect the SOA yield to depend solely on the OH concentration and not on the OH exposure.

Figure 5.1a shows the relationship between the measured OH concentrations and SOA yields for the experiments performed here as well as those from the literature. There is very good agreement between the chamber and CPOT experiments for similar OH concentration (shown in purple and orange, respectively). Moreover, the sharp increase in measured Y starting at [OH] $\approx 10^9$ molec cm^{-3} matches the hypothesis that there is a competitive process moderated by OH concentration.

Also plotted in Fig. 5.1a is the correlation between the [OH] and Y for experiments performed by Wu and Johnston (2017). These results, which were used by McDonald et al. (2018) for evaluating the contributions of D5 to aerosol levels in the Los Angeles Basin, were performed in a 50 L PFA photooxidation chamber with reported OH concentrations of ~10^8 molec cm^3 (the error of which "was difficult to assess") at 27°C and a relative humidity (RH) of 8–10%. Their data are neither vapor- nor wall-deposition corrected. For similar initial D5 concentrations (and, hence, for similar organic aerosol concentrations), the measured SOA yields were uniformly higher in experiments that were initiated with ammonium sulfate seed than those that were not (see Fig. 5.3b). We, therefore, show the seeded and unseeded experiments in Fig. 5.1 in blue and red, respectively. OH concentration in the experiments reported by Wu and Johnston (2017) were calculated by replacing the precursor with SO$_2$,
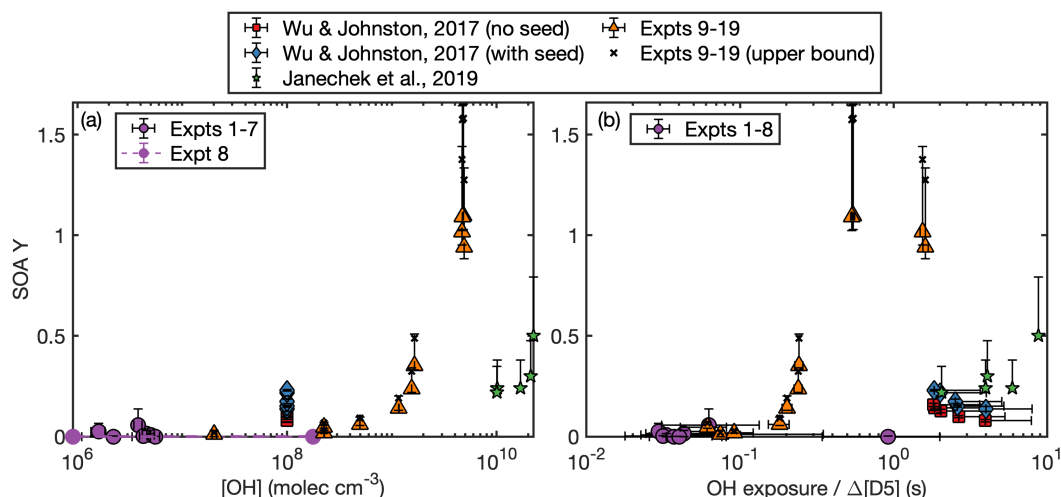
Figure 5.1: Measured SOA yield as a function of the (a) OH concentration and (b) OH exposure normalized to the amount of reacted D5 for the experiments performed here and by Janechek, Marek, et al. (2019) and Wu and Johnston (2017). In panel (a), Experiment 8, which was performed with methyl nitrite, is shown in purple and not outlined in black and the initial and final OH concentrations are connected with a purple dashed line. The vast majority of this experiment was performed under the lower OH concentration.

measuring the formation of aerosol, and assuming that all the SO_2 reacts with OH to form H_2SO_4 and all the sulfuric acid forms aerosol with minimal wall loss (Hall, Pennington, and Johnston, 2013). Because of the uncertainties present for each step of this measurement, it seems reasonable that this [OH] estimate could be too low by at least a factor of 2.

Other instrumental and analysis uncertainties might close the gap between the OH concentrations measured by Wu and Johnston (2017) and the OH concentrations found in the experiments performed here. For example, the CPOT experiments and the Wu and Johnston (2017) experiments calculate the total OH exposure experienced in the flow reactor and then find the OH concentration by taking the ratio of this exposure and the residence time. Since the reactor used by Wu and Johnston (2017) is a rectangular bag, regions will exist with differing OH concentrations. If this reactor has slightly higher concentrations in some points or its residence time is overestimated or if the residence time for CPOT is a slight underestimate (we calculated an uncertainty of ~2%), this could account for the remaining disagreement between the data from the two experimental setups.

Furthermore, differences in the analysis could change the relevant SOA yields calculated. For Experiments 10–19, we measured both the initial and the final D5

concentration and for Experiments 1–8 we continuously measured the concentration. Wu and Johnston (2017) measured the initial concentration and calculated the SOA yield by using the [OH] to estimate the amount of reacted D5. If Wu and Johnston (2017) underestimated the [OH], they might have correspondingly overestimated Y because they would have assumed less D5 reacted than in actuality. To achieve agreement to experiments performed here, then, the [OH] concentration could be different by less than a factor of 2 because of these confounding variables. We also assumed that the density of the SOA formed was 1.52 g cm^{-3} and Wu and Johnston (2017) collected the aerosol onto filters and directly measured the mass formed. Much secondary organic aerosol has a density of 1.4–1.6 g cm^{-3} (Kostenidou et al., 2007), but deviations from this range could account for some of the discrepancy between the sets of experiments. Additionally, since the CPOT experiments were unseeded, seeded experiments increased the measured Y, which could also have led to better agreement.

Data from Janechek, Marek, et al. (2019) show the opposite disagreement: OH concentrations are a factor of 2 too large to perfectly match the results presented here. Janechek, Marek, et al. (2019) performed their experiments in a 13.3 L potential aerosol mass oxidation flow reactor (PAM OFR) with OH concentrations on the order of 10^{10} molec cm^{-3}. They reported the total OH exposure and calculated it similarly to the method used for CPOT (using Equation 5.2) and we convert this to the [OH] plotted by dividing this OH exposure by the residence time (calculated from the size of the reactor and the reported flow rate) and assuming that OH concentrations throughout the reactor are approximately constant. Just as with the CPOT experiments, their experiments are unseeded, and they measure the initial and final D5 concentration directly. They used an SOA density of 0.959 g cm^{-3} to calculate Y and the positive error bars shown are an adjustment of their SOA yields to the 1.52 g cm^{-3} used in the experiments performed here. While they corrected for particle loss downstream of their reactors, they did not account for those particles lost within their reactor; this could have led to an underestimate of their SOA yields. While the methods to calculate [OH] were very similar, the CPOT and the PAM OFR are nevertheless different and, therefore, [OH] could vary locally in dissimilar ways between the reactors. Since the chemical mechanism shift would be based on the local OH concentration and not the average, a factor of 2 disagreement could be within the uncertainty. A comparison between predicted and estimated OH exposures for the PAM OFR indicates agreement only within a factor of 3 (Li et al., 2015; Janechek, Marek, et al., 2019), so a factor of 2 disagreement in [OH] would

seem to be with the uncertainties for the CPOT and the PAM OFR.

If the SOA yield depends on the OH exposure, instead of the OH concentration, we would expect that the dependence would actually be on the OH exposure normalized to the amount of reacted D5. That is, the number of OH radicals available per reacted D5 molecule, as is shown in Fig. 5.1b. This figure shows a factor of 10 disagreement between data from Wu and Johnston (2017) and Janechek, Marek, et al. (2019) and that from the experiments conducted here. From the CPOT, Experiments 18 (OH exposure/Δ[D5]=1.5 s, Y=102%) and 19 (OH exposure/Δ[D5]=1.6 s, Y=94%), which had [D5]$_0$=82 ppb, differ significantly from Experiments 16 and 17 (OH exposure/Δ[D5]=0.5 s, Y=109% and 110%), which had [D5]$_0$=246 ppb and otherwise identical experimental conditions. This suggests that OH exposure is not the driving force in determining the SOA yield.

The major difference in Experiments 16–17 and 18–19 is the percent of D5 that reacted by the end of the experiment: 97% for Experiment 16, 98% for Experiment 17, and 100% for Experiments 18–19. Figure 5.2 shows the fraction reacted compared to the SOA yield for experiments performed in this study and those in the literature. This fit could indicate that there are later generation oxidation products that form large amounts of aerosol and that the gas-phase reaction rate to form the low-volatility later-generation oxidation product is slower than the gas-phase reaction rate to form the first-generation product (Kroll and Seinfeld, 2008). However, if this were the case, Experiments 18–19 (Y=102% and 94%), in which all of the initial D5 reacted throughout the experiment, should show higher SOA yields than Experiments 16–17 (Y=109% and 110%), which they do not. Additionally, if later generation oxidation products produced more aerosol, there should be a correlation between Y and the OH exposure normalized to the amount of reacted D5 (Fig. 5.1b), which is also not accurate. The color axis in Fig. 5.2 indicates that across studies the fraction of D5 reacted correlates with the [OH]. So, there is no reason to suspect that it is the later-generation products that matter instead of the OH concentration for determining SOA yield.

If OH concentration is the strict determinant of the SOA yield, Experiments 16–17 should give the same SOA yields as Experiments 18–19. These experiments do have similar SOA yields, and Experiments 16–18 are all within error. If there is a difference, it might be attributed to a dependence on the organic aerosol mass concentration (M) at high [OH]. This would indicate that at high mass loadings, relatively more low-volatility products partition into the particle phase. This could
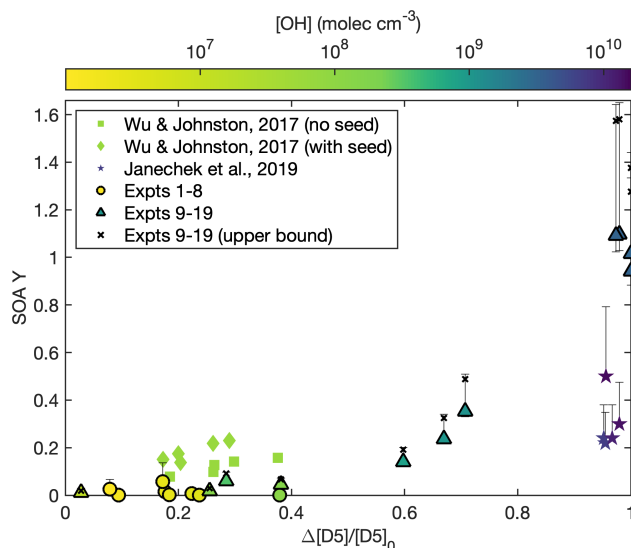
Figure 5.2: Measured SOA yield as a function of the fraction of D5 reacted at the end of the experiment. The color of each point indicates the OH concentration for the experiment. Experiments performed here are circles and triangles and are outlined in black, those by Janechek, Marek, et al. (2019) are stars, and those by Wu and Johnston (2017) are squares and diamonds. The wall-deposition-corrected data for Experiments 9–19 are shown as black Xs.

also explain the disagreement in Fig. 5.1a between the CPOT experiments and the data from Janechek, Marek, et al. (2019). Partitioning between the particle and gas phases does not significantly change the dependence of Y on [OH] for the experiments performed in this study: as shown in Fig. 5.3a, Experiment 15 (triangle with M=991 μg m^{-3}) has a similar M as Experiments 18 and 19 (triangles with M of 1267 and 1175 μg m^{-3}, respectively) but due to their differing [OH], they have very different SOA yields. Fig. 5.3b shows the same for a comparison between the lower [OH] experiments (Experiments 1–10); even at the same M, the OH concentration is what matters for determining Y. Note that the seed-surface-area dependence of experiments performed by Wu and Johnston (2017) is likely a result of the loss of oxidation product to the reactor's walls instead of to condensation onto particles suspended in the bulk of the chamber. The vast majority of the experiments performed under atmospherically relevant OH concentrations were also seeded and showed low SOA yields. For all experiments with [OH]$< 10^8$ molec cm^{-3}, the SOA yield is still $< 6\%$ and, in general, is closer to ~1%.

We do not expect that either relative humidity or temperature affect the SOA yield sufficiently that these would account for the vastly different measured SOA yields under different OH concentration. Experiments 1–8 were performed at RH levels
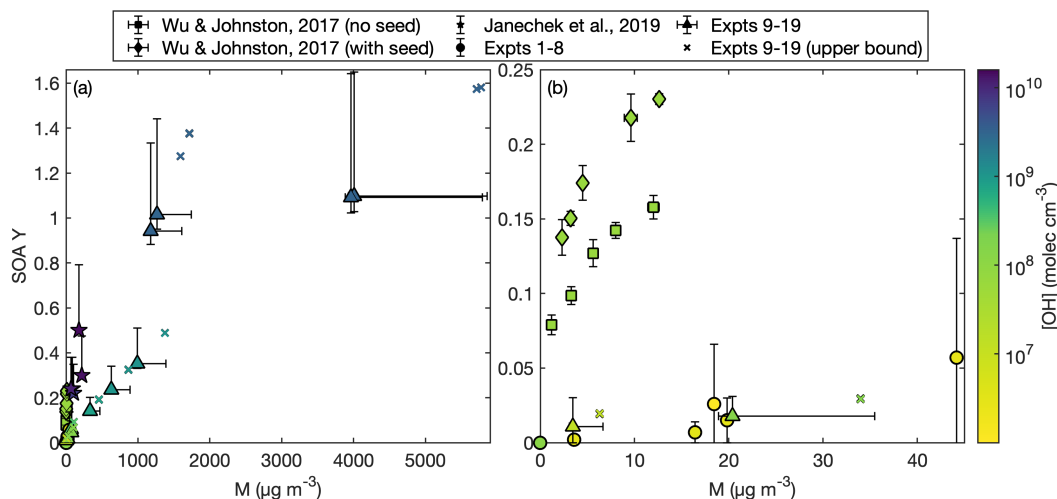
Figure 5.3: SOA yield as a function of organic aerosol mass concentration (M) as compared to that reported by Wu and Johnston (2017) and Janechek, Marek, et al. (2019). The color axis is the OH concentration. Even for similar M, an order of magnitude discrepancy exists in SOA yield. Panel (a) shows the entire scale and panel (b) focuses on experiments with M< 34 µg m^{-3}. Since the experiments reported by Wu and Johnston (2017) showed a dependence on the presence or absence of aerosol seed, those experiments are shown separately. CPOT experiments performed in this study were conducted without seed aerosol.

between 2 and 6%, Experiments 9–19 were between 0 and 30% RH, those by Wu and Johnston (2017) were performed at 27°C and a RH of 8–10%, and the experiments from Janechek, Marek, et al. (2019) were run at 24°C and an RH of 25% or 45%. At similar values of relative humidity but different OH concentrations (e.g., Experiments 9–12, which all have RH $\leq$ 6%), the OH concentration matters for determining the SOA yield. For Experiments 3 and 4, the lowest and highest temperatures studied here (17.7 and 27.6°C, respectively), the measured SOA Y varies by < 3%, which is within the uncertainty.

The NO$_x$ concentrations also do not seem to affect the SOA yield, as discussed in Appendix 5.A. While the D5 oxidation chemistry may depend on the NO mixing ratio (but not on the NO$_2$ mixing ratio), this has no effect on the measured SOA yield.

5.4 Conclusions

The atmospheric aerosol formation potential of D5 was investigated under a range of OH concentrations and exposures. While secondary organic aerosol (SOA) yields can reach 110% (158% at the upper limit) at OH mixing ratios of $\sim 5 \times 10^9$ molec

cm^{-3}, at atmospherically relevant OH concentrations ($[OH] \lesssim 10^{7.5}$ molec cm^{-3}), SOA yields do not exceed 6% and are likely ~1%. It is the OH concentration, and not the OH exposure, that affects the SOA yield.

This demonstrates the importance of extrapolating to the atmosphere at OH concentrations close to atmospheric levels and of using the appropriate reactor for the chemistry of a precursor to determine the secondary organic aerosol formation: if OH concentration is dominant, environmental chambers may be more useful, but if OH exposure matters, then flow tubes that have high OH mixing ratios may be the best tool.

Despite the relatively low SOA yields of D5 measured here at ambient OH concentrations, silicon has been observed in ambient aerosol and its concentration is likely somewhat population (and not vehicle) dependent (Bzdek et al., 2014; Pennington et al., 2012). Since D5 is so abundant, it could be possible that the silicon present is from D5 or other volatile methyl siloxanes, just in lower concentrations than expected. Another possibility is that silicon in the aerosol-phase comes from polydimethylsiloxanes (Weschler, 1988).

Since the aerosol formed from volatile chemical products (VCPs) may dominate the high concentrations of particulate matter found in urban areas (McDonald et al., 2018), understanding those VCPs that have high aerosol-formation potential and those which do not is important for formulating policy to reduce human exposure to organic aerosol.

APPENDIX

5.A NO$_x$-Dependence of SOA Yield

For atmospherically relevant OH concentrations, the SOA yield does not change depending on the NO$_x$ concentration: experiments with no NO$_x$ present are on both the lower and higher end of the SOA yields for the chamber experiments. Those with a continuous injection of NO throughout the experiment, which ensured that the NO/HO$_2$ ratio remained high even as the NO reacted, had SOA yields similar to both the no NO$_x$ and the initial NO experiments. This indicates that different NO mixing ratios did not have an effect on the measured SOA yield.

This does not imply that the chemistry is independent of NO concentration. Indeed, the concentrations of gas-phase fragments detected by the CIMS at m/z 139, 169, 243, and 317, which likely correspond to oxygenated fragments of D5, depend on the NO concentration but not the NO$_2$ concentration. Figure 5.A.1 shows the signal for these fragments normalized to the reagent ion as a function of the NO concentration at any time. Note that, since some of the methyl nitrite is detected as NO, data from Experiment 8 were not included. Figure 5.A.2 shows the NO and NO$_2$ concentrations in each experiment as a function of time.

Fu et al. (2020) found that the gas-phase rearrangement of methylsiloxanes is dependent on the NO/HO$_2$ ratio. A comparison of Figs. 5.A.1 and 5.A.3 shows that the concentration of some gas-phase fragments is dependent on the NO mixing ratio but not on the NO$_2$ mixing ratio. This is consistent with gas-phase products depending on the NO/HO$_2$ ratio. Note that at all NO/HO$_2$ ratios investigated, aerosol formation is still minimal when [OH] is small.
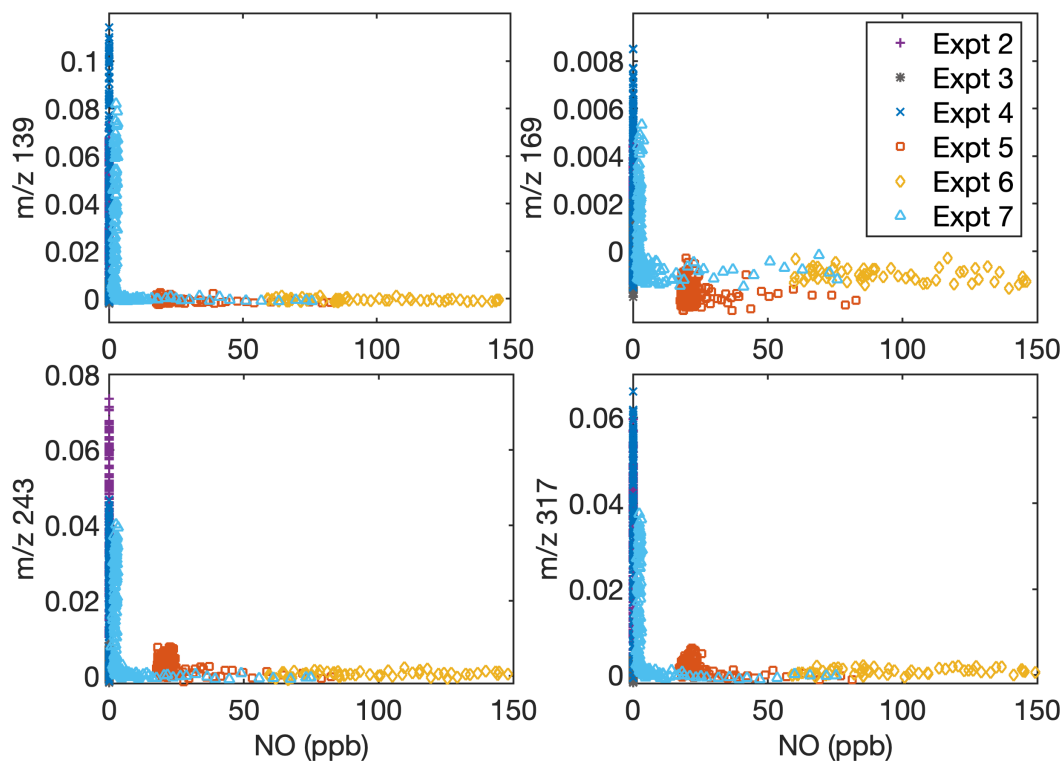
Figure 5.A.1: Dependence of gas-phase D5 oxidation products on the NO concentration in the chamber indicates that oxidation chemistry changes depending on NO concentrations. Signals normalized to the reagent concentrations with (a) m/z=139, (b) m/z=169, (c) m/z=243, and (d) m/z=317 are shown as a function of NO concentration. Experiment 6 has [NO] extending to >450 ppb, but since the normalized signal remains close to 0, data above [NO]=150 ppb are cut off for clarity. Because of the inaccuracy of NO measurements during oxidation when methyl nitrite is present, Experiment 8 is not included.
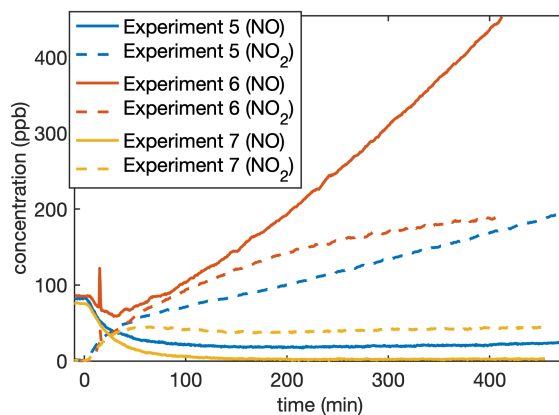
Figure 5.A.2: For the experiments that included NO_x, the NO and NO_2 concentrations as a function of the time since the onset of oxidation. Experiment 8 is not included, since methyl nitrite was present. The measurement uncertainty is ~5 ppb, but any organonitrates would also be measured as NO_2.
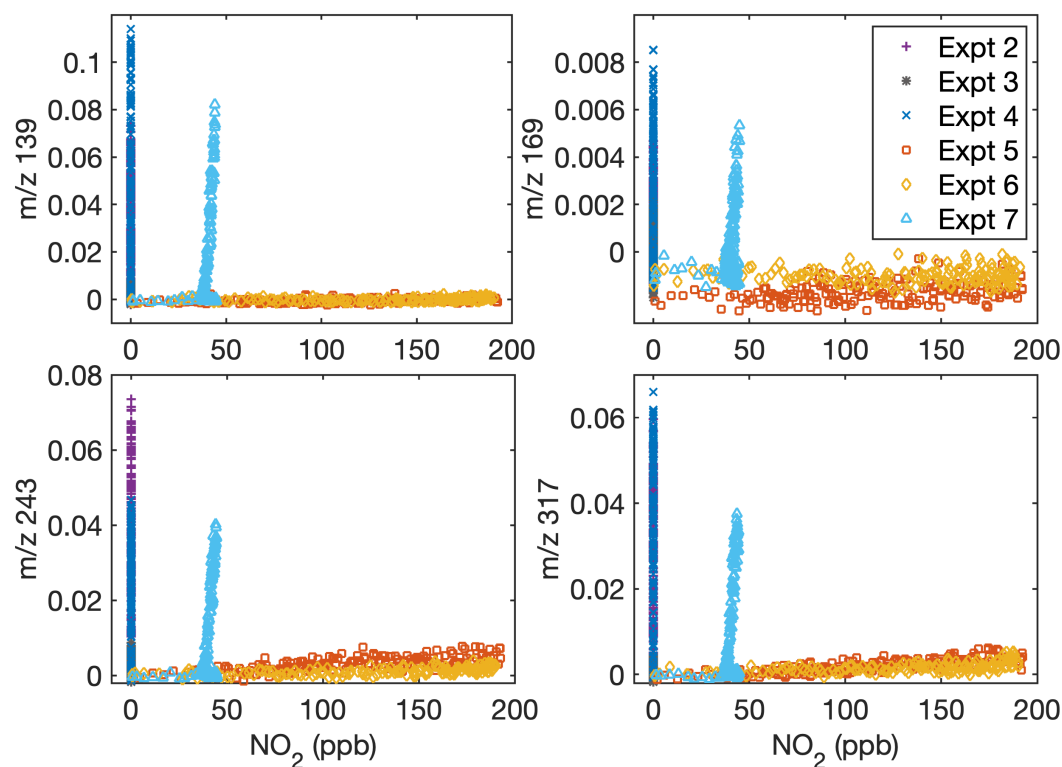
Figure 5.A.3: Dependence of gas-phase D5 oxidation products on the NO_2 concentration in the chamber indicates that oxidation chemistry does not depend on NO_2 (but does depend on NO, see Fig. 5.A.1). Signals normalized to the reagent concentrations with (a) m/z=139, (b) m/z=169, (c) m/z=243, and (d) m/z=317 are shown as a function of NO_2 concentration. Because of the inaccuracy of NO_2 measurements during oxidation when methyl nitrite is present, Experiment 8 is not included.

5.B Supplementary Information
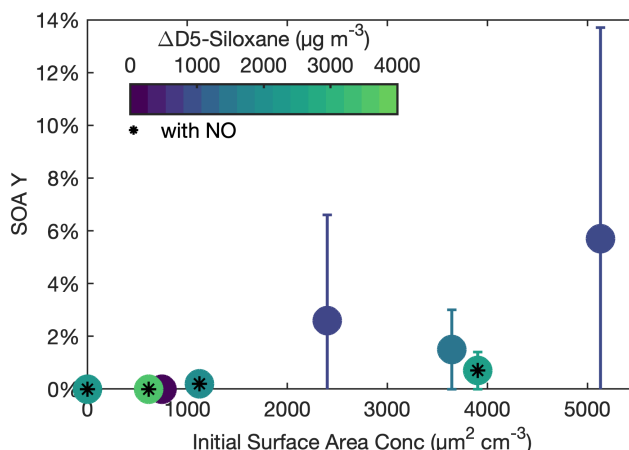
Figure 5.B.1: SOA yield at the end of each experiment with the associated uncertainty is shown as a function of the initial seed surface area concentration. The color of each point represents the amount of D5 that reacted throughout the entire experiment. Experiments with NO_x present include a black asterisk in their center.
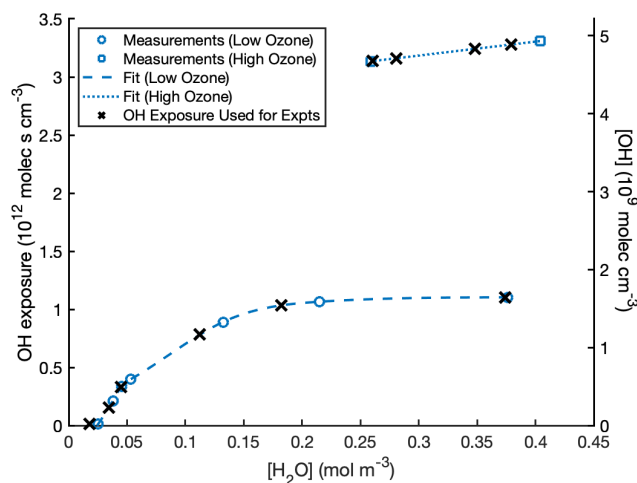
Figure 5.B.2: Determination of the OH exposure and, correspondingly, of the OH concentration of Experiments 9–19. Blue circles and squares are the measurements of the OH exposure using the reaction of SO_2 for the low and high O_3 cases, respectively. The dashed and dotted lines are the fits to these measurements and the black Xs are the corresponding OH exposure values used for Experiments 9–19.

References

Ahrens, Lutz, Tom Harner, and Mahiba Shoeib (Aug. 2014). "Temporal Variations of Cyclic and Linear Volatile Methylsiloxanes in the Atmosphere Using Passive Samplers and High-Volume Air Samplers." In: *Environ. Sci. Technol.* 48.16, pp. 9374–9381. DOI: 10.1021/es502081j.

Alton, Mitchell W. and Eleanor C. Browne (2020). "Atmospheric Chemistry of Volatile Methyl Siloxanes: Kinetics and Products of Oxidation by OH Radicals and Cl Atoms." In: *Environ. Sci. Technol.* 54.10, pp. 5992–5999. DOI: 10.1021/acs.est.0c01368.

Atkinson, Roger (1991). "Kinetics of the Gas-Phase Reactions of a Series of Organosilicon Compounds with OH and NO_3 Radicals and O_3 at 297 ± 2 K." In: *Environ. Sci. Technol.* 25.5, pp. 863–866. DOI: 10.1021/es00017a005.

Balducci, Catia, Mattia Perilli, Paola Romagnoli, and Angelo Cecinato (2012). "New Developments on Emerging Organic Pollutants in the Atmosphere." In: *Environ. Sci. Pollut. R.* 19.6, pp. 1875–1884. DOI: 10.1007/s11356-012-0815-2.

Burkholder, James B. et al. (2017). "The essential role for laboratory studies in atmospheric chemistry." In: *Environ. Sci. Technol.* 51.5, pp. 2519–2528. ISSN: 0013-936X. DOI: 10.1021/acs.est.6b04947.

Buser, Andreas M., Christian Bogdal, Matthew MacLeod, and Martin Scheringer (July 2014). "Emissions of Decamethylcyclopentasiloxane from Chicago." In: *Chemosphere* 107, pp. 473–475. DOI: 10.1016/j.chemosphere.2013.12.034.

Buser, Andreas M., Amelie Kierkegaard, Christian Bogdal, Matthew MacLeod, Martin Scheringer, and Konrad Hungerbühler (July 2013). "Concentrations in Ambient Air and Emissions of Cyclic Volatile Methylsiloxanes in Zurich, Switzerland." In: *Environ. Sci. Technol.* 47.13, pp. 7045–7051. DOI: 10.1021/es3046586.

Bzdek, Bryan R., Andrew J. Horan, M. Ross Pennington, Nathan J. Janechek, Jaemeen Baek, Charles O. Stanier, and Murray V. Johnston (Oct. 2014). "Silicon is a Frequent Component of Atmospheric Nanoparticles." In: *Environ. Sci. Technol.* 48.19, pp. 11137–11145. DOI: 10.1021/es5026933.

Carter, Layne, Jay Perry, Matthew J. Kayatin, Mark Wilson, Gregory J. Gentry, Elizabeth Bowman, Oscar Monje, Tony Rector, and John Steele (2015). "Process Development for Removal of Siloxanes from ISS Atmosphere." In: *45th International Conference on Environmental Systems (July 12–16, 2015)*. 74. Bellevue, Washington. URL: http://hdl.handle.net/2346/64361.

Charan, Sophia M., Reina S. Buenconsejo, and John H. Seinfeld (2020). "Secondary organic aerosol yields from the oxidation of benzyl alcohol." In: *Atmospheric Chemistry and Physics* 20.21, pp. 13167–13190. DOI: 10.5194/acp-20-13167-2020.

Charan Sophia M .and Kong, Weimeng, Richard C. Flagan, and John H. Seinfeld (2018). "Effect of particle charge on aerosol dynamics in Teflon environmental chambers." In: *Aerosol Sci. Technol.* 52.8, pp. 854–871. DOI: 10.1080/02786826.2018.1474167.

Coggon, Matthew M. et al. (2018). "Diurnal Variability and Emission Pattern of Decamethylcyclopentasiloxane (D5) from the Application of Personal Care Products in Two North American Cities." In: *Environ. Sci. Technol.* 52.10, pp. 5610–5618. DOI: 10.1021/acs.est.8b00506.

Finewax, Zachary, Demetrios Pagonis, Megan S. Claflin, Anne V. Handschy, Wyatt L. Brown, Olivia Jenks, Benjamin A. Nault, Douglas A. Day, Brian M. Lerner, Jose L. Jimenez, Paul J. Ziemann, and Joost A. de Gouw (2020). "Quantification and Source Characterization of Volatile Organic Compounds from Exercising and Application of Chlorine-Based Cleaning Products in a University Athletic Center." In: *Indoor Air* November, pp. 1–17. DOI: 10.1111/ina.12781.

Fu, Zihao, Hong Bin Xie, Jonas Elm, Xirui Guo, Zhiqiang Fu, Zhiqiang Fu, and Jingwen Chen (2020). "Formation of Low-Volatile Products and Unexpected High Formaldehyde Yield from the Atmospheric Oxidation of Methylsiloxanes." In: *Environ. Sci. Technol.* 54.12, pp. 7136–7145. DOI: 10.1021/acs.est.0c01090.

Gkatzelis, Georgios I., Matthew M. Coggon, Brian C. McDonald, Jeff Peischl, Kenneth C. Aikin, Jessica B. Gilman, Michael Trainer, and Carsten Warneke (2021). "Identifying Volatile Chemical Product Tracer Compounds in U.S. Cities." In: *Environ. Sci. Technol.* 55.1, pp. 188–199. DOI: 10.1021/acs.est.0c05467.

Hall, Wiley A., M. Ross Pennington, and Murray V. Johnston (2013). "Molecular Transformations Accompanying the Aging of Laboratory Secondary Organic Aerosol." In: *Environ. Sci. Technol.* 47.5, pp. 2230–2237. DOI: 10.1021/es303891q.

Hobson, J. F., R. Atkinson, and Carter W. P. L. (1997). "Chapter 6: Volatile Methylsiloxanes." In: *The Handbook of Environmental Chemistry Vol. 3 Part H: Organosilicon Materials*. Ed. by Grish Chandra. 9. Berlin: Springer, pp. 137–180. DOI: 10.1007/978-3-540-68331-5.

Huang, Yuanlong, Matthew M. Coggon, Ran Zhao, Hanna Lignell, Michael U. Bauer, Richard C. Flagan, and John H. Seinfeld (2017). "The Caltech Photooxidation Flow Tube reactor: Design, Fluid Dynamics and Characterization." In: *Atmos. Meas. Tech.* 10.10, pp. 839–867. DOI: 10.5194/amt-10-839-2017.

Huang, Yuanlong and John H. Seinfeld (2019). "A Note on Flow Behavior in Axially-Dispersed Plug Flow Reactors with Step Input of Tracer." In: *Atmos. Environ. X* 1, pp. 1–6. DOI: 10.1016/j.aeaoa.2019.100006.

Hughes, Lauren, Don Mackay, David E. Powell, and Jaeshin Kim (2012). "An Updated State of the Science EQC Model for Evaluating Chemical Fate in the Environment: Application to D5 (Decamethylcyclopentasiloxane)." In: *Chemosphere* 87.87, pp. 118–124. DOI: 10.1016/j.chemosphere.2011.11.072.

Janechek, Nathan J., Kaj M. Hansen, and Charles O. Stanier (2017). "Comprehensive Atmospheric Modeling of Reactive Cyclic Siloxanes and Their Oxidation Products." In: *Atmos. Chem. Phys.* 17, pp. 8357–8370. DOI: 10.5194/acp-17-8357-2017.

Janechek, Nathan J., Rachel F. Marek, Nathan Bryngelson, Ashish Singh, Robert L. Bullard, William H. Brune, and Charles O. Stanier (2019). "Physical Properties of Secondary Photochemical Aerosol from OH Oxidation of a Cyclic Siloxane." In: *Atmos. Chem. Phys.* 19, pp. 1649–1664. DOI: `10.5194/acp-19-1649-2019`.

Kim, Jaeshin and Shihe Xu (Dec. 2017). "Quantitative Structure-Reactivity Relationships of Hydroxyl Radical Rate Constants for Linear and Cyclic Volatile Methylsiloxanes." In: *Environ. Toxicol. Chem.* 36.12, pp. 3240–3245. DOI: `10.1002/etc.3914`.

Kostenidou, Evangelia, Spyros N. Pandis, Ravi K. Pathak, Spyros N. Pandis, Evangelia Kostenidou, and Spyros N. Pandis (2007). "An Algorithm for the Calculation of Secondary Organic Aerosol Density Combining AMS and SMPS Data." In: *Aerosol Sci. Technol.* 41.11, pp. 1002–1010. DOI: `10.1080/02786820701666270`.

Kroll, Jesse H. and John H. Seinfeld (May 2008). "Chemistry of Secondary Organic Aerosol: Formation and Evolution of Low-Volatility Organics in the Atmosphere." In: *Atmos. Environ.* 42.16, pp. 3593–3624. DOI: `10.1016/j.atmosenv.2008.01.003`.

Li, Rui, Brett B. Palm, Amber M. Ortega, James Hlywiak, Weiwei Hu, Zhe Peng, Douglas A. Day, Christoph Knote, William H. Brune, Joost A. De Gouw, and Jose L. Jimenez (2015). "Modeling the Radical Chemistry in an Oxidation Flow Reactor: Radical Formation and Recycling, Sensitivities, and the OH Exposure Estimation Equation." In: *J. Phys. Chem. A* 119.19, pp. 4418–4432. DOI: `10.1021/jp509534k`.

Mackay, Donald, Christina E. Cowan-Ellsberry, David E. Powell, Kent B. Woodburn, Shihe Xu, Gary E. Kozerski, and Jaeshin Kim (2015). "Decamethylcyclopentasiloxane (D5) Environmental Sources, Fate, Transport, and Routes of Exposure." In: *Environ. Toxicol. Chem.* 34.12, pp. 2689–2702. DOI: `10.1002/etc.2941`.

Mai, Huajun, Weimeng Kong, John H. Seinfeld, and Richard C. Flagan (Oct. 2018). "Scanning DMA Data Analysis II. Integrated DMA-CPC Instrument Response and Data Inversion." In: *Aerosol Sci. Technol.* 6826, pp. 1–35. ISSN: 0278-6826. DOI: `10.1080/02786826.2018.1528006`.

Malloy, Quentin G. J., Shunsuke Nakao, Li Qi, Rebecca Austin, Clayton Stothers, Hiroyuki Hagino, and David R. Cocker III (2009). "Real-Time Aerosol Density Determination Utilizing a Modified Scanning Mobility Particle Sizer—Aerosol Particle Mass Analyzer System." In: *Aerosol Sci. Technol.* 43.7, pp. 673–678. DOI: `10.1080/02786820902832960`.

McDonald, Brian C. et al. (Feb. 2018). "Volatile chemical products emerging as largest petrochemical source of urban organic emissions." In: *Science* 359.6377, pp. 760–764. ISSN: 0036-8075. DOI: `10.1126/science.aaq0524`.

McLachlan, Michael S., Amelie Kierkegaard, Kaj M. Hansen, Roger Van Egmond, Jesper H. Christensen, and Carsten A. Skjøth (2010). "Concentrations and Fate of Decamethylcyclopentasiloxane (D5) in the Atmosphere." In: *Environ. Sci. Technol.* 44.14, pp. 5365–5370. DOI: `10.1021/es100411w`.

Pennington, M. Ross, Joseph P. Klems, Bryan R. Bzdek, and Murray V. Johnston (2012). "Nanoparticle Chemical Composition and Diurnal Dependence at the CalNex Los Angeles Ground Site." In: *J. Geophys. Res.-Atmoss* 117.5, pp. 1–9. DOI: `10.1029/2011JD017061`.

Safron, Andreas, Michael Strandell, Amelie Kierkegaard, and Matthew Macleod (2015). "Rate Constants and Activation Energies for Gas-Phase Reactions of Three Cyclic Volatile Methyl Siloxanes with the Hydroxyl Radical." In: *Int. J. Chem. Kinet.* 47.7, pp. 420–428. DOI: `10.1002/kin.20919`.

Schwantes, Rebecca H., Sophia M. Charan, Kelvin H. Bates, Yuanlong Huang, Tran B. Nguyen, Huajun Mai, Weimeng Kong, Richard C. Flagan, and John H. Seinfeld (2019). "Low-volatility compounds contribute significantly to isoprene secondary organic aerosol (SOA) under high-NO_x conditions." In: *Atmospheric Chemistry and Physics* 19.11, pp. 7255–7278. DOI: `10.5194/acp-19-7255-2019`.

Tang, Xiaochen, Pawel K. Misztal, William W. Nazaroff, and Allen H. Goldstein (2015). "Siloxanes are the Most Abundant Volatile Organic Compound Emitted from Engineering Students in a Classroom." In: *Environ. Sci. Technol. Let.* 2.11, pp. 303–307. DOI: `10.1021/acs.estlett.5b00256`.

Trump, Erica R., Scott A. Epstein, Ilona Riipinen, and Neil M. Donahue (Nov. 2016). "Wall effects in smog chamber experiments: a model study." In: *Aerosol Sci. Technol.* 50.11, pp. 1180–1200. ISSN: 0278-6826. DOI: `10.1080/02786826.2016.1232858`.

Weschler, Charles J. (July 1988). "Polydimethylsiloxanes Associated with Indoor and Outdoor Airborne Particles." In: *Sci. Total Environ.* 73.1-2, pp. 53–63. DOI: `10.1016/0048-9697(88)90186-6`.

Wu, Yue and Murray V. Johnston (2017). "Aerosol Formation from OH Oxidation of the Volatile Cyclic Methyl Siloxane (cVMS) Decamethylcyclopentasiloxane." In: *Environ. Sci. Technol.* 51.8, pp. 4445–4451. DOI: `10.1021/acs.est.7b00655`.

Xiao, Ruiyang, Ian Zammit, Zongsu Wei, Wei Ping Hu, Matthew MacLeod, and Richard Spinney (2015). "Kinetics and Mechanism of the Oxidation of Cyclic Methylsiloxanes by Hydroxyl Radical in the Gas Phase: An Experimental and Theoretical Study." In: *Environ. Sci. Technol.* 49.22, pp. 13322–13330. DOI: `10.1021/acs.est.5b03744`.

Xu, N. and D. R. Collins (2021). "Design and Characterization of a New Oxidation Flow Reactor for Laboratory and Long-Term Ambient Studies." In: *Atmos. Meas. Tech.* 14.4, pp. 2891–2906. DOI: `10.5194/amt-14-2891-2021`.

Xu, Shihe, Nicholas Warner, Pernilla Bohlin-Nizzetto, Jeremy Durham, and Debra McNett (Aug. 2019). "Long-Range Transport Potential and Atmospheric Persistence of Cyclic Volatile Methylsiloxanes Based on Global Measurements." In: *Chemosphere* 228, pp. 460–468. DOI: `10.1016/j.chemosphere.2019.04.130`.

A p p e n d i x   A

COMPUTATIONAL SIMULATION OF THE DYNAMICS OF SECONDARY ORGANIC AEROSOL FORMATION IN AN ENVIRONMENTAL CHAMBER

Sunol, Alp M., Sophia M. Charan, and John H. Seinfeld (2018). "Computational simulation of the dynamics of secondary organic aerosol formation in an environmental chamber." In: *Aerosol Science and Technology* 52.4, pp. 470–482. DOI: 10.1080/02786826.2018.1427209.

Taylor & Francis
Taylor & Francis Group

Check for updates
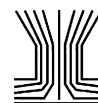
Computational simulation of the dynamics of secondary organic aerosol formation in an environmental chamber

A. M. Sunol, S. M. Charan, and J. H. Seinfeld

Division of Chemistry and Chemical Engineering, California Institute of Technology, Pasadena, California, USA

ABSTRACT

A key atmospheric process that is studied in laboratory chambers is the oxidation of volatile organic compounds to form low volatility products that condense on existing atmospheric particles (or nucleate) to form organic aerosol, so-called secondary organic aerosol. The laboratory chamber operates as a chemical reactor, in which a number of chemical and physical processes take place: gas-phase chemistry, transport of vapor oxidation products to suspended particles followed by uptake into the particles, deposition of vapors on the walls of the chamber, deposition of particles on the walls of the chamber, and coagulation of suspended particles. Understanding the complex interplay among these simultaneous physicochemical processes is necessary in order to interpret the results of chamber experiments. Here we develop and utilize a comprehensive computational model for dynamics of vapors and particles in a laboratory chamber and analyze chamber behavior over a range of physicochemical conditions.

1. Introduction

Understanding the chemical mechanisms by which volatile organic compounds (VOCs) are oxidized to low volatility products and secondary organic aerosol (SOA) is a major area of atmospheric chemistry research. The principal source of data on mechanisms of SOA formation is derived from laboratory chamber experiments, in which VOCs are caused to undergo oxidation, most frequently by the hydroxyl (OH) radical, to generate the low volatility products that condense into the particle phase (Schwantes et al. 2017). The SOA yield (Y) is determined as the ratio of the mass of organic aerosol formed to the mass of VOC reacted. To promote condensation of VOC oxidation products into the aerosol phase in the chamber, inert seed particles are customarily introduced to serve as sites for vapor condensation. Inevitably, the laboratory chamber contains walls, and interactions of vapors and particles with chamber walls must be accounted for in interpretation of data. For example, VOC oxidation products can condense onto growing aerosol or deposit onto the chamber wall, and even in the presence of seed aerosol, low volatility oxidation products may accumulate to a level at which they nucleate to form aerosol if the rate of generation of such products is sufficiently rapid to overcome the condensation sink. If an appreciable fraction of the VOC oxidation products deposits on the wall, then the SOA yield derived from the chamber data will be understated, perhaps significantly so. When such data are translated to the atmosphere, SOA yields would be correspondingly understated.

A common material used for flexible-walled environmental chambers is fluorinated ethylene propylene (FEP) Teflon film, customarily of thickness 0.05 mm. Irradiation of the chamber with actual or artificial sunlight is usually required to initiate photochemistry, and Teflon film has the attribute that it is essentially transparent to ultraviolet and visible radiation. From measurement of the size distribution of the aerosol suspended in the chamber over the course of an experiment, one can infer the mass of organic material that has condensed upon the original seed particles. There is ample evidence, however, that particles (Crump and Seinfeld 1981; McMurry and Grosjean 1985; McMurry and Rader 1985; Nah et al. 2017) and organic vapors (Matsunaga and Ziemann 2010; Yeh and Ziemann 2015; Zhang et al. 2015; Krechmer et al. 2016) can deposit on and adhere to Teflon chamber walls. To determine the SOA yield that would be produced in a "wall-less" chamber requires careful accounting for organic-containing

Color versions of one or more of the figures in the article can be found online at www.tandfonline.com/uast.

particles and low-volatility vapors that deposit on the chamber walls during the course of an experiment.

With recognition of the importance of competition between the suspended particles and the chamber wall for condensable vapors, strategies have been formulated to conduct VOC oxidation experiments using progressively higher concentrations of seed aerosol in order to enhance condensation of the low volatility vapors onto aerosol (Zhang et al. 2014; Nah et al. 2016, 2017). A consequence of this strategy is that, as the seed aerosol number concentration is increased, coagulation becomes increasingly important as a process affecting the aerosol size distribution (Pierce et al. 2008). The resulting complex coupling among aerosol condensational growth, wall deposition, and coagulation must be quantified.

The goal of the present work is to study numerically the temporal evolution of the vapor concentrations and the size- and composition-distributed aerosol in an environmental chamber undergoing gas-phase VOC oxidation over the range of parameter values characteristic of SOA formation. This includes particle growth by vapor condensation, deposition of vapor and particles to the chamber walls, and evolution of the particle size distribution due to simultaneous condensational growth and particle–particle coagulation. Several models exist based on numerical solution of the aerosol dynamic equations that address these phenomena. Meng et al. (1998) formulated a three-dimensional size-resolved and chemically resolved aerosol model, based in part on the work of Pilinis (1990), with gas-to-particle conversion represented by dynamic mass transfer between gas and aerosol phases. The model, which also includes explicit calculation of inorganic particle-phase thermodynamics, was applied to simulate gas and particle behavior in a 1987 air pollution episode in the South Coast Air Basin of California. Pierce et al. (2008) developed a model to simulate aerosol dynamics in a chamber involving simultaneous condensation, evaporation, coagulation, and wall deposition. The Pierce model was employed by Nah et al. (2016, 2017) to study effects of coagulation on particle wall deposition. Bian et al. (2015, 2017) used the TwO-Moment Aerosol Sectional (TOMAS) microphysics model (Adams and Seinfeld 2002; Pierce and Adams 2009; Pierce et al. 2011) to simulate organic species phase partitioning and particle and gas-phase wall losses during smog chamber characterization experiments involving wood smoke. The TOMAS model computes a size-resolved simulation of aerosol microphysics, conserving number and mass concentrations (see also Russell et al. 1998). Tian et al. (2017) derived a stochastic particle-resolved aerosol model (PartMC) that was applied to simulate coagulating ammonium sulfate particles in a cylindrical chamber, with special attention to fractal particle structure and wall loss. The computational model used in the present study is based on numerical solution of the aerosol dynamic equation (Seinfeld and Pandis 2016) to simulate particle growth by condensation, particle wall deposition, and coagulation, solved on a fixed particle size grid, with exact mass conservation of species.

2. Particle wall deposition

From the advent of environmental chambers, it was recognized that particles diffuse to and deposit on the chamber walls (Crump and Seinfeld 1981; McMurry and Grosjean 1985; McMurry and Rader 1985). Because the rate of particle deposition on the wall depends on the specific design parameters of each chamber (size, extent of mixing), the rate of wall deposition of particles as a function of particle size is generally determined experimentally by introducing particles of known sizes into the chamber, and after allowing time for mixing, measuring the size-dependent rates of wall deposition. The rate of deposition on the chamber walls is generally assumed to depend only on the particle size, so the rate of decay of the suspended particle number concentration distribution, $n_s(D_p, t)$, at diameter D_p is expressed as

$$\left(\frac{\partial n_s(D_p, t)}{\partial t}\right)_{wallloss} = -\beta(D_p)\, n_s\big(D_p, t\big) \qquad [1]$$

where the particle wall deposition coefficient $\beta(D_p)$ is determined by fitting the experimentally observed rates of decay of particles as a function of diameter.

If wall deposition is the sole process affecting aerosol number concentration in the chamber, determination of $\beta(D_p)$ from the rates of decay of particles of different sizes is relatively straightforward. However, if coagulation is appreciable, determination of $\beta(D_p)$ as solely representing particle wall deposition must account for the contribution of coagulation to the observed rate of particle decay. The dynamics of a suspended particle population $n_s(D_p, t)$ undergoing simultaneous coagulation and wall deposition is governed by

$$\frac{\partial n_s\big(D_p, t\big)}{\partial t} = \frac{1}{2}\int_0^{D_p} K\left(\left(D_p^3 - q^3\right)^{1/3}, q\right)$$

$$n_s\left(\left(D_p^3 - q^3\right)^{1/3}, t\right) n_s(q, t)\, dq$$

$$- n_s\big(D_p, t\big)\int_0^\infty K(q, D_p) n_s(q, t)\, dq$$

$$- \beta(D_p) n_s\big(D_p, t\big) \qquad [2]$$

subject to the initial condition $n_s(D_p, 0) = n_0(D_p)$, where $n_0(D_p)$ is the aerosol size distribution upon initial injection into the chamber, and $K(D_{p1}, D_{p2})$ is the coagulation coefficient between particles of diameters

D_{p1} and D_{p2}. Determining the value of $\beta(D_p)$ in the presence of coagulation requires finding $\beta(D_p)$ such that the solution of Equation (2) subject to $n_0(D_p)$ matches as closely as possible to the observed aerosol dynamics in the chamber, $n_s(D_p, t)$.

The combination of gravitational settling and Brownian diffusion gives rise to a functional form of $\beta(D_p)$ that, at the small end of the particle size spectrum, decreases as D_p increases, owing to decreasing Brownian diffusion, and at the large particle end of the size spectrum, increases as D_p increases, owing to increased particle settling velocity. Whereas the result is a characteristic U-shaped function, the precise $\beta(D_p)$ functionality must be determined experimentally for each chamber. An advantageous approach to determining $\beta(D_p)$ is to specify a $\beta(D_p)$ function having the proper characteristic functionality, with a set of unknown parameters to be determined by optimal fitting of the numerical solution of Equation (2) to the observed size distribution dynamics in the chamber in question (Pierce et al. 2008; Nah et al. 2017). This procedure requires iterative numerical solution of Equation (2), such that each revised set of parameters characterizing $\beta(D_p)$ moves the calculated $n_s(D_p, t)$ closer to the experimentally observed $n_s(D_p, t)$, as measured by a performance criterion of closeness of calculated $n_s(D_p, t)$ to observed $n_s(D_p, t)$.

The goal is to minimize the objective function,

$$J[\beta(D_p)] = \int_0^{t_f} \int_{D_{p,l}}^{D_{p,u}} [n_{s,\,obs}(D_p, t) - n_{s,\,pred}(D_p, t)]^2 dD_p dt$$

[3]

where $n_{s,\,obs}(D_p, t)$ is the observed size distribution and $n_{s,\,pred}(D_p, t)$ is that predicted using an assumed functional form of $\beta(D_p)$, here assumed to be

$$log_{10}[\beta(D_p)] = a + b log_{10}(D_p) + c[log_{10}(D_p)]^2$$

$$+ d[log_{10}(D_p)]^3$$

[4]

where a, b, c, d are the parameters that characterize $\beta(D_p)$. Before an optimal $\beta(D_p)$ is found from the minimization of $J[\beta(D_p)]$ in Equation (3), an initial guess for the four parameters (a, b, c, and d) must be chosen.

To evaluate the performance of the minimization of J, we performed 20-h simulations of simultaneous coagulation and wall deposition of an aerosol introduced into a chamber at $t = 0$ (Figure 1). $n(D_p, t)$ was discretized into 50 logarithmically distributed bins with mean diameters between 50 and 1,000 nm. The method for finding the initial guess is shown visually and explained in Figure 2 and its caption. Randomly distributed measurement uncertainty of 5% was added to particle number concentrations in each
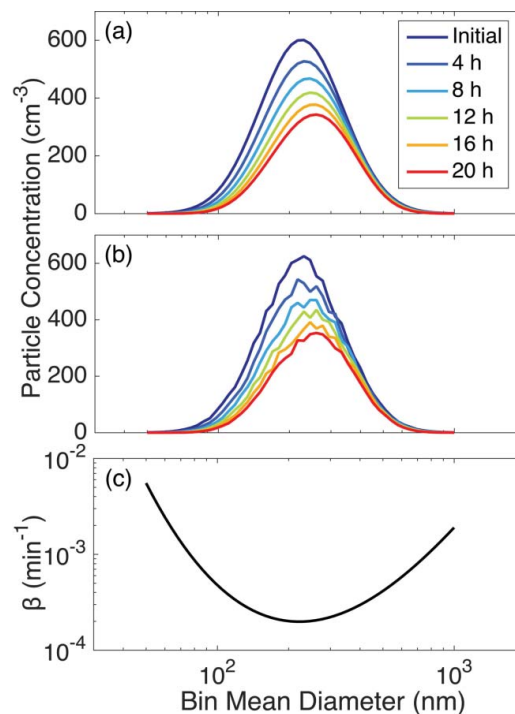
Figure 1. (a) and (b) show the evolution of a particle size distribution undergoing coagulation and particle wall deposition over 20 h for an initially lognormal distribution, assuming $\beta(D_p)$ shown in (c). The initial total number concentration is 10^4 cm^{-3}, and the initial lognormal distribution is centered at 225 nm with $\sigma_g = 1.5$. The mean diameters of the 50 bins are lognormally distributed between 50 and 1,000 nm. Data in (b) were generated by applying $\pm 5\%$ measurement uncertainty to the number concentration in each of the 50 bins.

bin. Figure 3 shows the results of optimization for 20 different simulations, each of these with the same base data but different realizations of the 5% measurement uncertainty.

3. Chamber physics and chemistry

3.1. Particle growth

During SOA formation, each particle that deposits on the wall of an environmental chamber carries with it the condensed organic mass from the inception of the experiment. In order to account for that particle-borne organic material in computing the overall SOA yield, it is necessary to keep track of particle size (and therefore the amount of condensed organic) upon deposition. Since the extent to which deposited particles continue to interact with the gas-phase contents of the chamber is unknown, two limiting assumptions have been invoked to estimate the contribution of the deposited particles to the amount of SOA (Hildebrandt et al. 2009; Loza et al. 2010): (1) The "lower bound" assumption states that once particles deposit on the wall, they cease interacting with the vapor
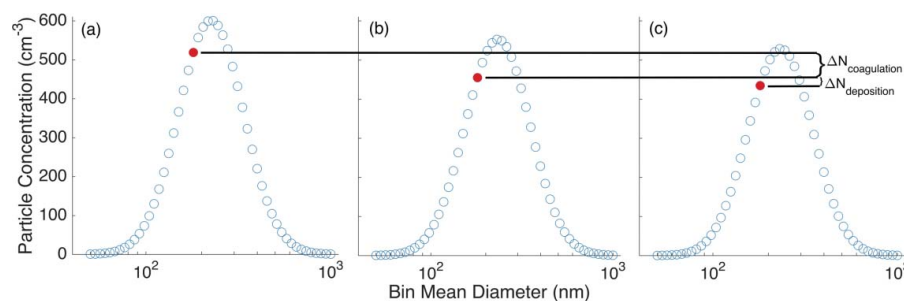
Figure 2. Process for choosing an initial guess for $\beta(D_p)$. The solid (red) dots represent the number concentration in the same size bin in all three distributions. (a) and (c) represent data points at times t_1 and t_2, respectively. When used to find an initial guess, time increments ($t_2 - t_1$) were chosen to be 6.5 min; in this figure, the time increment is 4 h, so that the procedure is visually obvious. (b) A simulation for one time increment with the distribution at t_1 as the initial condition and with $\beta(D_p) = 0$. Since (b) corresponds to a system in which particles from the distribution at t_1 are allowed to coagulate but not to deposit on the wall, the difference between the number concentration of a specific size bin from the t_2 distribution, shown in (b), and from the actual distribution at t_2, shown in (c), is then denoted $\Delta N_{\text{Deposition}}$. $\beta(D_p)$ is next calculated as $\beta\left(D_p, t_{1/2}\right) = \frac{\Delta N_{\text{Deposition}}}{N_{t_1}(t_2 - t_1)}$. A mean $\beta(D_p)$ can be found by averaging these values for a specific D_p over all the time points where the initial distribution has arbitrarily >10 particles cm^{-3} for that size bin. These average $\beta(D_p)$ values are next fit to the function in Equation (4) and these values of a, b, c, and d are used as an initial guess for the determination of $\beta(D_p)$.

in the chamber; and (2) The "upper bound" assumes that wall-deposited particles continue to absorb vapor as if they had remained suspended. Thus, the upper bound assumption is identical to that if the particles were still suspended. In treating the continued uptake of vapor by particles that have deposited on the chamber wall, one must assume an appropriate particle surface area for mass transport. The assumption made here is that, after deposition on the wall, the particle retains its spherical shape, and therefore its surface area remains the same as if it were still suspended. For a discussion of assumptions concerning the nature of deposited particles, the reader is referred to Trump et al. (2016).

The rate of vapor uptake by a particle is described in terms of the mass accommodation coefficient α_p, which is defined as the fraction of incoming vapor molecules that is taken up by the particle (Julin et al. 2014; Zhang et al. 2015). The mass accommodation coefficient α_p can be defined as either surface (α_{ps}) or bulk (α_{pb}) accommodation coefficient (Kolb et al. 2010), the difference being the extent to which the condensing molecule needs to be incorporated in the particle bulk to be considered as accommodated. Molecular-level simulations of molecule–surface interactions can distinguish between surface and bulk accommodation (Julin et al. 2014), but typical vapor–particle interactions in a laboratory chamber tend to be represented by a single overall mass accommodation coefficient, α_p. Rapid equilibration of an incoming vapor between the gas and particle phases is a reasonable assumption for a liquid-phase particle (Shiraiwa and Seinfeld 2012), although if the particle is solid or semisolid or if particle-phase chemistry plays an influential role in uptake, accommodation can be retarded. From a macroscopic point of view, the value of α_p for a particular

vapor–aerosol system is determined by fitting observed aerosol growth rate data to a dynamic growth model.

Particle-phase accretion reactions can produce effectively nonvolatile products. Such products can lead to an increase in the viscosity of the particle and reduced particle-phase diffusivity, retarding evaporation, and inhibiting gas–particle partitioning (Virtanen et al 2010a, b; Vaden et al. 2010, 2011; Abramson et al. 2013; Zaveri et al. 2014). In such a case, the timescale to achieve gas–particle equilibrium, $\tau_{g,p}$, may be long compared to the timescales for achieving gas–wall partitioning and for VOC oxidation, $\tau_{g,w}$ and τ_{rxn} (Zhang et al. 2012; Shiraiwa and Seinfeld 2012; Shiraiwa et al. 2013; Mai et al. 2015). Retarded gas–particle partitioning resulting from slow condensed-phase diffusion of vapor molecules will drive the vapor–particle system toward so-called *kinetically limited growth*. A vapor–particle accommodation coefficient, α_p, of order, say, 10^{-3}, leads to a vapor–particle equilibration timescale that is competitive with or can exceed that associated with the rate of change of vapor concentration due to both vapor-phase oxidation and vapor wall loss. When the production rate of condensable vapors is slow compared to the time needed to establish gas–particle equilibrium, the system exhibits *quasi-equilibrium growth*.

The magnitude of the timescale needed to establish gas–particle equilibrium, $\tau_{g,p}$, relative to the timescales for other processes in the system governs the extent to which the system is characterized by kinetically limited versus quasi-equilibrium growth. Gas–particle equilibrium is governed by the total organic mass in the system and is not explicitly dependent on the aerosol surface area. In contrast, kinetically limited condensation, for which $\tau_{g,p}$ is competitive with the timescale for VOC oxidation, depends on the aerosol surface area. The
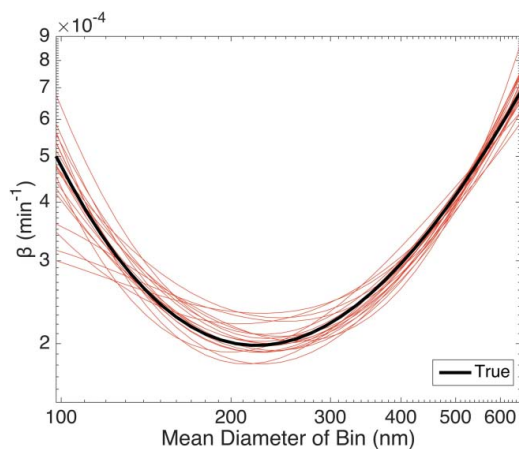
Figure 3. Optimization procedure to determine $\beta(D_p)$. The full optimization procedure to determine $\beta(D_p)$ was performed 20 times and each thin (red) curve represents one of these converged functions. Each of the optimized $\beta(D_p)$ functions was determined by taking the number concentrations in all of the 50 size bins shown in Figure 1a and subjecting these to a $\pm 5\%$ random; an example of the data used as an input is shown in Figure 1b. Once an initial guess of a, b, c, and d was found (the method for which is shown in Figure 2), these four parameters were used to minimize the function $J(\beta(D_p))$ in Equation (3). An average of 290 iterations were required for the optimization to converge. These values of a, b, c, and d then give the determined $\beta(D_p)$, which is shown as a thin (red) curve. In actual chamber experiments, the true value of $\beta(D_p)$ is unknown; using the method described here produces the set of thin (red) curves. To assess the performance of this method, we applied this procedure with simulated data with an assumed, true value of $\beta(D_p)$, which is shown both in Figure 1c and here in bold (black) to visually aid the comparison to each of the thin (red) lines. The range for the x-axis includes only bins with a number concentration >10 cm^{-3} for the duration of the 20-h experiment.

timescale for the production of condensable vapors, τ_{rxn}, is generally estimated on the basis of k_{rxn} [OH]. If $\tau_{g,p} > \tau_{rxn}$, condensation is kinetically limited. As α_p increases toward unity, $\tau_{g,p}$ decreases with respect to τ_{rxn}, and condensation shifts toward quasi-equilibrium growth.

3.2. Idealized kinetics

The essential characteristics of the gas-phase oxidation of a VOC to form SOA are the timescale of oxidation and the progression to lower volatility oxidation products. As a means of representing gas-phase kinetics in the simulations to follow, we use the idealized first-order kinetic scheme of McVay et al. (2014):

$$A \xrightarrow{k_1} B \xrightarrow{k_2} C \xrightarrow{k_3} D$$
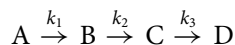
In this scheme, A represents the completely volatile parent VOC, and B, C, and D represent oxidation products, with successively decreasing volatility. The magnitudes of

the effective first-order rate constants, k_1, k_2, and k_3, govern the overall chemical reaction timescale of the system. The volatilities of the oxidation products are represented by their saturation mass concentrations, C_B^*, C_C^*, and C_D^*. In the present study, we do not consider particle-phase chemistry involving condensed B, C, and D. One could hypothesize generalized particle-phase reactions involving condensed B, C, and D that would further decrease (or possibly increase) the volatility of the aerosol, but this aspect is left for future work, especially in the case in which explicit particle-phase chemistry is established.

3.3. Vapor wall deposition

Vapor molecules in the generally well-mixed core of a chamber are transported through a boundary layer adjacent to the walls by a combination of molecular and turbulent diffusion (Zhang et al. 2015; Ye et al. 2016; Trump et al. 2016). As a vapor molecule i reaches the chamber wall, the fraction of encounters that lead to uptake is represented by the vapor wall accommodation coefficient, $\alpha_{w,i}$, which depends on the nature of the wall surface as well as the chemical composition of the species. Vapor species that deposit on the wall, in principle, may re-evaporate, eventually leading to an equilibrium between the gas phase and the wall. The absorptive nature of the wall has been characterized by a parameter defined as the equivalent absorbing organic mass on the wall, C_w (Matsunaga and Ziemann 2010; Yeh and Ziemann 2015). For an FEP Teflon-walled chamber, the quantity C_w can be regarded as characterizing the equilibrium solubility of individual vapor molecules in FEP Teflon polymer.

The rate of uptake of vapors by the wall can be characterized by the overall first-order vapor wall deposition coefficient, k_w, which depends on the surface area-to-volume ratio of the chamber, the degree of mixing in the chamber, the rate of gas-phase diffusion across the wall layer, and the vapor-wall accommodation coefficient, $\alpha_{w,i}$ (Zhang et al. 2015). The timescale characterizing the vapor wall deposition process is $\tau_{g,w} = k_w^{-1}$.

The rate of deposition of vapor to the chamber walls is represented as a first-order process, characterized by the first-order rate coefficient, k_w (s^{-1}) (Zhang et al. 2015). Vapor wall deposition is assumed to be reversible, with the vapor-wall partitioning coefficient, K_w:

$$K_w = \frac{R\,T}{M_w\,\gamma_w\,P_{sat}} \tag{5}$$

Here R is the ideal gas constant, T is temperature, M_w is the effective molecular weight of the absorbing wall material, γ_w is the effective activity coefficient of

the dissolved material in the wall, and P_{sat} is the saturation vapor pressure of the species of interest. Oxidation products, B, C, and D, are considered to condense on suspended particles as well as deposit reversibly onto the chamber walls. The governing equation for the concentration of a suspended vapor, such as B, is:

$$\frac{dB_g}{dt} = - k_{w,on,B}B_g + k_{w,off,B}B_w + k_1 A_g - k_2 B_g - J_B$$

[6]

where, $k_{w,on}$ and $k_{w,off}$ (s^{-1}) are the first-order rate coefficients for deposition on and evaporation from the wall, k_1 and k_2 are the oxidation rate constants of A and B, B_g and B_w are the concentrations of B suspended and on the wall, respectively, and J_B is the condensation rate of B onto particles. Vapor molecules are transported both to and from the wall. We express K_w in terms of $k_{w,on}$ and the first-order evaporation coefficient $k_{w,off}$. $k_{w,on}$ and $k_{w,off}$ are related through

$$K_w C_w = \frac{k_{w,on}}{k_{w,off}}$$

[7]

$k_{w,on}$ represents the overall rate of transport of vapor species from the core of the chamber to the edge of the wall boundary layer and through the boundary layer by molecular diffusion (McVay et al. 2014; Zhang et al. 2015),

$$k_{w,on} = \left(\frac{A}{V}\right) \frac{\frac{\alpha_w \bar{c}}{4}}{1 + \frac{\pi}{2} \left(\frac{\alpha_w \bar{c}}{4\sqrt{k_e D_i}}\right)}$$

[8]

$$k_{w,off} = \frac{k_{w,on} C^*}{C_w}$$

[9]

Here A/V is the surface area to volume ratio of the chamber; α_w is the mass accommodation coefficient of vapor species on the wall; k_e is the eddy diffusion coefficient for mixing in the chamber; D_i is the molecular diffusivity of the vapor in the thin layer adjacent to the wall; $\bar{c}$ is the mean thermal speed of the vapor, assumed for convenience to be the same for B, C, and D; C_w is the effective wall organic aerosol concentration; and C_i^* is the saturation mass concentration for species i. As noted earlier, C_w is the parameter that represents the capacity of the Teflon material itself to absorb organic molecules. Typical values of D_i and $\bar{c}$ for the classes of molecules important in SOA formation are $\sim 3 \times 10^6$ m^2 s^{-1} and 200 m s^{-1}, respectively. Values of k_e ranging from 10^{-3} to 1 s^{-1} correspond to chamber mixing timescales of 17 min to 1 s. A mixing timescale of 10^{-3} s^{-1} is characteristic of that in a typical chamber of volume exceeding ~ 20 m^3.

3.4. Aerosol conservation equation

The overall governing conservation equation for the suspended aerosol size distribution $n_s(D_p, t)$ is as shown below:

$$\frac{\partial n_s(D_p, t)}{\partial t} = \left(\frac{\partial n_s(D_p,t)}{\partial t}\right)_{coagulation}$$
$$+ \left(\frac{\partial n_s(D_p,t)}{\partial t}\right)_{condensation}$$
$$+ \left(\frac{\partial n_s(D_p,t)}{\partial t}\right)_{wallloss}$$

[10]

The rate of condensation of vapor molecules onto particles is given by:

$$J_i = 2\pi D_i D_p \left(G_i - G_i^{eq}\right) F_{FS}$$

[11]

where G_i is the gas-phase concentration of species i, G_i^{eq} is the equilibrium gas-phase concentration over a particle, and F_{FS} is the Fuchs–Sutugin correction factor for noncontinuum gas-phase diffusion (Seinfeld and Pandis 2016),

$$F_{FS} = \frac{0.75\ \alpha_p\ (1 + Kn)}{Kn^2 + Kn + 0.283\ Kn\ \alpha_p + 0.75\ \alpha_p}$$

[12]

The rate of change of the suspended aerosol size distribution owing to vapor condensation on suspended particles is:

$$\left(\frac{\partial n_s(D_p,t)}{\partial t}\right)_{condensation} = - \frac{\partial}{\partial D_p}[I(D_p, t) n_s(D_p, t)]$$

[13]

where $I(D_p, t)$ is the rate of change in particle diameter due to condensation or evaporation.

3.5. Key parameters

The principal parameter that controls the rate of particle growth by vapor condensation is α_p, the accommodation coefficient of a vapor species on particles. As noted earlier, α_p has been found to vary over the range of ~ 0.001 to close to 1.0 for different VOC systems (McVay et al. 2014). A related parameter, α_{pw}, describes the growth by vapor condensation of particles that have deposited on the wall. Of the two limiting assumptions that describe the growth of particles that have deposited on the wall, we adopt the lower bound assumption, in which once particles are lost to the walls, vapor condensation to these particles ceases, in which case, $\alpha_{pw} = 0$.

The oxidation rates of the vapor species, A, B, and C, as embodied in the first-order rate coefficients k_1, k_2, and k_3, establish the overall time scale for the temporal behavior of the system. The nominal initial oxidation rate constant for the simulations to be presented subsequently is $k_1 = 10^{-4}$ s^{-1}, with each subsequent oxidation rate coefficient assumed to increase by a factor of five. Vapor wall deposition is represented by the principal parameters, C_w the effective wall organic aerosol concentration, and α_w, the accommodation coefficient of vapor species onto the wall. The nominal value of α_w is assumed to be 10^{-5}. Matsunaga and Ziemann (2010) estimated a range of values, $C_w = 2$, 4, 10, and 24 mg m^{-3} for alkanes, alkenes, alcohols, and ketones. The nominal value used in the numerical studies here is $C_w = 10$ mg m^{-3}. Nominal values of parameters are summarized in Table 1, together with ranges used in simulations.

The size distribution of the seed aerosol at the start of an experiment is assumed to follow a log-normal distribution centered at a diameter of 225 nm, with geometric standard deviation $\sigma_g = 1.5$. The initial number concentration of seed particles is a key experimental variable. The base value of the initial seed number concentration is taken as 10^4 cm^{-3}.

3.6. Computational model

The computational model tracks the evolution of the particle size distribution in the chamber over time, and that of the gas-phase concentrations of A, B, C, and D, as well as the fraction of each that is suspended or on particles/the wall. Because the stoichiometric coefficients in the idealized gas-phase chemistry have been chosen to be unity, given adequate time in the chamber and the absence of wall deposition of particles or vapor, the theoretical maximum yield of SOA (the mass of SOA formed per mass of A reacted) that can be achieved is 1.0. Simulations are carried out for an experimental time of 20 h.

4. Computational simulations

The focus of the present work is exploring the relative importance of the physicochemical processes involving vapor molecules and particles in an environmental chamber, with particular attention to those competitive processes that arise as a consequence of the chamber itself. Here we present a range of simulations in which physicochemical parameters are systematically varied. Whereas there are several metrics that could be used to assess the characteristics of a particular chamber experiment, the SOA yield, Y, attained over a fixed experimental duration serves as the overall measure of the performance of the system.

4.1. Simultaneous vapor condensation on particles and vapor and particle deposition on chamber walls

Figure 4 shows the effect of variation of key parameters on SOA yield. Y increases as α_p increases since vapor condenses onto particles more readily (Figure 4a), and Y becomes less sensitive to α_p as α_p approaches unity. At the limit $\alpha_p = 1$, Y is only mildly sensitive to the value of α_w (Figure 4b) since vapor condensation on particles proceeds at its maximum rate; at $\alpha_p = 0.001$ a considerable portion of the vapor remains suspended for a longer period of time, and is therefore subject to vapor wall deposition, leading to a strong effect of increasing α_w on Y. As C_w decreases (Figure 4c), the capacity of the wall to take up vapor decreases, increasing Y. As the rate constants for A $\to$ B $\to$ C $\to$ D increase (Figure 4d), over a fixed experimental time, Y increases rapidly as α_p increases owing to the greater availability of lower volatility oxidation products, B, C, and D. As the values of C_B^*, C_C^*, and C_D^* decrease (Figure 4e), the overall lower volatility of oxidation products leads to an increase in Y, although at $\alpha_p = 0.001$, that increase is modest, since the value of α_p exerts a stronger control on Y than does the volatility C^*, at the assumed values of C_B^*, C_C^*, and C_D^*. Y increases as the initial number concentration of particles (Figure 4f) increases, particularly for $\alpha_p = 0.001$. This is

Table 1. Chamber parameters.

Parameter	Definition	Base value	Range of values considered
α_p	Accommodation coefficient of vapor species on suspended particles	10^{-3}	10^{-3} to 1
α_{pw}	Accommodation coefficient of vapor species on particles deposited on the wall	0	0 and α_p
α_w	Accommodation coefficient of vapor species deposited on the wall	10^{-5}	10^{-7} to 10^{-4}
k_1	First-order oxidation rate constant for A	1×10^{-4} s^{-1}	1×10^{-6} to 1×10^{-3} s^{-1}
k_2	First-order oxidation rate constant for B	5×10^{-4} s^{-1}	5×10^{-6} to 5×10^{-3} s^{-1}
k_3	First-order oxidation rate constant for C	25×10^{-4} s^{-1}	25×10^{-6} to 25×10^{-3} s^{-1}
C_w	Effective wall organic aerosol concentration	10 mg m^{-3}	10^{-2} to 10 mg m^{-3}
C_B^*	Saturation mass concentration for species B	10 µg m^{-3}	10^{-1} to 10^2 µg m^{-3}
C_C^*	Saturation mass concentration for species C	1 µg m^{-3}	10^{-2} to 10 µg m^{-3}
C_D^*	Saturation mass concentration for species D	10^{-1} µg m^{-3}	10^{-3} to 1 µg m^{-3}
N_t	Initial total number concentration of seed particles	10^4 cm^{-3}	10^3 to 10^6 cm^{-3}
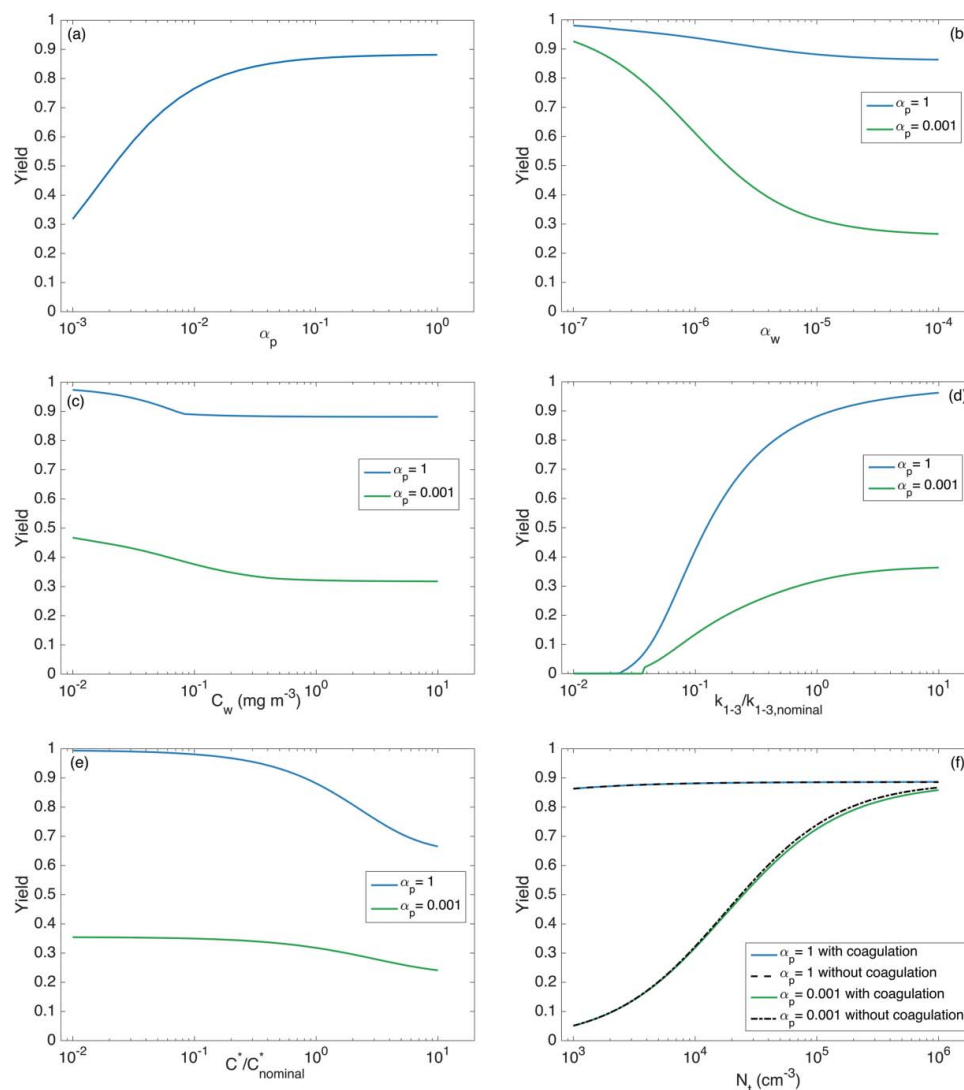
Figure 4. Secondary organic aerosol (SOA) yield Y for nominal parameter values in Table 1 with coagulation occurring. (a) α_p; (b) α_w; (c) C_w; (d) k_1; k_2; k_3; (e) C_B^*; C_C^*; C_D^*, (f) N_t. In (f), both the presence and absence of coagulation are considered.

because an increase in number concentration increases the suspended surface area and so preferences condensation onto suspended particles. When $\alpha_p = 1$, there is less competition in condensation between the wall and the suspended particles, so the effect of an increase in suspended surface area is dampened: since condensation onto suspended particles is already dominating condensation onto the walls, the change in this surface area due to coagulation – while still quite small – is noticeable, that is, in the absence of coagulation, the total available suspended surface area decreases since all particles are modeled as spheres.

The effect of α_p (0.001 vs. 0.01 vs. 1.0) on the distribution of products B, C, and D at the end of the experiment is shown in Figure 5. Under conditions of $\alpha_p = 0.001$, at the end of the simulation (Figure 5a), the majority of species B, C, and D is predicted to have deposited on the chamber wall. An increase in α_p by a factor of 10 to 0.01

(Figure 5b) has a substantial effect on the distribution of B, C, D, as Y is predicted to increase from 0.32 to 0.77. At $\alpha_p = 1$ (Figure 5c), the majority of products B, C, and D reside on suspended particles, and Y has increased to 0.88. In all three cases, little of the products reside in particles that have deposited on the chamber wall, owing to the fact that the surface area of deposited particles is much less than that of the suspended. There is little difference between the cases of $\alpha_p = 0.1$ and $\alpha_p = 1$ (not shown); an accommodation coefficient of 0.1 is essentially equal to $\alpha_p = 1.0$ in terms of the effect on the distribution of products.

Decreasing α_w (10^{-7} vs. 10^{-5}) at $\alpha_p = 0.001$, as seen in Figure 6, produces a dramatic change of product distribution Y from that at $\alpha_w = 10^{-5}$. At $\alpha_w = 10^{-7}$, the majority of B, C, and D are predicted to reside on suspended particles, and $Y = 0.93$ versus 0.32, with virtually no suspended vapor left in the chamber. For $\alpha_w > 10^{-5}$,

Figure 5. Variation of the distribution of oxidation products B, C, and D among suspended vapor, wall deposited vapor, suspended particles, and wall deposited particles for the nominal parameter values in Table 1. (a) $\alpha_p = 0.001$; (b) $\alpha_p = 0.01$; (c) $\alpha_p = 1.0$.

there is little change in the distribution of B, C, and D from that at $\alpha_w = 10^{-5}$ (not shown).

The effect of increased oxidation rate on the distribution of B, C, and D at the end of the simulated experiment for $\alpha_p = 0.001$ is shown in Figure 7. The nominal values of k_1, k_2, and k_3 are 0.0001 , 0.0005, and 0.0025 s^{-1}, respectively; at a factor of 10 increase, $k_1 = 0.001$ s^{-1}, $k_2 = 0.005$ s^{-1}, and $k_3 = 0.025$ s^{-1}, conversion of A to D occurs an order of magnitude more rapidly. This accelerated rate of conversion is not, however, accompanied by a concomitant increase in Y. Comparing Figures 5a and 7a, we note that Y increases only from 0.32 to 0.36. The explanation for this modest increase in Y can be attributed to the value of $\alpha_p = 0.001$; despite an order of magnitude increase in reaction rates, the low accommodation rate of vapor on particles ($\alpha_p = 0.001$) exerts the dominant influence on Y. When the order of magnitude increase in k_1, k_2, and k_3 occurs at $\alpha_p = 1.0$ (Figure 7b), the so-called *kinetic effect* is clearly demonstrated, with the overall Y increasing from 0.36 (Figure 7a) to 0.96 (Figure 7b).

Since α_{pw} is set to 0 throughout all the simulations described, the compounds are found on deposited particles only when they condense on suspended particles and these particles later deposit on the chamber walls. Since increasing

the oxidation rate shifts the condensation of compounds onto particles earlier in the experiment – when there are still numerous particles present – more of the compounds end up on particles that later deposit on the walls.

Experimental evidence suggests that C_w is likely to be relatively large (Matsunaga and Ziemann 2010). At values near the nominal value of $C_w = 10^4$ μg m^{-3}, Y does not vary appreciably for modest changes in C_w, but does vary significantly for values lower than the nominal value (Figure 4c). Y is most sensitive to C_w when the value of C_w is in the vicinity of that of C_{OA} (the concentration of organics). The effect of the value of C_w on Y is addressed in Figure 8. If C_w is decreased from its nominal value of 10^4 to 10 μg m^{-3}, at $\alpha_p = 0.001$ and $\alpha_w = 10^{-5}$, Y increases to 0.47 (Figure 8) from 0.32 (Figure 5a). At $\alpha_p = 1$, Y increases from 0.88 at $C_w = 10^4$ μg m^{-3} to 0.97 at $C_w = 10$ μg m^{-3} (distributions of B, C, D not shown).

The predicted value of Y corresponding to the two limiting assumptions regarding the extent to which particles on the wall continue to take up vapor can be assessed. We considered the distribution of B, C, D, in the two limiting cases in which wall-deposited particles either continue to or do not absorb vapors. For $\alpha_p = 0.001$, Y with ($\alpha_{pw} = \alpha_p$) and without particles in the wall growing is, respectively, 0.33 and 0.32. At $\alpha_p = 1.0$, $Y = 0.91$ for $\alpha_{pw} = 1$ and 0.88 for
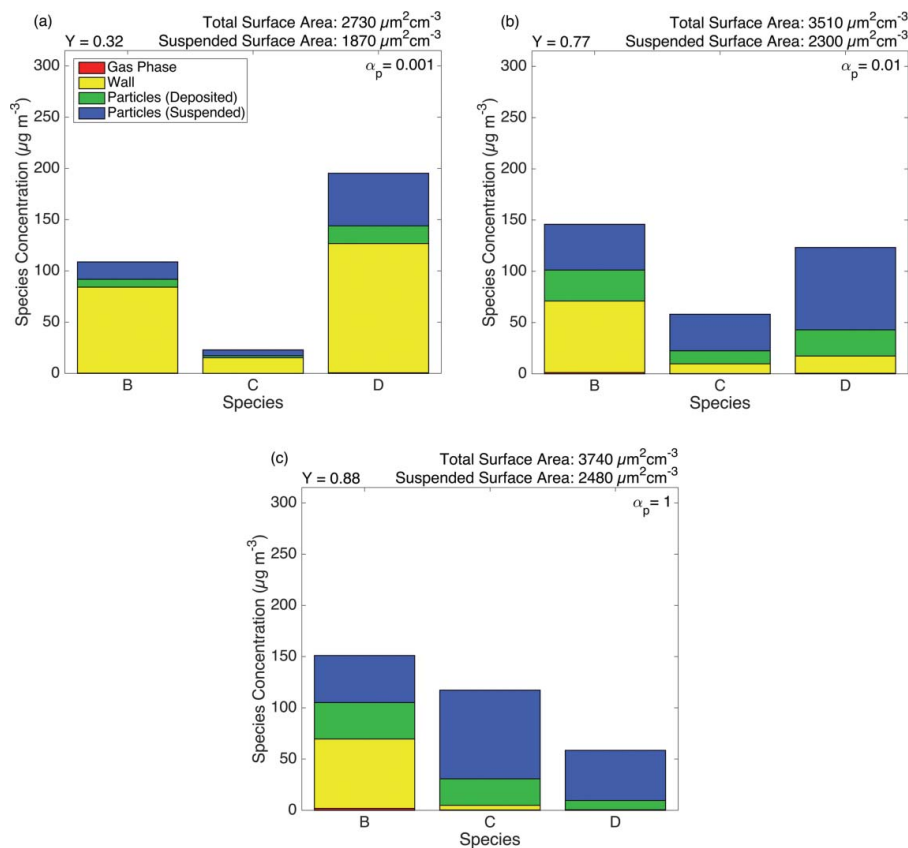
Figure 6. Variation of the distribution of oxidation products B, C, and D among suspended vapor, wall deposited vapor, suspended particles, and wall deposited particles for parameter values in Table 1 except for $\alpha_w = 10^{-7}$. By comparison with Figure 5a, note the strong effect of a two order of magnitude decrease in α_w on the distribution of B, C, and D among the suspended particles, wall deposited vapor, and deposited particles.

$\alpha_{pw} = 0$. These results demonstrate the relatively small difference in Y between the so-called upper and lower limit assumptions concerning the extent to which particles deposited on the wall continue to absorb vapors.

4.2. Effect of coagulation

Implementation of increasingly higher number concentrations of seed aerosol as a means to stimulate preferential condensation of vapor on particles is accompanied by increasing influence of coagulation on the dynamics of the particle size distribution (Nah et al. 2016, 2017). Also, as particles in the chamber grow due to accretion of vapor oxidation products,

the overall rate of wall deposition of particles evolves, in accordance with the particle size dependence of the wall deposition function, $\beta(D_p)$. Coagulation occurs simultaneously with particle growth, also serving to shift the overall particle size distribution to larger diameters, at the same time accompanied by a reduction in the overall particle number concentration. Coagulation leads to a decrease in the overall surface area of the suspended particles, since there are fewer particles, and because particles grow into sizes for which the deposition rate $\beta(D_p)$ is larger. The overall decrease in surface area is, therefore, a combined result of coagulation and increased wall deposition.

Vapor deposition on the walls of the chamber is controlled by the two parameters, α_w and C_w. Particles that deposit onto the wall serve to decrease both the amount of suspended oxidized products and the overall rate of condensation. Moreover, as N_t is increased with all other conditions the same, Y increases, since the effect of vapor wall loss is diminished, and at higher α_p, condensation competes more favorably with vapor wall deposition, leading to higher Y. In simulations carried out in the presence and absence of coagulation (not shown), coagulation has a modest effect on Y at high seed concentrations and low α_p. Furthermore, comparison of simulations with small and large mean diameters ($D_{pg} = 100$ and 400 nm) shows that coagulation has a larger effect on smaller diameter particles (not shown).

4.3. Kinetically limited versus quasi-equilibrium growth

The extent to which SOA yield increases with increasing seed aerosol surface area depends on the nature of the VOC oxidation system. In the toluene photoxidation system, Zhang et al. (2014) showed that Y
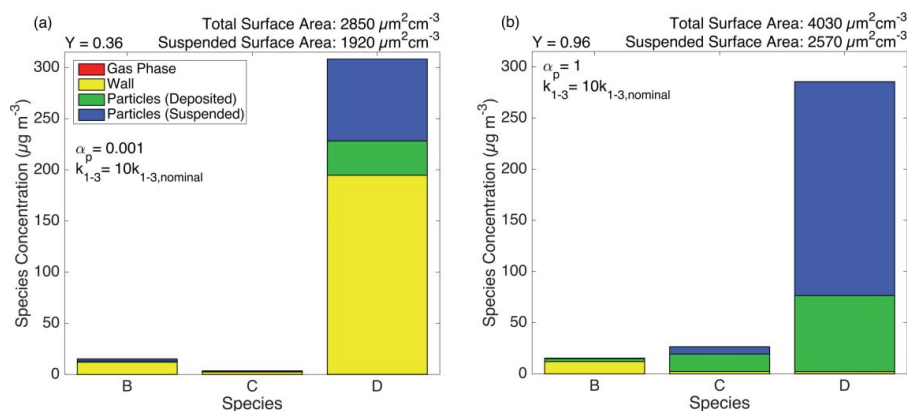
Figure 7. Variation of the distribution of oxidation products B, C, and D among suspended vapor, wall deposited vapor, suspended particles, and wall deposited particles for a tenfold increase in k_1, k_2, and k_3 over the nominal values at $\alpha_p = 0.001$ (a) and $\alpha_p = 1.0$ (b). For (a), the retarded rate of condensation of B, C, and D on suspended particles leads to an accumulation of wall deposited vapor and $Y = 0.36$, whereas for (b), the lack of retardation of condensation leads to $Y = 0.96$.
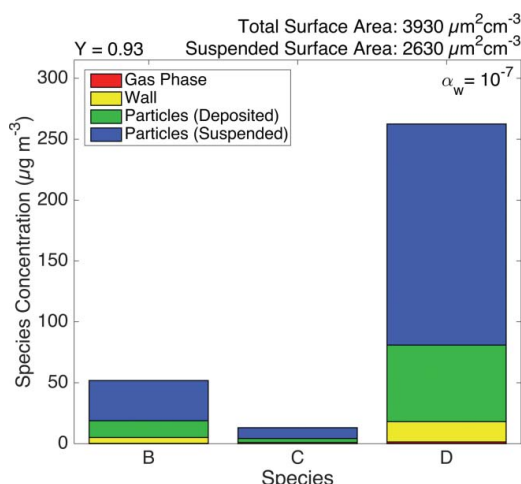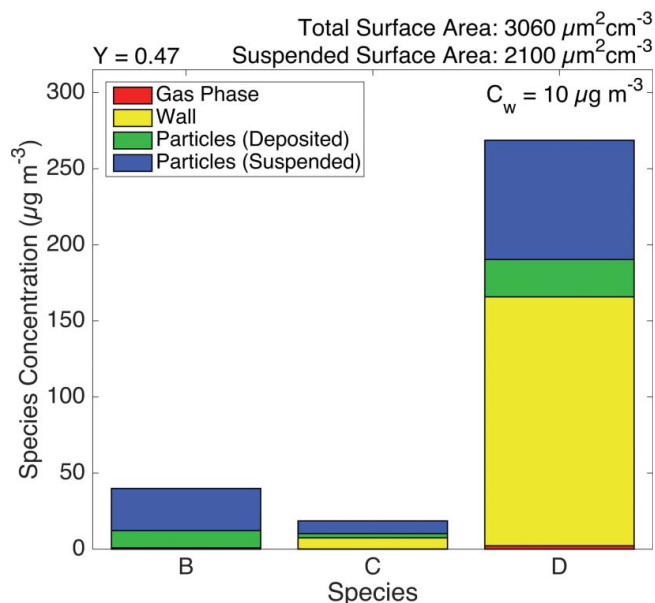
Figure 8. Variation of the distribution of oxidation products B, C, and D among suspended vapor, wall deposited vapor, and particles for $\alpha_p = 0.001$ and $C_w = 10$ μg m^{-3}. At $\alpha_p = 0.001$, the difference in Y corresponding to $C_w = 10$ μg m^{-3} and $C_w = 10^4$ μg m^{-3} (see Figure 5a) is a decrease from 0.47 to 0.32, reflecting the capacity of the wall to take up vapors.

increases with increasing seed aerosol surface area, whereas Nah et al. (2016) found in the α-pinene ozonolysis system that SOA growth rate and Y are essentially independent of seed surface over the range of seed surface area studied. Moreover, McVay et al. (2014) showed that Y depends on seed aerosol surface area only in systems in which the condensation of SOA-forming vapors onto seed aerosol particles is kinetically limited, that is, the timescale to establish gas–particle equilibrium is competitive with or greater than the timescales for VOC oxidation and vapor wall deposition. In addition to seed aerosol surface

area, VOC oxidation rate may also play an important role in establishing the effect of vapor wall deposition on SOA formation, with more rapid oxidation leading to higher Y. This is a consequence of the competition between growing particles and chamber walls for condensable VOC oxidation products. In the α-pinene ozonolysis SOA system of Nah et al. (2016), the best fit α_p value of 0.1 (or 1 with essentially the same statistical error) is consistent with the absence of significant limitations to vapor particle mass transfer, for which SOA formation is governed by quasi-equilibrium growth (Saleh et al. 2013; McVay et al. 2014).

The key parameter controlling the competition between the seed aerosol surface area effect and the oxidation rate effect is α_p (Figure 9). In general, for $\alpha_p \sim 0.1$ to 1.0 (Figure 9a has $\alpha_p = 1.0$), the oxidation rate dominates, and Y increases significantly as the VOC oxidation rate increases, while seed aerosol surface area has a negligible effect. For $\alpha_p = 0.001$ (Figure 9b), both effects can be observed: at low oxidation rate and high seed aerosol surface area, the oxidation rate effect dominates; at low seed aerosol surface area and rapid oxidation rate, the seed surface area dominates. In summary, the magnitude by which vapor wall deposition affects SOA yield depends on the extent to which the VOC system is characterized by kinetically limited SOA condensation growth. For either large α_p or large N_t, the chamber is effectively saturated with particles in terms of its competitiveness with the oxidation rate, so neither changing has much of an effect on Y. When comparing the cases in the presence and absence of coagulation (not shown), overall SOA yields are predicted to be lower in the presence of coagulation, owing to the decrease of the overall surface area of particles available for vapor condensation.
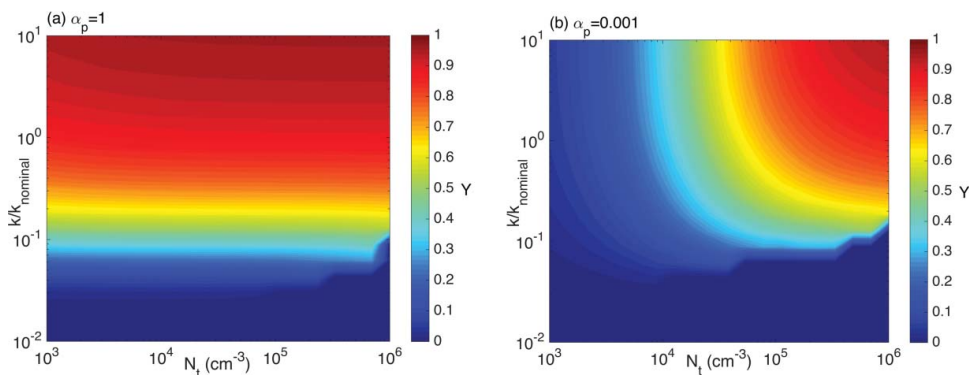
Figure 9. SOA yield as a function of initial seed concentration, N_t, and the oxidation rate, k, where the nominal oxidation rates are $k_1 = 0.0001$ s^{-1}, $k_2 = 0.0005$ s^{-1}, and $k_3 = 0.0025$ s^{-1}. For (a) $\alpha_p = 1.0$, the oxidation rate dominates since N_t has a negligible effect on Y. For (b) $\alpha_p = 0.001$, the oxidation rate dominates at low oxidation rates but the seed aerosol surface area dominates at rapid oxidation rates and relatively low seed aerosol surface area.

5. Conclusion

This work applies a computational model to simulate the dynamics of vapors and particles in an environmental chamber in which a VOC is undergoing oxidation to generate SOA. Here, we explore numerically the competitive processes involving vapors, particles, and the chamber walls in such a system. In order to avoid technicalities of actual gas-phase kinetics, we have utilized the canonical reaction system of A $\rightarrow$ B $\rightarrow$ C $\rightarrow$ D, in which each reaction product is characterized by decreasing volatility from its predecessor. Several key parameters emerge as strongly influencing the rate of generation of SOA; these include the accommodation coefficients of vapor species on growing particles and the wall, α_p and α_w, respectively, and the equilibrium solubility of vapors in the wall itself, C_w. We have also assessed the effect of particle–particle coagulation on particle dynamics and SOA formation. The challenge now remains to simulate chamber dynamics in actual VOC systems with explicit oxidation kinetics and array of reaction products.

Funding

References

Abramson, E., Imre, D., Beranek, J., Wilson, J., and Zelenyuk, A. (2013). Experimental Determination of Chemical Diffusion within Secondary Organic Aerosol Particles. *Phys. Chem. Chem. Phys.*, 15:2983–2991. doi:10.1039/c2cp44013j.

Adams, P. J., and Seinfeld, J. H. (2002). Predicting Global Aerosol Size Distributions in General Circulation Models. *J. Geophys. Res.*, 107:4370, doi: 10.1029/2001JD001010. doi:10.1029/2001JD001010.

Bian, Q., May, A. A., Kreidenweis, S. M., and Pierce, J. R. (2015). Investigation of Particle and Vapor Wall-Loss Effects on Controlled Wood-Smoke Smog-Chamber Experiments. *Atmos. Chem. Phys.*, 15:11027–11045. doi:10.5194/acp-15-11027-2015.

Bian, Q., Jathar, S. H., Kodros, J. K., Barsanti, K. C., Hatch, L. E., May, A. A., Kreidenweis, S. M., and Pierce, J. R. (2017). Secondary Organic Aerosol Formation in Biomass-Burning Plumes: Theoretical Analysis of Lab Studies and Ambient Plumes. *Atmos. Chem. Phys.*, 17:5459–5475. doi:10.5194/acp-17-5459-2017.

Crump, J. G., and Seinfeld, J. H. (1981). Turbulent Deposition and Gravitational Sedimentation of an Aerosol in a Vessel of Arbitrary Shape. *J. Aerosol Sci.*, 12:405–415. doi:10.1016/0021-8502(81)90036-7.

Hildebrandt, L., Donahue, D. M., and Pandis, S. N. (2009). High Formation of Secondary Organic Aerosol from the Photo-oxidation of Toluene. *Atmos. Chem. Phys.*, 9:2973–2986. doi:10.5194/acp-9-2973-2009.

Julin, J., Winkler, P. M., Donahue, N. M., Wagner, P. E., and Riipinen, I. (2014). Near-Unity Mass Accommodation Coefficient of Organic Molecules of Varying Structure. *Environ. Sci. Technol.*, 48:12083–12089. doi:10.1021/es501816h.

Kolb, C. E., Cox, R. A., Abbatt, J. P. D., Ammann, M., Davis, E. J., Donaldson, D. J., Garrett, B. C., George, C., Griffiths, P. T., Hanson, D. R., Kulmala, M., McFiggans, G., Pöschl, U., Riipinen, I., Rossi, M. J., Rudich, Y., Wagner, P. E., Winkler, P. M., Worsnop, D. R., and O'Dowd, C. D. (2010). An Overview of Current Issues in the Uptake of Atmospheric Trace Gases by Aerosols and Clouds. *Atmos. Chem. Phys.*, 10:10561–10605. doi:10.5194/acp-10-10561-2010.

Krechmer, J. E., Pagonis, D., Ziemann, P. J., and Jimenez, J. L. (2016). Quantification of Gas-Wall Partitioning in Teflon Environmental Chambers Using Rapid Bursts of Low-Volatility Oxidized Species. *Environ. Sci. Technol.*, 50:5757–5765. doi:10.1021/acs.est.6b00606.

Loza, C. L., Chan, A. W. H., Galloway, M. M., Kuetsch, F. N., Flagan, R. C., and Seinfeld, J. H. (2010). Characterization of Vapor Wall Loss in Laboratory Chambers. *Environ. Sci. Technol.*, 44:5074–5078. doi:10.1021/es100727v.

Mai, H., Shiraiwa, M., Flagan, R. C., and Seinfeld, J. H. (2015). Under What Conditions Can Equilibrium Gas-Particle Partitioning Be Expected to Hold in the Atmosphere? *Environ. Sci. Technol.*, 49:11485–11491. doi:10.1021/acs.est.5b02587.

Matsunaga, A., and Ziemann, P. J. (2010). Gas-Wall Partitioning of Organic Compounds in a Teflon Film Chamber and Potential Effects on Reaction Product and Aerosol Yield Measurements. *Aerosol Sci. Technol.*, 44:881–892. doi:10.1080/02786826.2010.501044.

McMurry, P. H., and Grosjean, D. (1985). Gas and Aerosol Losses in Teflon Film Smog Chambers. *Environ. Sci. Technol.*, 19:1176–1182. doi:10.1021/es00142a006.

McMurry, P. H., and Rader, D. J. (1985). Aerosol Wall Losses in Electrically Charged Chambers. *Aerosol Sci. Technol.*, 4:249–268. https://doi.org/10.1080/02786828508959054.

McVay, R. C., Cappa, C. D., and Seinfeld, J. H. (2014). Vapor-Wall Deposition in Chambers: Theoretical Considerations. *Environ. Sci. Technol.*, 48:10251–10258. doi:10.1021/es502170j.

Meng, Z., Dabdub, D., and Seinfeld, J. H. (1998). Size-Resolved and Chemically Resolved Model of Atmospheric Aerosol Dynamics. *J. Geophys. Res.*, 103:3419–3435. doi:10.1029/97JD02796.

Nah, T., McVay, R. C., Zhang, X., Boyd, C. M., Seinfeld, J. H., and Ng, N. L. (2016). Influence of Seed Aerosol Surface Area and Oxidation Rate on Vapor Wall Deposition and SOA Mass Yields: A Case Study with α-pinene Ozonolysis. *Atmos. Chem. Phys.*, 16:9361–9372. doi:10.5194/acp-16-9361-2016.

Nah, T., McVay, R. C., Pierce, J. R., Seinfeld, J. H., and Ng, N. L. (2017). Constraining Uncertainties in Particle-Wall Deposition Correction During SOA Formation in Chamber Experiments. *Atmos. Chem. Phys.*, 17:2297–2310. doi:10.5194/acp-17-2297-2017.

Pierce, J. R., Engelhart, G. J., Hildebrandt, L., Weitkamp, E. A., Pathak, R. K., Donahue, N. M., Robinson, A. L., Adams, P. J., and Pandis, S. N. (2008). Constraining Particle Evolution from

Wall Losses, Coagulation, and Condensation-Evaporation in Smog Chamber Experiments: Optimal Estimation Based on Size Distribution Measurements. *Aerosol Sci. Technol.*, 42:1001–1015. doi:10.1080/02786820802389251.

Pierce, J. R., and Adams, P. J. (2009). A Computationally Efficient Aerosol Nucleation/Condensation Method: Pseudo-Steady-State Sulfuric Acid. *Aerosol Sci. Technol.*, 43:216–226. doi:10.1080/02786820802587896.

Pilinis, C. (1990). Derivation and Numerical Solution of the Species Mass Distribution Equations for Multicomponent Particulate Systems. *Atmos. Environ.*, 24:1923–1928. doi:10.1016/0960-1686(90)90525-R.

Russell, L. M., and Seinfeld, J. H. (1998). Size- and Composition-Resolved Externally Mixed Aerosol Model. *Aerosol Sci. Technol.*, 28:403–416. doi:10.1080/02786829808965534.

Saleh, R., Donahue, N. M., and Robinson, A. L. (2013). Time Scales for Gas-Particle Partitioning Equilibration of Secondary Organic Aerosol Formed from Alpha-Pinene Ozonolysis. *Environ. Sci. Technol.*, 47:5588–5594. doi:10.1021/es400078d.

Schwantes, R. H., McVay, R. C., Zhang, X., Coggon, M. M., Lignell, H., Flagan, R. C., Wennberg, P. O., and Seinfeld, J. H. (2017). Science of the Environmental Chamber, in *Advances in Atmospheric Chemistry*, Volume I, World Scientific, Singapore, pp. 1–93.

Seinfeld, J. H., and Pandis, S. N. (2016). *Atmospheric Chemistry and Physics: from Air Pollution to Climate Change* 3rd Ed., Wiley, Hoboken, N.J.

Shiraiwa, M., Seinfeld, J. H. (2012). Equilibration Time Scale of Atmospheric Secondary Organic Aerosol Partitioning. *Geophys. Res. Lett.*, 39:L24801. doi:10.1029/2012GL054008.

Shiraiwa, M., Zuend, A., Bertram, A. K., and Seinfeld, J. H. (2013). Gas-Particle Partitioning of Atmospheric Aerosols: Interplay of Physical State, Non-ideal Mixing and Morphology. *Phys. Chem. Chem. Phys.*, 15:11441–11453. doi:10.1039/c3cp51595h.

Tian, J., Brem, B. T., West, M., Bond, T. C., Rood, M. J., and Riemer, N. (2017). Simulating Aerosol Chamber Experiments with the Particle-Resolved Aerosol Model Part MC. *Aerosol Sci. Technol.*, 51:856–867. doi:10.1080/02786826.2017.1311988.

Trump, E. R., Epstein, S. A., Riipinen, I., and Donahue, N. M. (2016). Wall Effects in Smog Chamber Experiments: A Model Study. *Aerosol Sci. Technol.*, 50:1180–1200. doi:10.1080/02786826.2016.1232858.

Vaden, T. D., Song, C., Zaveri, R. A., Imre, D., and Zeleyuk A. (2010). Morphology of Mixed Primary and Secondary Organic Particles and the Adsorption of Spectator Organic Gases During Aerosol Formation. *Proc. Natl. Acad. Sci. USA.*, 107:6658–6663. doi:10.1073/pnas.0911206107.

Vaden, T. D., Imre, D., Balanek, J., Shrivastava, M., and Zeleyuk, A. (2011). Evaporation Kinetics and Phase of Laboratory and Ambient Secondary Organic Aerosol. *Proc. Natl. Acad. Sci. USA.*, 108:2190–2195. doi:10.1073/pnas.1013391108.

Virtanen, A., Joutsensaari, J., Koop, T., Kannosto, J., Yli-Pirilä, P., Leskinen, J., Makela, J. M., Holopainen, K. J., Pöschl, U., Kulmala, M., Worsnop, D. R., and Laaksonen, A. (2010a). An Amorphous Solid State of Biogenic Secondary Organic Aerosol Particles. *Nature*, 467:824–827. doi:10.1038/nature09455.

Virtanen, A., Kannosto, J., Kuuluvainen, H., Arffman, A., Joutsensaari, J., Saukko, E., Hao, L., Yli-Pirilä, P., Tiitta, P., Holopainen, K. J., Keskinen, J., Worsnop, D. R., Smith, J. N., and Laaksonen, A. (2010b). Bounce Behavior of Freshly Nucleated Biogenic Secondary Organic Aerosol Particles. *Atmos. Chem. Phys.*, 11:8759–8766. doi:10.5194/acp-11-8759-2011.

Ye, P., Ding, X., Hakala, J., Hofbauer, V., Robinson, E. S., and Donahue, N. M. (2016). Vapor Wall Loss of Semi-volatile Organic Compounds in Teflon Chamber. *Aerosol Sci. Technol.*, 50:822–834. doi:10.1080/02786826.2016.1195905.

Yeh, G. K., and Ziemann, P. J. (2015). Gas-Wall Partitioning of Oxygenated Organic Compounds: Measurements, Structure-Activity Relationships and Correlation with Gas Chromatographic Retention Factor. *Aerosol Sci. Technol.*, 49:726–737. doi:10.1080/02786826.2015.1068427.

Zaveri, R. A., Easter, R. C., Shilling, J. E., and Seinfeld, J. H. (2014). Modeling Kinetic Partitioning of Secondary Organic Aerosol and Size Distribution Dynamics: Representing Effects of Volatility, Phase State, and Particle-Phase Reaction. *Atmos. Chem. Phys.*, 14:5153–5181. doi:10.5194/acp-14-5153-2014.

Zhang, X., Pandis, S. N., and Seinfeld, J. H. (2012). Diffusion-Limited versus Quasi-Equilibrium Aerosol Growth. *Aerosol Sci. Technol.*, 46:874–885. doi:10.1080/02786826.2012.679344.

Zhang, X., Cappa, C. D., Jathar, S. H., McVay, R. C., Ensberg, J. J., Kleeman, M. J., and Seinfeld, J. H. (2014). Influence of Vapor Wall Loss in Laboratory Chambers on Yields of Secondary Organic Aerosol. *Proc. Natl. Acad. Sci. USA.*, 111:5802–5807. doi:10.1073/pnas.1404727111.

Zhang, X., Schwantes, R. H., McVay, R. C., Lignell, H., Coggon, M. M., Flagan, R. C., and Seinfeld, J. H. (2015). Vapor Wall Deposition in Teflon Chambers. *Atmos. Chem. Phys.*, 15:4197–4214. doi:10.5194/acp-15-4197-2015.

UNIFIED THEORY OF VAPOR–WALL MASS TRANSPORT IN TEFLON-WALLED ENVIRONMENTAL CHAMBERS

Huang, Yuanlong, Ran Zhao, Sophia M. Charan, Christopher M Kenseth, Xuan Zhang, and John H. Seinfeld (2018). "Unified theory of vapor–wall mass transport in Teflon-Walled environmental chambers." In: *Environmental Science & Technology* 52.4, pp. 2134–2142. DOI: `10.1021/acs.est.7b05575`.

Unified Theory of Vapor−Wall Mass Transport in Teflon-Walled Environmental Chambers

Yuanlong Huang,[†] Ran Zhao,[‡] Sophia M. Charan,[‡] Christopher M. Kenseth,[‡] Xuan Zhang,[¶] and John H. Seinfeld*[,‡,§]

[†]Division of Geological and Planetary Sciences, California Institute of Technology, Pasadena, California 91125, United States
[‡]Division of Chemistry and Chemical Engineering, California Institute of Technology, Pasadena, California 91125, United States
[¶]National Center for Atmospheric Research, Boulder, Colorado 80301, United States
[§]Division of Engineering and Applied Science, California Institute of Technology, Pasadena, California 91125, United States

S *Supporting Information*

ABSTRACT: Secondary organic aerosol (SOA) formation is studied in laboratory chambers, in which volatile organic compounds (VOCs) are oxidized to produce low-volatility compounds that condense into the aerosol phase. It has been established that such oxidized low-volatility compounds can partition into the chamber walls, which traditionally consist of Teflon film. Several studies exist in which the rates of uptake of individual vapor compounds to the chamber walls have been measured, but a unified theory capable of describing the range of experimental measurements has been lacking. Here, a two-layer model of observed short and long vapor−wall interaction time scales in Teflon-walled environmental chambers is presented and shown to be consistent with experimental data on the rate of wall deposition of more than 90 compounds. Semiempirical relationships between key parameters in the model and vapor molecular properties are derived, which can be used to predict the fate of gas-phase vapor in the chamber under dry conditions.
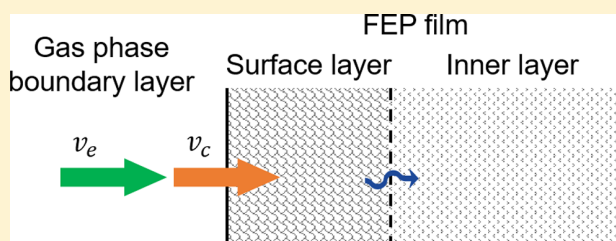
INTRODUCTION

The environmental chamber is a principal laboratory system used to study the formation, properties, and evolution of secondary organic aerosol (SOA).[1] The typical material from which chambers are constructed is Teflon film (fluorinated ethylene propylene, FEP). The process of SOA formation involves oxidation of a volatile organic compound (VOC) to generate low-volatility gas-phase products that subsequently condense into the aerosol phase. It has been established that these oxidized products may also partition into the Teflon chamber walls.[2−16] Such vapor−wall loss reduces the potential yield of SOA and must be accounted for in analysis of experiments. Current treatments of vapor−wall deposition in chambers consider the FEP film as an infinite medium into which vapor molecules dissolve.

The extent of partitioning of oxidized organic species typical of SOA into Teflon film has been studied experimentally by introducing species individually into a chamber and measuring their rate of decay from wall uptake. The uptake has been characterized by the time scale required to approach vapor−wall equilibrium (τ_w). Previous studies indicate that τ_w can be competitive with the time scales of other processes occurring in the chamber, such as the rate of VOC oxidation and the time scale associated with vapor−particle partitioning.[4,14] The time scale τ_w is governed by gas-phase diffusion through the boundary layer adjacent to the chamber wall, followed by uptake into the wall itself. Two major studies of vapor−wall uptake of individual

organic species typical of VOC oxidation products have reported significantly different time scales for vapor uptake, namely $\tau_w \sim$ 10 min[12] and $\tau_w \sim$ 10 h.[10] Possible reasons for the observed discrepancy in vapor−wall uptake rates include differences in the particular chemical systems studied or in the experimental protocol itself. The goal of the present work is to formulate and evaluate experimentally a unified theory of vapor−wall mass transport and uptake in Teflon-walled environmental chambers.

TWO-LAYER KINETIC SORPTION MODEL

We introduce a two-layer kinetic sorption model (Figure 1A), inspired by that proposed by Crank,[17] to explain the stress-dependent diffusion of vapor molecules into polymer film. In the two-layer model, after traversing a gas-phase boundary layer, vapor molecules enter a sharp, swollen outer layer in the Teflon that is thought to be stress-free, in which equilibrium with the gas phase is established relatively rapidly. It is estimated that a pseudosteady state profile in the gas-phase boundary layer is achieved on a time scale of order 10 s (Supporting Information, SI. I). Vapor molecules absorbed into the outer polymer layer (denoted the "Surface layer" in Figure 1A) then slowly diffuse into the interior of the polymer film (the "Inner layer" in Figure

Figure 1. Two-layer (dry) and three-layer (moist) models of vapor uptake at the surface of Teflon film in a laboratory chamber. (A) Two-layer kinetic sorption model. v_e and v_c are gas-phase boundary layer and interfacial mass transport coefficients, respectively. $C_g^b(t)$ is the bulk gas-phase concentration, $C_s(t)$ is the concentration (assumed to rapidly achieve uniformity) within the Surface Layer, and C_i is the transient concentratio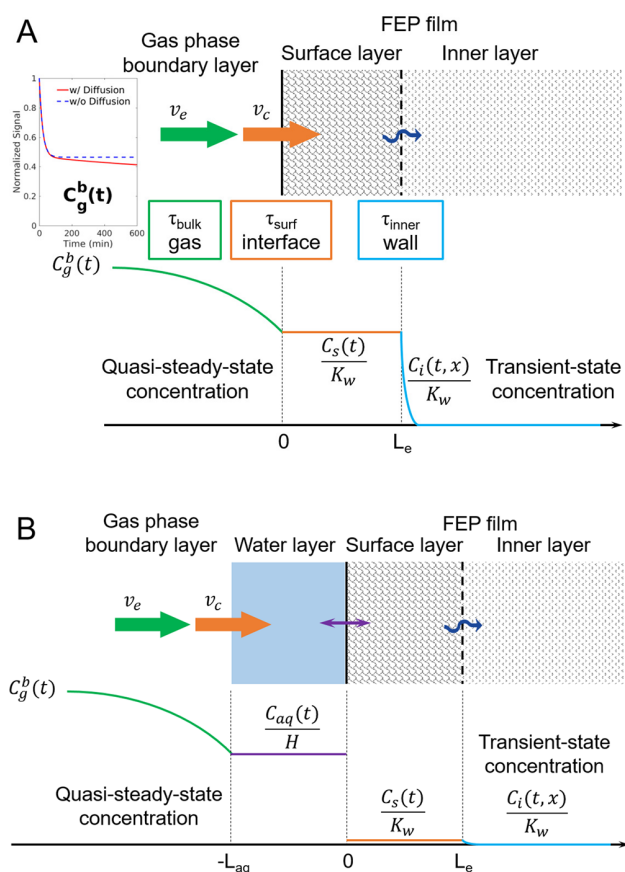n in the Inner Layer. The vapor−Teflon wall equilibrium constant, K_w, plays a role similar to that of a Henry's law dissolution constant. Time scales, τ_{bulk}, τ_{surf}, and τ_{inner}, corresponding to each layer are indicated. (B) Vapor uptake process in the presence of a thin aqueous film on the Teflon wall. Assumption of $H \gg K_w$, where H is the corresponding Henry's Law constant, is made. $C_{aq}(t)$ denotes the concentration of dissolved vapor in the aqueous film. L_e and L_{aq} represent the surface layer and aqueous film thicknesses, respectively.

1A) by breaking interchain bonds, impeded by the stress exerted by the polymer network.

Surface Layer. The Teflon FEP film is treated as a solution into which the molecules dissolve. Matsunaga and Ziemann[3] proposed that vapor-wall partitioning equilibrium can be represented by an effective organic mass concentration of the wall itself, C_w, by analogy to the effective aerosol mass concentration used in describing vapor-particle uptake.[18] Here, we introduce C_w and C_w', respectively, to distinguish between the compound-independent and -dependent equivalent mass concentration of the Teflon wall. These quantities are related by $C_w' = \frac{C_w}{\gamma^\infty}$, where γ^∞ is the activity coefficient of the solute vapor dissolved in an infinitely dilute solution of Teflon film. The compound-dependent C_w' reflects, therefore, the effect of the compound's activity in Teflon film. The process of partitioning into C_w corresponds to the surface layer absorption.

It is advantageous to define an effective thickness of the surface layer, L_e'. L_e' is related to C_w' by $L_e' = \frac{V}{A} \frac{C_w'}{\rho_w}$, where V and A are the volume and surface area of the chamber, respectively, and the density of FEP film[19] is $\rho_w = 2150 \text{ kg m}^{-3}$. Note that this effective thickness L_e' is related to the physical thickness of the surface layer L_e by $L_e' = \frac{L_e}{\gamma^\infty}$. Measurements of C_w suggest that L_e is of order 1 nm,[3,9,12] corresponding to a sharp air−polymer interface. This behavior is similar to that of a typical vapor−liquid interface, wherein the density increases sharply from the bulk vapor to the bulk liquid over a distance of order 1 nm (10−20 nominal molecular diameters).[20] For water molecules, this distance is ~3.3−8.4 Å.[21] For Teflon film, in determining C_w', Matsunaga and Ziemann[3] assumed an effective molecular weight of Teflon film of 200 g mol^{-1}; we adopt this assumption here, for which the effective Teflon molecular diameter is 0.54 nm. We tentatively take $L_e = 5$ nm, corresponding to a value of $C_w = 32.2 \text{ mg m}^{-3}$ (assuming $\gamma^\infty = 1$ and $\frac{A}{V} = 3 \text{ m}^{-1}$), consistent with the suggestions by Krechmer et al.[12] and Yeh and Ziemann.[9] The molecular diffusivity in the swollen and stress-free surface layer, that is of order $10^{-13} \text{ m}^2 \text{ s}^{-1}$,[22] establishes a time scale of ~1 ms to achieve concentration uniformity within the surface layer.

A key parameter in the kinetic sorption model is the vapor−wall equilibrium constant, K_w, similar to a Henry's law constant. The dimensionless $K_w = \frac{\rho_w}{\gamma^\infty c*} \frac{MW_{voc}}{MW_w}$, where MW_{voc} and MW_w are the mean molecular weights of the VOC vapor and FEP film, respectively, and $c*$ is the saturation mass concentration of the vapor. Typically, the activity coefficient of a compound in Teflon film, γ^∞, is the only unknown parameter in the expression for K_w. Limited information exists to constrain the value of γ^∞, and the activity coefficient γ^∞ is often assumed to be unity.[3,9,12] Within the consistent model framework developed here, γ^∞ is defined as the ratio of the physical thickness of the surface layer, L_e, to the effective thickness, L_e'; that is, $\gamma^\infty = \frac{L_e}{L_e'}$. If $\gamma^\infty = 1$, the FEP film behaves as an ideal solution. If $\gamma^\infty > 1$, the vapor molecules prefer to remain in the gas phase; if $\gamma^\infty < 1$, vice versa. The values of γ^∞ for a wide variety of compounds calculated from the literature[3,5,9,12] as a function of $c*$ estimated by EVAPORATION[23,24] as shown in Figure S2-A and Table 1 indicate that $\gamma^\infty > 1$. The inverse linear relationship between γ^∞ and $c*$ suggests that the FEP polymer is not generally hospitable for VOCs. This behavior, however, does not conflict with the presence of low volatility compounds in the Teflon film, since the vapor−wall equilibrium constant depends more strongly on $c*$ than γ^∞, such that compounds with lower $c*$ will haver higher K_w values (see Table 1 for dependence of γ^∞ on $c*$). Furthermore, the equilibrium fraction of the solute remaining in the gas phase, F_g, (Figure S2−B) is consistent with the observation that less volatile compounds tend to reside preferentially in the wall.

Inner Layer. The magnitude of the inner layer (Figure 1) effective diffusivity, $\mathcal{D}_{eff}$, is key to determining the temporal behavior of the bulk gas-phase concentration, $C_g^b(t)$, in a sufficiently long-duration experiment (~10 h). $\mathcal{D}_{eff}$ is considered to be influenced by the existence of FEP film in a glassy state, a coexistence of liquid and solid states, the latter of which comprises immobile microvoids.[25] Dual sorption theory[26] asserts that whereas free molecules can diffuse through the liquid layer, deeper diffusion must satisfy the Langmuir adsorption isotherm on the inner surface of local microvoids.[26] As a result, the molecular diffusivity in polymer is lower than that in pure liquid

Table 1. Parameters Representing Vapor−Wall Deposition in the Chambers[a]

	parameter	expression
k_1	forward rate (s^{-1})	$\left(\frac{A}{V}\right)v_l$
k_{-1}	backward rate (s^{-1})	$\frac{10^9}{L_e K_w}v_l$ or $\left(\frac{A}{V}\right)v_l\frac{\gamma^{\infty}c*}{10^3 C_w}\frac{MW_w}{MW_{voc}}$
k_2	first-order loss rate (s^{-1})	Figure 5 or from measurement[b]
L_e	surface layer thickness (nm)	5
K_w	dimensionless equilibrium constant	$\frac{10^9\rho_w}{\gamma^{\infty}c*}\frac{MW_{voc}}{MW_w}$
C_w	equivalent wall concentration (mg m^{-3})	$10.8\left(\frac{A}{V}\right)$
γ^{∞}	activity coefficient in FEP	$10^{3.299}(c*)^{-0.6407}$ (Figure S2-A)
v_l	wall deposition velocity (m s^{-1})	$\left(\frac{\pi}{2}\frac{1}{\sqrt{k_e\mathcal{D}_g}}+\frac{4}{\alpha_w\omega}\right)^{-1}$
α_w	wall accommodation coefficient	$10^{-2.744}(c*)^{-0.6566}$ (Figure S3)
$\mathcal{D}_{eff}$	effective diffusivity in FEP film (m^2 s^{-1})	$10^{-17.05}(\theta-110.9)^{-1.695}(c*)^{0.1831}$
ρ_w	Teflon FEP density[19] (kg m^{-3})	2150
$c*$	vapor saturation concentration (μg m^{-3})	species dependent (ref 23)
k_e	eddy diffusivity coefficient[12] (s^{-1})	$0.004 + 10^{-2.25}(V)^{0.74}$
V	chamber volume (m^3)	chamber dependent
A	chamber surface area (m^2)	chamber dependent
$\mathcal{D}_g$	diffusivity in gas phase (m^2 s^{-1})	5×10^{-6}
ω	mean molecular velocity (m s^{-1})	$\sqrt{\frac{8RT}{\pi MW_{voc}}}$
R	gas constant (kg m^2 s^{-2} K^{-1} mol^{-1})	8.314
MW_w	average molecular weight of FEP[3] (g mol^{-1})	200
MW_{voc}	vapor molecular weight (g mol^{-1})	species dependent
θ	molecular volume (cm^3 mol^{-1})	species dependent (Figure 3)

[a]The parameters listed here correspond to the dynamic system $X \underset{k_{-1}}{\overset{k_1}{\rightleftharpoons}} Y \overset{k_2}{\rightarrow} Z$, where X is the species of interest. Detailed discussion of the incorporation of this model framework into chamber models can be found in SI. VII. [b]It is recommended to fit the measured signal decay of species X to the analytical equation in SI. VI to obtain k_2, or simply use the asymptotic relationship $k_w^X = \frac{K_{eq}}{1+K_{eq}}k_2$, where k_w^X is the "apparent" first-order decay rate constant of species X, and $K_{eq} = \frac{k_1}{k_{-1}}$. In general, the use of the asymptote will not lead to a significant difference if the measurement lasts several hours.

$(10^{-13} - 10^{-9}$ m^2 s$^{-1})$.[27] The overall $\mathcal{D}_{eff}$ of molecules absorbed in the Teflon inner layer is of order 10^{-22} to 10^{-17} m^2 s^{-1}, well within the range of semisolid diffusivities.[28] By fitting time-dependent Teflon uptake rates of a variety of species, one can estimate the $\mathcal{D}_{eff}$ values.

Governing Equations Describing Uptake of Vapor Molecules in the Two-Layer Model. The mass transport coefficients across the gas-phase boundary layer and through the vapor-Teflon interface (Figure 1) can be written as $v_e = \frac{2}{\pi}\sqrt{k_e\mathcal{D}_g}$ and $v_c = \frac{\alpha_w\omega}{4}$, respectively, where k_e is the eddy diffusivity coefficient for mixing in the chamber, $\mathcal{D}_g$ is the vapor molecular diffusivity in air, α_w is the vapor−wall accommodation coefficient (see discussion in SI. II), and ω is the vapor molecular mean speed. From mass transfer resistance theory, the overall mass

transport coefficient across the gas-phase boundary layer and the air-Teflon interface is $v_l = \left(\frac{1}{v_e} + \frac{1}{v_c}\right)^{-1}$. For quasi-steady state gas-phase boundary layer diffusion (see discussion in SI. I), the bulk gas-phase mass flux J_b (μg s^{-1}) to the Teflon surface is

$$J_b = Av_l\left(C_g^b(t) - \frac{C_s(t)}{K_w}\right) \tag{1}$$

where C_g^b is the gas-phase concentration in the bulk chamber and C_s is the concentration of vapor dissolved in the wall surface layer. The mass balance for C_g^b involving vapor-wall mass transfer and gas-phase chemical reactions is

$$\frac{dC_g^b(t)}{dt} = -\left(\frac{A}{V}\right)v_l\left(C_g^b(t) - \frac{C_s(t)}{K_w}\right) + \sum^i R_i \tag{2}$$

where $\sum^i R_i$ represents the net generation or consumption of the species by chemical reaction.

Within the Teflon surface layer, the diffusive flux, J_d (μg s^{-1}), at the surface layer−inner layer boundary is

$$J_d = -A\mathcal{D}_{eff}\frac{\partial C_i(x, t)}{\partial x}\Bigg|_{x=L_e} \tag{3}$$

where C_i is the concentration of vapor molecules in the wall inner layer. Time-dependent mass conservation for C_s is given by

$$\frac{dC_s(t)}{dt} = \frac{v_l}{L_e}\left(C_g^b(t) - \frac{C_s(t)}{K_w}\right) + \frac{\mathcal{D}_{eff}}{L_e}\frac{\partial C_i(x, t)}{\partial x}\Bigg|_{x=L_e} \tag{4}$$

Diffusion of the dissolved solute in the inner Teflon layer obeys

$$\frac{\partial C_i(x, t)}{\partial t} = \mathcal{D}_{eff}\frac{\partial^2 C_i(x, t)}{\partial x^2} \tag{5}$$

Associated initial and boundary conditions are

$$C_g^b(0) = C_{g0}^b; \quad C_s(0) = C_{s0}; \quad C_i(x, 0) = 0;$$
$$C_i(0, t) = C_s(t); \quad C_i(\infty, t) = 0 \tag{6}$$

C_{g0}^b and C_{s0} are appropriate initial concentrations. For example, $C_{s0} = 0$ corresponds to a pristine chamber condition, while $C_{g0}^b = \frac{C_{s0}}{K_w}$ applies if the bulk gas-phase and surface layer concentrations are at equilibrium at the beginning of an experiment. The boundary condition as $x \rightarrow \infty$ expresses the consequence of the slow diffusion in the inner layer relative to the overall extent of the layer itself. If $\mathcal{D}_{eff}$ is sufficiently small such that penetration into the inner layer is negligible over an experiment, the mass conservation equations reduce to a single-layer sorption model, in which the corresponding vapor−wall equilibrium time scale (τ_{vwe}) is

$$\tau_{vwe} = \left(\frac{A}{V}\right)^{-1}\left(1 + \frac{V}{K_w L_e A}\right)^{-1}v_l^{-1} \tag{7}$$

Table 1 summarizes the key parameters that represent vapor−wall deposition in chamber experiment simulations.

Aqueous Film Model. Under sufficiently high relative humidity conditions (RH > 90%), it is assumed that an aqueous film of thickness L_{aq} exists on the chamber wall (Figure 1B). Since the diffusivity of vapor molecules in water $\mathcal{D}_{aq}$ is $\sim 1 \times 10^{-9}$

m^2 s^{-1},[29] the estimated time scale $\left(\frac{L_{aq}^2}{\mathcal{D}_{aq}}\right)$ for the dissolved vapor concentration to reach uniformity in this thin layer of water is sufficiently small (e.g., $\sim 10^{-1}$ s if $L_{aq} = 10\ \mu m$) such that the rate-limiting step for uptake is either gas-phase boundary layer diffusion or interfacial accommodation at the air−water interface.

Since oxidized VOCs tend to be polar molecules, γ^{∞} in aqueous solution should be smaller than that in a Teflon polymer solution, such that partitioning in the aqueous phase is preferred over the polymer phase. Thus, in this case, a reasonable assumption is that vapor partitioning does not proceed beyond the thin water film on the Teflon surface.

For this single-layer model, eq 7 can be directly applied to the aqueous film uptake, replacing K_w and L_e with the Henry's law constant H and L_{aq}, respectively. As described in SI. II, on the basis of measured time scale and equilibrium constants, it is possible to estimate the accommodation coefficient of the water surface.

■ EXPERIMENTAL STUDY OF VAPOR−WALL UPTAKE

To study vapor−wall interaction, we either (i) generated the compounds in situ by VOC oxidation in the chamber,[10,12,30−34] or (ii) injected the compounds of interest (purchased or synthesized) into the chamber.[2,3,9,28,35−38] The two-layer kinetic model is applied to two laboratory data sets from the Caltech Environmental Chamber (24 m^3, $\frac{A}{V} \sim 2$ m^{-1}) on the dynamics of vapor−wall deposition of individual compounds: (i) Zhang et al.[10] corresponding to in situ generation and (ii) deposition measurements of alcohols (1-hexanol 98%, 1-heptanol 98%, 1-octanol ≥ 99%, 1-nonanol 98%, 1-decanol ≥ 99%, 1-undecanol ≥ 97.5%, and 1-dodecanol 98%), aromatics (toluene 99.8%, *m*-xylene ≥ 99%, *o*-xylene 98%, and 1,3,5-trimethylbenzene 98%), alkanes (*n*-dodecane ≥ 99%, *n*-tridecane ≥ 99%, *n*-tetradecane ≥ 99%, *n*-octylcyclohexane 98%), and biogenics (isoprene 99%, methacrolein 95%, methyl vinyl ketone 99%, and α-pinene ≥ 99%) (all purchased through Sigma-Aldrich) by direct injection.

In the experiments conducted by Zhang et al.,[10] in situ oxidation of α-pinene, *n*-dodecane, toluene, and isoprene were carried out under high- and low-NO$_x$ conditions, with oxidation periods varying from 1 to 7 h. A customized CF$_3$O$^-$−CIMS[39] (chemical ionization mass spectrometry) was used to monitor the vapor-wall decay rates. Refer to Zhang et al.[10] for more experimental details. In the direct injection experiments, a bulb containing 10 to 50 μL of pure or mixed liquid VOCs was maintained at 65 °C (as well as the 50 cm stainless injection line, 3/8 in. OD) to ensure complete injection at a flow rate of 5 L min^{-1} of clean air ($\sim$100 ppb in the chamber, several orders of magnitude lower than the saturation vapor pressure). Before each injection, the chamber has been flushed with clean air at a flow rate of 370 L min^{-1} for 24 h at 45 °C. The injection period varied from minutes (biogenics) to hours (alcohols). After the injection period, 5 pulse injections of clean air were used to actively mix the chamber without significantly altering its volume. The chamber is considered to be well mixed $\sim$5 min after this operation, which is especially relevant for compounds with short injection periods. A series of RH-dependent studies were carried out in the chamber under 8% ± 5%, 50% ± 5%, and 80% ± 5% RH at 20 °C.

Over $\sim$18 h in the dark, a gas chromatograph with flame ionization detector (GC/FID, Agilent 6890N) was used to monitor the temporal concentration changes at a continuous sampling flow rate of 0.29 L min^{-1} through a perfluoroalkoxy

(PFA) Teflon tube (1/4 in. o.d., 3/16 in. i.d., and 2.0 m length). Pagonis et al.[40] note that the use of a PFA Teflon tube induces a response time lag for "sticky" compounds; the continuous flow through the sampling tube and lower sampling time resolution ($\sim$10 min) act to smooth this effect. A HP-5 column (30 m × 0.32 mm i.d. × 0.25 μm film thickness) was used for alcohols, aromatics, alkanes, and α-pinene, and a HP-PLOT Q column (15 m × 0.53 mm i.d. × 40 μm film thickness) was used for isoprene, methacrolein (MACR), and methyl vinyl ketone (MVK). For mixtures, the GC temperature ramping procedure was adjusted to obtain full peak resolution. It is challenging to clearly define the start time for GC measurements of compound dark decay. We ignore the first 3 to 5 data points of the GC measurements, which is $\sim$1 h after injection, on the assumption that the vapor concentrations in the gas phase and the surface layer have reached equilibrium.

Additionally, studies of in situ 20 s-pulse generated compounds[12] from isoprene oxidation under 8% ± 5%, 50% ± 5%, and > 90% RH were carried out. When RH was greater than 90%, an aqueous film was introduced to the surface of Teflon film by injecting water vapor into the chamber at 30 °C until the RH reached $\sim$80% and cooling to 20 °C to facilitate a uniform water film condensation on the wall, as evidenced visually by the blurry appearance of the chamber. Isoprene ($\sim$200 ppb), $\sim$1.2 ppm of NO (Airgas, 500 ppm ±1%), and $\sim$1.2 ppm of CH$_3$ONO (synthesized following Taylor et al.[41]) were injected to the chamber, respectively. UV lights were turned on for 20 s ($j_{NO_2} = 0.0044$ s^{-1}), and no nucleation was observed after lights off. Oxidation products were monitored with a custom-modified I$^-$-CIMS[42] with a 2 L min^{-1} sampling rate through $^1/_4$ in. PFA tube. A permeation tube with pure liquid CH$_3$I (Sigma-Aldrich, 99%) was used for reagent ion generation in I$^-$-CIMS, where vapor molecules X are detected as the cluster (X·I$^-$).

In the two-layer kinetic model simulation, the values of k_e and $\mathcal{D}_g$ used are 0.075 s^{-1} and 5 × 10^{-6} m^2 s^{-1}, respectively, for all compounds.[6] The accommodation coefficient α_w is calculated by a fitted empirical equation based on literature data (Table 1 and Figure S3, see SI. II for details). Activity coefficients for the compounds studied in Zhang et al.[10] are predicted by the equation in Table 1 and Figure S2-A. Since the oxidation period in Zhang et al.[10] varied from 1 to 7 h, it is reasonable to assume that an equilibrium state between the bulk chamber and the surface layer had been reached; that is, $C_g^b = \frac{C_s}{K_w}$, when lights are off. This assumption excludes the oxidation period from the fitting process. We will address subsequently the effect of the oxidation period on the temporal profile of bulk concentration.

■ RESULTS AND DISCUSSION

Effect of Oxidation Period on Vapor−Wall Partitioning. To study vapor−wall interaction, the species of interest is introduced to the chamber by either direct injection or in situ generation. During injection, the more volatile compounds generally require less time to inject but achieve wall partitioning more slowly (e.g., *n*-alkanes[3]), whereas less volatile compounds require a longer injection time, during which the bulk chamber and the wall may have already reached equilibrium when injection is completed. Even though the injection period can be shortened by heating the bulb and the injection line,[3,9] for passively mixed chambers the chamber mixing time scale may be the limiting factor to obtain a well-mixed concentration in the chamber. This mixing issue is avoided with in situ generation of

oxidation products. Ideally, the VOC oxidation period is short, so as to approximate as closely as possible a pulse input of oxidation products.[12] This is important, as the anticipated equilibration time between generation in the chamber and absorption by the surface layer of Teflon is of order 10^3 s.[12] However, generation of detectable concentration of products usually requires a relatively long oxidation time (OH concentration is typically $\sim 10^6$ molecules cm^{-3}), during which period equilibrium between the bulk chamber and the surface layer is likely to be achieved.

An idealized kinetic model is useful to describe the interplay between in situ oxidation and the approach to vapor−wall equilibrium. Let us assume that the VOC oxidation can be represented by the first-order reaction $G \xrightarrow{k_0} X$, where G is the VOC precursor, X is the oxidation product (i.e., the bulk concentration $C_g^b(t)$ in eq 2), and k_0 is an effective first-order rate constant. Since diffusion in the inner layer of the Teflon film is sufficiently slow, it is reasonable to ignore the inner layer uptake of the vapors during the oxidation period, that is, the second term in eq 4. By multiplying a scaling factor $\frac{A}{V}L_e$ to $C_s(t)$ in eq 4, the system can be represented kinetically by $G \xrightarrow{k_0} X \underset{k_{-1}}{\overset{k_1}{\rightleftharpoons}} Y$, where $Y = \frac{A}{V}L_e C_s(t)$, $k_1 = \frac{A}{V}v_1$, and $k_{-1} = \frac{1}{L_e K_w}v_1$. The equilibrium constant for this system is $K_{eq} = \frac{k_1}{k_{-1}} = K_w \frac{A}{V}L_e$. By this representation, vapor-wall partitioning during the VOC oxidation period is mathematically analogous to a classical equilibrium reaction system.

The departure from vapor-wall equilibrium at the end of the reaction period is defined by the normalized deviation $\epsilon = \frac{Y_e - Y_0}{Y_e} = \frac{X_0 - X_e}{X_e K_{eq}}$, where X_0 and Y_0 are the concentrations of X and Y at the end of the oxidation period, and X_e and Y_e are the concentrations at equilibrium. Thus, a value of $\epsilon = 0$ indicates that equilibrium has already been reached at the end of the oxidation period, whereas a value of ϵ close to 1 suggests that from the measured concentration change of X one can derive the characteristic time scale and equilibrium constant for vapor−wall deposition. Note that it is necessary only to focus on species X since that is the compound being measured. An analytical solution for the time-dependent dynamics of this kinetic system is given in SI. III.

For the compounds examined in this study and by Zhang et al.,[10] the oxidation period τ_{ox} varies from ~ 10 s to ~ 7 h. Assuming that 5% of the precursor G is consumed at the end of the oxidation period, the reaction rate constant k_0 follows the relationship $\tau_{ox} k_0 = 0.05$. The forward rate constant k_1 is determined by the mixing time scale in the chamber (k_e), as well as the surface accommodation coefficient (α_w). Using $k_e = 0.075$ s^{-1}, $\mathcal{D}_g = 5 \times 10^{-6}$ m^2 s^{-1}, and $\alpha_w = 10^{-5}$ (discussion in SI. II suggests that most of the compounds studied here are located in the gas-phase boundary layer diffusion regime, where the critical $\alpha_w \sim 10^{-6}$, for simplicity, a fixed value of 10^{-5} for α_w is assumed here), a value of $k_1 = 4.02 \times 10^{-4}$ s^{-1} is obtained, which is of the same order of magnitude as the values reported in the wall deposition study by Krechmer et al.[12] A contour plot (Figure 2) of ϵ as a function of vapor−wall equilibrium constant, $K_w \frac{A}{V}L_e$, and oxidation period, τ_{ox}, indicates that the majority ($\sim 75\%$) of the compounds studied in Zhang et al.[10] had already reached vapor−wall equilibrium at the end of the relatively lengthy oxidation period. In such a case, it is reasonable to estimate the
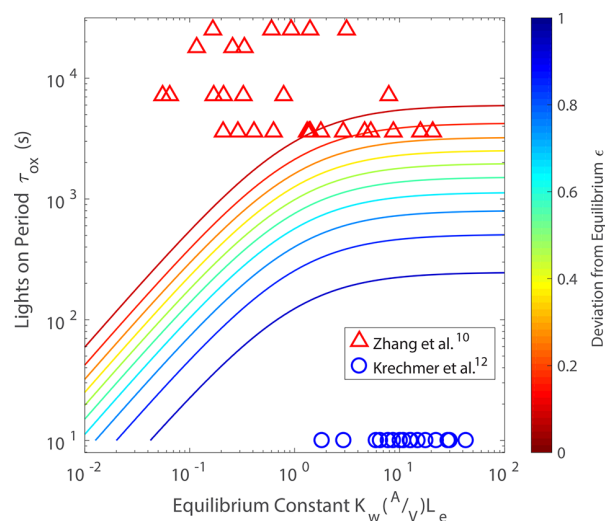
Figure 2. Deviation from equilibrium state at the end of oxidation period τ_{ox} as a function of equilibrium constant $K_W(A/V)L_e$ and oxidation period τ_{ox} for the system represented by $G \xrightarrow{k_0} X \underset{k_{-1}}{\overset{k_1}{\rightleftharpoons}} Y$, where $k_0 = 0.05/\tau_{ox}$ (s^{-1}, assume 5% of G is consumed at the end of oxidation period τ_{ox}), $k_1 = (A/V)v_1$ (s^{-1}), $k_{-1} = (1/L_e K_w)v_1$ (s^{-1}), A/V is the surface area to volume ratio of the chamber (m^{-1}), v_1 is the vapor-to-wall mass transport coefficient (m s^{-1}), L_e is the surface layer thickness (m), and K_w is the dissolution equilibrium constant of vapor molecule in the Teflon film. The equilibrium constant $K_{eq} = \frac{k_1}{k_{-1}} = K_w \frac{A}{V}L_e$.

diffusivity in the inner layer by assuming equilibrium between the bulk chamber and the surface layer. The small value of the wall accommodation coefficient reported by Zhang et al.[10] likely represents a combination of surface accommodation and inner layer diffusion. Figure 2 shows explicitly the effect of the length of the oxidation period on the surface-layer equilibrium process, since inner-layer diffusion will dominate the dynamics of the vapor sink in a long-duration oxidation experiment.

Diffusion in Teflon Polymer. The inferred diffusivities $\mathcal{D}_{eff}$ of species dissolved in Teflon film obtained by fitting data to the two-layer model as a function of the molecular saturation concentration c^* are shown in Figure 3A. $\mathcal{D}_{eff}$ values are in the range of 10^{-22} to 10^{-17} m^2 s^{-1}, which is of the order 10^6 smaller than those of small organic molecules in polymer film,[22,27,43] a result that is consistent with the higher energy barrier for larger molecules.[17,43] A transition state between solid and liquid diffusivities of this order of magnitude is well within the range of those in semisolid organic aerosol particles.[27]

With the assumption that the molecular diffusivity in the FEP film can be expressed as a function of molecular volume, we apply a semiempirical equation to correlate the diffusivity as a function of vapor molecular volume (θ in cm^3 mol^{-1})[44] and vapor saturation concentration (c^* in μg m^{-3}). c^* is used as the parameter that incorporates the contribution from different functional groups, and as noted earlier, is estimated by the empirical routine EVAPORATION.[23,24] The diffusivities obtained from the semiempirical eq (Table 1) are shown in Figure 3B. 95% of the predicted diffusivities lie within an order of magnitude of those inferred $\mathcal{D}_{eff}$. The high order of negative molecular volume dependence is consistent with the expectation that the larger the molecule, the smaller the diffusivity. The critical volume in the semiempirical eq (110.9 cm^3 mol^{-1}) can be viewed as a characteristic "hole" in the film; thus, small molecules
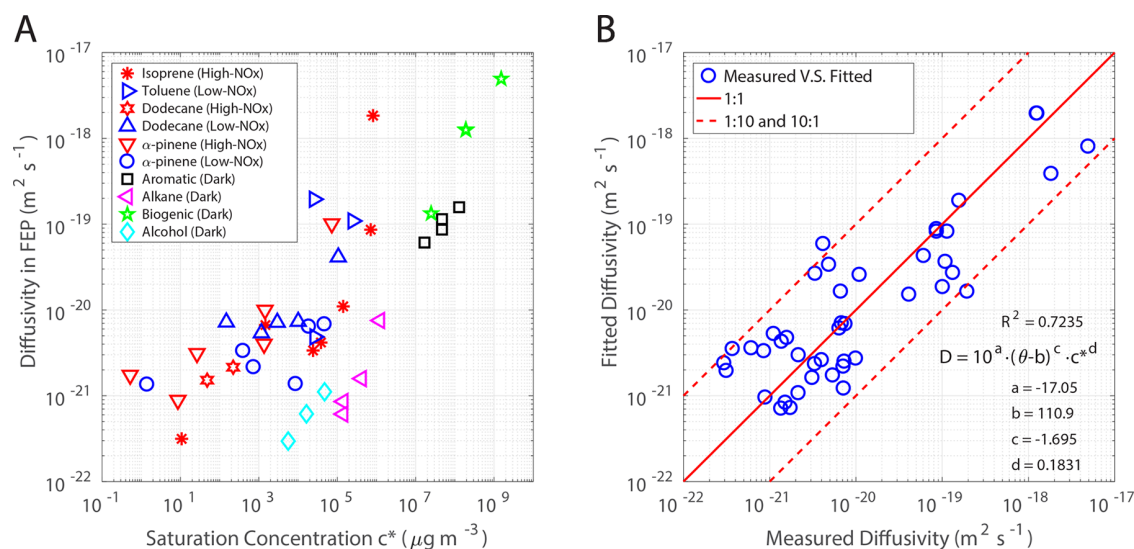
Figure 3. (A) Diffusivity in FEP film inferred from measurements by Zhang et al.[10] using CIMS and from this study using GC/FID as a function of saturation concentration (c^*) predicted by EVAPORATION.[23,24] (B) Comparison between measured and fitted diffusivity ($\mathcal{D}_{\text{eff}}$ in $m^2\,s^{-1}$) in Teflon film. The molecular volume (θ in $cm^3\,mol^{-1}$) and saturation vapor concentration (c^* in $\mu g\,m^{-3}$) dependent fitting equation in panel B is used. Molecular volume is estimated by summing the characteristic atomic volumes ($\theta = C \times 16.35 + H \times 8.71 + O \times 12.43 + N \times 14.39\ cm^3\,mol^{-1}$, where C, H, O, and N represent the number of carbon, hydrogen, oxygen, and nitrogen atoms in the compound).[44] Note: this equation applies only for molecules with a volume exceeding $110.9\ cm^3\,mol^{-1}$.
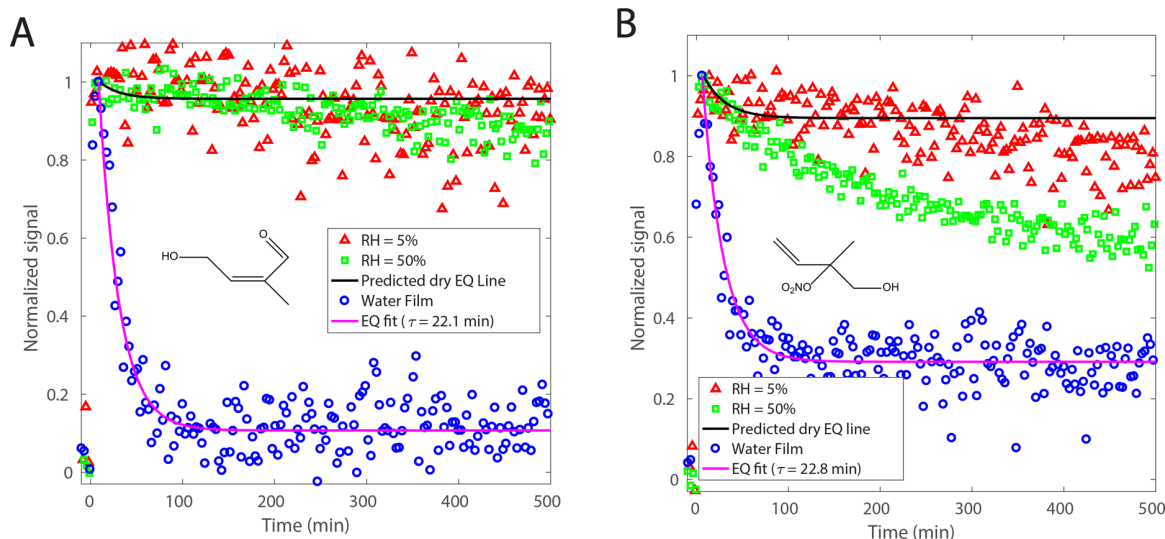
Figure 4. Signal decay after 20 s of in situ generation of isoprene oxidation products: (A) $C_5H_8O_2$ and (B) $C_5H_9O_4N$ at RH = 5%, 50%, and >90% (with aqueous film). Because of the signal decay caused by the "memory effect" arising from the sampling tube and instrument inlet,[40] the peaks show up ~5 min after lights off.

only have to overcome the cross-links between polymer chains. The fitted value of the critical volume is found to exceed those of most of the molecules studied previously;[22,43] thus the semiempirical relation given in Figure 3B cannot be used for molecules smaller than the critical volume. The diffusivity is found to be mildly dependent on vapor saturation concentration, reflecting the effect of the presence of functional groups (or molecular shape) on molecular diffusivity.

Diffusivities of vapor molecules in fresh and aged Teflon chambers have also been investigated. Though the absorption properties of the surface layer were reported to be unchanged in either fresh or aged Teflon chambers,[3] by fitting experimental data in the Caltech chamber,[10] we found that the inner layer

diffusivity increased with use of chambers, consistent with the observations by Loza et al.[2] Such behavior could be attributed to alteration of interchain bonds, such that subsequent diffusion is characterized by internal stress relaxation.[17,43] See the discussion in SI.IV for additional details.

Humidity Effect. For polymer film chambers, permeation of ubiquitous ambient water vapor through the film is possible given the small molecular volume and high diffusivity ($\sim 10^{-12}\ m^2\,s^{-1}$) of water in such polymer films.[45] The dissolution of water molecules in the Teflon film can exert an impact on the behavior of organic molecules therein. For hydrophilic compounds, the water could facilitate the absorption of the vapors into the film, while for hydrophobic compounds, it could exert a retarding

effect. In the high humidity case, in which an aqueous film is hypothesized to be present on the Teflon surface (panel B of Figure 1), it is evident that hydrophilic compounds would dissolve in the aqueous film.

The limited studies of RH-dependent vapor−wall interaction in chambers that exist report that the vapor−wall loss rate increases at higher RH (>50%).[2,35,37,38] It is notable that the compounds that have been studied in this regard are either reactive with water (e.g., IEPOX[35,37]) or highly water-soluble (e.g., HCOOH, H_2O_2,[38] and glyoxal[2]). These observations are consistent with the existence of water molecules in the Teflon film facilitating the absorption of hydrophilic compounds. We used two experimental strategies to investigate the role of RH in vapor−wall interaction.

In the first class of experiments, we injected into the chamber at different RH levels several groups of compounds (alcohols, alkanes, aromatics, and biogenics) that are not highly water-soluble and have relatively large molecular volume. A GC/FID was used to monitor the long-term dark decay of these compounds. The inferred diffusivities of the alcohols, alkanes, aromatics, and biogenics in Teflon are shown in Figure S5, indicating that most of the diffusivities decrease as RH increases. It is expected that at high RH, more water molecules dissolve in the Teflon film, such that intrusion of hydrophobic compounds is hindered.

Second, we carried out the same experimental protocol as that of Krechmer et al.[12] based on an in situ pulse generation of oxidation products (OH concentration is ∼10^8 molecules cm^{-3}). The temporal profiles of two isoprene oxidation products ($C_5H_8O_2$ and $C_5H_9O_4N$) are shown in Figure 4. Under dry conditions (RH ∼ 5%), $C_5H_8O_2$ and $C_5H_9O_4N$ exhibit essentially the same diffusivities as those observed by Zhang et al.[10] However, at RH ∼ 50%, the two compounds behave differently; a faster decay rate is observed for $C_5H_9O_4N$, which is likely attributable to hydrolysis of the compound containing a −ONO_2 group.[46] When a water film is introduced intentionally (RH > 90%), the signals of both compounds decrease rapidly after the lights are off at almost the same rates, reaching a constant level for the next 8 h. By fitting the data at RH > 90% in Figure 4 to the aqueous film model (Figure 1B), a characteristic time scale is found to be ∼22 min for each compound, considerably faster than that due to inner layer diffusion under dry conditions. This value is in the range of vapor−wall equilibrium time scales (τ_w) reported by Krechmer et al.[12] and Matsunaga and Ziemann.[3] With an estimated chamber eddy diffusivity of 0.075 s^{-1},[6] the calculated accommodation coefficients of $C_5H_8O_2$ and $C_5H_9O_4N$ at the water surface are 3.06×10^{-5} and 1.32×10^{-5}, respectively, consistent with gas-phase boundary layer mass transport being the rate-limiting step in the fast equilibrium sorption process.

The water film serves as a substantial reservoir given that both compounds are water active (soluble or reactive). By comparison, the inferred equilibrium constants, K_{eq}, for both compounds in the aqueous film exceed those in the dry Teflon film by factors of 186 and 21, suggesting that the majority of the vapor molecules remain within the aqueous layer. The results of this aqueous film experiment are consistent with the conclusion that in SOA formation experiments under high RH conditions, the presence of a condensed water film on the wall will exacerbate vapor−wall loss of hydrophilic oxidation products.

Mechanistic Representation of Vapor−Wall Deposition. After the introduction of vapors into the chamber (either by injection or in situ generation), loss due to wall uptake is

generally reported as first order. The experimental results reported here show that, in addition to the establishment of rapid equilibrium between the bulk gas phase and the surface layer of the chamber wall ($\tau_{surf} \sim 10^3$ s), inner layer diffusion as well as chemical reactions (e.g., hydrolysis) can lead to a continuous decay of the gas-phase vapors in the bulk chamber. This process can be represented kinetically by the following system: source $\rightarrow$ X $\underset{k_{-1}}{\overset{k_1}{\rightleftharpoons}}$ Y $\overset{k_2}{\rightarrow}$ Z, where "source" represents injection or in situ oxidation. Species X and Y represent the same compound in different phases, and species Z is the same compound in the third phase (e.g., the inner layer in this case). Correspondingly, k_2 represents either the first-order chemical reaction rate constant or the mass transfer coefficient. The forward and backward rate constants k_1 and k_{-1} govern the approach to phase equilibrium of X and Y.

When injection or in situ oxidation has ceased, the above dynamic system can be represented simply as X $\underset{k_{-1}}{\overset{k_1}{\rightleftharpoons}}$ Y $\overset{k_2}{\rightarrow}$ Z. If species X and Y have reached equilibrium, and if $k_2 \ll k_1 + k_{-1}$, a slow decay follows a rapid equilibrium. The time-dependent analytical solution of this kinetic system is presented in SI. VI. The apparent first-order decay rate constant, k_w^X, of species X exhibits the long-time asymptote $\frac{K_{eq}}{1 + K_{eq}} k_2$, where $K_{eq} = \frac{k_1}{k_{-1}}$ as defined above.

The net loss rate constant k_2 is a function of diffusivity $\mathcal{D}_{eff}$. To obtain a relationship between k_2 and $\mathcal{D}_{eff}$, an empirical equation can be fitted as shown in Figure 5, where k_2 and $\mathcal{D}_{eff}$ both emerge from fitting experimental data from the equilibrium reaction model and the two-layer diffusion model. For comparison, k_2 values derived from reported apparent first-order loss rates, k_w, by the asymptotic relationship, $k_w = \frac{K_{eq}}{1 + K_{eq}} k_2$, and the inferred diffusivities are shown in Figure 5. Many of these reported data
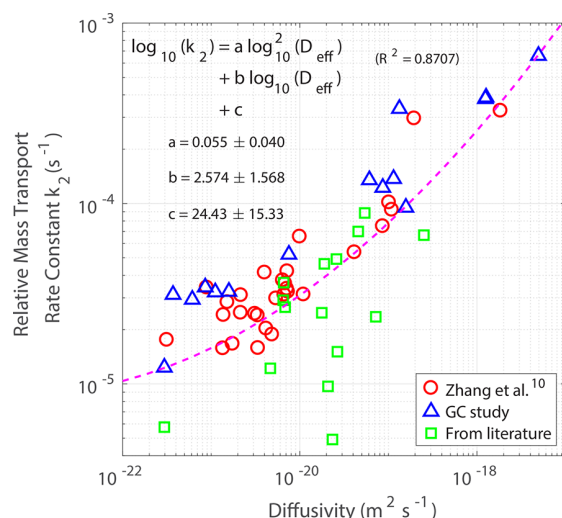
Figure 5. Empirical relationship between compound molecular diffusivity $\mathcal{D}_{eff}$ (m^2 s^{-1}) and relative inner layer mass transport rate constant k_2 (s^{-1}). k_2 is derived by fitting the analytical solution in SI.V to the experimental data, whereas data points from the literature[2,28,30−33,35,36] are calculated by the asymptotic relationship between k_w (reported data) and k_2. Diffusivity is predicted by the equation in Figure 3.

points lie within the uncertainty of the empirical relationship. The small reported k_2 values may be the result of different chamber conditions,[30,32,35] or the use of the asymptote, since some of the data are from the observation within 2 h (as indicated in SI. VI, in the short time period, the apparent k_w is small). Note that this empirical relationship does not account for the presence of heterogeneous reactions, which may change the value of k_2.

Atmospheric Implications. Teflon-walled laboratory chambers serve as the predominant system for the study of atmospheric SOA formation. Clear evidence exists for the deposition of VOC oxidation products on polymeric Teflon chamber walls. Such deposition removes products that would otherwise condense onto particles as SOA. Since the presence of wall deposition of vapors leads to an underestimate of the atmospheric SOA-forming potential of the parent VOC, data that have been influenced by such wall deposition will lead to an underprediction of SOA formation when extrapolated to the atmosphere.

The wall deposition process involves transport of vapor molecules from the core of the chamber to a boundary layer on the wall of the chamber, through which vapors are transported to the wall surface by a combination of molecular diffusion and macroscopic mixing. Vapor molecules diffuse into the Teflon polymer matrix by a process akin to that of uptake into a condensed phase. Observed rates of molecular uptake into Teflon polymer are found to be consistent with a model of the Teflon film consisting of two layers: (1) a thin surface layer into which vapor molecules penetrate first through the gas-phase boundary layer and second across the interface, over a time scale of order 10^3 s; and (2) a deeper layer of effectively semi-infinite extent into which the absorbed vapor molecules diffuse from the surface layer. The uptake rates by Teflon-walled chamber of over 90 individual organic vapor species are found to depend upon their molecular saturation vapor concentration ($c*$) and molecular size (θ).

Semiempirical equations have been formulated to describe the absorptive properties (γ^∞ and α_w) of the surface layer and the diffusivity in the inner layer of FEP film. Additional studies are needed to characterize the temperature effect on the vapor uptake process. Water molecules dissolved in the Teflon film provide extra sinks on the wall for hydrophilic compounds. Under sufficiently high RH conditions, where a thin film of condensed water is present on the Teflon surface, the wall becomes an increasingly competitive reservoir for hydrophilic compounds. The challenge is to design VOC oxidation chamber experiments under different RH levels so as to minimize vapor transport to the chamber walls. To better constrain the measured vapor—wall loss rate (e.g., the "apparent" first-order rate constant k_w), recommended parameters and guidelines are given in Table 1, which can facilitate a comprehensive consideration of the sinks of gas-phase species in a typical SOA formation experiment.

ASSOCIATED CONTENT

Supporting Information

This material is available free of charge via the Internet at http://pubs.acs.org/. The Supporting Information is available free of charge on the ACS Publications website at DOI: 10.1021/acs.est.7b05575.

> Discussion of the time scale of gas-phase boundary layer transport; parametrization of the activity and accommodation coefficients in the surface layer absorption; additional calculations; diffusivities in fresh and aged

Teflon chambers; humidity effect on Teflon inner layer diffusivity; application of the two-layer framework in chamber simulations (PDF)

AUTHOR INFORMATION

Corresponding Author
*Phone: +1 626 395 4635; fax: +1 626 568 8743; e-mail: seinfeld@caltech.edu.

ORCID
Ran Zhao: 0000-0002-1096-7632
Christopher M. Kenseth: 0000-0003-3188-2336
Xuan Zhang: 0000-0003-1548-8021
John H. Seinfeld: 0000-0003-1344-4068

Notes
The authors declare no competing financial interest.

REFERENCES

(1) Schwantes, R. H.; McVay, R. C.; Zhang, X.; Coggon, M. M.; Lignell, H.; Flagan, R. C.; Wennberg, P. O.; Seinfeld, J. H. *Advances in Atmospheric Chemistry*; World Scientific, 2017; Chapter 1 Science of the Environmental Chamber, pp 1−93.

(2) Loza, C. L.; Chan, A. W. H.; Galloway, M. M.; Keutsch, F. N.; Flagan, R. C.; Seinfeld, J. H. Characterization of vapor wall loss in laboratory chambers. *Environ. Sci. Technol.* **2010**, *44*, 5074−5078.

(3) Matsunaga, A.; Ziemann, P. J. Gas-wall partitioning of organic compounds in a Teflon film chamber and potential effects on reaction product and aerosol yield measurements. *Aerosol Sci. Technol.* **2010**, *44*, 881−892.

(4) McVay, R. C.; Cappa, C. D.; Seinfeld, J. H. Vapor-wall deposition in chambers: Theoretical considerations. *Environ. Sci. Technol.* **2014**, *48*, 10251−10258.

(5) Yeh, G. K.; Ziemann, P. J. Alkyl nitrate formation from the reactions of C8-C14 n-alkanes with OH radicals in the presence of NOx: Measured yields with essential corrections for gas-wall partitioning. *J. Phys. Chem. A* **2014**, *118*, 8147−8157.

(6) Zhang, X.; Cappa, C. D.; Jathar, S. H.; McVay, R. C.; Ensberg, J. J.; Kleeman, M. J.; Seinfeld, J. H. Influence of vapor wall loss in laboratory chambers on yields of secondary organic aerosol. *Proc. Natl. Acad. Sci. U. S. A.* **2014**, *111*, 5802−5807.

(7) Bian, Q.; May, A. A.; Kreidenweis, S. M.; Pierce, J. R. Investigation of particle and vapor wall-loss effects on controlled wood-smoke chamber experiments. *Atmos. Chem. Phys.* **2015**, *15*, 11027−11045.

(8) Krechmer, J. E.; et al. Formation of low volatility organic compounds and secondary organic aerosol from isoprene hydroxyhydroperoxide low-NO oxidation. *Environ. Sci. Technol.* **2015**, *49*, 10330−10339.

(9) Yeh, G. K.; Ziemann, P. J. Gas-wall partitioning of oxygenated organic compounds: Measurements, structure-activity relationships, and correlation with gas chromatographic retention factor. *Aerosol Sci. Technol.* **2015**, *49*, 727−738.

(10) Zhang, X.; Schwantes, R. H.; McVay, R. C.; Lignell, H.; Coggon, M. M.; Flagan, R. C.; Seinfeld, J. H. Vapor wall deposition in Teflon chambers. *Atmos. Chem. Phys.* **2015**, *15*, 4197−4214.

(11) Cappa, C. D.; Jathar, S. H.; Kleeman, M. J.; Docherty, K. S.; Jimenez, J. L.; Seinfeld, J. H.; Wexler, A. S. Simulating secondary organic aerosol in a regional air quality model using the statistical oxidation model - Part 2: Assessing the influence of vapor wall losses. *Atmos. Chem. Phys.* **2016**, *16*, 3041−3059.

(12) Krechmer, J. E.; Pagonis, D.; Ziemann, P. J.; Jimenez, J. L. Quantification of gas-wall partitioning in Teflon environmental chambers using rapid bursts of low-volatility oxidized species generated in situ. *Environ. Sci. Technol.* **2016**, *50*, 5757−5765.

(13) La, Y. S.; Camredon, M.; Ziemann, P. J.; Valorso, R.; Matsunaga, A.; Lannuque, V.; Lee-Taylor, J.; Hodzic, A.; Madronich, S.; Aumont, B. Impact of chamber wall loss of gaseous organic compounds on secondary organic aerosol formation: explicit modeling of SOA formation from alkane and alkene oxidation. *Atmos. Chem. Phys.* **2016**, *16*, 1417−1431.

(14) Nah, T.; McVay, R. C.; Zhang, X.; Boyd, C. M.; Seinfeld, J. H.; Ng, N. L. Influence of seed aerosol surface area and oxidation rate on vapor wall deposition and SOA mass yields: a case study with α-pinene ozonolysis. *Atmos. Chem. Phys.* **2016**, *16*, 9361−9379.

(15) Trump, E. R.; Epstein, S. A.; Riipinen, I.; Donahue, N. M. Wall effects in smog chamber experiments: A model study. *Aerosol Sci. Technol.* **2016**, *50*, 1180−1200.

(16) Ye, P.; Ding, X.; Hakala, J.; Hofbauer, V.; Robinson, E. S.; Donahue, N. M. Vapor wall loss of semi-volatile organic compounds in a Teflon chamber. *Aerosol Sci. Technol.* **2016**, *50*, 822−834.

(17) Crank, J. A theoretical investigation of the influence of molecular relaxation and internal stress on diffusion in polymers. *J. Polym. Sci.* **1953**, *11*, 151−168.

(18) Seinfeld, J. H.; Pankow, J. F. Organic atmospheric particulate material. *Annu. Rev. Phys. Chem.* **2003**, *54*, 121−140.

(19) PTFE, FEP, and PFA Specifications. Boedeker, 2014; http://www.boedeker.com/feppfa_p.htm.

(20) Frezzotti, A. Boundary conditions at the vapor-liquid interface. *Phys. Fluids* **2011**, *23*, 030609.

(21) Davidovits, P.; Jayne, J. T.; Duan, S. X.; Worsnop, D. R.; Zahniser, M. S.; Kolb, C. E. Uptake of gas molecules by liquids: a model. *J. Phys. Chem.* **1991**, *95*, 6337−6340.

(22) Tokarev, A.; Friess, K.; Machkova, J.; Sipek, M.; Yampolskii, Y. Sorption and diffusion of organic vapors in amorphous Teflon AF2400. *J. Polym. Sci., Part B: Polym. Phys.* **2006**, *44*, 832−844.

(23) Vapour pressure of Pure Liquid Organic Compounds. Tropo, 2014; http://tropo.aeronomie.be/models/evaporation_run.htm.

(24) Compernolle, S.; Ceulemans, K.; Müller, J.-F. EVAPORATION: a new vapour pressure estimation method for organic molecules including non-additivity and intramolecular interactions. *Atmos. Chem. Phys.* **2011**, *11*, 9431−9450.

(25) Frisch, H. L. Sorption and transport in glassy polymers - a review. *Polym. Eng. Sci.* **1980**, *20*, 2−13.

(26) Vieth, W.; Howell, J.; Hsieh, J. Dual sorption theory. *J. Membr. Sci.* **1976**, *1*, 177−220.

(27) Shiraiwa, M.; Ammann, M.; Koop, T.; Pöschl, U. Gas uptake and chemical aging of semisolid organic aerosol particles. *Proc. Natl. Acad. Sci. U. S. A.* **2011**, *108*, 11003−11008.

(28) Shiraiwa, M.; Yee, L. D.; Schilling, K. A.; Loza, C. L.; Craven, J. S.; Zuend, A.; Ziemann, P. J.; Seinfeld, J. H. Size distribution dynamics reveal particle-phase chemistry in organic aerosol formation. *Proc. Natl. Acad. Sci. U. S. A.* **2013**, *110*, 11746−11750.

(29) Schwarzenbach, R. P.; Gschwend, P. M.; Imboden, D. M. *Environmental Organic Chemistry*, 2nd ed.; John Wiley & Sons, Inc.: Hoboken, NJ, 2005.

(30) Praske, E.; Crounse, J. D.; Bates, K. H.; Kurtén, T.; Kjaergaard, H. G.; Wennberg, P. O. Atmospheric fate of methyl vinyl ketone: Peroxy radical reactions with NO and HO2. *J. Phys. Chem. A* **2015**, *119*, 4562−4572.

(31) Schwantes, R. H.; Teng, A. P.; Nguyen, T. B.; Coggon, M. M.; Crounse, J. D.; St. Clair, J. M.; Zhang, X.; Schilling, K. A.; Seinfeld, J. H.; Wennberg, P. O. Isoprene NO_3 oxidation products from the RO_2 + HO_2 pathway. *J. Phys. Chem. A* **2015**, *119*, 10158−10171.

(32) St. Clair, J. M.; Rivera-Rios, J. C.; Crounse, J. D.; Knap, H. C.; Bates, K. H.; Teng, A. P.; Jørgensen, S.; Kjaergaard, H. G.; Keutsch, F. N.; Wennberg, P. O. Kinetics and products of the reaction of the first-generation isoprene hydroxy hydroperoxide (ISOPOOH) with OH. *J. Phys. Chem. A* **2016**, *120*, 1441−1451.

(33) Schwantes, R. H.; Schilling, K. A.; McVay, R. C.; Lignell, H.; Coggon, M. M.; Zhang, X.; Wennberg, P. O.; Seinfeld, J. H. Formation of highly oxygenated low-volatility products from cresol oxidation. *Atmos. Chem. Phys.* **2017**, *17*, 3453−3474.

(34) Teng, A. P.; Crounse, J. D.; Wennberg, P. O. Isoprene peroxy radical dynamics. *J. Am. Chem. Soc.* **2017**, *139*, 5367−5377.

(35) Bates, K. H.; Crounse, J. D.; St. Clair, J. M.; Bennett, N. B.; Nguyen, T. B.; Seinfeld, J. H.; Stoltz, B. M.; Wennberg, P. O. Gas phase production and loss of isoprene epoxydiols. *J. Phys. Chem. A* **2014**, *118*, 1237−1246.

(36) Loza, C. L.; Craven, J. S.; Yee, L. D.; Coggon, M. M.; Schwantes, R. H.; Shiraiwa, M.; Zhang, X.; Schilling, K. A.; Ng, N. L.; Canagaratna, M. R.; Ziemann, P. J.; Flagan, R. C.; Seinfeld, J. H. Secondary organic aerosol yields of 12-carbon alkanes. *Atmos. Chem. Phys.* **2014**, *14*, 1423−1439.

(37) Nguyen, T. B.; Coggon, M. M.; Bates, K. H.; Zhang, X.; Schwantes, R. H.; Schilling, K. A.; Loza, C. L.; Flagan, R. C.; Wennberg, P. O.; Seinfeld, J. H. Organic aerosol formation from the reactive uptake of isoprene epoxydiols (IEPOX) onto non-acidified inorganic seeds. *Atmos. Chem. Phys.* **2014**, *14*, 3497−3510.

(38) Nguyen, T. B.; et al. Atmospheric fates of Criegee intermediates in the ozonolysis of isoprene. *Phys. Chem. Chem. Phys.* **2016**, *18*, 10241−10254.

(39) Crounse, J. D.; McKinney, K. A.; Kwan, A. J.; Wennberg, P. O. Measurement of gas-phase hydroperoxides by chemical ionization mass spectrometry. *Anal. Chem.* **2006**, *78*, 6726−6732.

(40) Pagonis, D.; Krechmer, J. E.; de Gouw, J.; Jimenez, J. L.; Ziemann, P. J. Effects of gas−wall partitioning in Teflon tubing and instrumentation on time-resolved measurements of gas-phase organic compounds. *Atmos. Meas. Tech.* **2017**, *10*, 4687−4696.

(41) Taylor, W. D.; Allston, T. D.; Moscato, M. J.; Fazekas, G. B.; Kozlowski, R.; Takacs, G. A. Atmospheric photodissociation lifetimes for nitromethane, methyl nitrite, and methyl nitrate. *Int. J. Chem. Kinet.* **1980**, *12*, 231−240.

(42) Lee, B. H.; Lopez-Hilfiker, F. D.; Mohr, C.; Kurtén, T.; Worsnop, D. R.; Thornton, J. A. An Iodide-adduct high-resolution time-of-flight chemical-ionization mass spectrometer: Application to atmospheric inorganic and organic compounds. *Environ. Sci. Technol.* **2014**, *48*, 6309−6317.

(43) Bagley, E.; Long, F. A. Two-stage sorption and desorption of organic vapors in cellulose acetate[1,2]. *J. Am. Chem. Soc.* **1955**, *77*, 2172−2178.

(44) Abraham, M. H.; McGowan, J. C. The use of characteristic volumes to measure cavity terms in reversed phase liquid chromatography. *Chromatographia* **1987**, *23*, 243−246.

(45) Linossier, I.; Gaillard, F.; Romand, M.; Feller, J. F. Measuring water diffusion in polymer films on the substrate by internal reflection fourier transform infrared spectroscopy. *J. Appl. Polym. Sci.* **1997**, *66*, 2465−2473.

(46) Bean, J. K.; Hildebrandt Ruiz, L. Gas-particle partitioning and hydrolysis of organic nitrates formed from the oxidation of α-pinene in environmental chamber experiments. *Atmos. Chem. Phys.* **2016**, *16*, 2175−2184.

Appendix C

LOW-VOLATILITY COMPOUNDS CONTRIBUTE SIGNIFICANTLY TO ISOPRENE SECONDARY ORGANIC AEROSOL (SOA) UNDER HIGH-NO$_x$ CONDITIONS

Schwantes, Rebecca H., Sophia M. Charan, Kelvin H. Bates, Yuanlong Huang, Tran B. Nguyen, Huajun Mai, Weimeng Kong, Richard C. Flagan, and John H. Seinfeld (2019). "Low-volatility compounds contribute significantly to isoprene secondary organic aerosol (SOA) under high-NO$_x$ conditions." In: *Atmospheric Chemistry and Physics* 19.11, pp. 7255–7278. DOI: 10.5194/acp-19-7255-2019.

Atmospheric
Chemistry
and Physics

Low-volatility compounds contribute significantly to isoprene secondary organic aerosol (SOA) under high-NO$_x$ conditions

Rebecca H. Schwantes[1,a], Sophia M. Charan[2], Kelvin H. Bates[2,b], Yuanlong Huang[1], Tran B. Nguyen[3], Huajun Mai[1], Weimeng Kong[2], Richard C. Flagan[2], and John H. Seinfeld[2,4]

[1]Division of Geological and Planetary Sciences, California Institute of Technology,
1200 East California Boulevard, Pasadena, California 91125, USA
[2]Division of Chemistry and Chemical Engineering, California Institute of Technology,
1200 East California Boulevard, Pasadena, California 91125, USA
[3]Department of Environmental Toxicology, University of California – Davis, Davis, California 95616, USA
[4]Division of Engineering and Applied Science, California Institute of Technology, Pasadena, California 91125, USA
[a]currently at: National Center for Atmospheric Research, Boulder, Colorado 80307, USA
[b]currently at: Faculty of Arts and Sciences, Harvard University, Cambridge, Massachusetts 02138, USA

Correspondence: Rebecca H. Schwantes (rschwant@ucar.edu)

Abstract. Recent advances in our knowledge of the gas-phase oxidation of isoprene, the impact of chamber walls on secondary organic aerosol (SOA) mass yields, and aerosol measurement analysis techniques warrant reevaluating SOA yields from isoprene. In particular, SOA from isoprene oxidation under high-NO$_x$ conditions forms via two major pathways: (1) low-volatility nitrates and dinitrates (LV pathway) and (2) hydroxymethyl-methyl-α-lactone (HMML) reaction on a surface or the condensed phase of particles to form 2-methyl glyceric acid and its oligomers (2MGA pathway). These SOA production pathways respond differently to reaction conditions. Past chamber experiments generated SOA with varying contributions from these two unique pathways, leading to results that are difficult to interpret. This study examines the SOA yields from these two pathways independently, which improves the interpretation of previous results and provides further understanding of the relevance of chamber SOA yields to the atmosphere and regional or global modeling. Results suggest that low-volatility nitrates and dinitrates produce significantly more aerosol than previously thought; the experimentally measured SOA mass yield from the LV pathway is ~ 0.15. Sufficient seed surface area at the start of the reaction is needed to limit the effects of vapor wall losses of low-volatility compounds and accurately measure the complete SOA mass yield. Under dry condi-

tions, substantial amounts of SOA are formed from HMML ring-opening reactions with inorganic ions and HMML organic oligomerization processes. However, the lactone organic oligomerization reactions are suppressed under more atmospherically relevant humidity levels, where hydration of the lactone is more competitive. This limits the SOA formation potential from the 2MGA pathway to HMML ring-opening reactions with water or inorganic ions under typical atmospheric conditions. The isoprene SOA mass yield from the LV pathway measured in this work is significantly higher than previous studies have reported, suggesting that low-volatility compounds such as organic nitrates and dinitrates may contribute to isoprene SOA under high-NO$_x$ conditions significantly more than previously thought and thus deserve continued study.

1 Introduction

In the atmosphere, submicrometer particulate matter is composed of a significant fraction of organic aerosol (Zhang et al., 2007). There are two forms of organic aerosol: primary, which is directly emitted into the atmosphere, and secondary, which is formed when gas-phase compounds partition to the particle phase. Processes governing secondary organic

aerosol (SOA) formation are particularly complex (Kroll and Seinfeld, 2008; Hallquist et al., 2009). SOA yields, the ratio of the mass of SOA formed to the mass of the parent volatile organic compound (VOC) reacted, are measured in environmental chambers and are used in models to reduce the complexity of SOA formation.

Isoprene is the dominant non-methane biogenic VOC emitted into the atmosphere. Because of the large flux of isoprene ($\sim 535\,\mathrm{Tg\,yr^{-1}}$) into the atmosphere (Guenther et al., 2012), oxidation of isoprene is a significant source of SOA even though SOA yields measured in chambers are relatively low (Carlton et al., 2009). Despite numerous experimental studies of isoprene SOA formation under varying conditions (Pandis et al., 1991; Edney et al., 2005; Kroll et al., 2005, 2006; Dommen et al., 2006; Kleindienst et al., 2006; Ng et al., 2006; Paulot et al., 2009; Chan et al., 2010; Chhabra et al., 2010; Surratt et al., 2010; Nguyen et al., 2011, 2014b, 2015; Zhang et al., 2011, 2012; Lin et al., 2013; Xu et al., 2014; Krechmer et al., 2015; Lambe et al., 2015; Brégonzio-Rozier et al., 2015; Clark et al., 2016, etc.), a consensus on the magnitude of SOA formed from isoprene oxidation by the hydroxyl radical (OH) is still lacking (Carlton et al., 2009; Brégonzio-Rozier et al., 2015; Clark et al., 2016). This lack of consensus in the experimental data leads recent global modeling studies (Marais et al., 2016; Stadtler et al., 2018) to implement SOA schemes that produce significantly different overall isoprene SOA yields. Isoprene SOA yields have been shown to depend on a variety of factors including RO_2 fate, NO_2/NO ratio, relative humidity, degree of oxidation, temperature, seed surface area, particle acidity, and chamber irradiation source (Carlton et al., 2009). These experimental conditions have not always been controlled or reported, which is likely a major reason for the variability seen in past isoprene SOA yields. By measuring isoprene SOA yields while controlling for seed surface area, RO_2 fate, NO_2/NO ratio, relative humidity, and temperature, we seek to resolve uncertainties in SOA formation in past yields.

Recent advances have improved our understanding of how chamber SOA yields should be measured and analyzed. This includes accounting carefully for particle wall deposition (Loza et al., 2012), vapor wall deposition (Zhang et al., 2014; Ehn et al., 2014), and particle coagulation (Nah et al., 2017). Advances have also taken place in the data processing of aerosol size distribution measurements by the differential mobility analyzer coupled to a condensation particle counter (DMA-CPC), the main instrument used to measure SOA yields (Mai and Flagan, 2018; Mai et al., 2018). Because isoprene SOA yields tend to be relatively small, the DMA data inversion technique and correction for CPC response time are quite important.

Additionally, there have been major recent advances in our understanding of isoprene gas-phase oxidation (Wennberg et al., 2018, and references therein) including theoretical (e.g., Peeters et al., 2009, 2014; Kjaergaard et al., 2012) and experimental (e.g., Teng et al., 2017; Nguyen et al.,

2015; Lee et al., 2014; Jacobs et al., 2014) studies. This improved understanding of isoprene gas-phase chemistry influences the processes governing isoprene SOA formation and informs the experimental design of the present work. This work focuses on the production of SOA from OH-initiated isoprene oxidation under high-NO_x conditions, which occurs via two major chemical pathways (Figs. 1 and 2). The first we define throughout as the low-volatility (LV) pathway representing all aerosol formed from the equilibrium gas–particle partitioning of compounds with sufficiently low volatility, which mostly include functionalized nitrates and dinitrates (e.g., red compounds in Fig. 1). The second we define as the 2-methyl glyceric acid (2MGA) pathway representing aerosol formed from 2-MGA, its oligomers, its organosulfates, and its organonitrates (blue compounds in Fig. 2). There are many definitions for high-NO_x conditions (Wennberg, 2013). Here we test two different high-NO_x chemical regimes. Experiments targeting the LV pathway are designed such that all peroxy radicals including acyl peroxy radicals dominantly react with NO and experiments targeting the 2-MGA pathway are designed such that all acyl peroxy radicals dominantly react with NO_2 and all other peroxy radicals dominantly react with NO.

Aerosol from the LV pathway is believed to be composed largely of isoprene dihydroxy dinitrates, which are produced from the first-generation hydroxy nitrate reacting with OH to form a peroxy radical that then reacts with NO. The gas-phase yield of isoprene dihydroxy dinitrates is quite uncertain (Lee et al., 2014). In general, the nitrate yields from highly functionalized RO_2 radicals have not been well studied (Wennberg et al., 2018) due mostly to difficulties in measuring such low-volatility compounds. The formation of some organic nitrate SOA precursors are summarized in Fig. 1, which is largely adapted from schemes presented in Wennberg et al. (2018) with the exception of the isoprene dihydroxy nitrooxy alkoxy radical 1,5 H shift. Wennberg et al. (2018) suggests the importance of a similar peroxy radical 1,5 H shift, which will not form in the present experiments due to the high levels of NO. However, based on past studies largely on alkane oxidation (Orlando et al., 2003; Atkinson, 2007), the equivalent alkoxy radical 1,5 H shift is expected to occur and has the potential to form low-volatility nitrates as further described in Sect. 5.1.

Throughout the text we use low volatility as a general term representing gas-phase compounds with a potential to exist partially in the particle phase. In this work, low-volatility compounds include the following volatility classes from Donahue et al. (2012): IVOC (intermediate), SVOC (semi), LVOC (low), and ELVOC (extremely low). When referring to specific volatility classes, the acronyms defined above are used.

Aerosol from the 2MGA pathway forms when methacrolein is oxidized under high-NO_2 conditions to form methylacryloyl peroxynitrate (MPAN). MPAN reacts with OH to form hydroxymethyl-methyl-α-lactone

Figure 1. Simplified chemical mechanism of isoprene OH-initiated oxidation under high-NO conditions, largely based on schemes in Wennberg et al. (2018), emphasizing SOA generated from the LV pathway, which includes low-volatility organic nitrates and dinitrates in red. Compounds detected in the gas phase by the chemical ionization mass spectrometer (CIMS) are highlighted with a blue square.

(HMML), and HMML either decomposes in the gas phase to form hydroxy acetone or interacts with a wet surface to form 2-methyl glyceric acid (2-MGA) (Kjaergaard et al., 2012; Nguyen et al., 2015). A minor channel to form methacrylic acid epoxide (MAE) also exists from methacrolein oxidation (Lin et al., 2013) but not from pure MPAN oxidation (Nguyen et al., 2015). Nguyen et al. (2015) demonstrated that MAE does not easily undergo ring-opening reactions to form particles. Thus, the yield of MAE from methacrolein (MACR) oxidation reported in Lin et al. (2013) should be adjusted to include only MAE detected in the gas phase, which corresponds to a yield of $\sim 1\,\%$–$2\,\%$.

Because SOA formed from the LV and 2MGA pathways is chemically distinct both in the route of formation and composition, the experiments reported here probed these chemical pathways separately. This experimental design is aimed to resolve inconsistencies associated with previously reported isoprene SOA yields (Carlton et al., 2009) and improve our understanding of isoprene SOA formation. Additionally, we seek to report updated isoprene SOA yields and trace the SOA yields to known gas-phase SOA precursors.
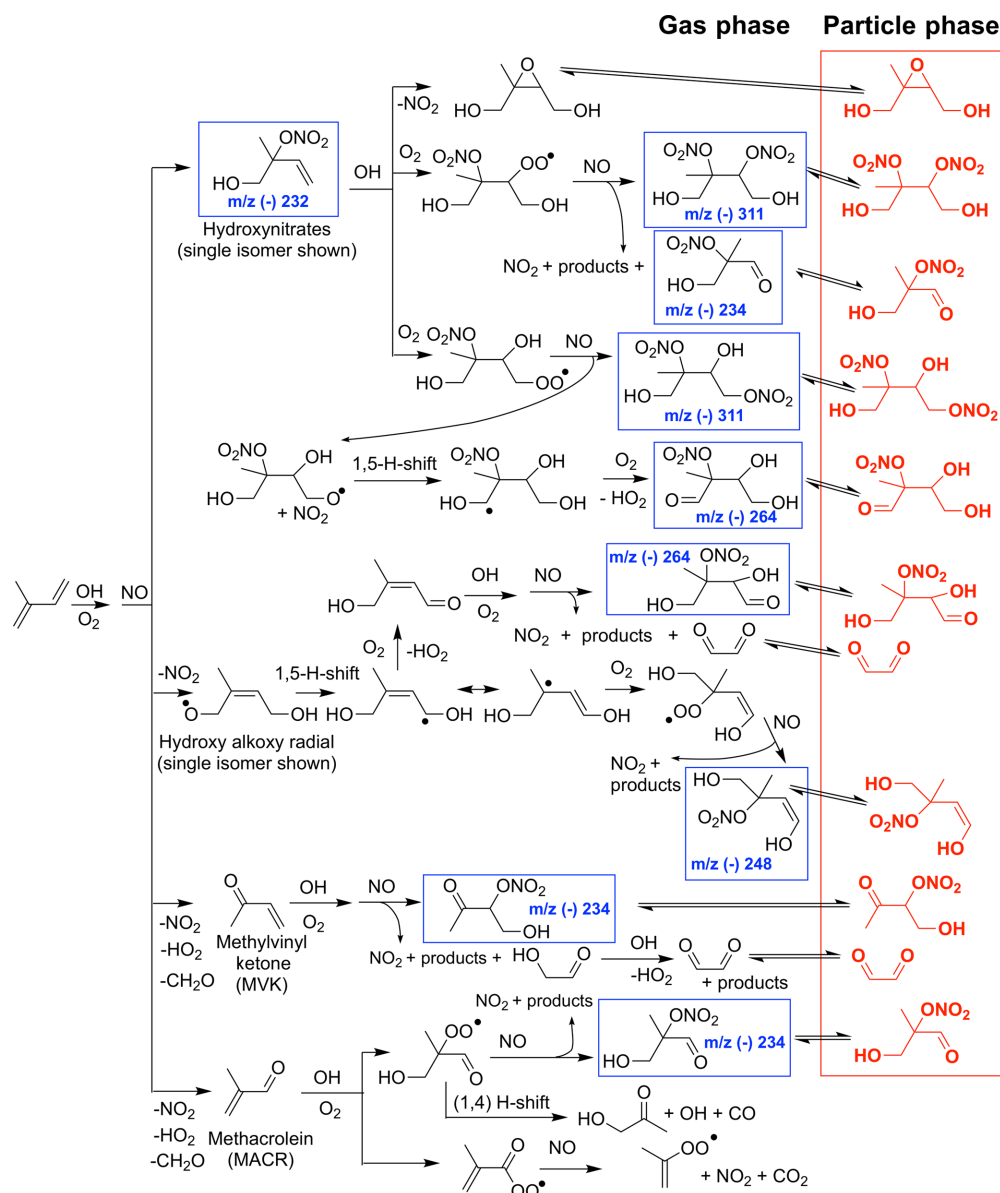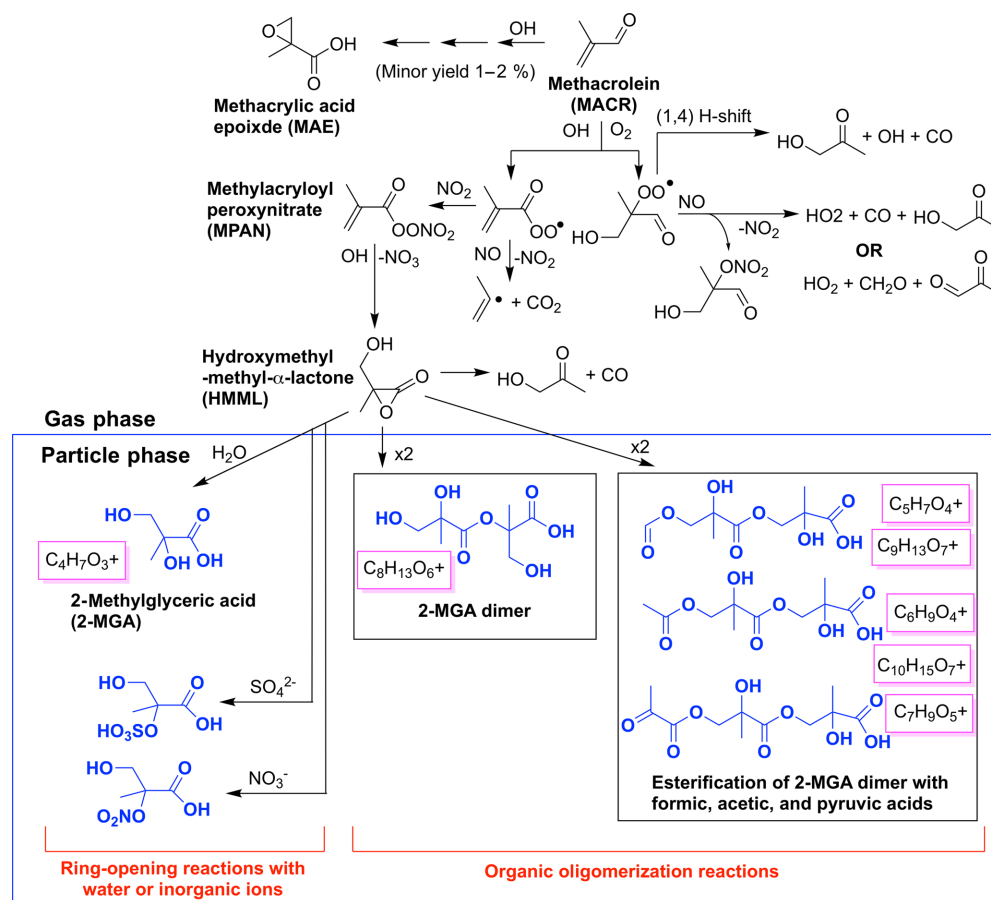
Figure 2. Simplified chemical mechanism of methacrolein OH-initiated oxidation under high-NO_2 conditions, largely based on schemes in Wennberg et al. (2018), emphasizing SOA generated from the 2MGA pathway including 2-methyl glyceric acid (2-MGA) and its oligomers in blue. Aerosol mass spectrometer (AMS) fragments likely corresponding to each compound are boxed in magenta.

2 Experimental methods

Chamber experiments were performed to study SOA formation from isoprene oxidation under high-NO_x conditions from two distinct pathways: (1) low-volatility nitrates and dinitrates (LV pathway) and (2) 2-MGA and its oligomers (2MGA pathway). Experiments targeting the LV pathway were performed using isoprene as the precursor, and an NO_2/NO ratio < 1.5 was maintained throughout the entire experiment (as verified by the kinetic mechanism) in order to favor the formation of nitrates and dinitrates and limit the formation of MPAN (Fig. 1). Experiments targeting the 2MGA pathway were performed using methacrolein as the precursor, and an NO_2/NO ratio > 11 was maintained throughout the entire experiment (as verified by the kinetic mechanism) with the exception of experiment M9, which maintained an NO_2/NO ratio > 8. This high NO_2/NO ratio accentuated the formation of MPAN, and thereby 2-MGA (Fig. 2), and was important for reducing variability between the experiments. If a lower NO_2/NO ratio was used, small fluctuations in the initial NO_2 or NO would result in large differences in the

NO_2/NO ratio. In order to completely separate the LV and 2MGA pathways, methacrolein had to be used as the VOC precursor for the 2MGA pathway experiments. If isoprene was used, even at the high NO_2/NO ratios used in the 2MGA pathway experiments, the SOA precursors from the LV pathway would form resulting in a mixed regime (i.e., chemistry in Fig. 1 is not dependent on NO_2 concentration). In each case, the effect of seed surface area, temperature, and humidity on the SOA yield was independently determined.

2.1 Experimental conditions

Experiments (see Table 1) were conducted in the Caltech dual chamber facility using a 21 m³ Teflon chamber. Prior to each experiment, the chamber was flushed with dry, purified air for 24 h. For humid experiments, the chamber was humidified prior to all injections. Ultrapure water (18 MΩ, Millipore Milli-Q) at 25 °C was recirculated through a Nafion membrane humidifier (FC200, Permapure LLC) while purified air flowed through the humidifier and into the chamber. First, isoprene (99 % purity) or methacrolein (95 % purity)

Table 1. Initial conditions and SOA yield for all experiments.

Expt no.	$[VOC]_0$ (ppb)	$[NO]_0$ (ppb)	$[NO_2]_0$ (ppb)	$[CH_3ONO]_0$ (ppb)	$[Aer\ Vol]_0$ ($\mu m^3\ cm^{-3}$)	$[Aer\ SA]_0$ ($\mu m^2\ cm^{-3}$)	Avg T (°C)	Avg RH (%)	OH (molec. cm^{-3})	SOA Yield
Dry control experiments										
C1	NA	NA	NA	NA	37	788	25.1	10.7	NA	NA
C2	NA	NA	NA	NA	109	2130	25.2	8.3	NA	NA
C3	NA	NA	NA	NA	183	3360	24.7	5.6	NA	NA
C4	NA	NA	NA	NA	375	5390	25.5	7.3	NA	NA
Experiments optimized for LV pathway (VOC precursor is isoprene)										
D1	59	585	6	118	0	0	25.6	5.0	2.6×10^6	0
D2	58	526	20	117	54	1170	26.4	5.6	2.5×10^6	0.04
D3	57	519	17	117	183	3420	25.9	7.5	2.5×10^6	0.17
D4	58	518	18	116	337	5770	26.4	7.9	2.4×10^6	0.16
D5	55	506	20	117	159	2830	12.8	16.4	1.7×10^6	0.15
D6	56	541	16	118	152	2660	32.4	5.9	2.7×10^6	0.16
D7	40	527	18	117	197	3580	25.9	8.1	2.6×10^6	0.18
D8	60	519	20	118	109	1790	25.5	44.7	2.3×10^6	NA
D9	55	489	20	119	166	2750	25.6	78.1	2.5×10^6	NA
D10	58	516	17	111	85	1580	25.8	5.1	2.2×10^6	0.04
D11	56	490	17	115	264	4770	25.8	5.2	2.4×10^6	0.16
Experiments optimized for 2MGA pathway (VOC precursor is methacrolein)										
M1	49	14	376	234	0	0	25.8	6.3	4.3×10^6	0.10
M2	48	15	365	235	82	1640	25.9	8.9	4.7×10^6	0.34
M3	46	23	345	236	118	2260	25.1	6.8	4.7×10^6	0.52
M4	50	17	356	235	50	1040	12.9	12.6	3.4×10^6	0.27
M5	58	18	375	235	87	1740	31.8	4.5	5.1×10^6	0.34
M6	52	12	334	235	104	1720	25.6	47.1	4.4×10^6	NA
M7	53	14	339	233	134	2340	25.6	67.4	4.6×10^6	NA
M8	56	18	352	236	141	2510	25.4	81.0	4.3×10^6	NA
M9	57	29	298	229	95	1910	25.9	5.1	4.7×10^6	0.24

Acronyms are defined as follows: VOC – volatile organic compound; NO – nitric oxide; NO_2 – nitrogen dioxide; CH_3ONO – methyl nitrite; T – temperature; RH – relative humidity. OH (hydroxyl radical) is estimated from the VOC decay over the first 3 h of each experiment. $[Aer\ Vol]_0$ is the particle wall-loss-corrected seed volume at the start of photooxidation, which is used to determine the uncertainty in the particle wall loss correction as explained in Sect. 4.1. $[Aer\ SA]_0$ is the surface area of the seed aerosol at the start of photooxidation not corrected for particle wall loss and is used to understand how the SOA yield changes depending on the surface area of the suspended particles (e.g., Fig. 5). The SOA yield is the mass fraction after 10 h of photooxidation.

was injected into a glass bulb using a gas-tight syringe and was carried by a flow of dry nitrogen into the chamber.

Second, methyl nitrite (CH_3ONO) was injected into the chamber. CH_3ONO was synthesized using the technique described in Taylor et al. (1980) and Chan et al. (2010) and was stored in liquid nitrogen. Prior to each experiment, an evacuated glass bulb was filled with CH_3ONO to the desired pressure, as measured by a capacitance manometer (MKS Baratron™). This bulb was then backfilled with nitrogen and flushed into the chamber. The bulb pressure was used to calculate the CH_3ONO mixing ratio in the chamber (see Table 1). After CH_3ONO was injected, pulses of purified air were added to the chamber to enhance mixing. Once the chamber was adequately mixed, NO (501 ppm in N_2, Scott Specialty Gases) or NO_2 (488 ppm in N_2, Scott Specialty Gases) was injected into the chamber through a calibrated

mass flow controller. Again the chamber was mixed by pulses of purified air.

Seed particles were generated from an atomizer using 0.06 M $(NH_4)_2SO_4$ seed solution. The seed aerosol was directed through a soft X-ray neutralizer (TSI Model 3088) prior to injection into the chamber to ensure a consistent initial particle charge distribution for all experiments. For humid experiments, the seed aerosol was directed through a wet-wall denuder after exiting the neutralizer in order to ensure the particles were deliquesced. After seed injection, mixing air was turned on for 1 min to enhance mixing. The seed aerosol particle number concentration had an approximately lognormal diameter distribution centered on average ~ 100 nm.

After injecting all gas-phase precursors and seed aerosol, photooxidation was delayed by 1 h for experiments with no

initial seed aerosol and 4 h for experiments with initial seed aerosol. The rate of particle wall deposition was measured for each experiment during this 4 h delay. Although NO_2 was not intentionally added for the LV pathway experiments, a modest NO_2 signal was observed to form during the 4 h delay and is reported in Table 1. This "NO_2" signal may be NO_2 itself or an interference in the NO_x monitor from an NO_y compound (e.g., known interferences include organic nitrates, nitrous acid, and CH_3ONO). The small signal of NO_2, or a different NO_y compound, is not expected to influence the results given the significantly larger initial NO levels (Table 1). When NO_2 or CH_3ONO were injected into the chamber, an NO signal was observed on the NO_x monitor. As the NO_x monitor has few interferences for NO, a small fraction of NO was likely formed from NO_2 or CH_3ONO photolysis in the Teflon injection lines. Thus, the slight increase in NO with the NO_2 and CH_3ONO injection was assumed and reported to be initial NO (Table 1).

The Caltech chamber uses ultraviolet (UV) broadband lights with the main emission peak centered at ~ 350 nm. Only 10 % of full light capacity ($j_{NO_2\ 10\%} = 4 \times 10^{-4}\,s^{-1}$) was used for these experiments because CH_3ONO photolyzes rapidly, and the lower light intensity minimizes chamber temperature increases ($\sim 0.4\,°C$ on average) caused by the UV lights. In all experiments, OH was produced by the photolysis of CH_3ONO as shown in the following reactions:

$$CH_3ONO + h\nu \rightarrow CH_3O + NO, \qquad (R1)$$

$$CH_3O + O_2 \rightarrow CH_2O + HO_2, \qquad (R2)$$

$$HO_2 + NO \rightarrow OH + NO_2. \qquad (R3)$$
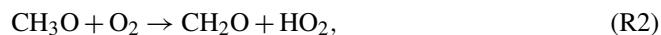
Relative to other OH precursors, CH_3ONO has a low Henry's law constant ($15\,M\,atm^{-1}$, calculated by theory) (Sander, 2015). During experiments with high relative humidity (RH), unlike other OH precursors, CH_3ONO is not expected to enhance OH production in the particle phase beyond atmospherically relevant levels.

2.2 Instrumentation

Temperature and RH were measured using a Vaisala HMM211 probe. NO and NO_2 were monitored using a Teledyne NO_x analyzer (T200). Because the Teledyne NO_x monitor detects CH_3ONO, organic nitrates, and other NO_y compounds as NO_2, only initial NO_2 measurements can be constrained with this instrument. For some experiments, NO_2 was also monitored using a luminol NO_2 and acyl peroxynitrate analyzer developed by Fitz Aerometric Technologies. This instrument separates NO_2 via chromatography at room temperature using a deactivated DB-5 column. NO_2 then reacts with luminol to produce a chemiluminescence response (Gaffney et al., 1998). The NO_2 measured by the luminol NO_2 and acyl peroxynitrate analyzer compares reasonably well with the simulated NO_2 from the kinetic model (Fig. S3 in the Supplement).

A gas chromatograph with a flame ionization detector (GC-FID; HP 6890N, column HP-Plot-Q) was used to measure the decay of isoprene and methacrolein. The GC-FID was calibrated with ~ 50–60 ppm of isoprene or methacrolein generated from analytical standards (Aldrich 95 %–99 % purity) and cross-calibrated by Fourier transform infrared absorption (FT-IR) spectroscopy (pathlength 19 cm) using the absorption cross sections measured by Pacific Northwest National Laboratory (PNNL) for isoprene or methacrolein (Sharpe et al., 2004). Linearity in the GC-FID calibration was determined to an error of ~ 1 % across a factor of 150 in dilution.

Aerosol organic and inorganic composition was recorded in situ using a high-resolution time-of-flight aerosol mass spectrometer (HR-AMS; Aerodyne Research, Inc.). The HR-AMS switched every 1 min between the high-resolution W mode and the lower-resolution, higher-sensitivity V mode. The data were analyzed with Igor Pro (Wave Metrics, Inc.), utilizing the Squirrel 1.56D and PIKA 1.15D analysis toolkits (from http://cires1.colorado.edu/jimenez-group/ToFAMSResources/ToFSoftware/index.html, last access: 14 April 2017). In-line filter runs conducted prior to each experiment were used to correct for air interferences (Aiken et al., 2008). Bulk SOA elemental composition was calculated following the methods and recommendations of Aiken et al. (2008) and Canagaratna et al. (2015).

Aerosol volume and number concentration were monitored using a differential mobility analyzer (DMA; TSI 3081 column) coupled with a condensation particle counter (CPC; TSI 3010), which measures all particles with a diameter between 20 and 800 nm. The voltage scan used by the DMA was 1 min hold at 15 V, 4 min increase to 9850 V, 1 min hold at 9850 V, and 0.5 min decrease back to 15 V. Only the up-scan data were used for the analysis. The longer up-scan and hold times used here, compared to previous studies (e.g., Loza et al., 2012 and Zhang et al., 2014), reduced biases caused by mixing in the CPC. Such CPC mixing biases particularly impact the measurement of large particles, which are important in SOA yield experiments as they contribute significantly to the total SOA volume.

The DMA data analysis includes an improved data inversion and a correction for particle mixing in the condensation particle counter, which influences the CPC response time (Mai and Flagan, 2018; Mai et al., 2018). The inversion technique is applicable only to particles ≤ 600 nm. Particle concentration between 600 and 800 nm was calculated assuming a nonlinear least squares lognormal fit applied to particles from 400 to 600 nm. For experiments with no initial seed aerosol, the inversion inconsistently determined the presence of particles beyond 400 nm. Such large particles are unlikely to be the result of nucleation and more likely to represent an artifact of the inversion; thus, only particles < 400 nm were used in the analysis of these experiments. Corrections to the DMA data for coagulation and particle wall loss are addressed in Sect. 4.1.

Isoprene oxidation products were measured using a CF_3O^- chemical ionization mass spectrometer (CIMS), which utilizes a custom-modified triple quadrupole mass analyzer (Varian 1200) (St. Clair et al., 2010). CF_3O^- interacts with a gas-phase compound (A) to form a complex that is detected at the molecular weight of $A + 85$ or, in some cases, to fragment. Various fragmentation products can form as explained in previous work (e.g., Paulot et al., 2009; Praske et al., 2015; Schwantes et al., 2017). In this work, the CIMS results are only used to identify the presence of highly functionalized organic nitrates and not for quantification, so only signals from the complex (i.e., $A \cdot CF_3O^-$) and not from fragmentation are reported.

3 Kinetic mechanism

All relevant reactions included in the Master Chemical Mechanism (MCM) v3.3.1 (http://mcm.leeds.ac.uk/MCM, last access: 7 September 2018) were used in the current kinetic model (Jenkin et al., 1997; Saunders et al., 2003). Isoprene oxidation chemistry was recently updated in MCM v3.3.1 by Jenkin et al. (2015). Additional reactions included in the kinetic model but not in MCM v3.3.1 are listed in Table S1. Updates include inorganic reactions needed for chamber studies with large NO_x levels (e.g., CH_3ONO photolysis) and small changes to the isoprene chemistry based largely on Wennberg et al. (2018) and consistent with Figs. 1 and 2. As shown in Table S1, these updates include the first-generation isoprene hydroxy nitrate yields, the rates and branching ratios for the oxidation of the first-generation isoprene hydroxy nitrates, and the HMML yield from the MPAN + OH reaction. In some cases, δ-isoprene hydroxy alkoxy radicals in MCM v3.3.1 decompose through peroxy radical H shifts directly to products that would not form under the high-NO conditions in this work. For simplicity, we change these reactions, so that the δ-isoprene hydroxy alkoxy radicals form unity yields of hydroxy aldehydes. BOXMOX, a box-model software package using the Kinetic PreProcessor (Knote et al., 2015), was used to simulate the chamber experiments. As listed in Table 1, the kinetic model was initialized for each experiment with the measured initial concentration of VOC, NO, NO_2, and CH_3ONO as well as the measured average temperature and relative humidity.

Saturation mass concentration (C^*) and the fraction of each compound in the particle phase (F_P) at 13, 26, and 32 °C are estimated for relevant organic nitrates and dinitrates produced in MCM v3.3.1 and listed in Table S2. C^* was calculated with the vapor pressure estimated from Nannoolal et al. (2004, 2008) using the online calculator located at http://www.aim.env.uea.ac.uk/aim/ddbst/pcalc_main.php (last access: 1 March 2019). F_P was calculated from the C^* values and gas-particle equilibrium theory as further explained in Sect. S1 (Seinfeld and Pandis, 2016).

As shown in Table 1, the inferred OH concentration was larger in experiments with higher temperatures. Because the temperature dependence of the CH_3ONO absorption cross section and quantum yield are not well established, the CH_3ONO photolysis rate constant was calculated from the CH_3ONO decay curve as measured by the GC-FID. Unfortunately, the GC-FID sensitivity to CH_3ONO was low, so only the 2MGA experiments produced a sufficiently large signal for this approach. The average CH_3ONO photolysis rate constant from experiments M1–M3, M4, M5, and M6–M8 were used for dry $\sim 25\,°C$ ($1.9 \times 10^{-4}\,s^{-1}$), dry $\sim 13\,°C$ ($1.4 \times 10^{-4}\,s^{-1}$), dry $\sim 32\,°C$ ($2.3 \times 10^{-4}\,s^{-1}$), and humid $\sim 25\,°C$ ($1.9 \times 10^{-4}\,s^{-1}$) experiments, respectively. This approach accurately captured the reaction of isoprene and methacrolein with OH in all experiments (Figs. S1 and S2), which implies that the simulated OH in the kinetic model is reasonably accurate even over varying temperature. All other photolysis rate constants are calculated from the absorption cross sections and quantum yields reported in Burkholder et al. (2015) and Jenkin et al. (2015). Additionally, the kinetic model captures NO and NO_2 reasonably well for both the LV and 2MGA pathway experiments (Fig. S3).

4 Results

First, corrections for particle coagulation and particle wall deposition, which are required for accurate calculation of SOA yields, are addressed (Sect. 4.1). Next, SOA produced from the LV (Sect. 4.2) and 2MGA (Sect. 4.3) pathways is discussed.

4.1 Corrections for particle coagulation and particle wall deposition

Past studies reporting particle wall deposition coefficients apply the measured particle number decay rate in each size bin to produce a wall deposition coefficient, ($\beta(D_p, t)$), that is a function of particle size (D_p) (Loza et al., 2012). Because larger seed particle number and surface area concentrations were used in these experiments, corrections to $\beta(D_p, t)$ that account for coagulation are needed (Pierce et al., 2008; Nah et al., 2017). The current work uses an approach similar to that of Nah et al. (2017) and Sunol et al. (2018) with updates to account for electrostatic charges on the chamber walls as described by Charan et al. (2018). To reduce the experimental uncertainty associated with these processes, particle wall deposition was calculated during each experiment. This approach accounted for the day-to-day fluctuations in particle coagulation processes, chamber wall charging, and chamber mixing. We summarize these approaches and describe any changes required for this analysis in Sect. S2 of the Supplement.

Four particle wall loss experiments were performed under dry conditions (RH < 10 %) at varying seed surface areas
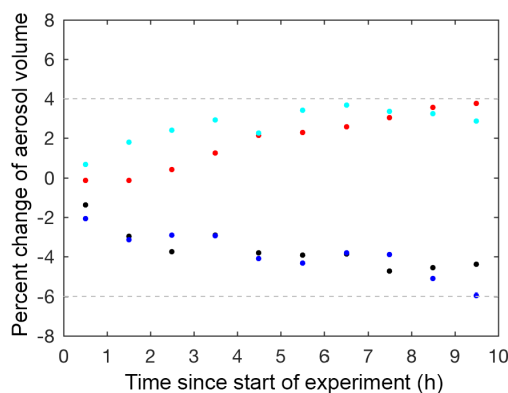
Figure 3. Percent change between the corrected aerosol volume over 10 h and the corrected aerosol volume at the start of photooxidation (60 min averages) for the following particle wall deposition control experiments: C1 ($V = 37\,\mu m^3\,cm^{-3}$; black dot), C2 ($V = 109\,\mu m^3\,cm^{-3}$; blue dot), C3 ($V = 183\,\mu m^3\,cm^{-3}$; red dot), and C4 ($V = 375\,\mu m^3\,cm^{-3}$; cyan dot), where V is the initial corrected particle volume.

as controls to verify the technique used to correct for particle wall loss, particle coagulation, and electrostatic charges on the chamber walls. These particle wall deposition experiments were performed by injecting ammonium sulfate seed into the chamber, as described in Sect. 2.1. Mixing air was added, and the ammonium sulfate seed aerosol was monitored in the dark chamber for at least 14 h. These controls confirmed that the wall loss correction calculated over the first 3.5 h could be extrapolated for an additional 10 h. Beyond 10 h, the wall loss correction was more uncertain, so only results from the first 10 h of each experiment are reported. The percent change between the aerosol volume over 10 h and the aerosol volume at the start of the control experiment was between $+4\%$ and -6% for all dry control experiments (Fig. 3).

The results of these control experiments verified the robustness of the correction technique and provided an estimate for the uncertainty. The reported uncertainty for the particle wall deposition correction is $+4\%$ and -6% of the corrected aerosol volume at the start of photooxidation. Experiments with larger seed aerosol volumes exhibit larger uncertainty in the reported SOA yield. However, such experiments are necessary despite the extra uncertainty, as larger seed surface areas minimize low biases in SOA yields due to vapor wall deposition of low-volatility compounds (Zhang et al., 2014; Ehn et al., 2014). For experiments with no initial seed aerosol, particle wall loss corrections were applied assuming the particles coagulated and deposited similarly to the lowest aerosol loading control experiment (C1). No uncertainty for the particle wall deposition correction was added to these experiments because the uncertainty derived here is applicable only to experiments with initial seed aerosol.

In experiments C1–C4, D1–D9, and M1–M8, electrostatic charges on the chamber walls were inferred to be present. After these experiments were completed, new Teflon chambers were acquired with negligible electrostatic charges on the chamber walls (Charan et al., 2018) likely due to their smaller volume ($18\,m^3$). Three additional new experiments (D10, D11, and M9) were completed using one of these new Teflon chambers to confirm that we had accurately corrected for the chamber wall charging effects. For the LV pathway experiments (Sect. 4.2), results for the new experiments were quite similar and within uncertainties of the old experiments. The new 2MGA pathway experiment produced slightly lower SOA yields than the old experiments but not necessarily because of the chamber wall charging corrections as described in Sect. 4.3.

Five control experiments were also performed under humid conditions. The DMA cannot measure hydrated particles owing to arcing in the DMA column at high RH. Thus, a Nafion dryer was used to dry particles before measurement. For the coagulation correction, the volume of the hydrated seed was calculated based on the dry DMA particle measurement, the RH in the chamber, and the hygroscopic growth curve for ammonium sulfate measured by Sjogren et al. (2007). The percent change for the aerosol volume was higher and less consistent in the humid control experiments than in the dry control experiments. Also, the optimized value of the electric field ($\overline{E}$) was higher in many of the humid experiments than in the dry experiments (Sect. S2, Table S3). Increased humidity is expected to decrease the electrostatic charges on the chamber walls (e.g., Ribeiro et al., 1992), but the inferred $\overline{E}$ suggests the opposite. Possibly, the humidifying process enhanced the electrostatic charges on the chamber walls or nitric acid, which is enhanced in the particle phase in the humid experiments under high-NO$_x$ conditions, impacts the coagulation or particle wall loss processes.

The aerosol mass spectrometer (AMS) data confirm that during the humid experiments, nitric acid partitioned to the particle phase and that organic aerosol was produced during photooxidation for all experiments. Nevertheless, the particle wall loss corrected volume measured by the DMA decayed below zero during photooxidation in the humid experiments. Potentially, this DMA volume decay suggests that nitric acid present in the particle phase changes the particle coagulation or wall loss characteristics. Even if we understood the impact of nitric acid on the particle coagulation or wall loss corrections, assessing how much of the particle growth is due to nitric acid versus organics would be difficult with the DMA, which measures only total aerosol volume and not composition. Further chamber characterization is required in order to assess isoprene SOA yields measured by the DMA from humid experiments under high-NO$_x$ conditions. Thus, in this work, only the AMS results will be discussed for the humid experiments and SOA yields are only reported for experiments performed under dry conditions (Table 1). None
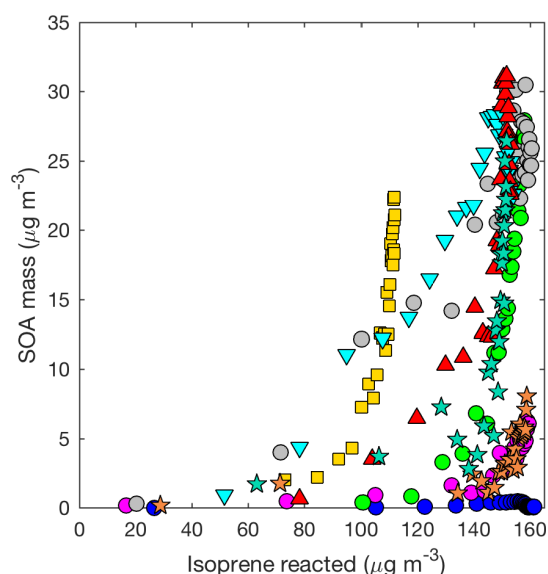
Figure 4. SOA mass yield (20 min averages) as measured by the DMA assuming a density of $1.4\,\mathrm{g\,cm^{-3}}$ for all LV pathway experiments: seed surface area (SA) – D1 (SA $= 0\,\mathrm{\mu m^2 cm^{-3}}$; blue dot), D2 (SA $= 1170\,\mathrm{\mu m^2\,cm^{-3}}$; magenta dot), D3 (SA $= 3420\,\mathrm{\mu m^2\,cm^{-3}}$; green dot), and D4 (SA $= 5770\,\mathrm{\mu m^2\,cm^{-3}}$; gray dot); temperature – D5 ($13\,^\circ$C; inverted cyan triangle) and D6 ($32\,^\circ$C; red triangle); isoprene loading – D7 (initial isoprene $110\,\mathrm{\mu g\,m^{-3}}$; yellow square); and new chamber with less wall charging – D10 (SA $= 1580\,\mathrm{\mu m^2\,cm^{-3}}$, orange star) and D11 (SA $= 4770\,\mathrm{\mu m^2\,cm^{-3}}$; teal star).

of the dry experiments exhibited the odd behavior observed in the humid experiments, and the AMS results confirm that under dry conditions minimal nitric acid partitioned to the aerosols (Fig. S10). For the dry experiments, the uncertainties are characterized well by the dry control experiments presented in Fig. 3.

4.2 SOA formation from the LV pathway

The SOA mass yields from isoprene for all LV pathway experiments (i.e., experiments targeting low-volatility compounds) are shown in Figs. 4 and 5. To convert aerosol volume measured by the DMA to aerosol mass, a density of $1.4\,\mathrm{g\,cm^{-3}}$ was assumed, consistent with past work (Dommen et al., 2006; Kroll et al., 2005, 2006; Brégonzio-Rozier et al., 2015). The kinetic mechanism suggests that in all experiments targeting the LV pathway, the formation of HMML was < 0.12 ppb even in experiments performed under cold conditions ($13\,^\circ$C). The AMS results also confirm that 2-MGA and its oligomers are not present in the LV pathway experiments (Sect. 5.2). Thus, the kinetic mechanism and AMS results verify that the experimental design correctly separates the two chemical regimes and 2-MGA is not substantially adding to the aerosol mass in the LV pathway experiments.
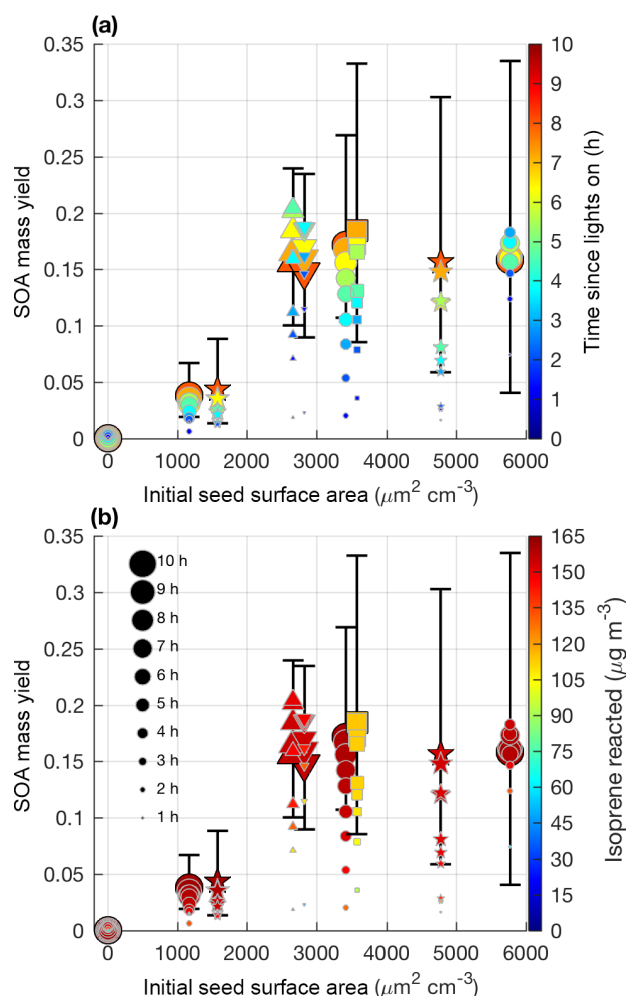
Figure 5. SOA mass yield (60 min averages) as a function of initial seed surface area for all LV pathway experiments. Colors represent time since lights on in panel **(a)** and extent of isoprene reacted in panel **(b)**. Marker size represents time since lights on. Uncertainty is shown in black lines as described in Sect. 4.1. Marker types indicate 25–26 $^\circ$C (dot), 13 $^\circ$C (inverted triangle), 32 $^\circ$C (triangle), lower loadings of isoprene (square), and new chamber with less wall charging (star).

Aerosol growth in the absence of seed aerosols was not observed in the LV pathway experiments (Fig. 4). As expected, SOA formed from gas–particle partitioning in the LV pathway exhibited a large dependence on seed surface area (Fig. 5). Without sufficient seed aerosol, low-volatility nitrates partition primarily to the chamber walls, and the resulting SOA yields are biased low. With the addition of inorganic seed aerosol like ammonium sulfate, vapor species are expected to partition more to particles relative to the chamber wall (Zhang et al., 2014). The gas-particle equilibrium is not expected to be dependent on the concentration of inorganic seed aerosol but instead is dependent on the concentration of organic aerosol. Depending on the saturation mass concentration (C^*), as the concentration of organic aerosol rises,

vapors are present more in the particle phase relative to the gas phase (Seinfeld and Pandis, 2016). C^* and the fraction of a compound expected to be in the particle phase (F_P) were estimated for a variety of organic nitrates and dinitrates in MCM v3.3.1 at 13, 26, and 32 °C (Table S2).

Similar to previous studies (e.g., Zhang et al., 2014), at a certain point increased seed surface area no longer substantially impacts the SOA yield (i.e., Fig. 5 after 2500 μm² cm⁻³). This point will heavily depend on the system and the saturation mass concentration (C^*) of the SOA precursors. As shown in Table S2, the isoprene SOA precursors are mostly classified as IVOCs and SVOCs (Donahue et al., 2012). Reaching a point where most of the vapors are in particles relative to the chamber wall is expected for IVOCs and SVOCs, which have moderate vapor wall losses in Teflon chambers especially under dry conditions (Zhang et al., 2014; Huang et al., 2018).

As expected the isoprene dihydroxy dinitrates had the lowest C^* values and high F_P at all temperatures. Based on the kinetic model, even assuming all of the isoprene dihydroxy dinitrates exist in the particle phase, the SOA formed would be much less than that detected in this study (Fig. S4). This is likely caused by too low of a production of the isoprene dihydroxy dinitrates and/or the importance of other SOA precursors. There are many additional compounds largely produced from hydroxy aldehyde oxidation or alkoxy [1,5]-H shifts (Fig. 1) with F_P at 26 °C between 0.05 and 0.4 (Table S2). The vapor pressures may be overpredicted for these specific compounds, but past studies suggest that in general, vapor pressure estimation methods like Nannoolal et al. (2004, 2008) underpredict rather than overpredict vapor pressure (Kurten et al., 2016). From the C^* calculations (Table S2), none of the multifunctional organic nitrates are expected to be appreciably in the particle phase. However, in a recent study, Lee et al. (2016) detected many multifunctional organic nitrates in aerosols in the ambient atmosphere, which has lower organic aerosol concentrations than chamber studies. Possibly, MCM underpredicts the formation of these IVOC and SVOC products (Fig. S4), such that even if only a fraction exists in the particle phase relative to the gas phase, an appreciable mass of aerosol still forms and/or these results suggest that volatility is not the only driver for aerosol formation from the LV pathway. All of the multifunctional nitrates here with estimated F_P at 26 °C between 0.05 and 0.4 have at least one hydroxy or aldehyde group (Table S2). Alcohols and aldehydes are well known to combine in particles to produce hemiacetals, whose vapor pressure is significantly lower than that of the initial reactants (Kroll and Seinfeld, 2008). Several past studies have confirmed that NO$_x$ in general, but not necessarily linearly, decreases the volatility of isoprene SOA (Kleindienst et al., 2009; Xu et al., 2014; D'Ambro et al., 2017). This decrease in volatility is likely due to accretion reactions. Whether the accretion reactions from hemiacetal formation versus those from 2MGA

oligomerization are responsible for the decrease in volatility is yet unknown.

Differences in the SOA yield at 10 h of photooxidation by varying temperatures (13–32 °C) lie within the experimental uncertainty. SOA forms earlier (i.e. with less isoprene reacted) at 13 °C than at 26 or 32 °C at comparable seed surface areas. This is consistent with the C^* values estimated in Table S2 and the above explanation demonstrating the likelihood of accretion reactions. Vapors that are only moderately in the particle phase at 26 °C (e.g., $F_P = 0.05$–0.4) will exist more appreciably in the particle phase at 13 °C (e.g., $F_P = 0.2$–0.8). From the above discussion, we expect that many of these compounds are SOA precursors not based only on their volatility but also on their potential to react in the particle phase to form lower-volatility products such as hemiacetals. Thus, if accretion reactions are the main factor, reducing temperature is expected to increase the rate of SOA production but not necessarily to impact the overall SOA yield.

Clark et al. (2016) have also measured isoprene SOA formation under high-NO$_x$ conditions at varying temperatures. Under the high-NO$_x$ conditions of their study, SOA is produced from both the 2MGA and LV pathways combined. Similarly to our study, Clark et al. (2016) do not find appreciable differences for temperatures from 27 to 40 °C. Contrary, to our work, Clark et al. (2016) found that reducing the temperature to 5 °C increases the SOA yield by a factor of 4. Unfortunately, there are no experiments between 5 °C and 27 °C to determine whether this shift is exponential or linear, so direct comparison of our results at 13 °C is difficult. Under the high-NO$_x$ conditions used by Clark et al. (2016), at colder temperatures MPAN will be more stable and so more HMML will form, which produces more SOA. Under this mixed regime, determining how much of the SOA increase is due to the LV versus the 2MGA pathway for direct comparison to this study is difficult. Additionally, Clark et al. (2016) start with significantly more isoprene than in our experiment, which enhances the concentration of organic aerosol, which will increase the fraction of a compound in the particle phase relative to the gas phase.

While vapor wall losses of LV compounds are expected to increase at colder temperatures (Zhang et al., 2015; Schwantes et al., 2017), the organic nitrate yields are also expected to be enhanced under colder temperatures (Orlando and Tyndall, 2012). Thus, the effects of these two temperature-dependent processes might cancel each other out. The increase in organic nitrate yield is expected to be moderate. For example, a ∼ 30 % increase from 32 to 13 °C is estimated for the yield of isoprene hydroxy nitrates (Wennberg et al., 2018). The loss of vapors to the walls could be much higher at colder temperatures, but this is hard to constrain as vapor wall deposition is dependent on the compound itself and the chamber used. The chamber used by Clark et al. (2016) (90 m³) is larger than our chamber (21 m³). Vapor wall losses are expected to be lower in larger chambers,

which have a lower chamber surface-area-to-volume ratio (Zhang et al., 2015). Significant seed aerosol is added into our chamber to reduce the influence of vapor wall deposition, but vapor wall deposition could certainly explain some of the differences at cold temperatures between our results and those from Clark et al. (2016).

Consistent with past work (e.g., Kroll et al., 2005; Ng et al., 2006), aerosol from the LV pathway is produced only after most of the isoprene is consumed, implying that aerosol from the LV pathway largely forms from later-generation chemistry (Fig. 4). As shown in Fig. 4, generally, SOA formation begins earlier (i.e., with less isoprene reacted) in experiments with larger seed aerosol. This is consistent with vapors partitioning more to particles relative to the chamber wall when seed aerosol is enhanced. The extent to which later-generation products are oxidized (i.e., the degree of oxidation) impacts the SOA yield as demonstrated by the varying slope (i.e., SOA yield) during each experiment in Fig. 4. We tested the OH/isoprene ratio on the SOA yield. Experiment D7 was performed with 40 ppb of isoprene compared to 55–60 ppb used in the other experiments, while the OH precursor concentration was kept constant. The kinetic model predicts that the production of important gas-phase SOA precursors from the LV pathway (e.g., isoprene dihydroxy dinitrates), when corrected for total isoprene reacted, is similar in experiment D7 to the other experiments (Fig. S4). The empirical results are consistent with these predictions. Although a lower isoprene loading decreases the competition of isoprene with OH, other compounds also react with OH quickly (e.g., NO). Under the conditions used in this study, differences in isoprene loading are not expected to greatly influence the isoprene SOA mass yield. However, detailed kinetic modeling of past experimental conditions would be necessary to understand how the degree of oxidation of later-generation products in this study compares to other studies.

In summary, the results (Fig. 5) suggest that one of the most important metrics for understanding the variability in SOA production from the LV pathway in various chamber experiments may be the initial seed surface area, instead of temperature or OH/isoprene ratio. Other parameters such as humidity and seed composition may also be important for SOA yields but were not tested in this study. Future experiments examining SOA yields should report the initial seed surface area and use a sufficient seed loading to reduce the impact of vapor wall deposition.

4.3 SOA formation from the 2MGA pathway

The SOA mass yields from methacrolein for all 2MGA pathway experiments (i.e., experiments targeting 2MGA and its oligomers) are shown in Figs. 6 and 7. Results from past experiments (Chan et al., 2010) have already demonstrated that fluctuations in the NO_2/NO ratio impact SOA formation through the production of MPAN. In this work, the NO_2/NO ratio is kept as consistent as possible to isolate other influ-
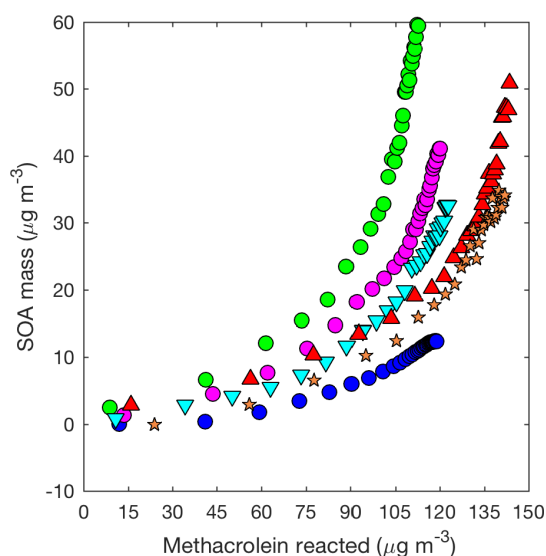
Figure 6. SOA mass yield (20 min averages) as measured by the DMA assuming a density of $1.4 \mu g \, cm^{-3}$ for 2MGA pathway experiments: seed surface area (SA) – M1 (SA $= 0 \mu m^2 \, cm^{-3}$; blue dot), M2 (SA $= 1640 \mu m^2 \, cm^{-3}$; magenta dot), and M3 (SA $= 2260 \mu m^2 \, cm^{-3}$; green dot), temperature – M5 (13 °C; inverted cyan triangle) and M6 (32 °C; red triangle), and new chamber with less wall charging – M9 (SA $= 1910 \mu m^2 \, cm^{-3}$; orange star).

ences on SOA production. The kinetic model suggests that the conditions for each experiment produce a consistent level of HMML (Fig. S4). Interestingly, because the experimental conditions heavily favored MPAN formation, the level of OH available to react with MPAN became the limiting reactant for aerosol formation in each experiment.

Contrary to the LV pathway, SOA in the 2MGA pathway experiments does not require seed particles to form. The process of SOA formation from these two pathways is very different. Lactone SOA precursors may polymerize in the presence of organics and water, which possibly explains why SOA from the 2MGA pathway readily forms particles without significant seed surface area, whereas in the LV pathway experiments volatility-based SOA formation results in aerosol yields that are particularly impacted by vapor partitioning. For the 2MGA pathway experiments, even though SOA formation occurred without initial seed aerosol, larger initial seed loadings still enhanced the SOA yield (Fig. 7). Possibly, similar to the LV pathway, larger seed surface areas limit vapor wall loss of HMML or its oligomerization partners. Alternatively, the presence of higher ammonium sulfate seed aerosol may also increase organosulfate formation, which could impact SOA composition and yield.

Temperature was varied between 13 and 32 °C. The NO_2/NO ratio used in this work was sufficiently high such that this temperature change did not greatly influence MPAN or HMML formation (Fig. S4). Thus, these experiments only

Figure 7. SOA mass yield (60 min averages) versus initial seed surface area for all 2MGA pathway experiments. Colors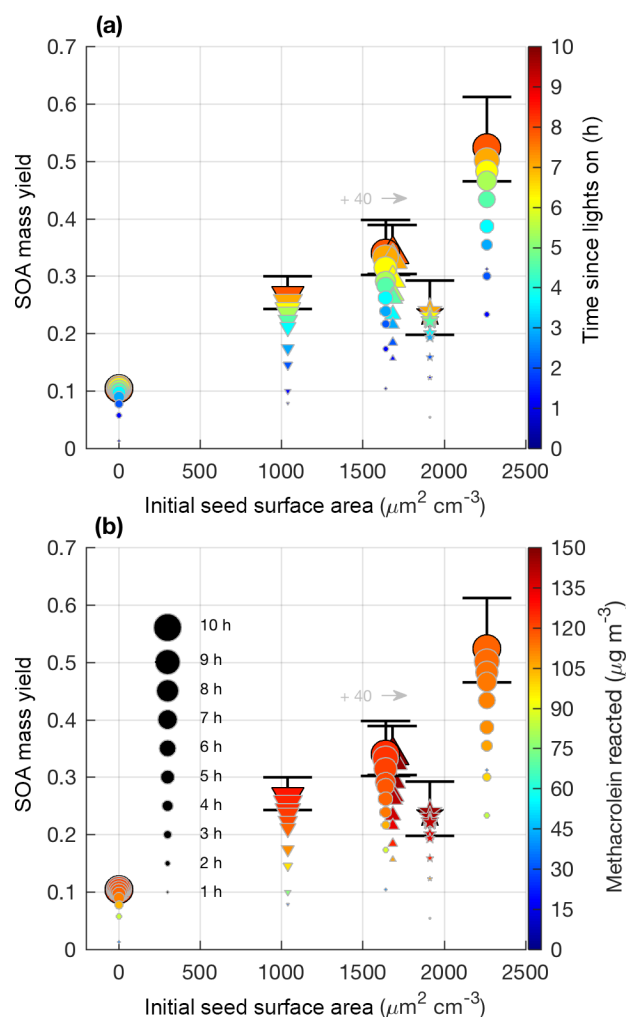 represent time since lights on **(a)** and extent of methacrolein reacted **(b)**. Marker size represents time since lights on. Uncertainty is shown in black lines and described in Sect. 4.1. Markers represent 25–26 °C (dot), 13 °C (inverted triangle), 32 °C (triangle), and new chamber with less wall charging (star). Two experiments were performed at nearly the same seed surface area. To enhance viewing, experiment M6 (32 °C; triangle) is shifted to the right by $40 \, \mu m^2 \, cm^{-3}$.

test whether aerosol properties and SOA yields are affected by temperature, as MPAN thermal decomposition is minimized. At the high NO_2/NO ratios used in this work, temperature does not impact SOA mass yield beyond given uncertainties (Fig. 7). Based on known gas-phase chemistry, past studies (e.g., Clark et al., 2016) with more moderate NO_2/NO ratios than that used in this work are expected to measure an enhanced SOA yield under colder temperatures due to a reduction in MPAN thermal decomposition and thereby an increase in HMML formation.

HMML, based on volatility alone, would exist mostly in the gas phase, but because HMML is very reactive (e.g.,

oligomerization or reaction with inorganic ions in the particle phase), HMML quickly produces aerosol (Kjaergaard et al., 2012; Nguyen et al., 2015). Based on HMML production simulated by the kinetic mechanism under the conditions used in these experiments, ~ 0.21 SOA mass yield from methacrolein is expected purely from the mass contained in HMML (molecular weight $= 102 \, g \, mol^{-1}$, Fig. S4). At first, the molecular weight of HMML itself is used because this is the mass of the majority of the oligomer monomers. This represents about half of the SOA mass yield (~ 0.5) measured from the experiment performed with the highest seed surface area. The rest of the aerosol is likely comprised of inorganic or organic compounds that react with HMML in the particle phase. For example, inorganic compounds such as water, nitrate, and sulfate can react with HMML through ring-opening reactions to produce total methacrolein SOA mass yields of ~ 0.25, ~ 0.34, and ~ 0.41, respectively (Fig. 2). Additionally, HMML can react with 2-MGA and other organic compounds through oligomerization processes (e.g., Chan et al., 2010; Nguyen et al., 2015; Zhang et al., 2011, 2012). Some of these organic oligomerization reactions bring into the particle phase additional organic compounds (e.g., organic acids) that ordinarily would exist primarily in the gas phase (Fig. 2). The details of these particle-phase reactions are further discussed in Sect. 5.2.

In general, there is much greater variability in the SOA mass yields measured from the 2MGA pathway than the LV pathway. The additional variability is only partially explained by the initial seed surface area (Fig. 7). Because the SOA yield is larger for experiments in which less methacrolein is oxidized (Figs. 6 and 7b), potentially, the extent of methacrolein oxidization contributes to this variability. The kinetic model suggests that the formation of gas-phase HMML is similar for all of the experiments (Fig. S4), but potentially slight variations in the NO_2/NO ratio and/or OH particularly near the end of each experiment are not well captured by the model. The kinetic model used here only simulates gas-phase oxidation. Chemistry occurring on surfaces such as the chamber walls or in the particle phase may be especially important for capturing the variability in the 2MGA pathway experiments. Considering that the 2MGA pathway experiments are very susceptible to small differences in chamber conditions, regional and global models should parameterize SOA formation from the 2MGA pathway through gas-phase formation of HMML and subsequent particle-phase reactions.

5 Discussion

The gas-phase compounds measured by the CIMS (Sect. 5.1) and aerosol composition measured by the AMS (Sect. 5.2) provide important insight into isoprene SOA chemical composition formed from both the LV and 2MGA pathways. Additionally, a comparison of the AMS and DMA results lends

insight into possible biases in the AMS measurements of organic aerosol in Sect. 5.3. The SOA yields measured in this study are compared with past measurements in Sect. 5.4, and the atmospheric contribution of the LV versus 2MGA pathways toward SOA formation from isoprene OH-initiated oxidation under high-NO$_x$ conditions is estimated in Sect. 5.5.

5.1 Specific low-volatility nitrates and dinitrates detected in the gas phase

Numerous nitrates and dinitrates are detected in the gas phase by the CF$_3$O$^-$ CIMS (i.e., compounds highlighted in blue boxes in Fig. 1). Many of these nitrates have been identified in previous studies (e.g., Lee et al., 2014). Yields for the low-volatility later-generation nitrates are either highly uncertain or unknown. Quantification is difficult for these low-volatility compounds due to high losses to sampling lines or chamber walls and lack of available standards. One study, Lee et al. (2014), was able to quantify the yield of dinitrates from the first-generation isoprene hydroxy nitrate standards. Assuming a sensitivity similar to the isoprene hydroxy nitrate standards, Lee et al. (2014) measured a dinitrate yield of 0.03–0.04 from OH-initiated oxidation of the δ-1-hydroxy,4-nitrate isomer.

Although most past studies have focused on dihydroxy dinitrates as the main contributor to isoprene high-NO SOA, other low-volatility nitrates are likely also important. In Fig. 8, the CIMS signals for the other low-volatility nitrates are comparable or larger than the dihydroxy dinitrate signal. The relative sensitivities for these compounds are unknown, but these results suggest that detection and quantification of all low-volatility dinitrates and nitrates is important. The peroxy radical formed from OH-initiated oxidation of an isoprene hydroxy nitrate can undergo a 1,5 or 1,6 α-hydroxy H shift to form a number of low-volatility nitrates that would occur in the ambient atmosphere (Wennberg et al., 2018). The NO concentrations are too high in these experiments for such shifts to occur. However, similarly, certain isomers of the alkoxy radical, formed from OH-initiated oxidation of a isoprene hydroxy nitrate, can undergo a 1,5 α-hydroxy H shift to form a dihydroxy carbonyl nitrate detected by the CIMS at m/z (-) 264 (Fig. 1 and 8). Additionally, various low-volatility nitrates in the gas phase are detected, which are potentially oxidation products from the δ-isoprene hydroxy alkoxy radical as depicted in Fig. 1.

Many multifunctional isoprene-derived organic nitrates have been detected in ambient aerosol (Lee et al., 2016). Although these low-volatility nitrates and dinitrates have low molar yields from isoprene OH-initiated oxidation, their mass is substantially larger than isoprene and so their contribution to the isoprene SOA mass yield is significant. The nitrate yield from straight-chain hydrocarbons is reasonably well understood, but few experimental measurements of the nitrate yield from highly oxidized compounds exist (Orlando and Tyndall, 2012; Wennberg et al., 2018). Further measure-
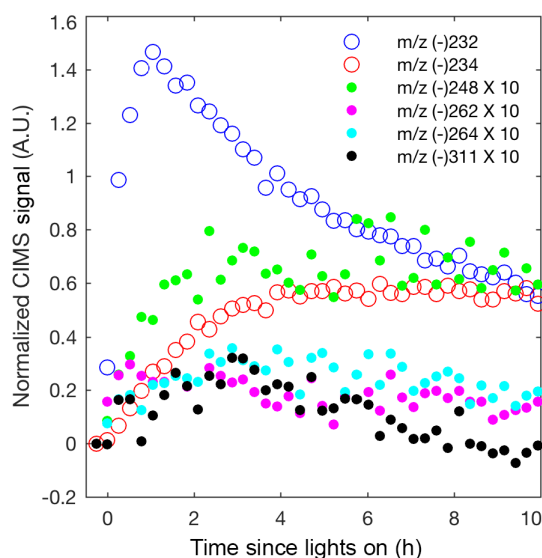
Figure 8. Normalized CIMS signal for known nitrates: C$_5$ hydroxy nitrate (m/z (–) 232; blue circle), methyl vinyl ketone or methacrolein nitrate (m/z (–) 234; red circle), and C$_5$ dihydroxy dinitrate (m/z (–) 311; black filled circle) and unknown nitrates, which are postulated in Fig. 1 as C$_5$ dihydroxy nitrate (m/z (–) 248; green filled circle), unknown (m/z (–) 262; magenta filled circle), and C$_5$ dihydroxy carbonyl nitrate (m/z (–) 264; cyan filled circle). As indicated in the legend, signals represented by filled circles are multiplied by 10.

ments of the yield of these low-volatility nitrates and dinitrates in the gas phase will be crucial for a better understanding of isoprene SOA formation under high-NO conditions.

5.2 Aerosol composition of high-NO isoprene SOA

Pieber et al. (2016) determined that inorganic aerosol such as ammonium nitrate or ammonium sulfate causes an interference on the AMS for the CO$_2^+$ ion signal. Although this interference is small for ammonium sulfate aerosol ($<$ 1 %, Pieber et al., 2016), a correction may be needed for experiments with high initial seed aerosol loadings. Here organic signals from the AMS rise when ammonium sulfate seed is injected into the chamber. We expect that this is due to the same interferences described in Pieber et al. (2016) and not due to contamination in ammonium sulfate solution or atomization technique. The background organic signal caused by the ammonium sulfate is subtracted from the overall results to produce Figs. 9, 10, and 11.

The AMS spectra from the LV pathway confirm that SOA formed from the LV pathway is not dominated by 2-MGA and its oligomers (cyan and red bars in Figs. 9 and S11). This is an important confirmation that isoprene SOA formed from the 2MGA and LV pathways are distinct. A small yield of isoprene epoxydiol (IEPOX) is produced from OH-initiated oxidation of isoprene hydroxy nitrates (Jacobs et al., 2014), and IEPOX SOA can be formed when particle liq-

Figure 9. High-resolution AMS organic mass spectra (averaged over 10 h of photooxidation – the sulfate background) for experiment D3 (RH = 8 %, panel **a**) and D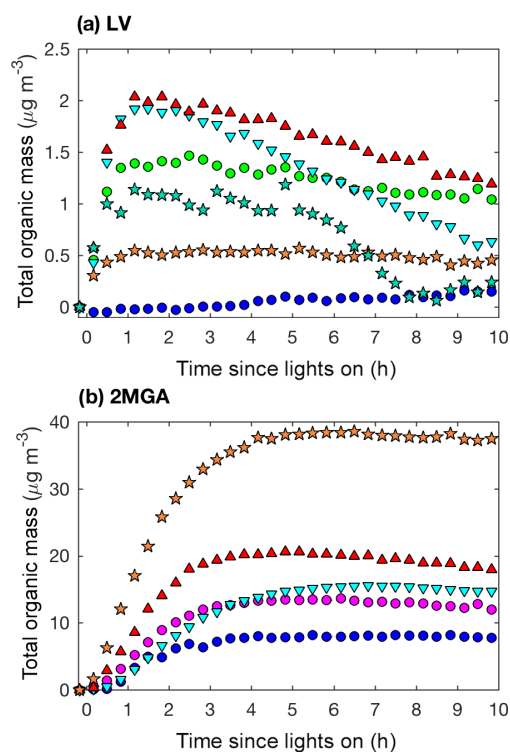9 (RH = 78 %, panel **b**) in gray. Fragments are labeled as 2-MGA monomer or dimer (cyan), esterification of 2-MGA with acids (red), isoprene epoxydiol (IEPOX) tracers (dark green), and examples of organonitrate fragments – $C_xH_yNO_z$ (purple).

Figure 10. High-resolution AMS organic mass spectra (averaged over 10 h of photooxidation – the sulfate background) for experiment M2 (RH = 9 %, panel **a**) and M8 (RH = 81 %, panel **b**) in gray. Fragments are labeled as 2-MGA monomer or dimer (cyan), esterification of 2-MGA with acids (red), examples of organosulfate fragments (dark green), and examples of organonitrate fragments – $C_xH_yNO_z$ (purple).

uid water is present (Nguyen et al., 2014a). NO levels remained high (> 100 ppb) throughout all LV pathway experiments (Fig. S3), ensuring that the RO_2 fate in these experiments was always $RO_2 + NO$. AMS fragments associated with IEPOX, which were identified by Lin et al. (2012), are slightly enhanced under humid conditions in the LV pathway experiments (Fig. 9). Some examples of organonitrate fragments ($C_xH_yNO_z^+$) are highlighted in Fig. 9. Some of these organonitrate fragments are enhanced under humid conditions (e.g., CH_3NO^+). In general, the AMS spectra are similar between all LV pathway conditions (i.e. varied humidity – Fig. 9; varied temperature – Fig. S11).

Prominent peaks in the AMS spectra from the 2MGA pathway clearly indicate that under dry conditions aerosol is comprised of various oligomerization products as mechanistically summarized in Fig. 2. These oligomerization processes include 2-MGA oligomerization with HMML (cyan bars in Fig. 10a) and, possibly, esterification of 2-MGA with carboxylic acids including formic, acetic, and pyruvic acids (red bars in Fig. 10a), which yield products that have been

detected in numerous studies (Chan et al., 2010; Zhang et al., 2011, 2012). Based on the AMS spectra, 2-MGA oligomerization appears to be more dominant without the presence of ammonium sulfate seed aerosol (Fig. S13). Varying temperature from 13 to 32 °C does not appear to substantially change the extent of 2-MGA oligomerization (Fig. S14).

Past studies have determined that HMML reaction with 2-MGA to form oligomers decreases under humid conditions, while HMML ring-opening reactions with water and inorganic ions to form organic nitrates and organic sulfates increase (Zhang et al., 2011, 2012; Nguyen et al., 2015). Consistent with these past studies, the 2-MGA oligomer fragments on the AMS (cyan and red) are no longer prominent signals for all humid experiments (Figs. 10 and S12). 2-MGA oligomer fragments are not substantially different at 47 %, 67 %, or 81 % RH, suggesting that the HMML oligomerization processes are impeded as soon as aerosol particles become deliquesced. Because isoprene is mostly emitted in regions with relatively high humidity, in the ambient atmosphere, HMML will more likely react with water and inor-

Figure 11. Total organic mass (20 min averages) as measured by the AMS for LV pathway experiments **(a)**: seed surface area (SA) – D1 (SA = 0 μm² cm⁻³; blue dot) and D3 (SA = 3420 μm² cm⁻³; green dot); temperature – D5 (13 °C; inverted cyan triangle) and D6 (32 °C; red triangle); and new chamber with less wall charging – D10 (SA = 1580 μm² cm⁻³; orange star) and D11 (SA = 4770 μm² cm⁻³; teal star). Total organic mass as measured by the AMS for 2MGA pathway experiments **(b)**: seed surface area – M1 (SA = 0 μm² cm⁻³; blue dot) and M2 (SA = 1640 μm² cm⁻³; magenta dot); temperature – M4 (13 °C; inverted cyan triangle) and M5 (32 °C; red triangle); and new chamber with less wall charging – M9 (SA = 1910 μm² cm⁻³; orange star).

ganic ions than undergo the various organic oligomerization reactions summarized in Fig. 2.

5.3 Comparison of AMS and DMA results

Based on the DMA measurements when assuming the same density, the SOA mass produced from the 2MGA pathway experiments is ∼ 2 times higher in magnitude than that from the LV pathway experiments (Figs. 4 and 6). However, the AMS results (Fig. 11) suggest that the SOA mass produced from the 2MGA pathway experiments is ≥ 8 times larger than that from the LV pathway experiments. This implies that the collection efficiency (CE) and/or the ionization efficiency of the AMS is quite different between these two regimes. Because the AMS is significantly more sensitive to aerosol formed from the 2MGA pathway, and not to SOA formed from the LV pathway, even ambient organic aerosol measurements have the potential to be impacted. Understand-

ing whether the AMS is systematically underestimating organic aerosol from organic nitrates and dinitrates in general, or if this is only relevant to the isoprene system is crucial as the AMS is used throughout the world to quantify organic aerosol. Moreover, ambient measurements over the isoprene-rich southeastern United States of particulate organic nitrates measured by the AMS are a factor of ∼ 5 lower than those measured by the thermal dissociation laser-induced fluorescence instrument (TD-LIF) (Lee et al., 2016). The relative CE differences between the LV and 2MGA pathways in this study and these field campaign results suggest that further AMS calibration of organic nitrates is necessary.

In this work, a CE of 0.5 is assumed for both regimes consistent with past work (Nguyen et al., 2014b). The exact CE is not relevant as no mass yields are reported here from the AMS. Docherty et al. (2013) determined that the CE could be estimated based on the f_{44}/f_{57} ratio. The f_{44}/f_{57} ratio for all experiments (2MGA and LV) is ≥ 6, which is where the CE vs. f_{44}/f_{57} curve plateaus at 0.2. Thus, the CE vs. f_{44}/f_{57} relationship developed by Docherty et al. (2013) is not able to explain the large difference in AMS sensitivity between aerosol formed from the LV and 2MGA pathways.

5.4 Comparison to previously reported SOA yields

SOA mass yields reported from past environmental chamber studies of OH-initiated oxidation of isoprene under high-NO$_x$ conditions vary over the range of 0.001–0.41 (Brégonzio-Rozier et al., 2015; Clark et al., 2016), suggesting isoprene SOA yields are highly dependent on chamber conditions (Carlton et al., 2009). In Table 2, past reported SOA mass yields are summarized along with the chamber conditions for both isoprene and methacrolein OH-initiated oxidation under high-NO$_x$ conditions. Only experiments that explicitly measure an SOA mass yield are listed in Table 2. Overall, our results suggest that the initial seed surface area has the greatest impact on SOA yield. Unfortunately, the initial seed surface area was not commonly reported in past studies. The closest metric is aerosol volume, which can roughly be used to understand differences.

As shown in Table 2, the range for isoprene SOA yields under high-NO$_x$ conditions even from the two most recent studies at comparable temperatures spans over an order of magnitude (0.004 at ∼ 21 °C for Brégonzio-Rozier et al., 2015, and 0.1 at 27 °C for Clark et al., 2016). Our results are most consistent with those of Clark et al. (2016). As shown in Table 2, a variety of NO$_x$ regimes (i.e., non-consistent NO$_2$/NO ratios) are all labeled as high-NO$_x$ in these past studies. Each study likely produces SOA in varying degrees from the LV and 2MGA pathways, which greatly complicates direct comparison between these past studies. By varying a large number of conditions and completely separating SOA production between the 2MGA and LV pathways, our results lend insight into the variation in these past experiments.

Table 2. Reported SOA mass yields and chamber conditions for isoprene and methacrolein OH-initiated oxidation under high-NO_x conditions.

Study	CV (m^3)	Oxidant	$[VOC]_0$ (ppb)	$[NO]_0$ (ppb)	$[NO_2]_0$ (ppb)	Light type	$[AS]_0$ ($\mu m^3\,cm^{-3}$)	Temp. (°C)	RH (%)	SOA yield (fraction)
Isoprene										
Edney et al. (2005)[a]	14.5	NO_x	1610–1680	∼ 630	0	UV	< 0.6–24[b]	29.7	30	0.002–0.028
Kroll et al. (2005)	28	HONO	25–500	75–138	98–165	UV	10–25	∼ 20	40–50	0.009–0.03
Dommen et al. (2006)	27	NO_x	180–2500	0–700	40–806	X	0	20	< 2–84	0.002–0.053
Kleindienst et al. (2006)[a]	14.5	NO_x	1600	406–485	7–69	UV	0.1–27[b]	25	30	0.003–0.018[c]
Chan et al. (2010)	28	HONO or CH_3ONO	33–523	259–316	510–859	UV	11–19	20–22	9–11	0.031–0.074
Chhabra et al. (2010)	28	HONO	81–286[d]	518–591	374–434	UV	11–14	NR	< 10	0.006–0.015
Zhang et al. (2011)	137	NO_x	400–790	138–253	1–9	N	10–30	281–303	15–88	0.007–0.03
Nguyen et al. (2011)	5	H_2O_2	∼ 250	600	100	UV	0	22–26	< 2–90	∼ 0.07
Xu et al. (2014)	10.6	H_2O_2	101–115	338–738	0	UV	0	∼ 25	< 5	0.015–0.085
Brégonzio-Rozier et al. (2015)	4.2	NO_x or HONO	439–846	14–143	< 1–79	X	0–16	16–24	< 5	0.001–0.01
Clark et al. (2016)	90	H_2O_2	250	500	0	UV	0	5–40	dry	0.1–0.41
Methacrolein										
Chan et al. (2010)	28	HONO or CH_3ONO	20–285	164–725	365–799	UV	11–16	20–22	9–11	0.019–0.392
Brégonzio-Rozier et al. (2015)	4.2	NO_x or HONO	396–927	19–123	4–100	X	0–15	19–24	< 5	0.005–0.042

CV: chamber volume. Acronyms are defined as follows: NR – not reported; UV – ultraviolet lights; N – natural; X – xenon arc lamps; AS – ammonium sulfate seed aerosol volume. [a] Chamber was operated in dynamic mode (residence time = 6 h). [b] Ammonium sulfate was injected throughout the experiment to generate the lower limit of initial seed aerosol. SO_2 was added in some experiments to generate the upper limit of initial seed aerosol. [c] Secondary organic carbon is converted to SOA using factor (2.47) reported in Kleindienst et al. (2007). [d] VOC reacted was reported and tabulated instead of VOC initial.

Many of the past SOA yield measurements were performed with no seed aerosol. Consistent with past results, when no seed aerosol was injected into the chamber (experiments D1 and M1), the SOA mass yield for the LV pathway (0 from isoprene) and 2MGA pathway (0.1 from methacrolein) were quite low. Past experiments performed with no seed aerosol only measured SOA from the 2MGA pathway, which is highly dependent on the NO_2/NO ratio (Chan et al., 2010), which varied greatly between these past studies. Clark et al. (2016), who measured high SOA yields (0.1 at 27 °C) in unseeded experiments, are the exception. Possibly, the larger chamber volume (90 m^3) used by Clark et al. (2016) compared to most studies listed in Table 2 reduced vapor wall losses and contributed to the enhanced SOA yield. However, other chamber characteristics might also be important because Zhang et al. (2011) measured quite low isoprene SOA yields (0.007–0.03) using a chamber larger than the one used in the Clark et al. (2016) study.

While the zero or low seed aerosol loading experiments in this study generally compare well with the past, SOA yields measured here using higher initial seed surface areas are substantially greater than most studies, especially for the LV pathway. The SOA yield from the LV pathway is ∼ 0.15 in this study, while past isoprene SOA yields are largely ≤ 0.07 with the exception of studies optimizing for high $RO_2 + NO_2$ reactions (Chan et al., 2010) or mixed regimes

– $RO_2 + HO_2/NO$ (Xu et al., 2014). The SOA yield from the LV pathway in this work is even larger than the SOA yield from Clark et al. (2016) (0.1 at 27 °C), which includes SOA from both the LV and 2MGA pathways. Possibly the larger chamber volume used by Clark et al. (2016) reduces vapor wall losses but not to the extent that enhanced seed surface area does in this work. The higher yields measured in this study are not unexpected given that recent publications have recognized the importance of using high initial seed surface areas when measuring SOA yields to reduce the impact of vapor wall deposition (e.g., Zhang et al., 2014; Ehn et al., 2014). The methacrolein SOA yields measured in this study from the 2MGA pathway are comparable to those measured by Chan et al. (2010) but larger than those measured by Brégonzio-Rozier et al. (2015).

Brégonzio-Rozier et al. (2015) measured low isoprene (0.001–0.01) and methacrolein (0.005–0.042) SOA mass yields and proposed that these lower yields were due to using xenon arc lamps as a light source, which are more representative of natural sunlight than the UV lamps used here and in most other studies. Dommen et al. (2006) also used xenon arc lamps and reported low yields. However, both of these studies used chambers with moderate to low chamber volumes (27–4.2 m^3) unlike the chamber used by Clark et al. (2016) and low levels of initial seed aerosol (0–16 $\mu m^3\,cm^{-3}$) unlike this work, which could also cause this low bias. Additionally,

the stainless steel chamber used by Brégonzio-Rozier et al. (2015) may have higher vapor wall losses than the Teflon chambers used in other studies. Further work is necessary to understand how vapor wall losses compare across different types of environmental chambers.

As discussed by Carlton et al. (2009), isoprene SOA forms mostly from oxidation of second and later-generation products (e.g., Ng et al., 2006). Towards the end of the experiment, SOA continues to grows even when isoprene is no longer reacting (e.g., the characteristic hook in Fig. 4). Differences in the level of oxidation of second and later-generation products could also explain some of the discrepancies between our results and past results. The isoprene SOA mass yields from the LV pathway are particularly sensitive to the extent of oxidation. More studies measuring the gas-phase yields and formation processes of low-volatility nitrates and dinitrates will be critical for further understanding isoprene SOA.

Many of the previous studies listed in Table 2 report the VOC/NO ratio when comparing experiments. A more useful metric is understanding the RO_2 fate and RO_2 lifetime. Simply injecting NO and/or NO_2 and reporting the initial concentrations are not sufficient to confirm that SOA was dominantly produced from the $RO_2 + NO$ channel or in the case of HMML formation from the $RO_2 + NO_2$ channel. For example, if NO decreases to zero before the end of the experiment, SOA has formed in a mixed regime; $RO_2 + NO$ reactions dominate in the beginning and $RO_2 + HO_2$ reactions dominate at the end. If large initial VOC loadings are used in the beginning of the experiment without comparable increases in NO, $RO_2 + RO_2$ reactions may become dominant.

Experiments here are specifically designed to test two different RO_2 fates, and the kinetic mechanism is used to confirm the fate of the RO_2. In the LV pathway experiments, high NO levels are maintained such that NO_2/NO ratio remains < 1.5 throughout the entire experiment, and RO_2 dominantly and consistently across the experiments reacts with NO. In the 2MGA pathway experiments, high NO_2 levels are used such that the acyl radical derived from methacrolein dominantly and consistently across experiments reacts with NO_2. By controlling for the RO_2 fate, the effects of temperature, seed surface area, and relative humidity on SOA formation become easier to resolve. The design of future experiments should optimize and report the RO_2 fate for which the experiment was designed, in addition to key reaction parameters such as seed surface area, rather than simply reporting an initial VOC/NO ratio.

5.5 Estimating the atmospheric contribution of the LV versus 2MGA pathways

This work was not only designed to independently study SOA formation from the two high-NO_x regimes (the 2MGA and LV pathways) but also to suggest alternative methods for parameterizing isoprene SOA under high-NO_x conditions in regional and global models. Because obtaining constant NO_2/NO ratios similar to the ambient atmosphere is near impossible for a chamber study (e.g., temporal variation in Fig. S3), creating isoprene SOA parameterizations based on NO_2/NO ratio that realistically extrapolate to the ambient atmosphere is not realistic. Instead, this work highlights a potential alternative. Aerosol from the 2MGA pathway could be incorporated directly from gas-phase HMML formation, and aerosol from the LV pathway could be included either from the formation of surrogate compounds such as isoprene dihydroxy dinitrates or with a volatility basis set scheme. By treating the SOA from these two independent regimes separately, this study sets up the experimental basis for such an approach.

In this study, direct comparison of the results from the 2MGA and LV pathways is difficult due to the difference in the extent of oxidation between the two regimes caused by the use of different VOC precursors and the variation in OH levels (Table 1). Thus, the kinetic model is used here to estimate the contribution of each pathway to the total under consistent oxidant levels. A detailed global modeling study is needed to precisely capture the contribution of the LV versus the 2MGA pathways toward SOA formation from isoprene OH-initiated oxidation under high-NO_x conditions. However, in order to demonstrate the significance of the new isoprene SOA yield from the LV pathway measured in this work, we roughly approximate the contribution of each pathway under typical atmospheric conditions. We use the same kinetic mechanism described in Sect. 3 but hold the following constant: $RH = 70\%$; $T = 298$ K; $NO_2 = 0.3$ ppb; $NO = 0.05$ ppb; isoprene $= 5$ ppb; $OH = 1.5 \times 10^6$ molec. cm^{-3}; $CO = 135$ ppb; $O_3 = 37$ ppb; and $HO_2 = 25$ ppt (Sanchez et al., 2018; Feiner et al., 2016; Pajunoja et al., 2016). Then gas-phase HMML and the gas-phase dinitrate SOA precursors are simulated as done for the experimental results in Fig. S4.

To estimate the aerosol contribution from the LV pathway, we assume that SOA production from the LV pathway scales with the production of isoprene dihydroxy dinitrates. Organic aerosol concentrations are higher in chamber experiments than the ambient atmosphere. By using low levels of VOC precursors compared to previous studies, this study attempts to reduce the organic aerosol concentrations to produce results more relevant to the ambient atmosphere. However, due to limitations in the DMA sensitivity, reducing the organic aerosol concentrations further to ambient levels is not possible. The ratio of the measured SOA yield (Fig. 5) versus the simulated gas-phase dihydroxy dinitrate SOA precursor yield (Fig. S4) is about 5. F_P is decreased by a factor of 2 for the dihydroxy dinitrates when C_{OA} is reduced from $\sim 25 \, \mu g \, cm^{-3}$ in the chamber to $\sim 4 \, \mu g \, cm^{-3}$ measured in the southeast US (Zhang et al., 2018). Thus, we multiply the dihydroxy dinitrate SOA precursors by 2.5 and we convert to mass by multiplying by the molecular weight of dihydroxy dinitrate. MCM v3.3.1 assumes a nitrate yield of 0.087–

0.104 from NO reacting with the peroxy radical derived from OH + isoprene hydroxy nitrate. Low-volatility nitrates such as dihydroxy hydroperoxy nitrates form when HO_2 reacts with the peroxy radical derived from OH + isoprene hydroxy nitrate. Such products would not form in the chamber conditions used in this work, where NO levels remained above 100 ppb, but would form in the ambient atmosphere. Considering these low-volatility species from mixed chemical regimes would further increase the SOA mass generated from the LV pathway.

For the 2MGA pathway, we convert to mass by multiplying gas-phase HMML by the molecular weight of 2-MGA (120 g mol^{-1}), 2-MGA nitrate (165 g mol^{-1}), and 2-MGA sulfate (200 g mol^{-1}), which are the expected condensed-phase products under the high humidity levels in the atmosphere. Laboratory studies confirm that 2-MGA forms under humid conditions and some of the 2-MGA partitions to the gas phase as expected based on its volatility (Nguyen et al., 2015). For simplicity, we assume most of the HMML forms 2-MGA nitrate and 2-MGA sulfate but acknowledge that further experimental and modeling studies are needed to fully understand HMML and 2-MGA aqueous phase chemistry.

Then based on the gas-phase SOA precursor distribution from the kinetic model and assumptions above, under typical atmospheric conditions the fraction of the total SOA mass from isoprene OH-initiated oxidation under high-NO$_x$ conditions is ~ 0.7 from the LV pathway and ~ 0.3 from the 2MGA pathway. This assumes that the dihydroxy dinitrates are valid surrogates for the isoprene SOA. Considering that many multifunctional isoprene-derived organic nitrates have been detected in ambient aerosol (Lee et al., 2016), all SOA precursors in Table S2 with $F_P > 0.05$ at 26 °C are combined and converted to mass. Extrapolating these to ambient organic aerosol concentrations is more difficult because these compounds are more likely to exist in the particle phase because of accretion reactions and not volatility. When these products are assumed to exist entirely in the particle phase and no factor is applied to correct for differences in organic aerosol concentration or for these products only representing about one-third of the isoprene SOA yield measured in this study (Fig. S4), the LV pathway is estimated to contribute to ~ 0.6 of the SOA formed under high-NO$_x$ conditions.

Thus, based on the simple calculations summarized above, the LV pathway may produce moderately more SOA mass than the 2MGA pathway in the atmosphere and consequently deserves equal attention. The conditions chosen here represent average atmospheric conditions around noon as measured during the Southern Oxidant and Aerosol Study (SOAS) field campaign, which occurred in the isoprene-rich southeastern United States (Sanchez et al., 2018; Feiner et al., 2016; Pajunoja et al., 2016). A more complete assessment using global and regional modeling is needed to more definitively determine the fraction of SOA formed via the LV versus 2MGA pathways as location, time of day, season, ambient aerosol concentration, and composition, etc.

will all impact the amount of SOA formed from each pathway. Additional studies addressing organic nitrate hydrolysis and aerosol acidity are also necessary to fully understand the relative impact of the two pathways on SOA formation. Additionally, the kinetic model used in this work only estimates gas-phase potential SOA precursors. Future analysis using a more complex model that explicitly simulates both the gas and particle phases would be useful for extrapolating the SOA yields measured here to the ambient atmosphere, which typically has lower organic aerosol concentrations than chamber experiments. This would need to be combined with additional analysis of the chemical constituents in the particle phase. From past work (Kleindienst et al., 2009; Xu et al., 2014; D'Ambro et al., 2017) demonstrating that isoprene-derived SOA under high-NO$_x$ conditions is lower in volatility than that derived under low-NO$_x$ conditions and the C^* values estimated in this work (Table S2), accretion reactions appear to be important even in the LV pathway experiments. The degree to which accretion reactions occur in the LV pathway experiments to form even lower-volatility products is quite uncertain and will greatly impact future analysis on how best to extrapolate isoprene SOA yields measured in chambers to the ambient atmosphere.

6   Conclusions

SOA from OH-initiated isoprene oxidation under high-NO$_x$ conditions forms from two major pathways: (1) low-volatility nitrates and dinitrates (LV pathway) and (2) 2-methyl glyceric acid and its oligomers (2MGA pathway). These SOA production pathways respond differently to experimental conditions, so this work examines the SOA yields from these two pathways independently. Results suggest that low-volatility nitrates and dinitrates produce significantly more aerosol than previously thought, with the isoprene SOA mass yield from the LV pathway being ~ 0.15. Sufficient initial seed aerosol is necessary to reduce the impact of vapor wall losses of low-volatility compounds and accurately measure the entire SOA mass yield. Even though previous studies have assumed that isoprene high-NO$_x$ SOA largely forms from 2-MGA and its oligomers (Chan et al., 2010; Zhang et al., 2011, 2012), results from this study confirm that low-volatility compounds are also important for isoprene SOA formed under high-NO$_x$ conditions. The fate of isoprene's RO$_2$ radicals and the environmental conditions will determine which pathways are active in the atmosphere at a certain time and location.

Under dry conditions, substantial amounts of SOA form from HMML reaction with 2-MGA to produce oligomers. The AMS results confirm that under humid conditions, these low-volatility oligomers are diminished in favor of higher-volatility monomer formation (and potentially subsequent volatilization of 2-MGA) to reduce the SOA mass. Thus, under atmospherically relevant humid conditions, aerosol

formed from the 2MGA pathway is limited to HMML reaction with water or inorganic ions such as nitrate and sulfate. The importance of SOA from the 2MGA pathway will also depend on the NO_2/NO ratio, while SOA formed from the LV pathway will be important under all NO_2/NO ratios. Under typical atmospheric conditions (RH $= 70$ %, $T = 298$ K, $NO_2/NO = 6$, NO $= 0.05$ ppb, isoprene $= 5$ ppb, and OH $= 1.5 \times 10^6$ molec. cm^{-3}), based on the simple assumptions discussed in Sect. 5.5 we now estimate that the LV pathway produces moderately more SOA mass than the 2MGA pathway due to the high isoprene SOA yield from the LV pathway measured in this work.

Given the high isoprene SOA mass yield from the LV pathway (~ 0.15) measured here, low-volatility compounds are as important as 2MGA-based compounds for isoprene SOA formed under high-NO_x conditions. Thus, further studies investigating the formation rates and yields of these low-volatility compounds are needed. Consistent with past work (e.g., Lee et al., 2014), a number of low-volatility nitrates and dinitrates, which are likely important precursors for SOA formed from the LV pathway, were detected in the gas phase by the CF_3O^- CIMS (Sect. 5.1). These low-volatility compounds are likely derived from OH-initiated oxidation of the first-generation isoprene hydroxy nitrates. Synthetic pathways toward standards of many of the isoprene hydroxy nitrates exist (Lee et al., 2014; Teng et al., 2017). Now that this study has confirmed that low-volatility products contribute significantly to isoprene SOA, measuring SOA mass yields under varying RO_2 fates using these isoprene hydroxy nitrate standards as the initial precursor instead of isoprene could be particularly valuable for decreasing the uncertainty in isoprene SOA yields. Additionally, an improved mechanistic understanding of isoprene SOA is needed. This would include an improved understanding of gas-phase reactions including measurements of highly functionalized peroxy radical isomerization rate constants, quantification of nitrate and hydroperoxide yields from highly functionalized RO_2 radicals reacting with NO or HO_2, respectively, and additional constraints on possible particle-phase accretion reactions leading to lower-volatility products (e.g., hemiacetal formation).

There are some limitations for how results from this study should be interpreted. In the atmosphere, the RO_2 lifetime is longer than that in chamber experiments from this study and most past studies measuring SOA yields. Due to limitations in the sensitivity of the DMA and high NO levels needed to control the RO_2 fate, performing SOA yield chamber experiments at conditions that favor a long RO_2 lifetime is difficult. At longer RO_2 lifetimes, the hydroxy nitrate isomer distribution shifts toward a higher percentage of β-isomers over δ-isomers (Peeters et al., 2014; Teng et al., 2017). Additionally, NO_x emissions are decreasing across many regions of the world due to improvements in emissions controls creating mixed regimes in the ambient atmosphere where a later-generation gas-phase product could form from $RO_2 + NO$ re-

action during the first generation and $RO_2 + HO_2$ during the second generation. Field measurements confirm the presence of such products. For example, Xiong et al. (2015) discuss the presence of dihydroxy hydroperoxy nitrates detected in the particle phase by Lee et al. (2016) during SOAS, a field campaign that took place during the summer in the southeastern United States. Dihydroxy hydroperoxy nitrates likely form when hydroxy nitrates, produced from the $RO_2 + NO$ pathway, react with OH and O_2 to form a peroxy radical that then reacts with HO_2. Additionally, because isoprene SOA from the LV pathway only forms once later-generation products become oxidized, the extent of oxidation is important but also difficult to compare across different studies.

Comparisons of the DMA and AMS results imply that the collection and/or ionization efficiency on the AMS for SOA formed from the LV pathway is significantly lower than that formed from the 2MGA pathway. This could have important consequences for the interpretation of ambient organic aerosol measured by the AMS. Further work calibrating organic hydroxy nitrates on the AMS is needed to better understand why the organic fraction analysis varied so significantly between the two pathways.

Results from this work combined with past work provide further insight into how isoprene SOA should be parameterized in global and regional atmospheric chemistry models. Under humid conditions, SOA formation from the 2MGA pathway is produced mostly from HMML ring-opening reactions to form monomer compounds 2-MGA, 2-MGA nitrate, and 2-MGA sulfate, which simplifies the parameterization of SOA from the 2MGA pathway as the organic oligomerization reactions can be ignored. The particle's liquid water and pH will be important to consider, as these metrics shift the equilibrium of 2MGA and its carboxylate and change the hydrolysis rates for the 2-MGA nitrate and 2-MGA sulfate. The gas-phase kinetics for MPAN formation and reaction with OH to form HMML have been reasonably well studied (e.g., Orlando et al., 1999, 2002; Nguyen et al., 2015). HMML formation and generation of SOA in the atmosphere would be best incorporated into models by directly forming SOA through the MPAN + OH reaction. This would best parameterize the effects of temperature and NO_2/NO ratio on MPAN formation and also the influence of OH on HMML formation. This study confirms the need to perform experiments with adequate seed aerosol to limit vapor wall deposition processes when measuring SOA yields from the LV pathway. When regional chemical transport models use SOA yields that account for vapor wall deposition, there are differences in the contribution of isoprene to the total SOA budget and improvements in the agreement between simulated and observed total SOA and diurnal variability (Cappa et al., 2016). Incorporating the isoprene SOA yields from the LV pathway measured in this work into models will further improve the accuracy of simulated isoprene SOA. Moreover, the results from this study along with future experiments studying the formation of low-volatility nitrates and dini-

trates on a mechanistic basis will be important for incorporating more explicit SOA formation into global models as has recently been done (e.g., Marais et al., 2016; Stadtler et al., 2018), thus replacing previous parameterizations that were typically based on a single chamber condition (e.g., Henze and Seinfeld, 2006; Henze et al., 2008; Heald et al., 2008).

References

Aiken, A. C., DeCarlo, P. F., Kroll, J. H., Worsnop, D. R., Huffman, J. A., Docherty, K. S., Ulbrich, I. M., Mohr, C., Kimmel, J. R., Sueper, D., Sun, Y., Zhang, Q., Trimborn, A., Northway, M., Ziemann, P. J., Canagaratna, M. R., Onasch, T. B., Alfarra, R. M., Prevot, A. S. H., Dommen, J., Du-

plissy, J., Metzger, A., Baltensperer, U., and Jimenez, J. L.: O/C and OM/OC ratios of primary, secondary, and ambient organic aerosols with high-resolution time-of-flight aerosol mass spectrometry, Environ. Sci. Technol., 42, 4478–4485, https://doi.org/10.1021/es703009q, 2008.

Atkinson, R.: Rate constants for the atmospheric reactions of alkoxy radicals: An updated estimation method, Atmos. Environ., 41, 8468–8485, https://doi.org/10.1016/j.atmosenv.2007.07.002, 2007.

Brégonzio-Rozier, L., Siekmann, F., Giorio, C., Pangui, E., Morales, S. B., Temime-Roussel, B., Gratien, A., Michoud, V., Ravier, S., Cazaunau, M., Tapparo, A., Monod, A., and Doussin, J.-F.: Gaseous products and secondary organic aerosol formation during long term oxidation of isoprene and methacrolein, Atmos. Chem. Phys., 15, 2953–2968, https://doi.org/10.5194/acp-15-2953-2015, 2015.

Burkholder, J. B., Sander, S. P., Abbatt, J., Barker, J. R., Huie, R. E., Kolb, C. E., Kurylo, M. J., Orkin, V. L., Wilmouth, D. M., and Wine, P. H.: Chemical Kinetics and Photochemical Data for Use in Atmospheric Studies, Evaluation No. 18, Tech. Rep. JPL Publication 15-10, Jet Propulsion Laboratory, Pasadena, CA, http://jpldataeval.jpl.nasa.gov (last access: 24 March 2017), 2015.

Canagaratna, M. R., Jimenez, J. L., Kroll, J. H., Chen, Q., Kessler, S. H., Massoli, P., Hildebrandt Ruiz, L., Fortner, E., Williams, L. R., Wilson, K. R., Surratt, J. D., Donahue, N. M., Jayne, J. T., and Worsnop, D. R.: Elemental ratio measurements of organic compounds using aerosol mass spectrometry: characterization, improved calibration, and implications, Atmos. Chem. Phys., 15, 253–272, https://doi.org/10.5194/acp-15-253-2015, 2015.

Cappa, C. D., Jathar, S. H., Kleeman, M. J., Docherty, K. S., Jimenez, J. L., Seinfeld, J. H., and Wexler, A. S.: Simulating secondary organic aerosol in a regional air quality model using the statistical oxidation model – Part 2: Assessing the influence of vapor wall losses, Atmos. Chem. Phys., 16, 3041–3059, https://doi.org/10.5194/acp-16-3041-2016, 2016.

Carlton, A. G., Wiedinmyer, C., and Kroll, J. H.: A review of Secondary Organic Aerosol (SOA) formation from isoprene, Atmos. Chem. Phys., 9, 4987–5005, https://doi.org/10.5194/acp-9-4987-2009, 2009.

Chan, A. W. H., Chan, M. N., Surratt, J. D., Chhabra, P. S., Loza, C. L., Crounse, J. D., Yee, L. D., Flagan, R. C., Wennberg, P. O., and Seinfeld, J. H.: Role of aldehyde chemistry and NOₓ concentrations in secondary organic aerosol formation, Atmos. Chem. Phys., 10, 7169–7188, https://doi.org/10.5194/acp-10-7169-2010, 2010.

Charan, S. M., Kong, W., Flagan, R. C., and Seinfeld, J. H.: Effect of particle charge on aerosol dynamics in Teflon environmental chambers, Aerosol Sci. Tech., 52, 854–871, https://doi.org/10.1080/02786826.2018.1474167, 2018.

Chhabra, P. S., Flagan, R. C., and Seinfeld, J. H.: Elemental analysis of chamber organic aerosol using an aerodyne high-resolution aerosol mass spectrometer, Atmos. Chem. Phys., 10, 4111–4131, https://doi.org/10.5194/acp-10-4111-2010, 2010.

Clark, C. H., Kacarab, M., Nakao, S., Asa-Awuku, A., Sato, K., and Cocker, D. R.: Temperature effects on secondary organic aerosol (SOA) from the dark ozonolysis and photooxidation of isoprene, Environ. Sci. Technol., 50, 5564–5571, https://doi.org/10.1021/acs.est.5b05524, 2016.

D'Ambro, E. L., Lee, B. H., Liu, J., Shilling, J. E., Gaston, C. J., Lopez-Hilfiker, F. D., Schobesberger, S., Zaveri, R. A., Mohr, C., Lutz, A., Zhang, Z., Gold, A., Surratt, J. D., Rivera-Rios, J. C., Keutsch, F. N., and Thornton, J. A.: Molecular composition and volatility of isoprene photochemical oxidation secondary organic aerosol under low- and high-NOx conditions, Atmos. Chem. Phys., 17, 159–174, https://doi.org/10.5194/acp-17-159-2017, 2017.

Docherty, K. S., Jaoui, M., Corse, E., Jimenez, J. L., Offenberg, J. H., Lewandowski, M., and Kleindienst, T. E.: Collection efficiency of the aerosol mass spectrometer for chamber-generated secondary organic aerosols, Aerosol Sci. Tech., 47, 294–309, https://doi.org/10.1080/02786826.2012.752572, 2013.

Dommen, J., Metzger, A., Duplissy, J., Kalberer, M., Alfarra, M. R., Gascho, A., Weingartner, E., Prevot, A. S. H., Verheggen, B., and Baltensperer, U.: Laboratory observation of oligomers in the aerosol from isoprene/NO_x photooxidation, Geophys. Res. Lett., 33, L13805, https://doi.org/10.1029/2006GL026523, 2006.

Donahue, N. M., Kroll, J. H., Pandis, S. N., and Robinson, A. L.: A two-dimensional volatility basis set – Part 2: Diagnostics of organic-aerosol evolution, Atmos. Chem. Phys., 12, 615–634, https://doi.org/10.5194/acp-12-615-2012, 2012.

Edney, E. O., Kleindienst, T. E., Jaoui, M., Lewandowski, M., Offenberg, J. H., Wang, W., and Claeys, M.: Formation of 2-methyl tetrols and 2-methylglyceric acid in secondary organic aerosol from laboratory irradiated isoprene/NO_x/SO_2/air mixtures and their detection in ambient $PM_{2.5}$ samples collected in the eastern United States, Atmos. Environ., 39, 5281–5289, https://doi.org/10.1016/j.atmosenv.2005.05.031, 2005.

Ehn, M., Thornton, J. A., E., K., Sipila, M., Junninen, H., Pullinen, I., Springer, M., Rubach, F., Tillmann, R., Lee, B., Lopez-Hilfiker, F., Andres, S., Acir, I.-H., Rissanen, M., Jokinen, T., Schobesberger, S., Kangasluoma, J., Kontkanen, J., Nieminen, T., Kurten, T., Nielsen, L. B., Jorgensen, S., Kjaergaard, H. G., Canagaratna, M., Dal Maso, M., Berndt, T., Petaja, T., Wahner, A., Kerminen, V.-M., Kulmala, M., Worsnop, D. R., Wildt, J., and Mentel, T. F.: A large source of low-volatility secondary organic aerosol, Nature, 506, 476–479, https://doi.org/10.1038/nature13032, 2014.

Feiner, P. A., Brune, W. H., Miller, D. O., Zhang, L., Cohen, R. C., Romer, P. S., Goldstein, A. H., Keutsch, F. N., Skog, K. M., Wennberg, P. O., Nguyen, T. B., Teng, A. P., De Gouw, J., Koss, A., Wild, R. J., Brown, S. S., Guenther, A., Edgerton, E., Baumann, K., and Fry, J. L.: Testing atmospheric oxidation in an Alabama forest, J. Atmos. Sci., 73, 4699–4710, https://doi.org/10.1175/JAS-D-16-0044.1, 2016.

Gaffney, J. S., Bornick, R. M., Chen, Y.-H., and Marley, N. A.: Capillary gas chromatographic analysis of nitrogen dioxide and PANs with luminol chemiluminescent detection, Atmos. Environ., 32, 1445–1454, https://doi.org/10.1016/S1352-2310(97)00098-8, 1998.

Guenther, A. B., Jiang, X., Heald, C. L., Sakulyanontvittaya, T., Duhl, T., Emmons, L. K., and Wang, X.: The Model of Emissions of Gases and Aerosols from Nature version 2.1 (MEGAN2.1): an extended and updated framework for modeling biogenic emissions, Geosci. Model Dev., 5, 1471–1492, https://doi.org/10.5194/gmd-5-1471-2012, 2012.

Hallquist, M., Wenger, J. C., Baltensperger, U., Rudich, Y., Simpson, D., Claeys, M., Dommen, J., Donahue, N. M., George,

C., Goldstein, A. H., Hamilton, J. F., Herrmann, H., Hoffmann, T., Iinuma, Y., Jang, M., Jenkin, M. E., Jimenez, J. L., Kiendler-Scharr, A., Maenhaut, W., McFiggans, G., Mentel, Th. F., Monod, A., Prévôt, A. S. H., Seinfeld, J. H., Surratt, J. D., Szmigielski, R., and Wildt, J.: The formation, properties and impact of secondary organic aerosol: current and emerging issues, Atmos. Chem. Phys., 9, 5155–5236, https://doi.org/10.5194/acp-9-5155-2009, 2009.

Heald, C. L., Henze, D. K., Horowitz, L. W., Feddema, J., Lamarque, J.-F., Guenther, A., Hess, P. G., Vitt, F., Seinfeld, J. H., Goldstein, A. H., and Fung, I.: Predicted change in global secondary organic aerosol concentrations in response to future climate, emissions, and land use change, J. Geophys. Res. Atmos., 113, D05211, https://doi.org/10.1029/2007JD009092, 2008.

Henze, D. K. and Seinfeld, J. H.: Global secondary organic aerosol from isoprene oxidation, Geophys. Res. Lett., 33, L09812, https://doi.org/10.1029/2006GL025976, 2006.

Henze, D. K., Seinfeld, J. H., Ng, N. L., Kroll, J. H., Fu, T.-M., Jacob, D. J., and Heald, C. L.: Global modeling of secondary organic aerosol formation from aromatic hydrocarbons: high-vs. low-yield pathways, Atmos. Chem. Phys., 8, 2405–2420, https://doi.org/10.5194/acp-8-2405-2008, 2008.

Huang, Y., Zhao, R., Charan, S. M., Kenseth, C. M., Zhang, X., and Seinfeld, J. H.: Unified theory of vapor-wall mass transport in Teflon-walled environmental chambers, Environ. Sci. Technol., 52, 2134–2142, https://doi.org/10.1021/acs.est.7b05575, 2018.

Jacobs, M. I., Burke, W. J., and Elrod, M. J.: Kinetics of the reactions of isoprene-derived hydroxynitrates: gas phase epoxide formation and solution phase hydrolysis, Atmos. Chem. Phys., 14, 8933–8946, https://doi.org/10.5194/acp-14-8933-2014, 2014.

Jenkin, M. E., Saunders, S. M., and Pilling, M. J.: The tropospheric degradation of volatile organic compounds: A protocol for mechanism development, Atmos. Environ., 31, 81–104, https://doi.org/10.1016/S1352-2310(96)00105-7, 1997.

Jenkin, M. E., Young, J. C., and Rickard, A. R.: The MCM v3.3.1 degradation scheme for isoprene, Atmos. Chem. Phys., 15, 11433–11459, https://doi.org/10.5194/acp-15-11433-2015, 2015.

Kjaergaard, H. G., Knap, H. C., Ornso, K. B., Jorgensen, S., Crounse, J. D., Paulot, F., and Wennberg, P. O.: Atmospheric fate of methacrolein. 2. Formation of lactone and implications for organic aerosol production, J. Phys. Chem. A., 116, 5763–5768, https://doi.org/10.1021/jp210853h, 2012.

Kleindienst, T. E., Edney, E. O., Lewandowski, M., Offenberg, J. H., and Jaoui, M.: Secondary organic carbon and aerosol yields from the irradiations of isoprene and α-pinene in the presence of NO_x and SO_2, Environ. Sci. Technol., 40, 3807–3812, https://doi.org/10.1021/es052446r, 2006.

Kleindienst, T. E., Jaoui, M., Lewandowski, M., Offenberg, J. H., Lewis, C. W., Bhave, P. V., and Edney, E. O.: Estimates of the contributions of biogenic and anthropogenic hydrocarbons to secondary organic aerosol at a southeastern US location, Atmos. Environ., 41, 8288–8300, https://doi.org/10.1016/j.atmosenv.2007.06.045, 2007.

Kleindienst, T. E., Lewandowski, M., Offenberg, J. H., Jaoui, M., and Edney, E. O.: The formation of secondary organic aerosol from the isoprene + OH reaction in the absence of NO_x, Atmos. Chem. Phys., 9, 6541–6558, https://doi.org/10.5194/acp-9-6541-2009, 2009.

Knote, C., Tuccella, P., Curci, G., Emmons, L., Orlando, J. J., Madronich, S., Baro, R., Jimenez-Guerrero, P., Luecken, D., Hogrefe, C., Forkel, R., Werhahn, J., Hirtl, M., Perez, J. L., San Jose, R., Giordano, L., Brunner, D., Yahya, K., and Zhang, Y.: Influence of the choice of gas-phase mechanism on predictions of key gaseous pollutants during the AQMEII phase-2 intercomparison, Atmos. Environ., 115, 553–568, https://doi.org/10.1016/j.atmosenv.2014.11.066, 2015.

Krechmer, J. E., Coggon, M. E., Massoli, P., Nguyen, T. B., Crounse, J. D., Hu, W., Day, D. A., Tyndall, G. S., Henze, D. K., Rivera-Rios, J. C., Nowak, J. B., Kimmel, J. R., Mauldin, R. L., Stark, H., Janye, J. T., Sipila, M., Junninen, H., St. Clair, J. M., Zhang, X., Feiner, P. A., Zhang, L., Miller, D. O., Brune, W. H., Keutsch, F. N., Wennberg, P. O., Seinfeld, J. H., Worsnop, D. R., Jimenez, J. L., and Canagaratna, M. R.: Formation of Low Volatility Organic Compounds and Secondary Organic Aerosol from Isoprene Hydroxyhydroperoxide Low-NO Oxidation, Environ. Sci. Technol., 49, 10330–10339, https://doi.org/10.1021/acs.est.5b02031, 2015.

Kroll, J. H. and Seinfeld, J. H.: Chemistry of secondary organic aerosol: Formation and evolution of low-volatility organics in the atmosphere, Atmos. Environ., 42, 3593–3624, https://doi.org/10.1016/j.atmosenv.2008.01.003, 2008.

Kroll, J. H., Ng, N. L., Murphy, S. M., Flagan, R. C., and Seinfeld, J. H.: Secondary organic aerosol formation from isoprene photooxidation under high-NO_x conditions, Geophys. Res. Lett., 32, L18808, https://doi.org/10.1029/2005GL023637, 2005.

Kroll, J. H., Ng, N. L., Murphy, S. M., Flagan, R. C., and Seinfeld, J. H.: Secondary organic aerosol formation from isoprene photooxidation, Environ. Sci. Technol., 40, 1869–1877, https://doi.org/10.1021/es0524301, 2006.

Kurten, T., Tiusanen, K., Roldin, P., Rissanen, M., Luy, J.-N., Boy, M., Ehn, M., and Donahue, N.: α-Pinene autoxidation products may not have extremely low saturation vapor pressures despite high O:C ratios, J. Phys. Chem. A., 120, 2569–2582, https://doi.org/10.1021/acs.jpca.6b02196, 2016.

Lambe, A. T., Chhabra, P. S., Onasch, T. B., Brune, W. H., Hunter, J. F., Kroll, J. H., Cummings, M. J., Brogan, J. F., Parmar, Y., Worsnop, D. R., Kolb, C. E., and Davidovits, P.: Effect of oxidant concentration, exposure time, and seed particles on secondary organic aerosol chemical composition and yield, Atmos. Chem. Phys., 15, 3063–3075, https://doi.org/10.5194/acp-15-3063-2015, 2015.

Lee, B. H., Mohr, C., Lopez-Hilfiker, F. D., Lutz, A., Hallquist, M., Lee, L., Romer, P., Cohen, R. C., Iyer, S., Kurten, T., Hu, W., Day, D. A., Campuzano-Jost, P., Jimenez, J. L., Xu, L., Ng, N. L., Guo, H., Weber, R. J., Wild, R. J., Brown, S. S., Koss, A., de Gouw, J., Olson, K., Goldstein, A. H., Seco, R., Kim, S., McAvey, K., Shepson, P. B., Starn, T., Baumann, K., Edgerton, E. S., Liu, J., Shilling, J. E., Miller, D. O., Brune, W., Schobesberger, S., D'Ambro, E. L., and Thornton, J. A.: Highly functionalized organic nitrates in the southeast United States: Contribution to secondary organic aerosol and reactive nitrogen budgets, P. Natl. Acad. Sci. USA, 113, 1516–1521, https://doi.org/10.1073/pnas.1508108113, 2016.

Lee, L., Teng, A. P., Wennberg, P. O., Crounse, J. D., and Cohen, R. C.: On rates and mechanisms of OH and O_3 reactions with isoprene-derived hydroxy nitrates, J. Phys. Chem. A, 118, 1622–1637, https://doi.org/10.1021/jp4107603, 2014.

Lin, Y.-H., Zhang, Z., Docherty, K. S., Zhang, H., Budisulistiorini, S. H., Rubitschun, C. L., Shaw, S. L., Knipping, E. M., Edgerton, E. S., Kleindienst, T. E., Gold, A., and Surratt, J. D.: Isoprene epoxydiols as precursors to secondary organic aerosol formation: acid-catalyzed reactive uptake studies with authentic compounds, Environ. Sci. Technol., 46, 250–258, https://doi.org/10.1021/es202554c, 2012.

Lin, Y.-H., Zhang, H., Pye, H. O. T., Zhang, Z., Marth, W. J., Park, S., Arashiro, M., Cui, T., Budisulistiorini, S. H., Sexton, K. G., Vizuete, W., Xie, Y., Luecken, D. J., Piletic, I. R., Edney, E. O., Bartolotti, L. J., Gold, A., and Surratt, J. D.: Epoxide as a precursor to secondary organic aerosol formation from isoprene photooxidation in the presence of nitrogen oxides, P. Natl. Acad. Sci. USA, 110, 6718–6723, https://doi.org/10.1073/pnas.1221150110, 2013.

Loza, C. L., Chhabra, P. S., Yee, L. D., Craven, J. S., Flagan, R. C., and Seinfeld, J. H.: Chemical aging of m-xylene secondary organic aerosol: laboratory chamber study, Atmos. Chem. Phys., 12, 151–167, https://doi.org/10.5194/acp-12-151-2012, 2012.

Mai, H. and Flagan, R. C.: Scanning DMA Data Analysis I. Classification Transfer Function, Aerosol Sci. Tech., 52, 1382–1399, https://doi.org/10.1080/02786826.2018.1528005, 2018.

Mai, H., Kong, W., Seinfeld, J. H., and Flagan, R. C.: Scanning DMA Data Analysis II. Integrated DMA-CPC Instrument Response and Data Inversion, Aerosol Sci. Tech., 52, 1400–1414, https://doi.org/10.1080/02786826.2018.1528006, 2018.

Marais, E. A., Jacob, D. J., Jimenez, J. L., Campuzano-Jost, P., Day, D. A., Hu, W., Krechmer, J., Zhu, L., Kim, P. S., Miller, C. C., Fisher, J. A., Travis, K., Yu, K., Hanisco, T. F., Wolfe, G. M., Arkinson, H. L., Pye, H. O. T., Froyd, K. D., Liao, J., and McNeill, V. F.: Aqueous-phase mechanism for secondary organic aerosol formation from isoprene: application to the southeast United States and co-benefit of SO_2 emission controls, Atmos. Chem. Phys., 16, 1603–1618, https://doi.org/10.5194/acp-16-1603-2016, 2016.

Nah, T., McVay, R. C., Pierce, J. R., Seinfeld, J. H., and Ng, N. L.: Constraining uncertainties in particle-wall deposition correction during SOA formation in chamber experiments, Atmos. Chem. Phys., 17, 2297–2310, https://doi.org/10.5194/acp-17-2297-2017, 2017.

Nannoolal, Y., Rarey, J., Ramjugernath, D., and Cordes, W.: Estimation of pure component properties Part 1. Estimation of the normal boiling point of non-electrolyte organic compounds via group contributions and group interactions, Fluid Phase Equilibr., 226, 45–63, https://doi.org/10.1016/j.fluid.2004.09.001, 2004.

Nannoolal, Y., Rarey, J., and Ramjugernath, D.: Estimation of pure component properties Part 3. Estimation of the vapor pressure of non-electrolyte organic compounds via group contributions and group interactions, Fluid Phase Equilibr., 269, 117–133, https://doi.org/10.1016/j.fluid.2008.04.020, 2008.

Ng, N. L., Kroll, J. H., Keywood, M. D., Bahreini, R., Varutbangkul, V., Flagan, R. C., and Seinfeld, J. H.: Contribution of first-versus second-generation products to secondary organic aerosols formed in the oxidation of biogenic hydrocarbons, Environ. Sci. Technol., 40, 2283–2297, https://doi.org/10.1021/es052269u, 2006.

Nguyen, T. B., Roach, P. J., Laskin, J., Laskin, A., and Nizkorodov, S. A.: Effect of humidity on the composition of isoprene pho-

tooxidation secondary organic aerosol, Atmos. Chem. Phys., 11, 6931–6944, https://doi.org/10.5194/acp-11-6931-2011, 2011.

Nguyen, T. B., Coggon, M. M., Bates, K. H., Zhang, X., Schwantes, R. H., Schilling, K. A., Loza, C. L., Flagan, R. C., Wennberg, P. O., and Seinfeld, J. H.: Organic aerosol formation from the reactive uptake of isoprene epoxydiols (IEPOX) onto non-acidified inorganic seeds, Atmos. Chem. Phys., 14, 3497–3510, https://doi.org/10.5194/acp-14-3497-2014, 2014a.

Nguyen, T. B., Crounse, J. D., Schwantes, R. H., Teng, A. P., Bates, K. H., Zhang, X., St. Clair, J. M., Brune, W. H., Tyndall, G. S., Keutsch, F. N., Seinfeld, J. H., and Wennberg, P. O.: Overview of the Focused Isoprene eXperiment at the California Institute of Technology (FIXCIT): mechanistic chamber studies on the oxidation of biogenic compounds, Atmos. Chem. Phys., 14, 13531–13549, https://doi.org/10.5194/acp-14-13531-2014, 2014b.

Nguyen, T. B., Bates, K. H., Crounse, J. D., Schwantes, R. H., Zhang, X., Kjaergaard, H. G., Surratt, J. D., Lin, P., Laskin, A., Seinfeld, J. H., and Wennberg, P. O.: Mechanism of the hydroxyl radical oxidation of methacryloyl peroxynitrate (MPAN) and its pathway toward secondary organic aerosol formation in the atmosphere, Phys. Chem. Chem. Phys., 17, 17914–17926, https://doi.org/10.1039/C5CP02001H, 2015.

Orlando, J. J. and Tyndall, G. S.: Laboratory studies of organic peroxy radical chemistry: an overview with emphasis on recent issues of atmospheric significance, Chem. Soc. Rev., 41, 6294–6317, https://doi.org/10.1039/C2CS35166H, 2012.

Orlando, J. J., Tyndall, G. S., and Paulson, S. E.: Mechanism of the OH-initiated oxidation of methacrolein, Geophys. Res. Lett., 26, 2191–2194, https://doi.org/10.1029/1999GL900453, 1999.

Orlando, J. J., Tyndall, G. S., Bertman, S. B., Chen, W., and Burkholder, J. B.: Rate coefficient for the reaction of OH with $CH_2=C(CH_3)C(O)OONO_2$ (MPAN), Atmos. Environ., 36, 1895–1900, https://doi.org/10.1016/S1352-2310(02)00090-0, 2002.

Orlando, J. J., Tyndall, G. S., and Wallington, T. J.: The atmospheric chemistry of alkoxy radicals, Chem. Rev., 103, 4657–4689, https://doi.org/10.1021/cr020527p, 2003.

Pajunoja, A., Hu, W., Leong, Y. J., Taylor, N. F., Miettinen, P., Palm, B. B., Mikkonen, S., Collins, D. R., Jimenez, J. L., and Virtanen, A.: Phase state of ambient aerosol linked with water uptake and chemical aging in the southeastern US, Atmos. Chem. Phys., 16, 11163–11176, https://doi.org/10.5194/acp-16-11163-2016, 2016.

Pandis, S. N., Paulson, S. E., Seinfeld, J. H., and Flagan, R. C.: Aerosol formation in the photooxidation of isoprene and β-pinene, Atmos. Environ., 25A, 997–1008, https://doi.org/10.1016/0960-1686(91)90141-S, 1991.

Paulot, F., Crounse, J. D., Kjaergaard, H. G., Kurten, A., St. Clair, J. M., Seinfeld, J. H., and Wennberg, P. O.: Unexpected epoxide formation in the gas-phase photooxidation of isoprene, Science, 325, 730–733, https://doi.org/10.1126/science.1172910, 2009.

Peeters, J., Nguyen, T. L., and Vereecken, L.: HO_x radical regeneration in the oxidation of isoprene, Phys. Chem. Chem. Phys., 11, 5935–5939, https://doi.org/10.1039/b908511d, 2009.

Peeters, J., Muller, J.-F., Stavrakou, T., and Nguyen, V.: Hydroxyl radical recycling in isoprene oxidation driven by hydrogen bonding and hydrogen tunneling: The upgraded LIM1 mechanism, J. Phys. Chem. A., 118, 8625–8643, https://doi.org/10.1021/jp5033146, 2014.

Pieber, S. M., Haddad, I. E., Slowik, J. G., Canagaratna, M. R., Jayne, J. T., Platt, S. M., Bozzetti, C., Daellenbach, K. S., Frohlich, R., Vlachou, A., Klein, F., Dommen, J., Miljevic, B., Jimenez, J. L., Worsnop, D. R., Baltensperger, U., and Prevot, A. S. H.: Inorganic salt interference on CO_2^+ in Aerodyne AMS and ACSM organic aerosol composition studies, Environ. Sci. Technol., 50, 10494–10503, https://doi.org/10.1021/acs.est.6b01035, 2016.

Pierce, J. R., Engelhart, G. J., Hildebrandt, L., Weitkamp, E. A., Pathak, R. K., Donahue, N. M., Robinson, A. L., Adams, P. J., and Pandis, S. N.: Constraining particle evolution from wall losses, coagulation, and condensation-evaporation in smog-chamber experiments: Optimal estimation based on size distribution measurements, Aerosol Sci. Tech., 42, 1001–1015, https://doi.org/10.1080/02786820802389251, 2008.

Praske, E., Crounse, J. D., Bates, K. H., Kurten, T., Kjaergaard, H. G., and Wennberg, P. O.: Atmospheric fate of methyl vinyl ketone: Peroxy radical reactions with NO and HO_2, J. Phys. Chem. A., 119, 4562–4572, https://doi.org/10.1021/jp5107058, 2015.

Ribeiro, P. A., Raposo, M., Marat-Mendes, J. N., and Giacometti, J. A.: Constant-current corona charging of biaxially stretched PVDF films in humidity-controlled atmospheres, IEEE T. Electr. Insul., 27, 744–750, https://doi.org/10.1109/14.155791, 1992.

Sanchez, D., Jeong, D., Seco, R., Wrangham, I., Park, J.-H., Brune, W., Koss, A., Gilman, J., de Gouw, J., Misztal, P., Goldstein, A., Baumann, K., Wennberg, P. O., Keutsch, F. N., Guenther, A., and Kim, S.: Intercomparison of OH and OH reactivity measurements in a high isoprene and low NO environment during the Southern Oxidant and Aerosol Study (SOAS), Atmos. Environ., 174, 227–236, https://doi.org/10.1016/j.atmosenv.2017.10.056, 2018.

Sander, R.: Compilation of Henry's law constants (version 4.0) for water as solvent, Atmos. Chem. Phys., 15, 4399–4981, https://doi.org/10.5194/acp-15-4399-2015, 2015.

Saunders, S. M., Jenkin, M. E., Derwent, R. G., and Pilling, M. J.: Protocol for the development of the Master Chemical Mechanism, MCM v3 (Part A): tropospheric degradation of non-aromatic volatile organic compounds, Atmos. Chem. Phys., 3, 161–180, https://doi.org/10.5194/acp-3-161-2003, 2003.

Schwantes, R. H., Schilling, K. A., McVay, R. C., Lignell, H., Coggon, M. M., Zhang, X., Wennberg, P. O., and Seinfeld, J. H.: Formation of highly oxygenated low-volatility products from cresol oxidation, Atmos. Chem. Phys., 17, 3453–3474, https://doi.org/10.5194/acp-17-3453-2017, 2017.

Seinfeld, J. H. and Pandis, S. N.: Atmospheric Chemistry and Physics: From Air Pollution to Climate Change, 3 edn., John Wiley & Sons, Inc., Hoboken, New Jersey, USA, 2016.

Sharpe, S. W., Johnson, T. J., Sams, R. L., Chu, P. M., Rhoderick, G. C., and Johnson, P. A.: Gas-phase databases for quantitative infrared spectroscopy, composite spectrum for ISOPREN_25T (Ver 1.0, Oct, 01) and composite spectrum for ISOBUTE-NAL_25T (Ver 1.0, Dec, 04), Appl. Spectrosc., 58, 1452–1461, https://doi.org/10.1366/0003702042641281, 2004.

Sjogren, S., Gysel, M., Weingartner, E., Baltensperger, U., Cubison, M., Coe, H., Zardini, A., Marcolli, C., Krieger, U., and Peter, T.: Hygroscopic growth and water uptake kinetics of two-phase aerosol particles consisting of ammonium sulfate, adipic and humic acid mixtures, J. Aerosol Sci., 38, 157–171, https://doi.org/10.1016/j.jaerosci.2006.11.005, 2007.

Stadtler, S., Kühn, T., Schröder, S., Taraborrelli, D., Schultz, M. G., and Kokkola, H.: Isoprene-derived secondary organic aerosol in the global aerosol–chemistry–climate model ECHAM6.3.0–HAM2.3–MOZ1.0, Geosci. Model Dev., 11, 3235–3260, https://doi.org/10.5194/gmd-11-3235-2018, 2018.

St. Clair, J. M., McCabe, D. C., Crounse, J. D., Steiner, U., and Wennberg, P. O.: Chemical ionization tandem mass spectrometer for the in situ measurement of methyl hydrogen peroxide, Rev. Sci. Instrum., 81, 094102, https://doi.org/10.1063/1.3480552, 2010.

Sunol, A. M., Charan, S. M., and Seinfeld, J. H.: Computational simulation of the dynamics of secondary organic aerosol formation in an environmental chamber, Aerosol Sci. Tech., 52, 470–482, https://doi.org/10.1080/02786826.2018.1427209, 2018.

Surratt, J. D., Chan, a. W. H., Eddingsaas, N. C., Chan, M. N., Loza, C. L., Kwan, a. J., Hersey, S. P., Flagan, R. C., Wennberg, P. O., and Seinfeld, J. H.: Reactive intermediates revealed in secondary organic aerosol formation from isoprene, P. Natl. Acad. Sci. USA, 107, 6640–6645, https://doi.org/10.1073/pnas.0911114107, 2010.

Taylor, W. D., Allston, T. D., Moscato, M. J., Fazekas, G. B., Kozlowski, R., and Takacs, G. A.: Atmospheric photo-dissociation lifetimes for nitromethane, methyl nitrite, and methyl nitrate, Int. J. Chem. Kinet, 12, 231–240, https://doi.org/10.1002/kin.550120404, 1980.

Teng, A. P., Crounse, J. D., and Wennberg, P. O.: Isoprene peroxy radical dynamics, J. Am. Chem. Soc., 139, 5367–5377, https://doi.org/10.1021/jacs.6b12838, 2017.

Wennberg, P. O.: Let's abandon the high NO_x and low NO_x terminology, IGACnews, 50, 3–4, 2013.

Wennberg, P. O., Bates, K. H., Crounse, J. D., Dodson, L. G., McVay, R. C., Mertens, L. A., Nguyen, T. B., Praske, E., Schwantes, R. H., Smarte, M. D., St Clair, J. M., Teng, A. P., Zhang, X., and Seinfeld, J. H.: Gas-Phase Reactions of Isoprene and Its Major Oxidation Products, Chem. Rev., 118, 3337–3390, https://doi.org/10.1021/acs.chemrev.7b00439, 2018.

Xiong, F., McAvey, K. M., Pratt, K. A., Groff, C. J., Hostetler, M. A., Lipton, M. A., Starn, T. K., Seeley, J. V., Bertman, S. B., Teng, A. P., Crounse, J. D., Nguyen, T. B., Wennberg, P. O., Misztal, P. K., Goldstein, A. H., Guenther, A. B., Koss, A. R., Olson, K. F., de Gouw, J. A., Baumann, K., Edgerton, E. S., Feiner, P. A., Zhang, L., Miller, D. O., Brune, W. H., and Shepson, P. B.: Observation of isoprene hydroxynitrates in the southeastern United States and implications for the fate of NO_x, Atmos. Chem. Phys., 15, 11257–11272, https://doi.org/10.5194/acp-15-11257-2015, 2015.

Xu, L., Kollman, M. S., Song, C., Shilling, J. E., and Ng, N. L.: Effects of NO_x on the volatility of secondary organic aerosol from isoprene photooxidation, Environ. Sci. Tech., 48, 2253–2262, https://doi.org/10.1021/es404842g, 2014.

Zhang, H., Surratt, J. D., Lin, Y. H., Bapat, J., and Kamens, R. M.: Effect of relative humidity on SOA formation from isoprene/NO photooxidation: enhancement of 2-methylglyceric acid and its corresponding oligoesters under dry conditions, Atmos. Chem. Phys., 11, 6411–6424, https://doi.org/10.5194/acp-11-6411-2011, 2011.

Zhang, H., Lin, Y. H., Zhang, Z., Zhang, X., Shaw, S. L., Knipping, E. M., Weber, R. J., Gold, A., Kamens, R. M., and Surratt, J. D.: Secondary organic aerosol formation from methacrolein photooxidation: roles of NO_x level, relative humidity and aerosol acidity, Environ. Chem., 9, 247–262, https://doi.org/10.1071/EN12004, 2012.

Zhang, H., Yee, L. D., Lee, B. H., Curtis, M. P., Worton, D. R., Isaacman-VanWertz, G., Offenberg, J. H., Lewandowski, M., Kleindienst, T. E., Beaver, M. R., Holder, A. L., Lonneman, W. A., Docherty, K. S., Jaoui, M., Pye, H. O. T., Hu, W., Day, D. A., Campuzano-Jost, P., Jimenez, J. L., Guo, H., Weber, R. J., de Gouw, J., Koss, A. R., Edgerton, E. S., Brune, W., Mohr, C., Lopez-Hilfiker, F. D., Lutz, A., Kreisberg, N. M., Spielman, S. R., Hering, S. V., Wilson, K. R., Thornton, J. A., and Goldstein, A. H.: Monoterpenes are the largest source of summertime organic aerosol in the southeastern United States, P. Natl. Acad. Sci. USA, 115, 2038–2043, https://doi.org/10.1073/pnas.1717513115, 2018.

Zhang, Q., Jimenez, J. L., Canagaratna, M. R., Allan, J. D., Coe, H., Ulbrich, I., Alfarra, M. R., Takami, A., Middlebrook, A. M., Sun, Y. L., Dzepina, K., Dunlea, E., Docherty, K., DeCarlo, P. F., Salcedo, D., Onasch, T., Jayne, J. T., Miyoshi, T., Shimono, A., Hatakeyama, S., Takegawa, N., Kondo, Y., Schneider, J., Drewnick, F., Borrmann, S., Weimer, S., Demerjian, K., Williams, P., Bower, K., Bahreini, R., Cottrell, L., Griffin, R. J., Rautiainen, J., Sun, J. Y., Zhang, Y. M., and Worsnop, D. R.: Ubiquity and dominance of oxygenated species in organic aerosols in anthropogenically-influenced Northern Hemisphere midlatitudes, Geophys. Res. Lett., 34, L13801, https://doi.org/10.1029/2007GL029979, 2007.

Zhang, X., Cappa, C. D., Jather, S. H., McVay, R. C., Ensberg, J. J., Kleeman, M. J., and Seinfeld, J. H.: Influence of vapor wall loss in laboratory chambers on yields of secondary organic aerosol, P. Natl. Acad. Sci. USA, 111, 5802–5807, https://doi.org/10.1073/pnas.1404727111, 2014.

Zhang, X., Schwantes, R. H., McVay, R. C., Lignell, H., Coggon, M. M., Flagan, R. C., and Seinfeld, J. H.: Vapor wall deposition in Teflon chambers, Atmos. Chem. Phys., 15, 4197–4214, https://doi.org/10.5194/acp-15-4197-2015, 2015.

Appendix D

CHARACTERIZATION OF AEROSOL HYGROSCOPICITY OVER THE NORTHEAST PACIFIC OCEAN: IMPACTS ON PREDICTION OF CCN AND STRATOCUMULUS CLOUD DROPLET NUMBER CONCENTRATION

Schulze, Benjamin C., Sophia M. Charan, Christopher M. Kenseth, Weimeng Kong, Kelvin H. Bates, Walt Williams, Andrew R. Metcalf, Haflidi H. Jonsson, Roy K. Woods, Armin Sorooshian, Richard C. Flagan, and John H. Seinfeld (2020). "Characterization of aerosol hygroscopicity over the northeast Pacific Ocean: impacts on prediction of CCN and stratocumulus cloud droplet number concentrations." In: *Earth and Space Science* 7.7, pp. 1–26. DOI: 10.1029/2020EA001098.

Characterization of Aerosol Hygroscopicity Over the Northeast Pacific Ocean: Impacts on Prediction of CCN and Stratocumulus Cloud Droplet Number Concentrations

B. C. Schulze[1], S. M. Charan[2], C. M. Kenseth[2], W. Kong[2], K. H. Bates[3], W. Williams[4], A. R. Metcalf[4], H. H. Jonsson[5], R. Woods[5], A. Sorooshian[6,7], R. C. Flagan[8,2], and J. H. Seinfeld[8,2]

[1]Department of Environmental Science and Engineering, California Institute of Technology, Pasadena, CA, USA, [2]Division of Chemistry and Chemical Engineering, California Institute of Technology, Pasadena, CA, USA, [3]Center for the Environment, Harvard University, Cambridge, MA, USA, [4]Department of Environmental Engineering and Earth Sciences, Clemson University, Anderson, SC, USA, [5]Naval Postgraduate School, Monterey, CA, USA, [6]Department of Chemical and Environmental Engineering, University of Arizona, Tucson, AZ, USA, [7]Department of Hydrology and Atmospheric Sciences, University of Arizona, Tucson, AZ, USA, [8]Division of Engineering and Applied Science, California Institute of Technology, Pasadena, CA, USA

Abstract During the Marine Aerosol Cloud and Wildfire Study (MACAWS) in June and July of 2018, aerosol composition and cloud condensation nuclei (CCN) properties were measured over the N.E. Pacific to characterize the influence of aerosol hygroscopicity on predictions of ambient CCN and stratocumulus cloud droplet number concentrations (CDNC). Three vertical regions were characterized, corresponding to the marine boundary layer (MBL), an above-cloud organic aerosol layer (AC-OAL), and the free troposphere (FT) above the AC-OAL. The aerosol hygroscopicity parameter (κ) was calculated from CCN measurements (κ_{CCN}) and bulk aerosol mass spectrometer (AMS) measurements (κ_{AMS}). Within the MBL, measured hygroscopicities varied between values typical of both continental environments (~0.2) and remote marine locations (~0.7). For most flights, CCN closure was achieved within 20% in the MBL. For five of the seven flights, assuming a constant aerosol size distribution produced similar or better CCN closure than assuming a constant "marine" hygroscopicity ($\kappa = 0.72$). An aerosol-cloud parcel model was used to characterize the sensitivity of predicted stratocumulus CDNC to aerosol hygroscopicity, size distribution properties, and updraft velocity. Average CDNC sensitivity to accumulation mode aerosol hygroscopicity is 39% as large as the sensitivity to the geometric median diameter in this environment. Simulations suggest CDNC sensitivity to hygroscopicity is largest in marine stratocumulus with low updraft velocities (<0.2 m s^{-1}), where accumulation mode particles are most relevant to CDNC, and in marine stratocumulus or cumulus with large updraft velocities (>0.6 m s^{-1}), where hygroscopic properties of the Aitken mode dominate hygroscopicity sensitivity.

1. Introduction

Marine stratocumulus (MSc) clouds, commonly observed off the Western coasts of North America, South America, Africa, and Australia, cover nearly one fifth of the Earth's surface and exert a large impact on its radiative balance (Wood, 2012). These cloud decks are particularly relevant to global climate due to their high albedo contrast with the underlying ocean and relatively low altitude, resulting in stronger shortwave reflectance than longwave absorption (Brenguier et al., 2000; Randall et al., 1984; Wood, 2012). Previous estimates suggest that a ~12% increase in the albedo of these clouds would produce a negative radiative forcing equivalent in magnitude to that of doubling atmospheric CO_2 concentrations (Latham et al., 2008; Stevens & Brenguier, 2009). Remote sensing, parcel modeling, and large eddy simulation (LES) studies have all established that MSc exhibit substantial albedo susceptibility to variations in cloud droplet number concentrations (CDNC) (Berner et al., 2015; Chen et al., 2011; Oreopoulos & Platnick, 2008; Platnick & Twomey, 1994; Sanchez et al., 2016). Understanding the sensitivity of MSc CDNC to aerosols acting as

cloud condensation nuclei (CCN) is therefore a critical aspect of reducing uncertainty in climate change predictions (Seinfeld et al., 2016).

The CDNC and albedo of MSc are substantially influenced by the abundance of below-cloud CCN. A recent satellite analysis suggested that variability in below-cloud CCN concentration may be responsible for ~45% of the variability in the radiative effect of marine boundary layer clouds (Rosenfeld et al., 2019). This influence results from the fact that increased CCN abundance enhances cloud reflectivity at constant liquid water path (Twomey, 1977) and has the potential to reduce MSc precipitation rates, increasing cloud lifetime (Ackerman et al., 1993; Albrecht, 1989; Goren & Rosenfeld, 2012; Rosenfeld, 2006). As a result, a major component of the uncertainty in the estimated indirect aerosol forcing has been attributed to the prediction of below-cloud CCN concentrations (Rosenfeld et al., 2014; Sotiropoulou et al., 2007). While the aerosol size distribution is generally thought to be the most important determinant of CCN activity (e.g., Dusek et al., 2006; Ervens et al., 2007; McFiggans et al., 2006; Reutter et al., 2009), particle composition has also been shown to exert a substantial influence (Jimenez et al., 2009; Liu & Wang, 2010; Mei et al., 2013; Quinn et al., 2008; Sanchez et al., 2016).

The propensity of a given aerosol particle to act as a CCN can be described using Köhler theory (Köhler, 1936; Seinfeld et al., 2016), provided sufficient information is known regarding particle size and solute properties (e.g., molecular weight, solubility, density, and activity). A novel framework, κ-Köhler theory, condenses these solute characteristics into a single parameter κ (the aerosol hygroscopicity) that can be easily incorporated into large-scale models (Petters & Kreidenweis, 2007). Substantial effort has, therefore, been devoted to quantifying κ values in a multitude of environments (Ervens et al., 2010; Gunthe et al., 2009; Pringle et al., 2010; Rose et al., 2010; Thalman et al., 2017). While κ values characteristic of inorganic aerosol components are relatively well-established, atmospheric organic aerosol is composed of numerous, highly diverse organic compounds, complicating representation of organic hygroscopicity using a single parameter (Kanakidou et al., 2005). Experimental studies have characterized κ values of secondary organic aerosol (SOA) (e.g., Asa-Awuku et al., 2010; Duplissy et al., 2008, 2011; Frosch et al., 2013; Lambe et al., 2011; Massoli et al., 2010; Zhao et al., 2015), and field studies have characterized the typical range of organic κ values (κ_{org}) observed in the atmosphere (Chang et al., 2010; Gunthe et al., 2009; Levin et al., 2014; Mei et al., 2013; Thalman et al., 2017; Wang et al., 2008). Generally, ambient κ_{org} values are found to be 0.1–0.2 for aged aerosol and primary marine organics and ~0 for freshly emitted combustion aerosol (e.g., soot) (Kreidenweis & Asa-Awuku, 2014). A linear relationship has been noted between observed κ_{org} values and organic aerosol oxygen-to-carbon (O:C) ratios in both the laboratory and the field (Chang et al., 2010; Lambe et al., 2011; Mei et al., 2013; Wang et al., 2019).

Ambient particle hygroscopicity data have been combined with aerosol size distribution measurements in CCN closure studies to assess the extent to which Köhler theory can be used to predict ambient CCN concentrations (e.g., Almeida et al., 2014; Asa-Awuku et al., 2011; Cubison et al., 2008; Medina et al., 2007; McFiggans et al., 2006; Moore et al., 2012; Ren et al., 2018; VanReken et al., 2003). Analyzing the accuracy of predicted CCN concentrations can provide insight into the influence of specific aerosol characteristics on CCN activity (Bougiatioti et al., 2011; Cubison et al., 2008; Medina et al., 2007; VanReken et al., 2003; Wang et al., 2010). For instance, size-resolved compositional (i.e., hygroscopicity) data are often required to accurately reproduce observed CCN concentrations in locations dominated by organic aerosol (Bhattu & Tripathi, 2015; Medina et al., 2007; Ren et al., 2018), while aerosol mixing state has been shown to strongly impact total CCN concentrations in urban environments (Cubison et al., 2008; Ervens et al., 2010; Quinn et al., 2008). By analyzing data from five ambient measurement campaigns, Ervens et al. (2010) found that for aerosol measured farther than a few tens of kilometers from the emission source, CCN activity could be predicted within a factor of two independent of either aerosol mixing state (i.e., internal or external) or organic solubility (i.e., insoluble or slightly soluble). Wang et al. (2010) further demonstrated that CCN concentrations can often be reproduced within 20% assuming internal mixing of aerosol components if the overall κ of the aerosol population is >0.1. The direct impact of variability in aerosol hygroscopicity on CCN concentrations is often assessed by assuming an invariant chemical composition, represented as a fixed κ, in CCN closure analyses. Field campaigns in continental environments ranging from polluted megacities to the pristine tropical rainforest have shown that CCN concentrations could be reproduced within 20% and 50%, respectively, assuming a constant $\kappa = 0.3$ (Gunthe et al., 2009; Rose et al., 2010), a value representative of average continental conditions (Andreae & Rosenfeld, 2008; Pringle et al., 2010). However, in coastal regions, MBL aerosol can result from a mixture of

distinct marine and continental emissions (e.g., Coggon et al., 2014; Mardi et al., 2018; Modini et al., 2015; Sorooshian et al., 2009), which complicates aerosol representation using regional or global models. CCN closure analysis can provide insight into the uncertainties in CCN concentrations that may result from inaccurate model representation of aerosol composition in these environments.

Due to the importance of the persistent stratocumulus cloud decks over the N.E. Pacific to global climate, aerosol characteristics in this region have received considerable attention. However, the diverse range of particle sources, including shipping exhaust (Coggon et al., 2012; Murphy et al., 2009; Prabhakar et al., 2014; Wonaschütz et al., 2013), primary and secondary natural marine emissions (Modini et al., 2015; Prabhakar et al., 2014; Sorooshian et al., 2009), anthropogenic and biogenic continental emissions (Coggon et al., 2014; Hegg et al., 2010; Moore et al., 2012), wildfire plumes (Brioude et al., 2009; Mardi et al., 2018), and aged aerosol from the Asian continent (Roberts et al., 2006, 2010), combined with strong temporal and spatial variability due to variable meteorological conditions, has hindered determination of general characteristics of the marine atmosphere in this location. This complexity is reflected in the diversity of hygroscopicity measurements previously reported in the marine boundary layer (MBL) and free troposphere (FT). For instance, average κ values reported from MBL measurements have varied from ~0.2–0.3 (Moore et al., 2012; Roberts et al., 2010) to ~0.5–0.7 (Royalty et al., 2017; Yakobi-Hancock et al., 2014). Measurements in the FT, while sparse, have been even more variable (κ ~0.05–1.0) (Roberts et al., 2006, 2010). While these measurements could largely be reconciled assuming various mixtures of continental (0.27 ± 0.2) and marine (0.72 ± 0.2) aerosol, determining the major emissions sources and meteorological patterns dictating these changes is important for improving model representation of the region (Pringle et al., 2010). CCN-based measurements of aerosol hygroscopicity and the resulting information about small particle composition can be especially useful in this regard, as knowledge of small particle composition can provide substantial insight into particle sources.

While hygroscopicity and mixing state characterization are important components of understanding the CCN activity of ambient aerosol, the dynamic processes controlling supersaturation, droplet nucleation, and droplet growth within clouds lead to nonlinear relationships between aerosol properties and CDNC. As a result, aerosol-cloud parcel modeling is instrumental to fully understand the role of aerosol hygroscopicity and mixing state on CDNC. Reutter et al. (2009) used such a model to distinguish three regimes of aerosol activation, defined as the aerosol-limited, updraft-limited, and transitional regimes, based on the ratio of updraft velocity to aerosol number concentration at the cloud base. The dependence of CDNC on aerosol hygroscopicity, while limited relative to other parameters such as particle number concentration and updraft velocity, was found to vary substantially between regimes. Additional modeling revealed that CDNC sensitivity to aerosol hygroscopicity is highly dependent on the below-cloud aerosol size distribution, with sensitivity increasing substantially with smaller median radii (Ward et al., 2010). Sanchez et al. (2016) concluded that modeled stratocumulus albedo is insensitive to the assumed hygroscopicity of the organic aerosol fraction; however, the sensitivity of CDNC to bulk hygroscopicity has yet to be fully evaluated in this environment.

The present study uses measurements of aerosol composition and CCN activity collected during the Marine Aerosol Cloud and Wildfire Study (MACAWS), combined with an aerosol-cloud parcel model, to gain insight into near-coastal aerosol hygroscopicity and its influence on prediction of CCN and MSc CDNC. Hygroscopicity measurements are combined with airmass backward trajectories and meteorological parameters to attribute observed particle characteristics to distinct sources when possible. CCN closure analyses are performed to investigate the impact of compositional and mixing state assumptions on CCN predictions. Finally, aerosol-cloud parcel model simulations constrained with MSc microphysical measurements are used to directly investigate the sensitivity of stratocumulus CDNC to aerosol hygroscopicity, mixing state, and size distribution properties.

2. Methodology

2.1. MACAWS Field Mission

The 2018 Marine Aerosol Cloud and Wildfire Study (MACAWS) consisted of 16 research flights operated out of the Center for Interdisciplinary Remotely-Piloted Aircraft Studies (CIRPAS) in Marina, California, during June and July. Measurements were performed on-board the CIRPAS Navy Twin Otter aircraft
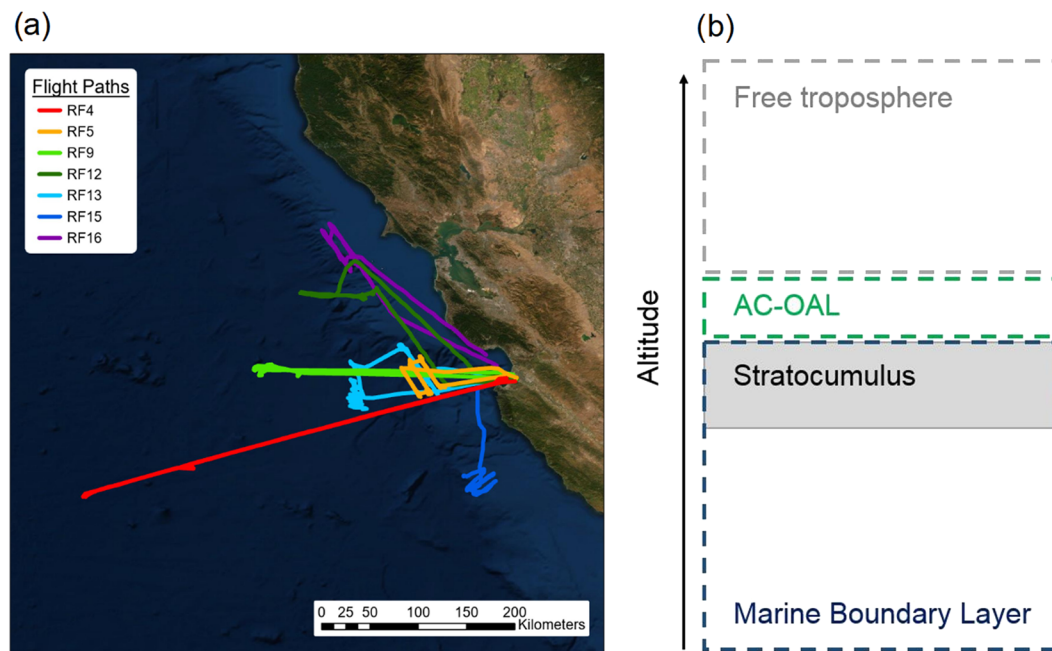
Figure 1. (a) Trajectories of the seven MACAWS research flights analyzed in this study. (b) Relative vertical locations of the marine boundary layer, the above-cloud organic-aerosol layer (AC-OAL), and the free troposphere.

(Coggon et al., 2012, 2014; Russell et al., 2013; Sorooshian et al., 2019; Wang et al., 2016). The scientific objectives of individual flights included characterization of marine aerosols and clouds, sampling of shipping vessel exhaust plumes, and investigation of nearby wildfire emissions. The present study focuses on seven research flights primarily aimed at characterization of the relationship between marine aerosol and the overlying stratocumulus cloud deck. Paths of these seven flights are depicted in Figure 1. Flight strategies typically involved a series of level legs at varying altitudes within the MBL and overlying FT. Slant or spiral soundings were generally performed before and after a series of level legs.

2.2. Twin Otter Instrumentation

The navigational and meteorological instrumentation utilized by the Twin Otter aircraft is described in detail by Sorooshian et al. (2018). Ambient aerosol was sampled using a forward-facing sub-isokinetic inlet (Hegg et al., 2005). Aerosol and cloud droplet number concentrations were characterized using a variety of instruments, including multiple condensation particle counters (CPC, TSI 3010, $D_p > 10$ nm; ultrafine CPC, TSI UFCPC, $D_p > 3$ nm), a passive cavity aerosol spectrometer probe (PCASP, $D_p \sim 0.11$–$3.4\,\mu$m), and forward scattering spectrometer probe (FSSP, Particle Measuring Systems [PMS], $D_p \sim 1.6$–$45\,\mu$m). Cloud liquid water content was measured using a PVM-100A probe (Gerber et al., 1994), and a threshold value of $0.02\,\text{g m}^{-3}$ was used to distinguish in-cloud sampling (Dadashazar et al., 2018; MacDonald et al., 2018).

Cloud condensation nuclei (CCN) number concentrations were measured at four supersaturations (SS) (0.1%, 0.3%, 0.43%, and 0.57%) using a Droplet Measurement Technologies (DMT) dual-column streamwise thermal-gradient cloud condensation nuclei counter (CCNC) (Lance et al., 2006; Roberts & Nenes, 2005). The CCNC operates by applying a linear temperature gradient to a cylindrical sampling tube with continuously wetted walls. As the thermal diffusivity of water vapor exceeds the diffusivity of air, supersaturated conditions are produced along the sampling column centerline. For this study, activated droplets grown to sizes larger than 0.75-μm diameter were counted and sized by an optical particle counter. The sheath and sample flows of each column were maintained at 0.45 and $0.05\,\text{L min}^{-1}$, respectively. Instrument pressure was maintained at 750 mb using a flow orifice and active pressure control system at the instrument inlet. Each column of the CCNC was calibrated using ammonium sulfate particles following standard methods as described in Rose et al. (2008). Calibrations were performed before and after the campaign, and observed

deviations in applied SS for a given temperature gradient imply uncertainties of ~6%, similar to the 5% value typical of field campaigns, as reported by Rose et al. (2008).

Aerosol size distributions and number concentrations for D_p between ~15 and 800 nm were measured with a custom-built scanning mobility particle sizer (SMPS) consisting of a differential mobility analyzer (DMA, TSI 3081) coupled to a condensation particle counter (TSI 3010). The DMA is operated in a closed-system configuration with a recirculating sheath and excess flow of 2.67 L min^{-1} and an aerosol flow of 0.515 L min^{-1}. The column voltage was scanned from 15 to 9,850 V over a ~2-min interval.

Aerosol chemical composition was measured using a high-resolution time-of-flight aerosol mass spectrometer (HR-ToF-AMS, Aerodyne Research Inc., hereafter referred to AMS) (DeCarlo et al., 2006). Incoming air enters the AMS through a 100-μm critical orifice, after which an aerodynamic lens produces a particle beam that is accelerated under high vacuum. The particle beam is flash-vaporized on a resistively heated surface (600°C), and the resulting gases are ionized by electron impaction (70 eV). Individual ion identity is determined using a high-resolution time-of-flight mass spectrometer. Due to the limited amount of aerosol mass present over the MBL, data were collected in high-sensitivity V-mode. The ionization efficiency (IE) of the AMS was calibrated using dry, 350-nm ammonium nitrate particles before each flight. Data were averaged over 1-min intervals, and all data were analyzed using standard AMS software (SQUIRREL v1.57 and PIKA v1.16l) within Igor Pro 6.37. The collection efficiency (CE) was determined using the composition-dependent calculator within the SQUIRREL and PIKA software packages (Middlebrook et al., 2012). Elemental H:C and O:C ratios were calculated using the "Improved-Ambient" elemental analysis method for AMS mass spectra (Canagaratna et al., 2015). Positive matrix factorization (PMF) analysis (Paatero & Tapper, 1994) was performed on the high-resolution AMS mass spectra in order to distinguish major classes and transformation processes of measured OA. Three factors were extracted, two of which factors correspond to OA subtypes characteristic of the MBL and above-cloud organic aerosol layer (AC-OAL), respectively, and resemble low-volatility oxygenated organic aerosol (LV-OOA). The third factor, which was rarely observed, is likely a result of primary anthropogenic emissions and resembles hydrocarbon-like organic aerosol (HOA). Further discussion of PMF data preparation and factor interpretation is included in the supporting information.

2.3. Determination of Aerosol Hygroscopicity

Aerosol hygroscopicity was calculated using two distinct methods based on measurements with the CCNC and AMS, respectively. Assuming a particle population is internally mixed, the critical activation diameter ($D_{p,c}$) (the diameter at which all larger particles will activate into cloud droplets) produced by a given SS can be determined by integrating the particle size distribution until the total CN concentration is equivalent to the measured CCN concentration:

$$N_{CCN} = \int_{D_{p,c}}^{\infty} n_{CN} dD_p \tag{1}$$

Knowledge of the critical diameter can then be used to calculate a single parameter representation of aerosol hygroscopicity from Köhler theory (Petters & Kreidenweis, 2007):

$$s = \frac{D_{wet}^3 - D_{p,c}^3}{D_{wet}^3 - D_{p,c}^3(1 - \kappa_{CCN})} \exp\left(\frac{4\sigma M_w}{RT\rho_w D_{wet}}\right) \tag{2}$$

where s is the equilibrium supersaturation, $D_{p,c}$ is the critical activation diameter, D_{wet} is the droplet diameter, R is the universal gas constant, T is the absolute temperature, ρ_w is the molar density of water, M_w is the molecular weight of water, and σ is the surface tension of the droplet at the point of activation. Following Rose et al. (2010), κ was determined by applying the observed activation diameter and varying both D_{wet} and κ until s is equivalent to the applied supersaturation of the CCNC and the maximum of a Köhler curve of CCN activation. The droplet surface tension is assumed equal to that of water for comparison with other studies (Collins et al., 2013; Petters & Kreidenweis, 2007; Roberts et al., 2010; Yakobi-Hancock et al., 2014). Hygroscopicity values calculated using this method are referred to as "CCN-derived." Since the likelihood of particle activation at a given SS tends to be a stronger function

of size than composition (Dusek et al., 2006), κ_{CCN} values correspond to particles with diameters near the calculated critical diameter.

A Monte Carlo approach was used to estimate the uncertainty in CCN-derived kappa values (Wang et al., 2019). A detailed description is provided in the supporting information. For a given measurement of the aerosol size distribution and CCN number concentration, the distribution of possible κ_{CCN} values calculated by varying these input parameters (i.e., CCN number concentration and size distribution) within their respective uncertainties is lognormally distributed. As a result, uncertainties attributed to κ_{CCN} are not symmetric about the geometric mean values. In general, we estimate 1σ uncertainties of $+55\%/-40\%$ for κ_{CCN} calculated at SS = 0.3%, $\sim+75\%/-45\%$ at SS = 0.43%, and $+100\%/-50\%$ to values calculated at SS = 0.57%. Due to the low CCN number concentrations observed at SS = 0.1% (<100 cm^{-3}) and possibility of counting unactivated particles (expected to only be a few per cm^{-3}), κ_{CCN} at SS = 0.1% are not reported, as small absolute deviations in particle number concentration measured by the CCNC and DMA due to differential inlet losses could strongly influence the resulting κ_{CCN} estimates.

Hygroscopicity estimates can also be made using component volume fractions measured by the HR-ToF-AMS using the following equation (Petters & Kreidenweis, 2007):

$$\kappa_{AMS} = \sum_{i}^{N} \epsilon_i \kappa_i \qquad (3)$$

where ϵ_i and κ_i represent the volume fraction and hygroscopicity of the ith NR-PM$_1$ component, respectively. While this calculation cannot capture the contribution of refractory components (sea salt, mineral dust, etc.), further analysis suggests their contribution is minor, as discussed in the supporting information. Organic aerosol density was assumed to be 1.4 g cm^{-3} for volume fraction calculations given the remote nature of the environments sampled and the oxidized character of the measured organic aerosol (e.g., O:C ratios of MBL and AC-OAL PMF factors were 0.91 and 0.76, respectively) (Hallquist et al., 2009; Roberts et al., 2010). The hygroscopicity of individual inorganic components is calculated using

$$\kappa_i = \left(\frac{M_w}{\rho_w}\right)\left(\frac{\rho_i}{M_i}\right) v_i \qquad (4)$$

where M_w and ρ_w are the molar mass and density of water, respectively, and M_i, ρ_i, and v_i are the molar mass, density, and van't Hoff factor of the inorganic component. Inorganic aerosol was dominated by sulfate and ammonium. The relative abundances of ammonium sulfate, ammonium bisulfate, and sulfuric acid were calculated using the molar ratio of ammonium to sulfate (Asa-Awuku et al., 2011; Nenes et al., 1998). Ammonium sulfate and bisulfate were assigned van't Hoff factors of 2.5, while sulfuric acid was assigned $\kappa = 0.9$ to align with previous measurements (Petters & Kreidenweis, 2007). Modifying the van't Hoff factors of ammonium sulfate and ammonium bisulfate and assumed κ of sulfuric acid within reasonable limits had a negligible influence on the presented results. Chloride measured by the AMS was assumed to represent sodium chloride and was assigned a hygroscopicity of 1.28 (Petters & Kreidenweis, 2007). AMS-measured nitrate aerosol was assumed to be ammonium nitrate with a hygroscopicity of 0.67 (Petters & Kreidenweis, 2007). The hygroscopicity of the organic component (κ_{org}) was assumed to be either 0 (non-hygroscopic), 0.1 (slightly-hygroscopic), or a function OA composition using a parameterization based on bulk O:C ratios developed in the literature (Lambe et al., 2011). Comparisons of κ_{CCN} and κ_{AMS} values, analysis of PMF factor composition, and evaluation of CCN-closure calculations are used to evaluate these different κ_{org} estimates.

An uncertainty analysis similar to that described for κ_{CCN} values was performed for κ_{AMS} values and is described in detail in the supporting information. For median conditions in the MBL and FT, the relative uncertainty in κ_{AMS} is estimated to be ~10–20%, due primarily to uncertainty in the estimated hygroscopicity of the organic component (κ_{org}). In the AC-OAL, the dominant contribution of organic aerosol increases the relative uncertainty to $\sim50\%$; however, due to the low absolute κ_{AMS} values observed in the AC-OAL, the absolute uncertainty is only ~0.1 or less.
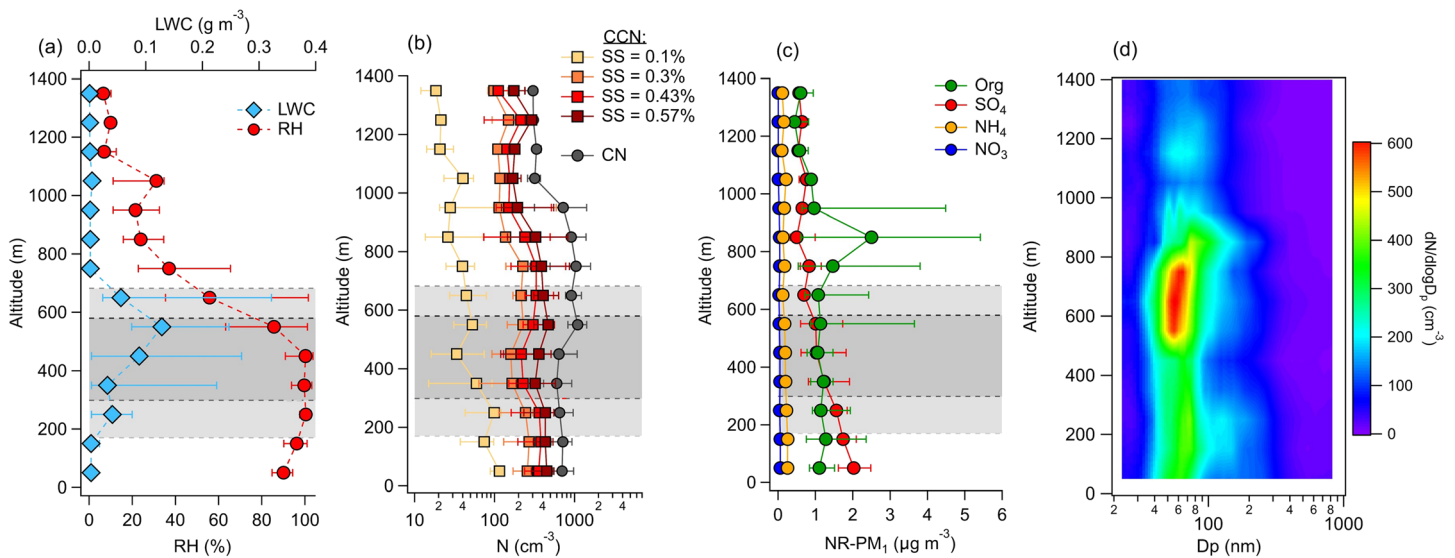
Figure 2. Vertical profiles of (a) RH and LWC, (b) CCN and CN concentrations, and (c) non-refractory (NR) PM$_1$ component mass loadings for the seven RFs in Figure 1. Markers represent median values, while horizontal bars span the interquartile range. (d) Vertical contour plot of median size distributions measured during the seven RFs. The dark grey region in panels a–c represents the average stratocumulus cloud depth (avg. cloud top height ≈ 570 m; avg. cloud bottom height ≈ 300 m). The lighter grey region represents the standard deviation of cloud top and bottom heights (e.g., avg. cloud top + cloud top height S.D. ≈ 680 m).

2.4. Aerosol-Cloud Parcel Model

The aerosol-cloud parcel model used in this study employs a user-specified updraft velocity to induce adiabatic cooling of an air parcel, leading to water vapor supersaturation. The predicted parcel supersaturation at each time step is determined by the relative rates of production through adiabatic cooling and loss through condensation of water vapor onto activated cloud droplets (Pruppacher & Klett, 1997; Seinfeld et al., 2016). In the present study, meteorological parameters such as ambient pressure, temperature, and lapse rate are obtained from MACAWS aircraft measurements and are specified before model execution. The below-cloud dry size distribution is assumed to contain Aitken and accumulation modes, the characteristics of which (i.e., number concentration, geometric mean diameter, hygroscopicity) are set by the user. Particles within each mode can be specified as either internally or externally mixed. Each compositional class, 1 per size mode if internally mixed or 2 per size mode if externally mixed, contains 300 lognormally spaced bins ranging from 1 nm to 3 μm. Droplet activation is assumed to occur when the ambient supersaturation of the parcel exceeds the critical supersaturation of the particles in a given size bin, as determined from κ-Kohler theory (Petters & Kreidenweis, 2007). Following activation, the growth of individual cloud droplet bins due to water vapor diffusion is explicitly represented. Additional physical processes such as droplet coagulation, coalescence, and deposition are not included, as previous parcel model studies have demonstrated that these processes have little influence on model predictions for typical marine stratocumulus conditions (Sanchez et al., 2016). Model execution proceeds until a user-specified liquid water content (0.4 g m^{-3} in this study) has been reached. Activated particle size bins larger than 1 μm are considered cloud droplets; however, using an alternative size threshold of 2 μm or 0.75 μm has a negligible influence on the results.

2.5. Air Mass Backward Trajectories

Air mass backward trajectories (120 hr) were calculated in the MBL for each flight using the NOAA HYSPLIT v4.2 model with the global data assimilation system (GDAS) 1° × 1° meteorological data set (Draxler & Hess, 1997, 1998; Stein et al., 2015). The higher spatial resolution EDAS 40 km × 40 km meteorological data set was not used due to its limited spatial range over the Pacific Ocean. The ending altitude of each trajectory was the approximate midpoint of the MBL during each flight.

Table 1

Median Aerosol Number (N) and Cloud Condensation Nuclei (CCN) Concentrations Measured in the Marine Boundary Layer (MBL), Above-Cloud Organic Aerosol Layer (AC-OAL), and Free Troposphere (FT)

Location	N (cm^{-3})	CCN: 0.1% (cm^{-3})	CCN: 0.3% (cm^{-3})	CCN: 0.43% (cm^{-3})	CCN: 0.57% (cm^{-3})
MBL	754 (509–978)	75 (33–106)	194 (146–285)	302 (187–410)	410 (229–522)
AC-OAL	1,662 (1,303–1,959)	58 (41–84)	363 (260–537)	574 (403–876)	781 (539–1,051)
FT	333 (296–555)	21 (14–35)	115 (89–145)	144 (102–194)	162 (118–240)

Note. Values in parentheses represent the interquartile range. CCN concentrations are provided as a function of the instrument supersaturation (%).

3. Results and Discussion

3.1. Aerosol Characteristics Over the N.E. Pacific

Results from the seven flights analyzed in this study are summarized in Figure 2 and Tables 1–3. In the subsequent analyses, "all flights" refers to these seven. Typical flight patterns included sampling within the MBL, FT, and, when present, the above-cloud organic aerosol layer (AC-OAL). The AC-OAL is operationally defined as the narrow altitude band (generally <200 m) directly above the marine stratocumulus cloud decks where OA mass loadings were relatively large (>1.5 μg m^{-3}) and a distinct AC-OAL PMF factor contributed >80% of total OA mass (Figure S6). This region occupies a similar location as the commonly referenced entrainment interface layer (EIL) above cloud decks (Dadashazar et al., 2018; Wood, 2012), but is defined by the aerosol characteristics described above rather than by turbulence and buoyancy characteristics, as is common for the EIL (Carman et al., 2012). Median aerosol properties are reported in Tables 1–3 for each of these three regions, while Figure 2 displays vertical profiles of aerosol and meteorological properties.

Distinct differences in particle properties were observed within each vertical region. Median aerosol number concentrations observed in the MBL (754 cm^{-3}) exceeded those in the FT (333 cm^{-3}), as expected. Observed particle concentrations were maximized within the AC-OAL (1,662 cm^{-3}), where intense actinic fluxes and elevated concentrations of the hydroxyl radical may drive new particle formation (Dadashazar et al., 2018; Mauldin et al., 1999). For all measured SS > 0.1%, observed CCN concentrations were also largest within the AC-OAL, rather than the MBL or FT, underscoring the importance of understanding the hygroscopicity of above-cloud CCN-active particles (Coggon et al., 2014; Sorooshian, Lu, et al., 2007; Sorooshian et al., 2007; Wang et al., 2008).

Observed aerosol composition in the MBL was relatively evenly divided between organic aerosol (OA) (43%) and sulfate (SO$_4$) (48%), with a minor contribution from ammonium (NH$_4$) (~10%) and negligible nitrate (NO$_3$) (≤1%). Prabhakar et al. (2014) have demonstrated that nitrate is preferentially distributed in super-micron particles in this marine environment, in agreement with the minor contribution observed with the AMS in this study. Using the "clean" versus "perturbed" threshold introduced by Coggon et al. (2012) for this region (where "clean" is defined by aerosol mass concentrations <1 μg m^{-3}), average MBL conditions were "perturbed" by shipping vessel emissions or other anthropogenic sources such as continental outflow. A distinct, highly oxidized MBL PMF factor was extracted from the data set (Figure S6). The oxidized nature of the MBL factor (O:C = 0.91) precludes the use of marker ions to distinguish individual sources; however, potential sources include shipping and biogenic emissions, as well as oxidized continental outflow aerosol (Coggon et al., 2012; Hegg et al., 2010; Sorooshian et al., 2009). In the AC-OAL, observed aerosol composition was dominated by organics (80%), as has been previously reported (Coggon et al., 2014;

Table 2

Median Mass Loadings of Total Non-Refractory PM1 (NR-PM$_1$), and Organic (Org.), Sulfate (SO$_4$), Ammonium (NH$_4$), and Nitrate (NO$_3$) Aerosol Components in the Marine Boundary Layer (MBL), Above-Cloud Organic Aerosol Layer (AC-OAL), and Free Troposphere (FT)

Location	NR-PM$_1$ (μg m^{-3})	Org. (μg m^{-3})	SO$_4$ (μg m^{-3})	NH$_4$ (μg m^{-3})	NO$_3$ (μg m^{-3})
MBL	2.8 (2.3–2.5)	1.1 (0.8–1.4)	1.5 (0.9–2.0)	0.2 (0.2–0.3)	0.0 (0.0–0.1)
AC-OAL	5.5 (4.5–7.5)	4.4 (3.2–6.1)	0.7 (0.6–1.1)	0.2 (0.2–0.3)	0.1 (0.0–0.1)
FT	1.5 (1.2–2.1)	0.7 (0.5–1.0)	0.6 (0.4–0.7)	0.1 (0.1–0.2)	0.0 (0.0–0.0)

Note. Values in parentheses represent the interquartile range.

Table 3

Median Values of the AMS-Derived (κ_{AMS}) and CCN-Derived (κ_{CCN}) Hygroscopicity Factor Measured in the Marine Boundary Layer (MBL), Above-Cloud Organic Aerosol Layer (AC-OAL), and Free Troposphere (FT)

Location	κ_{AMS}	κ_{CCN}: 0.3%	κ_{CCN}: 0.43%	κ_{CCN}: 0.57%
MBL	0.45 (0.35–0.52)	0.39 (0.20–0.61)	0.35 (0.24–0.50)	0.40 (0.27–0.54)
AC-OAL	0.19 (0.17–0.25)	0.13 (0.08–0.20)	0.19 (0.14–0.25)	0.17 (0.12–0.27)
FT	0.37 (0.30–0.43)	0.32 (0.18–0.65)	0.50 (0.29–0.88)	0.37 (0.21–0.72)

Note. Values in parentheses represent the interquartile range. κ_{CCN} are provided as a function of the instrument supersaturation (%).

Hersey et al., 2009; Sorooshian et al., 2007; Sorooshian, Ng, et al., 2007; Wang et al., 2008). A second, distinct factor displayed large mass loadings (up to 8 μg m^{-3}) within the AC-OAL (Figure S6) (O:C = 0.76), and the mass ratio of the AC-OAL to the MBL PMF factor is used as a tracer of AC-OAL entrainment into the MBL, as discussed in section 3.3.2. Possible aerosol production mechanisms in the AC-OAL include oxidation and transport of biogenic volatile organic compounds emitted by forested regions in the northwest United States, cloud droplet evaporation, and oxidation of sparingly soluble organics vented through the stratocumulus layer (Coggon et al., 2014; Heald et al., 2005; Sorooshian, Lu, et al., 2007). While large eddy simulations (LES) have demonstrated that the altitude of the top of the stratocumulus cloud deck can undergo diurnal variations of 10–100 m, providing a potential mechanism for AC-OAL aerosol production through droplet evaporation (Chen et al., 2011; Sorooshian, Lu, et al., 2007), the substantially larger mass fraction of organic aerosol in the AC-OAL than the MBL suggests that particle production is primarily a result of continental biogenic sources (Coggon et al., 2014). Observed aerosol mass loadings in the FT were the lowest sampled (1.5 μg m^{-3}) but agree well with previous aircraft measurements by Wang et al. (2008) off the coast of Pt. Reyes, CA, at a similar time of year (June–July).

3.2. Overview of Observed Aerosol Hygroscopicity

Figure 3 displays median aerosol number size distributions, κ_{AMS}, and κ_{CCN} values observed within the MBL, AC-OAL, and FT during each flight. For these comparisons, κ_{AMS} values are calculated assuming $\kappa_{org} = 0.1$, as is typical for non-urban regions (Mei et al., 2013; Moore et al., 2011, 2012). However, we note that using the parameterization developed by Lambe et al. (2011), the calculated κ_{org} values for the MBL and AC-OAL PMF factors are 0.19 and 0.17, respectively, due to their highly oxidized nature (Figure S6), suggesting the true κ_{org} values for large particles may be greater than 0.1.

Within the MBL, observed hygroscopicity values appear to cluster into three relatively distinct groups that span the range of values previously observed in this environment (Roberts et al., 2010; Royalty et al., 2017; Yakobi-Hancock et al., 2014). The strong temporal variation observed in both particle number size distributions and hygroscopicities underscores the complexity involved in accurately modeling CCN in coastal environments influenced by continental and marine sources. This is further demonstrated in Table 4, which depicts estimated organic and inorganic volume fractions of Aitken mode particles derived from MBL κ_{CCN} values. Assuming inorganic aerosol is entirely ammonium sulfate for these calculations, estimated organic fractions vary from effectively zero, as median κ_{CCN} during RF13 are larger than that of ammonium sulfate ($\kappa = 0.61$) to as high as 84%. The low hygroscopicities and subsequently large estimated organic fractions observed during flights RF9 and RF15 are uncharacteristic of remote marine environments and imply a continental influence on particle characteristics. κ_{AMS} values calculated during these flights are ~50–100% larger than κ_{CCN} values, implying addition of particle mass during growth that is more hygroscopic than the Aitken mode particles. While the difference between κ_{AMS} and κ_{CCN} values during these flights are nearly within the uncertainty range of the κ_{CCN} calculation, these observations align with those in many continental locations, where addition of inorganic mass to organic-rich Aitken mode particles growth is thought to lead to a positive relationship between particle hygroscopicity and size (Ervens et al., 2010; Kawana et al., 2016; Levin et al., 2014; Moore et al., 2012; Rose et al., 2011). On the other hand, κ_{AMS} and κ_{CCN} are quite similar during the other five flights, with relative deviations on the order of ~25% or less, which is well within the uncertainty of the κ_{CCN} measurements. A compilation of data reported by Royalty et al. (2017) suggests that minor variation of particle hygroscopicity with size is a common feature of remote marine aerosol, which generally exhibits elevated Aitken mode hygroscopicity. Four individual flights (RF4, RF5, RF13, and RF15) provide
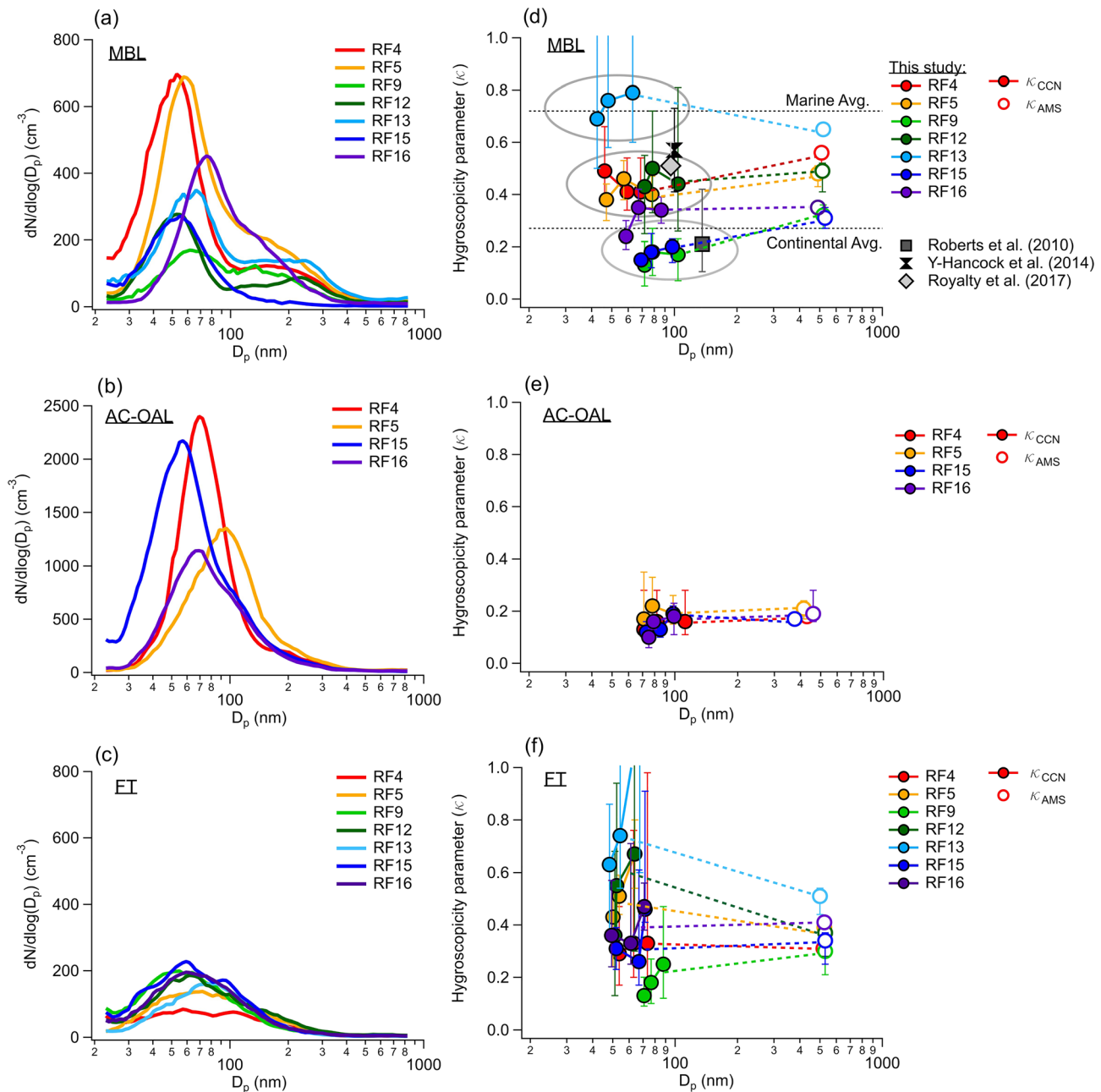
Figure 3. Median aerosol size distributions (a–c) and hygroscopicities (κ_{CCN} and κ_{AMS}) (d–f) measured in the marine boundary layer (MBL), above-cloud organic aerosol layer (AC-OAL), and free troposphere (FT), during the seven RFs. κ_{AMS} values are calculated assuming $\kappa_{org} = 0.1$ and are plotted at the median of the cumulative aerosol volume distribution. Vertical bars represent the interquartile range of hygroscopicity measurements. Previously observed values in the MBL are included for reference in (d), as are typical values for continental and marine environments from Pringle et al. (2010).

specific insight into the combined roles of aerosol sources and meteorological processes in determining aerosol hygroscopicity in the MBL, and these are discussed in further detail in section 3.3.2.

Within the AC-OAL, observed aerosol hygroscopicity is remarkably similar from flight-to-flight, and little difference is observed between κ_{CCN} and κ_{AMS} values. The combination of reduced hygroscopicity (i.e., κ ~0.2) and little variation with particle size suggests that within the AC-OAL, Aitken mode particles are organic-rich and grow through condensation of additional organic vapors, rather than addition of inorganic mass. Even under the assumption that the organic species in Aitken mode AC-OAL particles are entirely

Table 4

Calculated Aitken Mode Organic (f_{org}) and Inorganic (f_{inorg}) Volume Fractions Based on Median κ_{CCN} Values Derived From CCN Measurements at SS = 0.43% for MBL Measurements During Each Flight

Flight	κ_{CCN} − SS = 0.43%	Inorg. = $(NH_4)_2SO_4$		Inorg. = H_2SO_4	
		f_{org}	f_{inorg}	f_{org}	f_{inorg}
RF4	0.41	0.39	0.61	0.61	0.39
RF5	0.46	0.29	0.71	0.55	0.45
RF9	0.18	0.84	0.16	0.90	0.10
RF12	0.50	0.22	0.78	0.50	0.50
RF13	0.76	~	~	0.18	0.82
RF15	0.18	0.84	0.16	0.90	0.10
RF16	0.28	0.65	0.35	0.78	0.22

Note. Values of f_{org} and f_{inorg} are calculated assuming the inorganic aerosol component is either ammonium sulfate ($(NH_4)_2SO_4$) or sulfuric acid (H_2SO_4). Note that the hygroscopicity measured during RF13 cannot be reproduced assuming the inorganic component is entirely $(NH_4)_2SO_4$.

insoluble, total particle volume must be at least 66% organic to produce a hygroscopicity of 0.2 (assuming ammonium sulfate as the inorganic component). Chamber studies of monoterpene aerosol often observe κ_{org} of ~0.1–0.15 for Aitken mode particles (Alfarra et al., 2013; Zhao et al., 2015), which increases the estimated organic volume fraction to 80–89%. While the peak in the AC-OAL size distribution varies considerably between flights, the presence of a dominant Aitken mode in three out of four observations suggests particle formation may have occurred recently.

Coggon et al. (2014) first demonstrated that expansive dry air masses originating over the northwestern United States loft biogenic organic aerosol over the MBL and act as the main particle source to the AC-OAL. Our measurements support this conclusion; however, an additional contribution from organic gases vented through the stratocumulus layer cannot be ruled out. Comparing AC-OAL and MBL Aitken mode hygroscopicity suggests cloud droplet evaporation is at most a minor particle source to the AC-OAL, as during three of the four flights in which the AC-OAL was sampled, average MBL Aitken mode particles were substantially more hygroscopic than those in the AC-OAL (κ_{MBL} ~0.4; $\kappa_{AC\text{-}OAL}$ ~0.2). As the most hygroscopic particles in an air mass are likely to activate into cloud droplets, and as addition of inorganic mass is common during cloud processing in marine environments (Faloona, 2009; Seinfeld et al., 2016), it is unlikely that residual aerosol formed from evaporated cloud droplets would be less hygroscopic than the MBL aerosol population. Observations during RF15, discussed further in section 3.3.2, suggest entrainment during precipitation events can lead to a major AC-OAL signature in the MBL, directly demonstrating the importance of understanding the source of these particles.

Due to the low aerosol number concentrations in the FT, observed κ_{CCN} values vary widely between flights and exhibit large variability within individual flights. As a result, we hesitate to draw definitive conclusions based on these data. Other than RF13, average κ_{AMS} values from each flight are near or below 0.4, implying a substantial organic contribution to free tropospheric aerosol. In the absence of continental influence, observation of aerosols of such low hygroscopicity is unexpected, given that particle formation in the upper FT over tropical oceans is driven primarily by sulfuric acid nucleation and growth (Clarke, 1993; Clarke et al., 1998, 1999, 2013). Long range transport of organic aerosol layers from the Asian continent have been noted previously (Roberts et al., 2006, 2010), but estimates of aerosol hygroscopicity in such layers have varied dramatically. For instance, during the CIFEX experiments (Roberts et al., 2006), average κ attributed to aged aerosol layers were only ~0.04, whereas our measurements suggest a more moderate value of ~0.4, while observations by Roberts et al. (2010) indicated a value of 0.93 was more appropriate. While the substantial difference in particle concentrations in the MBL and FT observed during this campaign suggests FT aerosol plays a minor role in dictating MBL CCN activity on average, in remote marine environments, entrainment from the FT is the dominant source of MBL particles (Clarke, 1993; Clarke et al., 1996, 1998, 2013; Raes, 1995), and as such further research into the variability of FT aerosol composition is warranted.

3.3. Observation of Distinct Influences on MBL Particle Characteristics

Observations shown in Figure 3 indicate highly variable flight-averaged hygroscopicities in the MBL, suggesting that temporal variations in regional meteorology and/or particle source strengths can strongly influence CCN characteristics in this environment. Further analysis suggests that in four of the seven flights discussed in this study, specific meteorological patterns and emissions sources influencing particle characteristics can be identified. We discuss these observations to provide insight into the level of physicochemical detail (both in terms of emissions and atmospheric dynamics) required for atmospheric models to simulate MBL CCN concentrations with high fidelity.

3.3.1. Shipping Emissions

Aerosol properties measured during RF4 and RF5 suggest a prominent influence of regional shipping emissions on particle characteristics and hygroscopicity in this environment. During these flights, the dominance of an Aitken mode near ~50–60 nm with much larger concentrations than in the FT suggests relatively
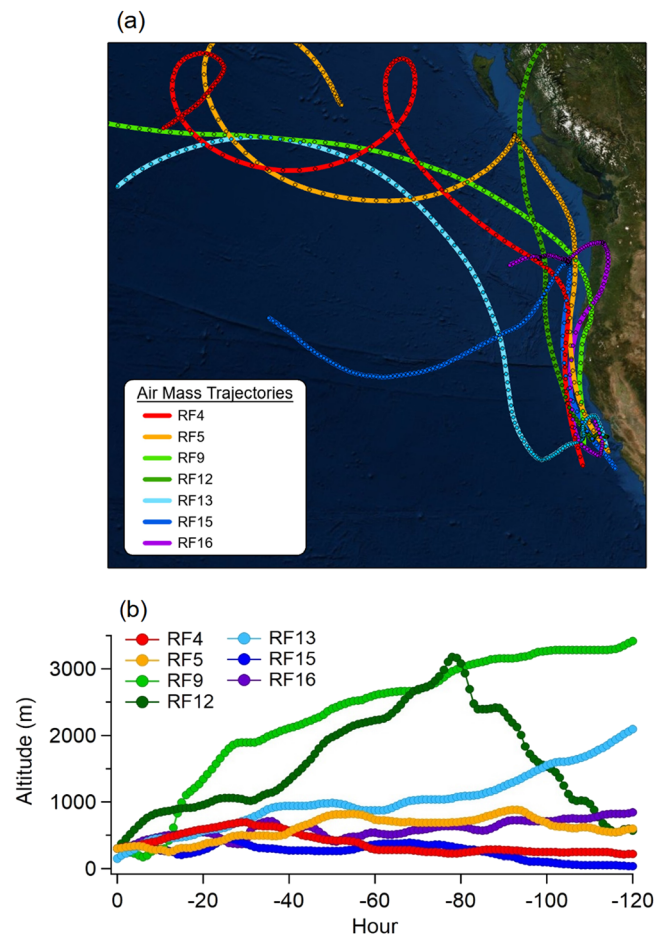
Figure 4. (a) 120-hr air mass backward trajectories calculated using the HYSPLIT model (Stein et al., 2015) from the approximate midpoint of each flight path at an altitude representative of the marine boundary layer. For six of the seven flights, the starting altitude was 300 m, while the starting altitude for the RF13 trajectory was 150 m due to the shallow height of the boundary layer. (b) Air mass altitude during the 120-hr transit to the measurement site.

recent formation from an MBL-based particle source. While such size distributions could hypothetically result from continental outflow (Moore et al., 2012), air mass backward trajectories remained over the ocean and near or within the MBL (<1,000 m) for the previous 5 days (Figure 4). Furthermore, trajectories transited primarily within the major shipping corridor along the coast, as observed for flights "perturbed" by shipping vessel emissions by Coggon et al. (2012), rather than recently arriving from the remote ocean (e.g., RF13). Downward mixing of AC-OAL particles is also ruled out as an Aitken mode particle source during these flights due to the distinctly different hygroscopicities observed in the MBL and AC-OAL (Figure 3). Finally, average wind speeds within the MBL were ~12 m s^{-1} and ~9 m s^{-1} during RF4 and RF5, respectively. Modini et al. (2015) previously noted that primary sea spray emissions produced particle concentrations of only 12 cm^{-3} during periods with similar windspeeds (12 m s^{-1}) in the same marine environment (equivalent to ~2% of particle number concentrations in the MBL during RF4 and RF5).

Shipping emissions have been previously noted as major contributors to aerosol and cloud properties in the N.E. Pacific environment (Cappa et al., 2014; Coggon et al., 2012; Lack et al., 2011; Murphy et al., 2009). Coggon et al. (2012) demonstrated that 70% of cloud residual particles measured in the California shipping lanes were impacted by nearby shipping emissions. Available compositional data further suggest that shipping emissions could be expected to produce Aitken mode hygroscopicities observed during RF4 and RF5. For instance, Lack et al. (2011) observed an effective κ value of 0.68–0.73 from exhaust produced by a
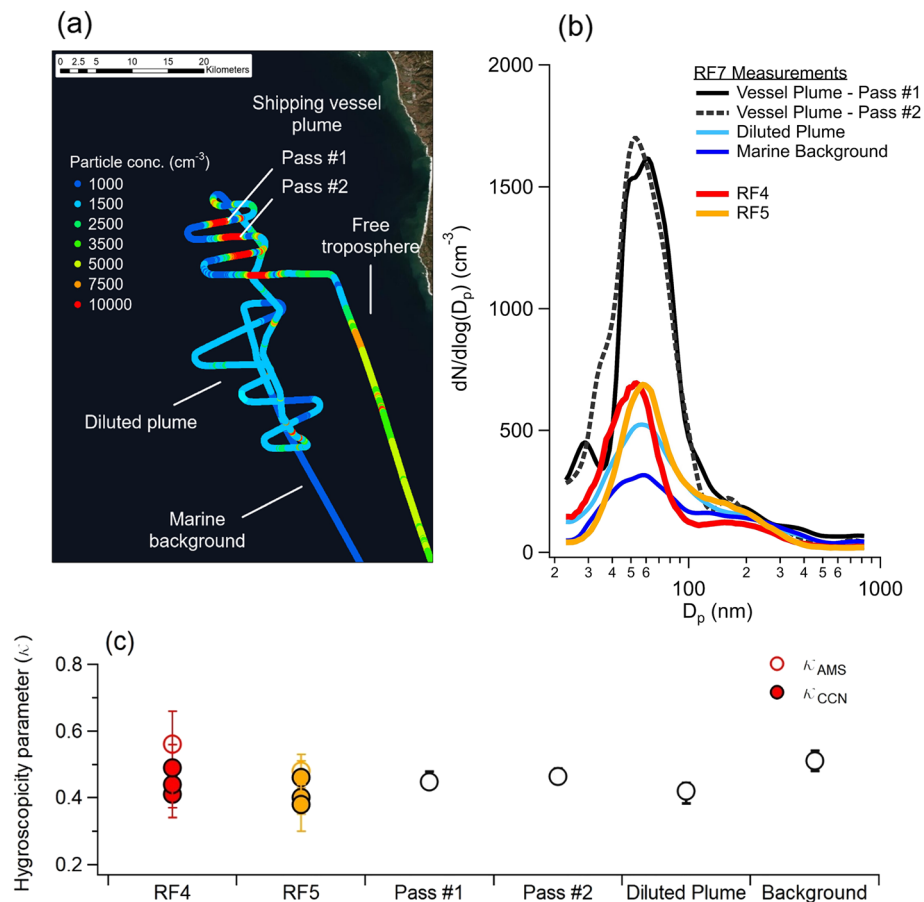
Figure 5. (a) Map of the Twin Otter trajectory during repeated sampling of the exhaust plume from a 330-m shipping vessel during RF7. Points are colored by the particle concentration measured by the CPC, and individual segments of the flight path are labeled. (b) Aerosol size distributions measured during the labeled segments in (a) compared to median distributions measured during RF4 and RF5. (c) Comparison of κ values derived from CCN and AMS measurements in RF4 and RF5 with those derived from AMS measurements during the flight segments shown in (a).

large (96,500 ton) container vessel, while the smaller Research Vessel Atlantis sampled during the same study produced a value of ~0.2. Hygroscopic growth factor measurements of shipping exhaust emitted by another large (90,000 ton) container vessel by Murphy et al. (2009) suggest an effective $\kappa = 0.1$–0.5.

Direct measurements of a large container vessel exhaust plume during RF7 provide further support for the attribution of aerosol characteristics to shipping emissions in RF4 and RF5. As shown in Figure 5, the strong Aitken mode peak in the size distribution measured directly within the plume aligns well with those measured in RF4 and RF5, while the total magnitude of the flight-median size distributions agree well with those measured in the diluted plume more than 20 km downwind. As the plume was relatively narrow directly behind the ship, κ_{CCN} values are not available, but κ_{AMS} measurements agree well with those in RF4 and RF5 (Figure 5c). However, given the variability in the measured κ values of particulate shipping exhaust just discussed, this agreement cannot be viewed as definitive. Ultimately, while the insights provided by the size distributions, backward trajectories, and κ_{AMS} values would not be definitive on their own, taken together they support a shipping emission signature on aerosol characteristics during these flights. This influence highlights the importance of accurate physicochemical representation of shipping vessel emissions within the California coastal zone. As an example, the implementation of recent regulations on the sulfur content of shipping fuel within coastal waters of the United States (up to 200 miles off the coast) should increase the organic:inorganic ratio of particulate shipping emissions in major shipping lanes over time (Cappa et al., 2014; Lack et al., 2011). Assuming, as a strictly upper limit estimate, that all Aitken mode particles observed during RF4 and RF5 are derived from shipping vessel emissions,
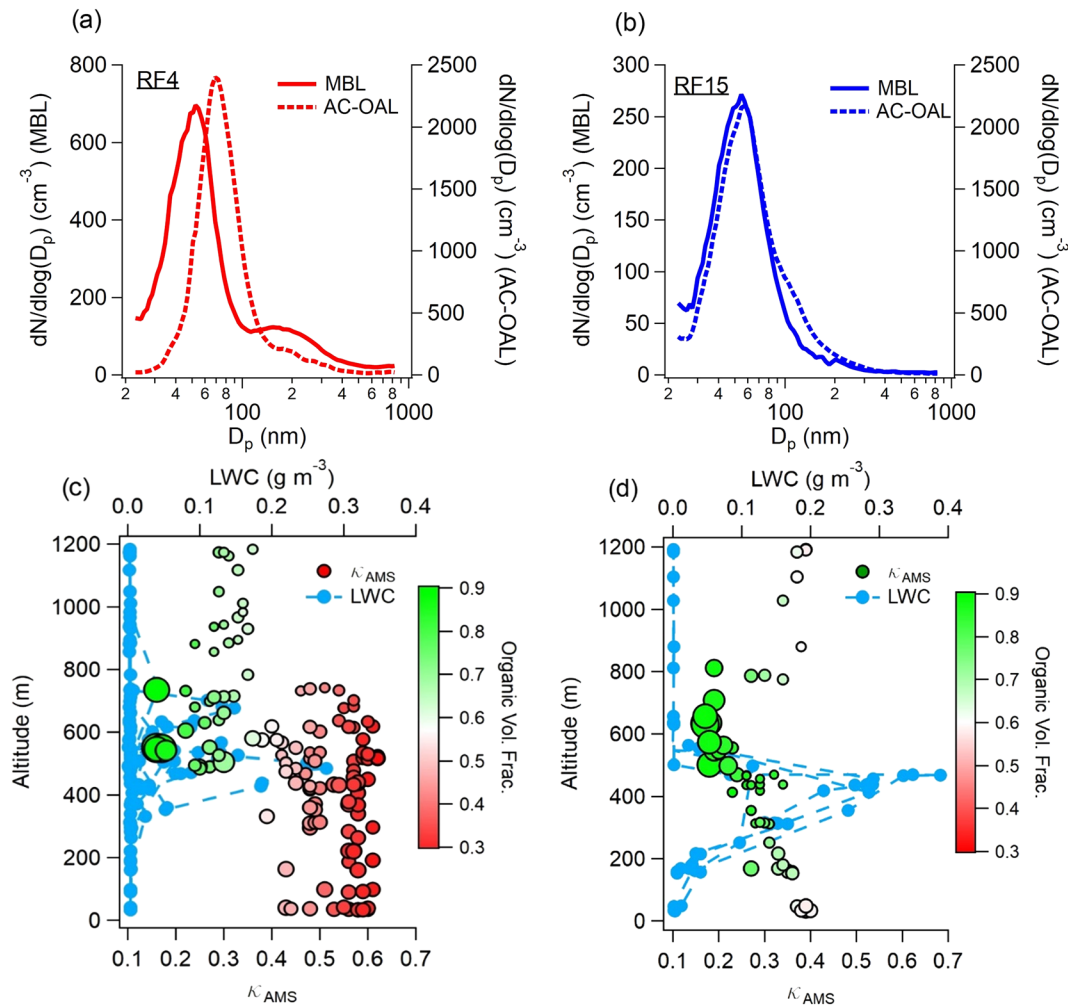
Figure 6. (Top) Median aerosol size distributions measured in the marine boundary layer (MBL) and above-cloud organic aerosol layer (AC-OAL) during RF4 (a) and RF15 (b). (Bottom) Vertical profile of AMS-derived hygroscopicity (κ_{AMS}) and liquid water content (LWC) during each flight. Values of κ_{AMS} are colored by the organic volume fraction measured by the AMS to aid interpretation of the figure.

changing the assumed hygroscopicity of these emissions from the value observed during ambient measurements in this study (~0.4–0.5) to a value of 0.1 (purely organic, partially hygroscopic), would change the CCN concentration at SS = 0.3% by 15–36%.

3.3.2. Entrainment From the AC-OAL

The observation of a single, dominant Aitken mode with reduced hygroscopicity during RF15 suggests an influence of the AC-OAL on MBL particle properties. According to Figure 4, the air mass sampled during RF15 had not recently transited over the continent or within the FT, which has previously shown to occasionally contain distinct layers of reduced hygroscopicity aerosol (Roberts et al., 2006, 2010). Clear evidence of entrainment from the AC-OAL is provided in Figure 6, which contrasts size distributions and κ_{AMS} values observed during RF15 and RF4, another flight with a prominent Aitken particle mode and relatively similar backward trajectory. During RF15, the MBL and AC-OAL size distributions are remarkably similar, exhibiting peak diameters at ~55 nm and lacking a larger accumulation mode. Liquid water contents measured within the MBL during RF15 demonstrate a fully developed stratocumulus layer encompassing roughly half of the MBL. κ_{AMS} values vary linearly with altitude from ~0.4 near the ocean surface to ~0.15–0.2 at the top of the cloud layer, aligning with the hypothesis of downward mixing of AC-OAL particles into the MBL. These observations are in stark contrast to those from RF4, where the Aitken mode diameter of the MBL and AC-OAL aerosol differ by ~20–25 nm, and importantly, the Aitken mode diameter in the MBL is smaller
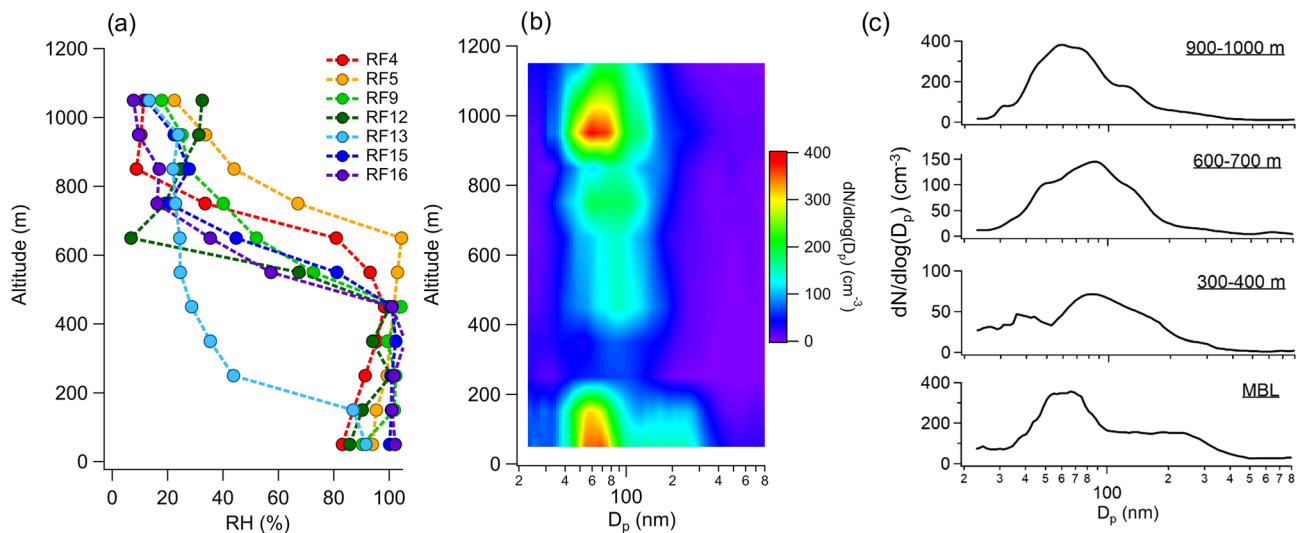
Figure 7. (a) Measured relative humidity vertical profile during each flight, demonstrating the reduced marine boundary layer (MBL) height during RF13. (b) Vertical profile of aerosol number size distributions during RF13. (c) Individual aerosol size distributions at different altitudes during RF13.

than the AC-OAL, suggesting a distinct particle source in each location. Finally, as the AC-OAL and MBL PMF factors are clearly distinguished in each flight where the AC-OAL layer was observed, the AC-OAL: MBL PMF factor mass ratio acts as a tracer for entrainment mixing. During RF15, the median AC-OAL: MBL PMF factor mass ratio was 0.81 in the MBL, in contrast to a value of 0.36 measured during RF4 and a median value of 0.42 in all flights other than RF15 where the AC-OAL was observed. The information obtained from the aerosol size distribution (no accumulation mode) and hygroscopicity (similar to the AC-OAL) in the MBL suggests that the distinct AC-OAL signature may result from entrainment following precipitation scavenging of the preexisting MBL aerosol. As typical AC-OAL particle concentrations are ~5 times as large as those in the overlying FT, failure to simulate this layer will result in underprediction of MBL particle concentrations during such distinct precipitation/entrainment events.

3.3.3. Transport From the Remote Pacific Ocean

Hygroscopicity measurements made during RF13 are notably larger than those from the other six flights, indicating a lack of organic aerosol across the particle size distribution. As expected, backward trajectories calculated within the MBL during this flight indicate recent arrival from the remote Pacific Ocean, rather than extended transport through the major shipping lanes along the coast. The boundary layer was substantially compressed (<300 m) and cloud-free during the flight, suggesting ongoing subsidence of free tropospheric air masses (Figure 7a). As new particle formation through sulfuric acid nucleation is known to be a notable source of CCN throughout the marine boundary layer (Clarke, 1993; Clarke et al., 1998, 2013), downwelling and entrainment of such nucleated particles is a possible explanation for the elevated Aitken mode hygroscopicities observed. While low number concentrations in the FT make κ_{CCN} estimates less reliable, the values observed in RF13 are relatively similar to those in the MBL, supporting entrainment. While aerosol size distribution measurements in the FT suggest such entrainment was not responsible for increases in Aitken mode particles locally, as concentrations directly above the MBL are substantially lower than those in the MBL, the elevated aerosol concentrations at ~1,000 m suggest entrainment may have produced MBL Aitken mode particles during transport (Figure 7b). Furthermore, the vertical profile of the aerosol size distribution in the FT is consistent with past observations of growth of nucleation-produced Aitken mode particles during large-scale subsidence (Clarke et al., 1999).

Due to the compressed height of the MBL during RF13, the potential contribution of primary sea spray aerosol to MBL particle characteristics is also enhanced. However, using the size distribution fitting technique established by Modini et al. (2015), the calculated concentration of primary sea spray aerosol is only 18 cm^{-3} or ~4% of the average MBL particle concentration during the flight, suggesting sea spray provides at most a minor contribution.
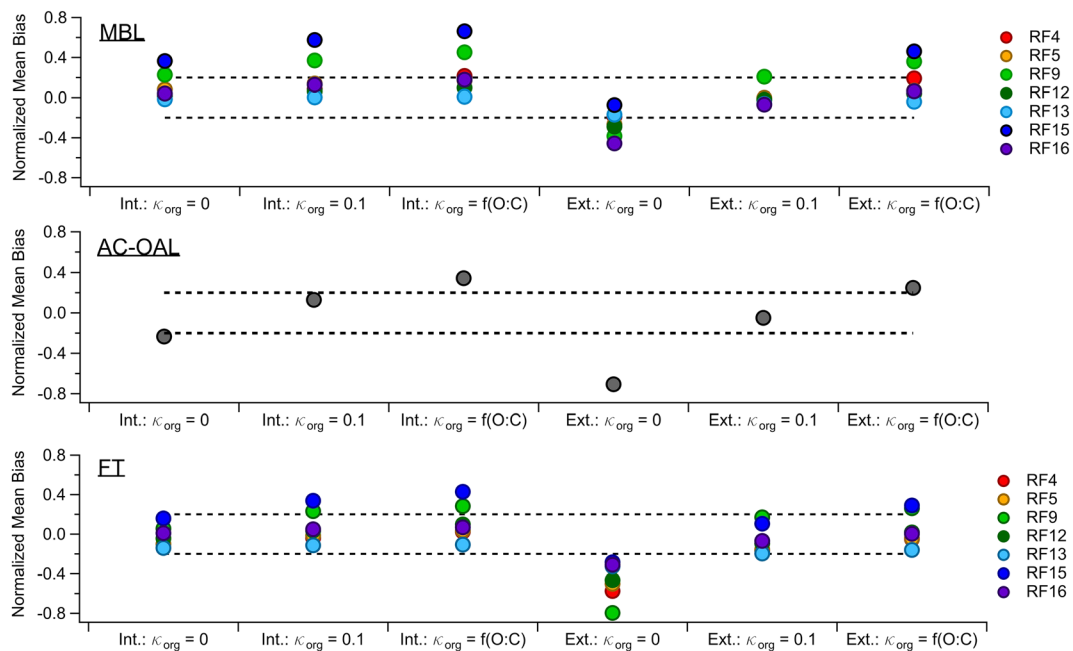
Figure 8. Normalized mean bias resulting from CCN closure analysis performed on data from each flight. A value of 0.2 is equivalent to an average overprediction of 20%. Int. indicates aerosol were assumed internally mixed, while Ext. indicates organic and inorganic aerosol were assumed to be externally mixed. κ_{org} represents the assumed hygroscopicity of the organic aerosol component, and f(O:C) indicates κ_{org} was calculated based on the bulk aerosol O:C ratio using the parameterization derived by Lambe et al. (2011).

3.4. CCN Closure Analysis

Figure 8 shows CCN closure results for the three sampled environments using six different assumptions regarding aerosol composition and mixing state. Three cases assume internally mixed aerosol components with composition determined by AMS measurements. These cases are differentiated by their assumptions regarding organic aerosol hygroscopicity, with κ_{org} increasing from 0 (first case), to 0.1 (second case), and finally to values predicted from time-varying measured OA O:C ratios according to the relationship developed by Lambe et al. (2011) (third case). The final three cases are similar to the internally mixed cases in their treatment of κ_{org}; however, the organic and inorganic aerosol components are assumed to be externally mixed. Bulk aerosol mass loadings were too low to obtain robust estimates of size-resolved composition, precluding more detailed treatment of composition in CCN closure calculations. Closure was assessed in terms of the normalized mean bias ($NMB = \sum (CCN_{pred,i} - CCN_{meas,i})/\sum CCN_{meas}$), similarly to Asa-Awuku et al. (2011), which provides a representation of the average CCN prediction error observed for each flight. Data for the MBL and FT are shown for individual flights, while data from the AC-OAL are aggregated from all flights where the layer was observed, as fewer size distributions were obtained from the AC-OAL during each flight (and the AC-OAL was not observed at all during three flights).

For the majority of analyzed flights (five out of seven), closure is obtained within 20% using AMS-measured bulk composition and an assumption of either insoluble ($\kappa_{org} = 0$) or slightly hygroscopic organics ($\kappa_{org} = 0.1$). While the assumption of insoluble organics disagrees with observed O:C ratios (e.g., the O:C ratio of the MBL PMF factor is 0.85), CCN closure studies often find this assumption is ideal when assuming internal mixing (Chang et al., 2007; Lance et al., 2009; Moore et al., 2011; Wang et al., 2008). The lack of strong dependence on κ_{org} suggests that in non-urban areas, regional models may be able to assign a single value to organic aerosol rather than attempt to dynamically model changes in organic aerosol hygroscopicity with aging (Wang et al., 2008). This is further highlighted by the fact that closure results assuming a constant κ_{org} value (0.1) are generally more accurate than those produced by parameterizing κ_{org} based on the observed O:C ratio (Lambe et al., 2011). As larger aerosols are more likely to have undergone cloud-processing, parameterizing organic hygroscopicity based on bulk measurements of the organic O:C ratio, which is biased by the largest particles, may also overpredict the oxidation state of particles near the

critical diameter of CCN activation. Without size-resolved compositional data, it is difficult to definitively conclude whether the overprediction observed when κ_{org} is parameterized based on the organic O:C ratio is due to such variability with size or is the result of a different relationship between O:C and κ_{org} for organic aerosols in this environment. However, other published parameterizations between O:C and κ_{org} in the literature either agree well with the Lambe parameterization (Chang et al., 2010; Massoli et al., 2010; Thalman et al., 2017) or predict more hygroscopic particles at the same O:C ratio (and as a result would lead to further overprediction if implemented in the CCN closure analysis) (Mei et al., 2013). The overprediction in CCN observed here when incorporating the Lambe parameterization therefore suggests that small particles near the critical activation diameter are less hygroscopic than larger particles that dominate the mass size distribution and thereby dictate AMS-measured composition.

Overall, generally good closure is expected in a semi-remote environment such as the California coastal zone, as previous studies have noted that closure is likely to be achieved within 20% when the bulk aerosol κ exceeds 0.1 (Wang et al., 2010). Furthermore, it is expected that aerosol in this coastal environment can be modeled as internally mixed, regardless of its true mixing state, due to the substantial contribution of inorganic constituents and distance from emission sources (Ervens et al., 2010; Fierce et al., 2016; Moore et al., 2012). Fierce et al. (2016) have demonstrated that in semi-remote environments (i.e., non-urban locations), initially externally mixed aerosol becomes internally mixed on a time scale of about 1 day, while the conversion is even faster (on the order of hours) in urban environments, in agreement with the results of Wang et al. (2010). Notable underpredictions (i.e., >20%) of CCN concentrations are produced when assuming externally mixed aerosol with insoluble organics, in agreement with the aged nature of the aerosol in this environment, which should lead to both oxidized organic aerosol and an appreciable amount of internal mixing.

CCN are strongly overpredicted in the MBL during RF9 (37%) and RF15 (57%) when assuming an internal mixture with hygroscopic organics. Aerosol composition during these flights was dominated by organic species in the MBL (59% and 58% of AMS-derived aerosol mass, respectively), indicative of a continental influence on aerosol properties. AMS-derived hygroscopicities are substantially larger than those derived from CCN measurements (Figure 3), suggesting that size-dependent composition may lead to the observed overprediction of CCN concentrations when using bulk AMS measurements of aerosol composition. Comparison of CCN closure results when assuming internal versus external mixing suggests that organic and inorganic components are externally mixed, implying either distinct particle sources or a lack of significant aging prior to measurement. In the case of RF15, this external mixing aligns with the hypothesis of downward mixing from the organic-rich AC-OAL. Figure S7 depicts the CCN closure normalized mean bias resulting from an assumption of internally mixed aerosols with hygroscopic organics as a function of the CCN-derived hygroscopicity. In general, CCN closure error increases rapidly as κ_{CCN} decreases past ~0.25, suggesting that detailed mixing state and/or size resolved compositional information is critical for accurate CCN prediction in this coastal environment during periods of intense organic aerosol intrusion into the MBL. As the aerosol hygroscopicity calculation used in this study relies on an assumption of internal mixing of organic and inorganic aerosol components, it is difficult to determine whether CCN closure error when assuming internal mixing during this flights is a result of externally mixed organic and inorganic aerosol or a result of variable composition with size. Ultimately, as these atypical organic aerosol-dominated marine conditions are the least likely to be accurately reproduced by regional models, further investigation of their frequency, particle characteristics, and resulting impact on cloud properties is warranted.

The analysis presented in Figure 8 implies that for typical conditions in the MBL (5 out of 7 flights in this study), mixing state and organic hygroscopicity have relatively little influence on CCN number concentrations. Additional closure analyses were performed assuming a constant κ equivalent to values attributed to average continental ($\kappa = 0.27$) and marine ($\kappa = 0.72$) environments (Pringle et al., 2010) (Figure 9). These results highlight the fact that assuming coastal aerosols have a strictly marine character leads to substantial errors in CCN prediction (>20% for 8 out of 9 flights) even if size distribution parameters are well characterized. Furthermore, for five out of the seven analyzed flights (RF4, RF5, RF9, RF13, RF16), assuming a constant marine κ (0.72) results in CCN prediction error similar to or larger than the error produced by assuming a constant aerosol size distribution derived from the median value measured in the MBL during this study. This underscores the importance of capturing organic contributions to coastal MBL aerosol, whether due to continental outflow, downwelling from the AC-OAL, shipping emissions, or marine biota.
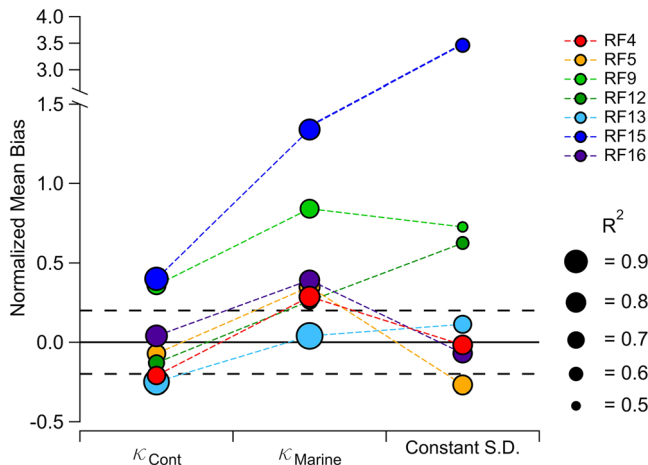
Figure 9. Normalized mean bias resulting from additional CCN closure analyses performed on data from each flight. κ_{Cont} and κ_{Marine} refer to analyses assuming a constant κ equivalent to values representative of continental (0.27) and marine (0.72) environments (Pringle et al., 2010). The Constant S.D. case assumes a constant aerosol number size distribution equivalent to the median value observed in the MBL during the campaign. Blacked dashed lines indicate closure error of $\pm20\%$. Marker size corresponds to the R^2 value computed from a linear fit of observed and predicted CCN from each flight. Note the split in the y-axis.

3.5. Sensitivity of Stratocumulus CDNC to Below-Cloud Aerosol Hygroscopicity

In order to directly investigate the sensitivity of N.E. Pacific stratocumulus CDNC to below-cloud aerosol properties, droplet activation was simulated using an aerosol-cloud parcel model constrained with detailed below-cloud aerosol measurements obtained from three cloud sampling passes performed during the campaign. While a number of previous cloud parcel modeling studies have assumed unimodal size distributions (Chen et al., 2016; Reutter et al., 2009 ; Ward et al., 2010), observed aerosol size distributions over the N.E. Pacific were frequently bimodal (Figure 3). As many current aerosol modules incorporated within global atmospheric chemistry models involve multiple aerosol size modes (Liu & Wang, 2010; Pringle et al., 2010; Rothenberg et al., 2018), we carried out parcel model runs to analyze CDNC sensitivity to properties of the Aitken and accumulation modes separately. Sensitivities were calculated following McFiggans et al. (2006), where $S(X_i) = \delta lnN_{CDNC}/\delta lnX_i$ and X_i is the parameter under investigation. Standard linear regressions of lnN_{CDNC} versus lnX_i were used to determine $S(X_i)$ values, as is convention (Reutter et al., 2009; Sánchez-Gácita et al., 2017; Ward et al., 2010). Measured aerosol and meteorological properties utilized as model constraints are summarized in Table 5. Sensitivity to hygroscopicity was computed across the range of κ = 0.2–0.6. Initial results confirmed that for observed MSc updraft velocities (w = 0.15–0.3 m s^{-1}), below-cloud particle number concentrations (~500–800 cm^{-3}), and typical hygroscopicities (κ ~ 0.2–0.4), properties of the Aitken mode have a minor impact on stratocumulus properties ($S(X_i)$ < 0.05), as minimum simulated activation diameters exceed 100 nm. Therefore, Figure 10 depicts the sensitivity of stratocumulus CDNC to properties of the accumulation mode and the simulated updraft velocity.

The average sensitivity of CDNC to aerosol hygroscopicity (0.19), while smaller than the sensitivity to size distribution parameters, is 39% as large as the sensitivity to the geometric mean diameter of the accumulation mode. This agrees with the consensus that particle size distribution properties have a larger influence on CCN concentration than particle composition (Dusek et al., 2006; McFiggans et al., 2006; Reutter et al., 2009), but also suggests accurate hygroscopicity reproduction should be included in future model improvement efforts. Observed below-cloud particle number concentrations and updraft velocities suggest that CCN activation occurs in the transitional regime according to the designations defined by Reutter et al. (2009), and simulated sensitivity to hygroscopicity agrees well with those previously reported for the transition regime (0.17–0.2) (Reutter et al., 2009; Ward et al., 2010).

Aging processes during transport likely lead to internally rather than externally mixed aerosol in the MBL. The simulated error in predicted CDNC when assuming fully externally mixed components is only 7.6–8.7% for the three modeled cases. This aligns with the observation of similarly accurate CCN closure results for the MBL when assuming internally or externally mixed components and a κ_{org} of 0.1 or larger. As the volume fraction of inorganic aerosol in the accumulation mode is likely to increase with increasing distance from the coast, this predicted mixing-state-related error may be an upper bound for marine conditions in general.

Previous aerosol-cloud parcel modeling studies have demonstrated that the sensitivity of predicted CDNC to aerosol hygroscopicity tends to decrease as bulk hygroscopicity increases, especially for the aerosol-limited and transitional aerosol activation regimes (Reutter et al., 2009; Sánchez-Gácita et al., 2017). If this is the case, accurate hygroscopicity characterization in marine regions subject to organic

Table 5

Below-Cloud Aerosol and Meteorological Data Used as Aerosol-Cloud-Parcel Model Constraints for Calculation of CDNC Sensitivities Depicted in Figure 10

Parameter	RF5-1	RF5-2	RF16
$N_{CN, Aitken}$ (cm^{-3})	296	301	128
$D_{pg, Aitken}$ (nm)	55	57	70
σ_{Aitken}	1.27	1.27	1.24
κ_{Aitken}	0.36	0.42	0.21
$N_{CN, Accum.}$ (cm^{-3})	492	465	406
$D_{pg, Accum.}$ (nm)	104	109	124
$\sigma_{Accum.}$	2.21	2.20	1.96
$\kappa_{Accum.}$	0.37	0.34	0.28
w (m s^{-1})	0.22	0.26	0.25
w/N_{CN} (m s^{-1} cm^{-3})	2.8×10^{-4}	3.4×10^{-4}	4.7×10^{-4}
Activation Regime	Trans.	Trans.	Trans.

Note. "Activation Regime" refers to the classifications of cloud droplet formation environments developed by Reutter et al. (2009). "Trans." = transitional.
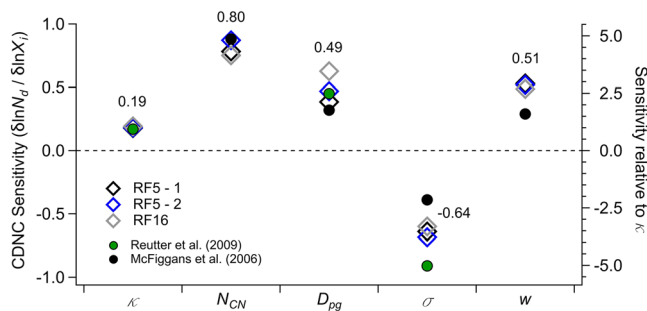
Figure 10. Sensitivity of calculated CDNC to accumulation mode aerosol hygroscopicity (κ), below-cloud aerosol particle number concentration (N_{CN}), accumulation mode geometric mean diameter (D_{pg}), accumulation mode standard deviation (σ), and updraft velocity (w). Data obtained during three cloud sampling passes were used as model constraints and are listed in Table 5. Numbers near each group of symbols represent average values from simulations in this study. Green symbols correspond to values reported by Reutter et al. (2009) for the transitional activation regime, while those in black correspond to values reported by McFiggans et al. (2006).

aerosol inputs, which contain aerosol with lower-than-average κ values, may be more important for global CDNC prediction accuracy than accurate hygroscopicity characterization in remote regions subject to aerosol sources with different, but elevated, hygroscopicities (e.g., ammonium sulfate [$\kappa = 0.61$] vs. sodium chloride [$\kappa = 1.28$]). To investigate this possibility, we calculated local CDNC sensitivity to aerosol hygroscopicity for four hypothetical marine aerosol size distributions. Rather than performing a linear regression on data obtained from a broad range of hygroscopicities, as was done for the data shown in Figure 10, local sensitivities refer to calculations performed on incremental variations in κ (e.g., $\kappa = 0.1$ vs. 0.2). Figure 11 displays the size distributions used as well as the sensitivity results. In order to span the likely range of size distributions observed in marine environments, the "Coastal" distribution is similar to median distributions observed during RF4 and RF5. A "Remote" distribution was generated using reported size distribution parameters from measurements over the remote subtropical N. Pacific by Ueda et al. (2016). Two additional size distributions were produced by interpolating between the "Coastal" and "Remote" distributions. Total particle concentrations in the simulations varied between 300 and 800 cm^{-3} depending on the size distribution used. Five different updraft velocities were simulated ($w = 0.1$–0.5 m s^{-1}), corresponding to the range typically observed within MSc over the Pacific (Zheng et al., 2016).

A few notable trends are evident in the results shown in Figure 11. As has been previously reported, CDNC sensitivity to aerosol hygroscopicity tends to decrease as hygroscopicity increases. However, even at low hygroscopicities, calculated sensitivities never exceed 0.3, suggesting that at a maximum, a 50% error in marine aerosol hygroscopicity should lead to an error of only 15% in predicted CDNC. Sensitivity slightly increases as the assumed particle concentration increases, and therefore, hygroscopicity is slightly less important in remote marine environments than in more polluted, coastal locations, as expected. In typical remote marine conditions ($\kappa \approx 0.6$) for instance, a 50% error in hygroscopicity is associated with only a ~2.5–7.5% error in predicted CDNC, while in coastal environments ($\kappa \approx 0.35$) the error is estimated to be ~7.5–15%.
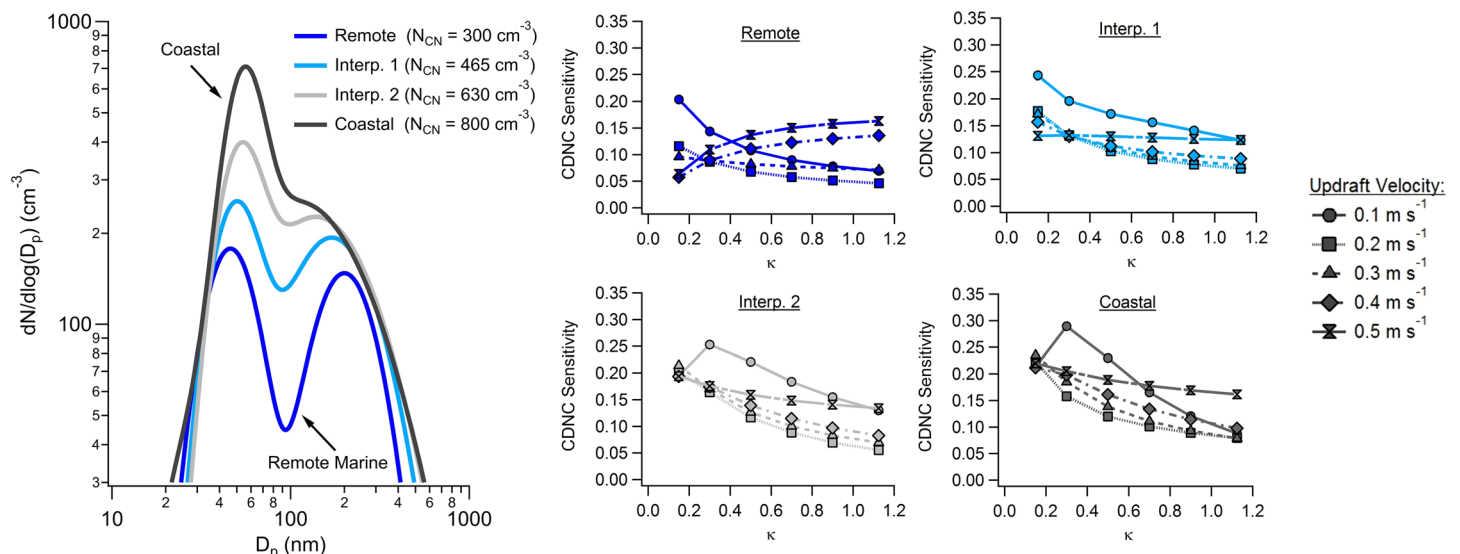

Figure 11. (Left) Aerosol number size distributions used as aerosol-cloud-parcel model inputs and (right) local CDNC sensitivities to aerosol hygroscopicity calculated using five updraft velocities. N_{CN} refers to the aerosol number concentration represented by each aerosol size distribution.
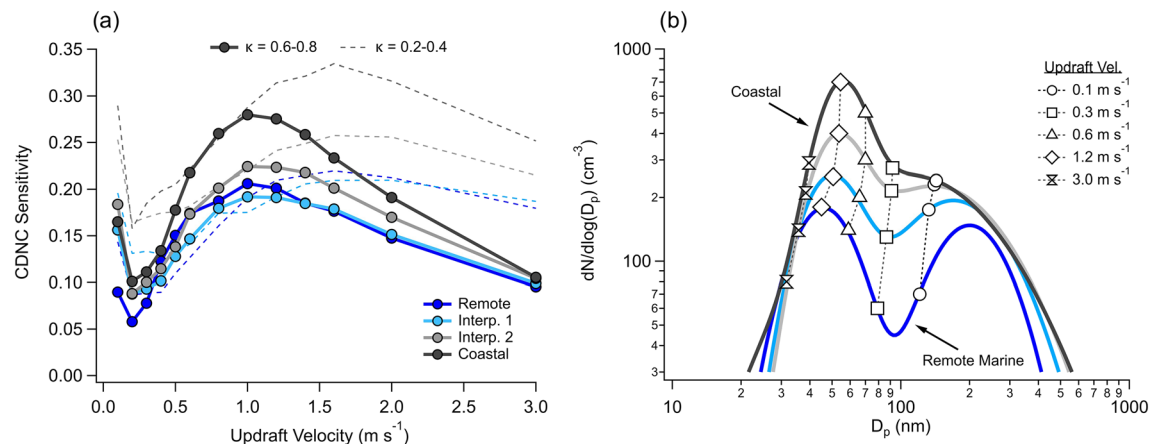
Figure 12. (a) Simulated local CDNC sensitivity to aerosol hygroscopicity in the range $\kappa = 0.6$–0.8 and $\kappa = 0.2$–0.4 as a function of updraft velocity. (b) Critical diameters (markers) calculated at the maximum supersaturation predicted by the aerosol-cloud-parcel model for five different updraft velocities assuming $\kappa = 0.6$.

When simulating certain combinations of updraft velocity and aerosol size distribution, the sensitivity of predicted CDNC to aerosol hygroscopicity does not decrease monotonically as hygroscopicity increases. Furthermore, at a given hygroscopicity value shown in Figure 11, CDNC sensitivity is a non-monotonic function of updraft velocity. Here, we demonstrate that these phenomena are a result of activation of the distinct Aitken aerosol mode. Variation in CDNC sensitivity to hygroscopicity with increasing updraft velocity is shown in Figure 12 for $\kappa = 0.6$–0.8. Local CDNC sensitivity to hygroscopicity initially decreases with increasing updraft velocity before increasing again at updraft velocities >0.2–0.3 m s^{-1}. This trend is consistent regardless of κ range analyzed; however, the shape of the curve becomes "stretched" horizontally as κ values decrease (Figure 12). Using a unimodal size distribution, Reutter et al. (2009) demonstrated that moving from the transitional to the aerosol-limited regime caused CDNC sensitivity to hygroscopicity to decline for all $\kappa > 0.05$. For the four marine size distributions simulated in this study, increasing the updraft velocity from 0.1 to 1.0 m s^{-1} shifts activation from the transitional regime to the aerosol-limited regime, implying CDNC sensitivity to hygroscopicity should subsequently decline. Our observation of the opposite phenomenon is due to the fact that at low ($w = 0.1$ m s^{-1}) and high ($w = 1$–1.5 m s^{-1}) updraft velocities, critical diameters produced within the rising air parcel occur near the peak of the accumulation and Aitken aerosol modes, respectively (Figure 12b). As the size distribution is peaked at these locations, subtle changes in aerosol hygroscopicity that induce small changes in the critical diameter result in a relatively large change in computed CDNC—hence elevated sensitivity to hygroscopicity. In contrast, for moderate ($w \sim 0.2$–0.3 m s^{-1}) updraft velocities, minimum critical diameters occur between the peaks of the Aitken and accumulation modes, and for very strong updraft velocities ($w > 1.5$–2 m s^{-1}) minimum critical diameters occur at sizes smaller than the peak of the Aitken mode, leading to lowered sensitivity (Figure 12b). This implies that in aerosol-limited environments with bimodal aerosol size distributions, the sensitivity of CDNC to hygroscopicity cannot necessarily be assumed to be negligible based solely on the ratio of the updraft velocity to particle number concentration. Ultimately, our results suggest that the sensitivity of marine CDNC to hygroscopicity is maximized in weak updraft conditions occurring in MSc ($w < 0.2$ m s^{-1}), where hygroscopicity of the accumulation, rather than the Aitken, mode is most relevant to accurate CDNC prediction, and in relatively strong updraft conditions ($0.5 < w < 2$ m s^{-1}) in either MSc or marine cumulus (Clarke et al., 1996), where Aitken mode hygroscopicity has a larger influence on CDNC than that of the accumulation mode.

4. Summary and Conclusions

Measurements of aerosol properties obtained over the N.E. Pacific Ocean during the MACAWS campaign in June and July 2018 were combined with results from an aerosol-cloud-parcel model to gain insight into aerosol hygroscopicity and its influence on CCN and MSc CDNC prediction in this environment. Three characteristic vertical regions were characterized, corresponding to the MBL, FT, and AC-OAL. Within the MBL,

flight-averaged hygroscopicities varied from values typical of continental environments ($\kappa = 0.27$), to those representative of remote marine locations ($\kappa = 0.72$) (Pringle et al., 2010). Distinct influences on MBL particle characteristics, including shipping emissions, entrainment from the AC-OAL, and transport from the remote Pacific, were identified through analysis of hygroscopicity data. In the AC-OAL, observed hygroscopicity suggests a dominant contribution of organic aerosol in both the Aitken and accumulation mode size ranges.

For the majority of flights, measured CCN concentrations could be reproduced within 20% using measurements of the aerosol size distribution, bulk hygroscopicity, and an assumption of either internally or externally mixed organic and inorganic components, in agreement with past results in non-urban locations (e.g., Ervens et al., 2010). Notably, for five of the seven flights, MBL CCN were better predicted when assuming a constant aerosol number size distribution derived from the median value measured in the MBL than when assuming a constant κ typical of remote marine locations (0.72).

Results from an aerosol-cloud-parcel model confirm that the sensitivity ($S(Xi) = \delta ln N_{CDNC}/\delta ln X_i$) of predicted CDNC to accumulation mode aerosol hygroscopicity (0.19) is substantially smaller than sensitivity to size distribution parameters, such as the accumulation mode geometric diameter (0.49) and standard deviation (-0.64). Simulations using a variety of possible MBL aerosol size distributions and hygroscopicities suggest that a 50% error in predicted hygroscopicity should rarely produce a CDNC error greater than 15%. However, model results further suggest that CDNC sensitivity to hygroscopicity does not monotonically decrease with increasing updraft velocity. Rather, sensitivity appears to decrease or remain constant with increasing updraft velocities from low to moderate values (e.g., 0.1–0.3 m s^{-1}) and then increase as updraft velocities increase further (>0.4 m s^{-1}) due to activation of the distinct Aitken mode of the aerosol size distribution. This phenomenon is observed despite the fact that at large updraft velocities (>0.4–0.5 m s^{-1}), marine conditions generally occupy the aerosol-limited regime of cloud droplet activation. Ultimately, CDNC sensitivity to hygroscopicity is predicted to be maximized in weak updraft conditions occurring in MSc (<0.2 m s^{-1}) and in strong updraft conditions (>0.5 m s^{-1}) expected to occur in either MSc or marine cumulus.

Data Availability Statement

Airborne field data used in this work can be accessed on the Figshare database (Sorooshian et al., 2017: https://doi.org/10.6084/m9.figshare.5099983.v10).

References

Ackerman, A. S., Toon, O. B., & Hobbs, P. V. (1993). Dissipation of marine stratiform clouds and collapse of the marine boundary layer due to the depletion of cloud condensation nuclei by clouds. *Science*, *262*(5131), 226–229. https://doi.org/10.1126/science.262.5131.226

Albrecht, B. A. (1989). Aerosols, cloud microphysics, and fractional cloudiness. *Science*, *245*(4923), 1227–1230. https://doi.org/10.1126/science.245.4923.1227

Alfarra, M. R., Good, N., Wyche, K. P., Hamilton, J. F., Monks, P. S., Lewis, A. C., & McFiggans, G. (2013). Water uptake is independent of the inferred composition of secondary aerosols derived from multiple biogenic VOCs. *Atmospheric Chemistry and Physics*, *13*(23), 11,769–11,789. https://doi.org/10.5194/acp-13-11769-2013

Almeida, G. P., Brito, J., Morales, C. A., Andrade, M. F., & Artaxo, P. (2014). Measured and modelled cloud condensation nuclei (CCN) concentration in São Paulo, Brazil: The importance of aerosol size-resolved chemical composition on CCN concentration prediction. *Atmospheric Chemistry and Physics*, *14*(14), 7559–7572. https://doi.org/10.5194/acp-14-7559-2014

Andreae, M. O., & Rosenfeld, D. (2008). Aerosol–cloud–precipitation interactions. Part 1. The nature and sources of cloud-active aerosols. *Earth-Science Reviews*, *89*(1), 13–41. https://doi.org/10.1016/j.earscirev.2008.03.001

Asa-Awuku, A., Moore, R. H., Nenes, A., Bahreini, R., Holloway, J. S., Brock, C. A., et al. (2011). Airborne cloud condensation nuclei measurements during the 2006 Texas Air Quality Study. *Journal of Geophysical Research*, *116*, D11201. https://doi.org/10.1029/2010JD014874

Asa-Awuku, A., Nenes, A., Gao, S., Flagan, R. C., & Seinfeld, J. H. (2010). Water-soluble SOA from alkene ozonolysis: Composition and droplet activation kinetics inferences from analysis of CCN activity. *Atmospheric Chemistry and Physics*, *10*(4), 1585–1597. https://doi.org/10.5194/acp-10-1585-2010

Berner, A. H., Bretherton, C. S., & Wood, R. (2015). Large eddy simulation of ship tracks in the collapsed marine boundary layer: A case study from the Monterey area ship track experiment. *Atmospheric Chemistry and Physics*, *15*(10), 5851–5871. https://doi.org/10.5194/acp-15-5851-2015

Bhattu, D., & Tripathi, S. N. (2015). CCN closure study: Effects of aerosol chemical composition and mixing state. *Journal of Geophysical Research: Atmospheres*, *120*, 766–783. https://doi.org/10.1002/2014JD021978

Bougiatioti, A., Nenes, A., Fountoukis, C., Kalivitis, N., Pandis, S. N., & Mihalopoulos, N. (2011). Size-resolved CCN distributions and activation kinetics of aged continental and marine aerosol. *Atmospheric Chemistry and Physics*, *11*(16), 8791–8808. https://doi.org/10.5194/acp-11-8791-2011

Brenguier, J.-L., Pawlowska, H., Schüller, L., Preusker, R., Fischer, J., & Fouquart, Y. (2000). Radiative properties of boundary layer clouds: Droplet effective radius versus number concentration. *Journal of the Atmospheric Sciences*, *57*(6), 803–821. https://doi.org/10.1175/1520-0469(2000)057%3C0803:RPOBLC%3E2.0.CO;2

Brioude, J., Cooper, O. R., Feingold, G., Trainer, M., Freitas, S. R., Kowal, D., et al. (2009). Effect of biomass burning on marine stratocumulus clouds off the California coast. *Atmospheric Chemistry and Physics*, *9*(22), 8841–8856. https://doi.org/10.5194/acp-9-8841-2009

Canagaratna, M. R., Jimenez, J. L., Kroll, J. H., Chen, Q., Kessler, S. H., Massoli, P., et al. (2015). Elemental ratio measurements of organic compounds using aerosol mass spectrometry: Characterization, improved calibration, and implications. *Atmospheric Chemistry and Physics*, *15*(1), 253–272. https://doi.org/10.5194/acp-15-253-2015

Cappa, C. D., Williams, E. J., Lack, D. A., Buffaloe, G. M., Coffman, D., Hayden, K. L., et al. (2014). A case study into the measurement of ship emissions from plume intercepts of the NOAA ship Miller Freeman. *Atmospheric Chemistry and Physics*, *14*(3), 1337–1352. https://doi.org/10.5194/acp-14-1337-2014

Carman, J. K., Rossiter, D. L., Khelif, D., Jonsson, H. H., Faloona, I. C., & Chuang, P. Y. (2012). Observational constraints on entrainment and the entrainment interface layer in stratocumulus. *Atmospheric Chemistry and Physics*, *12*(22), 11,135–11,152. https://doi.org/10.5194/acp-12-11135-2012

Chang, R. Y.-W., Liu, P. S. K., Leaitch, W. R., & Abbatt, J. P. D. (2007). Comparison between measured and predicted CCN concentrations at Egbert, Ontario: Focus on the organic aerosol fraction at a semi-rural site. *Atmospheric Environment*, *41*(37), 8172–8182. https://doi.org/10.1016/j.atmosenv.2007.06.039

Chang, R. Y.-W., Slowik, J. G., Shantz, N. C., Vlasenko, A., Liggio, J., Sjostedt, S. J., et al. (2010). The hygroscopicity parameter (κ) of ambient organic aerosol at a field site subject to biogenic and anthropogenic influences: Relationship to degree of aerosol oxidation. *Atmospheric Chemistry and Physics*, *10*(11), 5047–5064. https://doi.org/10.5194/acp-10-5047-2010

Chen, J., Liu, Y., Zhang, M., & Peng, Y. (2016). New understanding and quantification of the regime dependence of aerosol-cloud inter-action for studying aerosol-cloud indirect effects. *Geophysical Research Letters*, *43*, 1780–1787. https://doi.org/10.1002/2016GL067683

Chen, Y.-C., Xue, L., Lebo, Z. J., Wang, H., Rasmussen, R. M., & Seinfeld, J. H. (2011). A comprehensive numerical study of aerosol-cloud-precipitation interactions in marine stratocumulus. *Atmospheric Chemistry and Physics*, *11*(18), 9749–9769. https://doi.org/10.5194/acp-11-9749-2011

Clarke, A. D. (1993). Atmospheric nuclei in the Pacific midtroposphere: Their nature, concentration, and evolution. *Journal of Geophysical Research*, *98*(D11), 20,633–20,647. https://doi.org/10.1029/93JD00797

Clarke, A. D., Eisele, F., Kapustin, V. N., Moore, K., Tanner, D., Mauldin, L., et al. (1999). Nucleation in the equatorial free troposphere: Favorable environments during PEM-Tropics. *Journal of Geophysical Research*, *104*(D5), 5735–5744. https://doi.org/10.1029/98JD02303

Clarke, A. D., Freitag, S., Simpson, R. M. C., Hudson, J. G., Howell, S. G., Brekhovskikh, V. L., et al. (2013). Free troposphere as a major source of CCN for the equatorial pacific boundary layer: Long-range transport and teleconnections. *Atmospheric Chemistry and Physics*, *13*(15), 7511–7529. https://doi.org/10.5194/acp-13-7511-2013

Clarke, A. D., Li, Z., & Litchy, M. (1996). Aerosol dynamics in the equatorial Pacific marine boundary layer: Microphysics, diurnal cycles and entrainment. *Geophysical Research Letters*, *23*(7), 733–736. https://doi.org/10.1029/96GL00778

Clarke, A. D., Varner, J. L., Eisele, F., Mauldin, R. L., Tanner, D., & Litchy, M. (1998). Particle production in the remote marine atmosphere: Cloud outflow and subsidence during ACE 1. *Journal of Geophysical Research*, *103*(D13), 16,397–16,409. https://doi.org/10.1029/97JD02987

Coggon, M. M., Sorooshian, A., Wang, Z., Craven, J. S., Metcalf, A. R., Lin, J. J., et al. (2014). Observations of continental biogenic impacts on marine aerosol and clouds off the coast of California. *Journal of Geophysical Research: Atmospheres*, *119*, 6724–6748. https://doi.org/10.1002/2013JD021228

Coggon, M. M., Sorooshian, A., Wang, Z., Metcalf, A. R., Frossard, A. A., Lin, J. J., et al. (2012). Ship impacts on the marine atmosphere: Insights into the contribution of shipping emissions to the properties of marine aerosol and clouds. *Atmospheric Chemistry and Physics*, *12*(18), 8439–8458. https://doi.org/10.5194/acp-12-8439-2012

Collins, D. B., Ault, A. P., Moffet, R. C., Ruppel, M. J., Cuadra-Rodriguez, L. A., Guasco, T. L., et al. (2013). Impact of marine biogeo-chemistry on the chemical mixing state and cloud forming ability of nascent sea spray aerosol. *Journal of Geophysical Research: Atmospheres*, *118*, 8553–8565. https://doi.org/10.1002/jgrd.50598

Cubison, M. J., Ervens, B., Feingold, G., Docherty, K. S., Ulbrich, I. M., Shields, L., et al. (2008). The influence of chemical composition and mixing state of Los Angeles urban aerosol on CCN number and cloud properties. *Atmospheric Chemistry and Physics*, *8*(18), 5649–5667. https://doi.org/10.5194/acp-8-5649-2008

Dadashazar, H., Braun, R. A., Crosbie, E., Chuang, P. Y., Woods, R. K., Jonsson, H. H., & Sorooshian, A. (2018). Aerosol characteristics in the entrainment interface layer in relation to the marine boundary layer and free troposphere. *Atmospheric Chemistry and Physics*, *18*(3), 1495–1506. https://doi.org/10.5194/acp-18-1495-2018

DeCarlo, P. F., Kimmel, J. R., Trimborn, A., Northway, M. J., Jayne, J. T., Aiken, A. C., et al. (2006). Field-deployable, high-resolution, time-of-flight aerosol mass spectrometer. *Analytical Chemistry*, *78*(24), 8281–8289. https://doi.org/10.1021/ac061249n

Draxler, R. R., & Hess, G. D. (1997). Description of the HYSPLIT_4 modeling system. *NOAA. Tech. Memo. ERL ARL-224* (pp. 1–24). Silver Spring: NOAA Air Resources Laboratory.

Draxler, R. R., & Hess, G. D. (1998). An overview of the HYSPLIT_4 modelling system for trajectories, dispersion, and deposition. *Australian Meteorological Magazine*, *47*, 295–308.

Duplissy, J., DeCarlo, P. F., Dommen, J., Alfarra, M. R., Metzger, A., Barmpadimos, I., et al. (2011). Relating hygroscopicity and compo-sition of organic aerosol particulate matter. *Atmospheric Chemistry and Physics*, *11*(3), 1155–1165. https://doi.org/10.5194/acp-11-1155-2011

Duplissy, J., Gysel, M., Alfarra, M. R., Dommen, J., Metzger, A., Prevot, A. S. H., et al. (2008). Cloud forming potential of secondary organic aerosol under near atmospheric conditions. *Geophysical Research Letters*, *35*, L03818. https://doi.org/10.1029/2007GL031075

Dusek, U., Frank, G. P., Hildebrandt, L., Curtius, J., Schneider, J., Walter, S., et al. (2006). Size matters more than chemistry for cloud-nucleating ability of aerosol particles. *Science*, *312*(5778), 1375–1378. https://doi.org/10.1126/science.1125261

Ervens, B., Cubison, M., Andrews, E., Feingold, G., Ogren, J. A., Jimenez, J. L., et al. (2007). Prediction of cloud condensation nucleus number concentration using measurements of aerosol size distributions and composition and light scattering enhancement due to humidity. *Journal of Geophysical Research*, *112*, D10S32. https://doi.org/10.1029/2006JD007426

Ervens, B., Cubison, M. J., Andrews, E., Feingold, G., Ogren, J. A., Jimenez, J. L., et al. (2010). CCN predictions using simplified assump-tions of organic aerosol composition and mixing state: A synthesis from six different locations. *Atmospheric Chemistry and Physics*, *10*(10), 4795–4807. https://doi.org/10.5194/acp-10-4795-2010

Faloona, I. (2009). Sulfur processing in the marine atmospheric boundary layer: A review and critical assessment of modeling uncertainties. *Atmospheric Environment*, *43*(18), 2841–2854. https://doi.org/10.1016/j.atmosenv.2009.02.043

Fierce, L., Riemer, N., & Bond, T. C. (2016). Toward reduced representation of mixing state for simulating aerosol effects on climate. *Bulletin of the American Meteorological Society*, *98*(5), 971–980. https://doi.org/10.1175/BAMS-D-16-0028.1

Frosch, M., Bilde, M., Nenes, A., Praplan, A. P., Jurányi, Z., Dommen, J., et al. (2013). CCN activity and volatility of β-caryophyllene secondary organic aerosol. *Atmospheric Chemistry and Physics*, *13*(4), 2283–2297. https://doi.org/10.5194/acp-13-2283-2013

Gerber, H., Arends, B. G., & Ackerman, A. S. (1994). New microphysics sensor for aircraft use. *Atmospheric Research*, *31*(4), 235–252. https://doi.org/10.1016/0169-8095(94)90001-9

Goren, T., & Rosenfeld, D. (2012). Satellite observations of ship emission induced transitions from broken to closed cell marine stratocumulus over large areas. *Journal of Geophysical Research*, *117*, D17206. https://doi.org/10.1029/2012JD017981

Gunthe, S. S., King, S. M., Rose, D., Chen, Q., Roldin, P., Farmer, D. K., et al. (2009). Cloud condensation nuclei in pristine tropical rainforest air of Amazonia: Size-resolved measurements and modeling of atmospheric aerosol composition and CCN activity. *Atmospheric Chemistry and Physics*, *9*(19), 7551–7575. https://doi.org/10.5194/acp-9-7551-2009

Hallquist, M., Wenger, J. C., Baltensperger, U., Rudich, Y., Simpson, D., Claeys, M., et al. (2009). The formation, properties and impact of secondary organic aerosol: Current and emerging issues. *Atmospheric Chemistry and Physics*, *9*(14), 5155–5236. https://doi.org/10.5194/acp-9-5155-2009

Heald, C. L., Jacob, D. J., Park, R. J., Russell, L. M., Huebert, B. J., Seinfeld, J. H., et al. (2005). A large organic aerosol source in the free troposphere missing from current models. *Geophysical Research Letters*, *32*, L18809. https://doi.org/10.1029/2005GL023831

Hegg, D. A., Covert, D. S., Jonsson, H., & Covert, P. A. (2005). Determination of the transmission efficiency of an aircraft aerosol inlet. *Aerosol Science and Technology*, *39*(10), 966–971. https://doi.org/10.1080/02786820500377814

Hegg, D. A., Covert, D. S., Jonsson, H. H., & Woods, R. K. (2010). The contribution of anthropogenic aerosols to aerosol light-scattering and CCN activity in the California coastal zone. *Atmospheric Chemistry and Physics*, *10*(15), 7341–7351. https://doi.org/10.5194/acp-10-7341-2010

Hersey, S. P., Sorooshian, A., Murphy, S. M., Flagan, R. C., & Seinfeld, J. H. (2009). Aerosol hygroscopicity in the marine atmosphere: A closure study using high-time-resolution, multiple-RH DASH-SP and size-resolved C-ToF-AMS data. *Atmospheric Chemistry and Physics*, *9*(7), 2543–2554. https://doi.org/10.5194/acp-9-2543-2009

Jimenez, J. L., Canagaratna, M. R., Donahue, N. M., Prevot, A. S. H., Zhang, Q., Kroll, J. H., et al. (2009). Evolution of organic aerosols in the atmosphere. *Science*, *326*(5959), 1525–1529. https://doi.org/10.1126/science.1180353

Kanakidou, M., Seinfeld, J. H., Pandis, S. N., Barnes, I., Dentener, F. J., Facchini, M. C., et al. (2005). Organic aerosol and global climate modelling: A review. *Atmospheric Chemistry and Physics*, *5*(4), 1053–1123. https://doi.org/10.5194/acp-5-1053-2005

Kawana, K., Nakayama, T., & Mochida, M. (2016). Hygroscopicity and CCN activity of atmospheric aerosol particles and their relation to organics: Characteristics of urban aerosols in Nagoya, Japan. *Journal of Geophysical Research: Atmospheres*, *121*, 4100–4121. https://doi.org/10.1002/2015JD023213

Köhler, H. (1936). The nucleus in and the growth of hygroscopic droplets. *Transactions of the Faraday Society*, *32*(0), 1152–1161. https://doi.org/10.1039/TF9363201152

Kreidenweis, S. M., & Asa-Awuku, A. (2014). 5.13—Aerosol Hygroscopicity: Particle water content and its role in atmospheric processes. In H. D. Holland, & K. K. Turekian (Eds.), *Treatise on geochemistry* (Second ed.pp. 331–361). Oxford: Elsevier. https://doi.org/10.1016/B978-0-08-095975-7.00418-6

Lack, D. A., Cappa, C. D., Langridge, J., Bahreini, R., Buffaloe, G., Brock, C., et al. (2011). Impact of fuel quality regulation and speed reductions on shipping emissions: Implications for climate and air quality. *Environmental Science & Technology*, *45*(20), 9052–9060. https://doi.org/10.1021/es2013424

Lambe, A. T., Onasch, T. B., Massoli, P., Croasdale, D. R., Wright, J. P., Ahern, A. T., et al. (2011). Laboratory studies of the chemical composition and cloud condensation nuclei (CCN) activity of secondary organic aerosol (SOA) and oxidized primary organic aerosol (OPOA). *Atmospheric Chemistry and Physics*, *11*(17), 8913–8928. https://doi.org/10.5194/acp-11-8913-2011

Lance, S., Nenes, A., Mazzoleni, C., Dubey, M. K., Gates, H., Varutbangkul, V., et al. (2009). Cloud condensation nuclei activity, closure, and droplet growth kinetics of Houston aerosol during the Gulf of Mexico Atmospheric Composition and Climate Study (GoMACCS). *Journal of Geophysical Research*, *114*, D00F15. https://doi.org/10.1029/2008JD011699

Lance, S., Nenes, A., Medina, J., & Smith, J. N. (2006). Mapping the operation of the DMT continuous flow CCN counter. *Aerosol Science and Technology*, *40*(4), 242–254. https://doi.org/10.1080/02786820500543290

Latham, J., Rasch, P., Chen, C.-C., Kettles, L., Gadian, A., Gettelman, A., et al. (2008). Global temperature stabilization via controlled albedo enhancement of low-level maritime clouds. *Philosophical Transactions of the Royal Society A: Mathematical, Physical and Engineering Sciences*, *366*(1882), 3969–3987. https://doi.org/10.1098/rsta.2008.0137

Levin, E. J. T., Prenni, A. J., Palm, B. B., Day, D. A., Campuzano-Jost, P., Winkler, P. M., et al. (2014). Size-resolved aerosol composition and its link to hygroscopicity at a forested site in Colorado. *Atmospheric Chemistry and Physics*, *14*(5), 2657–2667. https://doi.org/10.5194/acp-14-2657-2014

Liu, X., & Wang, J. (2010). How important is organic aerosol hygroscopicity to aerosol indirect forcing? *Environmental Research Letters*, *5*(4), 044010. https://doi.org/10.1088/1748-9326/5/4/044010

MacDonald, A. B., Dadashazar, H., Chuang, P. Y., Crosbie, E., Wang, H., Wang, Z., et al. (2018). Characteristic vertical profiles of cloud water composition in marine stratocumulus clouds and relationships with precipitation. *Journal of Geophysical Research: Atmospheres*, *123*, 3704–3723. https://doi.org/10.1002/2017JD027900

Mardi, A. H., Dadashazar, H., MacDonald, A. B., Braun, R. A., Crosbie, E., Xian, P., et al. (2018). Biomass burning plumes in the vicinity of the California coast: Airborne characterization of physicochemical properties, heating rates, and spatiotemporal features. *Journal of Geophysical Research: Atmospheres*, *123*, 13,560–13,582. https://doi.org/10.1029/2018JD029134

Massoli, P., Lambe, A. T., Ahern, A. T., Williams, L. R., Ehn, M., Mikkilä, J., et al. (2010). Relationship between aerosol oxidation level and hygroscopic properties of laboratory generated secondary organic aerosol (SOA) particles. *Geophysical Research Letters*, *37*, L24801. https://doi.org/10.1029/2010GL045258

Mauldin, R. L., Tanner, D. J., Heath, J. A., Huebert, B. J., & Eisele, F. L. (1999). Observations of H2SO4 and MSA during PEM-Tropics-A. *Journal of Geophysical Research*, *104*(D5), 5801–5816. https://doi.org/10.1029/98JD02612

McFiggans, G., Artaxo, P., Baltensperger, U., Coe, H., Facchini, M. C., Feingold, G., et al. (2006). The effect of physical and chemical aerosol properties on warm cloud droplet activation. *Atmospheric Chemistry and Physics*, *6*(9), 2593–2649. https://doi.org/10.5194/acp-6-2593-2006

Medina, J., Nenes, A., Sotiropoulou, R.-E. P., Cottrell, L. D., Ziemba, L. D., Beckman, P. J., & Griffin, R. J. (2007). Cloud condensation nuclei closure during the International Consortium for Atmospheric Research on Transport and Transformation 2004 campaign: Effects of size-resolved composition. *Journal of Geophysical Research*, *112*, D10S31. https://doi.org/10.1029/2006JD007588

Mei, F., Setyan, A., Zhang, Q., & Wang, J. (2013). CCN activity of organic aerosols observed downwind of urban emissions during CARES. *Atmospheric Chemistry and Physics*, *13*(24), 12,155–12,169. https://doi.org/10.5194/acp-13-12155-2013

Middlebrook, A. M., Bahreini, R., Jimenez, J. L., & Canagaratna, M. R. (2012). Evaluation of composition-dependent collection efficiencies for the aerodyne aerosol mass spectrometer using field data. *Aerosol Science and Technology*, *46*(3), 258–271. https://doi.org/10.1080/02786826.2011.620041

Modini, R. L., Frossard, A. A., Ahlm, L., Russell, L. M., Corrigan, C. E., Roberts, G. C., et al. (2015). Primary marine aerosol-cloud interactions off the coast of California. *Journal of Geophysical Research: Atmospheres*, *120*, 4282–4303. https://doi.org/10.1002/2014JD022963

Moore, R. H., Bahreini, R., Brock, C. A., Froyd, K. D., Cozic, J., Holloway, J. S., et al. (2011). Hygroscopicity and composition of Alaskan Arctic CCN during April 2008. *Atmospheric Chemistry and Physics*, *11*(22), 11,807–11,825. https://doi.org/10.5194/acp-11-11807-2011

Moore, R. H., Cerully, K., Bahreini, R., Brock, C. A., Middlebrook, A. M., & Nenes, A. (2012). Hygroscopicity and composition of California CCN during summer 2010. *Journal of Geophysical Research*, *117*, D00V12. https://doi.org/10.1029/2011JD017352

Murphy, S. M., Agrawal, H., Sorooshian, A., Padró, L. T., Gates, H., Hersey, S., et al. (2009). Comprehensive simultaneous shipboard and airborne characterization of exhaust from a modern container ship at sea. *Environmental Science & Technology*, *43*(13), 4626–4640. https://doi.org/10.1021/es802413j

Nenes, A., Pandis, S. N., & Pilinis, C. (1998). ISORROPIA: A new thermodynamic equilibrium model for multiphase multicomponent inorganic aerosols. *Aquatic Geochemistry*, *4*(1), 123–152. https://doi.org/10.1023/A:1009604003981

Oreopoulos, L., & Platnick, S. (2008). Radiative susceptibility of cloudy atmospheres to droplet number perturbations: 2. Global analysis from MODIS. *Journal of Geophysical Research*, *113*, D14S21. https://doi.org/10.1029/2007JD009655

Paatero, P., & Tapper, U. (1994). Positive matrix factorization: a non-negative factor model with optimal utilization of error estimates of data values. *Environmetrics*, *5*(2), 111–126. https://doi.org/10.1002/env.3170050203

Petters, M. D., & Kreidenweis, S. M. (2007). A single parameter representation of hygroscopic growth and cloud condensation nucleus activity. *Atmospheric Chemistry and Physics*, *7*(8), 1961–1971. https://doi.org/10.5194/acp-7-1961-2007

Platnick, S., & Twomey, S. (1994). Determining the susceptibility of cloud albedo to changes in droplet concentration with the advanced very high resolution radiometer. *Journal of Applied Meteorology*, *33*(3), 334–347. https://doi.org/10.1175/1520-0450(1994)033%3C0334:DTSOCA%3E2.0.CO;2

Prabhakar, G., Ervens, B., Wang, Z., Maudlin, L. C., Coggon, M. M., Jonsson, H. H., et al. (2014). Sources of nitrate in stratocumulus cloud water: Airborne measurements during the 2011 E-PEACE and 2013 NiCE studies. *Atmospheric Environment*, *97*, 166–173. https://doi.org/10.1016/j.atmosenv.2014.08.019

Pringle, K. J., Tost, H., Pozzer, A., Pöschl, U., & Lelieveld, J. (2010). Global distribution of the effective aerosol hygroscopicity parameter for CCN activation. *Atmospheric Chemistry and Physics*, *10*(12), 5241–5255. https://doi.org/10.5194/acp-10-5241-2010

Pruppacher, H. R., & Klett, J. D. (1997). *Microphysics of clouds and precipitation*. Dordrecht, The Netherlands: Kluwer.

Quinn, P. K., Bates, T. S., Coffman, D. J., & Covert, D. S. (2008). Influence of particle size and chemistry on the cloud nucleating properties of aerosols. *Atmospheric Chemistry and Physics*, *8*(4), 1029–1042. https://doi.org/10.5194/acp-8-1029-2008

Raes, F. (1995). Entrainment of free tropospheric aerosols as a regulating mechanism for cloud condensation nuclei in the remote marine boundary layer. *Journal of Geophysical Research*, *100*(D2), 2893–2903. https://doi.org/10.1029/94JD02832

Randall, D. A., Coakley, J. A., Fairall, C. W., Kropfli, R. A., & Lenschow, D. H. (1984). Outlook for research on subtropical marine stratiform clouds. *Bulletin of the American Meteorological Society*, *65*(12), 1290–1301. https://doi.org/10.1175/1520-0477(1984)065%3C1290:OFROSM%3E2.0.CO;2

Ren, J., Zhang, F., Wang, Y., Collins, D., Fan, X., Jin, X., et al. (2018). Using different assumptions of aerosol mixing state and chemical composition to predict CCN concentrations based on field measurements in urban Beijing. *Atmospheric Chemistry and Physics*, *18*(9), 6907–6921. https://doi.org/10.5194/acp-18-6907-2018

Reutter, P., Su, H., Trentmann, J., Simmel, M., Rose, D., Gunthe, S. S., et al. (2009). Aerosol- and updraft-limited regimes of cloud droplet formation: Influence of particle number, size and hygroscopicity on the activation of cloud condensation nuclei (CCN). *Atmospheric Chemistry and Physics*, *9*(18), 7067–7080. https://doi.org/10.5194/acp-9-7067-2009

Roberts, G., Mauger, G., Hadley, O., & Ramanathan, V. (2006). North American and Asian aerosols over the eastern Pacific Ocean and their role in regulating cloud condensation nuclei. *Journal of Geophysical Research*, *111*, D13205. https://doi.org/10.1029/2005JD006661

Roberts, G. C., Day, D. A., Russell, L. M., Dunlea, E. J., Jimenez, J. L., Tomlinson, J. M., et al. (2010). Characterization of particle cloud droplet activity and composition in the free troposphere and the boundary layer during INTEX-B. *Atmospheric Chemistry and Physics*, *10*(14), 6627–6644. https://doi.org/10.5194/acp-10-6627-2010

Roberts, G. C., & Nenes, A. (2005). A continuous-flow streamwise thermal-gradient CCN chamber for atmospheric measurements. *Aerosol Science and Technology*, *39*(3), 206–221. https://doi.org/10.1080/027868290913988

Rose, D., Gunthe, S. S., Mikhailov, E., Frank, G. P., Dusek, U., Andreae, M. O., & Pöschl, U. (2008). Calibration and measurement uncertainties of a continuous-flow cloud condensation nuclei counter (DMT-CCNC): CCN activation of ammonium sulfate and sodium chloride aerosol particles in theory and experiment. *Atmospheric Chemistry and Physics*, *8*(5), 1153–1179. https://doi.org/10.5194/acp-8-1153-2008

Rose, D., Gunthe, S. S., Su, H., Garland, R. M., Yang, H., Berghof, M., et al. (2011). Cloud condensation nuclei in polluted air and biomass burning smoke near the mega-city Guangzhou, China—Part 2: Size-resolved aerosol chemical composition, diurnal cycles, and externally mixed weakly CCN-active soot particles. *Atmospheric Chemistry and Physics*, *11*(6), 2817–2836. https://doi.org/10.5194/acp-11-2817-2011

Rose, D., Nowak, A., Achtert, P., Wiedensohler, A., Hu, M., Shao, M., et al. (2010). Cloud condensation nuclei in polluted air and biomass burning smoke near the mega-city Guangzhou, China—Part 1: Size-resolved measurements and implications for the modeling of aerosol particle hygroscopicity and CCN activity. *Atmospheric Chemistry and Physics*, *10*(7), 3365–3383. https://doi.org/10.5194/acp-10-3365-2010

Rosenfeld, D. (2006). Aerosol-cloud interactions control of earth radiation and latent heat release budgets. *Space Science Reviews*, *125*(1-4), 149–157. https://doi.org/10.1007/s11214-006-9053-6

Rosenfeld, D., Andreae, M. O., Asmi, A., Chin, M., de Leeuw, G., Donovan, D. P., et al. (2014). Global observations of aerosol-cloud-precipitation-climate interactions. *Reviews of Geophysics*, *52*, 750–808. https://doi.org/10.1002/2013RG000441

Rosenfeld, D., Zhu, Y., Wang, M., Zheng, Y., Goren, T., & Yu, S. (2019). Aerosol-driven droplet concentrations dominate coverage and water of oceanic low-level clouds. *Science*, *363*, eaav0566. https://doi.org/10.1126/science.aav0566

Rothenberg, D., Avramov, A., & Wang, C. (2018). On the representation of aerosol activation and its influence on model-derived estimates of the aerosol indirect effect. *Atmospheric Chemistry and Physics*, *18*(11), 7961–7983. https://doi.org/10.5194/acp-18-7961-2018

Royalty, T. M., Phillips, B. N., Dawson, K. W., Reed, R., Meskhidze, N., & Petters, M. D. (2017). Aerosol properties observed in the subtropical North Pacific boundary layer. *Journal of Geophysical Research: Atmospheres*, *122*, 9990–10,012. https://doi.org/10.1002/2017JD026897

Russell, L. M., Sorooshian, A., Seinfeld, J. H., Albrecht, B. A., Nenes, A., Ahlm, L., et al. (2013). Eastern Pacific emitted aerosol cloud experiment. *Bulletin of the American Meteorological Society*, *94*(5), 709–729. https://doi.org/10.1175/BAMS-D-12-00015.1

Sanchez, K. J., Russell, L. M., Modini, R. L., Frossard, A. A., Ahlm, L., Corrigan, C. E., et al. (2016). Meteorological and aerosol effects on marine cloud microphysical properties. *Journal of Geophysical Research: Atmospheres*, *121*, 4142–4161. https://doi.org/10.1002/2015JD024595

Sánchez-Gácita, M., Longo, K. M., Freire, J. L. M., Freitas, S. R., & Martin, S. T. (2017). Impact of mixing state and hygroscopicity on CCN activity of biomass burning aerosol in Amazonia. *Atmospheric Chemistry and Physics*, *17*(3), 2373–2392. https://doi.org/10.5194/acp-17-2373-2017

Seinfeld, J. H., Bretherton, C., Carslaw, K. S., Coe, H., DeMott, P. J., Dunlea, E. J., et al. (2016). Improving our fundamental understanding of the role of aerosol−cloud interactions in the climate system. *PNAS*, *113*(21), 5781–5790. https://doi.org/10.1073/pnas.1514043113

Sorooshian, A., Anderson, B., Bauer, S. E., Braun, R. A., Cairns, B., Crosbie, E., et al. (2019). Aerosol-cloud-meteorology interaction airborne field investigations: Using lessons learned from the US West Coast in the design of ACTIVATE off the US East Coast. *Bulletin of the American Meteorological Society*, *100*(8), 1511–1528. https://doi.org/10.1175/BAMS-D-18-0100.1

Sorooshian, A., Lu, M.-L., Brechtel, F. J., Jonsson, H., Feingold, G., Flagan, R. C., & Seinfeld, J. H. (2007). On the source of organic acid aerosol layers above clouds. *Environmental Science & Technology*, *41*(13), 4647–4654. https://doi.org/10.1021/es0630442

Sorooshian, A., MacDonald, A. B., Dadashazar, H., Bates, K. H., Coggon, M. M., Craven, J. S., et al. (2017). A multi-year data set on aerosol-cloud-precipitation-meteorology interactions for marine stratocumulus clouds. *Figshare Dataset*. https://doi.org/10.6084/m9.figshare.5099983.v10

Sorooshian, A., MacDonald, A. B., Dadashazar, H., Bates, K. H., Coggon, M. M., Craven, J. S., et al. (2018). A multi-year data set on aerosol-cloud-precipitation-meteorology interactions for marine stratocumulus clouds. *Scientific Data*, *5*, 180026. https://doi.org/10.1038/sdata.2018.26

Sorooshian, A., Ng, N. L., Chan, A. W. H., Feingold, G., Flagan, R. C., & Seinfeld, J. H. (2007). Particulate organic acids and overall water-soluble aerosol composition measurements from the 2006 Gulf of Mexico Atmospheric Composition and Climate Study (GoMACCS). *Journal of Geophysical Research*, *112*, D13201. https://doi.org/10.1029/2007JD008537

Sorooshian, A., Padró, L. T., Nenes, A., Feingold, G., McComiskey, A., Hersey, S. P., et al. (2009). On the link between ocean biota emissions, aerosol, and maritime clouds: Airborne, ground, and satellite measurements off the coast of California. *Global Biogeochemical Cycles*, *23*, GB4007. https://doi.org/10.1029/2009GB003464

Sotiropoulou, R.-E. P., Nenes, A., Adams, P. J., & Seinfeld, J. H. (2007). Cloud condensation nuclei prediction error from application of Köhler theory: Importance for the aerosol indirect effect. *Journal of Geophysical Research*, *112*, D12202. https://doi.org/10.1029/2006JD007834

Stein, A. F., Draxler, R. R., Rolph, G. D., Stunder, B. J. B., Cohen, M. D., & Ngan, F. (2015). NOAA's HYSPLIT atmospheric transport and dispersion modeling system. *Bulletin of the American Meteorological Society*, *96*(12), 2059–2077. https://doi.org/10.1175/BAMS-D-14-00110.1

Stevens, B., & Brenguier, J.-L. (2009). *Cloud-controlling factors: Low clouds*. Cambridge, MA: The MIT Press. Retrieved from https://mitpress.universitypressscholarship.com/view/, https://doi.org/10.7551/mitpress/9780262012874.001.0001/upso-9780262012874-chapter-8

Thalman, R., de Sá, S. S., Palm, B. B., Barbosa, H. M. J., Pöhlker, M. L., Alexander, M. L., et al. (2017). CCN activity and organic hygroscopicity of aerosols downwind of an urban region in central Amazonia: Seasonal and diel variations and impact of anthropogenic emissions. *Atmospheric Chemistry and Physics*, *17*(19), 11,779–11,801. https://doi.org/10.5194/acp-17-11779-2017

Twomey, S. (1977). The influence of pollution on the shortwave albedo of clouds. *Journal of the Atmospheric Sciences*, *34*(7), 1149–1152. https://doi.org/10.1175/1520-0469(1977)034%3C1149:TIOPOT%3E2.0.CO;2

Ueda, S., Miura, K., Kawata, R., Furutani, H., Uematsu, M., Omori, Y., & Tanimoto, H. (2016). Number–size distribution of aerosol particles and new particle formation events in tropical and subtropical Pacific Oceans. *Atmospheric Environment*, *142*, 324–339. https://doi.org/10.1016/j.atmosenv.2016.07.055

VanReken, T. M., Rissman, T. A., Roberts, G. C., Varutbangkul, V., Jonsson, H. H., Flagan, R. C., & Seinfeld, J. H. (2003). Toward aerosol/cloud condensation nuclei (CCN) closure during CRYSTAL-FACE. *Journal of Geophysical Research*, *108*(D20), 4633. https://doi.org/10.1029/2003JD003582

Wang, J., Cubison, M. J., Aiken, A. C., Jimenez, J. L., & Collins, D. R. (2010). The importance of aerosol mixing state and size-resolved composition on CCN concentration and the variation of the importance with atmospheric aging of aerosols. *Atmospheric Chemistry and Physics*, *10*(15), 7267–7283. https://doi.org/10.5194/acp-10-7267-2010

Wang, J., Lee, Y.-N., Daum, P. H., Jayne, J., & Alexander, M. L. (2008). Effects of aerosol organics on cloud condensation nucleus (CCN) concentration and first indirect aerosol effect. *Atmospheric Chemistry and Physics*, *8*(21), 6325–6339. https://doi.org/10.5194/acp-8-6325-2008

Wang, J., Shilling, J. E., Liu, J., Zelenyuk, A., Bell, D. M., Petters, M. D., et al. (2019). Cloud droplet activation of secondary organic aerosol is mainly controlled by molecular weight, not water solubility. *Atmospheric Chemistry and Physics*, *19*(2), 941–954. https://doi.org/10.5194/acp-19-941-2019

Wang, Z., Ramirez, M. M., Dadashazar, H., MacDonald, A. B., Crosbie, E., Bates, K. H., et al. (2016). Contrasting cloud composition between coupled and decoupled marine boundary layer clouds. *Journal of Geophysical Research: Atmospheres*, *121*, 11,679–11,691. https://doi.org/10.1002/2016JD025695

Ward, D. S., Eidhammer, T., Cotton, W. R., & Kreidenweis, S. M. (2010). The role of the particle size distribution in assessing aerosol composition effects on simulated droplet activation. *Atmospheric Chemistry and Physics*, *10*(12), 5435–5447. https://doi.org/10.5194/acp-10-5435-2010

Wonaschütz, A., Coggon, M., Sorooshian, A., Modini, R., Frossard, A. A., Ahlm, L., et al. (2013). Hygroscopic properties of smoke-generated organic aerosol particles emitted in the marine atmosphere. *Atmospheric Chemistry and Physics*, *13*(19), 9819–9835. https://doi.org/10.5194/acp-13-9819-2013

Wood, R. (2012). Stratocumulus clouds. *Monthly Weather Review*, *140*(8), 2373–2423. https://doi.org/10.1175/MWR-D-11-00121.1

Yakobi-Hancock, J. D., Ladino, L. A., Bertram, A. K., Huffman, J. A., Jones, K., Leaitch, W. R., et al. (2014). CCN activity of size-selected aerosol at a Pacific coastal location. *Atmospheric Chemistry and Physics*, *14*(22), 12,307–12,317. https://doi.org/10.5194/acp-14-12307-2014

Zhao, D. F., Buchholz, A., Kortner, B., Schlag, P., Rubach, F., Kiendler-Scharr, A., et al. (2015). Size-dependent hygroscopicity parameter (κ) and chemical composition of secondary organic cloud condensation nuclei. *Geophysical Research Letters*, *42*, 10,920–10,928. https://doi.org/10.1002/2015GL066497

Zheng, Y., Rosenfeld, D., & Li, Z. (2016). Quantifying cloud base updraft speeds of marine stratocumulus from cloud top radiative cooling. *Geophysical Research Letters*, *43*, 11,407–11,413. https://doi.org/10.1002/2016GL071185

References From the Supporting Information

Aiken, A. C., DeCarlo, P. F., Kroll, J. H., Worsnop, D. R., Huffman, J. A., Docherty, K. S., et al. (2008). O/C and OM/OC ratios of primary, secondary, and ambient organic aerosols with high-resolution time-of-flight aerosol mass spectrometry. *Environmental Science &Technology*, *42*(12), 4478–4485. https://doi.org/10.1021/es703009q

Bahreini, R., Ervens, B., Middlebrook, A. M., Warneke, C., de Gouw, J. A., DeCarlo, P. F., et al. (2009). Organic aerosol formation in urban and industrial plumes near Houston and Dallas, Texas. *Journal of Geophysical Research*, *114*, D00F16. https://doi.org/10.1029/2008JD011493

Frossard, A. A., Russell, L. M., Burrows, S. M., Elliott, S. M., Bates, T. S., & Quinn, P. K. (2014). Sources and composition of submicron organic mass in marine aerosol particles. *Journal of Geophysical Research: Atmospheres*, *119*, 12,977–13,003. https://doi.org/10.1002/2014JD021913

Hegg, D. A., Covert, D. S., & Jonsson, H. H. (2008). Measurements of size-resolved hygroscopicity in the California coastal zone. *Atmospheric Chemistry and Physics*, *8*(23), 7193–7203. https://doi.org/10.5194/acp-8-7193-2008

Hildebrandt, L., Kostenidou, E., Lanz, V. A., Prevot, A. S. H., Baltensperger, U., Mihalopoulos, N., et al. (2011). Sources and atmospheric processing of organic aerosol in the Mediterranean: Insights from aerosol mass spectrometer factor analysis. *Atmospheric Chemistry and Physics*, *11*(23), 12,499–12,1515. https://doi.org/10.5194/acp-11-12499-2011

Huang, S., Wu, Z., Poulain, L., van Pinxteren, M., Merkel, M., Assmann, D., et al. (2018). Source apportionment of the organic aerosol over the Atlantic Ocean from 53°N to 53°S: Significant contributions from marine emissions and long-range transport. *Atmospheric Chemistry and Physics*, *18*(24), 18,043–18,062. https://doi.org/10.5194/acp-18-18043-2018

Jimenez, J. L., Jayne, J. T., Shi, Q., Kolb, C. E., Worsnop, D. R., Yourshaw, I., et al. (2003). Ambient aerosol sampling using the aerodyne aerosol mass spectrometer. *Journal of Geophysical Research*, *108*(D7), 8425. https://doi.org/10.1029/2001JD001213

Ng, N. L., Canagaratna, M. R., Zhang, Q., Jimenez, J. L., Tian, J., Ulbrich, I. M., et al. (2010). Organic aerosol components observed in northern hemispheric datasets from aerosol mass spectrometry. *Atmospheric Chemistry and Physics*, *10*(10), 4625–4641. https://doi.org/10.5194/acp-10-4625-2010

Ovadnevaite, J., Zuend, A., Laaksonen, A., Sanchez, K. J., Roberts, G., Ceburnis, D., et al. (2017). Surface tension prevails over solute effect in organic-influenced cloud droplet activation. *Nature*, *546*(7660), 637–641. https://doi.org/10.1038/nature22806

Schmale, J., Schneider, J., Nemitz, E., Tang, Y. S., Dragosits, U., Blackall, T. D., et al. (2013). Sub-Antarctic marine aerosol: Dominant contributions from biogenic sources. *Atmospheric Chemistry and Physics*, *13*(17), 8669–8694. https://doi.org/10.5194/acp-13-8669-2013

Suda, S. R., Petters, M. D., Yeh, G. K., Strollo, C., Matsunaga, A., Faulhaber, A., et al. (2014). Influence of functional groups on organic aerosol cloud condensation nucleus activity. *Environmental Science & Technology*, *48*(17), 10,182–10,190. https://doi.org/10.1021/es502147y

Ulbrich, I. M., Canagaratna, M. R., Zhang, Q., Worsnop, D. R., & Jimenez, J. L. (2009). Interpretation of organic components from positive matrix factorization of aerosol mass spectrometric data. *Atmospheric Chemistry and Physics*, *9*(9), 2891–2918. https://doi.org/10.5194/acp-9-2891-2009